frontiers | Research Topics

North pacific climate and ecosystem predictability on seasonal to decadal timescales

Edited by
Shoshiro Minobe, Antonietta Capotondi, Fei Chai, Michael Jacox, Masami Nonaka and Ryan Rykaczewski

Published in
Frontiers in Marine Science

ISSN 1664-8714
ISBN 978-2-83250-570-0
DOI 10.3389/978-2-83250-570-0

About Frontiers

Frontiers is more than just an open access publisher of scholarly articles: it is a pioneering approach to the world of academia, radically improving the way scholarly research is managed. The grand vision of Frontiers is a world where all people have an equal opportunity to seek, share and generate knowledge. Frontiers provides immediate and permanent online open access to all its publications, but this alone is not enough to realize our grand goals.

Frontiers journal series

The Frontiers journal series is a multi-tier and interdisciplinary set of open-access, online journals, promising a paradigm shift from the current review, selection and dissemination processes in academic publishing. All Frontiers journals are driven by researchers for researchers; therefore, they constitute a service to the scholarly community. At the same time, the *Frontiers journal series* operates on a revolutionary invention, the tiered publishing system, initially addressing specific communities of scholars, and gradually climbing up to broader public understanding, thus serving the interests of the lay society, too.

Dedication to quality

Each Frontiers article is a landmark of the highest quality, thanks to genuinely collaborative interactions between authors and review editors, who include some of the world's best academicians. Research must be certified by peers before entering a stream of knowledge that may eventually reach the public - and shape society; therefore, Frontiers only applies the most rigorous and unbiased reviews. Frontiers revolutionizes research publishing by freely delivering the most outstanding research, evaluated with no bias from both the academic and social point of view. By applying the most advanced information technologies, Frontiers is catapulting scholarly publishing into a new generation.

What are Frontiers Research Topics?

Frontiers Research Topics are very popular trademarks of the *Frontiers journals series*: they are collections of at least ten articles, all centered on a particular subject. With their unique mix of varied contributions from Original Research to Review Articles, Frontiers Research Topics unify the most influential researchers, the latest key findings and historical advances in a hot research area.

Find out more on how to host your own Frontiers Research Topic or contribute to one as an author by contacting the Frontiers editorial office: frontiersin.org/about/contact

North pacific climate and ecosystem predictability on seasonal to decadal timescales

Topic editors

Shoshiro Minobe — Hokkaido University, Japan

Antonietta Capotondi — University of Colorado Boulder, United States

Fei Chai — Second Institute of Oceanography, Ministry of Natural Resources, China

Michael Jacox — Environmental Research Division, Southwest Fisheries Science Center (NOAA), United States

Masami Nonaka — Japan Agency for Marine-Earth Science and Technology (JAMSTEC), Japan

Ryan Rykaczewski — Pacific Islands Fisheries Science Center, National Oceanic and Atmospheric Administration, United States

Citation

Minobe, S., Capotondi, A., Chai, F., Jacox, M., Nonaka, M., Rykaczewski, R., eds. (2022). *North pacific climate and ecosystem predictability on seasonal to decadal timescales*. Lausanne: Frontiers Media SA. doi: 10.3389/978-2-83250-570-0

Table of contents

frontiers | Frontiers in Marine Science

TYPE Editorial
PUBLISHED 19 December 2022
DOI 10.3389/fmars.2022.1111272

OPEN ACCESS

EDITED AND REVIEWED BY
Yngvar Olsen,
Norwegian University of Science and Technology, Norway

*CORRESPONDENCE
Shoshiro Minobe
minobe@sci.hokudai.ac.jp

SPECIALTY SECTION
This article was submitted to Marine Fisheries, Aquaculture and Living Resources, a section of the journal Frontiers in Marine Science

RECEIVED 29 November 2022
ACCEPTED 06 December 2022
PUBLISHED 19 December 2022

CITATION
Minobe S, Capotondi A, Chai F, Jacox MG, Nonaka M and Rykaczewski RR (2022) Editorial: North Pacific climate and ecosystem predictability on seasonal to decadal timescales.
Front. Mar. Sci. 9:1111272.
doi: 10.3389/fmars.2022.1111272

Editorial: North Pacific climate and ecosystem predictability on seasonal to decadal timescales

Shoshiro Minobe[1]*, Antonietta Capotondi[2,3], Fei Chai[4,5], Michael G. Jacox[3,6,7], Masami Nonaka[8] and Ryan R. Rykaczewski[9,10]

[1]Faculty of Science, Hokkaido University, Sapporo, Japan, [2]Cooperative Institute for Research in Environmental Sciences, University of Colorado, Boulder, CO, United States, [3]Physical Sciences Laboratory, National Oceanic and Atmospheric Administration (NOAA), Boulder, CO, United States, [4]School of Marine Sciences, University of Maine, Orono, ME, United States, [5]Second Institute of Oceanography, Ministry of Natural Resources, Hangzhou, China, [6]Southwest Fisheries Science Center, National Oceanic and Atmospheric Administration (NOAA), Monterey, CA, United States, [7]Institute of Marine Sciences, University of California, Santa Cruz, Santa Cruz, CA, United States, [8]Application Laboratory, Japan Agency for Marine-Earth Science and Technology, Yokohama, Japan, [9]Pacific Islands Fisheries Science Center, National Oceanic and Atmospheric Administration (NOAA), Honolulu, HI, United States, [10]Department of Oceanography, School of Ocean and Earth Science and Technology, University of Hawaii, Honolulu, HI, United States

KEYWORDS

climate variability, marine ecosystems, fisheries, observational data analysis, numerical modeling, regional modeling

Editorial on the Research Topic

North Pacific climate and ecosystem predictability on seasonal to decadal timescales

The present Research Topic aims to collect studies on all aspects contributing to marine ecosystem predictability and prediction, including observational and numerical studies, with a focus on the North Pacific Ocean north of 30°N. The scope of this Research Topic includes studies of climate predictability and climate-marine ecosystem relationships as the basis of marine ecosystem predictability. This Research Topic is organized by the Working Group on "Climate and Ecosystem Predictability", a joint working group between the North Pacific Marine Science Organization (PICES) and Climate and Oceans, Variability, Predictability and Change (CLIVAR). PICES is an intergovernmental organization for marine science over the North Pacific, that includes the countries along the North Pacific rim, i.e., the United States of America, Japan, People's Republic of China, Canada, Republic of Korea, and the Russian Federation. CLIVAR is one of six global core projects of the World Climate Research Programme. These international science organizations and projects have played important roles in the ocean and climate sciences. This working group is the first joint working group between PICES and CLIVAR, demonstrating the increasing need for collaboration between

physical ocean/climate studies, the main area of CLIVAR, and marine biological studies, the major focus of PICES.

The Research Topic includes twelve original papers and one perspective paper. The perspective paper by Minobe et al. outlined several steps required for marine biology forecasts, typically involving global climate model prediction of the physical environment, regional downscaling of those physical conditions, and marine biological estimation based on the physical environment. The paper reviewed existing projects pursuing physical ocean/climate prediction at lead times ranging from subseasonal to multi-annual, pointed out existing bottlenecks for using physical predictions to make marine biological forecasts, and described lessons learned from physical predictions. The workflow suggested by Minobe et al. is based on the assumption that the physical environment influences marine ecosystems on the timescales of interest but not vice versa. It is interesting to note that one paper in the Research Topic studied causality in the other direction, i.e., biology influencing physical conditions; using numerical experiments Ma et al. reported that the presence of phytoplankton substantially increases the subduction rate of the subtropical mode water and the central mode water in the North Pacific.

Four papers studied oceanic variability using data analysis and numerical modeling. Miyama et al. reported frequent occurrences of marine heatwaves in the Northwestern Pacific near Japan between 2010 and 2016 in summer, associated with a weakened first intrusion of the Oyashio current and increased frequency of warm core eddies detached from the Kuroshio Extension (KE) to the north of the KE. Nonaka et al. studied the intrinsic and atmospheric-forced components of KE eddy activity using an ensemble of ocean general circulation model runs with 0.1-degree horizontal resolution. They found that the intrinsic variability is dominant in the upstream KE, and in the downstream KE on interannual timescales. The atmospheric forced component, on the other hand, is dominant on decadal timescales in the downstream KE, in association with Rossby waves propagating from the central North Pacific with four-year time lags, implying potential predictability. Doi et al. investigated the predictability of sea-surface height using a climate prediction system and found a high predictability region in the central North Pacific at about 2-year lead time. Song et al. reported that the seasonal prediction skill of sea-surface temperatures is substantially better when the Ensemble adjustment Kalman filter is used for their data assimilation rather than Projection Optimal Interpolation, especially in the central North Pacific. They also found that inclusion of a wave model improves prediction in the Kuroshio-Oyashio Extension region.

Two papers described how the large-scale physical ocean and climate influence marine biology. Ma et al. investigated how fishery catches from China, Chinese Taipei, Japan and Korea are influenced by large scale climate modes including the Pacific Decadal Oscillation (PDO), the North Pacific Gyre Oscillation (NPGO) and the El Niño-Southern Oscillation, and found fishery-climate relationships to be non-stationary. By analyzing 120 marine biological indicators from the western (29 time series) and eastern (91 time series) North Pacific, Yati et al. found that the first principal component of the biological indicators is characterized by a long-term trend with multi-decadal fluctuations with the largest negative impacts on groundfishes (Figure 1). They found that this mode is strongly related to global warming. It is worth noting that their first mode is consistent with previous studies that analyzed a large number of biological indicators, but earlier studies did not investigate the impact of global warming (see references in Yati et al.).

Three papers investigate how regional physical conditions influence marine biology and how well marine biological conditions can be estimated using physical conditions. Gomez et al. found that the presence of swordfish is strongly related to warm core eddies around the Kuroshio Extension. Kuriyama et al. studied the spatial shared dynamics of temperature, salinity and ichthyoplankton abundance in the California Cooperative Oceanic Fisheries Investigations (CalCOFI) data, using an Empirical Dynamic Method known as "co-prediction". Their findings help identify the spatial structure of the physical and biological dynamics of the California Current System. Muhling et al. examined the performance of statistical models, including machine learning models, for fish habitat estimation in the California Current System. They found that models trained over periods without substantial marine heatwaves can be unreliable for the estimation of fish species and ages during marine heatwave conditions.

The other two papers investigated marine ecosystem forecasts with seasonal or multi-annual prediction lead times. Malick et al. examined the forecast skill of Pacific hake distributions, combining a statistical model for hake with regionally downscaled ocean forecasts provided by JISAO's Seasonal Coastal Oceanic Prediction of the Ecosystem (J-SCOPE). Navarra et al. used a physical-biological linear inverse model (LIM) for the prediction of fishery indicators (estimated biomasses, landings, and catches) in the Northwest Pacific, and found that the LIM outperforms persistence for up to 5-6 years. The influence of the physics on the biological indicators was found to play an important role in the forecast skill, with Rossby wave propagation from the central to western North Pacific potentially being responsible for the skill at multi-annual lead times.

The papers collected in this Research Topic clearly indicate the influence of physical ocean/climate conditions on marine ecosystems, as well as the importance and potential of prediction studies spanning from physics to biology. Some of the papers in this Research Topic have already had outstanding influence on the research community. At the time of writing, Muhling et al. have been cited by other publications 21 times and Miyama et al. 17 times. The study of Miyama et al. was also used as a

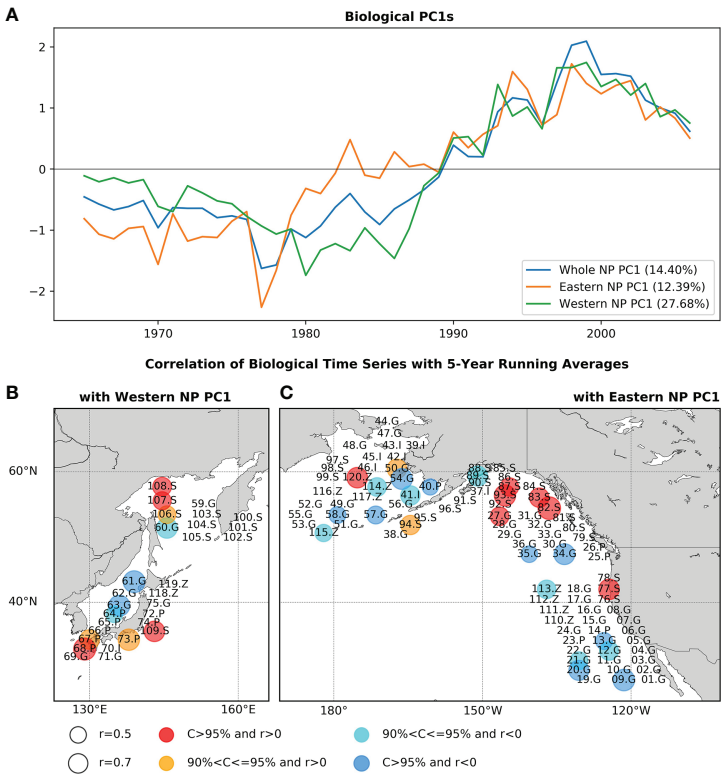

FIGURE 1
(A) The first Principal Components (PC1s) for the whole North Pacific (NP), eastern NP and western NP marine biological time series, and statistically significant correlations of marine biological time series **(B)** with the western NP PC1, **(C)** with the eastern NP PC1. Before calculating correlations 5-year running means are applied to PC1s and marine biological time series. In **(B, C)**, numbers indicate species ID in Table 1 of Yati et al., while S, G, P, Z and I indicate salmon, groundfish, small-pelagic, zooplankton and invertebrate, respectively. Circle size indicates the absolute values of correlations and colors of the circles (red, orange, cyan, blue) indicate the sign of correlations and the corresponding confidence levels. (After Yati et al.).

motivation for the new PICES working group on "Climate Extremes and Coastal Impacts in the Pacific". Yati et al. have been cited by the Sixth Assessment Report of the Intergovernmental Panel on Climate Change, Working Group II, in two chapters (Cooley et al., 2022; Shaw et al., 2022).

In the future, the importance and necessity of marine biological forecasting, especially those relating biological responses to physical variability, will further increase. Since marine biological forecasting can be conducted for many species, regions and timescales, a vast number of new studies is required. The topic editors hope that the present Research Topic illustrates the potential in this exciting and emerging research field.

Author contributions

All authors listed have made a substantial, direct, and intellectual contribution to the work and approved it for publication.

Funding

SM was supported by JSPS KAKENHI Grant Numbers JP18H04129, JP19H05704 and MN was supported by JP19H05701. RR was supported by NOAA Pacific Islands Fisheries Science Center, and AC was supported by the NOAA Climate Program Office Modeling, Analysis, Predictions and Projections (MAPP) program.

Acknowledgments

We thank PICES and CLIVAR for their support of the joint Working Group "Climate and Ecosystem Predictability", which organized this Research Topic.

Conflict of interest

The authors declare that the research was conducted in the absence of any commercial or financial relationships that could be construed as a potential conflict of interest.

Publisher's note

References

Cooley, S., Schoeman, D., Bopp, L., Boyd, P., Donner, S., Ghebrehiwet, D. Y., et al. (2022). "Oceans and coastal ecosystems and their services," in *Climate change 2022: Impacts, adaptation and vulnerability. contribution of working group II to the sixth assessment report of the intergovernmental panel on climate change*. Eds. H.-O. Pörtner, D. C. Roberts, M. Tignor, E. S. Poloczanska, K. Mintenbeck, A. Alegría and M. Craig (Cambridge, UK and New York, NY, USA: Cambridge University Press), 379–550. doi: 10.1017/9781009325844.005

Shaw, R., Luo, Y., Cheong, T. S., Abdul Halim, S., Chaturvedi, S., Hashizume, M., et al. (2022). "Asia," in *Climate change 2022: Impacts, adaptation and vulnerability. contribution of working group II to the sixth assessment report of the intergovernmental panel on climate change*. Eds. H.-O. Pörtner, D. C. Roberts, M. Tignor, E. S. Poloczanska, K. Mintenbeck, A. Alegría and M. Craig (Cambridge, UK and New York, NY, USA: Cambridge University Press), 1457–1579. doi: 10.1017/9781009325844.012

frontiers in Marine Science

ORIGINAL RESEARCH
published: 24 July 2020
doi: 10.3389/fmars.2020.00504

Evaluation of FIO-ESM v1.0 Seasonal Prediction Skills Over the North Pacific

*Yajuan Song[1,2], Yiding Zhao[3], Xunqiang Yin[1,2,4], Ying Bao[1,2,4] and Fangli Qiao[1,2,4]**

[1] First Institute of Oceanography, Ministry of Natural Resources, Qingdao, China, [2] Key Laboratory of Marine Science and Numerical Modeling, Ministry of Natural Resources, Qingdao, China, [3] North China Sea Marine Forecast Center, Ministry of Natural Resources, Qingdao, China, [4] Laboratory for Regional Oceanography and Numerical Modeling, Qingdao National Pilot National Laboratory for Marine Science and Technology, Qingdao, China

Accurate prediction over the North Pacific, especially for the key parameter of sea surface temperature (SST), remains a challenge for short-term climate prediction. In this study, seasonal predicted skills of the First Institute of Oceanography Earth System Model version 1.0 (FIO-ESM v1.0) over the North Pacific were assessed. Ensemble adjustment Kalman filter (EAKF) and Projection Optimal Interpolation (Projection-OI) data assimilation schemes were used to provide initial conditions for FIO-ESM v1.0 hindcasts that were started from the first day of each month between 1993 and 2017. Evolution and spacial distribution of SST anomalies over the North Pacific were reasonably reproduced in EAKF and Projection-OI assimilation output. Two hindcast experiments show that the skill of FIO-ESM v1.0 with the EAKF data assimilation scheme to predict SST over the North Pacific is considerably higher than that with Projection-OI data assimilation for all lead times of 1–6 months, especially in the central North Pacific where the subsurface ocean temperature in the initial conditions is significantly improved by EAKF data assimilation. For the Kuroshio–Oyashio extension (KOE) region, the errors in the initial conditions have more rapid propagation resulting in large discrepancies between simulated and observed values, which are reduced by inducing surface waves into the climate model. Incorporation of realistic initial conditions and reasonable physical processes into the coupled model is essential to improving seasonal prediction skill. These results provide a solid basis for the development of operational seasonal prediction systems for the North Pacific.

Keywords: seasonal prediction skill, FIO-ESM, North Pacific, ensemble adjustment kalman filter, assimilation scheme, sea surface temperature

OPEN ACCESS

Edited by:
Shoshiro Minobe,
Hokkaido University, Japan

Reviewed by:
Adam Thomas Devlin,
The Chinese University of Hong Kong, China
Jieshun Zhu,
University of Maryland, United States

***Correspondence:**
Fangli Qiao
qiaofl@fio.org.cn

Specialty section:
This article was submitted to Physical Oceanography, a section of the journal Frontiers in Marine Science

Received: *31 March 2020*
Accepted: *03 June 2020*
Published: *24 July 2020*

Citation:
Song Y, Zhao Y, Yin X, Bao Y and Qiao F (2020) Evaluation of FIO-ESM v1.0 Seasonal Prediction Skills Over the North Pacific. Front. Mar. Sci. 7:504. doi: 10.3389/fmars.2020.00504

INTRODUCTION

The seasonal prediction skill of short-term climate prediction systems has received increasing attention from the scientific community in recent decades (Kug et al., 2008; Kim et al., 2012; Wen et al., 2012). In the North Pacific, sea surface temperature (SST) is an essential parameter of the climate system, and its considerable variability has broad impacts on the weather, climate processes, and ocean environment both locally or around adjacent continents, such as North America and East Asia (Lau et al., 2004). Accurate prediction of SST based on the advanced seasonal prediction

systems will provide useful information for disaster prevention and damage reduction, as well as marine resource management. Improved skill to predict oceanographic conditions in the North Pacific is highly desirable.

Accurate prediction of SST anomalies (SSTAs) over the North Pacific remains a challenge for the seasonal prediction systems (Wen et al., 2012; Duan and Wu, 2014; Hu et al., 2014). Current state-of-the-art coupled general circulation models are unable to accurately simulate climatology and variations of SST in the North Pacific (Wang et al., 2014). Variability of SSTAs over the North Pacific, especially at mid and high latitudes, is mainly influenced by local air–sea interactions, Pacific Decadal Oscillation (PDO), and the El Niño–Southern Oscillation (ENSO, Liu and Alexander, 2007; Hu et al., 2014; Bayr et al., 2019). Associated with atmospheric teleconnection, ENSO is the primary source of global climate predictability at seasonal and interannual time scales (Kumar et al., 2014). Since the coupled ocean–atmosphere system was used for ENSO predictions (Cane et al., 1986), the seasonal prediction skill of ENSO has considerably improved, and SST over the equatorial Pacific can be successfully predicted two seasons in advance (Barnston et al., 1999, 2015; Luo et al., 2005; Song et al., 2015; Kim et al., 2017; Liu and Ren, 2017). However, the skill to predict SSTAs at the mid and high latitudes of the North Pacific is lower than that for the tropical eastern Pacific. The robust spring predictability barrier has limited seasonal prediction of ENSO for a long time (Zheng and Zhu, 2010). In the western central North Pacific, initial error growth also exhibits a distinctive seasonal dependence. The prediction skill is lowest in summer, giving rise to the summer predictability barrier (Zhao et al., 2012; Duan and Wu, 2014; Wu et al., 2016). Previous researches suggested that a shallow mixed-layer depth in the North Pacific accompanied by strong oceanic stratification in summer could result in a relatively weak correlation between SSTAs in the summer and temperature in the following winter (Alexander, 1999; Jacox et al., 2019), which could lead to poor prediction of SSTAs. With the exception of the Kuroshio–Oyashio Extension (KOE) region, SSTAs over most of the North Pacific can be predicted with reasonable skill with a lead time of two seasons (Wen et al., 2012). Hence, the ability of a model to predict SST over the KOE region is critical for the model's skill in short-term climate prediction over the North Pacific.

Seasonal prediction skill is controlled by physical processes in the dynamical model as well as the initial conditions (Rosati et al., 1997; Zhu et al., 2012, 2017a; Kim et al., 2017). Studies have found that low resolution and omission of critical physical processes in models can lead to systematic biases, which limit the seasonal prediction skill (Wen et al., 2012; Suranjana et al., 2014; Zhu et al., 2017a). With ensemble initialization, increased resolution, and comprehensive physics, seasonal prediction skill of coupled dynamical models can be considerable improved (Zhu et al., 2013). For example, Zhao et al. (2019a) show that incorporation of surface wave processes can effectively improve the simulation and prediction skills of SST in the North Pacific. In addition, small perturbations in initial conditions can lead to very different final results (Lorenz, 1969); therefore, more accurate initial conditions based on high-quality observation and data assimilation schemes are important for improving seasonal predictions (Alessandri et al., 2010; Zhu et al., 2012).

In recent decades, availability of ocean observation data and dramatically increased computer resources promotes the development and application of different data assimilation technologies, which combine the numerical model with observational data optimally to provide more accurate initial conditions for short-term climate prediction systems (Ratheesh et al., 2012). Several assimilation schemes, including optimal interpolation, three- or four-dimensional variational assimilation, and Kalman filtering have been widely used in weather and climate predictions (Eddy, 1964; Jones, 1965; Ezer and Mellor, 1997; Anderson, 2001; Yin et al., 2010). The Optimal Interpolation (OI) scheme requires few computing resources and is relatively simple and easy to implement. Yin et al. (2010) developed the improved Projection-OI scheme by projecting observed data obtained at the ocean surface onto layers below. The ensemble adjustment Kalman filter (EAKF) can make a joint adjustment on related variables; for example, the upper-ocean temperature, salinity, and velocity are in accordance with each other during the prediction (Anderson, 2001; Bishop et al., 2001; Chen et al., 2015). In addition, the ensemble method in EAKF effectively eliminates uncertainties caused by initial errors. Examining the impact of initial conditions, obtained from different data assimilation schemes, can benefit the development of prediction systems and improve seasonal prediction skills over North Pacific.

In this study, we evaluate the skill of FIO-ESM v1.0 in seasonal prediction of SST in North Pacific. The hindcast was initialized by EAKF and the Projection-OI data assimilation scheme. In addition, the effect of surface waves on the prediction skill is discussed. The remainder of the paper is organized as follows: climate model, assimilation schemes, hindcast experiments, and observed data used for validation are described in section "Model and Data Assimilation Schemes"; the assimilation results from two schemes are compared in section "Comparison of Assimilation Outputs"; in section "Evaluation of Prediction Skill", we investigate the seasonal dependence of prediction skill over the North Pacific, and we close with discussions and conclusions in section "Discussion".

MODEL AND DATA ASSIMILATION SCHEMES

Introduction of FIO-ESM v1.0

Hindcasts were conducted using FIO-ESM v1.0, which has been developed by the First Institute of Oceanography, Ministry of Natural Resources of China. There are five components in FIO-ESM v1.0. These include the Community Atmosphere Model Version 3.0 (CAM3.0) with a horizontal resolution of T42 (about 2.875° in latitude and longitude) and 26 vertical layers, the Community Land Model Version 3.5 (CLM3.5), the Los Alamos Sea Ice Model Version 4.0 (CICE4), the Parallel Ocean Program Version 2.0 (POP2.0), which is an ocean circulation component, and the wave model developed by the Key Laboratory of Marine Science and Numerical Modeling (MASNUM), Ministry

of Natural Resources of China. The horizontal resolution of POP2.0 and CICE4 is 0.3–1.1°, and there are 40 vertical layers in the ocean model. More details about FIO-ESM v1.0 can be found in Qiao et al. (2013).

FIO-ESM v1.0 is a fully coupled ocean–atmosphere general circulation model that considers ocean surface wave effects based on the theory of non-breaking surface wave-induced mixing (Qiao et al., 2004, 2010). A set of coordinated experiments, including historical and future scenarios simulations without flux correction, has been conducted and included in the Coupled Model Intercomparison Project phase 5 (CMIP5). The model can capture major features of the observed climatology in the historical period (Qiao et al., 2013), specially, it can reproduce SST distribution and evolution in historical experiments. By incorporating surface wave effects, the FIO-ESM v1.0 hindcasts are skillful in predicting SST over most of the North Pacific with lead times of 1–6 months (Zhao et al., 2019b). The reliable SST representation at mid-latitudes leads to improved simulated precipitation through the air–sea interaction (Chen et al., 2015). More details about model performance can be found in Zhao et al. (2019a).

Data Assimilation Schemes and Observation Data

The initial condition of the ocean state plays a crucial role in seasonal prediction. Outputs from two data assimilation methods, EAKF and Projection-OI, were used to initialize FIO-ESM v1.0.

Data assimilation using the EAKF includes ten ensembles spreading within a suitable scope. Ensembles were produced using the three-dimensional ocean temperature perturbation method with the magnitude of 10^{-3}°C.

$$T_{i,j,k}^{pert} = \left(1 + \alpha \cdot \beta_{i,j,k}\right) \cdot T_{i,j,k} \tag{1}$$

where the coefficient α is equal to 10^{-3}, $\beta_{i,j,k}$ is a random number between -1 and 1 varying at each grid, and $T_{i,j,k}^{pert}$ is the ocean temperature after perturbation. The perturbation simulation was conducted for 2 years before assimilation. During the perturbation simulation, the tiny perturbation grows, gradually stabilizes, and is used as the initialized condition for EAKF assimilation experiments (Chen et al., 2015). The EAKF avoids the perturbed observations in the traditional ensemble Kalman filter (Evensen, 1994); instead, background error covariance in the EAKF is calculated using ensemble samples. Spatial and temporal evolutions of covariance are determined by the dynamical processes of the model. Multiple variables are jointly adjusted in the EAKF, maintaining consistency of the dynamic relationships between elements before and after adjustment, thus ensuring rationality of the initial conditions. In addition, the method of the ensemble mean can effectively eliminate uncertainties caused by initial biases.

Projection-OI uses vertical projections to project observations at the ocean surface onto the three-dimensional model space (Yin et al., 2010). Differences between surface observations and model estimates were first calculated. Weight β_{SST} representing the covariant relations between the surface and the lower layer were then used to adjust the three-dimensional model state. Temperature variation in each layer is ΔT, $\beta_{SST} \cdot \Delta SST$ is the corresponding variation obtained through vertical projection, and Z is the difference between the two terms:

$$Z = \Delta T - \beta_{SST} \cdot \Delta SST \tag{2}$$

To minimize discrepancies, β_{SST} was determined using the least-square method by maintaining the gradient of Z at zero.

$$\beta_{SST} = \frac{cov(\Delta T, \Delta SST)}{\sigma^2_{\Delta SST}} \tag{3}$$

The time series of ΔT and ΔSST were constructed from anomalies. The Projection-OI assimilation experiment was conducted using a single member.

Two data assimilation experiments using the EAKF and the Projection-OI schemes were conducted for January 1993–December 2017 directly based on the fully coupled model FIO-ESM v1.0. Seasonal hindcasts under two initial conditions were started on the first day of each month. The same aerosol radiative forcing and greenhouse gas concentrations prescribed to the observation data in the historical experiments of CMIP5 were used. Influences of initial conditions on the skill of the model to predict seasonal SST in North Pacific were quantified by the same validation metrics.

A daily-averaged advanced very high resolution radiometer (AVHRR) SST from the National Oceanic and Atmospheric Administration (NOAA)/National Climate Data Center (NCDC) with horizontal resolution of 0.25° and sea level anomaly (SLA) from the Archiving, Validation and Interpretation of Satellite Data (AVISO) with horizontal resolution of 0.25° were assimilated in two hindcast experiments (Ducet et al., 2000; Reynolds et al., 2007). Observation data have higher horizontal resolution than the model and contain the signals of mesoscale processes. To ensure alignment with model resolution, spacial running averages of the observation data over 1.5° grid were used.

Monthly observed SST from NOAA Optimum Interpolation (OI) SST v2 for the period of 1993–2017 was used as the validation dataset (Banzon et al., 2016). Monthly subsurface ocean temperatures were obtained from version 4 of the Met Office Hadley Centre EN series of data sets (EN4), which is a global quality-controlled ocean temperature objective analysis. The horizontal resolution of EN4 is 1°, and there are 42 vertical layers (Good et al., 2013). Observation data were linearly interpolated to match the model grid.

SST is one of the key indicators to represent climate variabilities. In this study, we examined the skill of FIO-ESM v1.0 to predict SSTAs relative to monthly climatology averaged for 1993–2017 with different lead times. Several criteria are used to evaluate model performance. Specifically, the anomaly correlation coefficient (ACC), which is widely used to measure the relationship between predicted and observed anomalies, was used to quantify the prediction skill. Three-month running averages were applied before correlation analysis.

COMPARISON OF ASSIMILATION OUTPUTS

Climatology and evolution of SST from the assimilation output were compared with those from the validation dataset to examine whether the assimilation output can be used reliably to initialize prediction. Area-averaged time series of SSTAs over the North Pacific (20°–70°N, 110°E–100°W) are shown in **Figure 1**. Seasonal, interannual, and inter-decadal variabilities of SSTAs in EAKF and Projection-OI assimilation outputs are highly consistent with those of OISST v2 SSTAs. The correlation coefficient between OISST v2 and EAKF SSTAs (0.935) is higher than that between OISST v2 and Projection-OI (0.905), indicating that the ability to reproduce observed SSTAs is higher in EAKF than in Projection-OI. **Figure 2** shows the spacial distribution of ACC between OISST v2 and SST from two data assimilation experiments. High ACC scores indicate that the model with the data assimilation scheme has high ability in reproducing SST. For EAKF runs, the ACC reaches 0.9 over most of the North Pacific and is higher in the east than in the west. The same observation data are assimilated using Projection-OI scheme, but the ACC in the Projection-OI run is apparently lower than that in EAKF. For Projection-OI, ACC reaches 0.9 only distributing in the eastern North Pacific, off the coast of California. In general, SSTAs were reasonably reproduced with ACC exceeding 0.7 over most of the North Pacific, except for the western boundary region and the mid-latitudes of the central North Pacific where ACC is relatively lower. The FIO-ESM v1.0 with EAKF assimilation produces initial conditions for prediction that have higher accuracy than those produced by FIO-ESM v1.0 with Projection-OI assimilation.

Surface observation data, including SST and SLA, were assimilated into FIO-ESM v1.0 using EAKF and Projection-OI assimilation schemes. The ocean subsurface layer is considerably changed under the data assimilation. Here, the difference between EAKF and observed temperatures was calculated to estimate the error of the EAKF scheme; similarly, the difference between Projection-OI and observed temperatures was calculated to estimate the error of the Projection-OI scheme:

$$Temperature\ changes = |T_{EAKF} - T_{OBS}| - |T_{Projections-OI} - T_{OBS}| \quad (4)$$

where temperature changes refer to the difference between the absolute values of the errors of the two schemes; negative temperature changes indicate that the absolute difference between EAKF and observed temperatures is smaller than that between Projection-OI and observed temperatures. **Figure 3** shows temperature changes along 45°N in the North Pacific.

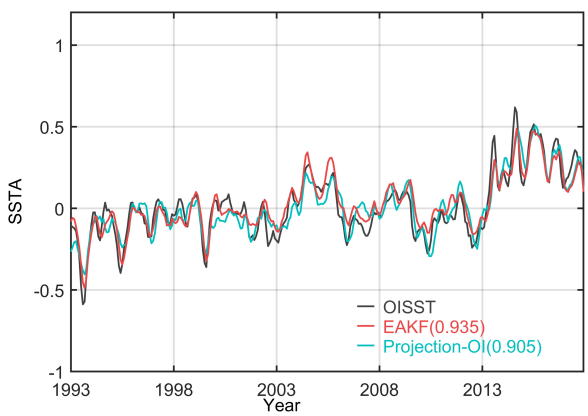

FIGURE 1 | Time series of area-averaged SSTAs (units: °C) over the North Pacific (20–70°N, 110°E–100°W) with respect to climatology for 1993–2017. Three-month-running smoothing is applied. The black line represents SSTAs from OISST v2 observation; red and blue lines represent EAKF and Projection-OI assimilation results, respectively. The values in brackets are correlation coefficients between assimilation results and observation.

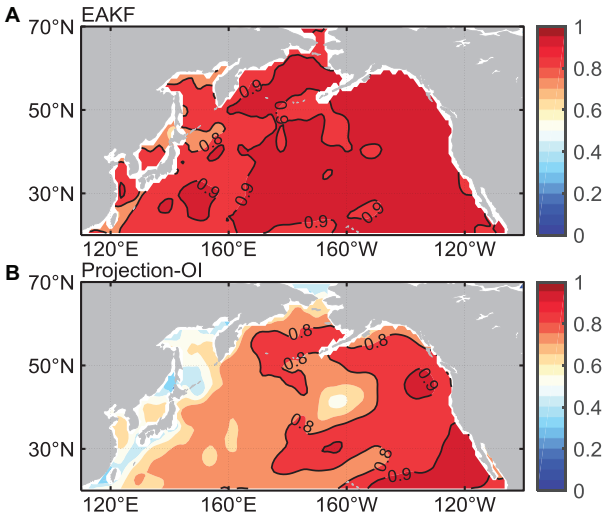

FIGURE 2 | The anomaly correlation coefficient (ACC) of sea surface temperature (SST) between OISST v2 and assimilation results for 1993–2017. **(A)** EAKF; **(B)** Projection-OI. ACC is significantly greater than zero at the 95% confidence level. Only the 0.8 and 0.9 contours are plotted.

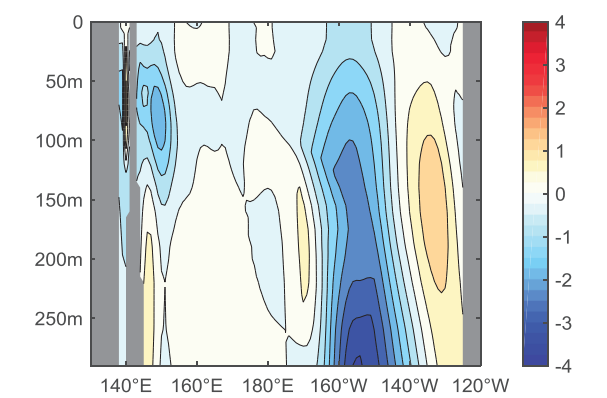

FIGURE 3 | The ocean temperature changes along 45°N in the North Pacific as the EAKF scheme compared with the Projection-OI assimilation scheme. This change was calculated according to Eq. (4) for 1993–2017 (units: °C). The negative value indicates improvement with EAKF data assimilation.

Negative temperature changes centered around 170–140°W from the surface to a depth of 300 m, and along the western coast at a depth of 100 m, indicating that EAKF is superior to Projection-OI in assimilating observed ocean temperatures for these locations. The EAKF and Projection-OI schemes use different projection methods to assimilate and project observed SST and SLA onto the subsurface vertical profile. The EAKF scheme uses the covariant relationship among different ensemble members, adjusting the temperature profile while also adjusting the current velocity coordinately, resulting in improved temperature simulation below the sea surface, which are superior to those obtained with the Projection-OI scheme. Distributions of subsurface negative temperature changes (centered around 170–140°W and 140–150°E in **Figure 3**) are consistent with that of high ACC skill (located in the central and western North Pacific as shown in **Figure 2**), indicating that the subsurface ocean temperature changes are directly associated with data assimilation techniques. Besides, this improvement is possible to be amplified via air–sea interaction in the coupled system. The improved SST, in turn, may derive inferior winds that contribute to better estimates of subsurface thermal conditions (Luo et al., 2005; Zhu et al., 2017a).

EVALUATION OF PREDICTION SKILL

Initialization of hindcasts with EAKF and Projection-OI data assimilation were conducted for 1993–2017. **Figure 4** shows ACC of SST with lead times of 2, 4, and 6 months between OISST v2 dataset and hindcast results. We explore the impact of two different data assimilation schemes on the seasonal prediction skill for SST in the North Pacific. For lead times of 2, 4, and 6 months, the skill of FIO-ESM v1.0 to hindcast seasonal SST in the North Pacific is higher with EAKF data assimilation and lower with Projection-OI data assimilation. ACC at a 2-month lead time exceeds 0.5 over most of the North Pacific and is higher than 0.9 in the eastern Pacific. The prediction based on Projection-OI assimilation shows lower prediction skills with the ACC below 0.5 in most parts of North Pacific. As the lead time of prediction increases from 2 to 6 months, values of AAC gradually decreased. For lead times of 2, 4, and 6 months, the spacial distribution of ACCs indicates low skill in SST prediction over the KOE region where the active mesoscale processed combined with strong air-sea interactions is present. The remarkable predicted bias over the KOE region is consistent with results from previous research (Wen et al., 2012) and is a common problem in seasonal prediction over the North Pacific.

To show the prediction skill initialized by two data assimilation methods more clearly, we examine the differences between ACC from EAKF and that from Projection-OI were calculated for each lead month. **Figure 5** shows a clear difference over the Western central Pacific, particularly in the Okhotsk Sea, Japan Sea, and China Seas in the first lead month. Starting from a 2-month lead, large positive values are found in the Bering Sea and the Gulf of Alaska of the eastern North Pacific and extend along the northeast–southwest banded area in central Pacific. This positive value indicating improvement with EAKF method varies with increasing lead months and remaining in place for lead times of 5 and 6 months. Due to the coordinated adjustment at the surface and the entire water column in vertical in EAKF, SST hindcasts with EAKF data assimilation are superior to those with Projection-OI data assimilation. The difference between the two ACCs does not decrease with increasing lead time. Prediction skill strongly depends on initial conditions, and the dependence can last for lead times of up to two seasons.

The times series of area-averaged (30–50°N, 150°E–150°W) SSTAs differences between hindcast and OISST v2 for 1993–2017 for different lead times is shown in **Figure 6**. Biases of SSTAs from EAKF and from Projection-OI are similar, characterized by strong interannual variation. When the bias from the EAKF experiment is positive, there is also a positive bias in the Projection-OI prediction, and vice versa, indicating that the direction of prediction SST shifts is probably related to the model, regardless of which data assimilation method is used. However, the prediction bias initialized with Projection-OI is considerable larger than those from EAKF. The EAKF scheme performs better in restraining the shifts of model due to coordinated adjustment. Generally, the prediction bias for a lead time of 6 months is larger than biases for lead times of 2 or 4 months, either for EAKF or Projection-OI experiments.

Seasonal dependence of prediction skill over the North Pacific was further investigated, and variation of ACC with horizontal axis of hindcast length and the vertical axis indicating the forecast starting month is shown in **Figure 7**. Hindcasts with EAKF data assimilation and that start from May are consistently high in skill, while the prediction skill is lower for hindcasts that start from November. The skill of Projection-OI hindcast is relatively low, but their ACC has the same characteristics of seasonal dependence as ACC of hindcasts with EAKF data assimilation. For both data assimilation schemes, hindcasts started from summer are lower in skill, which is consistent with the summer predictability barrier that is often encountered in short-term predictions. The differences show that the prediction skill is improved for all lead times by EAKF, especially for hindcasts that start in spring and autumn. The significant change with the differences exceeding 0.3 exists for lead times of 2–4 months. The FIO-ESM v1.0 with EAKF data assimilation tends to represent atmospheric and oceanic conditions relatively well and shows high skill of SST prediction over North Pacific.

To explore the factors underlying the superior performance of hindcasts with EAKF data assimilation, temperature changes (as defined in Eq. 4) in the subsurface layer in the initial condition and difference of prediction skills between EAKF and Projection-OI hindcasts averaged for 1–6 lead months are illustrated in **Figure 8**. The significant improvement of prediction skill distributes in the banded area from 160°E to 160°W and in the high latitudes. Realistic initial conditions improve a model's ability to capture climate variability and can improve the model's skill to predict ENSO with a lead time of up to two seasons (Song et al., 2015). Signals from the tropics can have profound impacts on subtropical regions. Previous studies suggest that SSTA evolution in the North Pacific is strongly influenced by ENSO because of atmospheric teleconnections (Kim et al., 2015; Zhu et al., 2017a). The well-predicted ENSO can also improve

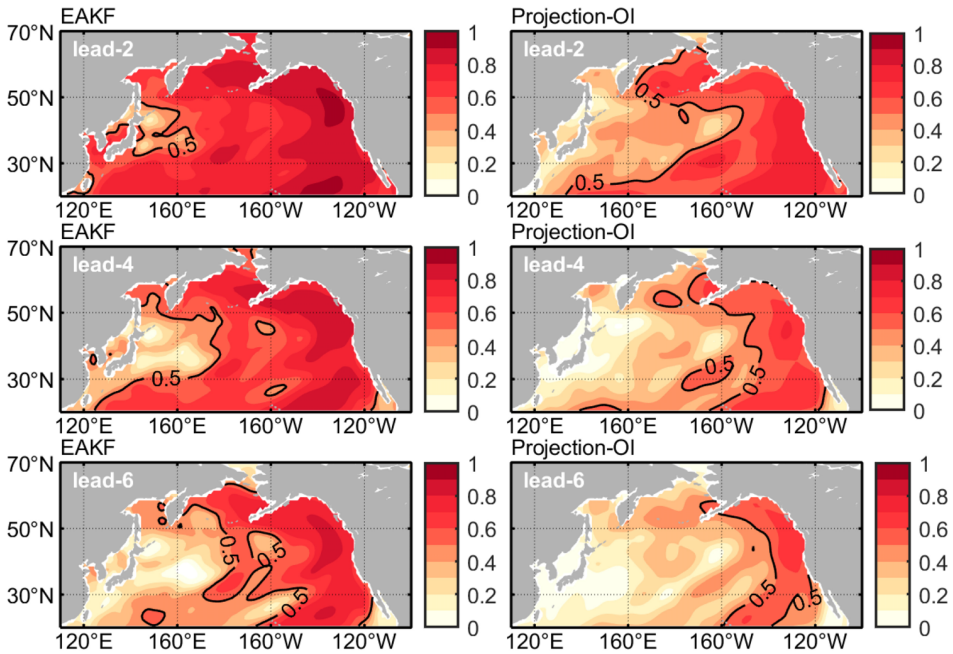

FIGURE 4 | Distributions of ACC between IOSST v2 and hindcasts using the EAKF and Projection-OI data assimilation methods for the 2-, 4-, 6-months lead in the North Pacific. Only the line of the 0.5 contour is plotted.

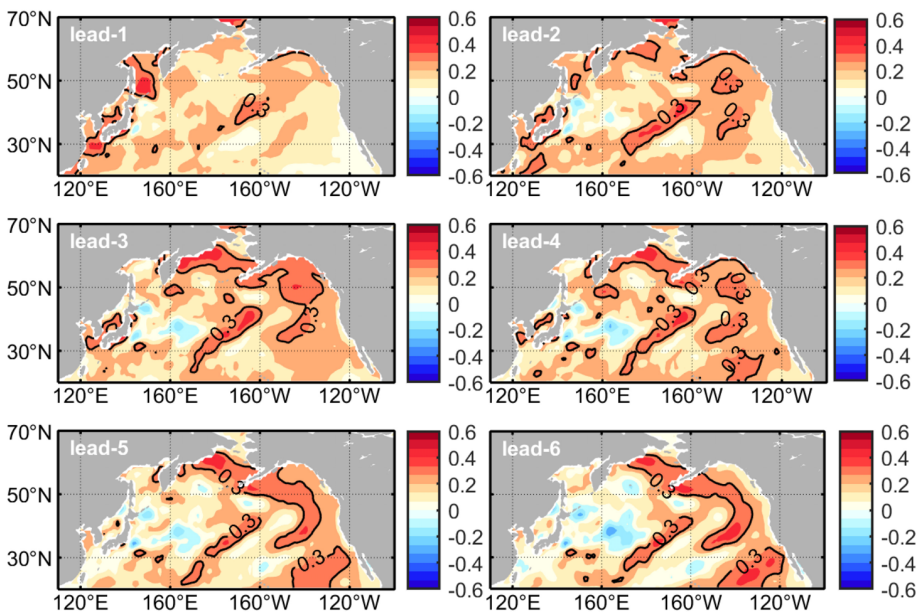

FIGURE 5 | The differences of ACC between the EAKF and Projection-OI hindcasts in each lead month averaged for 1993–2017. Only the line of 0.3 contour is plotted.

skill to predict SSTA over the mid and high latitudes. In addition, we found that significant improvement of ocean temperature in the subsurface layer of the initial condition up to 3°C is shown to be located over the central North Pacific between 160°E and 160°W, which is generally in accordance with the region where the prediction skill is much improved. It reveals that the accurate subsurface structure in the initial condition could improve seasonal prediction skill in this region. However, more accurate ocean temperatures in the initial conditions are insufficient to remove all prediction errors, for example over the KOE region, characterized by active air–sea interactions and mesoscale processes.

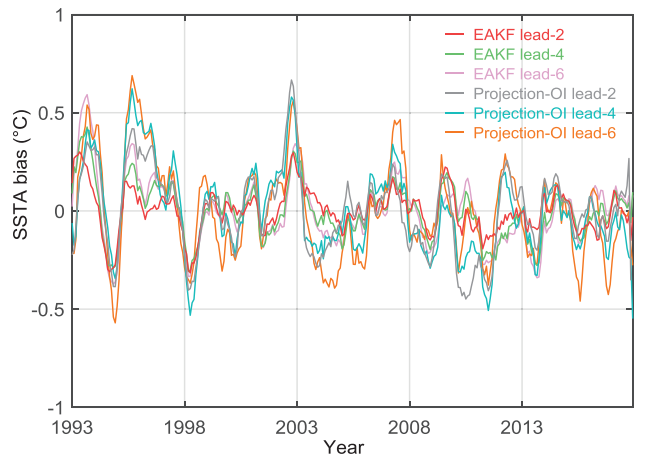

FIGURE 6 | Time series of area-averaged SSTAs prediction biases over the North Pacific (30–50°N, 150°E–150°W; units: °C) with respect to OISST v2 for 1993–2017. The lines in different colors represent SSTA biases at the 2-, 4-, and 6-lead months in EAKF and Projection-OI predictions, respectively.

DISCUSSION

In this paper, the impacts of initial conditions on the skill of FIO-ESM v1.0 to predict seasonal SST over the North Pacific were assessed. Several assimilation and hindcast experiments for 1993–2017 were conducted using FIO-ESM v1.0 and the EAKF and Projection-OI data assimilation scheme. Evaluation of data assimilation output shows that simulated SST in the North Pacific from the EAKF scheme has a higher accuracy than that from Projection-OI runs. Seasonal SST variability in assimilation outputs is consistent with those in observations, with ACC exceeding 0.7 over most of the North Pacific. Both EAKF and Projection-OI assimilate the same surface observation data, however, the model with EAKF data assimilation has higher accuracy than that with Projection-OI in simulating subsurface ocean temperature.

Oceanic initial conditions play an important role in improving seasonal prediction skill. We analyzed hindcasts initialized by EAKF and Projection-OI data assimilation for the lead times of 1–6 months for 1993–2017. Prediction skill, as represented by ACC, is higher in hindcasts with EAKF than those with Projection-OI. ACC exceeding 0.5 is found over almost the entire North Pacific at a 2-month lead time and even over the eastern North Pacific at the 6-month leading time with EAKF initialization. Specifically, significant improvement of ACC distributes over the central North Pacific, as well as from the Bering Sea to the eastern North Pacific. Seasonal dependence of prediction skill was further assessed, and we found that, like other prediction systems, FIO-ESM v1.0 also encounters the North Pacific summer predictability barrier. EAKF can mitigate the prediction bias in contrast to Projection-OI for all lead times of 1–6 months, especially for the prediction starting from spring and autumn.

The prediction skill of FIO-ESM v1.0 over the KOE region is relatively low, because the complex dynamic environment with strong air–sea interaction in this region, which is difficult to parameterize correctly in climate models. Previous research suggested that the SST evolution and climate variability in extratropical Pacific are influenced by ENSO through atmospheric teleconnection and other associated dynamic processes (Hu et al., 2014). The skill to predict SSTAs in the central Pacific increases under ENSO remote forcing during the cold phase (Zhu et al., 2017a). If the model fails to simulate the teleconnection pattern, it may limit the prediction skill over the North Pacific (Kim et al., 2015). Realistic oceanic

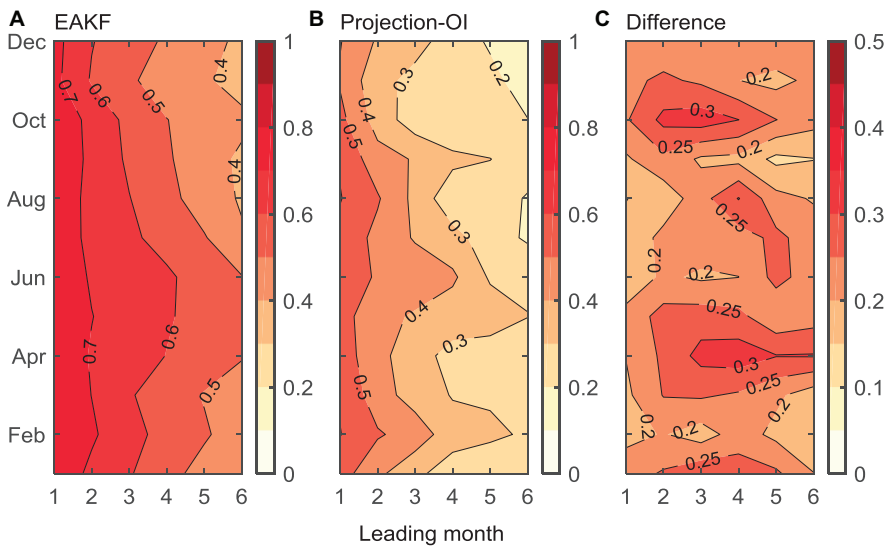

FIGURE 7 | Evolution of area-averaged ACC over the North Pacific (20–70°N, 110°E–100°W); the horizontal axis represents the length of hindcasts, and the vertical axis indicates the starting month. **(A)** EAKF; **(B)** Projection-OI; and **(C)** EAKF–Projection-OI.

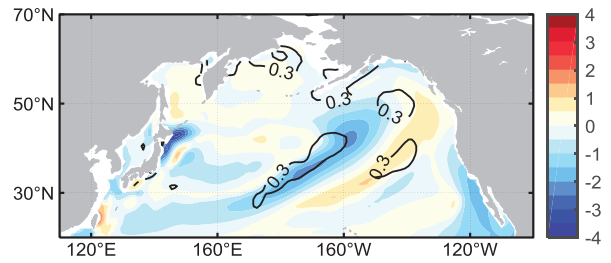

FIGURE 8 | The temperature changes between EAKF and Projection-OI averaged at the 50–150 m vertical depth (shaded; units: °C) in the initial condition and the differences of ACC between the EAKF and Projection-OI hindcasts averaged in all lead months (contour, only 0.3 and 0.4 contours are plotted). The depth of 50–150 m covers the annual variation of mixed-layer depth.

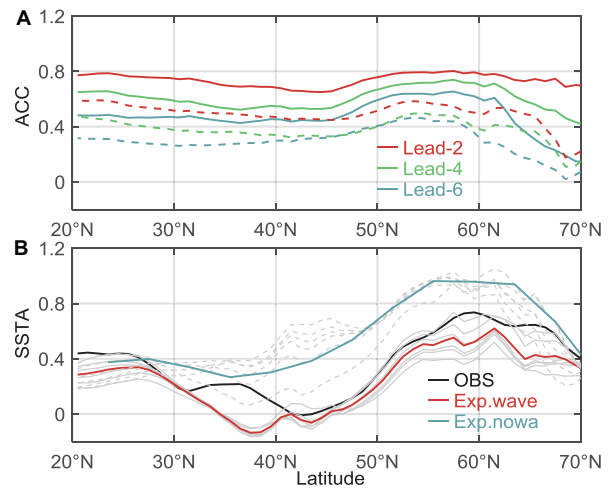

FIGURE 9 | (A) Zonal mean ACC (110°E–100°W) between IOSST v2 datasets and hindcast results in EAKF (solid line) and Projection-OI (dashed line) runs. Red, green, and blue lines represent for 2-, 4-, 6-month lead, respectively. **(B)** Zonal mean SSTAs (110°E–100°W; units: °C) with respect to 1993–2017 climatology in observation (black), Exp.wave (red) and Exp.nowa (blue) mean averaged for 1–6 lead months, and gray solid and dashed lines represent the different lead month in Exp.wave and Exp.nowa.

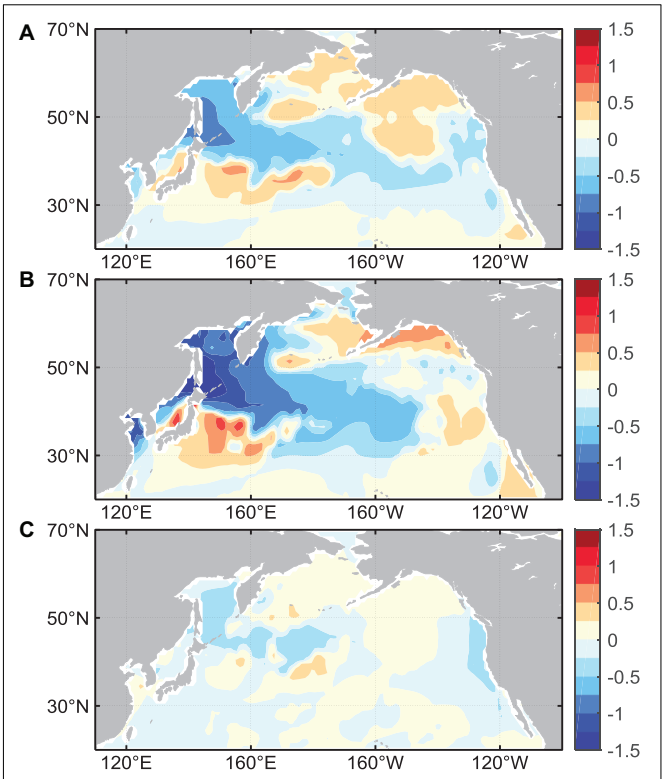

FIGURE 10 | The differences of absolute predicted biases between Exp.wave and Exp.nowa in 2016. **(A)** Annual mean; **(B)** Jan-Jun mean; and **(C)** Jul-Dec mean. The hindcasts with or without wave are respectively compared with OISST v2 to show the predicted biases. Then the difference of absolute values of the biased between Exp.wave and Exp.nowa are calculated. As definited above, the negative value, indicating that the absolute difference between EAKF and observation is smaller than that between Projection-OI and OISST v2, represents the improvement due to the surface wave effects.

initial conditions improve ENSO predictions, which in turn have profound impacts on SSTAs predictions over the extratropical Pacific. In this study, we found that the EAKF data assimilation scheme improves the subsurface layer temperature in the initial condition and results in highly predicted ACC over the central North Pacific, indicating that accurate oceanic initial conditions, especially in the subsurface layer, can effectively improve prediction skill over the North Pacific. The projection method of the data assimilation scheme in the subsurface layer or deep waters can improve the prediction system's performance. Development of short-term climate prediction systems has considerably improved seasonal prediction of SST over the North Pacific. For example, version 2 of the NCEP Climate Forecast System (CFSv2[1]), which belongs to the new generation of operational climate forecast systems and has improved physics and increased resolution in the atmosphere–ocean–land coupled model. The skill of seasonal forecasts of 2-m temperatures over the United States from CFSv2 is nearly double of that from the old version of the prediction system. Global SST forecasts are also considerably improved with CFSv2 (Suranjana et al., 2014). Guan et al. (2014) show that the maximum skill based on CFSv2 hindcasts is confined in the tropical Pacific, and the prediction skill at the mid-latitudes of North Pacific remains low. Compared with CFSv2, FIO-ESM v1.0 exhibits improved prediction skills in the mid and high latitudes ocean. As shown in **Figure 9**, the zonal mean of ACCs (110°E–100°W) varies between 0.7 and 0.4 for 1- to 6-month lead (latitudes ranging from 35 to 50°N) in the EAKF experiment. Except for the influences of initial condition on prediction, it demonstrated that the physical process, such as wave effect, also plays a constructive role in climate prediction in North Pacific. To show the impacts of wave-induced mixing on seasonal prediction, the hindcast without waves is conducted using FIO-ESM v1.0 for 2016 (denoted as Exp.nowa), and the

[1]http://cfs.ncep.noaa.gov

results were compared with the FIO-ESM v1.0 hindcast with EAKF data assimilation for 2016 (denoted as Exp.wave). Two experiments were started from each month of 2016 and initialized with the same initial conditions using the EAKF and ensemble method. When non-breaking wave-induced mixing effects are taken into account, the prediction bias of SSTAs is reduced by about 0.4°C for average lead times of 1–6 months at mid and high latitudes of the North Pacific (**Figure 9B**). Furthermore, bias reduction is found from the Okhotsk Sea across the mid-latitudes of the North Pacific (**Figure 10**) where low seasonal prediction skills have been persisting in other climate prediction systems. The prediction skill improvement due to surface wave exhibits seasonal dependence. Surface wave mixing has a stronger influence when the prediction starts in spring or early summer. As the prediction initiated from the second half of the year, ocean surface waves have little effect on prediction skill. The mixed-layer depth in the high latitude is shallow in summer, with the larger temperature gradient in the upper ocean. The enhanced vertical mixing bringing more cold water from the subsurface to the surface reduces SST. At low latitudes of the Pacific, the deep mixed-layer depth with weak wave-induced mixing results in a slight reduction in SST. In winter, the mixed-layer depth is deep, and the temperature gradient in the upper ocean is small. Due to the limitation of penetration depth, wave-induced mixing is unable to act on the water beneath the mixed layer. Furthermore, the decrease in the vertical diffusion coefficient reduces vertical water exchange, preventing downward heat transfer. As a result, upper ocean temperatures change little or even increase. The effect of surface wave on seasonal prediction of SST is more pronounced in summer, because of shallow mixed-layer depth (Zhao et al., 2019b). Seasonal predictions over the North Pacific over long lead times can be improved by incorporating realistic initial conditions produced by effective data assimilation schemes and reasonable physical processes in climate models.

DATA AVAILABILITY STATEMENT

The datasets of FIO-ESM v1.0 for this study can be found in: http://data.fio.org.cn/qiaofl/FIO-ESM-prediction.

AUTHOR CONTRIBUTIONS

FQ initially designed and organized the whole analysis. YS conducted the hindcast experiments and made some figures and the first draft. YZ assisted in the analysis and improvement of the figures and manuscript. XY, YZ, and YB implemented the EAKF and Projection-OI data assimilation schemes into the FIO-ESM v1.0 and set up the short-term climate prediction system. All authors contributed to the writing of the manuscript.

FUNDING

This research was jointly supported by the National Key Research and Development Program of China (2017YFC1404004 and 2018YFC1506004), the International Cooperation Project of Indo-Pacific Ocean Environment Variation and Air–Sea Interactions (GASI-IPOVAI-06&05 and GASI-04-QYQH-01), and the National Natural Science Foundation of China (41821004 and 41676020).

ACKNOWLEDGMENTS

We thank the National Supercomputer Center in Tianjin for providing computing resource. All experiments were carried out at National Supercomputer Center in Tianjin, and the calculations were performed on TianHe-1(A).

REFERENCES

Alessandri, A., Borrelli, A., Masina, S., Cherchi, A., Gualdi, S., Navarra, A., et al. (2010). The INGV-CMCC seasonal prediction system: improved ocean initial conditions. *Mon. Weather Rev.* 138, 2930–2952. doi: 10.1175/2010MWR3178.1

Alexander, M. A. (1999). The re-emergence of SST anomalies in the North Pacific Ocean. *J. Clim.* 12, 2419–2433. doi: 10.1175/1520-04421999012<2419:TROSAI<2.0.CO

Anderson, J. L. (2001). An Ensemble adjustment kalman filter for data assimilation. *Mon. Weather Rev.* 129, 2884–2903. doi: 10.1175/1520-04932001129<2884:AEAKFF<2.0.CO;2

Banzon, V., Smith, T. M., Chin, T. M., Liu, C., and Hankins, W. (2016). A long-term record of blended satellite and in situ sea-surface temperature for climate monitoring, modeling and environmental studies. *Earth Syst. Sci. Data* 8, 165–176. doi: 10.5194/essd-8-165-2016

Barnston, A., Tippett, M., Van den Dool, H., and Unger, D. (2015). Toward an improved multi-model ENSO prediction. *J. Appl. Meteorol. Climatol.* 54, 1579–1595. doi: 10.1175/JAMC-D-14-0188.1

Barnston, A. G., Glantz, M. H., and He, Y. (1999). Predictive skill of statistical and dynamical climate models in SST forecasts during the 1997/98 El Niño episode and the 1998 La Nifmars-07-00504a onset. *Bull. Am. Meteorol. Soc.* 80, 217–243. doi: 10.1175/1520-047719990802.0.CO;2

Bayr, T., Domeisen, D. I. V., and Wengel, C. (2019). The effect of the equatorial Pacific cold SST bias on simulated ENSO teleconnections to the North Pacific and California. *Clim. Dyn.* 53, 3771–3789. doi: 10.1007/s00382-019-04746-9

Bishop, C. H., Etherton, B. J., and Majumdar, S. J. (2001). Adaptive sampling with the ensemble transform kalman filter. *Part I: Theor. Aspects. Mon. Weather Rev.* 129, 420–436. doi: 10.1175/1520-049320011292.0.CO;2

Cane, M., Zebiak, A., and Dolan, S. C. (1986). Experimental forecasts of El Niño. *Nature* 321, 827–832. doi: 10.1038/321827a0

Chen, H., Yin, X., Bao, Y., and Qiao, F. (2015). Ocean satellite data assimilation experiments in FIO-ESM using ensemble adjustment Kalman filter. *Scie. China: Earth Sci.* 59, 484–494. doi: 10.1007/s11430-015-5187-2

Duan, W., and Wu, Y. (2014). Season-dependent predictability and error growth dynamics of Pacific Decadal Oscillation-related sea surface temperature anomalies. *Clim. Dyn.* 44, 1053–1072. doi: 10.1007/s00382-014-2364-5

Ducet, N., Traon, P., and Reverdin, G. (2000). Global high-resolution mapping of ocean circulation from TOPEX/Poseidon and ERS-1 and -2. *J. Geophys. Res. Oceans* 105, 19477–19498. doi: 10.1029/2000jc900063

Eddy, A. (1964). The objective analysis of horizontal wind divergence fields. *Q. J. R. Meteorol. Soc.* 90, 424–440. doi: 10.1002/qj.49709038606

Evensen, G. (1994). Sequential data assimilation with a nonlinear quasigeotropic model using Monte Carlo methods to forecast error statistics. *J. Geophys. Res.* 99, 143–162. doi: 10.1029/94jc00572

Ezer, T., and Mellor, G. (1997). Simulations of the Atlantic Ocean with a free surface sigma coordinate ocean model. *J. Geophys. Res. Atmospheres* 1021, 15647–15658. doi: 10.1029/97JC00984

Good, S. A., Martin, M. J., and Rayner, N. A. (2013). EN4: quality controlled ocean temperature and salinity profiles and monthly objective analyses with uncertainty estimates. *J. Geophys. Res. Oceans* 118, 6704–6716. doi: 10.1002/2013JC009067

Guan, Y., Zhu, J., Huang, B., Hu, Z. Z., and James, L. K. (2014). South Pacific Ocean dipole: a predictable mode on multiseasonal time scales. *J. Clim.* 27, 1648–1658. doi: 10.1175/jcli-d-13-00293.1

Hu, Z., Kumar, A., Huang, B., Zhu, J., and Guan, Y. (2014). Prediction Skill of North pacific variability in NCEP climate forecast system Version 2: impact of ENSO and Beyond. *J. Clim.* 27, 4263–4272. doi: 10.1175/JCLI-D-13-00633.1

Jacox, M. G., Alexander, M. A., Stock, C. A., and Hervieux, G. (2019). On the skill of seasonal sea surface temperature forecasts in the California Current System and its connection to ENSO variability. *Clim. Dyn.* 53, 7519–7533. doi: 10.1007/s00382-017-3608-y

Jones, R. H. (1965). Optimal estimation of initial conditions for numerical prediction. *J. Atmos. Sci.* 22, 658–663. doi: 10.1175/1520-046919650222.0.CO;2

Kim, H., Webster, P. J., and Curry, J. A. (2012). Seasonal prediction skill of ECMWF System 4 and NCEP CFSv2 retrospective forecast for the Northern Hemisphere Winter. *Clim. Dyn.* 39, 2957–2973. doi: 10.1007/s00382-012-1364-6

Kim, S., Jeong, H., and Jin, F. (2017). Mean bias in seasonal forecast model and ENSO prediction error. *Sci. Rep.* 7:6029. doi: 10.1038/s41598-017-05221-3

Kim, S., Kim, H., Min, S., Son, H., Won, D., Jung, H., et al. (2015). Intra-winter atmospheric circulation changes over East Asia and North Pacific associated with ENSO in a seasonal prediction model. *Asia Pacific J. Atmospheric Sci.* 51, 49–60. doi: 10.1007/s13143-014-0059-9

Kug, J. S., Kang, I., and Choi, D. (2008). Seasonal climate predictability with Tier-one and Tier-two prediction systems. *Clim. Dyn.* 31, 403–416. doi: 10.1007/s00382-007-0264-7

Kumar, A., Jha, B., and Wang, H. (2014). Attribution of SST variability in global oceans and the role of ENSO. *Clim. Dyn.* 43, 209–220. doi: 10.1007/s00382-013-1865-y

Lau, K. M., Lee, J., Kim, K., and Kang, I. (2004). The North pacific as a regulator of summertime climate over eurasia and North America. *J. Clim.* 17, 819–833. doi: 10.1175/1520-04422004017<0819:tnpaar<2.0.co;2

Liu, Y., and Ren, H. (2017). Improving ENSO prediction in CFSv2 with an analogue-based correction method. *Int. J. Climatol.* 37, 5035–5046. doi: 10.1002/joc.5142

Liu, Z., and Alexander, M. (2007). Atmospheric bridge, oceanic tunnel, and global climatic teleconnections. *Rev. Geophys.* 45:RG2005. doi: 10.1029/2005RG000172

Lorenz, E. N. (1969). Atmospheric predictability as revealed by naturally occurring analogues. *J. Atmos. Sci.* 26, 636–646. doi: 10.1175/1520-04691969262.0.CO;2

Luo, J., Masson, S., Behera, S., Shingu, S., and Yamagata, T. (2005). Seasonal Climate Predictability in a Coupled OAGCM Using a Different Approach for Ensemble Forecasts. *J. Clim.* 18, 4474–4497. doi: 10.1175/JCLI3526.1

Qiao, F., Song, Z., Bao, Y., Song, Y., Shu, Q., Huang, C., et al. (2013). Development and evaluation of an Earth system model with surface gravity waves. *J. Geophys. Res. Oceans* 118, 4514–4524. doi: 10.1002/jgrc.20327

Qiao, F., Yuan, Y., Ezer, T., Xia, C., Yang, Y., Lü, X., et al. (2010). A three-dimensional surface wave-ocean circulation coupled model and its initial testing. *Ocean Dynamics* 60, 1339–1355. doi: 10.1007/s10236-010-0326-y

Qiao, F., Yuan, Y., Yang, Y., Zheng, Q., Xia, C., and Ma, J. (2004). Wave-induced mixing in the upper ocean: distribution and application to a global ocean circulation model. *Geophys. Res. Lett.* 31, 293–317. doi: 10.1029/2004GL019824

Ratheesh, S., Sharma, R., and Basu, S. (2012). Projection-based assimilation of satellite-derived surface data in an indian ocean circulation model. *Mar. Geodesy* 35, 175–187. doi: 10.1080/01490419.2011.637855

Reynolds, R. W., Smith, T. M., Liu, C., Chelton, D. B., Casey, K. S., and Schlax, M. G. (2007). Daily high-resolution-blended analyses for sea surface temperature. *J. Clim.* 20, 5473–5496. doi: 10.1175/2007JCLI1824.1

Rosati, A., Miyakoda, K., and Gudgel, R. (1997). The impact of ocean initial conditions on ENSO forecasting with a coupled model. *Mon. Weather Rev.* 125, 754–772. doi: 10.1175/1520-04931997125<0754:TIOOIC<2.0.CO;2

Song, Z., Shu, Q., Bao, Y., Yin, X., and Qiao, F. (2015). The prediction on the 2015/16 El Niño event from the perspective of FIO-ESM. *Acta Oceanol. Sin.* 34, 67–71. doi: 10.1007/s13131-015-0787-4

Suranjana, S., Shrinivas, M., Wu, X., Wang, J., Nadiga, S., Tripp, P., et al. (2014). The NCEP climate forecast system version 2. *J. Clim.* 27, 2185–2208. doi: 10.1175/jcli-d-12-00823.1

Wang, C., Zhang, L., Lee, S., Wu, L., and Mechoso, C. R. (2014). A global perspective on CMIP5 climate model biases. *Nat. Clim. Change* 4, 201–205. doi: 10.1038/nclimate2118

Wen, C., Xue, Y., and Kumar, A. (2012). Seasonal Prediction of North Pacific SSTs and PDO in the NCEP CFS Hindcasts. *J. Clim.* 25, 5689–5710. doi: 10.1175/JCLI-D-11-00556.1

Wu, Y., Duan, W., and Rong, X. (2016). Seasonal predictability of sea surface temperature anomalies over the kuroshio-oyashio extension: low in summer and high in winter. *J. Geophys. Res. Oceans* 121, 6862–6873. doi: 10.1002/2016JC011887

Yin, X., Qiao, F., Xia, C., Lü, X., and Yang, Y. (2010). Reconstruction of eddies by assimilating satellite altimeter data into Princeton Ocean Model. *Acta Oceanol. Sin.* 29, 1–11. doi: 10.1007/s13131-010-0001-7

Zhao, X., Li, J., and Zhang, W. (2012). Summer persistence barrier of sea surface temperature anomalies in the Central Western North Pacific. *Adv. Atmospheric Sci.* 29, 1159–1173. doi: 10.1007/s00376-012-1253-2

Zhao, Y., Yin, X., Song, Y., and Qiao, F. (2019a). Seasonal prediction skills of FIO-ESM for North Pacific Sea surface temperature and precipitation. *Acta Oceanol. Sin.* 38, 5–12. doi: 10.1007/s13131-019-1366-x

Zhao, Y., Yin, X., Song, Y., and Qiao, F. (2019b). Effect of wave-induced mixing on sea surface temperature seasonal prediction in the North Pacific in 2016. *Haiyang Xuebao* 41, 52–61. doi: 10.3969/j.issn.0253-4193.2019.03.006

Zheng, F., and Zhu, J. (2010). Spring predictability barrier of ENSO events from the perspective of an ensemble prediction system. *Global Planet. Change* 72, 108–117. doi: 10.1016/j.gloplacha.2010.01.021

Zhu, J., Huang, B., Balmaseda, M. A., Kinter, J. L., Peng, P., Hu, Z., et al. (2013). Improved reliability of ENSO hindcasts with multi-ocean analyses ensemble initialization. *Clim. Dyn.* 41, 2785–2795. doi: 10.1007/s00382-013-1965-8

Zhu, J., Huang, B., Marx, L., Kinter, J. L., Balmaseda, M. A., Zhang, R., et al. (2012). Ensemble enso hindcasts initialized from multiple ocean analyses. *Geophys. Res. Lett.* 39:L09602. doi: 10.1029/2012GL051503

Zhu, J., Kumar, A., Lee, H. C., and Wang, H. (2017a). Seasonal predictions using a simple ocean initialization scheme. *Clim. Dyn.* 49, 3989–4007. doi: 10.1007/s00382-017-3556-6

Zhu, J., Kumar, A., Wang, W., Hu, Z. Z., Huang, B., and Balmaseda, M. A. (2017b). Importance of convective parameterization in ENSO predictions. *Geophys. Res. Lett.* 44, 6334–6342. doi: 10.1002/2017GL073669

Conflict of Interest: The authors declare that the research was conducted in the absence of any commercial or financial relationships that could be construed as a potential conflict of interest.

frontiers in Marine Science

ORIGINAL RESEARCH
published: 29 July 2020
doi: 10.3389/fmars.2020.00589

Predictability of Species Distributions Deteriorates Under Novel Environmental Conditions in the California Current System

Barbara A. Muhling[1,2], Stephanie Brodie[1,3], James A. Smith[1,2], Desiree Tommasi[1,2], Carlos F. Gaitan[4], Elliott L. Hazen[3], Michael G. Jacox[3,5], Toby D. Auth[6] and Richard D. Brodeur[7]*

[1] Institute of Marine Sciences, University of California, Santa Cruz, Santa Cruz, CA, United States, [2] NOAA Southwest Fisheries Science Center, San Diego, CA, United States, [3] NOAA Southwest Fisheries Science Center, Monterey, CA, United States, [4] Benchmark Labs, San Francisco, CA, United States, [5] NOAA Earth System Research Laboratory, Boulder, CO, United States, [6] Pacific States Marine Fisheries Commission, Newport, OR, United States, [7] NOAA Northwest Fisheries Science Center, Seattle, WA, United States

OPEN ACCESS

Edited by:
Liping Liu,
Shanghai Ocean University, China

Reviewed by:
Sam McClatchie,
Independent Researcher,
New Zealand
David Checkley,
University of California, San Diego,
United States

***Correspondence:**
Barbara A. Muhling
Barbara.Muhling@noaa.gov

Specialty section:
This article was submitted to Marine Fisheries, Aquaculture and Living Resources, a section of the journal Frontiers in Marine Science

Received: *31 March 2020*
Accepted: *26 June 2020*
Published: *29 July 2020*

Citation:
Muhling BA, Brodie S, Smith JA, Tommasi D, Gaitan CF, Hazen EL, Jacox MG, Auth TD and Brodeur RD (2020) Predictability of Species Distributions Deteriorates Under Novel Environmental Conditions in the California Current System. Front. Mar. Sci. 7:589. doi: 10.3389/fmars.2020.00589

Spatial distributions of marine fauna are determined by complex interactions between environmental conditions and animal behaviors. As climate change leads to warmer, more acidic, and less oxygenated oceans, species are shifting away from their historical distribution ranges, and these trends are expected to continue into the future. Correlative Species Distribution Models (SDMs) can be used to project future habitat extent for marine species, with many different statistical methods available. However, it is vital to assess how different statistical methods behave under novel environmental conditions before using these models for management advice, and to consider whether future projections based on these techniques are biologically reasonable. In this study, we built SDMs for adults and larvae of two ecologically important pelagic fishes in the California Current System (CCS): Pacific sardine (*Sardinops sagax*) and northern anchovy (*Engraulis mordax*). We used five different SDM methods, ranging from simple [thermal niche model (TNM)] to complex (artificial neural networks). Our results show that some SDMs trained on data collected between 2003 and 2013 lost substantial predictive skill when applied to observations from more recent years, when ocean temperatures associated with a marine heatwave were outside the range of historical measurements. This decrease in skill was particularly apparent for adult sardine, which showed non-stationary relationships between catch locations and sea surface temperature (SST) through time. While sardine adults and larvae shifted their distributions markedly during the marine heatwave, anchovy largely maintained their historical spatiotemporal distributions. Our results suggest that correlative relationships between species and their environment can become unreliable during anomalous conditions. Understanding the underlying physiology of marine species is therefore

essential for the construction of SDMs that are robust to rapidly changing environments. Developing distribution models that offer skillful predictions into the future for species such as sardine and anchovy, which are migratory and include separate sub-stocks, may be particularly challenging.

Keywords: Species Distribution Models, Pacific sardine, northern anchovy, California Current, marine heatwaves

INTRODUCTION

Climate change is leading to unprecedented conditions in marine ecosystems around the world, forcing ocean biota to adapt to new environmental states (Lima and Wethey, 2012; Poloczanska et al., 2013). Mobile marine animals may respond to physiologically stressful or otherwise unfavorable environments by moving away from impacted areas. These changes in spatial distributions can present challenges for the effective management of ecologically and economically important species and habitats (Mills et al., 2013; Cheung et al., 2015; Kleisner et al., 2017; Karp et al., 2019). The development of most stock assessment models, marine protected areas, and other resource management measures has traditionally assumed relatively constant species distributions through time (Link et al., 2011; Punt et al., 2013). Resilient management strategies for the future will thus need to be flexible enough to adapt to shifting species distributions, and changing spatial productivity regimes (Johnson and Welch, 2009).

Multivariate correlative Species Distribution Models (SDMs) are increasingly being used to anticipate these challenges by projecting future distributions of marine species. These types of model are popular due to their flexibility, and ability to represent complex relationships between a species and its ocean habitat (Guisan and Zimmermann, 2000; Elith and Leathwick, 2009). However, SDM projections can be misleading if models do not adequately capture the mechanistic drivers which underpin species responses to their environment (Buckley et al., 2010; Silber et al., 2017; Yates et al., 2018). These models can also behave in unexpected ways when confronted with novel environmental conditions, or when required to extrapolate in time or space (Hannemann et al., 2015; Norberg et al., 2019). The responses of different classes of SDM to novel conditions can also depend on the model structure, potentially introducing another significant source of uncertainty into projections of future species distributions.

The choice of covariates for use in SDMs can also be influential. The inclusion of environmentally invariant spatiotemporal covariates (e.g., longitude, latitude, month, day of the year) often improves SDM performance against present-day observations, because these covariates can represent important but unmeasured (or unknown) spatiotemporal processes (Brodie et al., 2020). However, as climate change increasingly leads to directional shifts in ocean conditions, historically relevant spatiotemporal predictors of species distributions may lose their skill. For species that move primarily in response to local, near-real-time environmental conditions, SDMs including spatiotemporal covariates are less likely to remain accurate into the future. In contrast, SDMs with spatiotemporal covariates may continue to be skillful for some future period of time for species which move depending on genetically determined migration behaviors, or in response to fixed geographical cues, such as coastal topography (Bauer et al., 2011; Winkler et al., 2014). These animals may continue to occupy historical habitats, even as the physiological suitability of these locations deteriorates (e.g., Crozier et al., 2008). The importance of understanding the physiology, predator-prey interactions, and movement ecology of species before attempting to project their future distributions is thus clearly important.

A combination of anthropogenic climate change overlaid on higher-frequency natural variability, such as the El Niño – Southern Oscillation, has led to unprecedented warm events in marine ecosystems in recent years (Holbrook et al., 2019; Jacox, 2019; Smale et al., 2019). These extreme events have been referred to as marine heatwaves, with a severity classification based on departures from climatological sea surface temperature (SST) (Hobday et al., 2018). The California Current System (CCS) experienced a severe (category 3) marine heatwave from 2014 to 2016 (**Figure 1**), which originated as an offshore anomaly known as "the Blob" (Bond et al., 2015). This heatwave evolved into a coastwide warming pattern (Di Lorenzo and Mantua, 2016), further fueled by a strong El Niño in 2015–2016 (Jacox et al., 2016). SSTs were up to 6°C warmer than usual, and primary productivity was anomalously low across parts of the continental shelf and offshore regions (Gentemann et al., 2017; Kahru et al., 2018). Many marine species responded strongly to the heatwave, showing highly anomalous abundances (e.g., Becker et al., 2018; Brodeur et al., 2019; Duguid et al., 2019), and distribution patterns (Cavole et al., 2016; Sakuma et al., 2016) compared to historical observations.

With novel environmental conditions, such as marine heatwaves, becoming increasingly common, there is a critical need to test if our predictions of species responses to these conditions are realistic (Guisan et al., 2013). The CCS marine heatwave can thus provide a useful out-of-sample robustness test for SDMs trained on prior years (Becker et al., 2018). If SDMs can reproduce the anomalous species distributions observed in 2014–2016, it instills confidence in their usefulness as tools for projecting species distributions decades into the future. Conversely, a strong loss of SDM skill during the heatwave years may suggest that the underlying mechanisms driving species distributions in the CCS have not been adequately captured.

Pacific sardine (*Sardinops sagax*: sardine hereafter) and northern anchovy (*Engraulis mordax*: anchovy hereafter) are ecologically important forage fish in the CCS, transferring energy from plankton to upper trophic levels (Koehn et al., 2016). Their dynamics are characterized by boom and bust cycles, even in the

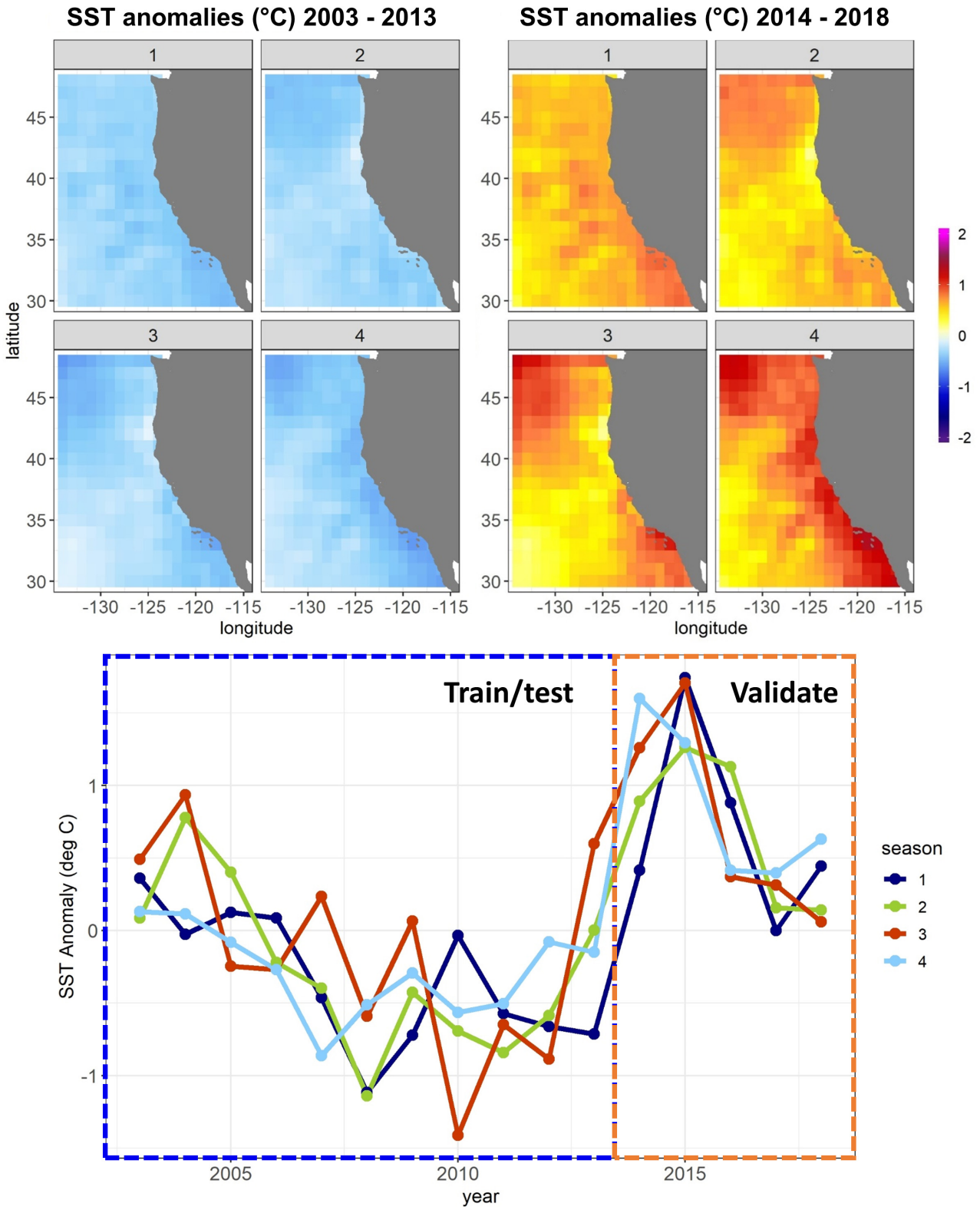

FIGURE 1 | Sea surface temperature (SST) anomalies against a 1980–2018 mean from the CCS ROMS by quarter (January–March, April–June, etc.) for the Experiment 1 SDM training/testing and validation time periods. Anomalies are averaged temporally and mapped spatially at 1° resolution **(top)** and averaged spatially across the whole model domain and plotted temporally **(bottom)**.

absence of industrial fishing (Baumgartner, 1992). In the past 10 years, sardine biomass has declined to very low levels, while anchovy abundance has increased strongly since 2017 (Lindegren et al., 2013; Gallo et al., 2019; Thompson et al., 2019; Zwolinski et al., 2019). Anchovy are associated with cool, upwelled waters in shallower coastal environments, and are generally non-migratory (Checkley et al., 2009). The central anchovy subpopulation ranges from Baja California to San Francisco, and spawns off southern and central California, while the northern subpopulation ranges from San Francisco to British Columbia, and spawns near the Columbia River plume (Emmett et al., 2005; Litz et al., 2008; Checkley et al., 2009; Duguid et al., 2019). Sardine reside in warmer, more oligotrophic waters between the California Current and the coastal upwelling region (Checkley et al., 2009). Two of the three sardine subpopulations undergo annual northward feeding migrations, the extent of which may depend on oceanographic conditions, population size, and age structure (Smith, 2005; Zwolinski et al., 2011; McDaniel et al., 2016). The southern subpopulation extends from southern Baja California to southern California, and spawns in summer and fall off southern Baja California. The northern subpopulation, and extends from northern Baja California to British Columbia (Valencia-Gasti et al., 2018), spawning off central and southern California in spring, and in spring-summer off Oregon and Washington in some years (Zwolinski et al., 2011; Auth et al., 2018).

Ongoing research surveys provide extensive distribution information for sardine and anchovy across life stages in the CCS, making them useful case study species. In this study, we thus assessed the ability of five different types of SDM to predict distributions of adults and larvae of sardine and anchovy in the region. Our chosen SDMs spanned a range of complexity from simple, single-variable thermal niche models (TNMs) to more complex machine learning models. We assessed the predictive skill for each SDM across two separate experiments. The first used data collected from 2003 to 2013 to train the SDMs, and then externally validated them against observations from 2014 to 2018, a time period including the 2014–2016 marine heatwave. The second experiment allowed the SDMs to use observations from the marine heatwave years for model training, and validated them against data from withheld years with near-average temperature conditions (2003–2007). We discuss our results in light of current knowledge on the ecology of sardine and anchovy in the CCS, and offer some potential explanations for differences in skill observed between the two experiments and across each life stage of each species.

MATERIALS AND METHODS

Biological Data Sources

Catch records for adult sardine and anchovy were obtained from trawl surveys conducted by the NOAA Southwest Fisheries Science Center (SWFSC). There were data from 1,777 hauls available for use, from 29 cruises conducted between July 2003 and September 2018. Sampling effort was primarily concentrated in spring (April: 657 hauls) and summer (July–August: 737 hauls), but some data were also available from other months between March and October. The trawl net was towed near the surface at night at a target speed of 3.5–4.0 knots. The net was fitted with an 8 mm mesh liner in the codend (more details are contained in Zwolinski and Demer, 2012; Zwolinski et al., 2012 and Weber et al., 2018). Sampling was concentrated on the continental shelf and slope.

Larval occurrence records for California waters were primarily sourced from the California Cooperative Oceanic Fisheries Investigations (CalCOFI) surveys. Collections under this program began in 1949, and CalCOFI cruises have occupied a standard grid of 66 stations off southern California since 1985. We used catches from standard oblique 0.71 m bongo net tows, which are fitted with 505 mm mesh and towed to 210 m depth (Kramer et al., 1972; Moser et al., 2001; Asch, 2015). Larval occurrence records for the northern California Current were sourced from various sampling programs conducted between 1998 and 2018 by the NOAA Northwest Fisheries Science Center (NWFSC) along the central Oregon coast. These catches derived from 1-m ring and 0.6–0.7 m bongo net tows fitted with 0.200–0.333 mm mesh towed to 20–100 m depth (Auth et al., 2015, 2018; Thompson et al., 2019). Larval data from the entire Oregon and southern Washington coasts were available from yearly (since 2013) NWFSC Prerecruit surveys using a 0.7 m bongo net with 0.333 mm mesh (Brodeur et al., 2019; Thompson et al., 2019).

Environmental Variables

Environmental predictors for the SDMs were sourced from a data assimilative CCS configuration of the Regional Ocean Modeling System (ROMS), with 42 terrain-following vertical levels. The ROMS domain covered from 30 to 48°N, inshore of 134°W at 0.1° horizontal resolution[1] (Veneziani et al., 2009; Neveu et al., 2016). The suite of predictors was the same as used by previous distribution modeling studies for marine vertebrates in the CCS (Scales et al., 2017; Becker et al., 2018; Brodie et al., 2018; Muhling et al., 2019; Smith et al., 2020), and is shown in **Table 1**. We included SST due to the known importance of temperature to physiological processes and habitat delineation in our species (Checkley et al., 2000; Zwolinski et al., 2011; Weber et al., 2018). Mesoscale oceanographic activity has been shown to delineate favorable spawning areas for small pelagic fishes (Asch and Checkley, 2013), and was captured through sea surface height and eddy kinetic energy. We also included predictors of current flow and wind stress (northward and eastward wind stress, current velocities, wind stress curl), as these are important in shaping retention characteristics and drivers of primary productivity in the region (Jacox et al., 2018). As Brodie et al. (2018) showed the importance of indicators of subsurface water column structure (such as isothermal layer depth and bulk buoyancy frequency) in predicting the distribution of large pelagic fishes and sharks in the CCS, we also included these variables. Isothermal layer depth captures the thickness of the well-mixed surface layer, while bulk buoyancy frequency indicates the stability of the upper water column. The spatial standard deviation of both SST and sea surface height at 0.7° resolution were also included as

[1] http://oceanmodeling.ucsc.edu/ccsnrt version 2016a

TABLE 1 | Predictors used to build SDMs, and SDM configurations which included each variable.

Variable	Source	Spatial resolution	Temporal resolution	SDM Config.
Bulk buoyancy frequency	ROMS	0.1	Daily	env, all
Wind stress curl	ROMS	0.5	Daily	env, all
Isothermal layer depth	ROMS	0.1	Daily	env, all
Eddy kinetic energy (log)	ROMS	0.1	Daily	env, all
Sea surface height	ROMS	0.1	Daily	env, all
Sea surface height s.d.	ROMS	0.1	Daily	env, all
Sea surface temperature	ROMS	0.1	Daily	env, all
Sea surface temperature s.d.	ROMS	0.1	Daily	env, all
Surface eastward current velocity	ROMS	0.1	Daily	env, all
Surface northward current velocity	ROMS	0.1	Daily	env, all
Surface eastward wind stress	ROMS	0.1	Daily	env, all
Surface northward wind stress	ROMS	0.1	Daily	env, all
Surface chlorophyll (4th root)	ESA reanalysis	0.04167	8 day	env, all
Moon phase	Date	Non-spatial	Daily	env, all
Stock biomass	Stock assessment or larval survey	Non-spatial	Annual	env, all
Latitude	Survey	Native	Daily	geo, all
Longitude	Survey	Native	Daily	geo, all
Month	Survey	Native	Monthly	geo, all

"s.d." denotes standard deviation. Note that wind stress curl was extracted at 0.5 resolution, to account for discrepancies in wind forcing datasets used across years (see Muhling et al., 2019).

predictors, to highlight areas of high variability such as frontal zones (Hazen et al., 2018). More information on the calculation of these parameters is available in Brodie et al. (2018) and Muhling et al. (2019). Although surface salinity is available from the ROMS, we chose not to include it as a predictor as it was inconsistent through time, across the two ROMS experiments (1980–2010 and 2011 – present: see Brodie et al., 2018). Values of each ROMS predictor were extracted at native 0.1° spatial resolution, for the date and location of biological sampling. As the CCS ROMS is physics-only (no biogeochemistry), we used satellite surface chlorophyll to approximate primary productivity. These data were obtained from chlorophyll re-analyses developed through the Ocean-Colour Climate Change Initiative (OC-CCI) using multiple ocean color sensors (Sathyendranath et al., 2019). Chlorophyll was extracted at 0.25° spatial resolution, and from 8-day composites overlapping biological sampling dates, to minimize the number of observations lost to cloud cover. Where no 8-day chlorophyll observations were available for a sampling station, we used monthly chlorophyll instead, as the correlation between 8-day and monthly chlorophyll was high ($r > 0.8$). This impacted <5% of the biological observations. Eddy kinetic energy and surface chlorophyll were both strongly right-skewed, and so were $\log_e$ and 4th root transformed, respectively, before inclusion in the SDMs. None of the environmental predictors were linearly correlated with each other at $r > 0.6$ or $r < -0.6$, and so all were included in the SDMs.

Following Weber and McClatchie (2010) and Muhling et al. (2019) we included annual biomass indicators as additional predictors for both species, to account for potentially different rates of occupation of environmentally suitable habitat at different stock sizes (**Supplementary Figure S1**). Previous studies have shown that actual occupied habitat is more spatiotemporally restricted than potential habitat for many fish species, particularly when stock biomass is low (Planque et al., 2007; Reiss et al., 2008). For sardine, we used annual standing stock biomass estimated from sardine stock assessments (Hill et al., 2014, 2018). For anchovy, we used 3-year running mean larval abundances from CalCOFI surveys to index anchovy stock biomass (following Zwolinski and Demer, 2012), as there is no current stock assessment for this species.

Species Distribution Models

All SDMs in this study predicted the probability of occurrence (presence or absence) of each species and life stage. The available biological data from both trawl and larval surveys were split into three sections for use in SDM training, testing, and external validation. Partitioning of observations among these three groups varied across two set experiments, described below.

In Experiment 1, SDMs were trained using a randomly selected 50% of all available observations collected between 2003 and 2013 (training dataset). Optimal SDM configurations were determined based on skill against the other 50% of data from these years (testing dataset). Model skill was quantified using the Area Under the Receiver Operating Characteristic (ROC) curve: (AUC). The AUC metric measures the skill of a classification model. The ROC curve plots the true positive rate against the false positive rate at different classification thresholds, and the area under this curve is used as a measure of model performance. An AUC of 1 indicates a perfect model, where all absences are correctly predicted as absences, and all presences are correctly predicted as presences, while a value of 0.5 indicates that the model's skill is no better than random. SDMs built using the optimal configuration were then scored against data from years 2014 to 2018 (validation dataset). Results reported for each SDM for each species/life stage thus include (1) a "test" skill, against data not used to build the model but within the same set of years, and (2) a "validation" skill, against data not used to build the model and from a different

set of years with novel environmental conditions (**Figure 1**). To estimate the uncertainty introduced from the random 50% split of 2003–2013 data into training and testing datasets, this split was repeated 10 times (setting the seed each time to allow reproducibility), with optimal SDM configurations re-determined, and a separate set of SDMs saved for each iteration. Mean SDM skill was then assessed across results from all 10 training/testing splits.

Our Experiment 1 training data for the SDMs were restricted to the years 2003–2013, to align with data availability for the trawl surveys. However, larval survey data extend much further back in time. We thus tested two modifications to Experiment 1 for larval sardine and larval anchovy SDMs: the first extended training and testing data back to September 1997, to align with the start of the satellite chlorophyll record. The second modification extended training and testing data back to 1980, to align with the start of the ROMS reanalysis, with chlorophyll dropped as a predictor. Skill against the withheld validation dataset from 2014 to 2018 was then re-tested in the same manner as for the larval SDMs trained using 2003–2013 data.

In Experiment 2, we aimed to assess whether changes in SDM skill between the testing and validation datasets observed in Experiment 1 depended primarily on the novel environmental conditions present during 2014–2018, or on the lack of temporal overlap between the training/testing data and the validation data. The first instance may suggest non-stationarity in relationships between species and their environment during extreme environmental events, or an inability of the SDMs to skillfully extrapolate to novel conditions. The second instance may suggest that the training and testing procedures outlined for Experiment 1 were generally insufficient to prevent overfitting of the SDMs. We thus repeated the SDM training procedure from Experiment 1 but used different splitting criteria. Here, we used 50% of the data from 2008 to 2018 as the training data, and the other 50% as the testing data. Years 2003–2007 were withheld to be used as validation data. In this experiment, the validation data were thus separated from the training/testing data temporally but were not particularly novel environmentally (**Figure 1**).

As strongly uneven class membership can bias classification models (Kuhn and Johnson, 2013), we used upsampling and downsampling in the *caret* package (Kuhn et al., 2019) on the training data for both experiments. Downsampling randomly samples the data so that the two classes (positive and negative) end up with the same frequency as the minority class. Upsampling samples the data with replacement to make the two class distributions equal. We upsampled the trawl data, as downsampling resulted in too few observations remaining for model training, but downsampled the much larger larval fish dataset to keep computation times feasible. The most unbalanced training dataset was for adult anchovy in the trawl dataset for Experiment 1 (6.18% positive stations), while the least unbalanced was for adult sardine in the trawl dataset, also for Experiment 1 (33.81% positive stations).

Within each experiment, we tested three subsets of predictors (**Table 1** and **Figure 2**). One set of SDMs was built using all environmental variables plus biomass indicators, longitude, latitude, and month. The next set was built using only environmental predictors and biomass indicators. The last set was built using only longitude, latitude, and month. These three configurations are referred to as "all," "env," and "geo," respectively, throughout the text.

Five different modeling methods were used to build SDMs for each species/life stage: three machine-learning methods and two forms of Generalized Additive Models (GAMs). These were chosen to represent a range of possible approaches to building SDMs for ecology, and all are well represented in the ecological literature (e.g., Özesmi et al., 2006; Olden et al., 2008; Elith, 2019; Brodie et al., 2020). All SDMs were built in R 3.6.1 (R Core Team, 2019) and are described in more detail below.

Boosted Regression Trees

Boosted Regression Trees (BRTs) are tree-based machine learning models, which are highly flexible and include interactions among predictors implicitly (Elith et al., 2008). BRTs for this study were built using Bernoulli distributions in the *dismo* and *gbm* packages (Hijmans et al., 2017; Greenwell et al., 2019). Different combinations of tree complexity, learning rate, and number of trees were tested using the *caret* package. Tree complexity was allowed to vary between 2 and 5 (with a step of 1), and the number of trees between 1200 and 2400 (step of 40). The best learning rate depends on the tree complexity, number of trees, and number of observations in the training data. We calculated a learning rate coefficient (lr.coeff) based on the number of observations as:

$$\text{lr.coeff} = 1.7\text{e}-06 \times \text{n} - 1.91\text{e}-04 \quad (1)$$

where n is the number of observations in the training data. We then allowed the learning rate for BRT training to vary between 4 and 8 times the lr.coeff. We found that this linear equation, determined iteratively, gave a useful range of learning rates to test. Once the "train" function in *caret* had selected the optimal values for tree complexity, learning rate, and number of trees, 5 BRTs were built using the same training data, to capture the stochasticity in the model building process (**Figure 2**).

Generalized Additive Models

Generalized Additive Models are semi-parametric regression models which can account for non-linear relationships between covariates and dependent variables using smoothing functions. We built our GAMs in the *mgcv* package (Wood, 2017). The only parameter tuned for the GAMs was the number of knots (k), which was allowed to vary between 3 and 7, and kept the same for all environmental variables. Although higher values of k can result in slightly more skillful models, this approach can also lead to biologically unreasonable relationships between predictors and dependent variables. Thin plate regression splines were used for all environmental variables, except month, which used a cyclic cubic regression spline. Latitude and longitude were included as a smoothed interaction term, and k was set to the square of the value used for single predictors [i.e., s(lon, lat, $k = \text{k} \times \text{k}$)]. This approach allowed the GAMs to realistically capture the 2-dimensional spatial structure of the observations (e.g., Zuur, 2012), without overfitting unreasonably in space. The value of k which produced the best AUC on the testing data was selected

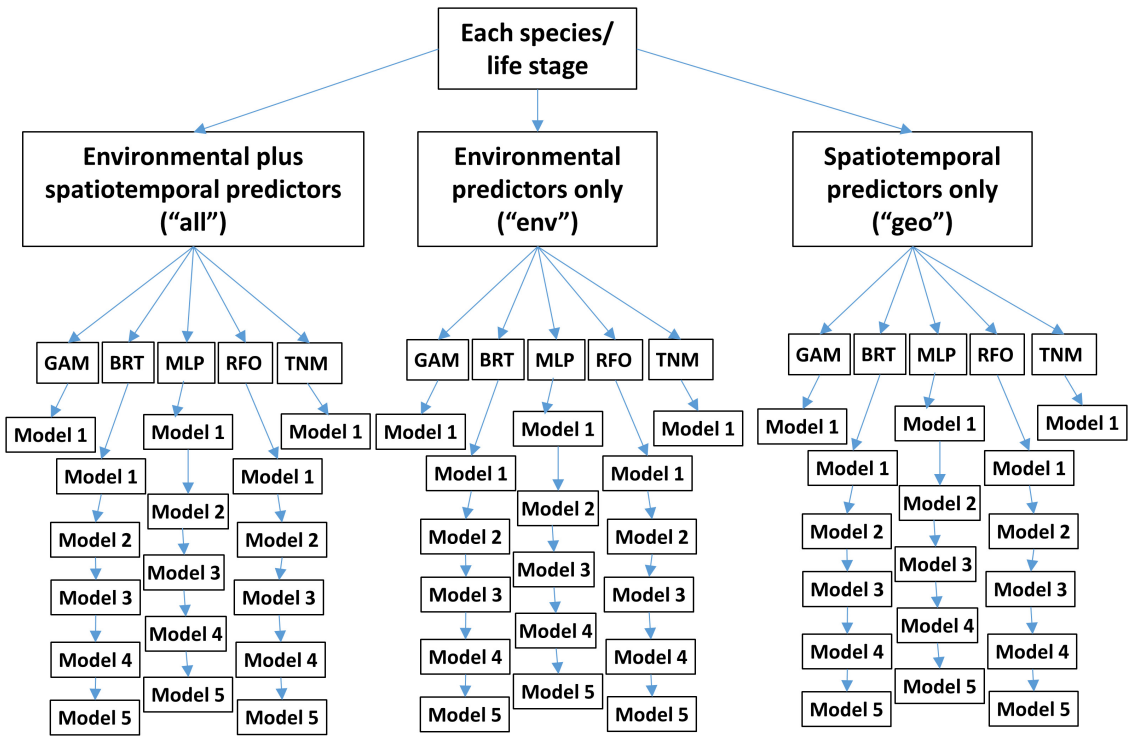

FIGURE 2 | Conceptual diagram of SDM ensembles used for each of the two modeling experiments. "GAM" denotes Generalized Additive Models, "BRT" Boosted Regression Trees, "MLP" Multilayer Perceptrons, "RFO" Random Forests, and "TNM" Thermal Niche Models. Note that these ensembles are replicated 10 times for different random splits of the training/testing data.

as optimal. Unlike the machine learning SDMs, multiple GAMs built on the same training data will be identical, and so only one GAM was built for each subset of the training data (**Figure 2**).

Multilayer Perceptron Artificial Neural Networks

Multilayer Perceptrons (MLPs) are a type of Artificial Neural Network machine learning model (Özesmi et al., 2006). We built our MLPs in the *neuralnet* package (Fritsch et al., 2019) using the resilient backpropagation with weight backtracking algorithm and a logistic activation function. MLPs were optimized by varying the number of neurons in the single hidden layer between 3 and 10. A maximum possible value of 10 was chosen as although models with >10 neurons sometimes had slightly higher skill against the testing data, they often did not converge, and required much longer computation times to build. Similarly to the BRTs, once an optimal number of neurons was chosen, five MLPs with this configuration were built for each set of the training data.

Random Forests

Random Forest models (RFOs) are also tree-based machine-learning models, but in contrast to BRTs, they use "bagging" (bootstrap aggregating) instead of sequential boosting to create model ensembles (Elith, 2019). We built our RFOs in the *randomForest* package (Liaw and Wiener, 2002), and optimized the models by varying the number of variables available for splitting at each tree node ("mtry"). This parameter was allowed to vary between a minimum of 2 and a maximum of the number of total predictors. Similarly to the BRTs and MLPs, once the best value of mtry was selected, five RFOs were built for each set of the training data.

Thermal Niche Model

Machine learning SDMs are sometimes criticized for presenting a "black box," or overly complex approach to distribution modeling (Özesmi et al., 2006; Olden et al., 2008). To examine this perspective for our region and species of interest, we also included a simple TNM in our suite of SDMs. The TNMs were GAMs including only SST as a predictor (and also latitude, longitude, and month for the "all" configuration). The number of knots (k) for SST was fixed at 3, to allow only simple parabolic relationships. Consistent with the approach to building the multivariate GAMs described above, latitude and longitude were included as a smoothed interaction term (except in the "env" configuration), with k set at the same optimal value determined for the full GAM. As with the full GAM, only one TNM was built for each subset of the training data.

RESULTS

Experiment 1: Novel Conditions

Species Distribution Model skill for years 2003–2013 was fair to good (AUCs > 0.7) for all four species/life stage combinations (**Figure 3**). Skill varied between different covariate

configurations, with those containing spatiotemporal predictors ("all" and "geo") generally outperforming environment-only SDMs ("env"). The exception was adult sardine, where distributions during this time period were generally best predicted using all available environmental and spatiotemporal predictors ("all" configuration), with the spatiotemporal-only SDMs ("geo") the least skillful and the environment-only SDMs ("env") showing intermediate skill. In contrast, larval sardine distributions during years 2003–2013 were near equally well predicted by either the "all" or "geo" SDMs, with the "env" SDMs substantially weaker. None of the three SDM configurations consistently outperformed the others for adult anchovy during the SDM training period, although the "env" TNM was particularly weak. This was also the case for sardine larvae and anchovy larvae, suggesting that simple univariate relationships with SST (i.e., the TNM) could not skillfully predict distributions of these species in 2003–2013. Larval anchovy distributions were best predicted by the "all" configuration, but most SDMs built using all three configurations showed good skill (AUCs > 0.75–0.80).

In contrast to the results for the SDM training period of 2003–2013, SDM skill for the marine heatwave years of 2014–2018 was markedly lower (**Figure 3**). AUCs were particularly low for adult sardine, being close to 0.5, or no better than a random model. The TNM for adult anchovy retained some skill, however, mean AUCs were still <0.7. In contrast to the other three species/life stage combinations, the larval anchovy SDMs did retain some skill for years 2014–2018. The "all" and "geo" models generally did the best, suggesting that this result was due to the persistence of previously observed spatiotemporal structure in larval anchovy distributions.

The observed loss of skill for years 2014–2018 was not consistent across seasons. Adult sardine and anchovy SDMs showed improved AUCs (although still <0.75 on average) for the spring period, but much lower skill during summer (**Supplementary Figure S2**). In contrast, the skill of the larval SDMs was much higher during summer than in spring. In particular, AUCs for the larval sardine BRTs, GAMs and TNMs averaged >0.75 for the "all" configurations during summer, but were generally <0.6 during spring.

The modifications to the Experiment 1 larval SDMs with a longer testing and training time period allowed the SDMs to use records from El Niño years with very warm temperatures in the early 1980s and late 1990s (**Figure 4**). However, validation skill on data from 2014 to 2018 did not change markedly for either sardine larvae or anchovy larvae depending on the testing and training years used. In fact, SDMs for both taxa showed a slight decline in validation skill when the testing and training data were extended back in time to 1997, and then to 1980.

None of the five SDM methods consistently out-performed the others across both time periods, for all species/life stage combinations (**Figures 3**, **4**). In particular, the prediction skill for the three machine learning methods was not substantially different to those from the GAMs. The skill of the simple TNM was often weaker during 2003–2013, but it was among the best SDMs for years 2014–2018 for adult sardine, adult anchovy, and larval anchovy.

Two-dimensional representations of SDM predictions were examined by binning observations and SDM predictions by SST and latitude, and averaging probabilities of occurrence within each bin. A comparison of these between the testing and validation time periods suggested some potential drivers of skill loss for the adult sardine SDMs (**Figure 5A**). During the model training time period (2003–2013), sardine were most likely to be collected where SSTs were between approximately 10 and 18°C, with somewhat higher probabilities of occurrence north of 42°N. This pattern was captured well by the SDMs. During the marine heatwave years, adult sardine were collected roughly within this same SST range in the northern study area, but patterns were much different in the south. Sardine were less likely to be collected south of 40°N at SSTs of 10–15°C than they were previously, but much more likely to be collected where SSTs were >19°C (**Figure 5A**). This shift was not captured by any of the SDMs, which all assumed very low probabilities of occurrence in these very warm conditions, in line with historical observations. This mismatch is also evident from one-dimensional partial relationships of adult sardine to SST, across all observations and SDMs (**Supplementary Figure S3**).

Two-dimensional representations of larval anchovy SDMs provide a contrast to the adult sardine SDMs (which performed the poorest on the validation dataset). Relationships between larval anchovy and SST with latitude remained much more constant between the training and validation time periods (**Figure 5B**). Larval anchovy were collected at SSTs of approximately 11–23°C throughout the time series, with two centers of abundance around 33–35°N, and 40–48°N. All of the SDMs captured these patterns well for the training years. While the SDMs were also able to predict the general patterns of distribution in the validation years, all underestimated overall probabilities of occurrence during 2014–2018, particularly at cooler SSTs < 19°C (**Figure 5B** and **Supplementary Figure S3**).

A comparison of observations and SDM predictions for two example years with relatively good sampling coverage (2008 and 2015) showed the contrasting responses of both species and life stages to the marine heatwave. Distributions of both adult and larval sardine appeared to move northward during spring 2015 (**Figure 6A**), although sampling coverage was not as comprehensive as in 2008. In 2008, both adult and larval sardine were concentrated south of 40°N during April and May, coinciding with areas of highest predicted probability from all of the SDMs. In 2015, adult sardine were not common in the trawl surveys, due to their low spawning stock biomass, but those that were present were located between 38 and 44°N. While the SDMs also predicted a northward shift in habitat, these predictions did not align exactly with observations, particularly for the GAMs and MLPs. Similarly, predictions from the larval sardine SDMs suggested a northward shift, but models underestimated the extent of the observed change in larval distributions (**Figure 6A**). The GAMs and MLPs did show some favorable habitat between 40 and 45°N, where larvae were collected, but also showed favorable habitat off southern California, where sampling collected very few larvae.

In contrast to sardine, adult and larval anchovy did not show strong northward shifts during summer 2015 (**Figure 6B**). Adult

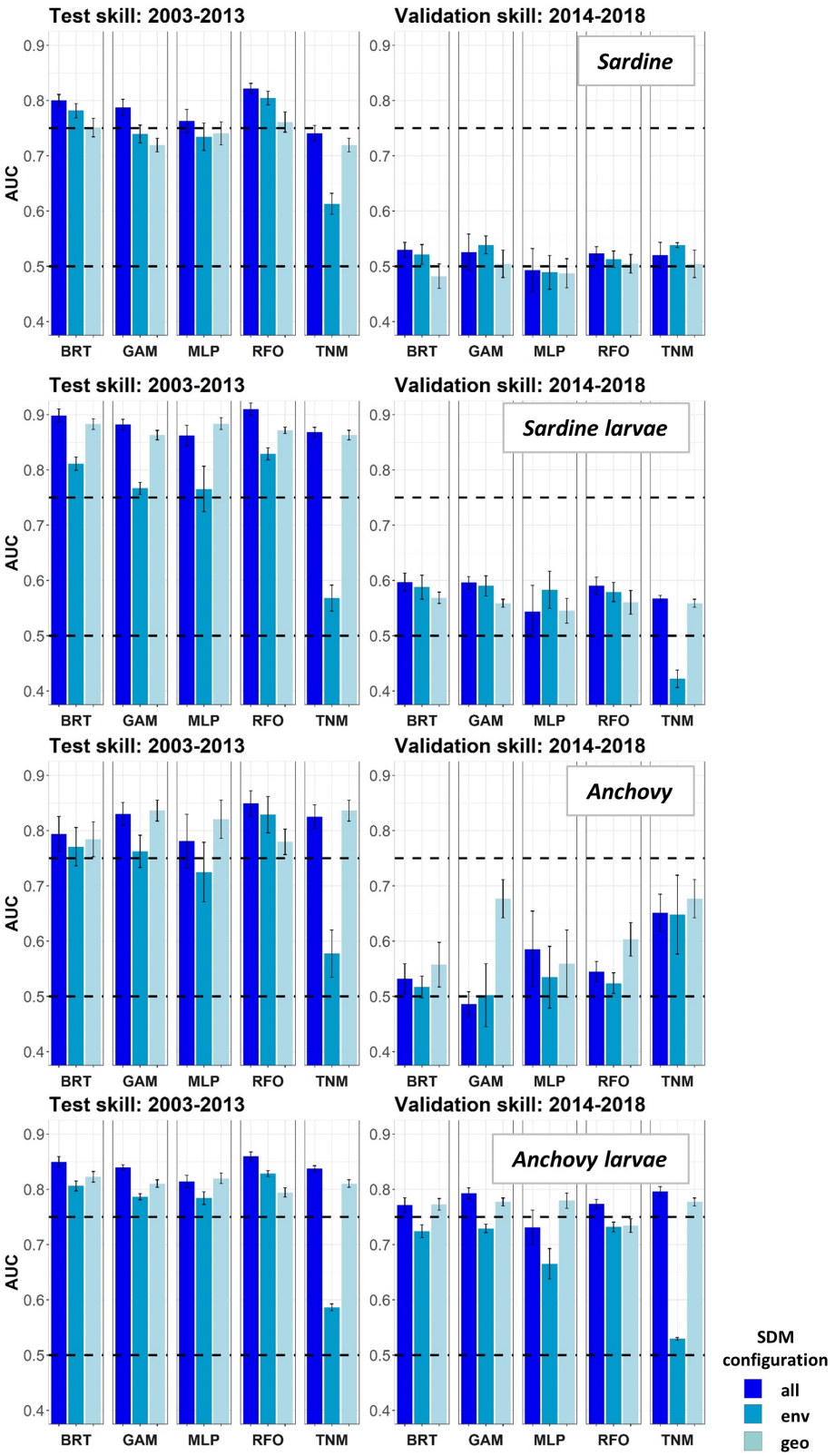

FIGURE 3 | Area Under the Receiver Operating Curve (AUC) skill metrics for Experiment 1 SDMs. Means and standard deviations across all SDM ensembles (see **Figure 1**) are shown for each life stage of each species. Colors of bars denote the SDM configuration ("all," "env," or "geo"). The horizontal black dashed lines show AUC values of 0.5 (no better than a random model), and 0.75 (a rough approximation of a "useful" model), for reference.

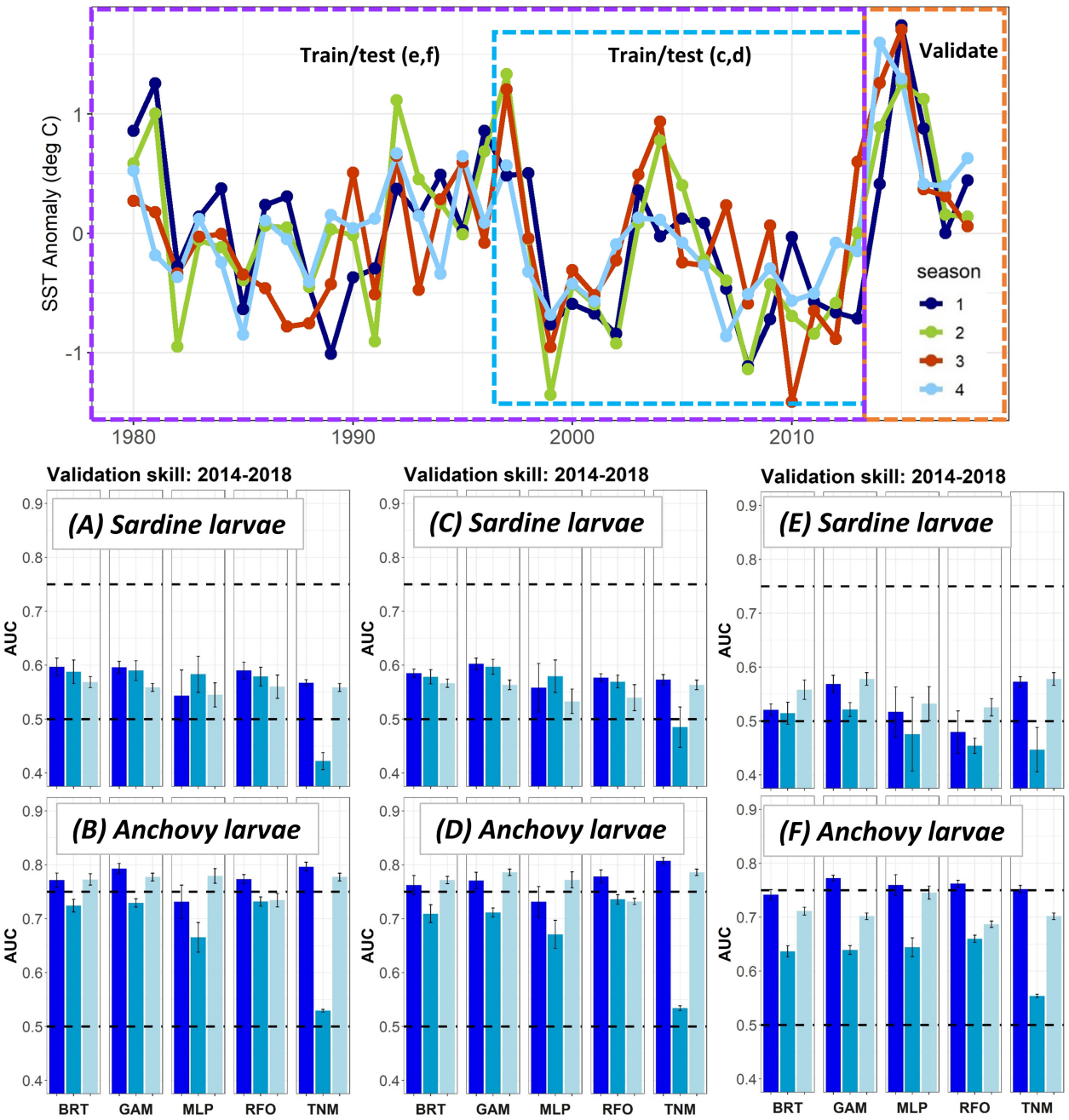

FIGURE 4 | SST anomalies averaged across the ROMS domain from 1980 to 2018 **(top)**, and validation AUCs for years 2014–2018 for larval sardine and larval anchovy SDMs trained using data from **(A,B)** 2003–2013 (i.e., Experiment 1), **(C,D)** 1997–2013, **(E,F)** 1980–2013. Means and standard deviations across all SDM ensembles (see **Figure 1**) are shown for each life stage of each species. Colors of bars denote the SDM configuration ("all," "env," or "geo"). The horizontal black dashed lines show AUC values of 0.5 (no better than a random model), and 0.75 (a rough approximation of a "useful" model), for reference.

anchovy were present between 37 and 48°N during July and August of both 2008 and 2015. This was captured better by the GAMs than the other SDMs for these particular years. Although larval sampling coverage differed between the years, the two centers of larval anchovy abundance appeared to persist during both 2008 and 2015 (**Figure 6B**). This persistence occurred despite strongly contrasting environmental conditions between the 2 years (**Figure 1**). However, while SST was moderately important to the larval anchovy SDMs, it was less influential than latitude and longitude (**Supplementary Figure S4**). SST was also not a strong contributor to the adult anchovy SDMs. Anchovy thus appeared more likely to maintain their historical spatiotemporal distribution patterns than sardine, partially due to weaker relationships with SST.

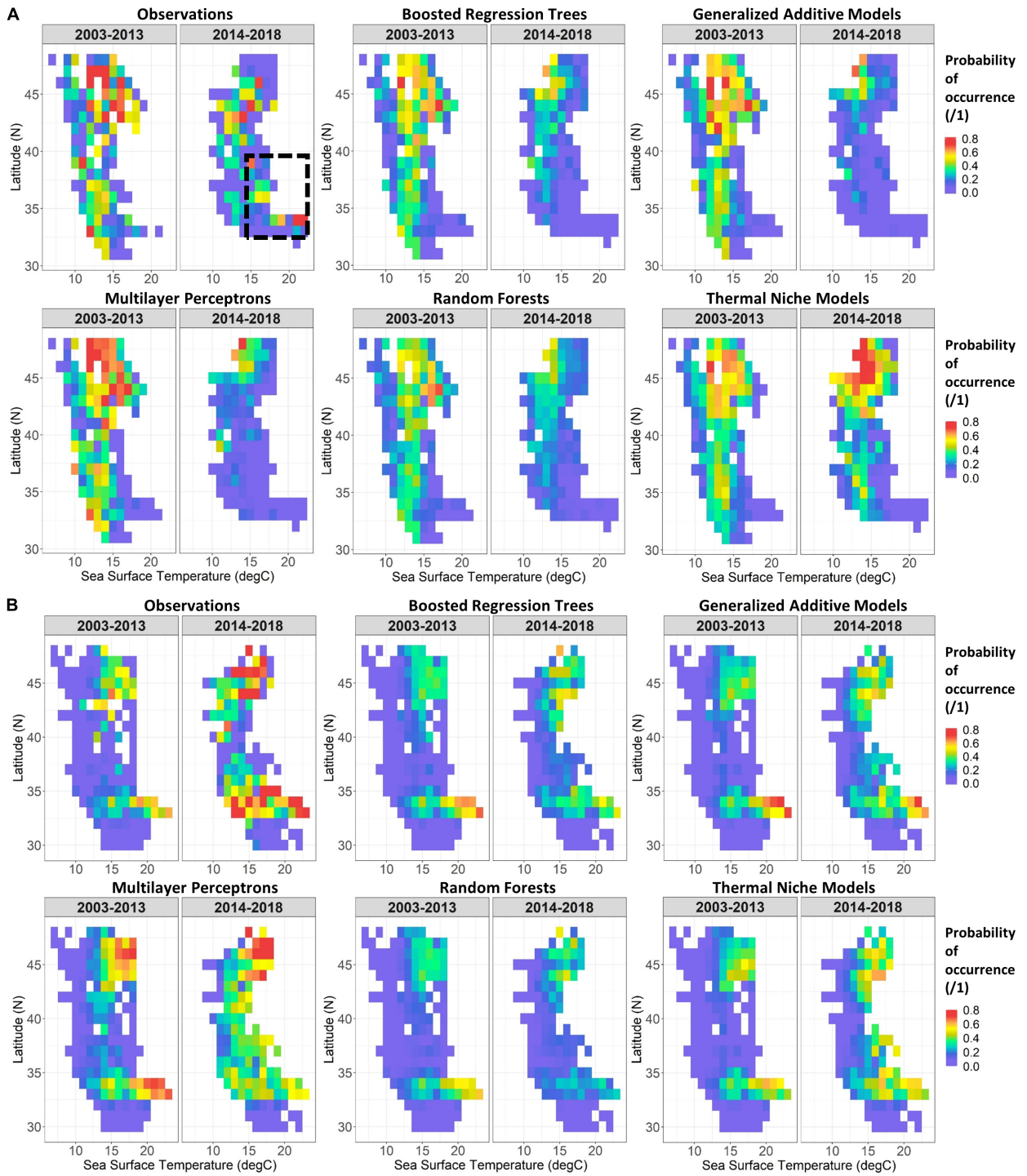

FIGURE 5 | Two-dimensional partial responses of Experiment 1 SDMs for adult sardine **(A)** and anchovy larvae **(B)** against SST and latitude, integrated across all other predictors. Predictions from the five SDM types are shown, as well as a summary of observations (mean probabilities of occurrence within 1° SST and latitude bins) for years 2003–2013 (left) and 2014–2018 (right). The black dash box in **(A)** draws attention to sardine observations from 2014 to 2018 which were poorly predicted by the SDMs.

The maps in **Figures 6A,B** suggested that the SDMs often captured some aspects of distribution patterns, but that predictions were not precisely aligned with observations. To test the effect of spatial resolution on SDM skill, we thus aggregated all predictions and observations to 2 × 2°, taking the maximum value of each within each cell. AUCs increased

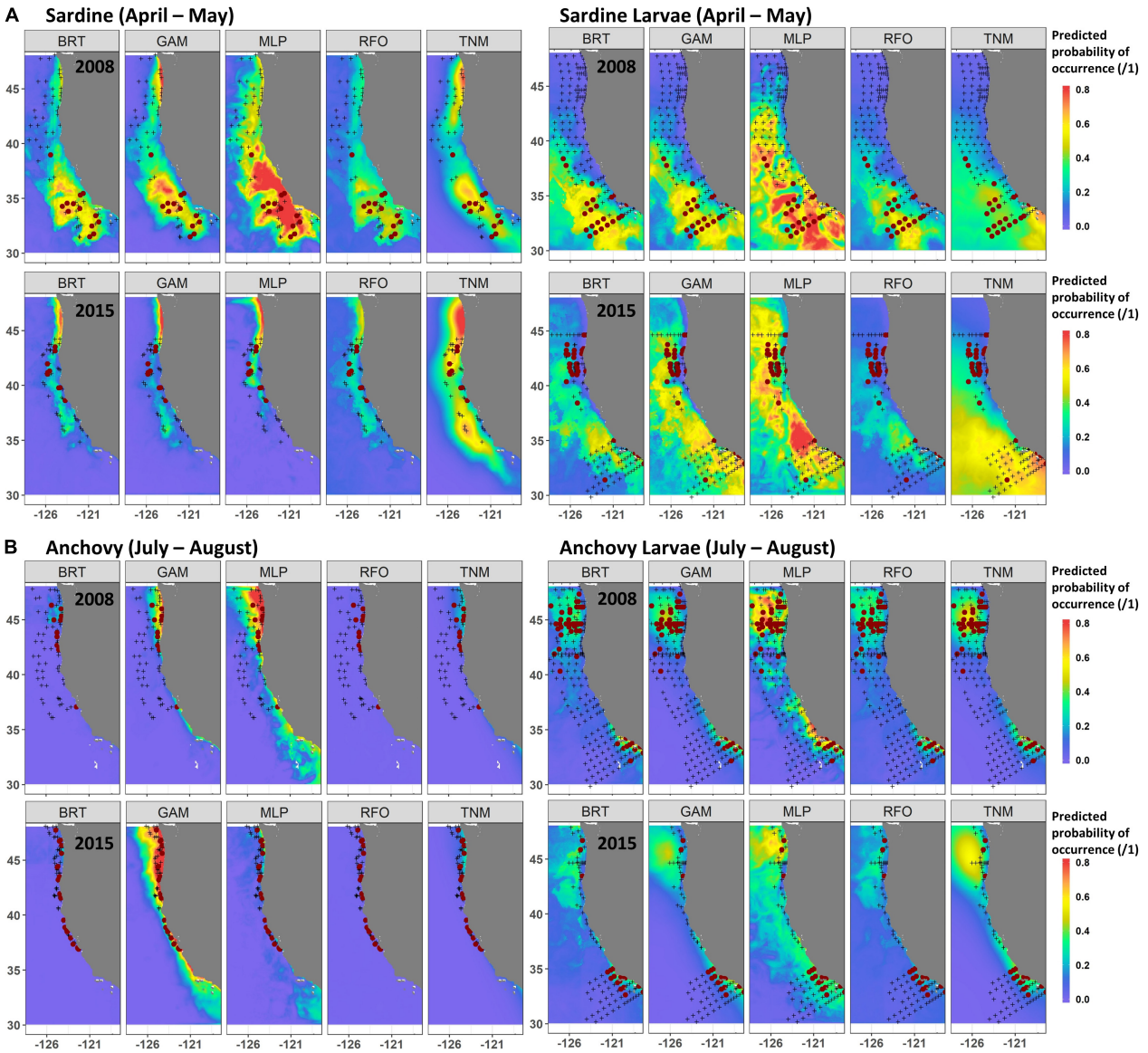

FIGURE 6 | Predicted and observed distributions of sardine and sardine larvae during April–May **(A)**, and anchovy and anchovy larvae during July–August **(B)**, for two examples years. SDM predictions are a mean across Experiment 1 SDM ensembles (see **Figure 2**). Observed presences are shown in maroon dots, observed absences by black crosses.

to >0.75 on average for most of the BRTs, GAMs, RFOs, and TNMs for sardine larvae, for the adult anchovy TNMs, and for the "env" GAMs and TNMs for adult sardine using these spatial coarsened data, but remained <0.75 for all other models (results not shown). Collapsing observed and predicted probabilities of occurrence even further, down to means within 2° latitudinal blocks, showed that SDMs were more successful at capturing the general direction of change than the magnitude of change (**Figure 7**). For example, both the adult and larval sardine SDMs captured the tendency for there to be more sardine in the northern CCS and less in the south during spring, but under-predicted the scales of these shifts. In contrast, the adult anchovy GAMs and MLPs correctly predicted an increase in overall probabilities of occurrence but were unable to reproduce the spatial patterns of these increases. The larval anchovy SDMs correctly predicted the spatial persistence of the two main spawning locations in 2014–2018 and the increase in probabilities of occurrence in the northern CCS (**Figures 6B**, **7**). However, the models were not able to predict the observed increases in probabilities of larval anchovy occurrence in the southern CCS.

Sampling coverage during the model training time period (2003–2013) was generally more spatially extensive and covered more negative habitat than during the validation period (2014–2018), a trend evident in **Figures 6A,B**. To assess the potential impact of this difference on 2014–2018 AUCs, we re-scored data from these years with some "dummy" negative stations

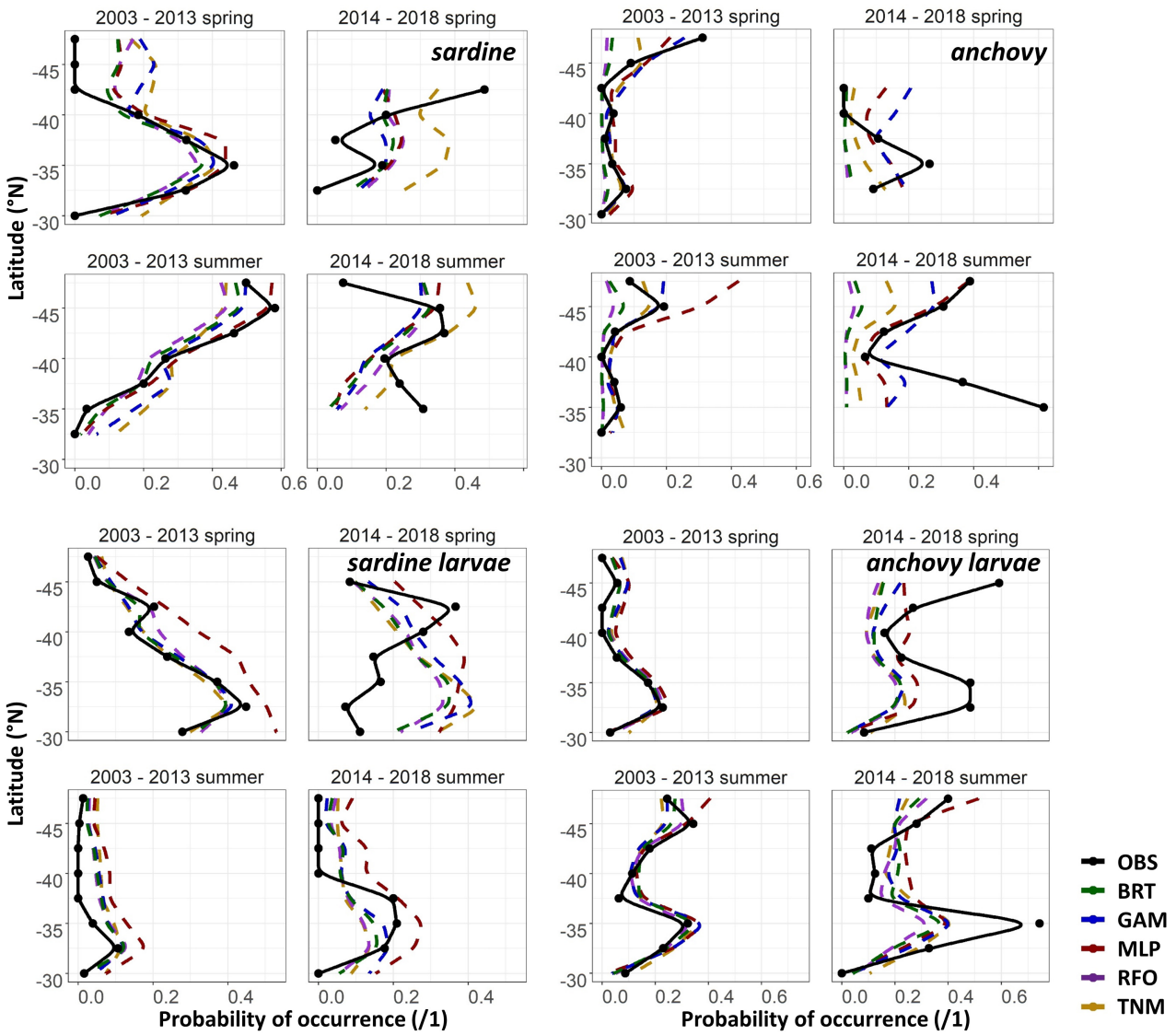

FIGURE 7 | Mean observed (black) and SDM predicted (colors) probabilities of occurrence of each life stage of each species in spring (April–May) and summer (July–August) by 2° latitude bins, for the test (2003–2013) and validation (2014–2018) time periods for Experiment 1.

added. These negative stations were located at aggregated 1 × 1° locations sampled only during 2003–2013 but not 2014–2018, and where no sardine or anchovy were recorded during the earlier period. Dummy negative stations were calculated and added separately for the trawl and larval datasets, with one station each added for each location in each year (2014–2018) at the end of April, and the end of July, to capture the two best sampled seasons. Environmental data were extracted at these new locations, and re-scored through the SDMs. AUCs for this new dataset including dummy negative stations were generally higher than for the original data (**Supplementary Figure S5**). This improvement was more marked for adult sardine and anchovy than for larvae, suggesting that lower and more inshore spatial coverage in trawl surveys in recent years may have led to lower AUCs for these life stages. However, the general patterns of skill loss remained consistent, with adult SDMs retaining better skill in spring versus summer, and larval SDMs retaining more skill during summer.

Experiment 2: Near-Average Conditions

Area Under the Receiver Operating Curves for validation years were generally higher in Experiment 2 than for the same taxa and SDMs in Experiment 1 (**Figure 8**). This result suggested that SDM predictions were more successful in unseen years if the training data covered a more complete range of environmental conditions and/or stock sizes. In particular, larval sardine distributions were well predicted for 2003–2007, in contrast to the strong loss of skill in Experiment 1. The most skillful SDM configurations for larval sardine were "all" and "geo," suggesting that this skill resulted from SDMs being better able to capture spatiotemporal structure

in distributions. Experiment 2 AUCs for withheld validation years also improved for adult sardine and adult anchovy, but mostly remained <0.75. Notably, the adult anchovy SDMs were the only ones to lose substantial skill between the test and validation time periods in Experiment 2. This was partially due to the comparative rarity of anchovy in these earlier years, a result of lower spawning stock biomass and less trawl sampling during summer. Anchovy larvae AUCs for Experiment 2 were slightly weaker than for Experiment 1, but still remained fair to good for all SDMs except for the "env" TNM. These results indicate that the SDMs were largely capable of retaining reasonable skill for years not included in the model training and testing process. The marked loss of skill observed for validation years in Experiment 1 may therefore have resulted mostly from the novel environmental conditions and unexpected species responses to those conditions, rather than SDM overfitting.

To provide a "best case" model comparison against results from Experiments 1 and 2, we lastly re-trained the SDMs using all available data from 2003 to 2018 (50% each for model training and testing, no data withheld for external validation). A comparison of mean AUC by year and SDM type suggested that the RFOs and BRTs were mostly able to maintain good predictive skill throughout the entire time series, as long as they were initially trained on data including observations from the marine heatwave years, and observations across a range of stock sizes (**Figure 9**). The MLPs, GAMs, and TNMs also showed useful skill in some years for most taxa, but usually performed less skillfully than the BRTs and RFOs, implying that the tree-based SDMs were best able to capture the complex responses of our species to their environment across different environmental regimes. Results from all sets of SDMs together thus indicate that although some of the machine-learning SDMs were flexible enough to maintain reasonable skill both before and during the marine heatwave, most could only do so if they had access to observations from heatwave years during the model training process. Otherwise, the models had no way to anticipate the non-stationary responses of species to anomalously warm temperatures, and lost much of their predictive skill.

DISCUSSION

Our results show that most SDMs lost substantial predictive skill during novel environmental conditions experienced during the recent marine heatwave, regardless of the type of model or the suite of covariates used. However, performance differed among species and life stages. There was no single best type of SDM, although including spatial variables was generally useful. We note that global statistical performance may not always completely represent model value, as some SDMs could capture the general spatial direction of change, even if they could not replicate the observed magnitude.

Importance of Robust SDM Validation

Loss of SDM skill on out-of-model validation datasets is not uncommon, and can be broadly attributed to four issues: (1) model overfitting during training (Elith, 2019), (2) unreasonable model behavior during extrapolation (Hannemann et al., 2015; Beaumont et al., 2016), (3) the selection of irrelevant predictors which do not impact distribution (Steen et al., 2017), and (4) non-stationarity in relationships between a species and its environment (Dormann et al., 2012; Yates et al., 2018). Some degree of over-fitting to the training data may be expected with the more flexible machine learning SDMs used in this study (i.e., BRTs, MLPs, RFOs). However, it was notable that (with the exception of adult anchovy), the GAMs and TNMs showed similarly poor skill to the more complex SDMs for the validation time period. The primary driver of skill loss for years 2014–2018 is thus unlikely to be simply a problem of overfitting in the more complex models. Similarly, the extrapolation behavior of the SDMs to anomalously warm temperatures did not appear to be biologically unreasonable. For example, adult sardine were most commonly collected at SSTs between 9 and 18°C in the Southern California Bight between 2003 and 2013. The SDMs all predicted that this pattern would continue during 2014–2018, and all predicted low probabilities of occurrence where SSTs were warmer than 18°C. In contrast, observations showed that adult sardine were collected with relatively high occurrence in these southern locations, in waters as warm as 21.7°C. These very warm temperatures were rarely sampled between 2003 and 2013.

The third and fourth issues identified above are likely more relevant to our results. Statistical relationships between our species and their environment changed between the model training and validation time periods, particularly for adult sardine. While the relative importance of each predictor to the SDMs frequently varied across model type, all SDMs tended to show similar skill loss during 2014–2018. This suggests that none of the SDMs successfully captured the true drivers of spatial distribution for sardine and anchovy in our study region. The exception was larval anchovy, where the SDMs successfully predicted that the main distribution drivers were environmentally invariant geospatial predictors. However, we note that aggregating observations and predictions to a coarser spatial resolution improved the validation skill of some SDMs to more acceptable levels, and did qualitatively capture the northward shifts in adult and larval sardine distributions during the marine heatwave years. The spatial contraction of sampling effort in recent years may also have led to some relative loss of skill from reduced sampling in strongly negative habitats. In addition, breaking results down by season showed that the larval sardine SDMs performed better during summer, while the adult SDMs showed some improvement in skill during spring. These results suggest that better understanding of spatial processes and spawning phenology should allow the development of more reasonable predictive models in the future.

Our results highlight another important recommendation for the prediction of species distributions, which is the need to validate SDM predictions on an entirely withheld dataset. Results from Experiment 2 show that even when the validation dataset does not include previous unobserved values for environmental predictors (e.g., very warm SSTs), some loss of predictive skill is still possible for some taxa. However, Experiment 2 SDMs (validated against near-average conditions) generally maintained much better skill than those built under Experiment

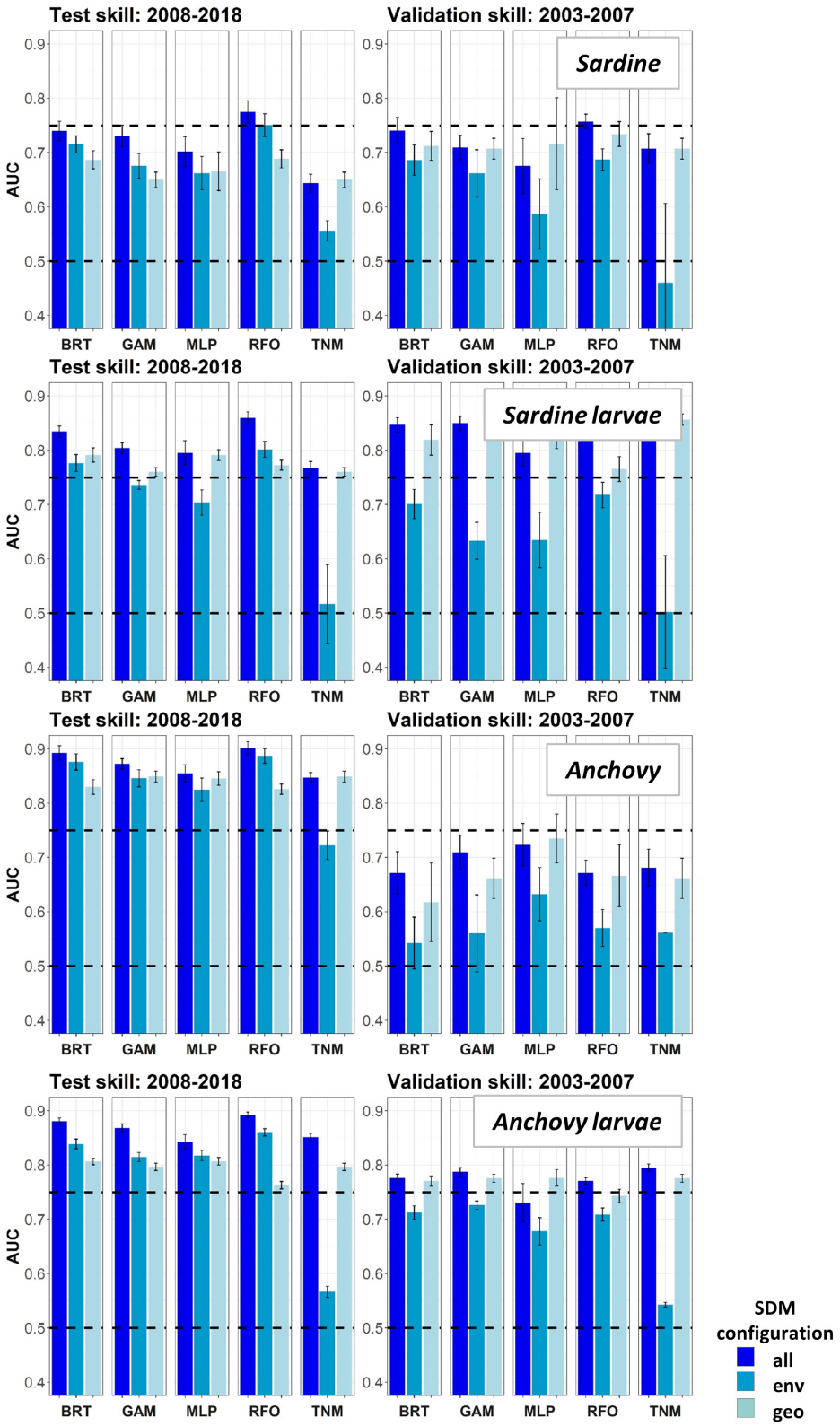

FIGURE 8 | Area Under the Receiver Operating Curve (AUC) skill metrics for Experiment 2 SDMs. Means and standard deviations across all SDM ensembles (see **Figure 1**) are shown for each life stage of each species. Colors of bars denote the SDM configuration ("all," "env," or "geo"). The horizontal black dashed lines show AUC values of 0.5 (no better than a random model), and 0.75 (a rough approximation of a "useful" model), for reference.

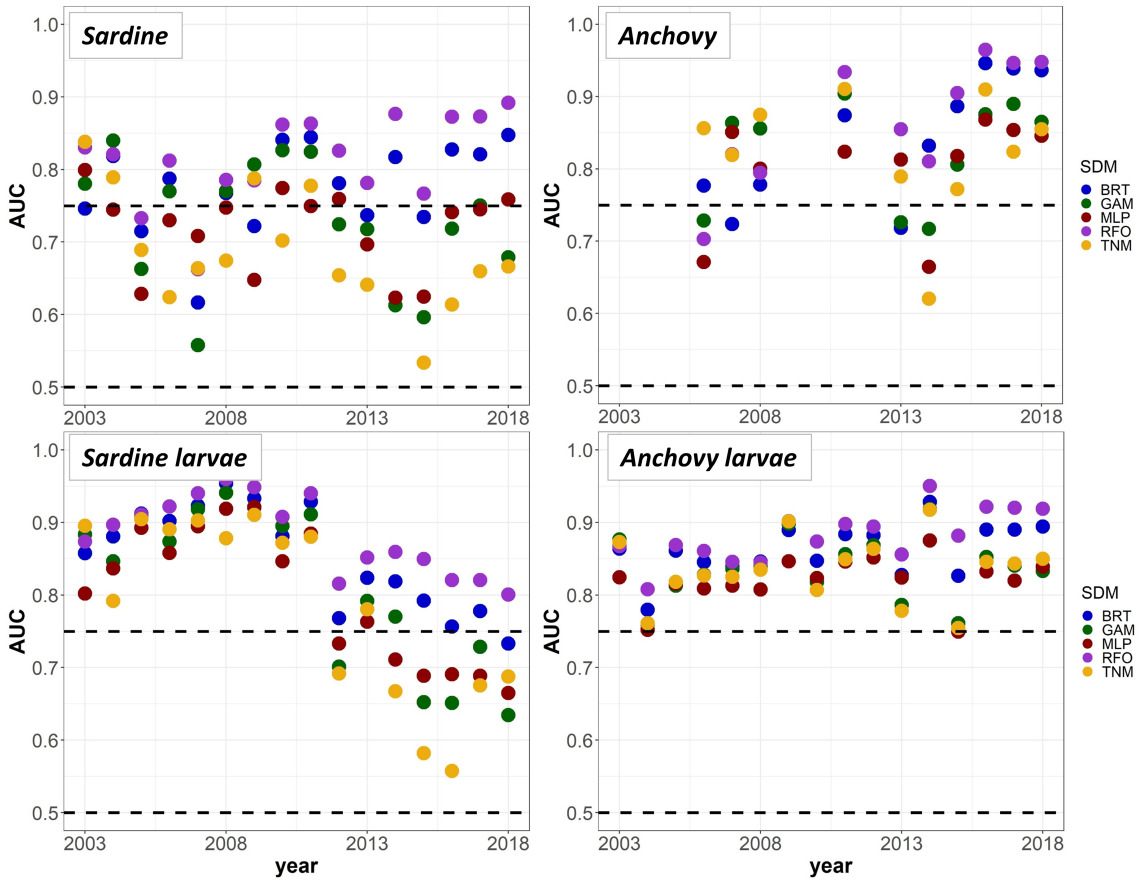

FIGURE 9 | Mean Area Under the Receiver Operating Curve (AUC) test skill metrics for SDMs trained on random 50% splits of all available data from 2003 to 2018, for the "all" covariate configuration only. Colors denote the SDM type. The horizontal black dashed lines show AUC values of 0.5 (no better than a random model), and 0.75 (a rough approximation of a "useful" model), for reference.

1 (validated against novel conditions). If there are sufficient observations, the splitting of data into a model training, testing, and external validation set should be standard practice for properly assessing model skill, particularly for the highly flexible machine learning SDMs (Özesmi et al., 2006). This is particularly important if SDMs are to be transferrable to times, locations, or environmental conditions not included within the training data.

Influence of Species Ecology on SDM Performance

Environmental associations of sardine and anchovy in the CCS have been closely studied for more than 50 years (e.g., Lasker and Smith, 1977; Fiedler et al., 1986; Lindegren et al., 2013; Gallo et al., 2019). Extensive previous research suggests that both species have distinct temperature preferences, especially during spawning (Lluch-Belda et al., 1991; Green-Ruiz and Hinojosa-Corona, 1997; Zwolinski et al., 2011; Weber et al., 2018). We may therefore have reasonably expected that both species would respond in a predictable way during the unusual environmental conditions observed in recent years. However, although our results qualitatively captured some of the phenological shifts in spawning recorded by previous studies (e.g., McClatchie et al., 2016; Auth et al., 2018), our SDMs showed a substantial loss of predictive skill across both species and life stages for years 2014–2018, with the exception of larval anchovy.

Relationships between adult sardine and the ocean environment appeared to be especially non-stationary. In particular, none of the SDMs predicted the occurrence of sardine in warm (>18°C) waters during 2014–2018. This observation may be partially due to the increased incursion of adult sardine from the southern sub-stock into United States waters. The current stock assessment uses a SST cutoff rule, where sardine caught at < = 16.7°C are assumed to be from the northern sub-stock and those caught at >16.7°C from the southern sub-stock (Félix-Uraga et al., 2004; García-Morales et al., 2012; Demer and Zwolinski, 2014; Hill et al., 2019). However, re-training and re-validating the adult sardine SDMs only on observations where SST was <16.7°C, to remove the influence of the southern sub-stock, did not improve model validation skill, with all AUCs for 2014–2018 remaining <0.6 (results not shown). Thus, although the low historical sampling coverage in waters warmer than 20°C may have limited the ability of the SDMs to predict to these novel conditions in 2014–2018, relationships between

sardine and their environment also changed substantially during the heatwave years even within cooler temperatures. In addition, re-training the larval sardine SDMs using data back to 1980 did not result in more skillful predictions in 2014–2018. These results suggest that distribution patterns and environmental associations for early life stages of sardine during the marine heatwave were unprecedented over the 38 years where larval data were available, despite several strong El Niño events occurring during this timeframe.

In contrast to the other species/life stage combinations, adult sardine SDM skill for both Experiment 2 and for the full models trained on years 2003–2018 mostly remained fair to poor. This result suggests that even when sardine SDMs were able to use observations from the marine heatwave years, they struggled to usefully generalize relationships between this species and its environment. This issue may partially stem from sardine migratory behavior. When biomass is high, the two sardine sub-stocks migrate seasonally. The northern sub-stock moves between southern California in winter and the Pacific Northwest in summer, while the southern sub-stock reaches southern California during summer and returns to coastal Baja California in winter (Lo et al., 2011; Demer et al., 2012). The two sub-stocks thus overlap strongly in space but much less so in time, giving the appearance of largely separate temperature habitats between the two groups. However, laboratory studies show that sardine larvae and adults from both sub-stocks can tolerate very similar, and broad ($\sim$ 9–27°C), thermal ranges if given the opportunity to acclimate (Lasker, 1964; Brewer, 1976; Martínez-Porchas et al., 2009; Pribyl et al., 2016). The strong importance of SST to the sardine SDMs (**Supplementary Figure S4**) is thus unlikely to represent a purely physiological constraint. Previous studies have also found relationships between sardine and temperature to be complex. For example, McClatchie et al. (2010) showed that a long-standing SST-recruitment relationship for sardine was non-stationary through time, and had reduced predictive skill when applied to more recent data.

During the anomalous conditions of the marine heatwave, adult sardine may also have changed their migration and spawning phenology in response to conditions experienced weeks or months before sampling, leading to observed distribution shifts that did not follow historical environmental associations (see **Figure 5A**). As older, mature sardine comprise the bulk of the migrant population (Lo et al., 2011; McDaniel et al., 2016), the poor prediction skill during the marine heatwave period may also have been associated with changes in sardine age structure. The 2015–2018 sardine population was not only low in abundance, but trawl acoustic survey data showed younger age classes dominating the age composition (Hill et al., 2019). Younger fish may not have migrated as far north during these years, which may have contributed to the observed latitudinal mismatch between observations and SDM predictions for sardine.

The only species and life stage to retain good skill during the marine heatwave years was larval anchovy. However, this skill derived mostly from the inclusion of geospatial predictors in the SDMs, suggesting that anchovy spawning did not shift markedly in space or time in recent years. This was confirmed by the map comparisons in **Figure 6B**, showing the spatial persistence of two spawning areas for anchovy in summer during a near-average year (2008) and a heatwave year (2015). This was an unexpected result, as including fixed geospatial predictors in SDMs should theoretically reduce their usefulness for extrapolating to novel environmental conditions. However, previous studies have shown that anchovy in the northern CCS can be associated with the Columbia River plume during warmer months (Emmett et al., 2005; Litz et al., 2008). Spawning anchovy may therefore have maintained their association with this oceanographic feature during the heatwave years, despite the presence of anomalously warm temperatures.

Although the spatial structure of anchovy spawning activity persisted during the marine heatwave, their ability to maintain historical spawning areas under future warming is not clear (e.g., Howard et al., 2020). Climate change is expected to result in mean upper ocean temperature increases of 2–4°C in the CCS by 2100 under the RCP8.5 "business as usual" scenario, with future marine heatwaves leading to even higher SST extremes (Woodworth-Jefcoats et al., 2017; Alexander et al., 2018). While SDMs including geospatial predictors often did better for the marine heatwave test case described in this study, it is probably not reasonable to assume that these relationships will continue to hold decades into the future. Our results therefore highlight the ongoing need for improved mechanistic understanding of movement and distribution drivers for sardine and anchovy in the CCS, if climate change impacts on these species are to be realistically predicted over longer time horizons.

The difficulties inherent to predicting the distributions of migratory species with broad physiological tolerances are also apparent from our results, and have been described for other species previously (e.g., Dambach and Rödder, 2011; Yates et al., 2018). Sardine migratory behavior depends on population size, sub-stock structure, and age composition (Lluch-Belda et al., 1986; Demer et al., 2012; McDaniel et al., 2016). As a result, the presence or absence of sardine and their larvae in the CCS may depend partially on environmental conditions at the time of sampling, and partially on environmental and population drivers of migration and spawning condition earlier in the season. In addition, the same environmental conditions which cause shifts in suitable habitats can also impact recruitment and biomass, which are themselves linked to migration and distribution patterns. During the marine heatwave years, sardine biomass declined to very low levels while anchovy biomass increased sharply (Harvey et al., 2019; Hill et al., 2019). As a result, both environmental conditions and stock biomass for both species during 2014–2018 were outside the ranges of the training period. A combination of both factors, and interactions between them, likely contributed to loss of SDM skill. This is a central problem with using SDMs to predict or project species distributions into the future: it is often more straightforward to anticipate shifts in potential environmental niches than it is to model the complex relationships between stock productivity, movements, and realized habitat use (e.g., Koenigstein et al., 2016).

Other complex factors can drive decoupling of species distributions from their immediate environment, including the persistence of anomalous range extensions even after environmental conditions have returned to normal [e.g., bottlenose dolphin (*Tursiops truncatus*) off central California: Wells et al., 1990]. Migratory schooling animals may also show inertia in their behaviors deriving from collective memory (Macdonald et al., 2018), or from interactions between environmentally invariant and environmentally responsive movement behaviors (Bauer et al., 2011; Winkler et al., 2014). Taken together, these considerations suggest that caution is required when attempting to use statistical SDMs for future projections of pelagic species habitats. It is worth noting that a similar study predicting marine mammal distributions in the CCS during the 2014–2016 marine heatwave showed higher model skill than we describe here (Becker et al., 2018). Correlative SDMs may therefore still have use for certain climate prediction problems within some ecosystems. Progression toward more mechanistically informed distribution models which incorporate processes such as metabolism, energy budgets, foraging ecology, and migratory behavior can alleviate some of the drawbacks of statistical SDMs (e.g., Lehodey et al., 2008; Planque et al., 2011; Deutsch et al., 2015; Fiechter et al., 2015; Rose et al., 2015; Koenigstein et al., 2016; Howard et al., 2020). However, a sound understanding of physiological drivers across different species is required before the best modeling framework can be identified (Yates et al., 2018), and there are insufficient data available on these processes for many marine taxa.

Conclusion and Recommendations

Overall, our results suggest that statistical relationships defined in correlative SDMs can break down when confronted with novel environmental conditions. This loss of skill was relatively consistent across the five SDMs examined, despite strong differences in model complexity. While a lack of transferability of SDMs in time or space can result from multiple mechanisms (Yates et al., 2018), in our case, the non-stationary responses of our two test species to changes in their ocean environment were particularly influential. Whether the rate of change of the environment contributed to this non-stationarity is unclear (heatwaves represent sudden anomalous change), and validation of long time series would be a valuable test of longer term non-stationarity. Although sardine and anchovy are well-studied forage species in the CCS, their complex environmental associations and behaviors challenged our ability to effectively model their distributions across different oceanographic regimes. Our results thus show the importance of understanding the mechanistic drivers of range shifts in marine species, and the difficulties intrinsic to modeling the distributions of mobile, migratory animals.

We recommend that future work explores methods for including migration and spawning phenology in SDMs for sardine and anchovy in the CCS, for example via correlative SDMs which include spatially remote or time-lagged processes (Thorson et al., 2020), further development of mechanistic models (e.g., Rose et al., 2015), or exploration of hybrid correlative-mechanistic approaches. Development of distribution models by age group, or use of a measure of age composition as an additional covariate may also be beneficial for sardine SDMs. Consistent sampling across a wider range of thermal environments may also allow better definition of potential versus realized habitats for both species. Ultimately, if the SDMs described in this study can be improved to better represent the underlying processes driving distribution shifts in sardine and anchovy, they will be more useful for anticipating the potential impacts of climate change and anomalous environmental events on the future assessment and management of these species, and on the broader CCS.

DATA AVAILABILITY STATEMENT

The CalCOFI larval fish observations are available at: https://coastwatch.pfeg.noaa.gov/erddap/tabledap/erdCalCOFIlrvcntEDtoEU.html and https://coastwatch.pfeg.noaa.gov/erddap/tabledap/erdCalCOFIlrvcntQtoSA.html, while the adult trawl survey data are available at: https://coastwatch.pfeg.noaa.gov/erddap/tabledap/FRDCPSTrawlLHHaulCatch.html. Chlorophyll re-analysis fields are also on the Coastwatch ERDDAP server at: https://coastwatch.pfeg.noaa.gov/erddap/griddap/pmlEsaCCI42OceanColor8Day.html. Northern CCS larval survey data are available upon request from author T.D.A. ROMS environmental fields are available upon request by contacting the corresponding author.

AUTHOR CONTRIBUTIONS

BM, SB, JS, DT, EH, and MJ conceived and designed the study. RB, TA, and CG contributed to data and essential background for the work. BM, SB, JS, CG, DT, EH, MJ, RB, and TA wrote and reviewed the manuscript. BM conducted the statistical analyses and prepared the manuscript figures. All authors contributed to the article and approved the submitted version.

FUNDING

The authors would like to acknowledge NOAA's Fisheries and the Environment (FATE) program and Coastal and Ocean Climate Applications (COCA) program for funding portions of this work, including the Future Seas project (grant number NA17OAR4310268) and ongoing data collections in the region.

ACKNOWLEDGMENTS

We thank the vessels, scientists and crews involved in collecting the biological observations central to this study, as well as Y. Gu and B. Macewicz for data provision. J. Zwolinski, A. Thompson, W. Watson, and Y. Gu provided helpful comments and guidance on data and earlier manuscript drafts. This research was first developed as part of a North Pacific Marine Science Organization (PICES) workshop on "Application of Machine

Learning to Ecosystem Change Issues in the North Pacific" convened by C. Hannah, C. Werner, H. Hasumi, and M. St. John in Victoria, BC, Canada October 2019. We also thank the two peer-reviewers for providing helpful feedback which substantially improved the manuscript.

SUPPLEMENTARY MATERIAL

The Supplementary Material for this article can be found online at: https://www.frontiersin.org/articles/10.3389/fmars.2020.00589/full#supplementary-material

REFERENCES

Alexander, M. A., Scott, J. D., Friedland, K. D., Mills, K. E., Nye, J. A., Pershing, A. J., et al. (2018). Projected sea surface temperatures over the 21st century: changes in the mean, variability and extremes for large marine ecosystem regions of Northern Oceans. *Elementa* 6:9. doi: 10.1525/elementa.191

Asch, R. G. (2015). Climate change and decadal shifts in the phenology of larval fishes in the California current ecosystem. *Proc. Natl. Acad. Sci. U.S.A.* 112, E4065–E4074.

Asch, R. G., and Checkley, D. M. Jr. (2013). Dynamic height: a key variable for identifying the spawning habitat of small pelagic fishes. *Deep Sea Res. Part I* 71, 79–91. doi: 10.1016/j.dsr.2012.08.006

Auth, T. D., Brodeur, R. D., and Peterson, J. O. (2015). Anomalous ichthyoplankton distributions and concentrations in the northern California current during the 2010 El Niño and La Niña events. *Prog. Oceanogr.* 137, 103–120. doi: 10.1016/j.pocean.2015.05.025

Auth, T. D., Daly, E. A., Brodeur, R. D., and Fisher, J. L. (2018). Phenological and distributional shifts in ichthyoplankton associated with recent warming in the northeast Pacific Ocean. *Global Change Biol.* 24, 259–272. doi: 10.1111/gcb.13872

Bauer, S., Nolet, B. A., Giske, J., Chapman, J. W., Åkesson, S., Hedenström, A., et al. (2011). "Cues and decision rules in animal migration," in *Animal Migrations: A Synthesis*, eds E. J. Milner-Gulland, J. M. Fryxell, and A. R. E. Sinclair, Chap. 6 (New York: Oxford University Press Inc.), 68–87. doi: 10.1093/acprof:oso/9780199568994.003.0006

Baumgartner, T. R. (1992). Reconstruction of the history of the Pacific sardine and northern anchovy populations over the past two millenia from sediments of the Santa Barbara basin, California. *Calif. Coop. Oceanic Fish. Invest. Rep.* 33, 24–40.

Beaumont, L. J., Graham, E., Duursma, D. E., Wilson, P. D., Cabrelli, A., Baumgartner, J. B., et al. (2016). Which species distribution models are more (or less) likely to project broad-scale, climate-induced shifts in species ranges? *Ecol. Modelling* 342, 135–146. doi: 10.1016/j.ecolmodel.2016.10.004

Becker, E. A., Forney, K. A., Redfern, J. V., Barlow, J., Jacox, M. G., Roberts, J. J., et al. (2018). Predicting cetacean abundance and distribution in a changing climate. *Divers. Distrib.* 25, 626–643. doi: 10.1111/ddi.12867

Bond, N. A., Cronin, M. F., Freeland, H., and Mantua, N. (2015). Causes and impacts of the 2014 warm anomaly in the NE Pacific. *Geophys. Res. Lett.* 42, 3414–3420. doi: 10.1002/2015gl063306

Brewer, G. D. (1976). Thermal tolerance and resistance of the northern anchovy, *Engraulis mordax*. *Fish. Bull.* 74, 433–445.

Brodeur, R. D., Auth, T. D., and Phillips, A. J. (2019). Major shifts in pelagic micronekton and macrozooplankton community structure in an upwelling ecosystem related to an unprecedented marine heatwave. *Front. Mar. Sci.* 6:212. doi: 10.3389/fmars.2019.00212

Brodie, S., Jacox, M. G., Bograd, S. J., Welch, H., Dewar, H., Scales, K. L., et al. (2018). Integrating dynamic subsurface habitat metrics into species distribution models. *Front. Mar. Sci.* 5:219. doi: 10.3389/fmars.2018.00219

Brodie, S. J., Thorson, J. T., Carroll, G., Hazen, E. L., Bograd, S., Haltuch, M. A., et al. (2020). Trade-offs in covariate selection for species distribution models: a methodological comparison. *Ecography* 43, 11–24. doi: 10.1111/ecog.04707

Buckley, L. B., Urban, M. C., Angilletta, M. J., Crozier, L. G., Rissler, L. J., and Sears, M. W. (2010). Can mechanism inform species' distribution models? *Ecol. Lett.* 13, 1041–1054.

Cavole, L. M., Demko, A. M., Diner, R. E., Giddings, A., Koester, I., Pagniello, C. M., et al. (2016). Biological impacts of the 2013–2015 warm-water anomaly in the Northeast Pacific: winners, losers, and the future. *Oceanography* 29, 273–285.

Checkley, D., Ayon, P., Baumgartner, T., Bernal, M., Coetzee, J. C., Emmett, R. L., et al. (2009). "Habitats in Checkley," in *Climate Change and Small Pelagic Fish*, eds C. Roy, J. Alheit, Y. Oozeki, and D. Checkley (Cambridge, MA: Cambridge University Press), 12–44.

Checkley, D. M., Dotson, R. C. Jr., and Grif?th, D. A. (2000). Continuous, underway sampling of eggs of Pacific sardine (*Sardinops sagax*) and northern anchovy (*Engraulis mordax*) in spring 1996 and 1997 off southern and central California. *Deep Sea Res. Part II* 47, 1139–1155. doi: 10.1016/s0967-0645(99)00139-3

Cheung, W. W., Brodeur, R. D., Okey, T. A., and Pauly, D. (2015). Projecting future changes in distributions of pelagic fish species of Northeast Pacific shelf seas. *Prog. Oceanogr.* 130, 19–31. doi: 10.1016/j.pocean.2014.09.003

Crozier, L. G., Hendry, A. P., Lawson, P. W., Quinn, T. P., Mantua, N. J., Battin, J., et al. (2008). Potential responses to climate change in organisms with complex life histories: evolution and plasticity in Pacific salmon. *Evol. Appl.* 1, 252–270. doi: 10.1111/j.1752-4571.2008.00033.x

Dambach, J., and Rödder, D. (2011). Applications and future challenges in marine species distribution modeling. *Aquat. Conserv.* 21, 92–100. doi: 10.1002/aqc.1160

Demer, D. A., and Zwolinski, J. P. (2014). Corroboration and refinement of a method for differentiating landings from two stocks of Pacific sardine (*Sardinops sagax*) in the California current. *ICES J. Mar. Sci.* 71, 328–335. doi: 10.1093/icesjms/fst135

Demer, D. A., Zwolinski, J. P., Byers, K. A., Cutter, G. R., Renfree, J. S., Sessions, T. S., et al. (2012). Prediction and confirmation of seasonal migration of Pacific sardine (*Sardinops sagax*) in the California current ecosystem. *Fish. Bull.* 110, 52–70.

Deutsch, C., Ferrel, A., Seibel, B., Pörtner, H. O., and Huey, R. B. (2015). Climate change tightens a metabolic constraint on marine habitats. *Science* 348, 1132–1135. doi: 10.1126/science.aaa1605

Di Lorenzo, E., and Mantua, N. (2016). Multi-year persistence of the 2014/15 North Pacific marine heatwave. *Nat. Clim. Change* 6, 1042–1047. doi: 10.1038/nclimate3082

Dormann, C. F., Schymanski, S. J., Cabral, J., Chuine, I., Graham, C., Hartig, F., et al. (2012). Correlation and process in species distribution models: bridging a dichotomy. *J. Biogeogr.* 39, 2119–2131. doi: 10.1111/j.1365-2699.2011.02659.x

Duguid, W. D., Boldt, J. L., Chalifour, L., Greene, C. M., Galbraith, M., Hay, D., et al. (2019). Historical fluctuations and recent observations of Northern Anchovy *Engraulis mordax* in the Salish Sea. *Deep Sea Res. Part II Top. Stud. Oceanogr.* 159, 22–41. doi: 10.1016/j.dsr2.2018.05.018

Elith, J., and Leathwick, J. R. (2009). Species distribution models: ecological explanation and prediction across space and time. *Annu. Rev. Ecol. Evol. Syst.* 40, 677–697. doi: 10.1146/annurev.ecolsys.110308.120159

Elith, J., Leathwick, J. R., and Hastie, T. (2008). A working guide to boosted regression trees. *J. Anim. Ecol.* 77, 802–813. doi: 10.1111/j.1365-2656.2008.01390.x

Elith, J. (2019). "Machine learning, random forests, and boosted regression trees," in *Quantitative Analyses in Wildlife Science*, eds L. A. Brennan, A. N. Tri, and B. G. Marcot, Chap. 15 (Baltimore, MD: Johns Hopkins University Press), 281–297.

Emmett, R. L., Brodeur, R. D., Miller, T. W., Pool, S. S., Krutzikowsky, G. K., Bentley, P. J., et al. (2005). Pacific sardines (*Sardinops sagax*) abundance, distribution, and ecological relationships in the Pacific Northwest. *Calif. Coop. Oceanic Fish. Invest. Rep.* 46, 122–143.

Félix-Uraga, R., Gómez-Muñoz, V. M., Quiñonez-Velazquez, C., Melo-Barrera, F. N., and García-Franco, W. (2004). On the existence of Pacific sardine groups off the west coast of Baja California and southern California. *Calif. Coop. Oceanic Fish. Invest. Rep.* 45, 146–151.

Fiechter, J., Rose, K. A., Curchitser, E. N., and Hedstrom, K. S. (2015). The role of environmental controls in determining sardine and anchovy population cycles in the California current: analysis of an end-to-end model. *Prog. Oceanogr.* 138, 381–398. doi: 10.1016/j.pocean.2014.11.013

Fiedler, P. C., Methot, R. D., and Hewitt, R. P. (1986). Effects of California El Niño 1982–1984 on the northern anchovy. *J. Mar. Res.* 44, 317–338.

Fritsch, S., Guenther, F., and Wright, M. N. (2019). *neuralnet: Training of Neural Networks. R Package Version 1.44.2*. Avaliable at: https://CRAN.R-project.org/package=neuralnet.(accessed February 07, 2019).

Gallo, N. D., Drenkard, E., Thompson, A. R., Weber, E. D., Wilson-Vandenberg, D., McClatchie, S., et al. (2019). Bridging from monitoring to solutions-based thinking: Lessons from CalCOFI for understanding and adapting to marine climate change impacts. *Front. Mar. Sci.* 6:695. doi: 10.3389/fmars.2019.00695

García-Morales, R., Shirasago-German, B., Félix-Uraga, R., and Pérez-Lezama, E. L. (2012). Conceptual models of Pacific sardine distribution in the California current System. *Curr. Dev. Oceanogr.* 5, 23–47.

Gentemann, C. L., Fewings, M. R., and García-Reyes, M. (2017). Satellite sea surface temperatures along the West Coast of the United States during the 2014–2016 northeast Pacific marine heat wave. *Geophys. Res. Lett.* 44, 312–319. doi: 10.1002/2016gl071039

Green-Ruiz, Y. A., and Hinojosa-Corona, A. (1997). Study of the spawning area of the Northern anchovy in the Gulf of California from 1990 to 1994, using satellite images of sea surface temperatures. *J. Plankton Res.* 19, 957–968. doi: 10.1093/plankt/19.8.957

Greenwell, B., Boehmke, B., Cunningham, J., and GBM Developers (2019). *gbm: Generalized Boosted Regression Models. R Package Version 2.1.5*. Avaliable at: https://CRAN.R-project.org/package=gbm (accessed January 14, 2019).

Guisan, A., Tingley, R., Baumgartner, J. B., Naujokaitis-Lewis, I., Sutcliffe, P. R., and Tulloch, A. I. (2013). Predicting species distributions for conservation decisions. *Ecol. Lett.* 16, 1424–1435.

Guisan, A., and Zimmermann, N. E. (2000). Predictive habitat distribution models in ecology. *Ecol. Modelling* 135, 147–186. doi: 10.1016/s0304-3800(00)00354-9

Hannemann, H., Willis, K. J., and Macias-Fauria, M. (2015). The devil is in the detail: unstable response functions in species distribution models challenge bulk ensemble modelling. *Global Ecol. Biogeogr.* 25, 26–35. doi: 10.1111/geb.12381

Harvey, C., Garfield, N., Williams, G., Tolimieri, N., Schroeder, I., Andrews, K., et al. (2019). *Ecosystem Status Report of the California Current for 2019: A Summary of Ecosystem Indicators Compiled by the California Current Integrated Ecosystem Assessment Team (CCEIA)*. Washington, DC: U.S. Department of Commerce, 149.

Hazen, E. L., Scales, K. L., Maxwell, S. M., Briscoe, D. K., Welch, H., Bograd, S. J., et al. (2018). A dynamic ocean management tool to reduce bycatch and support sustainable fisheries. *Sci. Adv.* 4:eaar3001. doi: 10.1126/sciadv.aar3001

Hijmans, R. J., Phillips, S., Leathwick, J., and Elith, J. (2017). *dismo: Species Distribution Modeling. R Package Version 1.1-4*. Avaliable at: https://CRAN.R-project.org/package=dismo (accessed January 09, 2017).

Hill, K. T., Crone, P. R., Demer, D. A., Zwolinski, J., Dorval, E., and Macewicz, B. J. (2014). "Assessment of the Pacific sardine resource in 2014 for US management in 2014-15," in *National Oceanic and Atmospheric Administration Technical Memorandum NMFS-SWFSC-531*, (Washington, DC: US Department of Commerce).

Hill, K. T., Crone, P. R., and Zwolinski, J. P. (2018). "Assessment of the Pacific sardine resource in 2018 for US management in 2018-19," in *National Oceanic and Atmospheric Administration Technical Memorandum NMFS-SWFSC-*600, (Washington, DC: US Department of Commerce).

Hill, K. T., Crone, P. R., and Zwolinski, J. P. (2019). "Assessment of the Pacific sardine resource in 2019 for US management in 2019-20," in *National Oceanic and Atmospheric Administration Technical Memorandum NMFS-SWFSC-615*, (Washington, DC: US Department of Commerce).

Hobday, A. J., Oliver, E. C., Gupta, A. S., Benthuysen, J. A., Burrows, M. T., Donat, M. G., et al. (2018). Categorizing and naming marine heatwaves. *Oceanography* 31, 162–173.

Holbrook, N. J., Scannell, H. A., Gupta, A. S., Benthuysen, J. A., Feng, M., Oliver, E. C., et al. (2019). A global assessment of marine heatwaves and their drivers. *Nat. Commun.* 10, 1–13.

Howard, E. M., Penn, J. L., Frenzel, H., Seibel, B. A., Bianchi, D., Renault, L., et al. (2020). Climate-driven aerobic habitat loss in the California current system. *Sci. Adv.* 6:eaay3188. doi: 10.1126/sciadv.aay3188

Jacox, M. G. (2019). Marine heatwaves in a changing climate. *Nature* 571, 485–487. doi: 10.1038/d41586-019-02196-1

Jacox, M. G., Edwards, C. A., Hazen, E. L., and Bograd, S. J. (2018). Coastal upwelling revisited: ekman, Bakun and improved upwelling indices for the U.S. West Coast. *J. Geophys. Res.* 123, 7332–7350. doi: 10.1029/2018jc014187

Jacox, M. G., Hazen, E. L., Zaba, K. D., Rudnick, D. L., Edwards, C. A., Moore, A. M., et al. (2016). Impacts of the 2015–2016 El Niño on the California current system: early assessment and comparison to past events. *Geophys. Res. Lett.* 43, 7072–7080. doi: 10.1002/2016gl069716

Johnson, J. E., and Welch, D. J. (2009). Marine fisheries management in a changing climate: a review of vulnerability and future options. *Rev. Fish. Sci.* 18, 106–124. doi: 10.1080/10641260903434557

Kahru, M., Jacox, M. G., and Ohman, M. D. (2018). CCE1: decrease in the frequency of oceanic fronts and surface chlorophyll concentration in the California current system during the 2014–2016 northeast Pacific warm anomalies. *Deep Sea Res. Part I Oceanogr. Res. Pap.* 140, 4–13. doi: 10.1016/j.dsr.2018.04.007

Karp, M. A., Peterson, J. O., Lynch, P. D., Griffis, R. B., Adams, C. F., Arnold, W. S., et al. (2019). Accounting for shifting distributions and changing productivity in the development of scientific advice for fishery management. *ICES J. Mar. Sci.* 76, 1305–1315.

Kleisner, K. M., Fogarty, M. J., McGee, S., Hare, J. A., Moret, S., Perretti, C. T., et al. (2017). Marine species distribution shifts on the US Northeast Continental Shelf under continued ocean warming. *Prog. Oceanogr.* 153, 24–36. doi: 10.1016/j.pocean.2017.04.001

Koehn, L. E., Essington, T. E., Marshall, K. N., Kaplan, I. C., Sydeman, W. J., Szoboszlai, A. I., et al. (2016). Developing a high taxonomic resolution food web model to assess the functional role of forage fish in the California current ecosystem. *Ecol. Modelling* 335, 87–100. doi: 10.1016/j.ecolmodel.2016.05.010

Koenigstein, S., Mark, F. C., Gößling-Reisemann, S., Reuter, H., and Pörtner, H. O. (2016). Modeling climate change impacts on marine fish populations: process-based integration of ocean warming, acidification and other environmental drivers. *Fish Fish.* 17, 972–1004. doi: 10.1111/faf.12155

Kramer, D., Kalin, M. J., Stevens, E. G., Thrailkill, J. R., and Zweifel, J. R. (1972). "Collecting and processing data on fish eggs and larvae in the California current region," in *National Oceanic and Atmospheric Administration Technical Report NMFS-CIRC-370*, Vol. 370, (Seattle, WA: US Department of Commerce).

Kuhn, M., and Johnson, K. (2013). *Remedies for Severe Class Imbalance. In: Applied Predictive Modeling*. New York, NY: Springer.

Kuhn, M., Wing, J., Weston, S., Williams, A., Keefer, C., Engelhardt, A., et al. (2019). *caret: Classification and Regression Training. R Package Version 6.0-84*. Avalaiable at: https://CRAN.R-project.org/package=caret (accessed March 20, 2020).

Lasker, R. (1964). An experimental study of the effect of temperature on the incubation time, development, and growth of Pacific sardine embryos and larvae. *Copeia* 2, 399–405.

Lasker, R., and Smith, P. E. (1977). Estimation of the effects of environmental variations on the eggs and larvae of the northern anchovy. *Calif. Coop. Oceanic Fish. Invest. Rep.* 19, 128–137.

Lehodey, P., Senina, I., and Murtugudde, R. (2008). A spatial ecosystem and populations dynamics model (SEAPODYM)–Modeling of tuna and tuna-like populations. *Prog. Oceanogr.* 78, 304–318. doi: 10.1016/j.pocean.2008.06.004

Liaw, A., and Wiener, M. (2002). Classification and Regression by randomForest. *R News* 2, 18–22.

Lima, F. P., and Wethey, D. S. (2012). Three decades of high-resolution coastal sea surface temperatures reveal more than warming. *Nat. Commun.* 3, 1–13.

Lindegren, M., Checkley, D. M., Rouyer, T., MacCall, A. D., and Stenseth, N. C. (2013). Climate, fishing, and fluctuations of sardine and anchovy in the California current. *Proc. Natl. Acad. Sci. U.S.A.* 110, 13672–13677. doi: 10.1073/pnas.1305733110

Link, J. S., Nye, J. A., and Hare, J. A. (2011). Guidelines for incorporating fish distribution shifts into a fisheries management context. *Fish Fish.* 12, 461–469. doi: 10.1111/j.1467-2979.2010.00398.x

Litz, M. N., Heppell, S. S., Emmett, R. L., and Brodeur, R. D. (2008). Ecology and distribution of the northern subpopulation of northern anchovy (*Engraulis mordax*) off the US west coast. *Cali. Coop. Oceanic Fish. Invest. Rep.* 49, 167–182.

Lluch-Belda, D., Lluch-Cota, D. B., Hernandez-Vazquez, S., Salinas-Zavala, C. A., and Schwartzlose, R. A. (1991). Sardine and anchovy spawning as related to temperature and upwell in the California current system. *Calif. Coop. Oceanic Fish. Invest. Rep.* 32, 105–111.

Lluch-Belda, D., Magallón, F. J., and Schwartzlose, R. A. (1986). Large fluctuations in the sardine fishery in the Gulf of California: possible causes. *Calif. Coop. Oceanic Fish. Invest. Rep.* 27, 136–140.

Lo, N. C., Macewicz, B. J., and Griffith, D. A. (2011). Migration of Pacific sardine (*Sardinops sagax*) off the west coast of United States in 2003–2005. *Bull. Mar. Sci.* 87, 395–412. doi: 10.5343/bms.2010.1077

Macdonald, J. I., Logemann, K., Krainski, E. T., Sigurðsson, b, Beale, C. M., Huse, G., et al. (2018). Can collective memories shape fish distributions? A test, linking space-time occurrence models and population demographics. *Ecography* 41, 938–957. doi: 10.1111/ecog.03098

Martínez-Porchas, M., Hernández-Rodríguez, M., and Bückle-Ramírez, L. F. (2009). Thermal behavior of the Pacific sardine (*Sardinops sagax*) acclimated to different thermal cycles. *J. Thermal Biol.* 34, 372–376. doi: 10.1016/j.jtherbio.2009.07.002

McClatchie, S., Goericke, R., Auad, G., and Hill, K. (2010). Re-assessment of the stock-recruit and temperature-recruit relationships for Pacific sardine (*Sardinops sagax*). *Can. J. Fish. Aquat. Sci.* 67, 1782–1790. doi: 10.1139/f10-101

McClatchie, S., Goericke, R., Leising, A., Auth, T. D., Bjorkstedt, E., Robertson, R. R., et al. (2016). State of the California current 2015-16: comparisons with the 1997-98 El Niño. *Calif. Coop. Oceanic Fish. Invest.* 57, 1–57.

McDaniel, J., Piner, K., Lee, H. H., and Hill, K. (2016). Evidence that the migration of the northern subpopulation of Pacific sardine (*Sardinops sagax*) off the west coast of the United States is age-based. *PLoS One* 11:e0166780. doi: 10.1371/journal.pone.0166780

Mills, K. E., Pershing, A. J., Brown, C. J., Chen, Y., Chiang, F. S., Holland, D. S., et al. (2013). Fisheries management in a changing climate: lessons from the 2012 ocean heat wave in the Northwest Atlantic. *Oceanography* 26, 191–195.

Moser, H. G., Charter, R. L., Smith, P. E., Ambrose, D. A., Watson, W., Charter, S. R., et al. (2001). Distributional atlas of fish larvae and eggs in the Southern California Bight region, 1951-1998. *Calif. Coop. Oceanic Fish. Invest. Atlas* 34:166.

Muhling, B. A., Brodie, S., Jacox, M., Snodgrass, O., Dewar, H., Tommasi, D., et al. (2019). Dynamic habitat use of albacore and their primary prey species in the California current system. *Calif. Coop.Oceanic Fish. Invest. Rep.* 60, 1–15.

Neveu, E., Moore, A. M., Edwards, C. A., Fiechter, J., Drake, P., Crawford, W. J., et al. (2016). An historical analysis of the California current circulation using ROMS 4D-Var: system configuration and diagnostics. *Ocean Modelling* 99, 133–151. doi: 10.1016/j.ocemod.2015.11.012

Norberg, A., Abrego, N., Blanchet, F. G., Adler, F. R., Anderson, B. J., Anttila, J., et al. (2019). A comprehensive evaluation of predictive performance of 33 species distribution models at species and community levels. *Ecol. Monogr.* 89:e01370.

Olden, J. D., Lawler, J. J., and Poff, N. L. (2008). Machine learning methods without tears: a primer for ecologists. *Q. Rev. Biol.* 83, 171–193. doi: 10.1086/587826

Özesmi, S. L., Tan, C. O., and Özesmi, U. (2006). Methodological issues in building, training, and testing artificial neural networks in ecological applications. *Ecol. Modelling* 195, 83–93. doi: 10.1016/j.ecolmodel.2005.11.012

Planque, B., Bellier, E., and Lazure, P. (2007). Modelling potential spawning habitat of sardine (*Sardina pilchardus*) and anchovy(*Engraulis encrasicolus*) in the Bay of Biscay). *Fish. Oceanogr.* 16, 16–30. doi: 10.1111/j.1365-2419.2006.00411.x

Planque, B., Loots, C., Petitgas, P., Lindstrøm, U. L. F., and Vaz, S. (2011). Understanding what controls the spatial distribution of fish populations using a multi-model approach. *Fish. Oceanogr.* 20, 1–17. doi: 10.1111/j.1365-2419.2010.00546.x

Poloczanska, E. S., Brown, C. J., Sydeman, W. J., Kiessling, W., Schoeman, D. S., Moore, P. J., et al. (2013). Global imprint of climate change on marine life. *Nat. Clim. Change* 3, 919–925.

Pribyl, A. L., Hyde, J. R., Robertson, L., and Vetter, R. (2016). Defining an ideal temperature range for the northern subpopulation of Pacific sardine. *Sardinops sagax* caeruleus. Environ. Biol. Fish 99, 275–291. doi: 10.1007/s10641-016-0473-1

Punt, A. E., A'mar, T., Bond, N. A., Butterworth, D. S., de Moor, C. L., De Oliveira, J. A., et al. (2013). Fisheries management under climate and environmental uncertainty: control rules and performance simulation. *ICES J. Mar. Sci.* 71, 2208–2220. doi: 10.1093/icesjms/fst057

R Core Team (2019). *R: A Language and Environment for Statistical Computing*. Vienna: R Foundation for Statistical Computing.

Reiss, C. S., Checkley, D. M. Jr., and Bograd, S. J. (2008). Remotely sensed spawning habitat of Pacific sardine (*Sardinops sagax*) and Northern anchovy (*Engraulis mordax*) within the California current. *Fish. Oceanogr.* 17, 126–136. doi: 10.1111/j.1365-2419.2008.00469.x

Rose, K. A., Fiechter, J., Curchitser, E. N., Hedstrom, K., Bernal, M., Creekmore, S., et al. (2015). Demonstration of a fully-coupled end-to-end model for small pelagic fish using sardine and anchovy in the California current. *Prog. Oceanogr.* 138, 348–380. doi: 10.1016/j.pocean.2015.01.012

Sakuma, K. M., Field, J. C., Mantua, N. J., Ralston, S., Marinovic, B. B., and Carrion, C. N. (2016). Anomalous epipelagic micronekton assemblage patterns in the neritic waters of the California current in spring 2015 during a period of extreme ocean conditions. *Calif. Coop. Oceanic Fish. Invest. Rep.* 57, 163–183.

Sathyendranath, S., Brewin, R. J., Brockmann, C., Brotas, V., Calton, B., Chuprin, A., et al. (2019). An ocean-colour time series for use in climate studies: the experience of the ocean-colour climate change initiative (OC-CCI). *Sensors* 19:4285. doi: 10.3390/s19194285

Scales, K. L., Hazen, E. L., Maxwell, S. M., Dewar, H., Kohin, S., Jacox, M. G., et al. (2017). Fit to predict? Eco-informatics for predicting the catchability of a pelagic fish in near real time. *Ecol. Appl.* 27, 2313–2329. doi: 10.1002/eap.1610

Silber, G. K., Lettrich, M. D., Thomas, P. O., Baker, J. D., Baumgartner, M., Becker, E. A., et al. (2017). Projecting marine mammal distribution in a changing climate. *Front. Mar. Sci.* 4:413. doi: 10.3389/fmars.2017.00413

Smale, D. A., Wernberg, T., Oliver, E. C., Thomsen, M., Harvey, B. P., Straub, S. C., et al. (2019). Marine heatwaves threaten global biodiversity and the provision of ecosystem services. *Nat. Clim. Change* 9, 306–312. doi: 10.1038/s41558-019-0412-1

Smith, J. A., Tommasi, D., Sweeney, J., Brodie, S., Welch, H., Hazen, E. L., et al. (2020). Lost opportunity: quantifying the dynamic economic impact of time-area fishery closures. *J. Appl. Ecol.* 57, 502–513. doi: 10.1111/1365-2664.13565

Smith, P. E. (2005). A history of proposals for subpopulation structure in the Pacific sardine (*Sardinops sagax*) population off western North America. *Calif. Coop. Oceanic Fish. Invest. Rep.* 46:75.

Steen, V., Sofaer, H. R., Skagen, S. K., Ray, A. J., and Noon, B. R. (2017). Projecting species' vulnerability to climate change: which uncertainty sources matter most and extrapolate best? *Ecol. Evol.* 7, 8841–8851. doi: 10.1002/ece3.3403

Thompson, A. R., Harvey, C. J., Sydeman, W. J., Barceló, C., Bograd, S. J., Brodeur, R. D., et al. (2019). Indicators of pelagic forage community shifts in the California current large marine ecosystem, 1998–2016. *Ecol. Ind.* 105, 215–228. doi: 10.1016/j.ecolind.2019.05.057

Thorson, J. T., Ciannelli, L., and Litzow, M. A. (2020). Defining indices of ecosystem variability using biological samples of fish communities: a generalization of empirical orthogonal functions. *Prog. Oceanogr.* 181:102244. doi: 10.1016/j.pocean.2019.102244

Valencia-Gasti, J. A., Durazo, R., Weber, E. D., Mcclatchie, S., Baumgartner, T., and Lennert-Cody, C. E. (2018). Spring spawning distribution of Pacific sardine in US and Mexican waters. *Calif. Coop. Oceanic Fish. Invest. Rep.* 59, 79–85.

Veneziani, M., Edwards, C. A., Doyle, J. D., and Foley, D. (2009). A central California coastal ocean modeling study: 1. Forward model and the influence of realistic versus climatological forcing. *J. Geophys. Res. Oceans* 114:C04015. doi: 10.1029/2008JC004774

Weber, E. D., Chao, Y., and Chai, F. (2018). Performance of fish-habitat classifiers based on derived predictors from a coupled biophysical model. *J. Mar. Syst.* 186, 105–114. doi: 10.1016/j.jmarsys.2018.06.012

Weber, E. D., and McClatchie, S. (2010). Predictive models of northern anchovy *Engraulis mordax* and Pacific sardine *Sardinops sagax* spawning habitat in the California current. *Mar. Ecolo. Prog. Ser.* 406, 251–263. doi: 10.3354/meps08544

Wells, R. S., Hansen, L. J., Baldridge, A. B., Dohl, T. P., Kelly, D. L., and Defran, R. H. (1990). "Northward extension of the range of bottle-nose dolphins along the California coast," in *The Bottlenose Dolphin*, eds S. Leatherwood and R. R. Reeves (San Diego, CA: Academic Press Inc), 421–431.

Winkler, D. W., Jørgensen, C., Both, C., Houston, A. I., McNamara, J. M., Levey, J., et al. (2014). Cues, strategies, and outcomes: how migrating vertebrates track environmental change. *Mov. Ecol.* 2:10.

Wood, S. N. (2017). *Generalized Additive Models: An Introduction With R*, 2nd Edn. London: Chapman and Hall/CRC.

Woodworth-Jefcoats, P. A., Polovina, J. J., and Drazen, J. C. (2017). Climate change is projected to reduce carrying capacity and redistribute species richness in North Pacific pelagic marine ecosystems. *Global Change Biol.* 23, 1000–1008. doi: 10.1111/gcb.13471

Yates, K. L., Bouchet, P. J., Caley, M. J., Mengersen, K., Randin, C. F., Parnell, S., et al. (2018). Outstanding challenges in the transferability of ecological models. *Trends Ecol. Evol.* 33, 790–802.

Zuur, A. F. (2012). *A Beginner's Guide to Generalized Additive Models With R*. Newburgh, NY: Highland Statistics Limited, 1–206.

Zwolinski, J. P., and Demer, D. A. (2012). A cold oceanographic regime with high exploitation rates in the Northeast Pacific forecasts a collapse of the sardine stock. *Proc. Natl. Acad. Sci. U.S.A.* 109, 4175–4180. doi: 10.1073/pnas.1113806109

Zwolinski, J. P., Demer, D. A., Byers, K. A., Cutter, G. R., Renfree, J. S., Sessions, T. S., et al. (2012). Distributions and abundances of Pacific sardine (Sardinops sagax) and other pelagic fishes in the California current ecosystem during spring 2006, 2008, and 2010, estimated from acoustic–trawl surveys. *Fish. Bull.* 110, 110–122.

Zwolinski, J. P., Emmett, R. L., and Demer, D. A. (2011). Predicting habitat to optimize sampling of Pacific sardine (*Sardinops sagax*). *ICES J. Mar. Sci.* 68, 867–879. doi: 10.1093/icesjms/fsr038

Zwolinski, J. P., Stierhoff, K. L., and Demer, D. A. (2019). "Distribution, biomass, and demography of coastal pelagic fishes in the California current ecosystem during summer 2017 based on acoustic-trawl sampling," in *NOAA Technical Memorandum NMFS NOAA-TM-NMFS-SWFSC-610*, (Silver Spring, MA: NOAA), 76.

Disclaimer: The scientific results and conclusions, as well as any views or opinions expressed herein, are those of the author(s) and do not necessarily reflect the views of NOAA or the Department of Commerce.

Conflict of Interest: CG co-founded the company Benchmark Labs.

The remaining authors declare that the research was conducted in the absence of any commercial or financial relationships that could be construed as a potential conflict of interest.

frontiers in Marine Science

ORIGINAL RESEARCH
published: 28 August 2020
doi: 10.3389/fmars.2020.00680

Mesoscale Warm-Core Eddies Drive Interannual Modulations of Swordfish Catch in the Kuroshio Extension System

Gloria Silvana Durán Gómez[1,2]*, *Takeyoshi Nagai*[1] *and Kotaro Yokawa*[3]

[1] *Department of Ocean Sciences, Tokyo University of Marine Science and Technology, Tokyo, Japan,* [2] *Facultad de Pesquería, Universidad Nacional Agraria La Molina, Lima, Peru,* [3] *National Research Institute for Far Seas Fisheries, Fisheries Research and Education Agency (FRA), Shizuoka, Japan*

Recent observational and numerical studies have suggested that the decadal modulation of the Kuroshio Extension system, driven by mesoscale eddies, profoundly affect the basin scale physical and biogeochemical oceanography. However, it remains unclear how these decadal changes affect distribution and abundance of fish species in this region. In this study, 26,964 swordfish catch data obtained by longliners during 2004–2010 in the western North Pacific are analyzed with an eddy-resolving ocean reanalysis by using mesoscale dynamic parameters and an eddy detection technique, to clarify the effects of mesoscale eddies and their variabilities on the swordfish relative abundance. During this period, the Kuroshio Extension underwent two different dynamic phases: stable path state in 2004, 2005, and 2010; and unstable path state during 2006–2009. Based on our analyses, we show here that swordfish are more concentrated in and near the anticyclonic warm-core eddies in the northern site, 36–45°N, of the Kuroshio Extension system, especially during the unstable path phase. This is found to be caused by the interannual modulation of mesoscale eddy activities due to more warm-core rings generated from the unstable Kuroshio Extension, making it easier for fishermen to target swordfish in this region.

Keywords: interannual modulation, mesoscale eddies, Kuroshio Extension decadal modulation, eddy detection technique, swordfish fishery, CPUE

OPEN ACCESS

Edited by:
Shoshiro Minobe,
Hokkaido University, Japan

Reviewed by:
Yasumasa Miyazawa,
Japan Agency for Marine-Earth Science and Technology (JAMSTEC), Japan
Oscar Sosa-Nishizaki,
Center for Scientific Research and Higher Education in Ensenada (CICESE), Mexico

***Correspondence:**
Gloria Silvana Durán Gómez
silvanadg20@hotmail.com

Specialty section:
This article was submitted to Marine Fisheries, Aquaculture and Living Resources, a section of the journal Frontiers in Marine Science

Received: *27 March 2020*
Accepted: *27 July 2020*
Published: *28 August 2020*

Citation:
Durán Gómez GS, Nagai T and Yokawa K (2020) Mesoscale Warm-Core Eddies Drive Interannual Modulations of Swordfish Catch in the Kuroshio Extension System. Front. Mar. Sci. 7:680. doi: 10.3389/fmars.2020.00680

1. INTRODUCTION

Ocean accommodates variety of marine life from small plankton to large migratory fish species, including swordfish. Within this marine ecosystem, phytoplankton are the most important primary producers of the vital energy source for most of the marine life, forming the foundation of the food web. These marine primary producers are nearly passive to the flow, and their abundance depends strongly on the availability of nutrients and light. The enhanced nutrient injection near ocean fronts (Mahadevan and Archer, 2000; Lévy et al., 2001) and active restratification of the mixed layer eddies (Mahadevan et al., 2012) may sustain primary producers and their grazers. So, the enhanced primary and secondary productions near fronts and eddies not only provide controls over biogeochemical flows but also attract large migratory fish species (Braun et al., 2019). In addition to this bottom-up influence through the trophic supply, physical structures in the ocean, such as fronts and eddies, have been known to influence the distributions of marine organisms. They may

act as barriers or migration routes, giving greater feeding opportunities and a preferred thermal habitat, thus influencing the behavior and distribution of various marine species (Seki et al., 2002; Watanabe et al., 2009). To this regard, using satellite tracking of shark movements, satellite remote sensing and a numerical forecasting model, Braun et al. (2019) have recently shown that the blue sharks in the Gulf Stream regions prefer warm swirls or warm-core rings, which has been believed to be oligotrophic ocean desert. For swordfish, Bigelow et al. (1999) have reported, using Hawaii based swordfish longline fishery data, that important factors to model catch-per-unit-effort (CPUE) include latitude, time, longitude, sea surface temperature (SST), and frontal energy. However, the detailed mechanisms of how the mesoscale frontal processes affect these factors are not discussed. Also, Hsu et al. (2015) recently reported high swordfish catch found outside of eddies, by using satellite altimeter data in the surroundings of the Gulf Stream. Although the direct comparison of fishery catch data with the mesoscale eddies detected using satellite altimeter data is pioneering, the study region was limited to the western North Atlantic. In the western North Pacific, previous studies using limited short-term physical and fishery data have shown the influence of mesoscale eddies on the distributions of pelagic fish (Sugimoto and Tameishi, 1992). However, it is still unclear how evolving mesoscale flows with interannual timescale affect distributions and relative abundance of fish species, including the swordfish. In the Pacific Ocean, the swordfish *Xiphias gladius* has a distribution between the latitudes 50°N–50°S (Bedford and Hagerman, 1983), with areas of apparent concentrations in the western North Pacific within the latitudes 20–45°N. The main habitat of the swordfish in this area is the subtropical region (Watanabe et al., 2009), where the Kuroshio Extension flows along its northern boundary.

The Kuroshio Extension (KE) is a western boundary current of the subtropical gyre in the North Pacific. It is one of the most dynamic regions of the world ocean, rich in mesoscale eddies and with the largest heat loss from the ocean to the atmosphere (Qiu et al., 2004). It presents two dynamic states: "stable" and "unstable" driven by the Aleutian low variation and associated westward propagating mesoscale eddies (Qiu and Chen, 2005; Taguchi et al., 2007; Sugimoto and Hanawa, 2009; Qiu et al., 2014). During the stable period, the KE flows steadily along relatively stable paths, while during the unstable period, it flows more convoluted paths evolving with timescales of weeks to months. Due to this interannual variation, it has been shown that ecosystem in the KE region can be influenced from its lowest trophic level (Lin et al., 2014).

However, it has still been unclear how the KE interannual modulation affects the distributions and the relative abundance of higher trophic levels such as secondary producers, migrating fish species including swordfish, in relation to the mesoscale eddies.

In this study, by using a state-of-the-art ocean reanalysis product and available pelagic longline swordfish fishery data from 2004 through 2010 in the KE region, it becomes possible to investigate the effects of the spatiotemporal variations in the mesoscale eddies on the relative abundance of swordfish. The objective of this study is to assess the influence of mesoscale eddies over the swordfish *X. gladius* relative abundance, represented as the catch-per-unit-effort (CPUE) in the KE region. Section 2 includes data and methods, section 3 presents the results of the analysis using dynamic parameters for the mesoscale flow with the swordfish CPUE and their modulations in response to the KE state. Section 4 provides discussion, and finally, conclusions are presented in section 5.

2. DATA AND METHODS

2.1. Fishery Data

The fishery data used in this study consist of catch and effort data collected in the region 25–45°N, 138°E–160°W from 2004 through 2010 by Japanese offshore surface longliners based on the Kesennuma fishing port. This operational data contains information of time (year, month, and day), fishing locations, number of swordfish catches, and effort in number of hooks deployed. A total of 26,964 catch data were collected and summarized by the National Research Institute for Far Seas Fisheries (**Table 1**). Since our focus is the swordfish abundance in the mesoscale-eddy-rich KE system, the swordfish catch data in the region 140–175°E, 25–45°N are used in this study.

The catch-per-unit-effort (CPUE) of a specie can be used to estimate the relative abundance, generally under the assumption that there is a linear relationship between these two (Skalski et al., 2010), or that both of these values are proportional (Cushing, 1981). For the analysis of the relative abundance of swordfish in this study, we use a nominally defined CPUE calculated by the following equation

$$\mathrm{CPUE} = 100 \times \frac{\text{Total \# of fish catch}}{\text{Total \# of hooks}}, \tag{1}$$

expressing the catch and effort as the total number of fish catch per 100 hooks. Although this non-standardized CPUE may bias the abundance depending on the environmental factors,

TABLE 1 | Number of fishery records for the period 2004–2010.

	Year							Total
Month	**2004**	**2005**	**2006**	**2007**	**2008**	**2009**	**2010**	
1		536	502	591	534	459	432	3,054
2		505	474	499	440	404	338	2,660
3		500	458	462	515	488	396	2,819
4		516	469	465	458	348	361	2,617
5		455	275	398	448	318	381	2,275
6		299	302	415	509	357	93	1,975
7	2	221	315	312	380	218		1,448
8	123	217	147	265	146	134		1,032
9	301	383	343	398	299	212		1,936
10	444	408	373	453	439	315		2,432
11	433	364	336	440	372	406		2,351
12	412	372	326	504	386	365		2,365
Total	1,715	4,776	4,320	5,202	4,926	4,024	2,001	26,964

such as temperature, salinity and/or specifications of fishing gears (Bigelow et al., 1999; Bellido et al., 2001), important factors revealed by this study in the following sections, such as mesoscale dynamic parameters, can be useful to improve the standardization.

2.2. Ocean Data Analyses

For the respective analysis of the oceanographic conditions in the KE, we used the Four-dimensional Variational Ocean Re-Analysis for the western North Pacific over 30 years (FORA-WNP30) provided by the Japan Agency for Marine-Earth Science and Technology (JAMSTEC) and the Japan Meteorological Research Institute (Usui et al., 2017). We worked with data of sea surface height, temperature, salinity and lateral velocity with a resolution of 1/10° in the western North Pacific during the time corresponding to the period of the fishery data.

To characterize the mesoscale flow field, several dynamic parameters are computed using the reanalysis data. For the mesoscale eddy detection, the Okubo-Weiss parameter (OW) is computed, since it can distinguish two-dimensional flow of rotating regime (OW < 0) from that of deformation regime (OW > 0) (Okubo, 1979; Weiss, 1991). The OW is defined as

$$\mathrm{OW} = 4\left[\left(\frac{\partial u}{\partial x}\right)^2 + \frac{\partial v}{\partial x}\frac{\partial u}{\partial y}\right], \tag{2}$$

where u and v are zonal and meridional velocities, respectively, and x and y represent the respective zonal and meridional directions.

In a region where the rotation dominates over the deformation flow (OW < 0), it is typically inside the isolated eddies. The directions of the rotating flows of the detected mesoscale eddies are determined by computing the vertical component of the relative vorticity, ζ. The sign convention for direction is that the vorticity is positive (negative) when rotation is anticlockwise (clockwise),

$$\zeta = \frac{\partial v}{\partial x} - \frac{\partial u}{\partial y} \tag{3}$$

The available reanalysis data do not include vertical velocity, and the exact discretized form for the continuity equation of the model is not provided. Therefore, to deduce the tendency of the adiabatic subinertial vertical water movement, the divergence of the Q-vector, $\nabla_h \cdot \mathbf{Q}$ is computed. Positive and negative signs of $\nabla_h \cdot \mathbf{Q}$ have been shown to correspond to the tendency of downwelling and upwelling, respectively (Gill, 1982; Nagai et al., 2015). $\nabla_h \cdot \mathbf{Q}$ is defined as,

$$\nabla_h \cdot \mathbf{Q} = -\frac{\partial}{\partial x}\left(\frac{\partial u}{\partial x}\frac{\partial b}{\partial x} + \frac{\partial v}{\partial x}\frac{\partial b}{\partial y}\right) - \frac{\partial}{\partial y}\left(\frac{\partial u}{\partial y}\frac{\partial b}{\partial x} + \frac{\partial v}{\partial y}\frac{\partial b}{\partial y}\right), \tag{4}$$

where $b = -g\rho/\rho_o$ is buoyancy with water density ρ and its reference value ρ_o, gravitational acceleration g, and $\nabla_h = (\partial/\partial x, \partial/\partial y)$ is the horizontal derivative operator. In addition to the divergence of the Q-vector, a frontogenetical function is also computed using upper 100 m average horizontal flow. The frontogenetical function F is equated as,

$$F = \frac{1}{2}\frac{D\left|\nabla_h b\right|^2}{Dt} = \mathbf{Q}\cdot\nabla_h b = -\left(\frac{\partial u}{\partial x}\frac{\partial b}{\partial x} + \frac{\partial v}{\partial x}\frac{\partial b}{\partial y}\right)\frac{\partial b}{\partial x} - \left(\frac{\partial u}{\partial y}\frac{\partial b}{\partial x} + \frac{\partial v}{\partial y}\frac{\partial b}{\partial y}\right)\frac{\partial b}{\partial y}. \tag{5}$$

When the frontogenetical function F is positive, it is equivalent to the increase trend of the lateral buoyancy gradient of the front under the frontogenesis, while a negative value means decrease in the lateral buoyancy gradient caused by the frontolysis (Pettersen, 1956; Bluestein, 1993). To investigate the relationships between the swordfish CPUE and these mesoscale dynamic parameters, the CPUEs are computed as a function of these parameters with the following resolutions, every $0.02f$ for ζ/f (where f is the Coriolis parameter); 2×10^{-10} s^{-2} for OW; 2×10^{-17} ms^{-3} for $\nabla_h \cdot \mathbf{Q}$.

2.3. Eddy Detection and Eddy Kinetic Energy

To analyze the swordfish CPUE distributions with respect to mesoscale eddies, and to investigate their temporal variations in the Kuroshio Extension system, an eddy detection technique is used. The eddy detection method is based on the closed contours of the OW-parameter (2) at a value of -5×10^{-11} s^{-2}. The OW parameter for the eddy detection is computed from upper 100 m average lateral flow data. Only eddies with equivalent radius from 15 to 200 km are considered to detect mesoscale eddies of $\mathcal{O}$(100 km) under the limit of available resolution of the reanalysis $\sim$ 10 km. Whether a detected eddy is a cyclonic or an anticyclonic ring is determined by averaging the vertical component of relative vorticity ζ (3) within the eddy.

To understand the effects of eddies on the swordfish CPUE, the geographically closest eddy to each fishing position is determined by computing the distance between each fishing location and all the positions of eddy center, which is defined as the average longitudes and latitudes inside an eddy. The maps of the mean CPUE as a function of zonal and meridional distance from the eddy center are then obtained by averaging each CPUE, computed for each fishing point, on the grid over 500 km centered at the eddy with the resolution of 10 km for both zonal and meridional directions. Lastly, to investigate the spatiotemporal modulations in eddy activities, the upper 100 m average eddy kinetic energy (EKE) is computed as,

$$\mathrm{EKE} = \frac{1}{2}\left({u'_{100}}^2 + {v'_{100}}^2\right), \tag{6}$$

where u'_{100} and v'_{100} are fluctuating (eddy) components of the zonal and meridional upper 100 m average velocities obtained by subtracting long-term (1982–2014) mean velocities $\overline{\mathbf{u}}$ from each component of daily velocity $\mathbf{u}$, i.e., $\mathbf{u}' = \mathbf{u} - \overline{\mathbf{u}}$ before averaging them over upper 100 m.

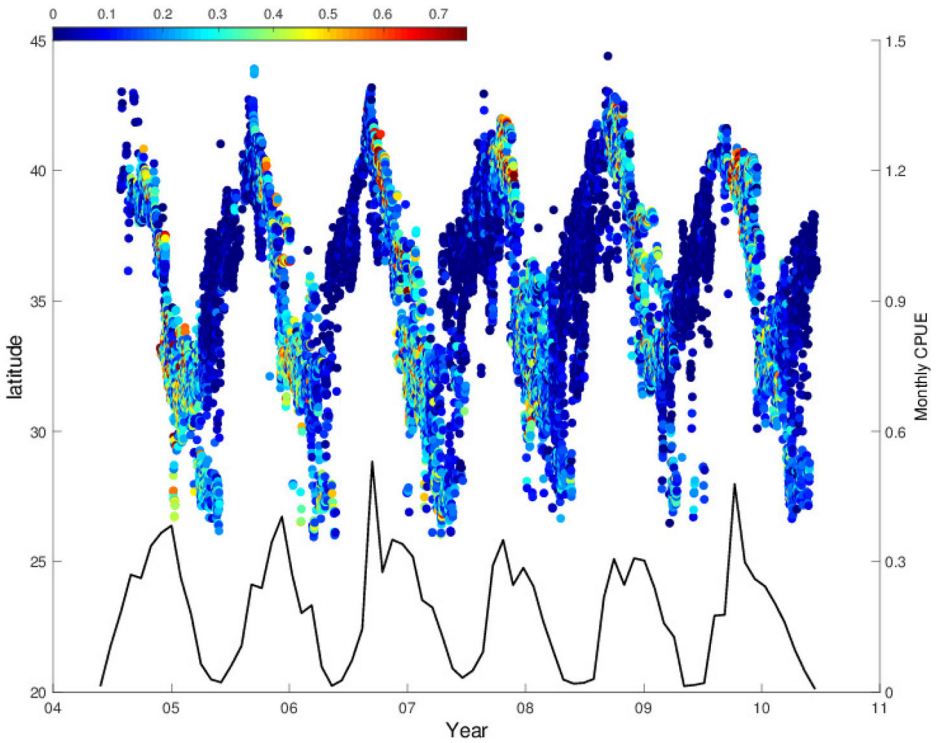

FIGURE 1 | Time series of daily average latitudinal fishing position with swordfish CPUE in color (*n*/100 hooks, where *n* is a number of catch) from 2004 to 2010 and the black line shows monthly CPUE.

3. RESULTS

3.1. Seasonal Variation of Swordfish Catch

The latitudinal positions of longline fishing reflect a seasonal feeding migration pattern of swordfish moving over the latitudes 25°N-45°N (**Figure 1**). From autumn to winter seasons the surface longliners chase swordfish migrating southward more than 2,000 km, meanwhile from spring to summer seasons, they migrate northward from the center of the subtropical gyre at 25°N to the northern edge of the KE system, the Kuroshio-Oyashio mixed water region at 42–43°N.

During this swordfish migration, CPUE values recorded on the daily basis show seasonal variations which can be clearer after computing them monthly (black line in **Figure 1**). When the fishing positions reach northernmost regions, and reverse to the south in late autumn, the values of CPUE start increasing significantly which is followed by a rapid decrease in early winter. After this, there is also a CPUE increase when the southward migration reaches around 33–35°N. The monthly CPUE shows a repeated seasonal pattern that coincides with this migration previously described. Accordingly, the monthly CPUE exhibits two peaks in most of the years analyzed, due to CPUE increases in the northern and southern fishing sites in different seasons. The high CPUE values are observed during late autumn in the northern fishing site, whereas they appear during winter season in the southern site. These two seasonal CPUE peaks could be demonstrated clearly by separating the CPUE data into two groups according to the fishing site: southern region, 25–36°N and northern region, 36–45°N (**Figure 2A**). In the southern region, CPUE peaks occur mostly in winter season (Dec-Jan, red line in **Figure 2A**), while they appear mostly during autumn to winter season (Oct–Dec) in the northern region except early 2009 (blue line in **Figure 2A**).

3.2. Interannual Variation in the Kuroshio Extension System

Besides the seasonal variations presented in the previous section, both regions also display interannual variations in their CPUE values during the study period 2004–2010, which could be attributed to the decadal modulations of the Kuroshio Extension reported extensively in the previous studies (Qiu and Chen, 2005; Lin et al., 2014). Swordfish CPUE presents a decreasing trend from 2006 through 2009 in the southern (red curve in **Figure 2A**), and an increasing trend from 2004 through 2007 followed by a decreasing trend after 2007 in the northern fishing site (blue line in **Figure 2A**). In order to illustrate the interannual transitions of the Kuroshio Extension system, we computed the KE path defined as the longest contour at SSH = 0 in the region 30–40°N, 140–155°E. The obtained KE paths present the interannual phase transitions between stable and unstable period (**Figures 2B,D**). Since this result is consistent with a previous study by Qiu and Chen (2010) showing the same path transitions, our study period was divided into two, i.e., stable phase which

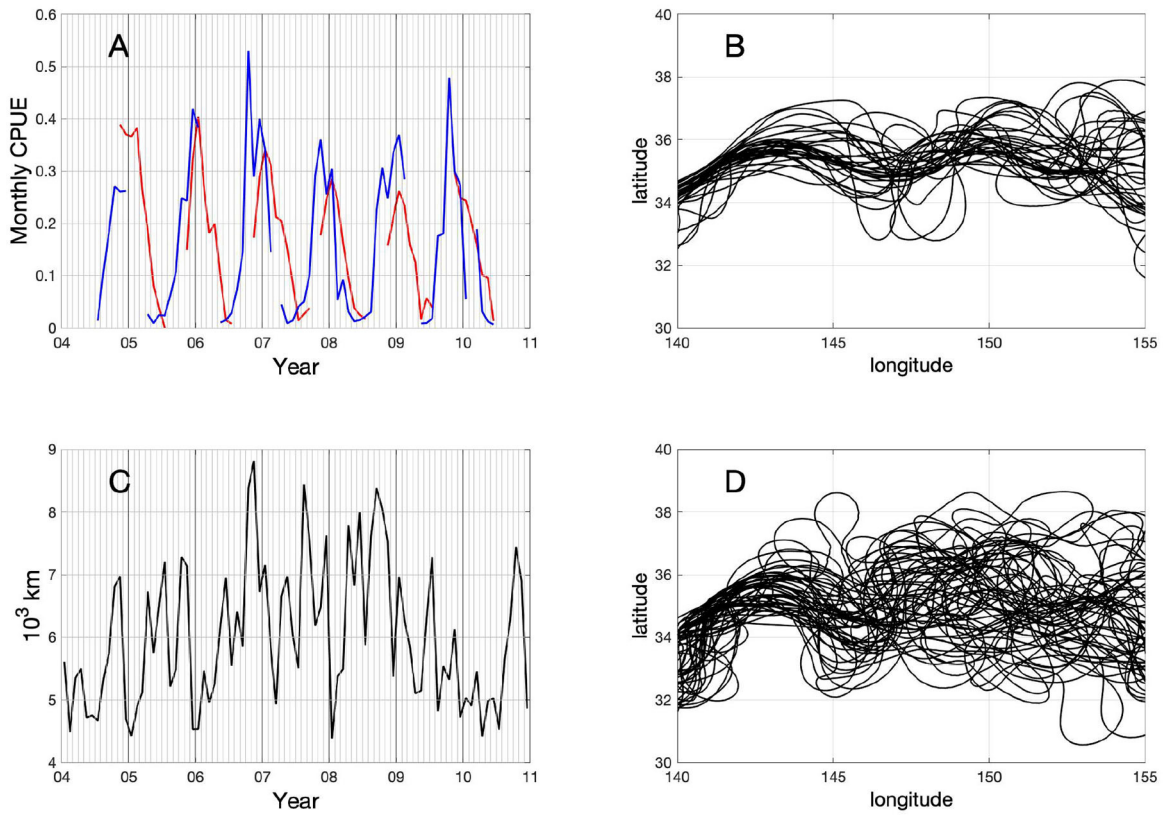

FIGURE 2 | Time series of **(A)** the monthly CPUE from 2004 to 2010 in the range 140–175°E for (red) southern region 25–36°N and (blue) northern region 36–45°N and of **(C)** monthly Kuroshio Extension path length (10^3 km) between 140 and 175°E. Monthly averaged paths of the Kuroshio Extension defined by the longest contour of sea surface height (SSH) at 0 m using FORA-WNP30 data for **(B)** stable paths for the years 2004, 2005, and 2010, and **(D)** unstable paths during the period 2006–2009. The abscissa is longitude (°E) and the ordinate is latitude (°N).

includes the years of 2004, 2005, and 2010, and the unstable phase from 2006 through 2009.

During the stable phase (2004, 2005, 2010), the KE shows relatively straight paths, defining clearly two quasi-stationary meander crests located at 144 and 150°E (**Figure 2B**). On the contrary, during the unstable phase (2006–2009), apparently more convoluted paths are observed (**Figure 2D**). At the same time, during the latter described unstable phase, the KE paths become longer reaching up to 9,000 km of their length in late 2006, whereas path lengths are relatively shorter during the stable phase (**Figure 2C**).

By comparing the path length of the KE with the swordfish CPUE in each region (southern region, 25–36°N and northern region, 36–45°N) separately, it is observed that the swordfish CPUE in the northern region modulates similarly to the KE path length with the longer path length resulting in the higher CPUE, although there is an exceptional CPUE peak in late 2009 with a shorter path length (blue line in **Figure 2A** and black line in **Figure 2C**). The CPUE in the northern region shows a distinct peak in late 2006, which coincides well with the peak in the KE path length at the same time. On the other hand, the CPUE in the southern region shows an opposite trend to that of the KE path length and CPUE in the northern region with a largest CPUE value in early 2006 followed by a decreasing trend until middle of 2009 (red line in **Figure 2A**).

Despite these interannual changes in the CPUE, seasonal north-south migration shows the periodic annual cycle, i.e., the northward migration during spring to summer and the southward migration during autumn to winter (**Figure 1**). In contrast, longitudinal CPUE distributions are found to exhibit interannual transitions (**Figure 3**). In the northern region (36–45°N), the CPUE in the western region, 143–155°E shows relatively high values in autumn to winter season during the unstable period (**Figure 3A**). Note that during autumn to winter, swordfish migrate from north to south. On the other hand, during most of the stable years, 2004–2005, the CPUE values in the western part are relatively low. In the southern region, the longitudinal transitions in CPUE distributions are not as clear as that in the northern region. However, during most of the stable years, 2004–2005, relatively high CPUE values are found also in the western region 143–155°E during winter to spring season (**Figure 3B**). In the latter season, swordfish start migrating northward. Thus, the CPUE in the western region 143–155°E is most likely to be a key to induce observed interannual modulations both in the northern and the southern regions. The CPUE-weighted-mean zonal positions of longliners,

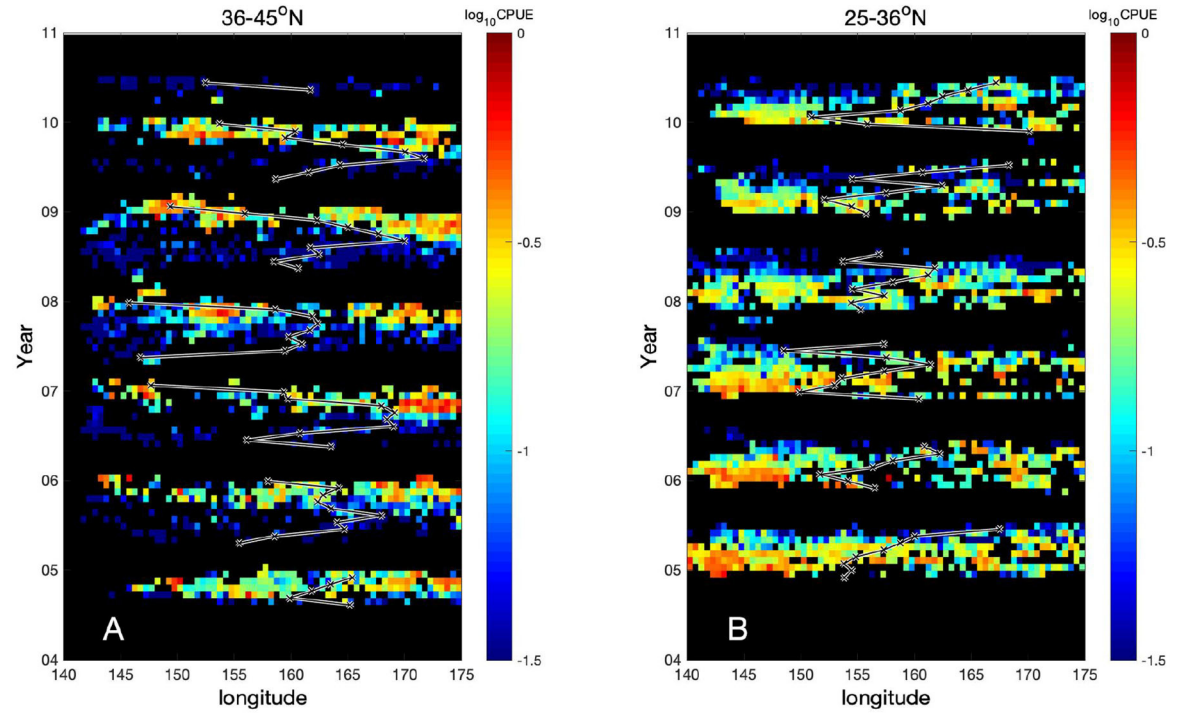

FIGURE 3 | CPUE as a function of longitude and time for **(A)** northern region 36–45°N and for **(B)** southern region 25–36°N. Black lines are the CPUE-weighted-mean zonal positions of longliners, which is computed by Σ_{long}[longitude × CPUE/ Σ_{long}CPUE], where Σ_{long} is sum along longitude every month so that sum of CPUE/ Σ_{long}CPUE is 1.

shown as black lines in **Figure 3**, reflect the pattern of zonal seasonal migration of the swordfish. In the northern region, it moves mostly eastward during spring to summer, while it turns westward during autumn to winter (**Figure 3A**). During the unstable period, it can approach to the western region 143–155°E in winter where the high CPUE values appear in the same period, while it does not reach to the western region during the stable period. On the contrary, the CPUE-weighted-mean zonal positions are relatively stationary in the southern region (**Figure 3B**). This suggests that in the northern region, swordfish distribute more heterogeneously in the zonal direction, depending on seasons and years than the southern region. Because smooth and convoluted KE paths, during the respective stable and unstable phase in the same western part 143–155°E (**Figures 2B,D**), are caused by less and more active mesoscale eddies, these results imply that the KE stability state and associated mesoscale variabilities in the western region affect largely on the swordfish CPUE values hence also on their relative abundance.

3.3. Physical Conditions for High Swordfish CPUE

The results in the previous section suggest that the decadal KE variability causes the interannual modulations in the swordfish CPUE. To investigate the CPUE dependency on the water property and its interannual changes, time series of CPUE is computed as a function of temperature and salinity averaged over upper 200 m. In the southern region, high CPUE values (>0.3) are found with high temperature (>18°C) and salinity (>34.7) throughout the study period (**Figures S1C,D**). On the other hand, in the northern region, high CPUE values are found with wide ranges of temperature (8–23°C) and salinity (33.4–34.9) during the unstable period, 2006–2009 (**Figures S1A,B**). On the contrary, during the stable phase, these high CPUE values are found only with high temperature and salinity in both regions. Similarly, the CPUE computed on the Temperature-Salinity (T-S) diagram during the unstable period in the northern region shows higher values in the widest ranges of temperature and salinity amongst the regions and periods (**Figure S2**). These high CPUE values in the northern region, during the unstable phase, are found in higher temperature ranges if compared with those of the same salinity, and in relatively lower salinity ranges at the same temperature (**Figure S2A**). On the other hand, during the stable period in the northern region, the ranges of temperature and salinity with high CPUE are narrowed and the CPUE values are lower than those in unstable period (**Figure S2B**). Meanwhile, for southern region, there is no clear difference between unstable and stable period, concentrating high CPUE values at high temperature and salinity ranges (**Figures S2C,D**), similar to **Figures S1C,D**.

Since the KE modulation is known to be driven by mesoscale eddies, it is suspected that the swordfish CPUE can also be influenced by the mesoscale flows, leading to the observed interannual CPUE modulations. To understand the role of

mesoscale eddies in driving the interannual variations of the CPUE, several dynamic parameters to characterize the mesoscale flows are examined. **Figure 4A** indicates that, in the northern region, higher CPUE values are mostly associated with negative values of OW (rotating regime) and with negative values of vorticity (anticyclonic vorticity, clockwise rotating flow in the northern hemisphere), suggesting that some physical structures and biological conditions associated with anticyclonic warm-core eddies lead to the high swordfish CPUE. Besides that, CPUE values are higher with slightly positive values of divergence of Q-vector, $\nabla_h \cdot \mathbf{Q}$ (convergence zones), i.e., downwelling motions (**Figures 4B,C**). The results of these dynamic parameter analyses suggest that the higher CPUE in the northern region is found with negative OW, negative vorticity and positive $\nabla_h \cdot \mathbf{Q}$ (downwelling motions). On the other hand, this tendency (negative vorticity, negative OW and positive $\nabla_h \cdot \mathbf{Q}$) is subtle in the southern region. This indicates that here these parameters are not useful as in the northern region (**Figures 4D–F**).

To investigate the effects of the KE path modulations on the relationships between above physical parameters and the CPUE, the same analyses are conducted separately for the unstable and the stable KE phases. The results for the unstable phase are found to be very similar to that for the entire period, in which higher CPUE values are found with negative vorticity, negative OW, and slightly positive $\nabla_h \cdot \mathbf{Q}$ in the northern region (**Figures 5A–C**). It should be noted that these high CPUE values in the unstable phase are even higher compared to that computed for the entire period (**Figures 4A–C**, **5A–C**). In contrast, high CPUE values associated with these parameter ranges are absent in the northern region during the stable phase (**Figures 6A–C**), being clearly distinguishable in comparison to the unstable phase (**Figures 5A–C**). In the southern region, no clear trend is found with these parameters regardless of stable or unstable states of the KE (**Figures 5D–F**, **6D–F**).

3.4. Eddy Detection Analysis

So far, the results indicate that the higher values of CPUE are formed within anticyclonic eddies with downwelling motion. However, these analyses have not considered eddies explicitly. For this reason, the eddy detection analysis is conducted in order to determine if mesoscale eddies do affect the swordfish CPUE.

The mean CPUE computed for anticyclone (warm-core eddies) (**Figure 7A**) and cyclone (cold-core eddies) as a function of zonal and meridional distance from the closest detected mesoscale eddy (**Figure 7B**) shows clearly that the CPUEs in and near the anticyclonic eddies are higher than in cyclonic eddies roughly by a factor of 2–3. It should be noted that, in the anticyclonic eddies, higher CPUEs are found on the northeastern side of the warm-core eddies within the regions of 100 km from the eddy center (**Figure 7A**). From the mesoscale

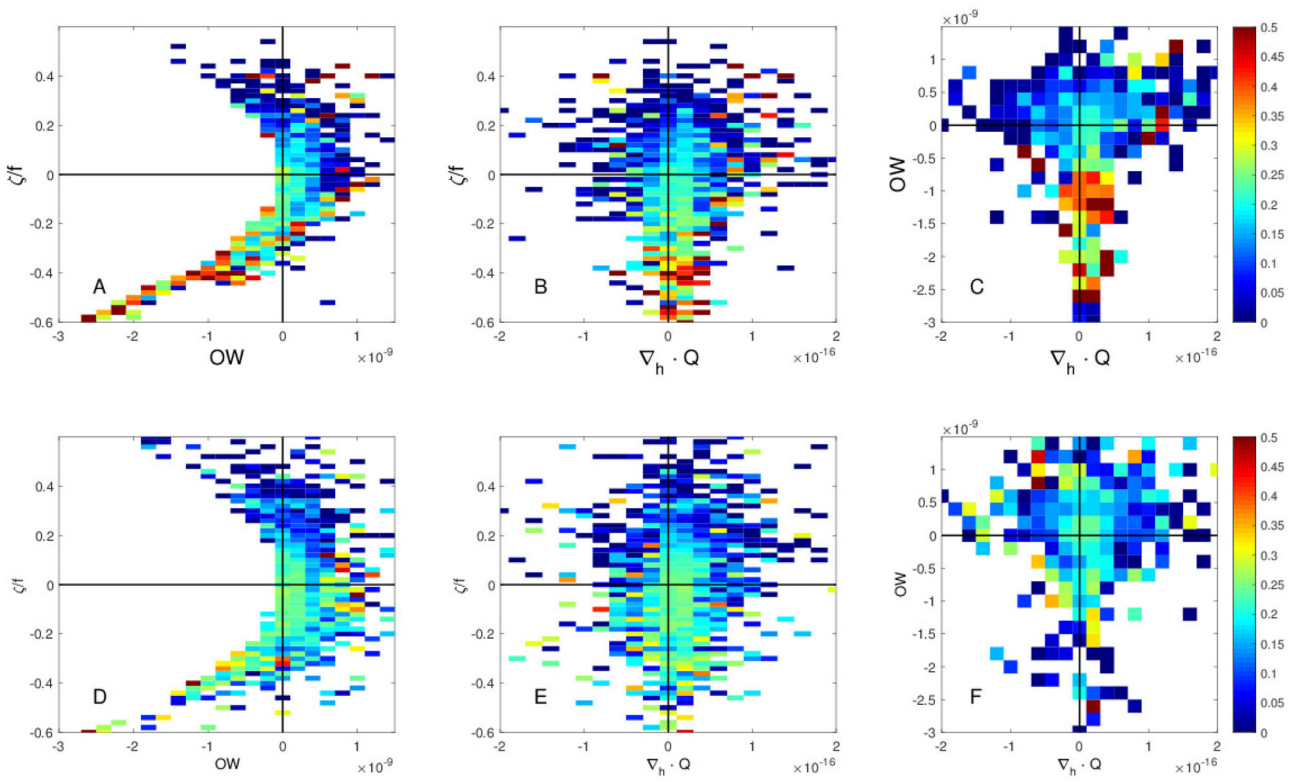

FIGURE 4 | Swordfish CPUE as a function of **(A,D)** Okubo-Weiss (OW) parameter (2) and vorticity (3) normalized by f Coriolis parameter, ζ/f, **(B,E)** divergence of Q-vector, $\nabla_h \cdot \mathbf{Q}$ (4) and normalized vorticity ζ/f, and **(C,F)** divergence of Q-vector and OW for **(A–C)** the northern region 36–45°N, and for **(D–F)** the southern region 25–36°N.

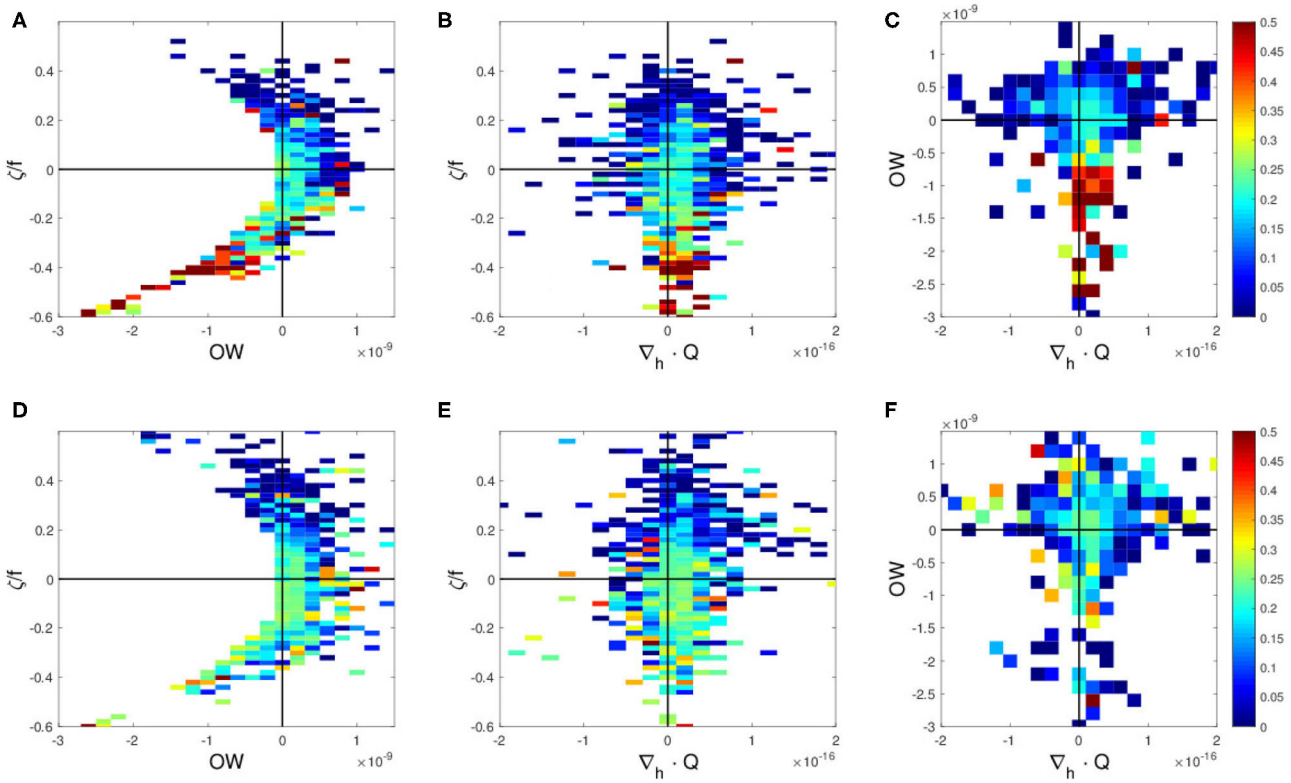

FIGURE 5 | Swordfish CPUE during the unstable period 2006–2009 as a function of **(A,D)** Okubo-Weiss (OW) parameter (2) and vorticity (3) normalized by *f* Coriolis parameter, ζ/f, **(B,E)** divergence of Q-vector, $\nabla_h \cdot \mathbf{Q}$ (4) and normalized vorticity ζ/f, and **(C,F)** divergence of Q-vector and OW for **(A–C)** the northern region 36–45°N, and for **(D–F)** the southern region 25–36°N.

dynamic parameter analyses presented in the previous section, it is found that the high CPUE values are associated with negative OW, negative relative vorticity, and positive $\nabla_h \cdot \mathbf{Q}$, which can be interpreted as anticyclonic warm-core eddies with downwelling tendency. This is further supported explicitly by the eddy detection analysis, in which the high CPUE values are found more in and near the anticyclonic warm-core eddies.

To clarify where this downwelling tendency accompanied by the higher CPUE occurs with respect to the warm-core eddies, the divergence of Q-vector ($\nabla_h \cdot \mathbf{Q}$) is averaged as a function of distance from the closest eddy for each fishing location regardless of the CPUE values. In the northern region, the average $\nabla_h \cdot \mathbf{Q}$ shows positive values on the eastern side and negative ones on the western side, suggesting that the downwelling and upwelling occur on the eastern and western side of the anticyclones, respectively (**Figures 8A,B**). On the other hand, for cyclones, downwelling tendency ($\nabla_h \cdot \mathbf{Q} > 0$) is found on the western side, and upwelling ($\nabla_h \cdot \mathbf{Q} < 0$) is observed on the eastern side.

In addition to the $\nabla_h \cdot \mathbf{Q}$, the frontogenetical function, $\mathbf{Q} \cdot \nabla_h b$ is averaged similarly as a function of zonal and meridional distance from the closest detected mesoscale eddy. In the northern fishing region, anticyclonic eddies present a trend to increase the lateral buoyancy gradient with $\mathbf{Q} \cdot \nabla_h b > 0$ on the eastern edge of the warm-core eddies (**Figure 8C**). Meanwhile, for cyclones $\mathbf{Q} \cdot \nabla_h b > 0$ is found near the center but on the southwestern side (**Figure 8D**). Both positive values of $\mathbf{Q} \cdot \nabla_h b$ are found in the region of the downwelling tendency, reflecting the typical downwelling ($\mathbf{Q} \cdot \nabla_h b$) expected on the dense side of the front under the frontogenesis ($\mathbf{Q} \cdot \nabla_h b > 0$) (Hoskins, 1971).

To investigate how the interannual variabilities, shown in the previous section, are related with the detected mesoscale eddies, the eddy detection results are analyzed further for the stable and the unstable phases separately. During the unstable phase, the mean CPUE in and near the mesoscale anticyclonic warm-core eddies shows roughly two times higher values than those during the stable phase (**Figures 9A,C**). The same tendency of higher CPUE during the unstable phase than the stable phase is found for the cyclonic cold-core eddies, although the values of CPUE are about three times smaller than those for the anticyclonic warm-core eddies (**Figures 9B,D**). Results of the same eddy detection analysis, but limited for the northern region, 36 - 45°N, show the same tendency that the higher CPUEs are found more on the northeastern side of the anticyclonic warm-core rings during the unstable phase (**Figure 10**). However, this tendency is much weaker in the southern region, 25–36°N where the difference of the CPUEs between stable and unstable phases decreases to about a half of that in the northern region

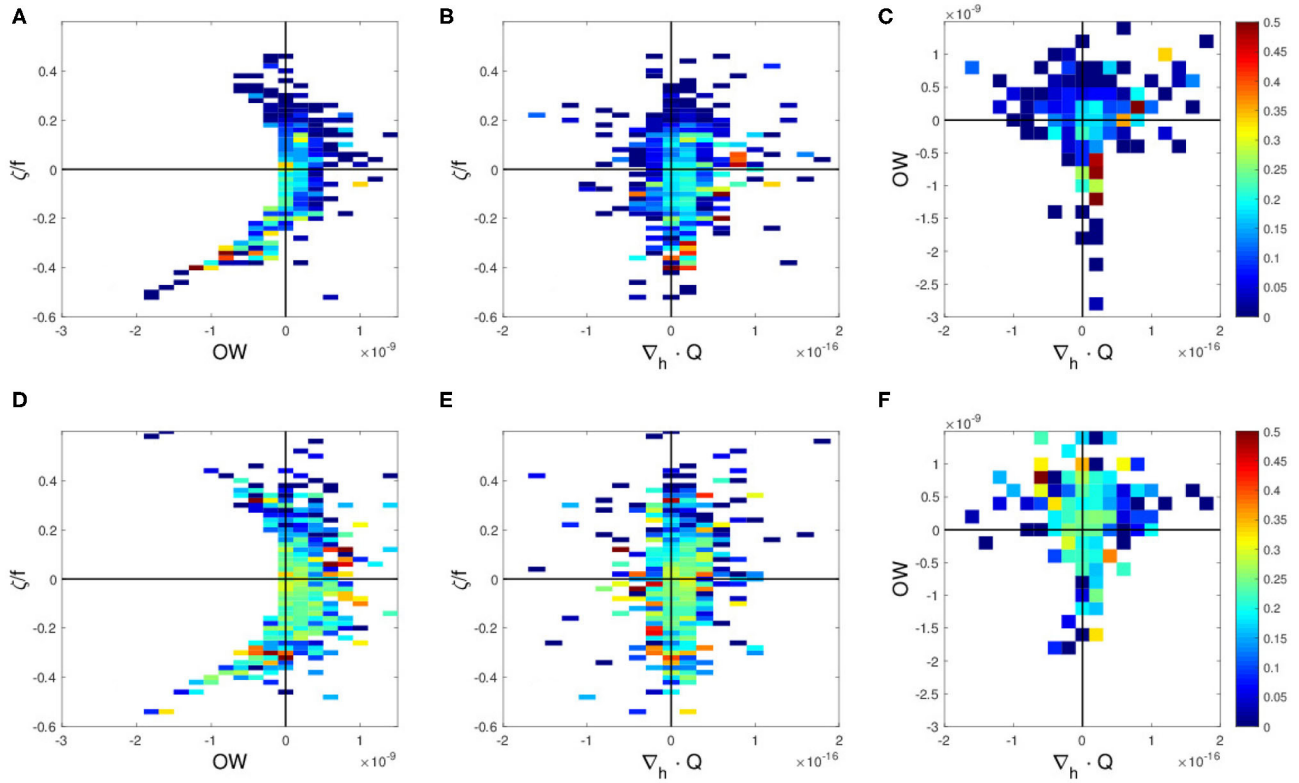

FIGURE 6 | Swordfish CPUE during the stable years 2004–2005 and 2010 as a function of **(A,D)** Okubo-Weiss (OW) parameter (2) and vorticity (3) normalized by f Coriolis parameter, ζ/f, **(B,E)** divergence of Q-vector, $\nabla_h \cdot \mathbf{Q}$ (4) and normalized vorticity ζ/f, and **(C,F)** divergence of Q-vector and OW for **(A–C)** the northern region 36–45°N, and for **(D–F)** the southern region 25–36°N.

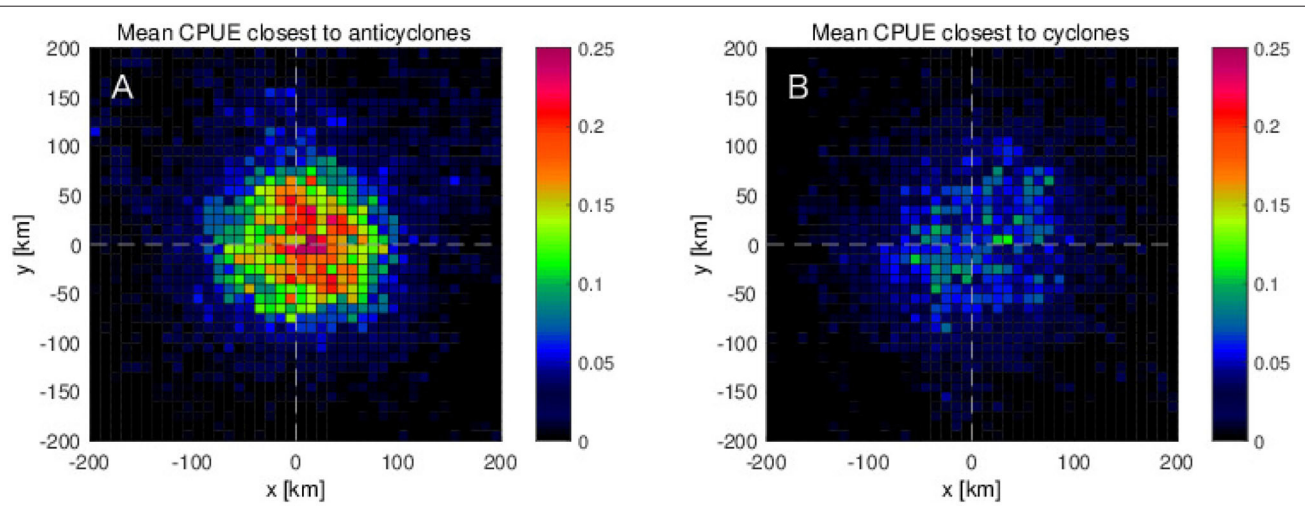

FIGURE 7 | Mean CPUE as a function of distances from the center of eddies along zonal and meridional directions for **(A)** anticyclonic eddies (or warm-core rings: WCR) and **(B)** cyclonic eddies (or cold-core rings: CCR), which are closest to each swordfish fishing position.

(**Figures 10**, **11**). What is more, in the southern region, the peak of CPUE formed on the northeastern side of the anticyclonic warm-core eddies found in the northern region disappears (**Figures 10A**, **11A**).

These results from the eddy detection analyses suggest that the interannual changes of the swordfish CPUE in the northern region are caused by environmental changes associated with the mesoscale anticyclonic warm-core eddies. Therefore, the number

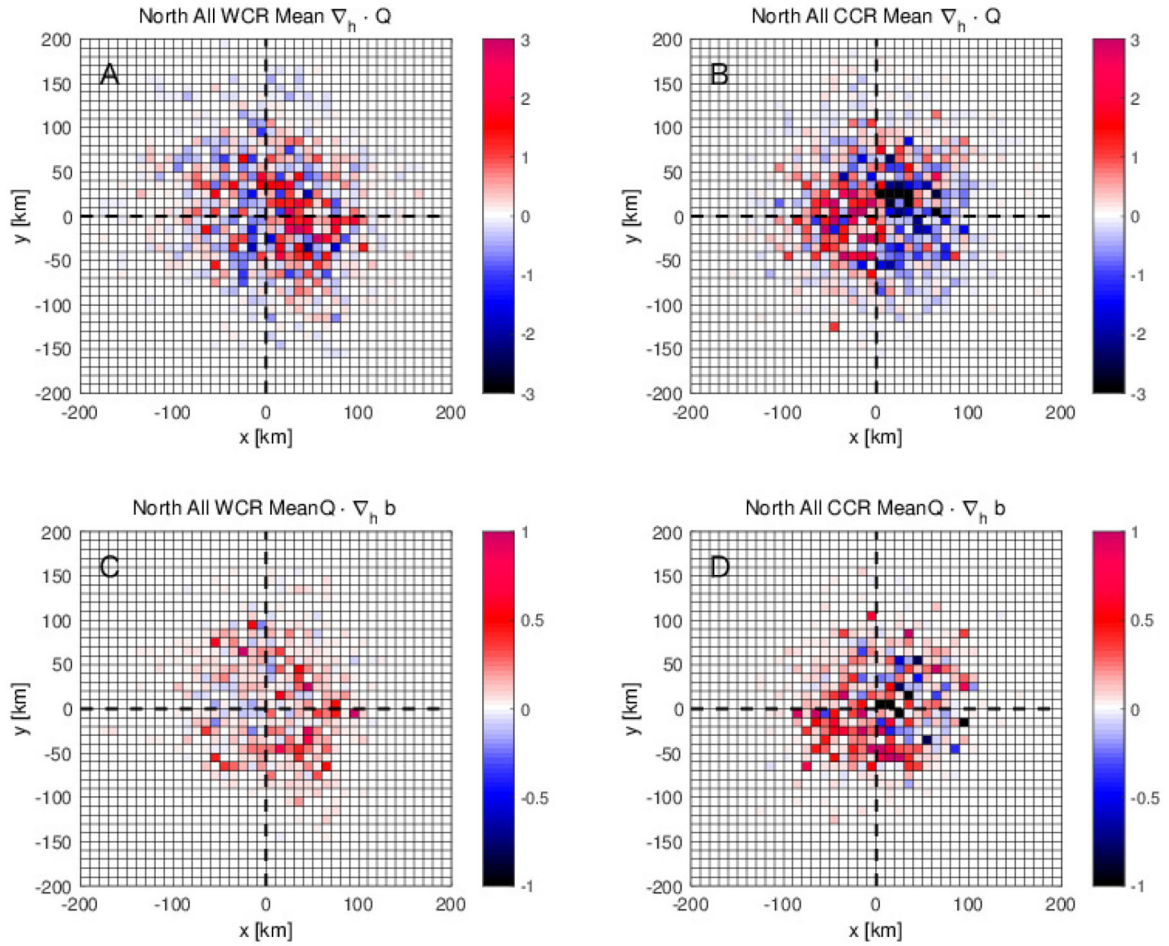

FIGURE 8 | (A,B) Average divergence of Q-vector $\nabla_h \cdot \mathbf{Q}$ (4) and **(C,D)** average frontogenetical function $\mathbf{Q} \cdot \nabla_h b$ (5) as a function of zonal and meridional distance from the center of the closest eddy to the fishing location for **(A,C)** warm-core rings (WCR) and for **(B,D)** cold-core rings (CCR) in the northern fishing site.

of detected warm-core eddies in the northern region are counted. During the unstable phase in the northern region, 36–45°N, the number of anticyclonic warm-core eddies increases by 15% in comparison to those formed in the stable period. Also, this number exhibits distinct high-frequency seasonal changes with higher values in spring to summer for most of the years except late 2008 (**Figure 12**).

The Eddy Kinetic Energy (EKE), averaged in the upper 100 m depth in the KE region, also shows interannual modulations in response to the variation of the KE states (**Figure 13**), which is consistent with that in the number of detected mesoscale anticyclonic warm-core rings. During the stable phase (2004–2005, 2010), high EKE values (>0.3 m^{2}s^{-2}) are confined in the relatively narrow region along the straight path with the two meander crests at 144 and 150°E (similar to **Figure 2B**). On the other hand, during the unstable phase of 2006–2009, the high EKE is more accumulated in the western region, where the Kuroshio Current separates from the Japanese coast. At the same time, the latitudinal extent of the high EKE (>0.3 m^{2}s^{-2}) becomes wider, covering more area in the northern latitudes. These results suggest that the wider high EKE latitudinal extent to the northern region during the unstable phase is caused by more mesoscale eddies including anticyclonic warm-core rings in the same region and period.

4. DISCUSSION

Although several previous studies have found effects of mesoscale physical features, such as the formation of meanders, eddies, and filaments on the distribution of marine species (Sugimoto and Tameishi, 1992; Correa-Ramírez et al., 2007; Vásquez et al., 2013; Hsu et al., 2015; Braun et al., 2019), some of their analyses were limited only to short-term fishery data with a few mesoscale events. Therefore, it has been unclear how the reported results are robust under seasonal and interannual variabilities. Even with intensive dataset over a longer period of time, studies on the interannual changes of pelagic fish distributions and abundance in relation to the mesoscale processes are still very limited. In contrast, the results of this study using relatively long-term (7 years) fishery data with eddy-resolving ocean reanalysis clearly

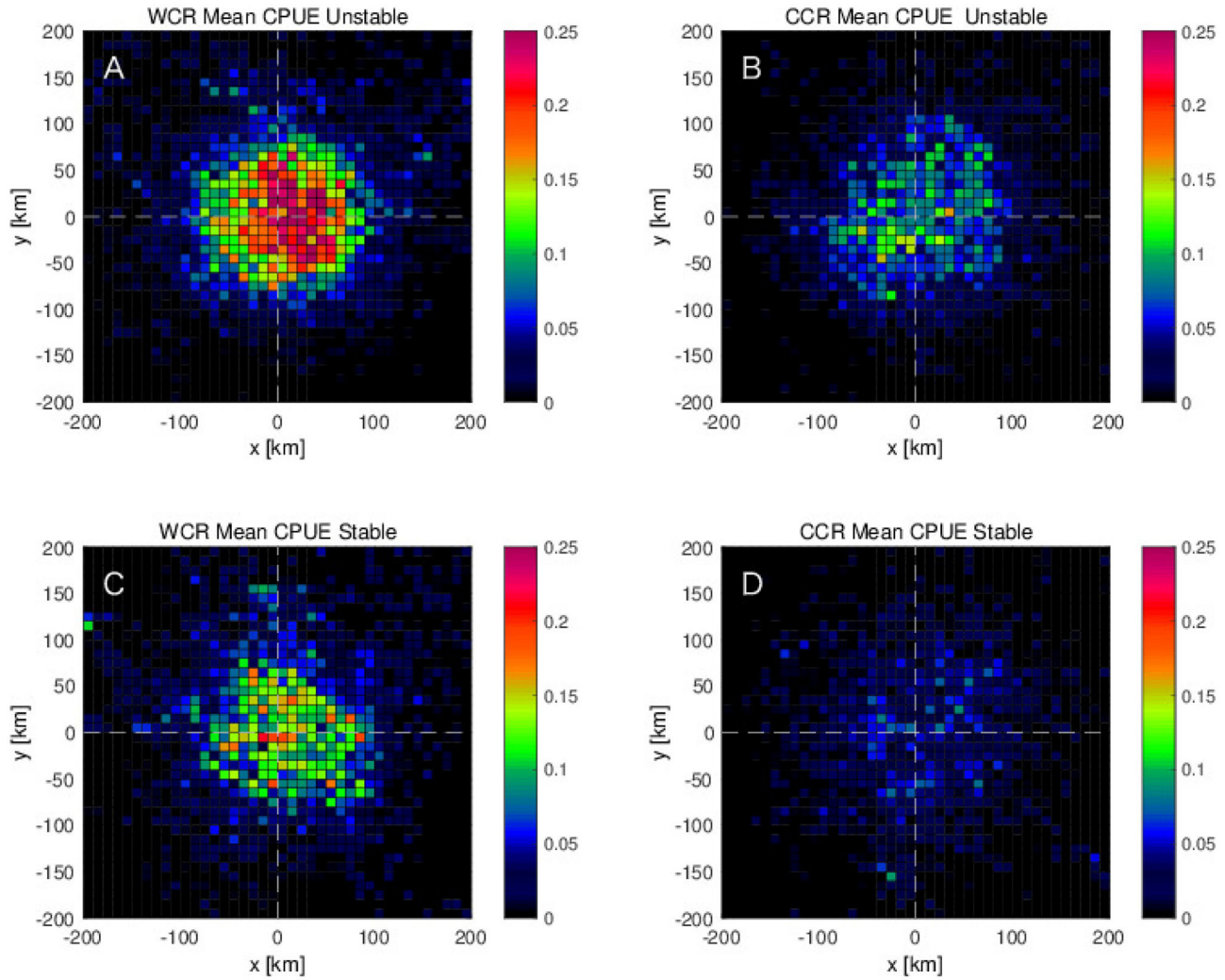

FIGURE 9 | Mean CPUE as a function of distances from the center of eddies along zonal and meridional directions for **(A,C)** anticyclonic eddies (or warm-core rings: WCR) and **(B,D)** cyclonic eddies (or cold-core rings: CCR), which are closest to each swordfish fishing position in **(A,B)** unstable period 2006–2009 and in **(C,D)** stable period for years 2004, 2005, and 2010.

indicate that high swordfish CPUEs are found in and near the anticyclonic eddies. The results are contradictory comparing to the previous study made by Hsu et al. (2015) in the western North Atlantic, in which the high swordfish relative abundance was negatively correlated with presence of mesoscale eddies. It should be noted that these effects on the catch may differ depending on the swordfish stock behavior. Also, the clear tendency of more swordfish in anticyclones, warm-core eddies in the western North Pacific in this study would be the result of the absence of topographic features in the upstream KE region. In contrast, it has been reported in the North Atlantic that swordfish appear to be attracted to complex high-relief bottom structures and complex thermal structures, such as the topography relief of the Charleston Bump (Sedberry, 2001; Sedberry and Loefer, 2001).

In this study, the period for the analyses is divided into two phases based on the interannual KE path modulation, the stable phase for years 2004, 2005, and 2010, and the unstable phase from 2006 through 2009. The results of our analyses using several dynamic parameters, the eddy detection technique, and the eddy kinetic energy in relation to the swordfish CPUE reveal also that the well-known variation in the KE system (Qiu and Chen, 2005; Jiang et al., 2017) could have large influences on the swordfish relative abundance. The swordfish CPUE in the northern region (36–45°N) increases proportionally to the KE path length with higher values during the unstable KE phase, whereas that in the southern region (25–36°N) exhibits an opposite tendency with low values during the unstable phase. These opposite interannual CPUE trends in the northern and southern regions are reminiscent of the north-south seesaw decadal variability found in the surface chlorophyll concentration by Lin et al. (2014). However, while phytoplankton are mostly passive to the flow, swordfish migrates seasonally between subtropical

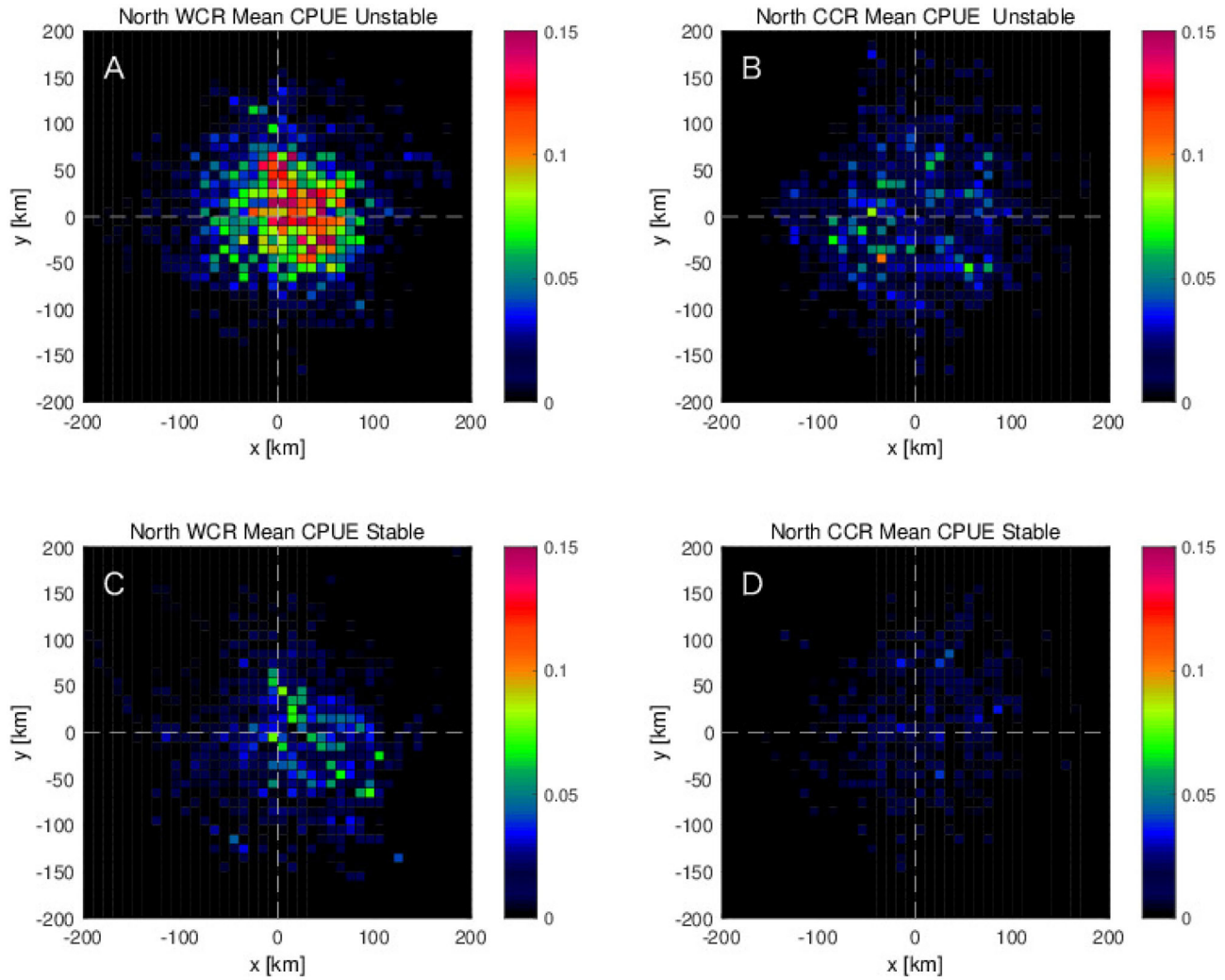

FIGURE 10 | Mean CPUE for the northern region, 140–175°E and 36–45°N as a function of distances from the center of eddies along zonal and meridional directions for **(A,C)** anticyclonic eddies (or warm-core rings: WCR) and **(B,D)** cyclonic eddies (or cold-core rings: CCR), which are closest to each swordfish fishing position in **(A,B)** unstable period 2006–2009 and in **(C,D)** stable period for years 2004, 2005, and 2010.

region and the Kuroshio-Oyashio confluent region over several thousands of kilometers.

According to Watanabe et al. (2009), south-north swordfish migrations in the western North Pacific are strongly affected by their feeding ecology, i.e., prey distributions. More presence in the subtropical region (29–34°N) from winter to spring seasons and in the transition zone (35–41°N) from summer to autumn is because of the better feeding conditions. Their defined subtropical region corresponds to the southern region, and the transition zone to the northern region of this study. Therefore, the CPUE peak in late autumn in the northern region, just before the southward migration, and the other peak during winter in the southern region, are due to more presence of swordfish prey in each region. Our results of the north-south seasonal transitions in the CPUE are strikingly similar and consistent with the reported patterns of the swordfish feeding migration (Watanabe et al., 2009), suggesting that seasonal distribution of swordfish in the study area is mainly controlled by the zoogeographical distribution patterns of their prey species.

Besides this feeding migration, it should be noted that swordfish are distributed relative to preferred thermal habitats, i.e., temperature fronts, for energetic gains by riding currents and enhanced feeding regime (Seki et al., 2002). Swordfish migrates toward more favorable areas for their feeding and physical conditions. Even though it is known that this species can be found within the temperature range of 5–27°C and it is frequently found in surface waters at 13°C (Nakamura, 1985), swordfish prefer warm temperatures within the range of 18–22°C (Uda, 1960). This condition is consistent with our results shown in **Figures S1C,D**, **S2C,D**, highlighting their preferred warm (18–22°C) and high salinity (>34.7) conditions in the southern region, regardless of the KE stability. Note that temperature and

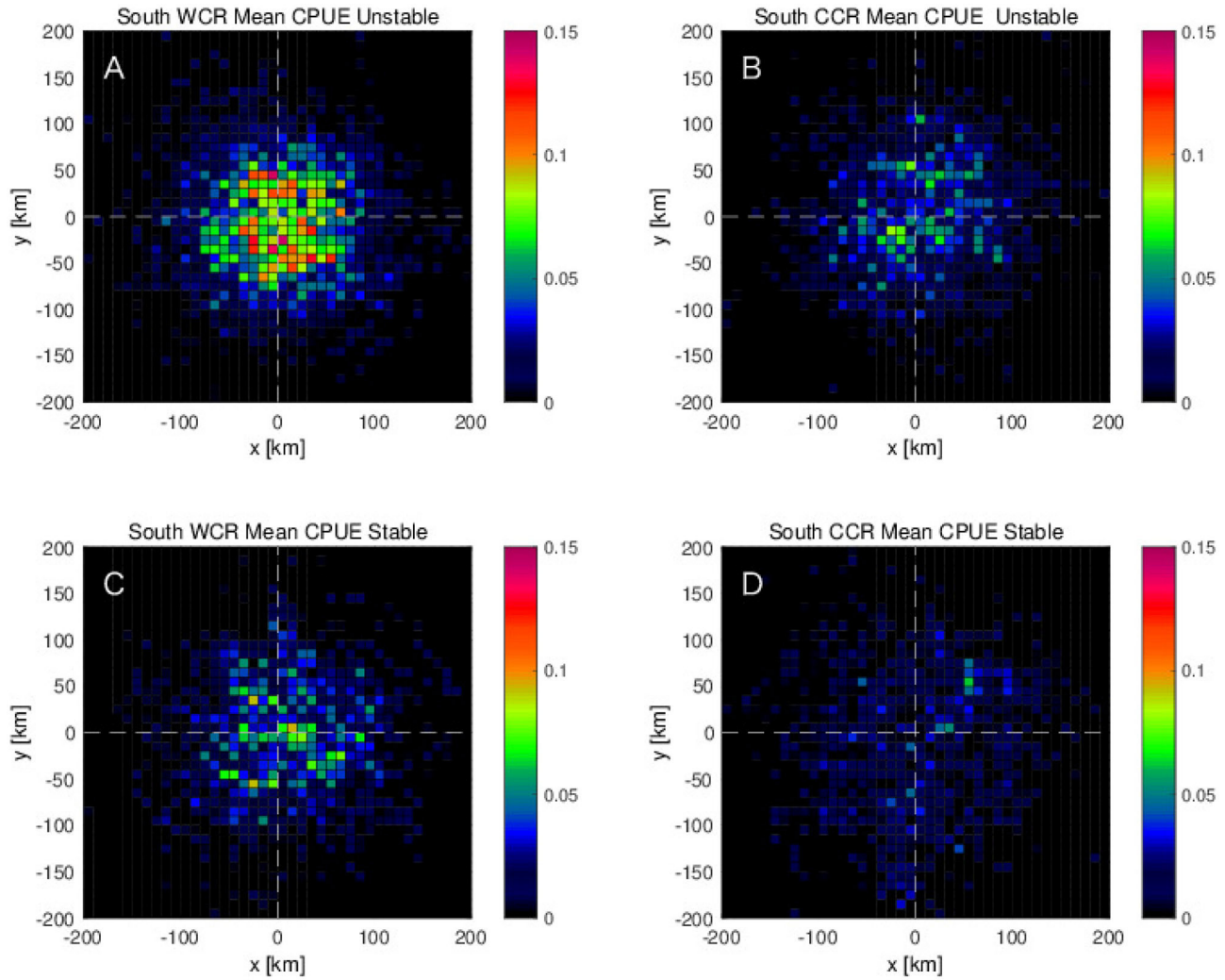

FIGURE 11 | Mean CPUE for the southern region, 140–175°E and 25–36°N as a function of distances from the center of eddies along zonal and meridional directions for **(A,C)** anticyclonic eddies (or warm-core rings: WCR) and **(B,D)** cyclonic eddies (or cold-core rings: CCR), which are closest to each swordfish fishing position in **(A,B)** unstable period 2006–2009 and in **(C,D)** stable period for years 2004, 2005, and 2010.

salinity for this analysis were averaged over upper 200 m, which could be deeper than the warm layers at the edges of warm-core eddies and streamers in the northern region, but thinner than the warm salty mode water in the recirculation gyre south of the KE. Therefore, the high CPUE values associated with much wider temperature and salinity ranges in the northern region, especially during the unstable KE phase (**Figures S1A,B**, **S2A**), suggest that swordfish can distribute following the surface trapped warm-salty waters of the streamers and warm-core eddies which are more frequently seen during the unstable phase in the region north of the KE.

The most important agents to drive the interannual modulations of CPUE in this northern region are found to be anticyclonic warm-core eddies, especially in the western region 143–155°E (**Figures 3A**, **6**, **12**). The high EKE values (>0.3 m^{2}s^{-2}) in the western KE region during unstable phase, with its wider latitudinal extent toward north (**Figure 13**), are consistent with the increasing number of anticyclonic warm-core eddies in the unstable period (**Figure 12**). While these anticyclonic eddies move westward as the first baroclinic mode Rossby waves, the warm streamers that are more abundant during the unstable phase, can fuel warm-salty water to the warm-core eddies (Sugimoto et al., 1992; Yasuda et al., 1992). At the same time, near the Japanese coast, these rings move generally northward (Mizuno and White, 1983; Tomosada, 1986; Yasuda et al., 1992), providing more suitable conditions that swordfish can distribute in the northern region. For migrating swordfish, it becomes easier to find warm-salty water due to more warm-core eddies during unstable phase, which the swordfish can utilize during their migrations to the northern feeding sites or to the southern warm-salty habitats and spawning sites.

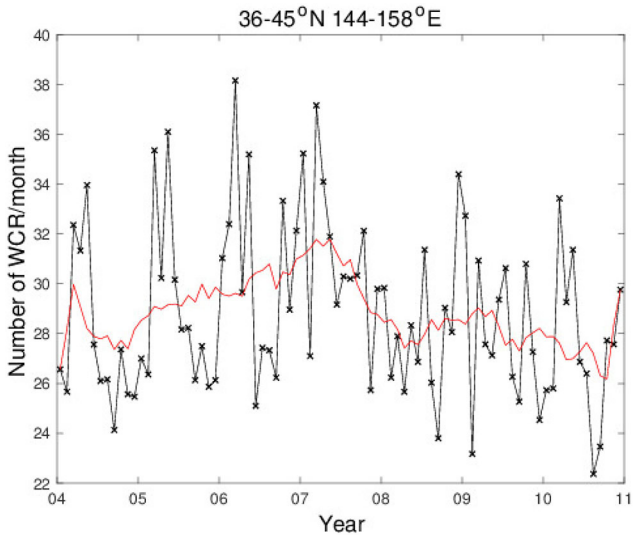

FIGURE 12 | Temporal variation of number of detected warm-core eddies per month, from 2004 through 2010 in the western North Pacific region 144–158°E and 36–45°N, is represented by black cross and line. The red curve shows moving average with a period of a year.

According to the eddy detection analysis, high CPUE values are found on the northeastern side of the closest anticyclonic warm-core eddies (**Figure 9A**), especially in the northern region, 36–45°N during the unstable phase (**Figure 10A**). The high CPUE values on the northeastern side of these anticyclonic warm-core eddies are found to coincide with the positive divergence of Q-vector ($\nabla_h \cdot \mathbf{Q} > 0$), suggesting that swordfish high CPUE values are accompanied by adiabatic downward flow. The result also shows upwelling tendency ($\nabla_h \cdot \mathbf{Q} < 0$) on the western side of the warm-core eddies with relatively lower CPUE values. The reasons of upwelling and downwelling on the western and eastern sides of the anticyclonic eddy is, however, unclear. Although recent numerical studies have reported that the dipole pattern of the vertical velocity arises in mesoscale eddies, similar to the patterns shown in **Figures 8A,B**, adiabatic up- and downwelling do not necessarily occur on the western and eastern side, respectively, of an anticyclone. Their orientation with respect to an eddy depends on how the eddy is detached from a main current (Pilo et al., 2018), and how the Q-vector distributes (Estrada-Allis et al., 2018). Before an anticyclonic ring is detached from the anticyclonic meander of the KE, the upwelling and the downwelling are seen from the meander trough to the crest, and from the crest to the trough, respectively (Bower and Rossby, 1989). The former is on the western side and the latter on the eastern side of the meander crest, where the anticyclonic meander leads respective northward and southward flow on the western and eastern side, while the background isopycnal shoals northward. This implies that the anticyclonic eddies which accommodate swordfish are relatively young, and close to the generation sites keeping the aforementioned up- and downwelling tendencies associated with the meandering patterns. This could be the reason why downwelling tendency is found on the eastern side of the anticyclonic warm-core eddies, where the high CPUE values coincide (**Figure 8A**).

By extracting the divergence of Q-vector $\nabla_h \cdot \mathbf{Q}$ at each fishing point located only on the northeastern side of the warm-core eddies (a green shape in **Figure S3B**), it is observed that higher values of $\nabla_h \cdot \mathbf{Q}$ appear in the western regions at 143°E, 148°E, and 152–155°E in the northern fishing site (black line in **Figure S3**). Furthermore, number of these eddies accompanied by fishing activities on their northeastern side is larger in the same region (red line in **Figure S3**). This indicates that the warm-core eddies, in the western region, are the main contributors to increase the divergence of Q-vector on the northeastern side of the warm-core eddies. In this western region, the Kuroshio Extension has its meander crests, where many warm-core eddies are generated, supporting our prior speculations that high CPUEs associated with downwelling tendency ($\nabla_h \cdot \mathbf{Q} > 0$) on the northeastern side are caused by swordfish being attracted to the young warm-core eddies in the western region.

However, the vertical velocity, induced by the subinertial deformation flow is very small $\mathcal{O}(10^{-4}$–10^{-3} ms$^{-1})$ in comparison to the typical swimming speed of swordfish, that goes from $\mathcal{O}(1$ ms$^{-1})$ as sustainable cruising speeds for saving energetic costs (Block and Booth, 1992) to the maximum speed $\mathcal{O}(10$ ms$^{-1})$ (He, 2011). Therefore, the downwelling tendency is unlikely to be a controlling factor of swordfish distributions, but some other conditions that coincide with the downwelling tendency should affect them.

Further analysis, using the eddy detection technique with frontogenetical function $\mathbf{Q} \cdot \nabla_h b$, shows that high swordfish CPUEs on the northeastern side of the anticyclonic eddies coincide with the $\mathbf{Q} \cdot \nabla_h b > 0$ (**Figure 8C**), i.e., frontogenesis or sharpening of the front. The sharp thermal or environmental front generated by the frontogenesis on the eastern side of the young anticylones may act as a lateral environmental barrier. At the same time, sharpened front on the eastern side of a warm-core eddy increases the southward flow. Based on the above analysis, the high CPUEs found in the northern region during unstable KE phase are associated with the young warm-core eddies in the western region 143–155°E (**Figure 3A**, **Figure S3**). Note that these high CPUE values occur during autumn to winter seasons, when swordfish migrate north to south. During these returning migrations to the subtropical region, they most likely can encounter the warm-salty water on the northern edge of the warm-core eddies. Following the current of these warm-core eddies, swordfish could use strong southward flows along their eastern side to migrate further south. Although the swordfish can swim against the eddy flow, the strong current of the young anticyclones could induce a net advection effect with their relatively slow cruising swimming speed $\mathcal{O}(1$ ms$^{-1})$.

In addition to these physical structures of the young warm-core eddies, bottom-up biological processes may also attract swordfish. The isothermal shoaling on the western side of the anticyclones could induce upwelling of nutrients, which triggers phytoplankton bloom (Flierl and Davis, 1993) and zooplankton accumulations in the downstream, presumably at the northeastern side of the warm-core eddies. Since swordfish feed on small fish and squids attracted by plankton, these

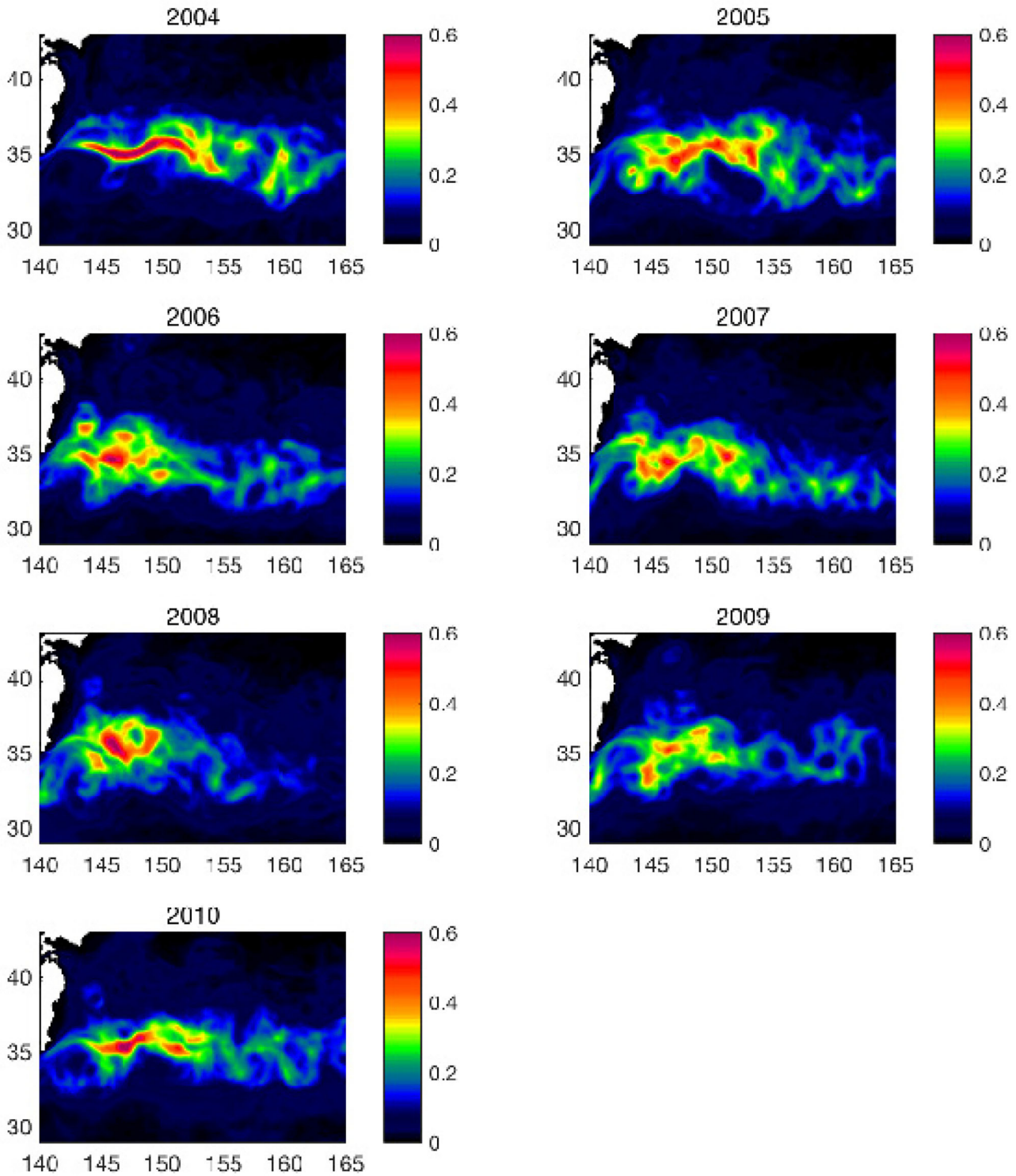

FIGURE 13 | Top 100-m annual mean eddy kinetic energy m^2s^{-2} from 2004 through 2010 obtained from FORA-WNP30 data using (6). The abscissa is longitude (°E) and the ordinate is latitude (°N).

bottom-up mechanisms would also boost the CPUE of the swordfish migrating southward on the northeastern side of the young warm-core eddies. For instance, the neon flying squid *Ommastrephes bartramii* is one of the swordfish main preys (Watanabe et al., 2009), which presents a similar seasonal latitudinal migration with preference of slightly colder and

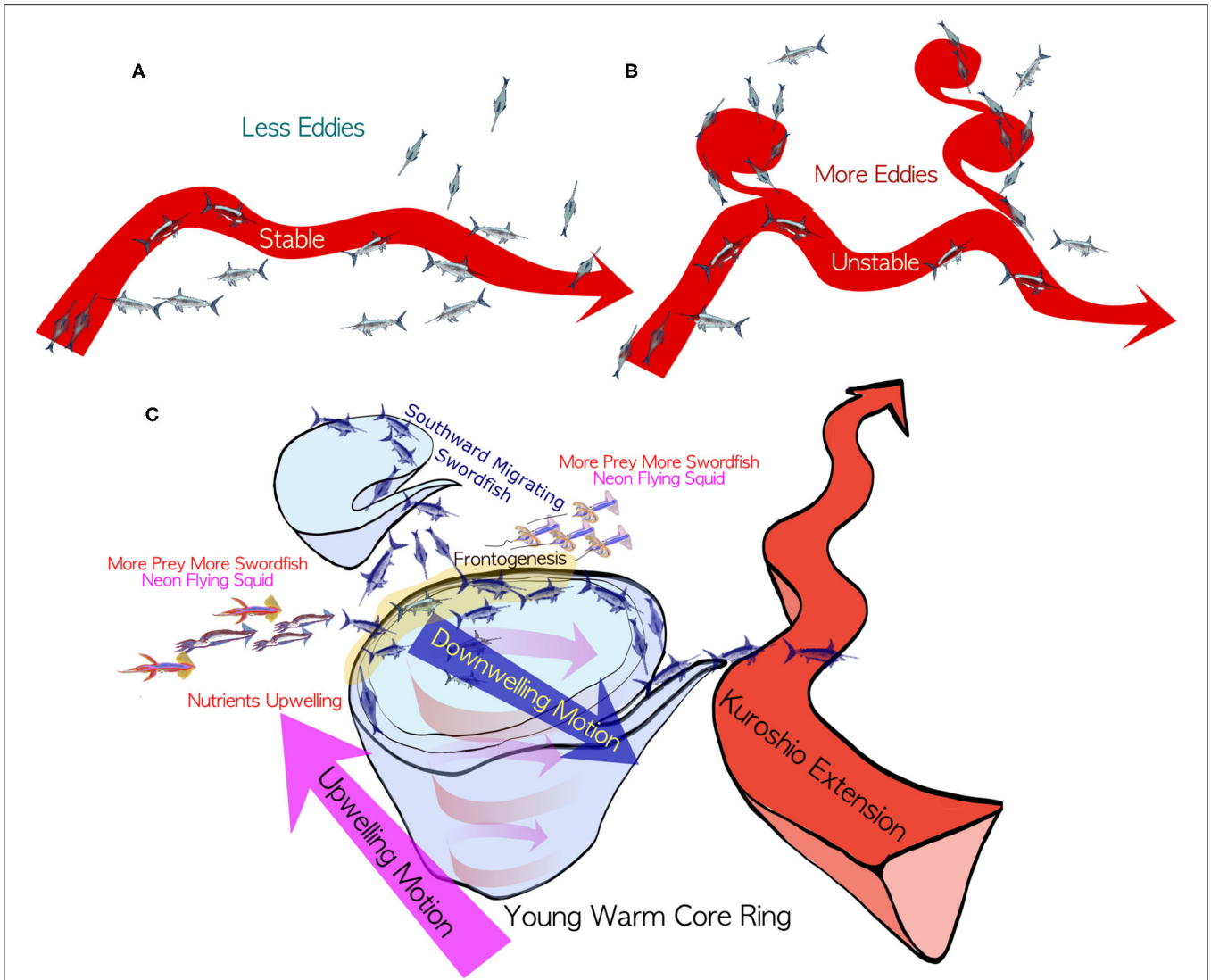

FIGURE 14 | Summary of this study. Schematics for the modulations of the swordfish distributions associated with the Kuroshio Extension path states for **(A)** stable period in which Kuroshio Extension takes relatively straight path without many warm-core rings and with less northward spreading of swordfish population and for **(B)** unstable period in which the Kuroshio Extension path exhibits meandering with more warm-core eddies and more swordfish are caught on their northeastern side during southward swordfish migration. The latter **(B)** unstable period can be characterized by the higher and lower swordfish CPUE in the northern and the southern regions, respectively. The situation reverses during **(A)** stable period with the lower and higher swordfish CPUE in the northern and the southern regions, respectively. **(C)** Hypothesis to form high swordfish CPUE on the northeastern side of an anticyclonic warm-core ring. During their southward migration in autumn to winter, they can encounter their favorable warm-salty environment on the north side of the warm-core eddies. Following the flow of the eddies they might be able to migrate south efficiently with the southward flow on the eastern side of the warm-core eddies. When they reach just north of the Kuroshio Extension, they might be attracted by prey enhanced on the northeastern side of the young warm-core eddies by the upwelling on the western side. Note that there is a downwelling tendency on the northeastern side of the young warm-core eddies. See also a supplementary animation at https://doi.org/10.6084/m9.figshare.12818846.v2.

fresher waters (Tian et al., 2009). The neon flying squid are often found at the edges of warm-core rings for better feeding conditions (Igarashi et al., 2018). When the Oyashio Current reaches to the northern edge of these young warm-core eddies, just north of the KE, it is reported that the abundance of the neon flying squid increases there (Igarashi et al., 2011). This situation would allow the swordfish to feed on the neon flying squid on the northeastern edges, while keeping themselves still inside the preferred thermal habitat near the warm-core eddies. These interpretations for the results in this study can be synthesized into one hypothesis that top-down physical and bottom-up biological processes may sustain high CPUE on the northeastern side of the young warm-core eddies, making swordfish inside the eddies even more easily targeted (**Figure 14C**).

The above hypothesis is partially supported by the CPUE distributions from autumn to winter season in 2006 to 2007 (see **Movie S1**). In this movie, a warm-core eddy is pinched off from the KE in the middle of October 2006, followed by an

appearance of a moderate value of CPUE on the northern edge of this war-core ring in the middle of November. Then, early in December, high CPUE values are seen on the northeastern side of this eddy, which persist until end of December 2006. After this, high CPUE values appear in the recirculation gyre south of the KE without clear associations with the mesoscale eddies until middle of January 2007. It should be noted that the high CPUE values are found along the warm streamer connecting between this warm-core eddy and the meander crest of the KE in the end of January, which are probably due to the southward migrating swordfish using the streamer connected to the subtropical region.

Also, this tendency of higher CPUEs on the northeastern side of the warm-core eddies accompanied by $\nabla_h \cdot \mathbf{Q} > 0$ are clearer during the unstable period (**Figures 9A,C**), suggesting that more young warm-core eddies in the western region during the unstable period attract more swordfish. Moreover, as shown in the results, the higher CPUE values during unstable phase in the northern region (**Figure 2A**) are caused by the higher CPUE in the same western region, 143–155°E (**Figure 3A**). Therefore, there is clearly an importance of young warm-core eddies in the western region just north of the KE as the drivers of the interannual changes of the swordfish CPUE.

Although the Kuroshio has been known to be nutrient poor near the surface, recent studies have pointed out that the Kuroshio in its subsurface layer is a nutrient stream, similar to the Gulf Stream, transporting a large amount of nutrients from south to the subpolar region, and that the concentrations of nitrate within the nutrient stream is relatively higher compared to ambient water of the same density (Saito, 2019). The higher nutrient concentrations along the Kuroshio nutrient stream is found to persist even in the downstream, the Kuroshio Extension (Nagai et al., 2019). Therefore, warm-core eddies originated from the KE could maintain the positive anomaly in the nutrient concentrations in the subsurface layer, which may enhance the nutrient supply with other physical processes near eddies (Yoshimori et al., 1995; McGillicuddy Jr and Robinson, 1997; Mahadevan and Tandon, 2006; McGillicuddy et al., 2007). These bottom-up processes could possibly sustain relatively better food availability for warm water favorite pelagic fish species within warm-core eddies.

Our analyses using the mesoscale dynamic parameters shown above illustrate that the swordfish CPUE in the northern region is higher when the OW < 0, vorticity $\zeta < 0$, and $\nabla_h \cdot \mathbf{Q} > 0$, within the anticyclonic eddies with downwelling flow. However, these parameters do not show any clear trend for the CPUE in the southern region. In the subtropical region, it has been reported that the surface mixed layer eddies generate submesoscale frontal structures, so called submesoscale soup (McWilliams, 2019), which are enhanced during the winter season (Sasaki et al., 2014) when swordfish migrates back to this region. How these submesoscale fronts influence on the distributions of the migrating fish species are currently unknown due to the coarse resolutions of the observation data. While the resolution of the reanalysis data in this study is eddy resolving $\sim$ 10 km, it is still too coarse to reproduce these submesoscale processes. Also, despite the typical lengths of the lines for the longline fishing exceed several tens of kilometers, the locations of the catches were represented by the ship position when they recovered the gear, that most likely limits the accuracy of the fishing positions. Nevertheless, the results show a clear dependency of the swordfish relative abundance on the mesoscale parameters and anticyclonic eddies, which would have even finer structures to reveal with the improved accuracy and resolutions in future studies.

5. SUMMARY AND CONCLUSIONS

In this study, using mesoscale parameters derived from FORA-WNP30 dataset and swordfish catch records from pelagic longline fishery data from 2004 through 2010, the swordfish relative abundance in association with the mesoscale physical parameters and their interannual modulations were investigated, with a special emphasis on the mesoscale eddies in the Kuroshio Extension system.

For a clearer understanding of the effects of the KE modulations on the swordfish CPUE, the study area is separated into two regions, the northern region that is between 36 and 45°N, and the southern region between 25 and 36°N, reflecting the seasonal feeding migration of the swordfish (**Figure 1**). Besides this seasonal variation, interannual changes in the swordfish CPUE are also observed in both regions, which depend strongly on the mesoscale dynamic parameters such as the vorticity, the Okubo-Weiss parameter, and the divergence of Q-vector (**Figures 4–6**). When the Kuroshio Extension is stable for the years 2004, 2005, and 2010, the eddy kinetic energy shows high values in limited regions along the narrow and stable Kuroshio Extension axis, and the annual swordfish CPUE shows low and high values in the northern and the southern region, respectively. In contrast, when the Kuroshio Extension is unstable for the years 2006 through 2009, the high values of EKE ($> 0.3\ m^2s^{-2}$) are more concentrated in the western Kuroshio Extension region, and the annual swordfish CPUE tends to be high and low in the northern and the southern region, respectively, opposite to the stable phase.

The CPUE as a function of the mesoscale dynamic parameters suggests that higher CPUE values are clearly associated with the negative vorticity and the negative Okubo-Weiss parameter (i.e., anticyclonic rotating flows, **Figure 4**). Consistently, the eddy detection analysis with the CPUE data shows explicitly that the high CPUE values are found in and near the anticyclonic warm-core eddies, especially on their northeastern side (**Figure 9**). This is probably because, during the southward migration, swordfish encounter the warm-salty waters at the northern edge of the warm-core eddies, and uses the southward flow on their eastern side to migrate south keeping themselves within their preferred warm-salty water environment. Another ecological reason for this is that their main prey, neon flying squid *O. bartramii* are known to prefer to stay at the edges of warm-core eddies (**Figure 14**). The further analyses suggest that, in the northern region, the CPUE values in and near the detected anticyclonic eddies are higher during unstable

phase than in the stable phase by several factors (**Figure 10**). These results indicate that the spatiotemporal variabilities in the mesoscale warm-core eddies have a large impact on the swordfish CPUE in the northern fishing site, with more warm-core eddies accompanied by the higher CPUE values during the unstable phase.

In conclusion, more swordfish can be found efficiently on the northeastern side of the warm-core rings emanated from the Kuroshio Extension jet during its unstable phase. It should be noted that, for the first time, the clear interannual modulations in the swordfish CPUE, which can be tightly correlated with the mesoscale warm-core eddies, are shown in the northern Kuroshio Extension region in this study. In the southern region, however, no clear relationship is found between the same set of mesoscale parameters and the swordfish CPUE, despite the clear interannual modulation of CPUE, suggesting that unresolved physical and biological structures, such as those associated with submesoscale processes (Tandon and Nagai, 2019) are more important to control the swordfish relative abundance in this subtropical southern regions. These results and remaining issues call for more studies to correlate more detailed oceanographic parameters with relative abundance of many fish species in the KE system, which has been long-known as one of the richest fishing grounds in the world ocean.

DATA AVAILABILITY STATEMENT

The fishery datasets for this article are not publicly available because the swordfish catch and effort data were collected by cooperation with the captains and crews of commercial longline fisheries vessels in Kesennuma port, Japan, with a legal contract to protect their privacy. Requests to access the datasets should be directed to Fisheries Agency of Japan. However, all the codes to analyze data are available upon request to the corresponding author. The ocean reanalysis data, Four-dimensional Variational Ocean Reanalysis for the western North Pacific (FORA-WNP30), is available from (http://synthesis.jamstec.go.jp/FORA/e/index.html).

AUTHOR CONTRIBUTIONS

KY summarized the fishery data. GD and TN analyzed fishery data and ocean reanalysis data, and provided the figures of the paper. TN conducted eddy-detection analysis. GD provided the first draft of the manuscript. GD, TN, and KY edited the manuscripts. All authors contributed to the article and approved the submitted version.

ACKNOWLEDGMENTS

GD and TN thank JASSO (Japan Student Services Organization) for providing support for GD's exchange student program in the academic year 2018 at TUMSAT, PICES for support to let GD give the FIS committee award winning talk on this study in Victoria Canada at PICES 2019, Dr. Akiko Okamoto (Robinson Farm, Amami Island, https://www.robinson-ikka.com/), FRA, Captains, and crew members of fishing vessels at Kesennuma port for the swordfish data. GD thanks continuous supports from parents and Prof. Icochea at UNALM, Peru. This study is supported by Fishery Agency of Japan (JV-Project), and partially supported by SKED (JPMXD0511102330). This study utilized the dataset Four-dimensional Variational Ocean Reanalysis for the western North Pacific (FORA-WNP30), which was produced by Japan Agency for Marine-Science and Technology (JAMSTEC) and Meteorological Research Institute of Japan Meteorological Agency (JMA/MRI).

SUPPLEMENTARY MATERIAL

The Supplementary Material for this article can be found online at: https://www.frontiersin.org/articles/10.3389/fmars.2020.00680/full#supplementary-material

REFERENCES

Bedford, D. W., and Hagerman, F. B. (1983). The billfish fishery resource of the California Current. *Calif. Coop. Ocean. Fish. Invest. Rep*. 24, 70–78.

Bellido, J., Pierce, G., and Wang, J. (2001). Modelling intra-annual variation in abundance of squid *Loligo forbesi* in Scottish waters using generalised additive models. *Fish. Res.* 52, 23–39. doi: 10.1016/S0165-7836(01)00228-4

Bigelow, K. A., Boggs, C. H., and He, X. (1999). Environmental effects on swordfish and blue shark catch rates in the US North Pacific longline fishery. *Fish. Oceanogr*. 8, 178–198. doi: 10.1046/j.1365-2419.1999.00105.x

Block, B. A., and Booth, D. (1992). Direct measurement of swimming speeds and depth of blue marlin. *J. Exp. Biol*. 166, 267–284.

Bluestein, H. B. (1993). *Synoptic-dynamic Meteorology in Midlatitudes. Volume II: Observations and Theory of Weather Systems*. New York, NY: Oxford University Press.

Bower, A. S., and Rossby, T. (1989). Evidence of cross-frontal exchange processes in the Gulf Stream based on isopycnal rafos float data. *J. Phys. Oceanogr*. 19, 1177–1190. doi: 10.1175/1520-0485(1989)019<1177:EOCFEP>2.0.CO;2

Braun, C. D., Gaube, P., Sinclair-Taylor, T. H., Skomal, G. B., and Thorrold, S. R. (2019). Mesoscale eddies release pelagic sharks from thermal constraints to foraging in the ocean twilight zone. *Proc. Natl. Acad. Sci. U.S.A*. 116, 17187–17192. doi: 10.1073/pnas.1903067116

Correa-Ramírez, M., Hormazabal, S., and Yuras, G. (2007). Mesoscale eddies and high chlorophyll concentrations off central Chile (29°"39° S). *Geophys. Res. Lett*. 34:L12604. doi: 10.1029/2007GL029541

Cushing, D. H. (1981). *Fisheries Biology: A Study in Population Dynamics*. Madison, WI: University of Wisconsin Press.

Estrada-Allis, S. N., Barceló-Llull, B., Pallás-Sanz, E., Rodríguez-Santana, A., Souza, J. M. A. C., Mason, E., et al. (2018). Vertical velocity dynamics and mixing in an anticyclone near the Canary Islands. *J. Phys. Oceanogr*. 49, 431–451. doi: 10.1175/JPO-D-17-0156.1

Flierl, G. R., and Davis, C. S. (1993). Biological effects of Gulf Stream meandering. *J. Mar. Res*. 51, 529–560. doi: 10.1357/0022240933224016

Gill, A. (1982). Atmospheric-ocean dynamics. *Int. Geophys. Ser*. 30:662.

He, P. (2011). *Behavior of Marine Fishes: Capture Processes and Conservation Challenges*. Iowa, IA: John Wiley & Sons. doi: 10.1002/9780813810966

Hoskins, B. J. (1971). Atmospheric frontogenesis models: some solutions. *Q. J. R. Meteorol. Soc*. 97, 139–153. doi: 10.1002/qj.49709741202

Hsu, A. C., Boustany, A. M., Roberts, J. J., Chang, J.-H., and Halpin, P. N. (2015). Tuna and swordfish catch in the US northwest Atlantic longline fishery in relation to mesoscale eddies. *Fish. Oceanogr*. 24, 508–520. doi: 10.1111/fog.12125

Igarashi, H., Awaji, T., Kamachi, M., Ishikawa, Y., Usui, N., Fujii, Y., et al. (2011). "A statistical approach to identify optimal habitat suitability of neon flying squid in Northwestern North Pacific by using satellite datasets and 3-D ocean data assimilation product," in *North Pacific Marine Science Organization (PICES)-2011 Meeting* (Khabarovsk).

Igarashi, H., Saitoh, S.-I., Ishikawa, Y., Kamachi, M., Usui, N., Sakai, M., and Imamura, Y. (2018). Identifying potential habitat distribution of the neon flying squid (*Ommastrephes bartramii*) off the eastern coast of Japan in winter. *Fish. Oceanogr*. 27, 16–27. doi: 10.1111/fog.12230

Jiang, W., Peng, L., Jin, T., and Zhang, S. (2017). Variability of the Kuroshio Extension system in 1992-2013 from satellite altimetry data. *Geodesy Geodyn*. 8, 103–110. doi: 10.1016/j.geog.2016.12.004

Lévy, M., Klein, P., and Treguier, A.-M. (2001). Impact of sub-mesoscale physics on production and subduction of phytoplankton in an oligotrophic regime. *J. Mar. Res*. 59, 535–565. doi: 10.1357/002224001762842181

Lin, P., Chai, F., Xue, H., and Xiu, P. (2014). Modulation of decadal oscillation on surface chlorophyll in the Kuroshio Extension. *J. Geophys. Res*. 119, 187–199. doi: 10.1002/2013JC009359

Mahadevan, A., and Archer, D. (2000). Modeling the impact of fronts and mesoscale circulation on the nutrient supply and biogeochemistry of the upper ocean. *J. Geophys. Res*. 105, 1209–1225. doi: 10.1029/1999JC900216

Mahadevan, A., D'Asaro, E., Lee, C., and Perry, M. J. (2012). Eddy-driven stratification initiates North Atlantic spring phytoplankton blooms. *Science* 337, 54–58. doi: 10.1126/science.1218740

Mahadevan, A., and Tandon, A. (2006). An analysis of mechanisms for submesoscale vertical motion at ocean fronts. *Ocean Model*. 14, 241–256. doi: 10.1016/j.ocemod.2006.05.006

McGillicuddy, D. J., Anderson, L. A., Bates, N. R., Bibby, T., Buesseler, K. O., Carlson, C. A., et al. (2007). Eddy/wind interactions stimulate extraordinary mid-ocean plankton blooms. *Science* 316, 1021–1026. doi: 10.1126/science.1136256

McGillicuddy, D. Jr, and Robinson, A. (1997). Eddy-induced nutrient supply and new production in the Sargasso Sea. *Deep-Sea Res. Part I* 44, 1427–1450. doi: 10.1016/S0967-0637(97)00024-1

McWilliams, J. C. (2019). A survey of submesoscale currents. *Geosci. Lett*. 6, 1–15. doi: 10.1186/s40562-019-0133-3

Mizuno, K., and White, W. B. (1983). Annual and interannual variability in the Kuroshio Current system. *J. Phys. Oceanogr*. 13, 1847–1867. doi: 10.1175/1520-0485(1983)013<1847:AAIVIT>2.0.CO;2

Nagai, T., Clayton, S., and Uchiyama, Y. (2019). "Multiscale routes to supply nutrients through the Kuroshio nutrient stream," in *Kuroshio Current: Physical, Biogeochemical and Ecosystem Dynamics*, eds T. Nagai, H. Saito, K, Suzuki, M. Takahashi (Washington, DC: AGU-Wiley), 105–125. doi: 10.1002/9781119428428.ch6

Nagai, T., Gruber, N., Frenzel, H., Lachkar, Z., McWilliams, J. C., and Plattner, G.-K. (2015). Dominant role of eddies and filaments in the offshore transport of carbon and nutrients in the California Current System. *J. Geophys. Res*. 120, 5318–5341. doi: 10.1002/2015JC010889

Nakamura, I. (1985). *FAO Species Catalogue: Vol. 5. Billfishes of the World*. FAO Fisheries Synopsis. 125:65.

Okubo, A. (1979). Horizontal dispersion of floatable particles in the vicinity of velocity singularities such as convergences. *Deep Sea Research and Oceanographic Abstracts*, 17, 445–454.

Pettersen, S. (1956). *Weather Analysis and Forecasting: Volume I: Motion and Motion Systems*. New York, NY: McGraw-Hill.

Pilo, G. S., Oke, P. R., Coleman, R., Rykova, T., and Ridgway, K. (2018). Patterns of vertical velocity induced by eddy distortion in an ocean model. *J. Geophys. Res*. 123, 2274–2292. doi: 10.1002/2017JC013298

Qiu, B., and Chen, S. (2005). Variability of the Kuroshio Extension jet, recirculation gyre, and mesoscale eddies on decadal time scales. *J. Phys. Oceanogr*. 35, 2090–2103. doi: 10.1175/JPO2807.1

Qiu, B., and Chen, S. (2010). Eddy-mean flow interaction in the decadally modulating Kuroshio Extension system. *Deep-Sea Res. Part II* 57, 1098–1110. doi: 10.1016/j.dsr2.2008.11.036

Qiu, B., Chen, S., and Hacker, P. (2004). Synoptic-scale air-sea flux forcing in the western North Pacific: observations and their impact on SST and the mixed layer. *J. Phys. Oceanogr*. 34, 2148–2159. doi: 10.1175/1520-0485(2004)034<2148:SAFFIT>2.0.CO;2

Qiu, B., Chen, S., Schneider, N., and Taguchi, B. (2014). A coupled decadal prediction of the dynamic state of the Kuroshio Extension system. *J. Clim*. 27, 1751–1764. doi: 10.1175/JCLI-D-13-00318.1

Saito, H. (2019). "The Kuroshio: its recognition, scientific activities and emerging issues," in *Kuroshio Current: Physical, Biogeochemical and Ecosystem Dynamics*, eds T. Nagai, H. Saito, K, Suzuki, M. Takahashi (Washington, DC, AGU-Wiley), 1–11. doi: 10.1002/9781119428428.ch1

Sasaki, H., Klein, P., Qiu, B., and Sasai, Y. (2014). Impact of oceanic-scale interactions on the seasonal modulation of ocean dynamics by the atmosphere. *Nat. Commun*. 5:5636. doi: 10.1038/ncomms6636

Sedberry, G., and Loefer, J. (2001). Satellite telemetry tracking of swordfish, *X*iphias gladius, off the eastern United States. *Mar. Biol*. 139, 355–360. doi: 10.1007/s002270100593

Sedberry, G. R. (2001). *The Charleston Bump: An Island of Essential Fish Habitat in the Gulf Stream*. Island in the stream: Oceanography and fisheries of the Charleston Bump, 3–24.

Seki, M. P., Polovina, J. J., Kobayashi, D. R., Bidigare, R. R., and Mitchum, G. T. (2002). An oceanographic characterization of swordfish (*Xiphias gladius*) longline fishing grounds in the springtime subtropical North Pacific. *Fish. Oceanogr*. 11, 251–266. doi: 10.1046/j.1365-2419.2002.00207.x

Skalski, J. R., Ryding, K. E., and Millspaugh, J. (2010). *Wildlife Demography: Analysis of Sex, Age, and Count Data*. Elsevier.

Sugimoto, S., and Hanawa, K. (2009). Decadal and interdecadal variations of the Aleutian low activity and their relation to upper oceanic variations over the North Pacific. *J. Meteorol. Soc. Jpn. Ser. II* 87, 601–614. doi: 10.2151/jmsj.87.601

Sugimoto, T., Kawasaki, Y., and Li, J. (1992). A description of the time-dependent hydrographic structure of the warm streamer around the Kuroshio warm-core ring 86B. *Deep-Sea Res. Part A* 39, S77–S96. doi: 10.1016/S0198-0149(11)80006-3

Sugimoto, T., and Tameishi, H. (1992). Warm-core rings, streamers and their role on the fishing ground formation around Japan. *Deep-Sea Res. Part A* 39, S183–S201. doi: 10.1016/S0198-0149(11)80011-7

Taguchi, B., Xie, S.-P., Schneider, N., Nonaka, M., Sasaki, H., and Sasai, Y. (2007). Decadal variability of the Kuroshio Extension: observations and an eddy-resolving model hindcast. *J. Clim*. 20, 2357–2377. doi: 10.1175/JCLI4142.1

Tandon, A., and Nagai, T. (2019). "Mixing associated with submesoscale processes," in *Encyclopedia of Ocean Sciences, 3rd Edition*, eds H. K. Cochran, H. J. Bokuniewicz, and P. L. Yger (Amsterdam: Elsevier). doi: 10.1016/B978-0-12-409548-9.10952-2

Tian, S., Chen, X., Chen, Y., Xu, L., and Dai, X. (2009). Evaluating habitat suitability indices derived from CPUE and fishing effort data for *Ommatrephes bratramii* in the northwestern Pacific Ocean. *Fish. Res*. 95, 181–188. doi: 10.1016/j.fishres.2008.08.012

Tomosada, A. (1986). Generation and decay of Kuroshio warm-core rings. *Deep-Sea Res. Part A* 33, 1475–1486. doi: 10.1016/0198-0149(86)90063-4

Uda, M. (1960). Fisheries oceanography in Japan, especially on the principles of fish distribution, concentration, dispersal and fluctuation. CalCOFI Reports 8, 25–31.

Usui, N., Wakamatsu, T., Tanaka, Y., Hirose, N., Toyoda, T., Nishikawa, S., et al. (2017). Four-dimensional variational ocean reanalysis: a 30-year high-resolution dataset in the western North Pacific (FORA-WNP30). *J. Oceanogr*. 73, 205–233. doi: 10.1007/s10872-016-0398-5

Vásquez, S., c, M., Parada, C., and Sepúlveda, A. (2013). The influence of oceanographic processes on jack mackerel (*Trachurus murphyi*) larval distribution and population structure in the southeastern Pacific Ocean. *ICES J. Mar. Sci*. 70, 1097–1107. doi: 10.1093/icesjms/fst065

Watanabe, H., Kubodera, T., and Yokawa, K. (2009). Feeding ecology of the swordfish *Xiphias gladius* in the subtropical region and transition

zone of the western North Pacific. *Mar. Ecol. Prog. Ser.* 396, 111–122. doi: 10.3354/meps08330

Weiss, J. (1991). The dynamics of enstrophy transfer in two-dimensional hydrodynamics. *Phys. D* 48, 273–294. doi: 10.1016/0167-2789(91)90088-Q

Yasuda, I., Okuda, K., and Hirai, M. (1992). Evolution of a Kuroshio warm-core ring–variability of the hydrographic structure. *Deep-Sea Res. Part A* 39, S131–S161. doi: 10.1016/S0198-0149(11)80009-9

Yoshimori, A., Ishizaka, J., Kono, T., Kasai, H., Saito, H., Kishi, M., et al. (1995). Modeling of spring bloom in the western subarctic Pacific (off Japan) with observed vertical density structure. *J. Oceanogr.* 51, 471–488. doi: 10.1007/BF02286393

Conflict of Interest: The authors declare that the research was conducted in the absence of any commercial or financial relationships that could be construed as a potential conflict of interest.

frontiers in Marine Science

ORIGINAL RESEARCH
published: 16 September 2020
doi: 10.3389/fmars.2020.546882

Climate Variability Patterns and Their Ecological Effects on Ecosystems in the Northwestern North Pacific

Shuyang Ma[1], Yongjun Tian[1,2,3], Jianchao Li[1], Haiqing Yu[1], Jiahua Cheng[4], Peng Sun[1,3,5]*, Caihong Fu[6], Yang Liu[1,3] and Yoshiro Watanabe[1]*

[1] Laboratory of Fisheries Oceanography, Fisheries College, Ocean University of China, Qingdao, China, [2] Laboratory for Marine Fisheries Science and Food Production Processes, Pilot National Laboratory for Marine Science and Technology, Qingdao, China, [3] Frontiers Science Center for Deep Ocean Multispheres and Earth System, Ocean University of China, Qingdao, China, [4] East China Sea Fisheries Research Institute, Chinese Academy of Fishery Sciences, Shanghai, China, [5] Department of Biological Sciences, University of Bergen, Bergen, Norway, [6] Fisheries and Oceans Canada, Pacific Biological Station, Nanaimo, BC, Canada

Climate-induced ecosystem variability is an increasing concern in recent years. Integrated researches in the northeastern North Pacific have proved the ecological importance of the Pacific Decadal Oscillation (PDO), North Pacific Gyre Oscillation (NPGO), and El Niño–Southern Oscillation (ENSO) to the ecosystem variability. While in the northwestern North Pacific, researches have been independent of each other over different regional ecosystems, and identified relatively weak linkages between these climatic indices (e.g., PDO, NPGO, and ENSO) and variations in the regional ecosystems. Such disassociated researches with unidentified important climate variability patterns may have hampered a holistic understanding of climate-induced ecosystem variability in the northwestern North Pacific. Furthermore, non-stationarity in climate–biology relationships has been proven to be important for ecosystems in the northeastern North Pacific but has not yet been studied in the northwestern North Pacific. Therefore, this research compiles biological, environmental, and climatic data in ecosystems in the northwestern North Pacific and employs a suite of analytical techniques, aiming to provide a holistic understanding of the climate-induced ecosystem variability. It shows that ecosystems in the northwestern North Pacific had a leading regime shift in the late 1980s in response to climate variability. The Siberian High, Arctic Oscillation, and East Asian Monsoon exhibit greater ecological importance to ecosystem variability than the PDO, NPGO, and ENSO. Their variations contribute greatly to sea surface temperature changes and thus variations in ecosystems. Furthermore, modified models considering non-stationary relationships achieve better performances than stationary models, suggesting the existence of non-stationarity in climate–biology relationships in the northwestern North Pacific. This non-stationarity resulted from the decline in variance of the sea level pressure in Siberian High rather than the Aleutian Low as suggested by previous studies in the northeastern North Pacific. Our research provides an improved understanding of the climate-induced ecosystem variability in the northwestern North Pacific, offering implications for further research on the entire North Pacific.

Keywords: climate variability, ecosystem, ecological responses, non-stationarity, northwestern North Pacific

OPEN ACCESS

Edited by:
Shoshiro Minobe,
Hokkaido University, Japan

Reviewed by:
Fabio Pranovi,
Ca' Foscari University of Venice, Italy
Takashi Kitagawa,
The University of Tokyo, Japan

***Correspondence:**
Yongjun Tian
yjtian@ouc.edu.cn
Peng Sun
sunpeng@ouc.edu.cn

Specialty section:
This article was submitted to Marine Fisheries, Aquaculture and Living Resources, a section of the journal Frontiers in Marine Science

Received: *30 March 2020*
Accepted: *18 August 2020*
Published: *16 September 2020*

Citation:
Ma S, Tian Y, Li J, Yu H, Cheng J, Sun P, Fu C, Liu Y and Watanabe Y (2020) Climate Variability Patterns and Their Ecological Effects on Ecosystems in the Northwestern North Pacific. Front. Mar. Sci. 7:546882. doi: 10.3389/fmars.2020.546882

INTRODUCTION

Climate-induced ecosystem variability has been one of the most noteworthy issues at a global scale in the 21st century (Doney et al., 2012). The North Pacific is characterized by pronounced decadal climate variability and has received much attention on the responses of ecosystems to changing climatic and environmental conditions (Hare and Mantua, 2000; Biondi et al., 2001; Overland et al., 2008; Yatsu et al., 2013; Reid et al., 2016). In the northeastern North Pacific, integrated studies based on the data compiled from multiple sources have provided holistic understandings of the climate-induced ecosystem variability (Benson and Trites, 2002; Mantua, 2004; Litzow and Mueter, 2014). Contrastingly, studies in the northwestern North Pacific (**Figure 1**) have been carried out independent of each other in different regions. Studies in Chinese (Ma et al., 2019), Korean (Zhang et al., 2000, 2007), and Japanese waters (Tian et al., 2006, 2008; Yatsu et al., 2013) have all demonstrated strong linkages between regional ecosystems and climatic/environmental conditions. However, these regional studies have not yet been integrated to show general patterns in climate–ecosystem relationships, which prevents from a holistic understanding of climate-induced ecosystem variability in the northwestern North Pacific. Therefore, an integrated study targeting at the northwestern North Pacific is in urgent need, which can promote understanding on the basin-scale climate-induced ecosystem variability in the North Pacific.

Studies have shown that low-frequency climate variability (red noise) in the North Pacific may have produced decadal-scale periods of stability separated by climatic regime shifts (Hsieh et al., 2005; Di Lorenzo and Ohman, 2013). It is also widely accepted that these shifts could result in community-level, basin-scale ecosystem regime shifts (Benson and Trites, 2002). Therefore, determining the specific climate variability pattern with ecological importance is of great necessity in understanding the climate-induced ecosystem variability and predicting ecosystem dynamics. Relevant studies in the North Pacific have proved the leading role of the Aleutian Low pressure system on regional climate and ecosystem variability (Minobe, 1999; Di Lorenzo and Ohman, 2013). In addition, the Pacific Decadal Oscillation (PDO), North Pacific Gyre Oscillation (NPGO), and El Niño–Southern Oscillation (ENSO) are presented as the primary climate variability patterns with considerable ecological importance and have been extensively used in the ecosystem variability researches in the northeastern North Pacific (Zhang et al., 1997; Mantua and Hare, 2002; Mantua, 2004; Di Lorenzo et al., 2008). However, spatial modes of these climate variability patterns exhibit weaker representation (small loadings) in the northwestern North Pacific than in the central and northeastern North Pacific. Therefore, these climate variability patterns may contribute less to ecosystem variability in the northwestern North Pacific. Aside from the patterns in the PDO, NPGO, and ENSO (SOI), studies in the northwestern North Pacific always consider the Arctic Oscillation Index (AOI), East Asian Monsoon Index (MOI), and Siberian High Index (SHI, variations in Siberian High pressure system) in order to explore more potential links between climate variability patterns and regional environment and ecosystem variability (Tian et al., 2014; Jung et al., 2017; Liu et al., 2019; Ma et al., 2019). However, the ecological importance of these climate variability patterns has not been evaluated, which may hamper predictions of climate-induced ecosystem variability in the northwestern North Pacific. Thus, it is imperative to determine the driving climate variability patterns that have ecological importance in the northwestern North Pacific for better understanding of climate-induced ecosystem variability and predicting ecosystem dynamics.

Traditionally, the relationships between ecosystem variability and environmental conditions have been modeled as a stochastic process with a fixed probability density without considering time-dependent non-stationarity (Wolkovich et al., 2014). However, time-dependent non-stationarity can be important to take into account in light of changing climatic conditions. An example of the non-stationary relationships between physical drivers and biological responses is the changing climate–salmon relationships in around 1988/89 in the Gulf of Alaska, which is attributed to the altered importance of PDO and NPGO, forced by declined variance in the sea level pressure of the Aleutian Low (Litzow et al., 2018). Consequently, traditional understanding of the stationary pressure–state relationships could be subjected to climate variability, and statistical models based on the stationary assumption tend to be biased, resulting in the loss of their predictive skills and the failure to warn of potential ecological risks (Williams and Jackson, 2007; Dormann et al., 2013). Therefore, considering the existence of non-stationary relationships and their underlying mechanisms is crucial for the better illustration of climate–ecosystem relationships and the development of adaptive management strategies.

Considering the above demands, we conducted an integrated study to explore ecologically important climate variability patterns and to determine non-stationary driver–response relationships between climate variability patterns and ecosystem variability in the northwestern North Pacific. Marine fishery catch data from China, Japan, and Korea, as well as sea surface temperature and climatic indices were compiled for this integrated study. We employed traditional statistical approaches, their modified versions for tackling non-stationarity, as well as machine learning methods to explore the possible linkages between climate/environment drivers and ecosystem responses. This study aims to: (1) explore long-term variability in ecosystem, environment, and climate in the northwestern North Pacific; (2) evaluate the ecological importance of candidate climate variability patterns; (3) identify non-stationarity in relationships between biological responses and physical drivers; and (4) compare the climate-induced ecosystem variability in the northwestern and northeastern North Pacific.

MATERIALS AND METHODS

Data

Based on the availability of qualified long-term time-series, we compiled fishery catch data of various taxa (with raw catch data shown in **Supplementary Figure S1**) from four countries/regions (i.e., China, Chinese Taipei, Japan, and Korea)

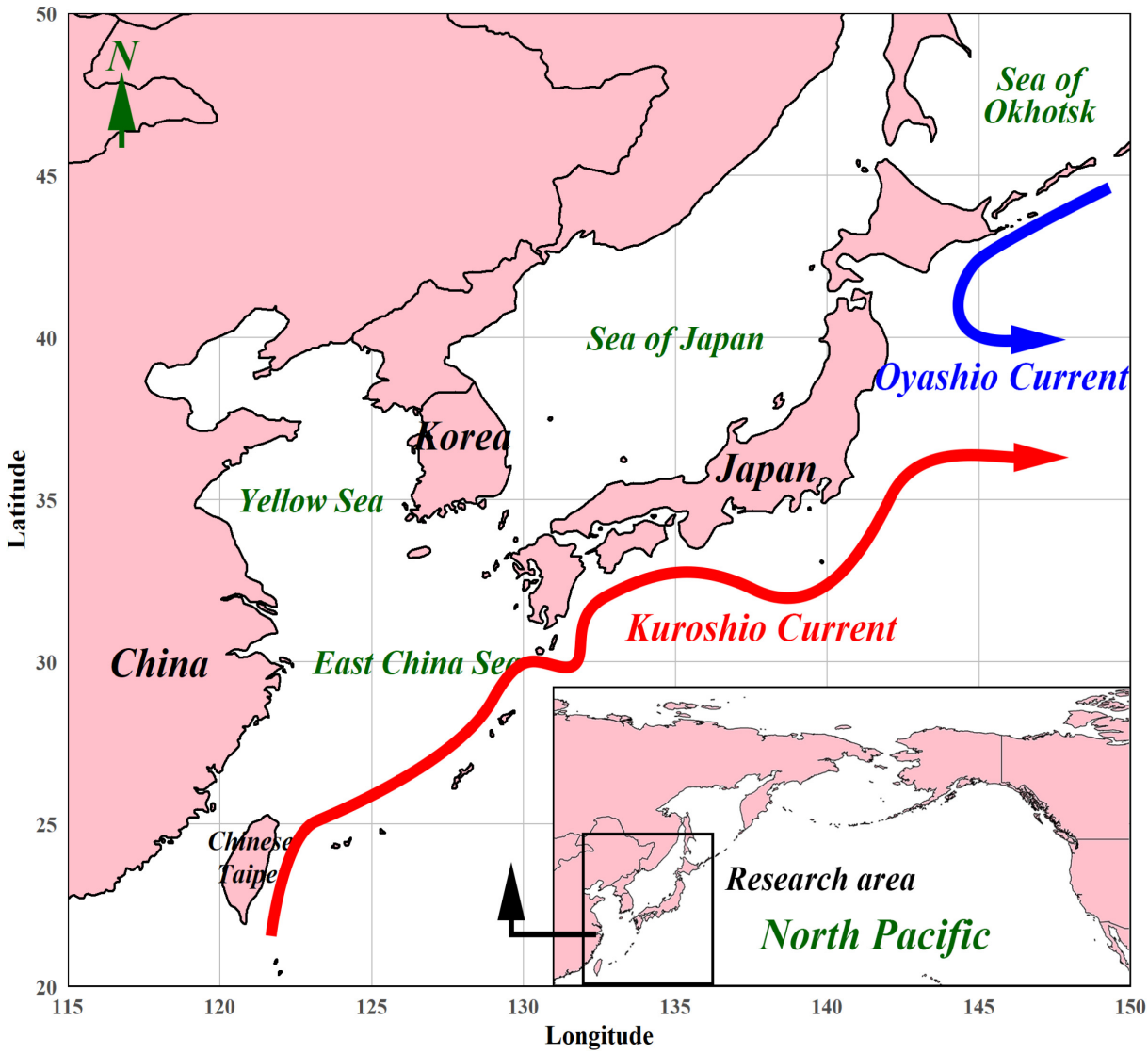

FIGURE 1 | Map of the northwestern North Pacific.

for the period of 1963–2016 (the longest time period considering both data availability and comprehensiveness). Although the taxa from different countries/regions may differ, they generally fall into three major categories, large predatory, demersal, and small pelagic (**Supplementary Table S1**), such that they well represent the ecosystem structures (Tian et al., 2014). Within each country/region, taxa that account for a small amount of catch (<1% of total catch) are excluded to avoid the effects of potential recording errors. Missing data (24 missing grids in a total of 3,240 data grids with a missing rate of 0.74%) were filled with the averages of two adjacent years' data. Each catch data time-series by species and by fishing country/region were standardized with a mean of 0 and a variance of 1 such that temporal variabilities in the different data sets are comparable.

Monthly sea surface temperature (SST) grid data with a resolution of 0.5°(latitude × longitude) for the range of 20°–50°N, 115°–150°E and for the period of 1963–2010 were obtained from the Simple Ocean Data Assimilation Reanalysis (SODA) (Carton and Giese, 2008). Winter (from January to March, a period that is frequently used in relevant researches in northwestern North Pacific) (e.g., Ma et al., 2019) means in each SST grid were calculated for further analyses.

The PDO, NPGO, SOI, AOI, SHI, and MOI have been used to define climate variability in the North Pacific (Ropelewski and Jones, 1987; Thompson and Wallace, 1998; Hare and Mantua, 2000; Gong et al., 2001; Mantua and Hare, 2002; Wu and Wang, 2002; Di Lorenzo et al., 2008). All these large-scale climatic indices (short as CIs) are derived from open-access online databases and have a monthly temporal scale for the period 1963–2016. These CIs are well documented and largely associated with variations in the fish communities and ecosystems in the North Pacific (Tian et al., 2014; Liu et al., 2019; Ma et al., 2019).

Large-scale climate processes, such as the Siberian High, Aleutian Low, Arctic Oscillation, and Asian Monsoon are most active in winter. Therefore, winter (from December to February, a period that is frequently used in relevant researches) average for each index was calculated to represent climatic variability. Details for CIs are provided in **Supplementary Table S2**.

Data Analyses

Intensive increasing trends were observed in the catch data from China (**Supplementary Figure S1**). Such increasing trends may have been caused by socioeconomic factors such as the growing consumption of seafoods and the increasing marine fishing effort, which can lead to biased results. Therefore, we used engine power of the total Chinese marine fishing boats (from Chinese Fishery Statistics, **Supplementary Figure S2**) as a surrogate for fishing effort to remove the potential socioeconomic trends in catch data from China. The detrend analyses were applied through linear regressions with catch data from China as response variables and engine power as an explanatory variable. Residuals from the linear regressions were then used as the detrended catch time-series for further analyses. The detrend analyses were not conducted for catch data from the other three countries/regions as no obvious socioeconomic trend was observed in their catch time-series (**Supplementary Figure S1**).

Principal component analysis (PCA) is often used to identify the most important patterns of common variability in catch data sets (e.g., Hare and Mantua, 2000; Litzow and Mueter, 2014). We applied PCA to the fishery catch data of all taxa within the four countries/regions and calculated the principal component scores (short as PCs) to represent ecosystem variability. Empirical orthogonal function (EOF) analysis is often used to identify the most important SST variability pattern in the North Pacific (Weare and Nasstrom, 1982; Litzow et al., 2018). We calculated spatial modes and time coefficients (short as EOFs) to represent the regional SST variability. Both PCA and EOF were conducted by singular value decomposition (SVD) of the centered and scaled (average 0 and variance 1) data matrix, which was considered a preferred method for numerical accuracy (Venables and Ripley, 2002). Both PCA and EOF analyses were conducted by the "prcomp" routine (psych package) in R (R Core Team, 2018).

The sequential *t*-test analysis of regime shift (STARS) developed by Rodionov (2004) was applied to detect trends and regime shifts in the PC scores. Because of the presence of autocorrelation in the PC scores, we used a "prewhitening" procedure before applying the STARS algorithm (ver.3) (Rodionov, 2006). STARS results are determined by the cut-off length for proposed regimes (L) and the Huber weight parameters (H), which defines the range of departure from the observed mean beyond which observations are considered as outliers. By exploratory analyses with STARS, L is set here to 15 and H to 1 with a significant level of 5%. STARS is written in Visual Basic for Application (VBA) for Microsoft Excel and is available at www.BeringClimate.noaa.gov (Rodionov and Overland, 2005).

Linear correlations among PCs, EOFs, and CIs were estimated using Pearson correlation analyses similar to those of Ma et al., 2019. The number of degrees of freedom of coefficients obtained from the significance tests was adjusted based on the potential autocorrelation in the covariates (Pyper and Peterman, 1998). Analyses were conducted using the "corr.test" routine (psych package) with supplementary scripts for the recalculation of effective degrees of freedom in R (R Core Team, 2018).

Gradient Forest (GF) analysis was employed to identify contributions of climatic (CIs) and environmental variability (EOFs) to biological variability (PCs). The gradient forest method is built upon random forests to capture complex relationships between potentially correlated predictors and multiple response variables by integrating individual random forest analyses over the different response variables (Ellis et al., 2012). In essence, random forests are regression trees that partition the response variable into two groups at a specific split value for each predictor p to maximize homogeneity. Along with other measures, gradient forests provide the goodness-of-fit, R^2, for each response variable f and the importance weighted by R^2. In this study, we ran the gradient forests 1,000 times to obtain the variability of R^2. The run with the highest overall performance (R^2) is then used for calculating weighted importance of predictors on responses. Analyses are conducted using the "gradientForest" package available online at http://gradientforest.r-forge.r-project.org/.

Generalized additive models (GAM) and threshold generalized additive models (TGAM) were applied to identify the types of relationships (stationary or non-stationary) between PCs (biological responses) and EOFs/CIs (physical drivers). A "stationary" relationship is better fitted by a single function throughout the entire period of time-series, and it is formulated using a GAM (Ciannelli et al., 2004):

$$Y = \alpha + s\,(X) + \varepsilon \tag{1}$$

where Y is the response variable PC, X is the predictor (or driver) EOF or CI, and s, α, and ε are smooth function (with $k \leq 3$ to avoid overfitting), intercept, and error terms, respectively. By contrast, a "non-stationary" relationship is better fitted by different functions for different time periods, and the responses to drivers have an abrupt change over a threshold year (Litzow et al., 2018). The non-stationary relationship is formulated using a TGAM (with specific to two time periods) (Puerta et al., 2019):

$$Y_t = \begin{cases} \alpha_1 + s_1\,(X) + \varepsilon_t, & if\ t < y \\ \alpha_2 + s_2\,(X) + \varepsilon_t, & if\ t \geq y \end{cases} \tag{2}$$

where y is the threshold year that separates two periods with different responses to drivers. The y is between the 0.1 lower and the 0.9 upper quantiles of the time-series and is selected by minimizing the generalized cross validation score (GCV) of the model (Casini et al., 2009). To compare the fitness of stationary (GAMs) and non-stationary (TGAMs) models, the "genuine" cross validation squared prediction error (gCV) is computed, which accounts for the estimation of the threshold line and the estimation of the degrees of freedom for the functions appearing in all stationary and non-stationary formulations (Ciannelli et al., 2004). Analyses were conducted by the "mgcv" package in R (R Core Team, 2018).

Analyses flow is shown in **Figure 2**.

RESULTS

Ecosystem, Environment, and Climate Variability

The first four PCs explain 63.19% of the total variance in ecosystem variability (**Figure 3**) with loadings on PCs shown in **Supplementary Figure S3**. PC1 has an increasing trend since the mid-1970s with a step-like change in 1986/87. PC2 decreases around the early 1970s before increasing in the late 1980s with step-like changes in 1974/75 and 1989/90. Prior to the late 1980s, PC3 was relatively stable before the late 1980s; however, it decreases till the mid-2000s with step-like changes in 1989/90 and 2004/05. PC4 has dramatic fluctuations before stabilizing in the 1980s with step-like changes in 1993/94 and 2006/07. PCs are characterized by significant multidecadal to decadal variability patterns with the most concentrated step-like changes in the late 1980s, which indicates that an ecosystem regime shift in the northwestern North Pacific may have happened in the late 1980s.

The first four EOFs have an explanation of 51.65% of the total variance in SST variability (**Figure 4**). Spatial modes of EOFs are provided in **Supplementary Figure S4**. EOF1 shows an abrupt increase in the late 1980s with a step-like change in 1987/88. EOF2 decreases in the 1970s but increases in the late 1980s with step-like changes in 1989/90. EOF3 has a sharp increase in the early 1980s before showing interannual fluctuations with a step-like change in 1980/81. EOF4 shows large interannual fluctuations without any step-like change. Variability in EOFs has obvious decadal scale with step-like changes concentrated in the late 1980s, which indicates that possible regime shift in SST in the northwestern North Pacific happened in the late 1980s.

The CIs clearly show decadal-scale patterns (**Figure 5**). The PDO shows a step-like change in 1976/77, and the NPGO shows a step-like change in 1997/98. The SOI has relatively high-frequency variations without any noticeable step-like change. The AOI, SHI, and MOI have concentrated step-like changes in 1988/89.

Relationships Among Climate, Environment, and Ecosystem Variability

Correlations among CIs, EOFs, and PCs have diverse patterns (**Figure 6**). First, PC1 is positively correlated with EOF1 but negatively with EOF4; PC2 shows a negative correlation with

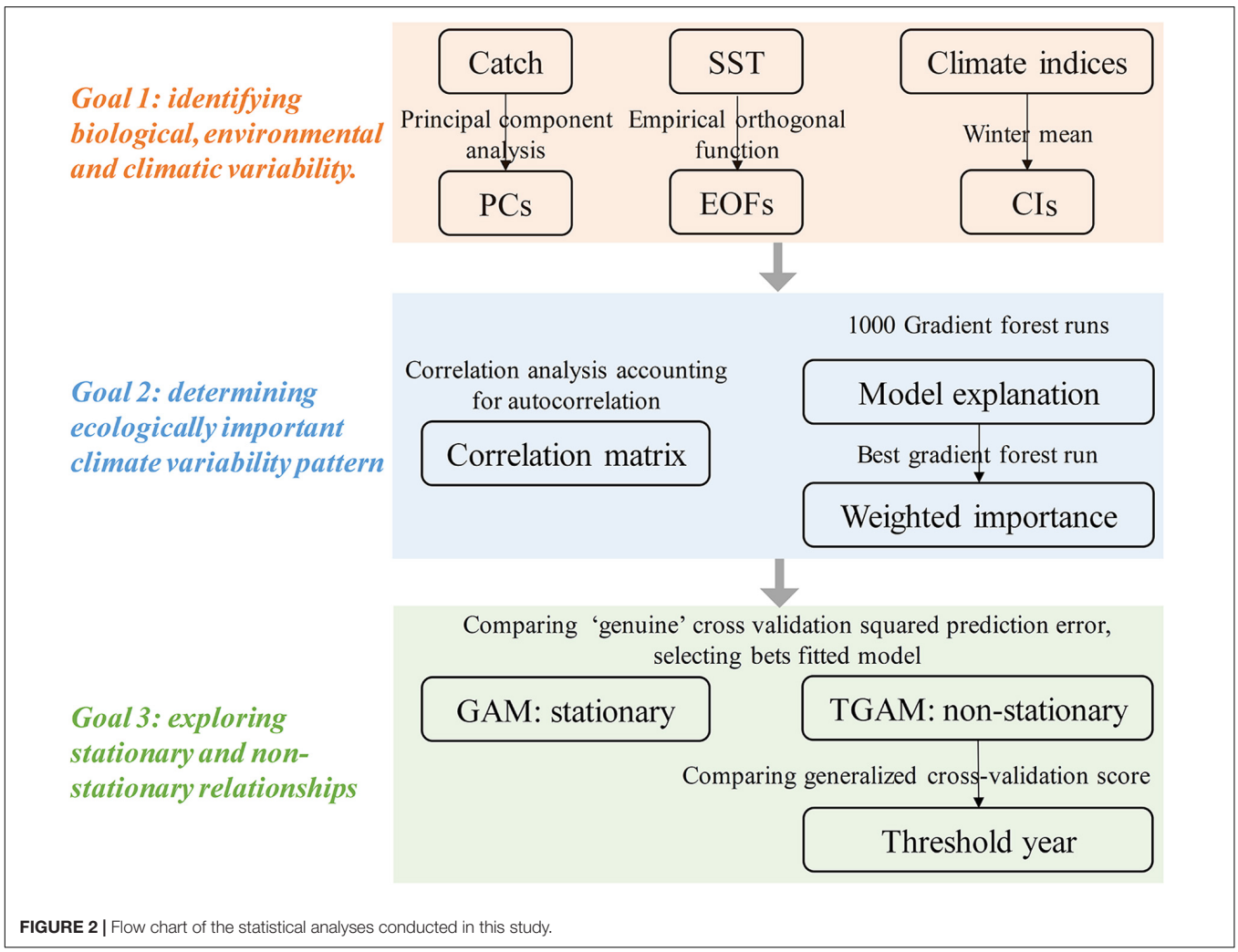

FIGURE 2 | Flow chart of the statistical analyses conducted in this study.

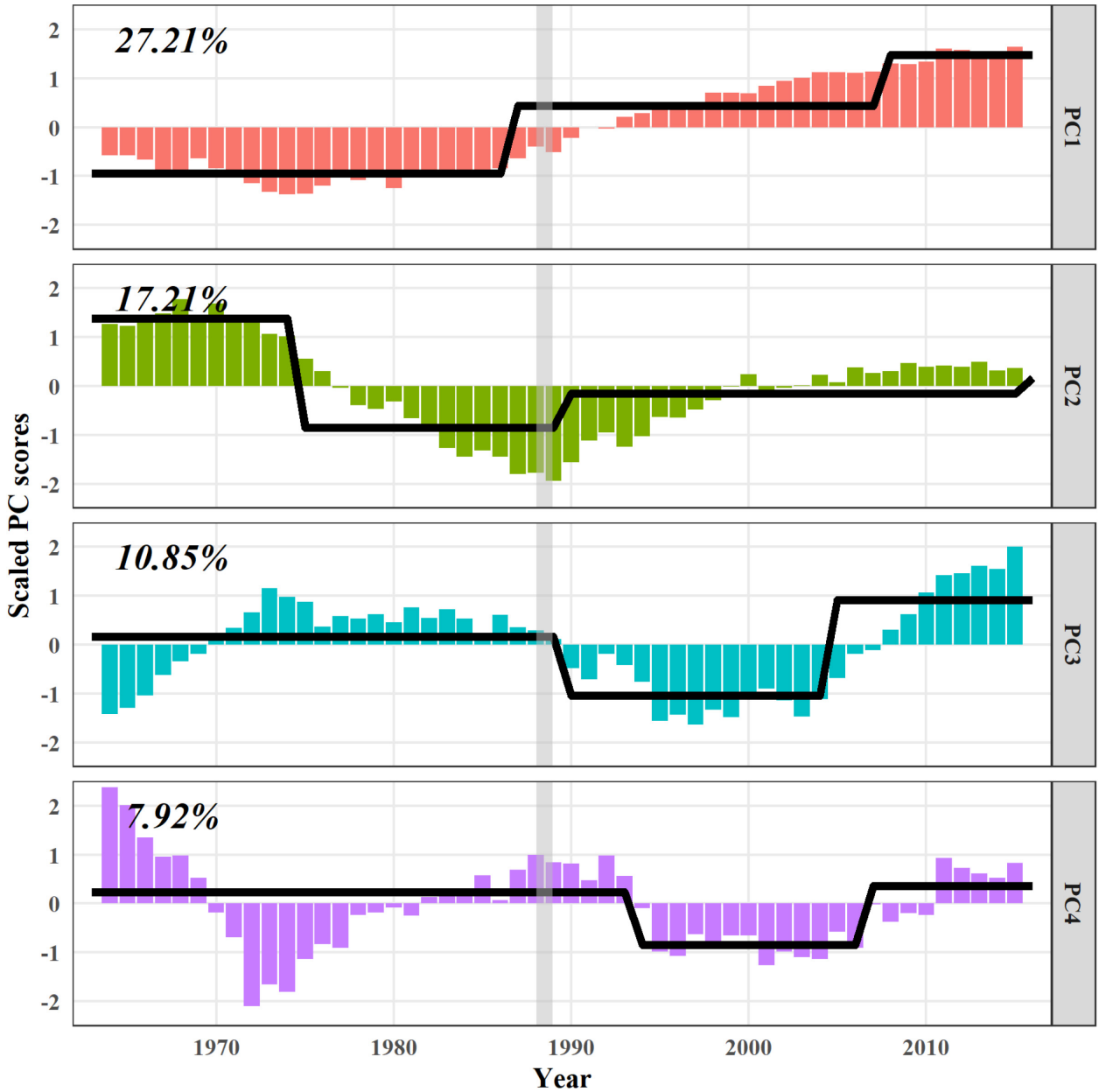

FIGURE 3 | Trajectories of the first four principal components (PCs). Numbers indicate the percentage of variance explained by each PC. Black lines represent regime means calculated by STARS, and gray lines represent the concentrated step-like changes in the late 1980s.

PDO. Other PCs show no correlations with EOFs due to the autocorrelations. Second, EOF1 is negatively correlated with the SHI and MOI; EOF2 is negatively correlated with the PDO, SHI, and MOI, but positively with the AOI; EOF3 shows a relatively weak correlation with the PDO. Third, the SHI is negatively correlated with the AOI but positively with MOI. The PDO is negatively correlated with the SOI.

Gradient forest analysis reveals that PC1 is best explained by EOFs and CIs followed by PC2. PC3 and PC4, on the other hand, failed to be explained by these drivers (**Figure 7A**). In addition, weighted importance shows that EOF1, SHI, and EOF3 are the first three contributors to the variations in PCs. The PDO shows less weighted importance than the SHI, indicating its relatively weaker effects on PCs (**Figure 7B**).

Non-stationary Relationships Between CIs/EOFs and PCs

For all the models relating PCs to CIs and EOFs, the non-stationary models generally resulted in lower gCV (**Figure 8**), indicating better model performances compared with the stationary models. In the case of PC1, the reduction in gCV by

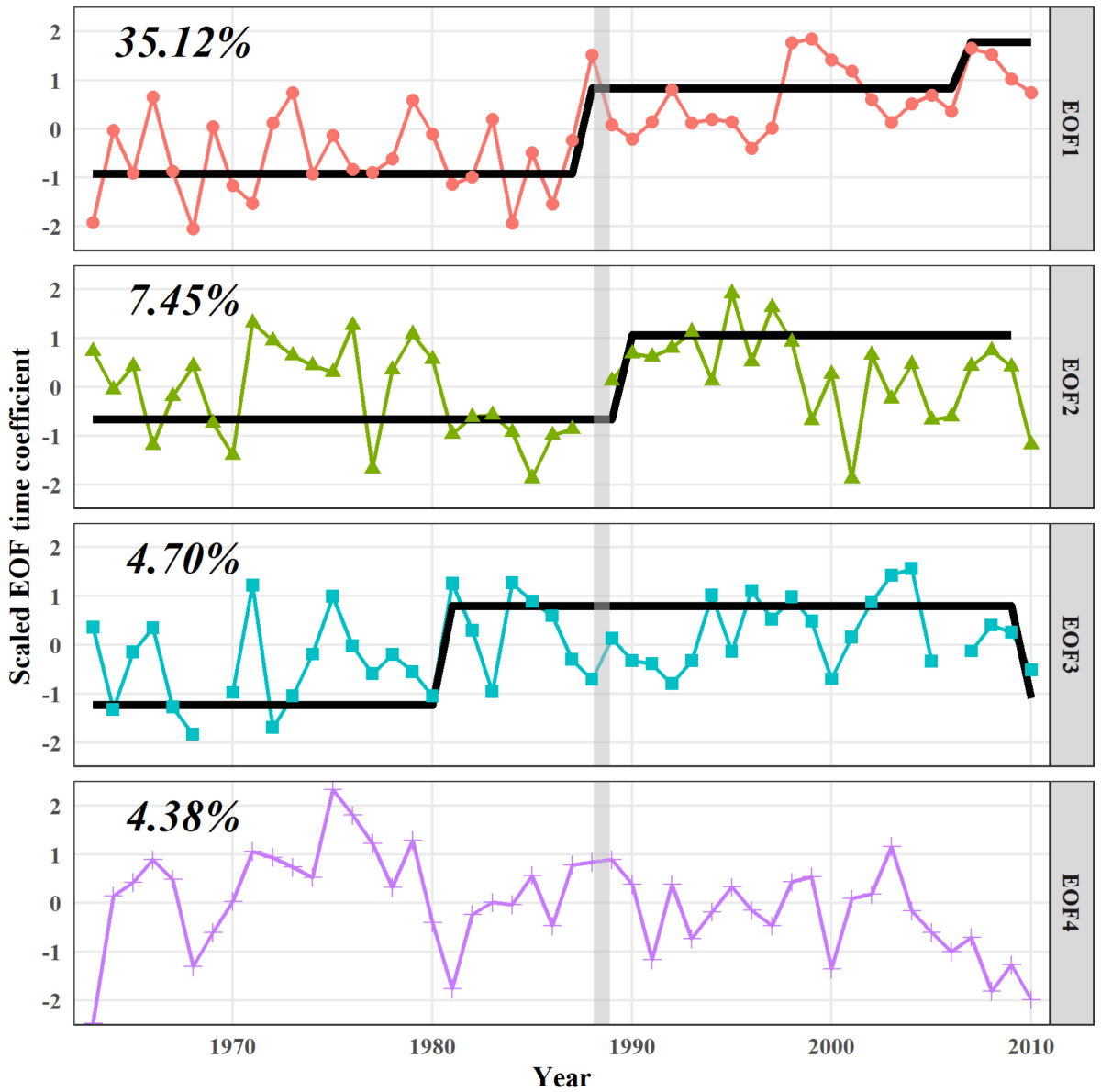

FIGURE 4 | Trajectories of the first four modes of empirical orthogonal functions (EOFs). Numbers indicate the percentage of variance explained by each EOF. Black lines represent regime means calculated by STARS, and gray lines represent the concentrated step-like changes in the late 1980s in contrast to those in **Figure 3**.

implementing non-stationary models are the greatest compared with other PCs. The best fitted model for PC1 (with the lowest gCV) is a non-stationary model with EOF2 as the driver. In the case of PC2, a non-stationary model with EOF1 as the driver achieves the lowest gCV. In the case of PC3, the best model is non-stationary with EOF4 as the driver. For PC4, a non-stationary model with SHI as the driver has a significantly lower gCV and becomes the best fitted one.

According to variations in GCV, threshold years were selected to distinguish eras for fitting driver–response relationships separately (**Supplementary Figure S5**). Two or three eras were identified in the relationships between PCs and CIs/EOFs (**Figure 9**). In relating PC1 to EOF2, two eras were distinguished by the threshold year 1990/91 with similar negative relationships for both eras. However, PC1 is tightly aggregated with EOF2 in Era1 but dispersive in Era2, indicating a more stable relationship in Era1 than in Era2. Relationships between PC2 and EOF1 are divided into two eras by threshold years 1976/77. A positive relationship is shown in Era2 with high dispersion, and an inverted dome-shaped relationships are shown in Era1, suggesting that EOF1 is relatively weak to explain variations in PC2 after the mid-1970s. In the fitting of PC3 and EOF4, contrasting relationships are shown in the two eras with the threshold year 1992/93. Relationships between the SHI and PC4 are negative, negative and inverted dome-shaped in the three eras, with threshold

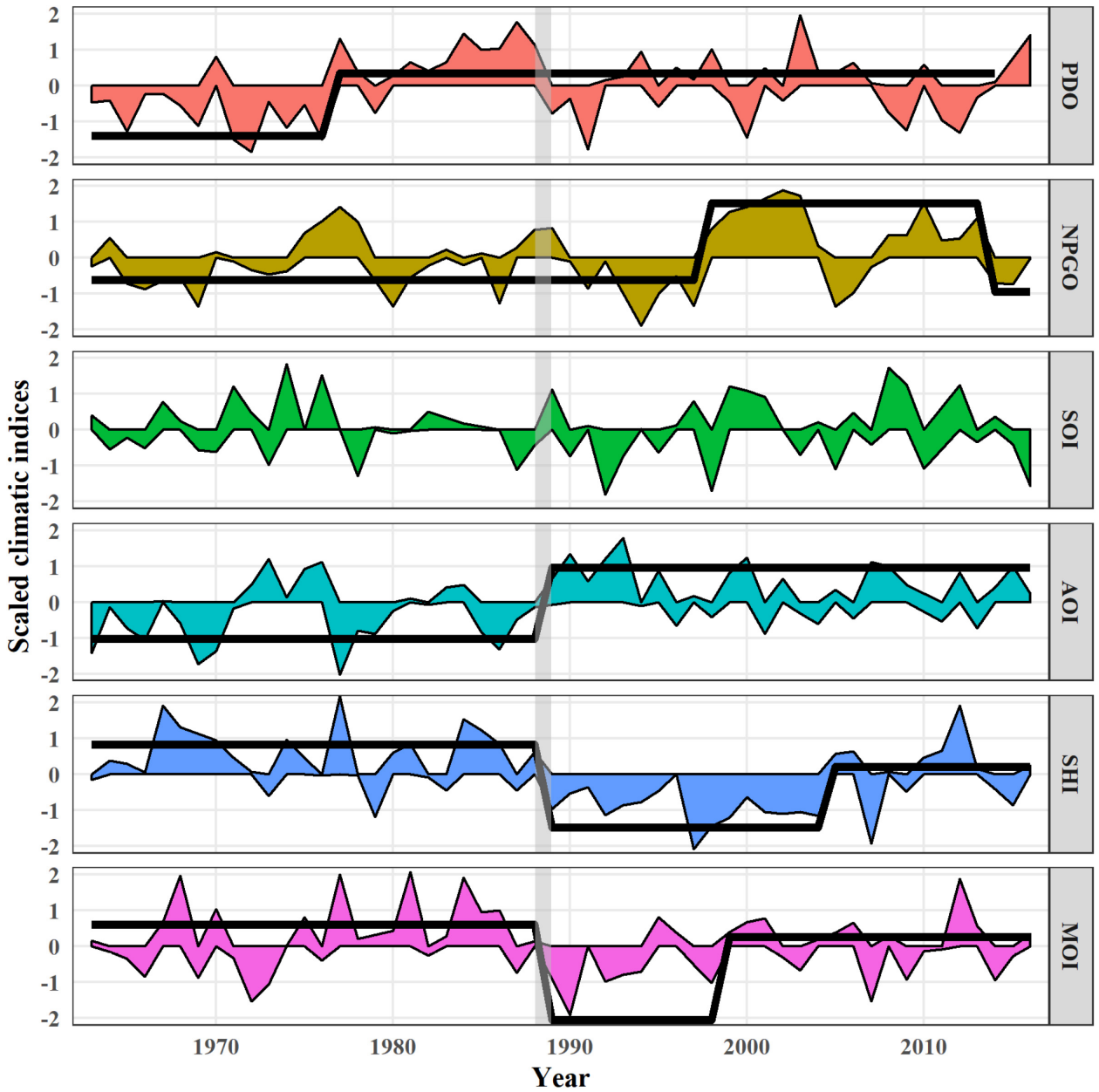

FIGURE 5 | Trajectories of the climatic indices (CIs). Black lines represent regime means calculated by STARS, and gray lines represent the concentrated step-like changes in the late 1980s in contrast to those in **Figures 3**, **4**.

years 1969/70 and 1994/95, and the weakest relationship is shown in Era2.

DISCUSSION

Climate-Induced Ecosystem Variability in the Northwestern North Pacific

In this research, catch data of various taxa from four countries/regions were compiled to provide a holistic perspective on ecosystem variability in the northwestern North Pacific. The problem of missing data always exists in researches with enormous data demands as well as ours. However, with a relatively low missing rate (0.74%), we think it would not affect our results as we focus on the long-term general patterns in ecosystem variability instead of short-term population variability. Significant socioeconomic trends were observed in catch data from China, which may lead to confused results when focusing on climate-induced variability. Therefore, it is imperative to remove the trends by detrend analysis. Although lacking taxa-specific fishing effort data, the engine power of the total Chinese fishing boats could reflect the general pattern in socioeconomic

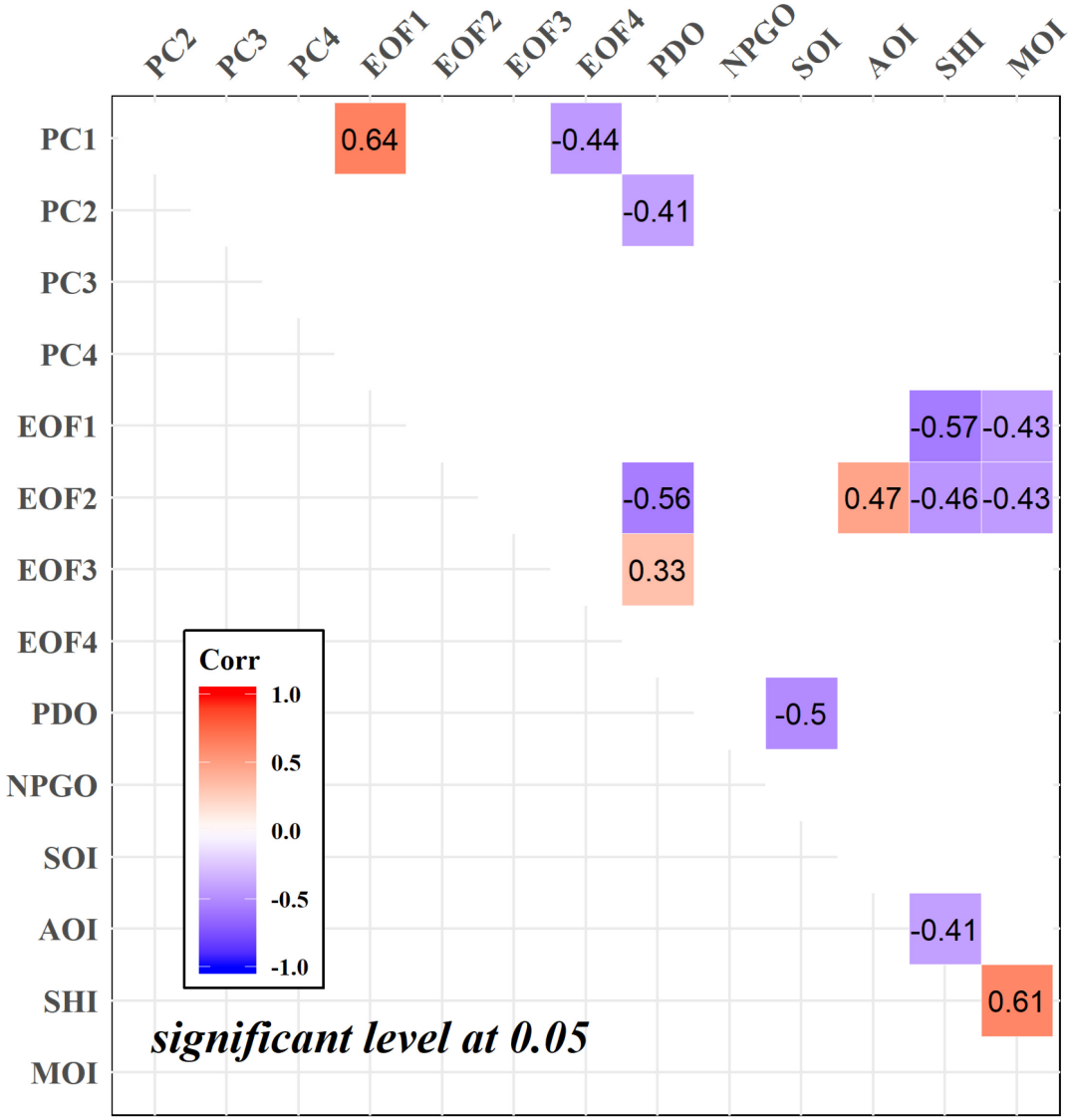

FIGURE 6 | Correlations among principal components (PCs), modes of empirical orthogonal functions (EOFs), and climatic indices (CIs). Colored grids represent significant relationships at a significant level of 0.05 with consideration on the potential autocorrelation. Numbers are correlation coefficients (Corr).

variations in China and could satisfy our demand in the detrend analysis. In addition, catch data from Japan and Korea were extensively used in relevant researches with satisfactory representatives on the biomass (e.g., Tian et al., 2014; Jung et al., 2017). Catch data from Chinese Taipei shown in **Supplementary Figure S1** exhibit inconspicuous socioeconomic influences. Therefore, the detrend analyses were not conduced in catch data from the above three countries/regions.

We employed an analytical framework that integrates both traditional and advanced statistical methods. The traditional statistical methods such as PCA, EOF, STARS, and correlation analyses were extensively used in researches on climate-induced ecosystem variability in the North Pacific (e.g., Mantua and Hare, 2002; Litzow and Mueter, 2014; Ma et al., 2019). The advanced methods including GF and TGAM thrived in recent years with their unique characters that cater to the present research demands. Specifically, the GF captures complex relationships between potentially correlated predictors and multiple response variables, which greatly benefit researches focusing on obscure climate–environment–ecosystem covariations with colinearity in the predictors (e.g., climatic indices and environmental variables) (Fu et al., 2019). The TGAM considers the non-stationary driver–response relationships and has been successfully used in detecting the critical transitions and for ecosystem resilience assessment (Vasilakopoulos and Marshall, 2015; Vasilakopoulos et al., 2017). Therefore, the analytical framework serves as an effective approach in investigating climate-induced ecosystem variability.

Our integrated study across different regions of the northwestern North Pacific indicates that ecosystem variability in this part of the North Pacific is featured by significant

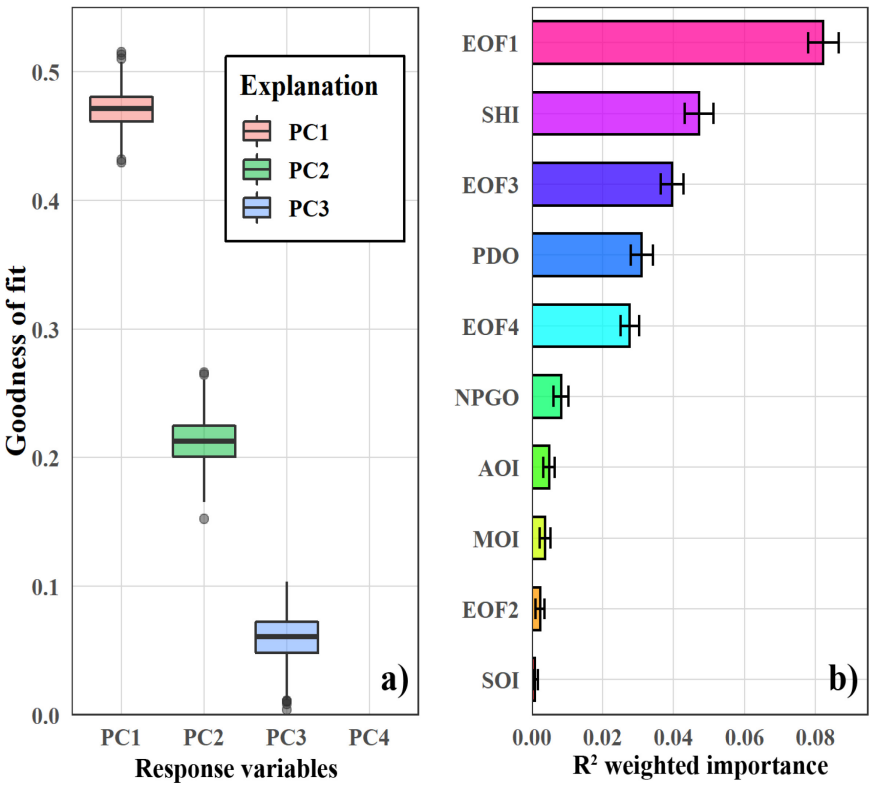

FIGURE 7 | Gradient forest analysis shows **(A)** model performance (goodness-of-fit R^2) for principal components (PCs) and **(B)** weighted importance of modes of empirical orthogonal functions (EOFs) and climatic indices (CIs) on PCs. Error bars represent standard deviations from 1,000 model runs.

decadal-scale and synchrony with climate variability. In particular, the climatic regime shift in the late 1980s (step-like changes in CIs and EOFs) resulted in the ecosystem regime shift (step-like changes in PCs). In the late 1980s, the SHI shifted from a positive phase to a negative phase, representing the weakening pressure in the Siberian High area. Previous research has reported that the decline in the SHI could lead to the decline in MOI (Wu and Wang, 2002). As a result, the MOI also shifted from a positive phase to a negative phase in the late 1980s, representing the weakening monsoon. In addition, the AOI shifted from a negative phase to a positive phase, indicating the strengthening of the Arctic wind vortex, which could hinder the southward intrusion of cold air and also impact the SHI and MOI (Gong et al., 2001; Wu and Wang, 2002). Consequently, the weakening monsoon and decreasing intrusion of cold air directly caused the increase in water temperature, shown as step-like changes in EOFs in the late 1980s. Increasing water temperature could be beneficial for warm-water species but harmful for cold-water species, which have caused the ecosystem regime shift in the late 1980s (Tian et al., 2008; Reid et al., 2016). Our research presents apparent evidence that supports the dominance shift from cold-water taxa to warm-water taxa in the late 1980s. For instance, PC1, PC2, and PC3 all show great changes around the late 1980s. The warm-water yellowtail (J5, positive loading on PC1), Japanese anchovy (J20 and K12, positive loadings on PC2 and PC1, respectively), and Japanese jack mackerel and Japanese scad (J16, negative loading on PC3) had abrupt increases in the late 1980s. By contrast, cold-water Japanese sardine (J19 and K11, negative loadings on PC2), Pacific cod (J8, negative loadings on PC1 and PC2), and walleye pollock (J9 and K4, negative loadings on PC1 and PC2) decreased sharply in the late 1980s. Such taxa shift has impacted fisheries that have fixed gears (such as stow-net and trap-net) or fixed fishing ground, resulting in increased (decreased) percentages of warm-water (cold-water) species (Cheung et al., 2013). Furthermore, the warming has led to north movement of target species, resulting in north movement of fishing grounds of flexible fishery and the increased percentages of low-latitude species in catches of high-latitude countries/regions (Tian et al., 2012).

In addition to the synchrony in climatic and ecosystem regime shifts, correlations among CIs, EOFs and PCs have also been identified by our results. PC1 shows primary correlations with EOF1. PC1 represents the most common variability pattern in ecosystems in the northwestern North Pacific with the highest explained variance and high loadings of most taxa. Besides, EOF1 primarily represents SST variations in the eastern part of East China Sea and variations in the Kuroshio Current path south of Kyushu, Japan (**Supplementary Figure S4**). These two areas have been identified as wintering and/or spawning grounds for many migratory species, such as sardine, anchovy, Japanese jack mackerel, and bluefin tuna (Kitagawa et al., 2000; Kasai et al., 2008; Yatsu et al., 2013; Sassa, 2019; Yatsu, 2019).

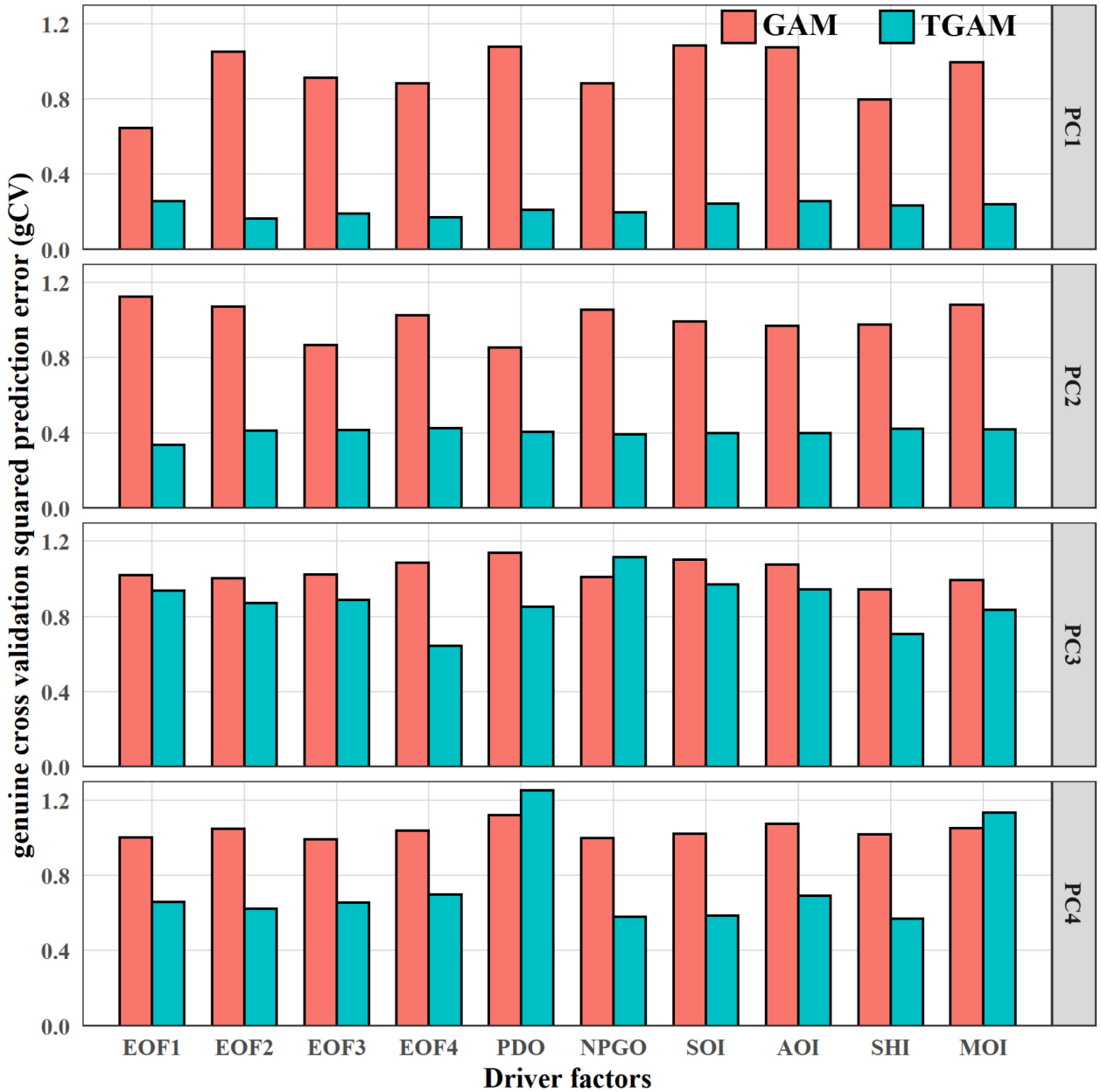

FIGURE 8 | Model comparisons between stationary and non-stationary models. Red bars show the "genuine" cross validation squared prediction error (gCV) of stationary models (GAMs), and blue bars show gCV of non-stationary models (TGAMs).

Environmental changes in these wintering and/or spawning grounds have great impacts on wintering mortality, early life-stage growth and survival of migratory species, and thus play a decisive role on their recruitment process. In addition, the SHI and MOI are negatively correlated with EOF1, but not correlated with PCs, indicating that climate variability impacts biological variability through the intermediary environment variability. It provides evidence that climate-induced biological variability in the northwestern North Pacific may follow the "atmosphere–ocean–ecosystem" process as well as the "double-integration" process (Di Lorenzo and Ohman, 2013; Ma et al., 2019). Furthermore, PC2 is negatively correlated with the PDO. PC2 represents mainly the cold-water species Japanese sardine and walleye pollock (high loadings on PC2) whose catches boomed during the 1970s to 1980s but decreased sharply in the late 1980s. Aside from the above climate variability patterns, it corresponded to PDO that had a shift from a cold regime to the warm regime in the mid-1970s followed by a sharp decline in the late 1980s (Yatsu, 2019).

Our research evaluates the ecological importance of climate variability patterns, and the results show that the SHI may have the highest ecological importance to ecosystems in the

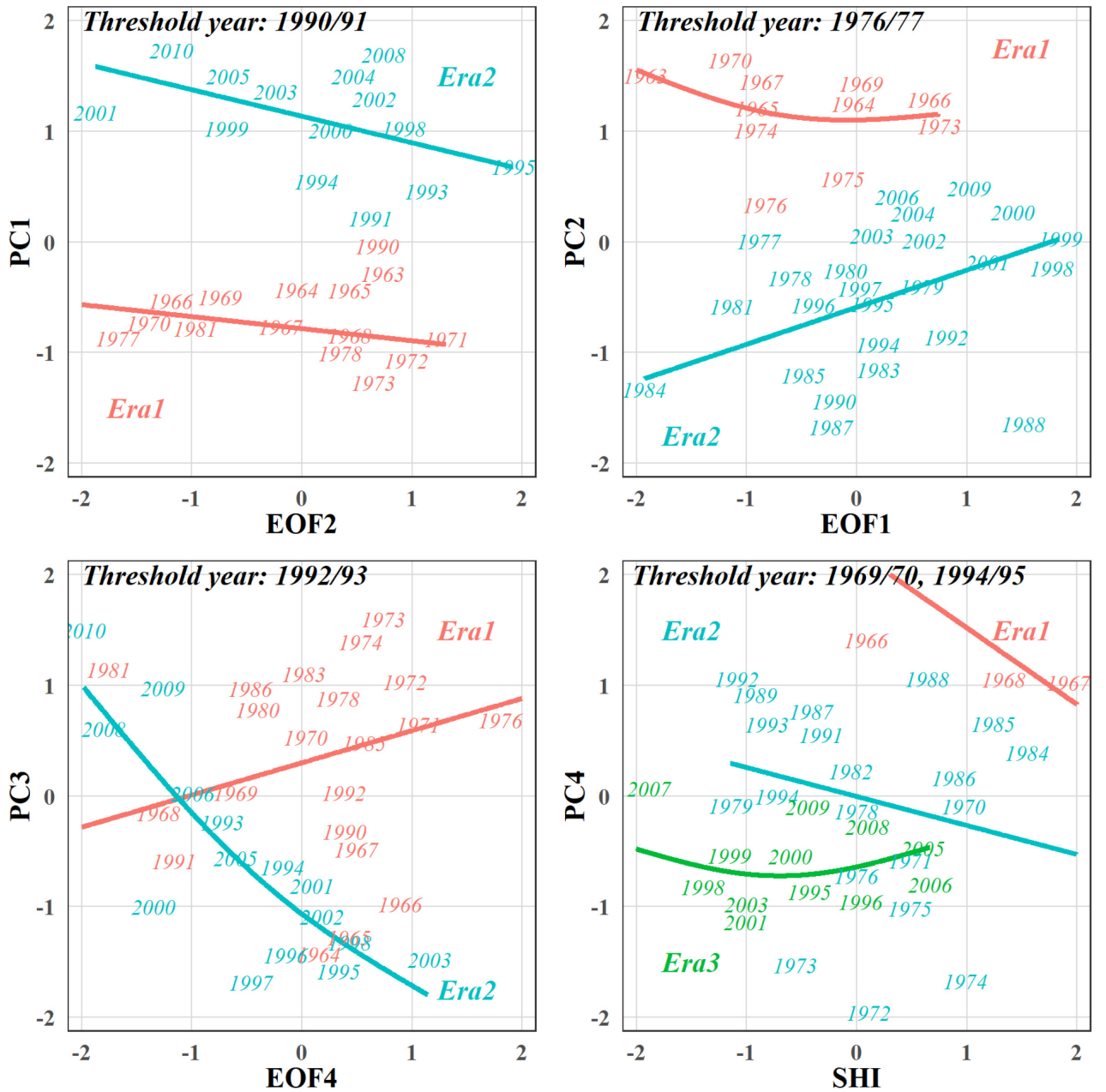

FIGURE 9 | Fitting relationships by the best fitted models. Colors represent different eras with distinguished models.

northwestern North Pacific. On the one hand, SHI combining with AOI and MOI have large impacts on EOF1 that could affect the PC1, while PDO is correlated with EOF2 and PC2 that account for relatively little variance in the ecosystem. On the other hand, gradient forest identifies that EOF1, SHI, and EOF3 are the top three contributors to variations in PCs, followed by PDO, which provides direct evidence for higher ecological importance of SHI than PDO. Nevertheless, this is not a denial of the importance of PDO in the northwestern North Pacific. The PDO has strong linkage with the Kuroshio Current transport (Andres et al., 2009). Besides, the PDO in tandem with ENSO could affect the east Asian winter monsoon (Wang et al., 2008). Therefore, the PDO could still exert on ecosystems by the above intermediaries, which is not investigated here. Based on our results, the SHI should be further considered in future researches on climate-induced biological variability in the northwestern North Pacific. Furthermore, global warming may also have effects on the ecosystem variability in the northwestern North Pacific as temperature increasing in the western boundary current area was observed (Wu et al., 2012). The long-term increasing pattern of EOF1 is likely related to global warming. Meanwhile, EOF1 also has good correspondence to the Siberian High, Arctic

Oscillation, and East Asian Monsoon as we discussed earlier, which was consistent with other researches (e.g., Park et al., 2012). The coincidence of both climate variability and global warming makes it difficult, if not impossible, to separate their effects. Furthermore, other research found that global warming could impact the Siberian High and monsoon system (Hori and Ueda, 2006), which also increases the difficulty in the isolation. Although our research highlighted the ecological importance of the climate variability patterns, global warming could also impact ecosystem variations in the northwestern North Pacific.

Non-stationarity in Climate/Environment–Ecosystem Relationships

Non-stationarity in relationships between climate/environment drivers and ecosystem responses is verified by our research. Previous researches present clear evidences for the non-stationarity in climate–biology relationships in the northeastern North Pacific (Litzow et al., 2018, 2019b; Puerta et al., 2019). Our research points to the non-stationarity in the northwestern North Pacific and enriches proofs for the non-stationarity in the entire North Pacific.

Non-stationarity in relationships between PCs and drivers is characterized by varied fitness or opposite fitting trends in different eras. For example, although the fitted non-stationary relationships between PC1 and EOF2 are negative in both eras, higher dispersion is discovered in Era2 than in Era1 (root mean squared errors, RMSEs are 0.31 and 0.43 in Era1 and Era2, respectively), indicating the lower control of EOF2 on PC1 in Era1 than in Era2. In addition, the fitted non-stationary relationship between PC3 and EOF4 is positive in Era1 but negative in Era2, suggesting different driver–response relationships in the two eras. These two patterns have also been reported in other researches (Puerta et al., 2019). Furthermore, relationships between PCs and drivers have different threshold years, suggesting the asynchronous non-stationarity in the ecosystems, which could be caused by different sensitivities of fish populations in their responses to environmental drivers (Beaugrand, 2015).

The non-stationarity in the northeastern North Pacific has been attributed to the Aleutian Low-forced change in the relative importance of PDO and NPGO to the regional environment variability (Litzow et al., 2018). Such change in the relative importance of alternative climatic indices may also exist in the northwestern North Pacific (**Supplementary Figure S6**). For example, the MOI gradually lost its control on EOF1 since the 1980s, while NPGO showed increased correlations with EOF1. Similarly, correlations between PDO and EOF2 decreased from the 1980s to the early 1990s, and by contrast, correlations between NPGO and EOF2 increased consistently during this same period. While the decline in variance of the Aleutian Low was responsible for the change in the relative importance of PDO and NPGO (Litzow et al., 2018), the same reason may also apply to their correlations with EOF2. As for EOF1, the altered relative importance of MOI and NPGO may be attributed to the decline in variance of the Siberian High that decreased sharply since the late 1980s (**Supplementary Figure S7**). Strong variances in these pressure systems may drive coherent variability in regional ocean physical processes. Therefore, these climatic indices would have good representation of environmental conditions and, thus, relate well with biological variability. However, low variances in these pressure systems would reduce the strength of association among individual environmental variables, accompanied by weaker representation of environmental conditions and disappearing relationships with biological variability. It could explain the weaker driver–response relationships for the era after the threshold years.

While numerous studies address the role of climate forcing in the biological variability of the North Pacific, most of these tend to model relationships among climatic, environmental, and biological variables as stationary properties (Wolkovich et al., 2014). Our studies, demonstrate the existence of non-stationarity between physical drivers and biological responses, in line with a few others (e.g., Litzow et al., 2018, 2019a,b; Puerta et al., 2019). We also preliminarily explored the mechanism behind the relationships in the northwestern North Pacific. Based on our findings, we stress that recognizing climate states (or eras) is vital for the identification of non-stationarity in climate–biology relationships. In addition, analytical techniques considering the non-stationarity achieve better fitting than models with stationary relationships, thus, these techniques are suggested to be used in future researches. Relaxing assumptions of stationary relationships among environmental variables and ecosystem responses may be an important step in understanding climate-induced biological variability.

Comparisons of Climate-Induced Patterns in Ecosystems Between the Northwestern and Northeastern North Pacific

Long-term variabilities in ecosystems in the northwestern and northeastern North Pacific are both characterized by decadal variations largely affected by climate variability. It is widely known that climate-induced ecosystem regime shifts in the North Pacific occurred in the mid-1970s, late 1980s, and late 1990s, and they matched well with the synchronous climatic regime shifts (Overland et al., 2008). However, in the northeastern North Pacific, ecosystem responses to the climatic regime shifts were stronger in the mid-1970s and late 1990s, but weaker in the late 1980s (**Supplementary Figure S8**) (Litzow and Mueter, 2014). By contrast, we found that ecosystems in the northwestern North Pacific had the strongest regime shift in response to the climatic regime shift in the late 1980s (**Supplementary Figure S8**). Asynchronous ecosystem regime shifts were induced by the different climate variability patterns that have ecological importance. Climatic regime shifts dominated by the PDO and NPGO contributed to the ecosystem regime shifts in the mid-1970s and late 1990s, while climatic regime shifts dominated by the SHI, AOI, and MOI resulted in an ecosystem regime shift in the late 1980s. Therefore, identification of climate variability pattern with ecological importance is vital in understanding climate-induced biological variability.

Based on this study and those of others (e.g., Litzow et al., 2019a,b), non-stationarity in climate–biology relationships exists in both northwestern and northeastern North Pacific and is driven by the decline in variances of pressure systems. In addition, non-stationarity in both northwestern and northeastern North Pacific is shown as variations in driver–response relationships over threshold years. However, the decline in the variance of Siberian High was greater in magnitude and longer in duration compared to the Aleutian Low (**Supplementary Figure S7**), which may imply more profound non-stationary effects on ecosystems in the northwestern than in the northeastern North Pacific. Furthermore, accompanied with weakening activities of Siberian High and Aleutian Low, the NPGO seems to replace the MOI and PDO and exhibits control over thermal variability in both the northwestern and northeastern North Pacific, providing bases for unified climate-induced biological variability in the North Pacific.

DATA AVAILABILITY STATEMENT

The raw data supporting the conclusions of this article will be made available by the authors, without undue reservation.

AUTHOR CONTRIBUTIONS

SM, YT, and PS conceived the study. CF, YW, JC, and YL provided guidance in the methods. JL and HY conducted the data compilation and analysis. SM, YT, PS, and CF wrote and revised the manuscript. YT, JL, PS, and YL obtained funding for the study. All authors contributed to the article and approved the submitted version.

FUNDING

This work was supported by the National Natural Science Foundation of China (Grant Nos. 41861134037, 41930534, 41976210, and 41806190), the Shandong Key R&D Program (Grant No. 2019GHY112014), and the Fundamental Research Funds for the Central Universities to Ocean University of China (Grant No. 201713054).

ACKNOWLEDGMENTS

We want to thank the online open-access data and scripts providers, and the two reviewers for their invaluable comments on the manuscript.

SUPPLEMENTARY MATERIAL

The Supplementary Material for this article can be found online at: https://www.frontiersin.org/articles/10.3389/fmars.2020.546882/full#supplementary-material

REFERENCES

Andres, M., Park, J. H., Wimbush, M., Zhu, X. H., Nakamura, H., Kim, K., et al. (2009). Manifestation of the Pacific decadal oscillation in the kuroshio. *Geophys. Res. Lett.* 36, 1–5.

Beaugrand, G. (2015). Theoretical basis for predicting climate-induced abrupt shifts in the oceans. *Philos. Trans. R. Soc. B Biol. Sci.* 370:20130264. doi: 10.1098/rstb.2013.0264

Benson, A. J., and Trites, A. W. (2002). Ecological effects of regime shifts in the Bering Sea and eastern North Pacific Ocean. *Fish Fish.* 3, 95–113. doi: 10.1046/j.1467-2979.2002.00078.x

Biondi, F., Gershunov, A., and Cayan, D. R. (2001). North Pacific decadal climate variability since 1661. *J. Clim.* 14, 5–10. doi: 10.1175/1520-0442(2001)014<0005:npdcvs>2.0.co;2

Carton, J. A., and Giese, B. S. (2008). A reanalysis of ocean climate using simple ocean data assimilation (SODA). *Month. Weather Rev.* 136, 2999–3017. doi: 10.1175/2007mwr1978.1

Casini, M., Hjelm, J., Molinero, J.-C., Lövgren, J., Cardinale, M., Bartolino, V., et al. (2009). Trophic cascades promote threshold-like shifts in pelagic marine ecosystems. *Proc. Natl. Acad. Sci. U.S.A.* 106, 197–202. doi: 10.1073/pnas.0806649105

Cheung, W. W. L., Watson, R., and Pauly, D. (2013). Signature of ocean warming in global fisheries catch. *Nature* 497, 365–368. doi: 10.1038/nature12156

Ciannelli, L., Chan, K.-S., Bailey, K. M., and Stenseth, N. C. (2004). Nonadditive effects of the environment on the survival of a large marine fish population. *Ecology* 85, 3418–3427. doi: 10.1890/03-0755

Di Lorenzo, E., and Ohman, M. D. (2013). A double-integration hypothesis to explain ocean ecosystem response to climate forcing. *Proc. Natl. Acad. Sci. U.S.A.* 110, 2496–2499. doi: 10.1073/pnas.1218022110

Di Lorenzo, E., Schneider, N., Cobb, K. M., Franks, P., Chhak, K., Miller, A. J., et al. (2008). North Pacific gyre oscillation links ocean climate and ecosystem change. *Geophys. Res. Lett.* 35:L08607.

Doney, S. C., Ruckelshaus, M., Emmett Duffy, J., Barry, J. P., Chan, F., English, C. A., et al. (2012). Climate change impacts on marine ecosystems. *Annu. Rev. Mar. Sci.* 4, 11–37.

Dormann, C. F., Elith, J., Bacher, S., Buchmann, C., Carl, G., Carré, G., et al. (2013). Collinearity: a review of methods to deal with it and a simulation study evaluating their performance. *Ecography* 36, 27–46. doi: 10.1111/j.1600-0587.2012.07348.x

Ellis, N., Smith, S. J., and Pitcher, C. R. (2012). Gradient forests: calculating importance gradients on physical predictors. *Ecology* 93, 156–168. doi: 10.1890/11-0252.1

Fu, C., Xu, Y., Bundy, A., Gruss, A., Coll, M., Heymans, J. J., et al. (2019). Making ecological indicators management ready: assessing the specificity, sensitivity, and threshold response of ecological indicators. *Ecol. Indic.* 105, 16–28. doi: 10.1016/j.ecolind.2019.05.055

Gong, D. Y., Wang, S. W., and Zhu, J. H. (2001). East Asian winter monsoon and Arctic oscillation. *Geophys. Res. Lett.* 28, 2073–2076. doi: 10.1029/2000gl012311

Hare, S. R., and Mantua, N. J. (2000). Empirical evidence for North Pacific regime shifts in 1977 and 1989. *Prog. Oceanogr.* 47, 103–145. doi: 10.1016/s0079-6611(00)00033-1

Hori, M. E., and Ueda, H. (2006). Impact of global warming on the East Asian winter monsoon as revealed by nine coupled atmosphere-ocean GCMs. *Geophys. Res. Lett.* 33:L03713.

Hsieh, C. H., Glaser, S. M., Lucas, A. J., and Sugihara, G. (2005). Distinguishing random environmental fluctuations from ecological catastrophes for the North Pacific Ocean. *Nature* 435, 336–340. doi: 10.1038/nature03553

Jung, H. K., Rahman, S. M., Kang, C.-K., Park, S.-Y., Lee, S. H., Park, H. J., et al. (2017). The influence of climate regime shifts on the marine environment and ecosystems in the East Asian Marginal Seas and their mechanisms. *Deep Sea Res. Part II Top. Stud. Oceanogr.* 143, 110–120. doi: 10.1016/j.dsr2.2017.06.010

Kasai, A., Komatsu, K., Sassa, C., and Konishi, Y. (2008). Transport and survival processes of eggs and larvae of jack mackerel *Trachurus japonicus* in the East China Sea. *Fish. Sci.* 74, 8–18. doi: 10.1111/j.1444-2906.2007.01491.x

Kitagawa, T., Nakata, H., Kimura, S., Itoh, T., Tsuji, S., and Nitta, A. (2000). Effect of ambient temperature on the vertical distribution and movement of Pacific bluefin tuna *Thunnus thynnus* orientalis. *Mar. Ecol. Prog. Ser.* 206, 251–260. doi: 10.3354/meps206251

Litzow, M. A., Ciannelli, L., Cunningham, C. J., Johnson, B., and Puerta, P. (2019a). Nonstationary effects of ocean temperature on Pacific salmon productivity. *Can. J. Fish. Aquat. Sci.* 76, 1923–1928. doi: 10.1139/cjfas-2019-0120

Litzow, M. A., Ciannelli, L., Puerta, P., Wettstein, J. J., Rykaczewski, R. R., and Opiekun, M. (2019b). Nonstationary environmental and community relationships in the North Pacific Ocean. *Ecology* 100:e02760.

Litzow, M. A., Ciannelli, L., Puerta, P., Wettstein, J. J., Rykaczewski, R. R., and Opiekun, M. (2018). Non-stationary climate-salmon relationships in the Gulf of Alaska. *Proc. R. Soc. B* 285:20181855. doi: 10.1098/rspb.2018.1855

Litzow, M. A., and Mueter, F. J. (2014). Assessing the ecological importance of climate regime shifts: an approach from the North Pacific Ocean. *Prog. Oceanogr.* 120, 110–119. doi: 10.1016/j.pocean.2013.08.003

Liu, S., Liu, Y., Fu, C., Yan, L., Xu, Y., Wan, R., et al. (2019). Using novel spawning ground indices to analyze the effects of climate change on Pacific saury abundance. *J. Mar. Syst.* 191, 13–23. doi: 10.1016/j.jmarsys.2018.12.007

Ma, S., Liu, Y., Li, J., Fu, C., Ye, Z., Sun, P., et al. (2019). Climate-induced long-term variations in ecosystem structure and atmosphere-ocean-ecosystem processes in the Yellow Sea and East China Sea. *Prog. Oceanogr.* 175, 183–197. doi: 10.1016/j.pocean.2019.04.008

Mantua, N. (2004). Methods for detecting regime shifts in large marine ecosystems: a review with approaches applied to North Pacific data. *Prog. Oceanogr.* 60, 165–182. doi: 10.1016/j.pocean.2004.02.016

Mantua, N. J., and Hare, S. R. (2002). The Pacific decadal oscillation. *J. Oceanogr.* 58, 35–44.

Minobe, S. (1999). Resonance in bidecadal and pentadecadal climate oscillations over the North Pacific: role in climatic regime shifts. *Geophys. Res. Lett.* 26, 855–858. doi: 10.1029/1999gl900119

Overland, J., Rodionov, S., Minobe, S., and Bond, N. (2008). North Pacific regime shifts: definitions, issues and recent transitions. *Prog. Oceanogr.* 77, 92–102. doi: 10.1016/j.pocean.2008.03.016

Park, Y.-H., Yoon, J.-H., Youn, Y.-H., and Vivier, F. (2012). Recent warming in the western north pacific in relation to rapid changes in the atmospheric circulation of the siberian high and aleutian low systems. *J. Clim.* 25, 3476–3493. doi: 10.1175/2011jcli4142.1

Puerta, P., Ciannelli, L., Rykaczewski, R. R., Opiekun, M., and Litzow, M. A. (2019). Do Gulf of Alaska fish and crustacean populations show synchronous non-stationary responses to climate? *Prog. Oceanogr.* 175, 161–170. doi: 10.1016/j.pocean.2019.04.002

Pyper, B. J., and Peterman, R. M. (1998). Comparison of methods to account for autocorrelation in correlation analyses of fish data. *Can. J. Fish. Aquat. Sci.* 55, 2127–2140. doi: 10.1139/f98-104

R Core Team (2018). *R: A Language and Environment for Statistical Computing*. Vienna: R Core Team.

Reid, P. C., Hari, R. E., Beaugrand, G., Livingstone, D. M., Marty, C., Straile, D., et al. (2016). Global impacts of the 1980s regime shift. *Glob. Chang. Biol.* 22, 682–703. doi: 10.1111/gcb.13106

Rodionov, S., and Overland, J. E. (2005). Application of a sequential regime shift detection method to the Bering Sea ecosystem. *ICES J. Mar. Sci.* 62, 328–332. doi: 10.1016/j.icesjms.2005.01.013

Rodionov, S. N. (2004). A sequential algorithm for testing climate regime shifts. *Geophys. Res. Lett.* 31:L09204.

Rodionov, S. N. (2006). Use of prewhitening in climate regime shift detection. *Geophys. Res. Lett.* 33:L12707.

Ropelewski, C. F., and Jones, P. D. (1987). An extension of the Tahiti-Darwin southern oscillation index. *Month. Weather Rev.* 115, 2161–2165. doi: 10.1175/1520-0493(1987)115<2161:aeotts>2.0.co;2

Sassa, C. (2019). reproduction and early life history of mesopelagic fishes in the kuroshio region: a review of recent advances. *Kuroshio Curr.* 2019, 273–294. doi: 10.1002/9781119428428.ch17

Thompson, D. W., and Wallace, J. M. (1998). The arctic oscillation signature in the wintertime geopotential height and temperature fields. *Geophys. Res. Lett.* 25, 1297–1300. doi: 10.1029/98gl00950

Tian, Y., Kidokoro, H., and Watanabe, T. (2006). Long-term changes in the fish community structure from the Tsushima warm current region of the Japan/East Sea with an emphasis on the impacts of fishing and climate regime shift over the last four decades. *Prog. Oceanogr.* 68, 217–237. doi: 10.1016/j.pocean.2006.02.009

Tian, Y., Kidokoro, H., Watanabe, T., Igeta, Y., Sakaji, H., and Ino, S. (2012). Response of yellowtail, *Seriola quinqueradiata*, a key large predatory fish in the Japan Sea, to sea water temperature over the last century and potential effects of global warming. *J. Mar. Syst.* 91, 1–10. doi: 10.1016/j.jmarsys.2011.09.002

Tian, Y., Kidokoro, H., Watanabe, T., and Iguchi, N. (2008). The late 1980s regime shift in the ecosystem of Tsushima warm current in the Japan/East Sea: evidence from historical data and possible mechanisms. *Prog. Oceanogr.* 77, 127–145. doi: 10.1016/j.pocean.2008.03.007

Tian, Y., Uchikawa, K., Ueda, Y., and Cheng, J. (2014). Comparison of fluctuations in fish communities and trophic structures of ecosystems from three currents around Japan: synchronies and differences. *ICES J. Mar. Sci.* 71, 19–34. doi: 10.1093/icesjms/fst169

Vasilakopoulos, P., and Marshall, C. T. (2015). Resilience and tipping points of an exploited fish population over six decades. *Glob. Chang. Biol.* 21, 1834–1847. doi: 10.1111/gcb.12845

Vasilakopoulos, P., Raitsos, D. E., Tzanatos, E., and Maravelias, C. D. (2017). Resilience and regime shifts in a marine biodiversity hotspot. *Sci. Rep.* 7, 1–11.

Venables, W. N., and Ripley, B. D. (2002). *Modern Applied Statistics with S*. Berlin: Springer Publishing Company.

Wang, L., Chen, W., and Huang, R. (2008). Interdecadal modulation of PDO on the impact of ENSO on the east Asian winter monsoon. *Geophys. Res. Lett.* 35:L20702.

Weare, B. C., and Nasstrom, J. S. (1982). Examples of extended empirical orthogonal function analyses. *Month. Weather Rev.* 110:481. doi: 10.1175/1520-0493(1982)110<0481:eoeeof>2.0.co;2

Williams, J. W., and Jackson, S. T. (2007). Novel climates, no-analog communities, and ecological surprises. *Front. Ecol. Environ.* 5, 475–482. doi: 10.1890/070037

Wolkovich, E., Cook, B., McLauchlan, K., and Davies, T. (2014). Temporal ecology in the anthropocene. *Ecol. Lett.* 17, 1365–1379. doi: 10.1111/ele.12353

Wu, B., and Wang, J. (2002). Winter arctic oscillation, siberian high and east asian winter monsoon. *Geophys. Res. Lett.* 29:3. doi: 10.1029/2002gl015373

Wu, L., Cai, W., Zhang, L., Nakamura, H., Timmermann, A., Joyce, T., et al. (2012). Enhanced warming over the global subtropical western boundary currents. *Nat. Clim. Chang.* 2:161. doi: 10.1038/nclimate1353

Yatsu, A. (2019). Review of population dynamics and management of small pelagic fishes around the Japanese archipelago. *Fisher. Sci.* 85, 611–639. doi: 10.1007/s12562-019-01305-3

Yatsu, A., Chiba, S., Yamanaka, Y., Ito, S., Shimizu, Y., Kaeriyama, M., et al. (2013). Climate forcing and the Kuroshio/Oyashio ecosystem. *ICES J. Mar. Sci.* 70, 922–933. doi: 10.1093/icesjms/fst084

Zhang, C. I., Lee, J. B., Kim, S., and Oh, J.-H. (2000). Climatic regime shifts and their impacts on marine ecosystem and fisheries resources in Korean waters. *Prog. Oceanogr.* 47, 171–190. doi: 10.1016/s0079-6611(00)00035-5

Zhang, C. I., Yoon, S. C., and Lee, J. B. (2007). Effects of the 1988/89 climatic regime shift on the structure and function of the southwestern Japan/East Sea ecosystem. *J. Mar. Syst.* 67, 225–235. doi: 10.1016/j.jmarsys.2006.05.015

Zhang, Y., Wallace, J. M., and Battisti, D. S. (1997). ENSO-like interdecadal variability: 1900-93. *J. Clim.* 10, 1004–1020. doi: 10.1175/1520-0442(1997)010<1004:eliv>2.0.co;2

Conflict of Interest: The authors declare that the research was conducted in the absence of any commercial or financial relationships that could be construed as a potential conflict of interest.

frontiers in Marine Science

ORIGINAL RESEARCH
published: 30 September 2020
doi: 10.3389/fmars.2020.547442

Atmospheric-Driven and Intrinsic Interannual-to-Decadal Variability in the Kuroshio Extension Jet and Eddy Activities

Masami Nonaka[1], Hideharu Sasaki[1], Bunmei Taguchi[2] and Niklas Schneider[3]*

[1] Japan Agency for Marine-Earth Science and Technology, Yokohama, Japan, [2] Faculty of Sustainable Design, University of Toyama, Toyama, Japan, [3] International Pacific Research Center, University of Hawai'i at Mānoa, Honolulu, HI, United States

OPEN ACCESS

Edited by:
Robin Robertson, Xiamen University Malaysia, Malaysia

Reviewed by:
Xiaopei Lin, Ocean University of China, China
Ru Chen, Tianjin University, China
Thierry Penduff, UMR5001 Institut des Géosciences de l'Environnement (IGE), France

***Correspondence:**
Masami Nonaka
nona@jamstec.go.jp

Specialty section:
This article was submitted to Physical Oceanography, a section of the journal Frontiers in Marine Science

Received: *01 April 2020*
Accepted: *02 September 2020*
Published: *30 September 2020*

Citation:
Nonaka M, Sasaki H, Taguchi B and Schneider N (2020) Atmospheric-Driven and Intrinsic Interannual-to-Decadal Variability in the Kuroshio Extension Jet and Eddy Activities. Front. Mar. Sci. 7:547442. doi: 10.3389/fmars.2020.547442

To investigate the influences of oceanic intrinsic/internal variability and its interannual-to-decadal modulations on the Kuroshio Extension (KE) jet speed and associated eddy activity, a ten-member ensemble integration of an eddy-resolving ocean general circulation model forced by the 1965–2016 atmospheric reanalysis is conducted. We found a distinct time–scale dependence in the ratio of forced and intrinsic variability of the KE jet speed. On the decadal time scale, the ratio of the magnitude of intrinsic variability to that of the atmospheric–driven variability is 0.73, suggesting it is largely atmospheric–driven. In contrast, on the interannual time scales, the KE jet speed has a large ensemble spread, indicating that it is strongly affected by intrinsic variability and has substantial uncertainty. For eddy activity, the ratios of atmospheric–driven and intrinsic variability also depend on the region. In the downstream KE [32°–38°N, 153°–165°E], variability in the atmospheric–driven eddy activity dominates (1.36 times) over the intrinsic variability on the decadal time scale, and is positively correlated with the current speed. Consistent with the westward propagation of atmospheric–driven jet speed anomalies shown by the ensemble mean, the eddy activity in the downstream KE region is correlated with the current speed variability in the central North Pacific 4 years earlier. This linkage is robust even for each ensemble member with the significant lagged correlation found in seven out of ten ensemble members as well as the ensemble mean (r = 0.59), suggesting the possibility of prediction of the eddy activity. In contrast, the eddy activity in the upstream KE [32°–38°N, 141°–153°E] shows a very large intrinsic and limited atmospheric–driven variability with a ratio of the former to the latter of 2.73. These results suggest that the intrinsic variability needs to be considered in the interannual variability of strong ocean jet. The dependence of these findings to the model specificities needs to be further explored.

Keywords: kuroshio extension, eddy activity, interannual-to-decadal variability, predictability, ensemble simulation

INTRODUCTION

The Kuroshio is the western boundary current of the subtropical gyre in the North Pacific. After departing from the Japan coast at Cape Inubo at the eastern edge of the Honshu Island, it continues as an eastward free jet in the Kuroshio Extension (KE) and is associated with the strongest mesoscale eddy activity in the North Pacific Ocean (e.g., Qiu and Chen, 2005).

The Kuroshio and KE system transports heat from the tropics to the mid-latitude, and release huge amounts of heat to the atmosphere (about 1.7×10^8 W in the annual mean net surface heat flux from the KE region [30°–40°N, 141°–165°E], compared to 7.9×10^8 W in the whole Northern Hemisphere oceans to the north of 30°N based on the third version of the Japanese Ocean Flux Data Sets with the Use of Remote Sensing Observations (J-OFURO3; Tomita et al., 2018) to impact the atmosphere aloft. Through such processes, the strong warm currents and associated sea surface temperature (SST) frontal structure affect the development of cyclones (Kuwano-Yoshida and Minobe, 2017; Hirata et al., 2018) and the large-scale atmospheric circulations (Minobe et al., 2008; Frankignoul et al., 2011; O'Reilly and Czaja, 2015), inducing basin–scale air–sea interactions (Qiu et al., 2014) extending to the tropical Pacific (Joh and Di Lorenzo, 2019). In addition, the decadal variability in the strength of the currents can affect SST, mixed layer depth, and further marine ecosystem in the Kuroshio Extension region (e.g., Nishikawa et al., 2011).

Eddies associated with the KE jet (Itoh and Yasuda, 2010; Sasaki and Minobe, 2015) are an important agent for water mass exchanges across the KE jet and associated oceanic frontal zones, and influence distributions of temperature (Sugimoto and Hanawa, 2011), potential vorticity (Qiu and Chen, 2006; Oka et al., 2015), nutrients (e.g., Sasai et al., 2019), and oxygen (Oka et al., 2015, 2019). The eddy activity modifies also the KE jet itself (Ma et al., 2016). Further, eddies in the region may affect the ocean–to–atmosphere feedbacks (Ma et al., 2015). Because of these possible influences on the atmosphere and ocean, including geochemical variables, it is important to improve our understandings of variability in the KE and associated eddies.

Continuous satellite altimeter observations from the early 1990s have revealed that the KE jet has interannual-to-decadal variability in its strength, latitude, and its stability, which are tightly linked with the eddy activity (Qiu and Chen, 2005). The altimeter observations also unveiled that the interannual-to-decadal variability in the KE jet strength is associated with the sea surface height anomalies that are generated in the central/eastern part of the North Pacific by wind–stress variability and propagate westward as Rossby waves (Qiu and Chen, 2005), indicating that the variability is atmospherically driven. On the other hand, idealized ocean model experiments suggest that strong western boundary currents have variability under steady atmospheric forcing (e.g., Dijkstra and Ghil, 2005). Similarly, a substantial interannual-to-decadal variability of the KE jet has been found in the layer and ocean general circulation models (OGCMs) that realistically represent the ocean circulation (Pierini, 2006; Taguchi et al., 2007; Sérazin et al., 2015) when driven by seasonally-varying atmospheric field without the interannual variability. To investigate atmospherically-forced and intrinsic oceanic variability and their non-linear interaction, ensemble OGCM simulations have been performed in recent years. The OCCIPUT project (OceaniC Chaos-ImPacts, strUcture, predicTability, Penduff et al., 2014) conducted and analyzed an ensemble of 50 eddy-permitting (1/4° horizontal resolution) ocean model integrations subject to realistic atmospheric forcing for 56 years. This large ensemble revealed statistical properties of the atmospherically-forced and intrinsic oceanic variability around the globe (Penduff et al., 2019; Close et al., 2020) and in the Atlantic Meridional Overturning Circulation (AMOC; Leroux et al., 2018). South of the subpolar gyre, the AMOC simulated in 1/4 and 1/12° horizontal resolution OGCMs showed no significant differences in the variance of intrinsic variability, validating the use of eddy-permitting models to investigate AMOC's intrinsic variability (Gregorio et al., 2015). Detailed structures of intrinsic variability of AMOC were further investigated by an eddy-resolving ensemble of multi-decadal integrations for the North Atlantic Ocean (Jamet et al., 2019). Prominent intrinsic interannual variability in the KE jet was found in a 3-member ensemble of eddy-resolving (1/10° horizontal resolution), 18-year integration of a realistic OGCM forced by interannually varying atmospheric forcing under slightly different conditions (Nonaka et al., 2016). The result indicates that part of the KE jet fluctuations are caused intrinsically by non-linear interaction of the strong current and eddies. However, the limited ensemble size and integration period of Nonaka et al. (2016) experiment precluded a separation of interannual and decadal variability due to intrinsic ocean processes and atmospheric forcing, and pacing of intrinsic variability in the KE jet by atmospheric variability (Taguchi et al., 2007; Pierini, 2014).

The same question arises with respect to the interannual and decadal variability of ocean eddy activity. Interannual-to-decadal variability in the KE jet strength, stability, and associated eddy activity induced by Rossby wave propagation (Qiu and Chen, 2005) suggests a wind-driven component of interannual variability in eddy activity. Meanwhile, as eddies are basically formed by oceanic dynamical instability, their activities could be inherently uncertain. In addition, the aforementioned intrinsic interannual variability in the KE jet speed (Pierini, 2014; Nonaka et al., 2016) is likely to induce intrinsic variability in eddy activity. Indeed, recent studies have shown that smaller horizontal-scale oceanic variability like mesoscale eddy activity is more strongly affected by oceanic intrinsic variability (Penduff et al., 2011; Sérazin et al., 2015). To further understand the interannual-to-decadal variability and predictability/uncertainty of mesoscale eddy activity, it is necessary to clarify the potential importance of intrinsic variability.

The purpose of the present study is to investigate the importance of oceanic intrinsic variability in the KE jet strength and associated eddy activity on interannual-to-decadal time scales. This requires available computational resources be used to secure eddy-resolving horizontal resolution, albeit with a limited ensemble size. We conduct a 10 member ensemble of 52-year integrations of a realistic, eddy-resolving OGCM. In section 2, we introduce the OGCM and ensemble experiment, and show

the long-term mean and its spread among ensemble members in section 3. We investigate the KE jet variability and eddy activity in sections 4 and 5, respectively. Section 6 and 7 are for the discussions and summary.

MATERIALS AND METHODS

OFES2

The second version of the OGCM for the Earth Simulator (OFES2) interannual integration has been conducted for the period from 1958 to 2017 (Sasaki et al., 2018). For OFES2, we have modified the first version of OFES (Masumoto et al., 2004; Sasaki et al., 2008) in vertical mixing and tidal mixing parameterization, and coupled the ocean model with a sea-ice model (Komori et al., 2005). The integration has been performed with a horizontal resolution of 1/10° in the model's near-global domain, from 76°S to 76°N. The topography of OFES2 is obtained from ETOPO1 (Amante and Eakins, 2009) with a maximum depth of 7,500 m. The model's vertical coordinate has 105 levels with 44 levels in the upper 300 m. The first version of OFES was integrated from 1950 (Sasaki et al., 2008) after a 50-year spin-up with climatological atmospheric field (Masumoto et al., 2004). OFES2's integration branched off this integration with the temperature and salinity initial conditions taken from the simulated fields of OFES on January 1st, 1958.

To estimate wind-stress at the sea surface, wind speeds relative to ocean currents are used in OFES2. The wind fields are obtained from the Japanese 55-year atmospheric reanalysis based surface dataset for driving ocean-sea-ice models (JRA-55do; Tsujino et al., 2018), in which wind fields are adjusted to the satellite-observed wind speeds. As the satellites observe sea surface wind speeds relative to the surface ocean currents, the OGCM double counts the effect of the surface currents (Zhai and Greatbatch, 2007). Furthermore, the OGCM is driven by the atmospheric reanalysis field that does not include responses to the modeled SST variability, and could underestimate the western boundary currents and associated eddy activities (Renault et al., 2019, 2020).

Sasaki et al. (2020) shows further details of the model setup and comparisons between observations and modeled fields in OFES2. The model represents well observed fields with some exceptions, for example, a northward turn of the extension of the Gulf Stream in the North Atlantic.

Ensemble Experiment

In addition to the original OFES2 eddy-resolving interannual integration mentioned above, we conducted a 10-member ensemble integration of OFES2 for the period from the beginning of 1965 to the end of 2016 (OFES2_ensemble). Ensemble members differ in their initial conditions but are driven by the identical JRA-55do atmospheric reanalysis fields that were also used in the original OFES2 integration. Initial conditions are obtained by sampling the original OFES2 integration every 2 days over an 18 days period between January 3rd and 21st, 1965. Those fields were applied on January 1st, 1965 and then integrated to December 31st, 2016. From the slight differences in the initial conditions, differences among the ensemble members increase with time and saturate in about 5 years (not shown). We analyze the model output from 1970 to 2016. This method to generate the ensemble simulations is basically similar to that used by Jamet et al. (2019). As the differences developed under identical atmospheric variabilities, we attribute differences among the realizations to oceanic intrinsic variability. Temporal variability of the ensemble mean is assumed to largely result from atmospheric forcing, although the ensemble mean can include some components that are not atmospheric driven due to limited number of ensemble members.

Definition of KE Jet Speed and Eddy Kinetic Energy

In the present study, we define the KE jet speed as the current velocity at 2.5-m depth along its axis based on monthly-mean data. At each zonal grid point within the latitudinal band of 30°–40°N, we define the axis of the KE jet as the meridional grid point with the maximum current velocity. The occasional impact of mesoscale features on the jet axis is minimized by the use of a 10-degree longitude average and 13-month running mean (mentioned below).

We estimate the eddy kinetic energy (EKE) as $(u'^2+v'^2)/2$, where u' and v' are temporally high-pass filtered zonal and meridional velocity at 2.5-m depth, respectively, and u' and v' are calculated by subtracting the 13-month running mean fields from their original monthly time series. In the present study, we further apply 13-month running mean to the EKE and other time series to focus on the variability on interannual and longer time scales. To avoid long-term trends and/or multi-decadal variability, which could be induced by oceanic intrinsic variability (Sérazin et al., 2016) and can affect the analysis of time series, we removed the linear trends before the following analysis except for the analysis of the long-term mean fields for **Figure 2E** and relating discussion.

Observational Data

For observed data, we used the surface geostrophic currents distributed by the Copernicus Marine Environment Monitoring Service for comparison with the simulated data. The product identifier of the data is SEALEVEL_GLO_PHY_L4_REP_OBSERVATIONS_008_047. These currents are available on a 0.25° × 0.25° grid, and we use monthly-mean values estimated from the daily-mean data in this study. With the observational data, we estimate the KE jet speed and EKE in the same way as for the simulated data. We also use the indices of the North Pacific Gyre Oscillation (NPGO; Di Lorenzo et al., 2008) and the Pacific Decadal Oscillation (PDO; Mantua et al., 1997) obtained from the web sites of the Georgia Institute of Technology[1] and Joint Institute for the Study of the Atmosphere and Ocean, University of Washington[2], respectively. Data between 1970 and 2015 are used to examine correlations of the EKE in the KE region with these indices. J-OFURO3 data are obtained from the Asia-Pacific Data-Research Center at the International Pacific Research Center, University of Hawaii[3].

[1] http://www.o3d.org/npgo/npgo.php

[2] http://research.jisao.washington.edu/pdo/PDO.latest.txt

[3] http://apdrc.soest.hawaii.edu/datadoc/jofuro3.php

Estimation of Magnitudes of Atmospheric-Forced and Intrinsic Variabilities

In the following analyses, we hypothesize that the variability of the ensemble mean $\langle f \rangle$ of variable f represents the ocean response to time dependent atmospheric forcing, and that deviations $f - \langle f \rangle$ of each ensemble member from the ensemble mean are caused by intrinsic oceanic variability. Here, the angled brackets represent the ensemble mean, $\langle f \rangle = \frac{1}{M}\sum_{m=1}^{M} f$, and an overbar temporal average, $\bar{f} = \frac{1}{T}\sum_{t=1}^{T} f$, where M is the ensemble size and T is number of months for the analysis period. We define the ensemble spread as the standard deviation among ensemble members from the ensemble mean:

$$\sqrt{\frac{1}{M-1}\sum_{m=1}^{M}\left(f - \langle f \rangle\right)^2}.$$

Following Rowell et al. (1995), see also Leroux et al., 2018), the variance of intrinsic variability is estimated by:

$$\sigma_{int}^2 = \frac{1}{T(M-1)}\sum_{t=1}^{T}\sum_{m=1}^{M}\left(f - \langle f \rangle\right)^2,$$

the variance of the ensemble mean is:

$$\sigma_{em}^2 = \frac{1}{T-1}\sum_{t=1}^{T}\left(\langle f \rangle - \overline{\langle f \rangle}\right)^2,$$

and the variance of the response to variable atmospheric forcing is:

$$\sigma_{atm}^2 = \sigma_{em}^2 - \frac{1}{M}\sigma_{int}^2 = \frac{1}{T-1}\sum_{t=1}^{T}\left(\langle f \rangle - \overline{\langle f \rangle}\right)^2 - \frac{1}{TM(M-1)}\sum_{t=1}^{T}\sum_{m=1}^{M}\left(f - \langle f \rangle\right)^2.$$

In σ_{atm}^2, the term of $-\frac{1}{M}\sigma_{int}^2$ is added to take into account the influence of the limited number of ensemble members. The magnitudes of the intrinsic and atmospheric–driven variability are characterized by σ_{int}, and σ_{atm}.

RESULTS

Long-Term Mean and Ensemble Spread

Global Distributions

We first examine the influence of oceanic intrinsic variability on long-term, 30-year (1986–2015), mean fields. **Figure 1A**

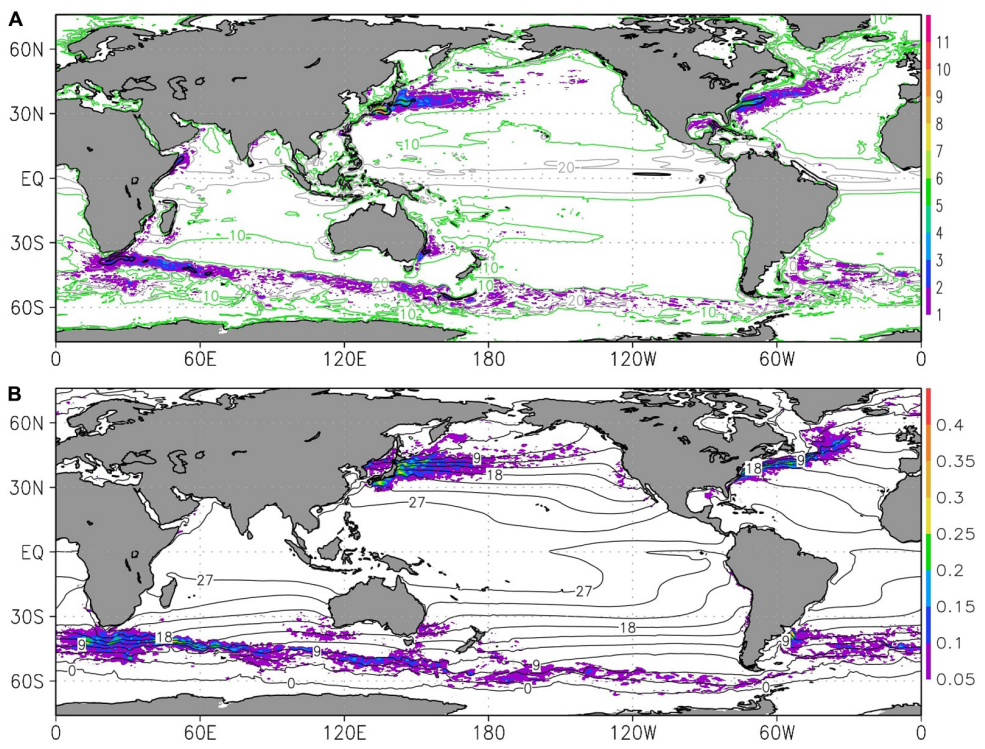

FIGURE 1 | Global map of the long-term (1986–2015) mean **(A)** surface (2.5-m depth) current speed, and **(B)** SST. Contours (shadings) indicate the ensemble mean (spread). Contour intervals are 10 cm s^{-1} (3°C) for **(A,B)** panel. Unit for the current speed is cm s^{-1}, for SST °C.

indicates that even in the 30-year mean current speed, there are spreads among the ensemble members in the western boundary currents and the Antarctic Circumpolar Current regions. Corresponding ensemble spreads are also found in the same regions in the 30-year mean sea surface temperature (SST) field (**Figure 1B**). While the modeled SST field tends to be restored to observed surface air temperature field through the estimation of surface heat fluxes based on the bulk formulae, SSTs are strongly influenced by oceanic dynamics in the strong current regions and can have the ensemble spreads associated with the spreads of the current field. The distribution of the spread in the long-term mean fields is consistent with regions of high intrinsic variability found in the previous studies based on climatological atmospheric forcing (Nonaka et al., 2016) and realistic atmospheric forcing (Close et al., 2020). Such intrinsic variability induces differences among the ensemble members even in the long-term mean fields. However, due to limited number of 10 ensemble members, estimates of the ensemble spread have uncertainties corresponding to the particular ensemble size as discussed below.

The Kuroshio Extension Current

The long-term (30-year) and ensemble mean of the surface current in the North Pacific (**Figure 2**) indicates that the mean current distributions are well represented in the model, although speeds are lower than the observations (**Figure 2A**), even if we compare the observed data to the ensemble member with the strongest current in the KE region (**Figure 2B**) or change the averaging interval to the overlapping period from 1993 to 2016 (not show). The surface boundary condition for the wind stress based on the wind speeds relative to ocean currents could be a reason for the weaker surface current.

As discussed above, the ensemble spreads of the long-term mean surface current are large along the Kuroshio and KE, and extends to around 170°E (**Figure 2D**). While absolute values of the ensemble spreads are limited to less than 5 cm s^{-1}, except for the Kuroshio large meander region, they exceed the atmospherically-forced variability in different 30-year averages of the ensemble mean. Indeed, the ensemble spread (**Figure 2D**) is generally larger than the differences between the two 30-year averaged ensemble means for distinct averaging intervals such as [1971–2000] and [1986–2015] (**Figure 2E**), the most separated 30-year means in the period of 1970–2016. Mean differences among four 30-year averaged ensemble means for the averaging intervals starting in 1971, 1976, 1981, and 1986 are further small (not show), and thus smaller than the ensemble spread.

Oceanic internal dynamics leave a clear difference in the long-term mean jet structures averaged from 160°E to 170°E, an area of large ensemble spreads and weaker mean current speed of the KE. **Figure 3** shows that the mean KE has substantially different structures among the ensemble members: some members have rather broad single jet, while other members have double or even triple jet structures (**Figures 3A–C**). Consistently, the relatively large (about 1 cm s^{-1}) ensemble spreads extend vertically to about 300 m (**Figure 3E**), the typical depth of the jet structure found in the ensemble mean (**Figure 3D**). Ensemble spreads of temperature are found in the thermocline layer below the enhanced spread of the current speed, consistent with the thermal wind relationship (**Figure 3F**). This suggests that the observed jet

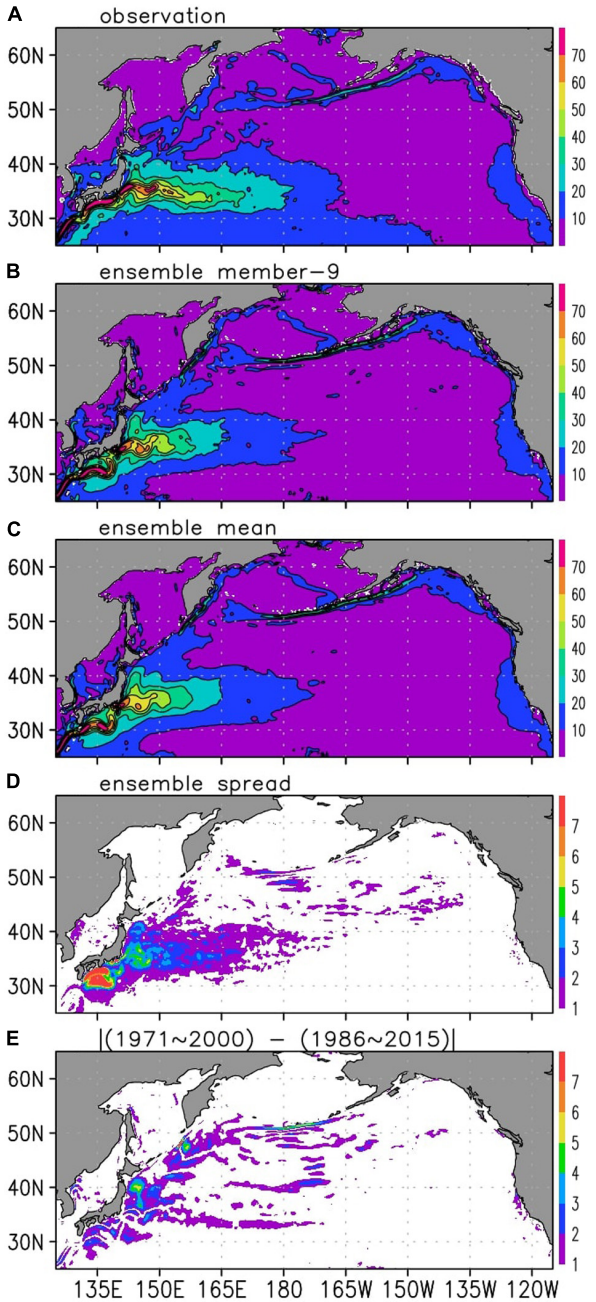

FIGURE 2 | (A) Horizontal map of the long-term (1993–2018) mean observed surface current speed. **(B,C)** Same as the top panel but for panel **(B)** the ensemble member with the largest current speed in the KE jet (30–40N, east of 141E) and **(C)** the ensemble mean of the simulated field averaged for the periods (1986–2015). **(D)** Same as panel **(C)** but for the ensemble spread. **(E)** Absolute value of difference between two long-term mean simulated surface current fields for the periods of (1971–2000) and (1986–2015). Unit is cm s^{-1}.

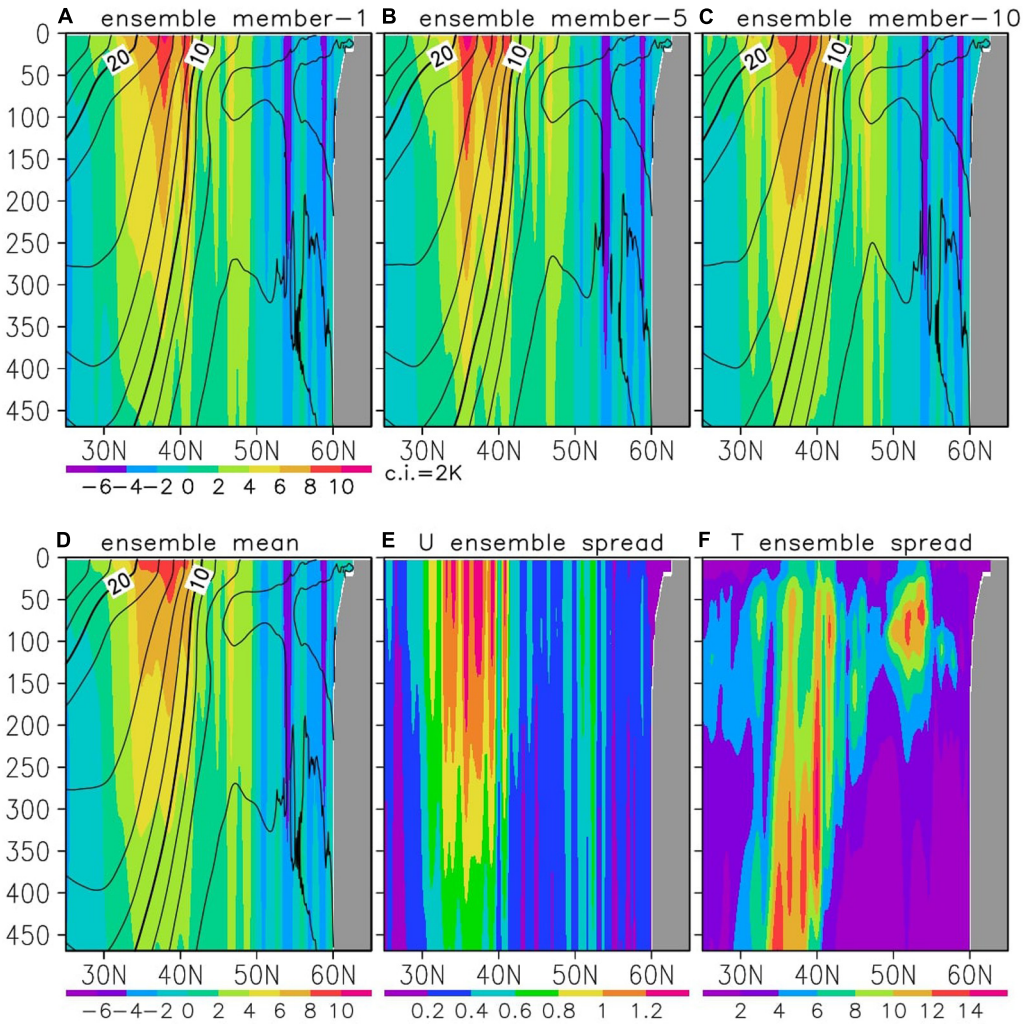

FIGURE 3 | Latitude–depth sections of the long-term (1986–2015) mean, 160°E–170°E zonally averaged fields. **(A–D)** Eastward current speed (shadings, cm s^{-1}) and temperature (contours, with intervals of 2°C) for panels **(A–C)** ensembles 1, 5, and 10, and **(D)** ensemble mean. **(E,F)** Ensemble spread of panel **(E)** the eastward current (unit is cm s^{-1}) and **(F)** temperature (unit is 0.01°C). Color bar for panels **(A–C)** is indicated under panel **(A)**.

structures are difficult to reproduce in eddy-resolving OGCMs in this particular region due to its substantial uncertainty.

Interannual-to-Decadal Variability in the KE Jet Speed

Figure 4A depicts the time series of the KE jet speed for each ensemble member and ensemble mean for the integration period, excluding the first 5 years when the difference among the ensemble members develops. The ensemble spread has a substantial amplitude compared to the total variability of the ensemble average low pass filtered with a 13-month running mean. Indeed, the magnitude of its intrinsic variability, σ_{int} (4.1 cm s^{-1}), is comparable to the magnitude of atmospheric–driven variability, σ_{atm} (4.4 cm s^{-1}), and their ratio is 0.93. However, on decadal time scales, the spread among the ensemble members is rather limited, and all members have similar variations with peaks around 1974, 1980, 1990, and 2005. To focus on the decadal time scales, the KE jet speed time series is smoothed by a 37-month running mean: in this time series, which are dominated by decadal variability (not show), the ratio of magnitude of intrinsic variability σ_{int} (2.8 cm s^{-1}) to that of atmospheric–driven one σ_{atm} (3.8 cm s^{-1}), 0.73, is lower than the counterpart, 0.93, for the variability after 13-month running mean. In contrast, on interannual time scales, the spread among the ensemble members is substantial compared to the variability of the ensemble mean. For the band-pass filtered time series of [13-month running mean]−[37-month running mean], which are dominated by interannual variability (not shown), the magnitude of intrinsic variability σ_{int} (2.7 cm s^{-1}) is larger than that of atmospheric–driven one σ_{atm} (1.4 cm s^{-1}), and the ratio of it is 1.92. In short, in the ensemble members, the KE jet speed exhibits on the interannual and longer time-scale a similar magnitude of atmospheric–driven and intrinsic variability, but its decadal and interannual

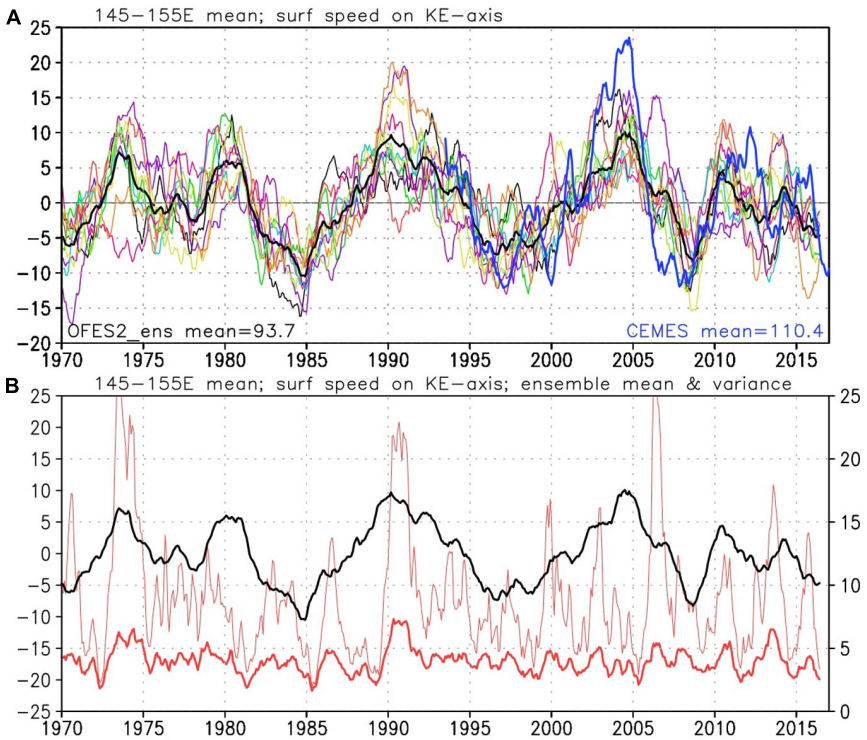

FIGURE 4 | Time series of the Kuroshio Extension jet speed at 2.5-m depth on its axis averaged in 145°–155°E for panel **(A)** each ensemble member (thin curves), the ensemble mean (thick black curve), and observation (thick blue curve). The temporal means are estimated for the period from July 1993 to June 2016, the common period for the model and observation data, and shown in the left-bottom (model) and right-bottom (observation) of the panel **(A)**. **(B)** For ensemble mean (thick black curve, left axis) and ensemble spread (thick red curve, right axis). Red thin curve indicates a 95% confidence interval of the ensemble spread (only upper boundary is shown) following Leroux et al. (2018). Unit is cm s^{-1}. A 13-month running mean is applied and the linear trend is removed.

components are dominated by atmospheric–driven and intrinsic variability, respectively.

Comparing the time series of the ensemble mean and ensemble spread confirms above-mentioned features (**Figure 4B**). Although the spread tends to be high (low) around decadal local maxima (minima) of the ensemble mean in 1974 and 1990 (1985 and 1997), such a relationship is not present in other peaks of the ensemble mean, and we do not find clear relationships between the variability in the ensemble mean and spread. It is indeed very clear that different time scales are at play: the ensemble mean is dominated by decadal time scale, and variability in the spread does not show clear decadal signal and is dominated by interannual time-scale. This is consistent with the rather limited ensemble spread on the decadal time scale and means that the decadal variability in the KE jet speed is more atmospheric–driven, and the KE jet speed has a large uncertainty on the interannual time scale. The thin red curve in **Figure 4B** indicates robustness of the variance among the ensemble members following the method of Leroux et al. (2018, Eq. A1). Due to the limited number of ensemble members in the present study, the uncertainty is very large compared to the ensemble spread itself. Therefore, we need to consider the ensemble spread as a result of the limited number of samples and to interpret the results with sufficient care.

Comparison of the model results with observations (blue thick curve) consistent with the time-scale dependent uncertainty of the KE jet speed (**Figure 4A**). As discussed with **Figure 2**, the time mean KE jet speed is lower in the model (93.7 cm s^{-1} in July 1993–June 2016, the common period for the model and observation) than the observation (110.4 cm s^{-1}). Meanwhile, the ensemble mean represents very well the observed variability on the decadal time scale. Their correlation coefficient r = 0.76 (0.90) for the time series applied 13-month (37-month) running mean, 95 (99) % significant with the effective degree of freedom N = 7 (5) estimated following Metz (1991). In contrast, the band-pass filtered ensemble mean and observation, which are dominated by the interannual time scale, are unrelated (r = 0.17, not significant at 90% level with N = 23).

Eddy Activity in the KE Region

In addition to the simulated KE jet being slightly weaker than the observed (**Figure 2**), EKE in the model is underestimated compared to the observations (**Figure 5A**) even in the ensemble member with the maximum EKE level in the high EKE region (**Figure 5B**). However, the distribution of EKE is similar in the ensemble member with the minimum EKE in the region (**Figure 5C**) and also in the ensemble mean (**Figure 5D**), and the model represents the long-term mean horizontal distributions well. Then, we investigate the temporal variability of simulated

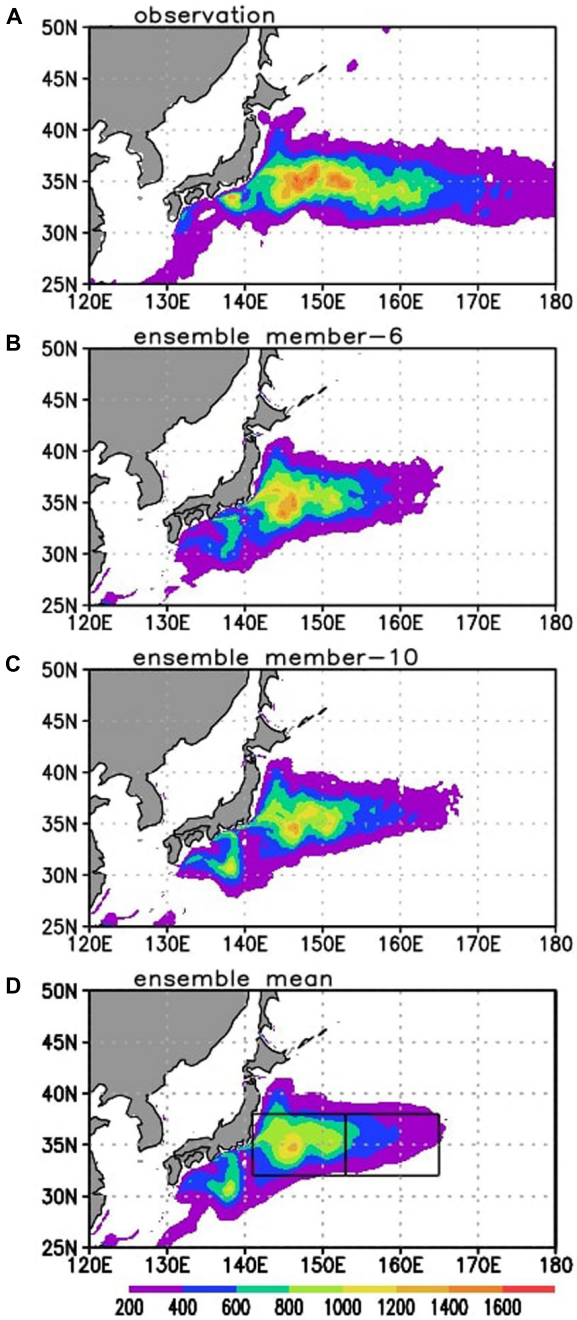

FIGURE 5 | (A) Long-term (July 1994–Jun 2016) averaged observed EKE. **(B–D)** Same as the top panel but for the simulated EKE (cm s^{-1})^2 for the ensemble member with a **(B)** maximum and **(C)** minimum area-mean EKE in the high EKE region [32°–38°N, 141°–165°E], and for panel **(D)** the ensemble mean. The rectangles in the panel **(D)** indicate the upstream [32°–38°N, 141°–153°E] and downstream [32°–38°N, 153°–165°E] KE regions.

eddy activity in the KE upstream and downstream regions. Following Qiu and Chen (2005), we define the KE upstream and downstream regions as [32°–38°N, 141°–153°E] and [32°–38°N, 153°–165°E], respectively (shown by the rectangles in **Figure 5D**).

KE Downstream

In contrast with the KE upstream region (**Figure 6A**) that will be discussed later, EKE time series in ensemble members in the downstream region show only small differences among the ensemble members especially on the decadal time scales (**Figure 6B**). Indeed, the atmospheric–driven variability in the eddy activity dominates (1.36 times) over the intrinsic variability on the decadal time scales (37-month running mean filtered time series), while the ratio is 0.34 on an interannual time scale (band-pass filtered time series). Also, the ensemble mean corresponds well with the observed time series except for the last several years (r = 0.73 for 1994–2010, 99% significant, N = 12, r = 0.41 for 1994–2015, not significant). The reasons for the difference between the observation and the simulation after 2010 are unclear at this stage. This means that in this region, at least in this particular model, the modulation of the eddy activity has a substantial atmospherically–driven component and thus, some potential predictability.

To investigate the mechanisms for the variability in eddy activities, we compare the longitude-time section of anomalies of the ensemble member 2 of EKE and current speed meridionally averaged from 32° to 38°N in **Figure 7A**. Both anomalies tend to propagate westward from the central North Pacific with an intensification of the EKE amplitude toward the western boundary region, and tend to co-vary in the KE downstream region. Indeed, the time series of area means in the KE downstream region (**Figure 7B**) are synchronized with each other: high current speed is accompanied by high EKE (r = 0.79, 98% significant, N = 8). For each ensemble member, the corresponding correlation varies from r = 0.79 to 0.93, but all of them are significant at 98% or higher level. The ensemble member 2 shown in **Figures 7A,B** is the member that has the lowest correlation between the time series shown in **Figure 7B**, among the all members. The relationship between the current speed and EKE is also suggested in the observations (**Figure 7C**, r = 0.89, 99% significant, N = 7). The westward propagation of the signals (**Figure 7D**) and correlation between the area averaged EKE and current speed in the KE downstream region (**Figure 7E**) are also found in the ensemble mean (r = 0.93, 99% significant, N = 6), indicating that the variabilities include the atmospheric–driven component.

As the current speed anomalies include the atmospheric–driven component and tend to propagate westward (**Figure 7D**), the propagation of anomalies could provide predictability for EKE in the KE downstream region. To explore this hypothesis, we first attribute changes of EKE to atmospheric forcing by examining the ensemble mean (**Figures 8A–D**). Predictability and comparison with the single observed realization further require estimation of the signal to noise ratio, estimated from the relative variances due to atmospheric forcing and intrinsic variations, and illustrated by the correlations for individual ensemble members (**Figures 8E,F**). In the lagged correlation maps, a high correlation region is found with current speeds even in 4 years earlier in the central North Pacific (**Figure 8C**), and then propagates westward for a shorter lead-time (**Figures 8A,B**). This feature is consistent with Taguchi et al. (2010) who showed that the low-frequency modulation of EKE in the KE region

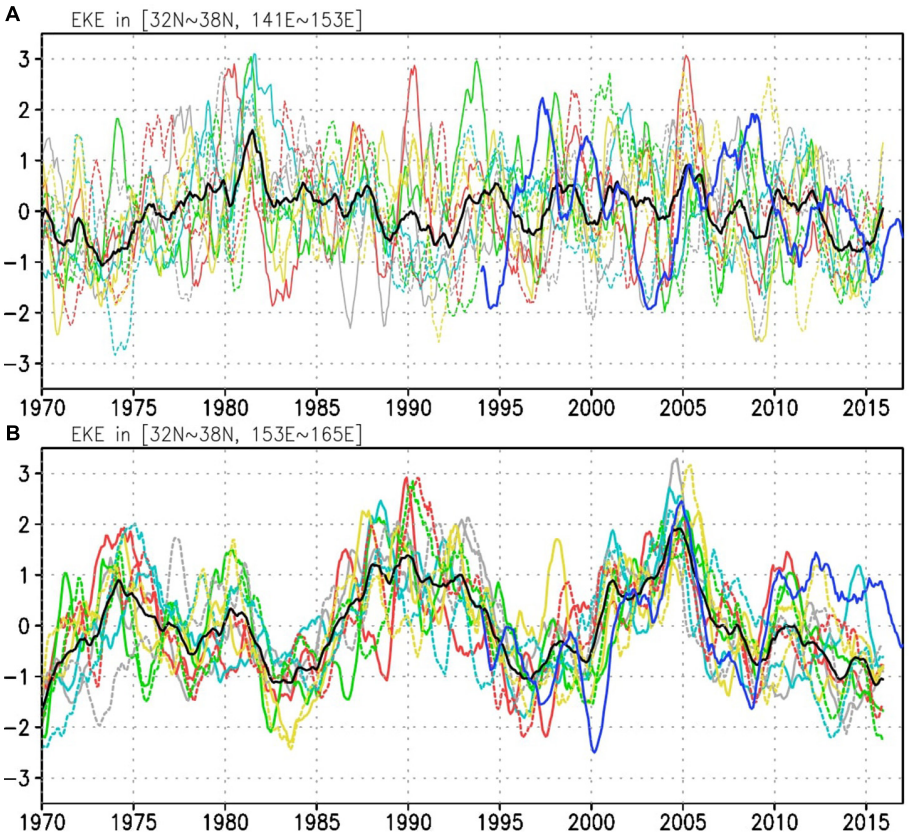

FIGURE 6 | Time series of the standardized area-mean EKE anomalies in panel **(A)** the KE upstream region [32°–38°N, 141°–153°E] and **(B)** the KE downstream [32°–38°N, 153°–165°E] for each ensemble member (thin curves), the ensemble mean (thick black curve), and the observation (thick blue curve). The time series of observation and each ensemble member are standardized by dividing the original time series by their standard deviations. The ensemble mean is divided by the mean of standard deviations of all ensemble members.

is associated with the incoming, westward-propagating Rossby wave signals. The time series of area averaged current speed in the central North Pacific (34°–36°N, 175°W–165°W) correlates well with the eddy activities in the KE downstream region in 4 years later (r = 0.59, 90% significant, N = 12), indicating a potential of predictability of the ensemble mean eddy activities in the region (**Figure 8D**). While **Figure 8B** suggests that the current in the same region also correlates with the eddy activities in the KE downstream 2 years later, the correlation is slightly lower (r = 0.50) and not significant. Also, the westward propagating signals are not found in the 6-year lead correlation map (not shown).

In the actual prediction, however, we need to consider the lagged correlation for each ensemble member rather than the ensemble mean as real observation is equivalent to one realization of the ensembles. For each ensemble member, the lagged correlation between the area averaged current speed in the central North Pacific and EKE in the KE downstream region 4 years later varies from r = 0.264 (ensemble member 6, **Figure 8F**) to 0.602 (ensemble member 3, **Figure 8E**) and their average is r = 0.446. While seven of ten members show the lagged correlation statistically significant at 90% level, the correlations are not significant for three members. (It should be noted that as the ensemble mean has smoother time series, the effective degree of freedom is smaller than that for each ensemble member, and correlation coefficients at 90% significance higher for the ensemble mean than for each ensemble member). This means that while the ensemble mean shows a potential of a 4-year lead prediction of eddy activity in the KE downstream region, it is not always expected for each ensemble member due to the intrinsic variability and, thus for real observation.

Indeed, a similar 4-year lagged correlation between the current speed in the central North Pacific (40°–42°N, 160°W–150°W) and EKE in the KE downstream region is also found in the observed data (r = 0.60), but it is not statistically significant (not shown). While this result can be due to intrinsic variability included in the observation, the less robust statistical relation could be also due to the limited length of observed time series. Therefore, to determine the potential predictability in EKE in the KE downstream region with several years lead-time in the real North Pacific Ocean has to await a longer observed record.

KE Upstream

In contrast to the downstream region, the time series in the KE upstream region of EKE for each ensemble member (**Figure 6A**) shows substantial differences and there is almost no common

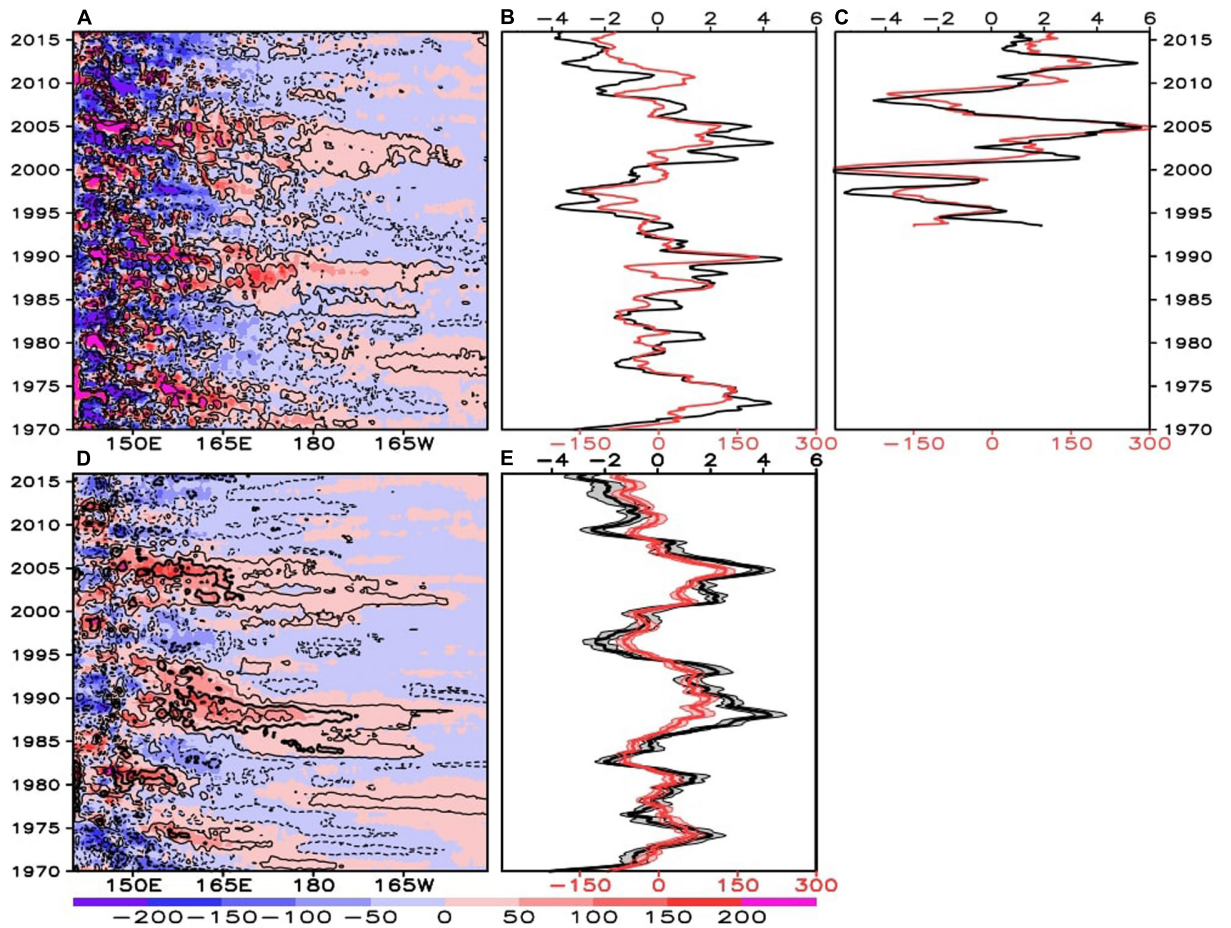

FIGURE 7 | Anomalies of the eddy activity and current speed at 2.5-m-depth meridionally averaged in 32°–38°N. **(A)** Longitude-time section of the eddy activity anomaly (shadings) and current speed anomaly (contours at ±1, 5 cm s^{-1}). **(B)** Time series of an individual member EKE (red, bottom axis) and current speed (black, top axis) anomalies averaged in 153°–165°E. **(A,B)** Are for the ensemble member 2, which has the lowest correlation between the two time series among the all ensemble members. **(C)** Time series of the observed eddy activity (red) and current speed (black) anomalies averaged in 153°–165°E. **(D)** Same as **(A)** but for the ensemble mean (contours at ±1, 3, 5 cm s^{-1}). **(E)** Same as **(B)** but for the ensemble mean. Shadings indicate the corresponding error bars as ± (ensemble spread/$M^{1/2}$). M = 10, the number of the ensemble members. Unit for current speed is cm s^{-1}, for EKE (cm s^{-1})^2.

temporal variability among the ensemble members. Indeed, the ratio of the magnitude of intrinsic variability of EKE to that of the atmospheric–driven variability is 2.73 in this region. Hence, at least in this particular model, the variability in the eddy activity in the region is strongly uncertain, and consistently, the time series based on observation does not agree with the model ensemble mean ($r = -0.16$, not significant). Nevertheless, the observed time series is in the range of the ensemble spread except for some years in the mid and late 1990s, implying that the observation is basically within the simulated uncertainty. We will discuss the high uncertainty of EKE in this region and the influence of model biases on the uncertainty in section "Discussion About the Simulated Eke in the KE Upstream Region."

Map of Potential Predictability

In the above analyses, we have investigated uncertainty/potential predictability of the eddy activity focusing on the two particular regions, the KE upstream and downstream regions defined by Qiu and Chen (2005). To examine horizontal distributions of this property in the whole KE region, we further plot the horizontal map of potential predictability for the interannual and longer time scale variability (**Figure 9**). Here, we define the potential predictability (PP) as follows: $\mathrm{PP} = \sigma^2_{atm} / \left(\sigma^2_{atm} + \sigma^2_{int}\right)$ (Rowell et al., 1995; Sugi et al., 1997). PP represents the ratio of deterministic, atmospheric–driven, variance to the total variance, considering the variability in the ensemble mean is deterministic.

In **Figure 9**, we plot the square root of PP estimated for 5°–longitude and 5°–latitude mean eddy activities after applying a 13-month running mean to focus on the interannual and longer variability. The linear trends are also removed. The plot shows that PP is generally higher in the downstream side with peaks around 160°E to the north of the KE jet, and has a local minimum around the KE jet (∼37°N) in the further downstream region. It is clear that PP is low in the upstream of the KE jet around its axis, consistent with the difference found in the specific KE upstream and downstream regions in the previous subsections.

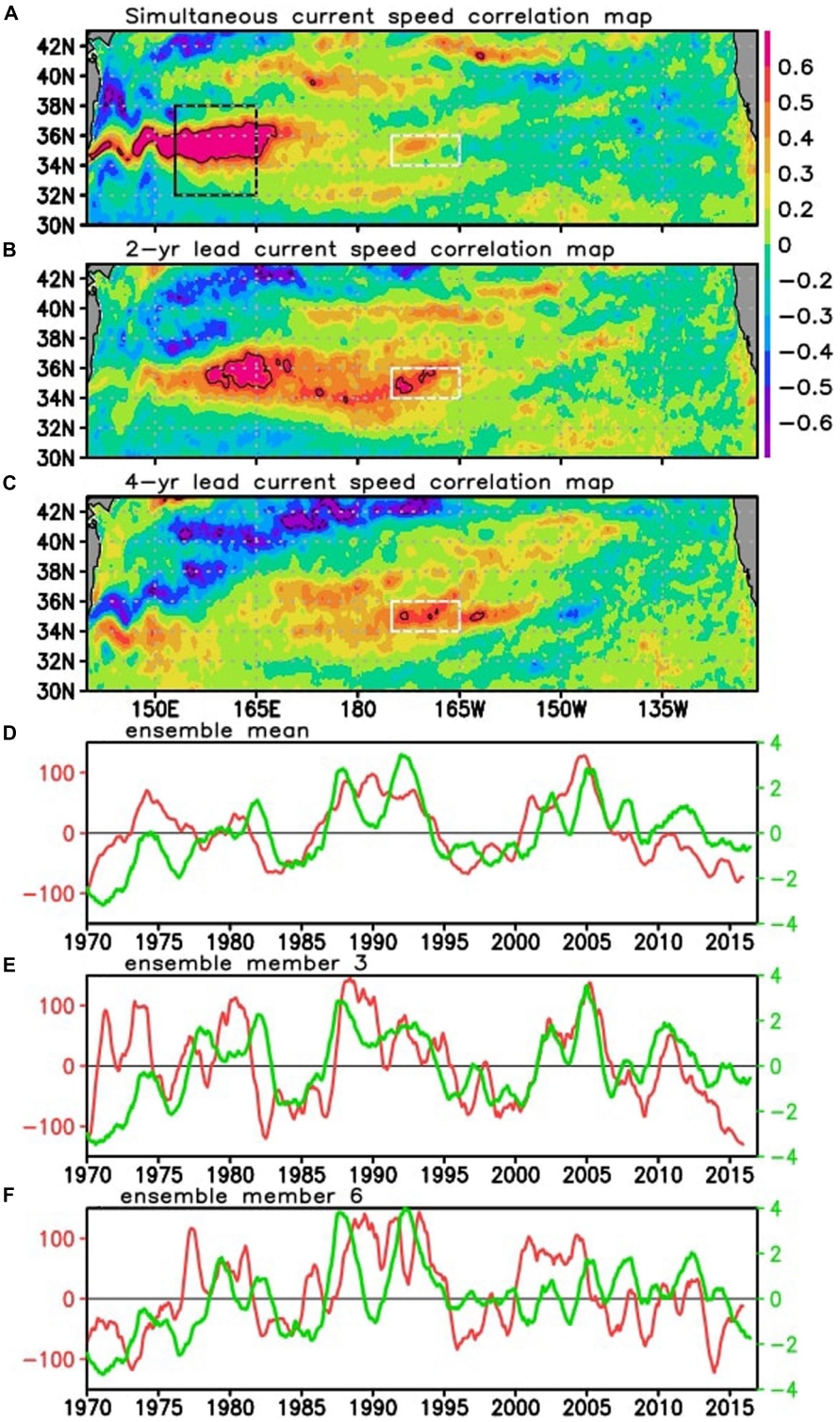

FIGURE 8 | (A–C) Lagged correlation map of the surface current speed in the North Pacific with the EKE in the KE downstream [red curve in panel **(D)**] with **(A)** 0-, **(B)** 2-, and **(C)** 4-year lead current speed fields for the ensemble mean fields. Black contours indicate the significant region at 90% level. **(D)** Time series of anomalies of the area mean EKE (red) in the KE downstream region [32°–38°N, 153°–165°E] [black rectangle in panel **(A)**], and the 4-year lead surface current speed (green) averaged in the central North Pacific [34°–36°N, 175°W–165°W] [white rectangle in panels **(A–C)**]. **(E,F)** Same as **(D)** but for ensemble members **(E)** 3 and **(F)** 6, each of which has the highest and lowest correlation between the time series among the all ensemble members, respectively. Unit for current speed is cm s^{-1}, for EKE (cm s^{-1})^2.

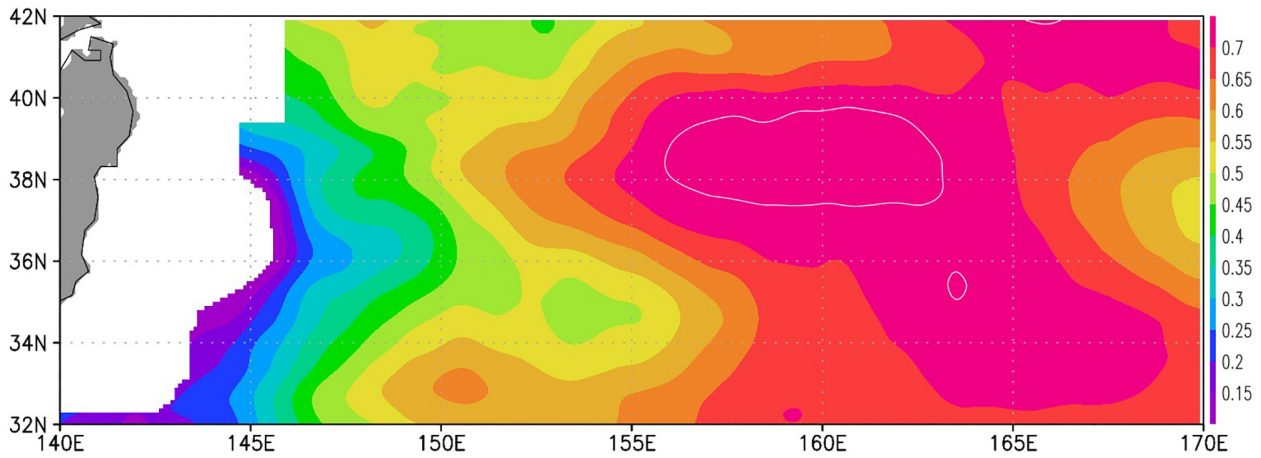

FIGURE 9 | Horizontal map of the square root of the potential predictability (PP) of the simulated 5°–longitude and 5°–latitude averaged EKE. The value is plotted at the grid point of the center of the 55°–longitude and 5°–latitude area. White contours indicate 0.75. A 13-month running-mean is applied to and the linear trend is removed from EKE before estimating PP.

Comparison with the long-term mean horizontal distribution of eddy activity (**Figure 5**) implies that PP tends to be lower with higher eddy activity in the KE region.

DISCUSSION OF THE SIMULATED EKE IN THE KE UPSTREAM REGION

The relationship between EKE and the current speed found in the KE downstream region can be explained by dynamical stability. Given the geostrophic/thermal wind relationship with weak currents at depth, the stronger surface zonal current is associated with a stronger meridional temperature/density gradient. Stronger meridional temperature gradients are more baroclinically unstable and induce higher eddy activity. Stronger meridional shear associated with the stronger zonal currents favors barotropic instability.

The relationship we identified in the KE downstream region is, however, opposite to what Qiu and Chen (2005) found based on satellite observations in the KE upstream region. They show that a high (low) eddy activity is associated with a low (high) current speed on the decadal time scale. In the KE upstream region, as found in **Figure 6A**, the model does not capture the observed EKE variability. Furthermore, the observed relationship between the current speed and EKE variability is not clearly reproduced even in each ensemble member (only two of ten members show significant negative correlation between them consistent with the observation) as well as in the ensemble mean. So, the discrepancy in the region could be a model deficiency. Alternatively, this may imply that EKE activity in the KE upstream region is highly uncertain in the real ocean, so that the observed time series cannot be reproduced in ocean GCMs.

Sugimoto and Hanawa (2012) show from observational data that when the Kuroshio takes its offshore non-large meander path and passes the southern part (32°–33°N) of the Izu Ridge (around 140°E), eddy activity tends to be high in the upstream KE region. While OFES2 has a bias in the path of Kuroshio south of Japan, and tends to have the large meander path more often compared to the observations as suggested in **Figure 2**, we have confirmed that the model tends to take a near shore path at the Izu Ridge more often than in the observation (not shown). Based on the results of Sugimoto and Hanawa (2012), this means that the bias of the model Kuroshio path does not enhance the eddy activity in the upstream KE region. Also, as discussed with **Figure 5**, the model has slightly weaker EKE in the KE region compared to the observation, and the high uncertainty in the KE upstream region is not due to too strong eddy activity in the region.

The uncertainty in EKE in the upstream KE region can be further explored by correlating across all the ensemble members the intrinsic (unforced) component of SSH anomalies onto the intrinsic component of the EKE in the upstream KE region (**Figure 10**). Positive EKE deviations in the upstream KE region that exceed the ensemble mean are associated with a negative (positive) SSH deviations from the ensemble mean to the south (north) of the upstream KE jet (**Figure 10A**). Hence, as the intrinsic variability, the stronger EKE is associated with a weaker southern recirculation gyre and a weaker SSH meridional gradient, while there is a possibility that the weaker recirculation and meridional SSH gradient results from the stronger EKE. This property is consistent with observation (Qiu and Chen, 2005), although the observed data includes both the atmospheric–forced and intrinsic components. Interestingly, stronger EKE in the upstream KE region is also associated with positive SSH deviations in the Kuroshio south of Japan, and the lagged correlation maps (**Figures 10B,C**) show that the signal appears first in the region and then expands into the upstream KE region. The positive SSH deviations to the north of the mean Kuroshio meandered path (depicted by the contours) tends to straighten the Kuroshio path and this leads to stronger EKE in the upstream KE region 2 years later. The analysis suggests that the self-sustained intrinsic path variations of Kuroshio south of Japan (e.g., Qiu and Miao, 2000) may have a down-stream influence on

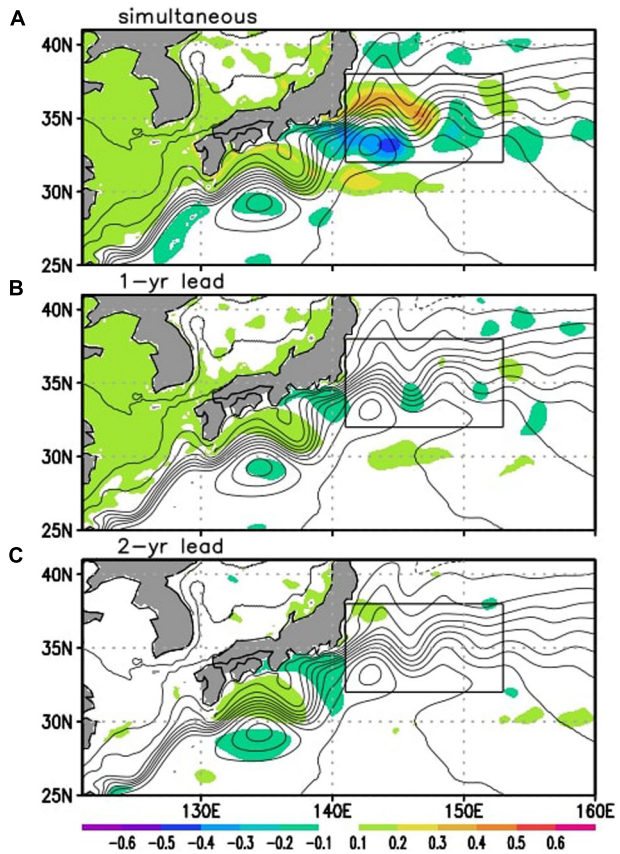

FIGURE 10 | Correlation maps of SSH difference from its ensemble mean with EKE deviations from its ensemble mean in the KE upstream region (indicated by the black rectangle) from all the ensemble members. **(A)** The simultaneous correlation. **(B,C)** The lagged correlation maps with SSH fields lead by panel **(B)** 1 year and **(C)** 2 years. Regions over a 95% confidence level (N = 380) are indicated. For the estimation of the correlations, simultaneous and lagged covariances of deviations of SSH and EKE from their ensemble mean, and their variances are calculated from the whole ensemble members.

the uncertainty of the KE's southern recirculation gyre and the EKE in the upstream KE region.

SUMMARY

To investigate the possible influence of oceanic intrinsic variability and its interannual-to-decadal modulations in the KE jet speed and associated eddy activities, we conducted a 10-member ensemble, 52-year integration of an eddy-resolving OGCM with time-varying surface forcing and slightly different initial conditions. We show that, on the decadal time scales, variability in the KE jet speed has a limited ensemble spread, suggesting that the decadal jet speed variability is mostly atmospheric–driven. In contrast, on interannual time scales, the KE jet speed has a large ensemble spread, indicating that it is strongly affected by intrinsic variability, has substantial uncertainty, and is difficult to predict. The present study confirms with a longer integration results of Nonaka et al. (2016). This time-scale dependence is similar to that found in the Atlantic Meridional Overturning Circulation (Jamet et al., 2019). While Pierini (2006) suggests the importance of intrinsic variability to decadal KE variability, the present study suggests that the intrinsic variability is more important on the interannual time scale. The pacing of intrinsic variability in the KE jet by atmospheric variability proposed by previous studies (Taguchi et al., 2007; Pierini, 2014) could not be identified in the relation between the intrinsic and atmospheric–forced variability of the upstream KE jet speed. Further exploration is necessary.

In the KE upstream region, observations show that eddy activity is high (low) when the KE jet is weak (strong) (Qiu and Chen, 2005). However, in our simulations, the eddy activity in the KE upstream region shows high uncertainty and limited atmospheric–driven variability. In contrast, the eddy activities in the KE downstream region have a small ensemble spread especially on the decadal time scale, indicating they are predominantly atmospheric–driven. Further, the eddy activity is highly correlated with the surface current speed averaged in the same region. This relationship is consistent with the enhanced baroclinic instability associated with stronger currents and meridional density gradients. Through westward propagation of surface current variability signals shown by the lagged correlation maps based on the ensemble mean field, which can represent atmospheric–driven potentially predictable component of variability, the eddy activity in the KE downstream region correlates well (r = 0.59, 90% significant) with the ensemble mean surface current speed variability in the central North Pacific 4 years earlier. Even for each ensemble member, the significant lagged correlation is also found in seven out of ten ensemble members, suggesting a possibility of prediction of the eddy activity in the region based on westward propagation of wind-driven current speed anomalies. Consistent with this, the ensemble mean of eddy activity in the KE downstream has lagged correlation with the index of NPGO, which leads the KE jet variability with several years lag. Their correlation is r = 0.41 (90% significant, N = 22) when the NPGO index leads a 39 months with applying 13-month running mean. Interestingly, the ensemble mean of eddy activity in the KE upstream correlates with PDO (r = 0.42, 99% significant, N = 48), when the PDO index leads 13 months. As we discussed above, however, the wind-driven component is limited in the KE upstream region and this correlation is not found for each ensemble member at least in our simulation due to the large uncertainty caused by intrinsic variability.

While it has been widely recognized in the atmospheric science that observations are just one realization of possible fields, the oceanography community is only beginning to explore this aspect (e.g., Penduff et al., 2018), except for the fields directly relating to eddies, and should consider oceanic fields in the similar way. There are a few emerging projects that have pointed out the importance of oceanic intrinsic variability (see Introduction). Among them, statistical properties of the atmospheric–forced and intrinsic oceanic variability have been revealed globally with a large ensemble OGCM simulations performed under the OCCIPUT project (e.g., Penduff et al., 2019; Close et al., 2020). In the present study, as we used more

computational resources for high horizontal resolutions to represent the KE jet structure and to resolve mesoscale eddies, the number of ensemble members (10) is limited compared to the OCCIPUT experiment (50). While this choice precluded us from the robust estimates of ensemble spreads and Gaussianity of distribution (Penduff et al., 2019), our higher-resolution ensemble simulations complement the OCCIPUT simulations. By better resolving the eddy activity and jet structures, we have documented the atmospheric–forced and intrinsic variability on the interannual-to-decadal time scales in the KE region. The present results confirm that, even on the interannual time-scale that is longer than a typical eddy lifetime, it is necessary to consider uncertainty in variability of the strong jets. Nevertheless, we found possibility of predictability in the eddy activity in the KE downstream region. Since intrinsic variability is likely model dependent, these results should be explored with other models or using multi-model comparisons as well as larger number of ensemble members.

DATA AVAILABILITY STATEMENT

The raw data supporting the conclusions of this article will be made available by the authors, without undue reservation.

AUTHOR CONTRIBUTIONS

MN, BT, and NS contributed to the conception and design of the study. MN and HS conducted the numerical simulations. MN performed the analysis and wrote the first draft of the manuscript. All authors contributed to the manuscript revision, read, and approved the submitted version.

FUNDING

This study was supported by the KAKENHI JP19H05701, JP18H03726, and JP17K05665, the Japan Science and Technology Agency through Belmont Forum CRA "InterDec," US National Science Foundation grant NSF1357015, and JAMSTEC-IPRC Collaborative Research (JICore).

ACKNOWLEDGMENTS

OFES2_ensemble integration was conducted on the Earth Simulator with the support of JAMSTEC.

REFERENCES

Amante, C., and Eakins, B. W. (2009). *ETOPO1 1 Arc-Minute Global Relief Model: Procedures, Data Sources and Analysis. NOAA Technical Memorandum NESDIS NGDC-24*. Silver Spring, MD: NOAA.

Close, S., Penduff, T., Speich, S., and Molines, J.-M. (2020). A means of estimating the intrinsic and atmospherically-forced contributions to sea surface height variability applied to altimetric observations. *Prog. Oceanogr.* 184:102314. doi: 10.1016/j.pocean.2020.102314

Di Lorenzo, E., Schneider, N., Cobb, K. M., Chhak, K., Franks, P. J. S., Miller, A. J., et al. (2008). North Pacific gyre oscillation links ocean climate and ecosystem change. *Geophys. Res. Lett.* 35:L08607. doi: 10.1029/2007GL032838

Dijkstra, H. A., and Ghil, M. (2005). Low-frequency variability of the large-scale ocean circulation: a dynamical systems approach. *Rev. Geophys.* 43:RG3002.

Frankignoul, C., Sennèchael, N., Kwon, Y.-O., and Alexander, M. (2011). Influence of the meridional shifts of the Kuroshio and the Oyashio extensions on the atmospheric circulation. *J. Clim.* 24, 762–777. doi: 10.1175/2010jcli3731.1

Gregorio, S., Penduff, T., Serazin, G., Molines, J.-M., and Barnier, B. (2015). Intrinsic variability of the Atlantic meridional overturning circulation at interannutl-to-multidecadal time scales. *J. Phys. Oceanogr.* 45, 1929–1946. doi: 10.1175/JPO-D-14-0163.1

Hirata, H., Kawamura, R., Kato, M., and Shinoda, T. (2018). A positive feedback process related to the rapid development of an extratropical cyclone over the Kuroshio/Kuroshio extension. *Mon. Weather Rev.* 146, 417–433. doi: 10.1175/MWR-D-17-0063.1

Itoh, S., and Yasuda, I. (2010). Characteristics of mesoscale eddies in the Kuroshio-Oyashio extension region detected from the distribution of the sea surface height anomaly. *J. Phys. Oceanogr.* 40, 1018–1034. doi: 10.1175/2009jpo4265.1

Jamet, Q., Dewar, W. K., Wienders, N., and Deremble, B. (2019). Spatiotemporal patterns of chaos in the atlantic overturning circulation. *Geophys. Res. Lett.* 46, 7509–7517. doi: 10.1029/2019GL082552

Joh, Y., and Di Lorenzo, E. (2019). Interactions between Kuroshio extension and central tropical pacific lead to preferred decadal-timescale oscillations in pacific climate. *Sci. Rep.* 9:13558. doi: 10.1038/s41598-019-49927-y

Komori, N., Takahashi, K., Komine, K., Motoi, T., Zhang, X., and Sagawa, G. (2005). Description of sea-ice component of coupled ocean-sea-ice model for the Earth Simulator (OIFES). *J. Earth Simulat.* 4, 31–45.

Kuwano-Yoshida, A., and Minobe, S. (2017). Storm-track response to SST fronts in the northwestern Pacific region in an AGCM. *J. Clim.* 30, 1081–1102. doi: 10.1175/JCLI-D-16-0331.1

Leroux, S., Penduff, T., Bessières, L., Molines, J.-M., Brankart, J.-M., Sérazin, G., et al. (2018). Intrinsic and atmospherically forced variability of the AMOC: insights from a large-ensemble ocean hindcast. *J. Clim.* 31, 1183–1203. doi: 10.1175/JCLI-D-17-0168.1

Ma, X., Chang, P., Saravanan, R., Montuoro, R., Hsieh, J.-S., Wu, D., et al. (2015). Distant influence of Kuroshio eddies on North Pacific weather patterns? *Sci. Rep.* 5:17785. doi: 10.1038/srep17785

Ma, X., Jing, Z., Chang, P., Liu, X., Montuoro, R., Small, R. J., et al. (2016). Western boundary currents regulated by interaction between ocean eddies and the atmosphere. *Nature* 535, 533–537. doi: 10.1038/nature18640

Mantua, N. J., Hare, S. R., Zhang, Y., Wallace, J. M., and Francis, R. C. (1997). A Pacific interdecadal climate oscillation with impacts on salmon production. *Bull. Amer. Meteorol. Soc.* 78, 1069–1079. doi: 10.1175/1520-0477(1997)078<1069:apicow>2.0.co;2

Masumoto, Y., Sasaki, H., Kagimoto, T., Komori, N., Ishida, A., Sasai, Y., et al. (2004). A fifty-year eddy-resolving simulation of the world ocean -Preliminary outcomes of OFES (OGCM for the Earth Simulator). *J. Earth Simulat.* 1, 35–56.

Metz, W. (1991). Optimal relationship of large-scale flow patterns and the barotropic feedback due to high-frequency eddies. *J. Atm. Sci.* 48, 1142–1159.

Minobe, S., Kuwano-Yoshida, A., Komori, N., Xie, S.-P., and Small, R. J. (2008). Influence of the Gulf Stream on the troposphere. *Nature* 452, 206–209. doi: 10.1038/nature06690

Nishikawa, H., Yasuda, I., and Itoh, S. (2011). Impact of winter-to-spring environmental variability along the Kuroshio jet on the recruitment of Japanese sardine. *Fish. Oceanogr.* 20, 570–582. doi: 10.1111/j.1365-2419.2011.00603.x

Nonaka, M., Sasai, Y., Sasaki, H., Taguchi, B., and Nakamura, H. (2016). How potentially predictable are midlatitude ocean currents? *Sci. Rep.* 6:20153. doi: 10.1038/srep20153

Oka, E., Qiu, B., Takatani, Y., Enyo, K., Sasano, D., Kosugi, N., et al. (2015). Decadal variability of subtropical mode water subduction and its impact on biogeochemistry. *J. Oceanogr.* 71, 389–400. doi: 10.1007/s10872-015-0300-x

Oka, E., Yamada, K., Sasano, D., Enyo, K., Nakano, T., and Ishii, M. (2019). Remotely forced decadal physical and biogeochemical variability of North Pacific subtropical mode water over the last 40 years. *Geophys. Res. Lett.* 46, 1555–1561. doi: 10.1029/2018GL081330

O'Reilly, C. H., and Czaja, A. (2015). The response of the Pacific storm track and atmospheric circulation to Kuroshio extension variability. *Quart. J. R. Meteor. Soc.* 141, 52–66. doi: 10.1002/qj.2334

Penduff, T., Barnier, B., Terray, L., Bessières, L., Sérazin, G., Grégorio, S., et al. (2014). "Ensembles of eddying ocean simulations for climate," in *Proceedings of the CLIVAR Exchanges, Special Issue on High Resolution Ocean Climate Modelling, 65, International CLIVAR Project Office*, Southampton.

Penduff, T., Le Sommer, J., Barnier, B., Zika, J., Dewar, W. K., Treguier, A.-M., et al. (2011). Sea level expres- sion of intrinsic and forced ocean variabilities at interannual time scales. *J. Clim.* 24, 5652–5670. doi: 10.1175/jcli-d-11-00077.1

Penduff, T., Llovel, W., Close, S., Garcir-Gomez, I., and Leroux, S. (2019). Trends of coastal sea level between 1993 and 2015: imprints of atmospheric forcing and oceanic chaos. *Surv. Geophys.* 40, 1543–1562. doi: 10.1007/s10712-019-09571-7

Penduff, T., Sérazin, G., Leroux, S., Close, S., Molines, J.-M., Barnier, B., et al. (2018). Chaotic variability of ocean heat content: climate-relevant features and observa- tional implications. *Oceanography* 31, 63–71. doi: 10.5670/oceanog.2018.210

Pierini, S. (2006). Kuroshio extension system model study: decadal chaotic self-sustained oscillations. *J. Phys. Oceanogr.* 36, 1605–1625. doi: 10.1175/JPO2931.1

Pierini, S. (2014). Kuroshio extension bimodality and the North Pacific oscillation: a case of intrinsic variability paced by external forcing. *J. Clim.* 27, 448–454. doi: 10.1175/jcli-d-13-00306.1

Qiu, B., and Chen, S. (2005). Variability of the Kuroshio extension jet, recirculation gyre and mesoscale eddies on decadal timescales. *J. Phys. Oceanogr.* 35, 2090–2103. doi: 10.1175/jpo2807.1

Qiu, B., and Chen, S. (2006). Decadal variability in the formation of the North Pacific subtropical mode water: oceanic versus atmospheric control. *J. Phys. Oceanogr.* 36, 1365–1380. doi: 10.1175/JPO2918.1

Qiu, B., Chen, S., Schneider, N., and Taguchi, B. (2014). A coupled decadal prediction of the dynamic state of the Kuroshio extension system. *J. Clim.* 27, 1751–1764. doi: 10.1175/jcli-d-13-00318.1

Qiu, B., and Miao, W. (2000). Kuroshio path variations south of Japan: bimodality as a self-sustained internal oscillation. *J. Phys. Oceanogr.* 30, 2124–2137. doi: 10.1175/1520-0485(2000)030<2124:kpvsoj>2.0.co;2

Renault, L., Marchesiello, P., Masson, S., and McWilliams, J. C. (2019). Remarkable control of western boundary currents by eddy killing, a mechanical air-sea coupling process. *Geophys. Res. Lett.* 46, 2743–2751. doi: 10.1029/2018GL081211

Renault, L., Masson, S., Arsouze, T., Madec, G., and McWilliams, J. C. (2020). Recipes for how to force oceanic model dynamics. *J. Adv. Model. Earth Syst.* 12:e2019MS001715. doi: 10.1029/2019MS001715

Rowell, D. P., Folland, C., Maskell, K., and Ward, M. N. (1995). Variability of summer rainfall over tropical north Africa (1906-92): observations and modelling. *Q. J. R. Meteor. Soc.* 121, 669–704. doi: 10.1256/smsqj.52310

Sasai, Y., Honda, M. C., Siswanto, E., Kato, S., Uehara, K., Sasaki, H., et al. (2019). "Impact of Ocean physics on marine ecosystems in the Kuroshio and Kuroshio extension regions," in *Kuroshio Current: Physical, Biogeochemical, and Ecosystem Dynamics, Geophysical Monograph 243*, eds T. Nagai, H. Saito, K. Suzuki, and M. Takahashi (Hoboken, NJ: John Wiley & Sons Inc.), doi: 10.1002/9781119428428.ch11

Sasaki, H., Kida, S., Furue, R., Aiki, H., Komori, N., Masumoto, Y., et al. (2020). A global eddying hindcast ocean simulation with OFES2. *Geosci. Model Dev. Discuss.* 13, 3319–3336. doi: 10.5194/gmd-13-3319-2020

Sasaki, H., Kida, S., Furue, R., Nonaka, M., and Masumoto, Y. (2018). An increase of the Indonesian Throughflow by internal tidal mixing in a high-resolution quasi-global ocean simulation. *Geophys. Res. Lett.* 45, 8416–8424. doi: 10.1029/2018gl078040

Sasaki, H., Nonaka, M., Masumoto, Y., Sasai, Y., Uehara, H., Sakuma, H., et al. (2008). "An eddy-resolving hindcast simulation of the quasi-global ocean from 1950 to 2003 on the Earth Simulator," in *High Resolution Numerical Modelling of the Atmosphere and Ocean*, eds K. Hamilton, and W. Ohfuchi (New York, NY: Springer), 157–185. doi: 10.1007/978-0-387-49791-4_10

Sasaki, Y. N., and Minobe, S. (2015). Climatological mean features and interannual to decadal variability of ring formations in the Kuroshio Extension region. *J. Oceanogr.* 71, 499–509. doi: 10.1007/s10872-014-0270-4

Sérazin, G., Meyssignac, B., Penduff, T., Terray, L., Barnier, B., and Molines, J.-M. (2016). Quantifying uncertainties on regional sea level change induced by multidecadal intrinsic oceanic variability. *Geophys. Res. Lett.* 43, 8151–8159. doi: 10.1002/2016GL069273

Sérazin, G., Penduff, T., Grégorio, S., Barnier, B., Molines, J.-M., and Terray, L. (2015). Intrinsic variability of sea- level from global 1/12 ocean simulations: spatio-temporal scales. *J. Clim.* 28, 4279–4292. doi: 10.1175/JCLI-D-14-00554

Sugi, M., Kawamura, R., and Sato, N. (1997). A studyof SST-forced variability and potential predictability of seasonal mean fields using the JMA global model. *J. Meteor. Soc. Jpn.* 75, 717–736. doi: 10.2151/jmsj1965.75.3_717

Sugimoto, S., and Hanawa, K. (2011). Roles of SST anomalies on the wintertime turbulent heat fluxes in the Kuroshio-Oyashio confluence region: influences of warm eddies detached from the Kuroshio extension. *J. Clim.* 24, 6551–6561. doi: 10.1175/2011jcli4023.1

Sugimoto, S., and Hanawa, K. (2012). Relationship between the path of the Kuroshio in the south of Japan and the path of the Kuroshio extension in the east. *J. Oceanogr.* 68, 219–225. doi: 10.1007/s10872-011-0089-1

Taguchi, B., Qiu, B., Nonaka, M., Sasaki, H., Xie, S.-P., and Schneider, N. (2010). Decadal variability of the Kuroshio extension: mesoscale eddies and recirculations. *Ocean Dyn.* 60, 673–691. doi: 10.1007/s10236-010-0295-1

Taguchi, B., Xie, S.-P., Schneider, N., Nonaka, M., Sasaki, H., and Sasai, Y. (2007). Decadal variability of the Kuroshio extension: observations and an eddy-resolving model hindcast. *J. Clim.* 20, 2357–2377. doi: 10.1175/jcli4142.1

Tomita, H., Hihara, T., Kako, S., Kubota, M., and Kutsuwada, K. (2018). An introduction to J-OFURO3, a third-generation Japanese ocean flux data set using remote-sensing observations. *J. Oceanogr.* 75, 171–194. doi: 10.1007/s10872-018-0493-x

Tsujino, H., Urakawa, S., Nakano, H., Small, R. J., Kim, W. M., Yeager, S. G., et al. (2018). JRA-55 based surface dataset for driving ocean-sea-ice models (JRA55-do). *Ocean Model.* 130, 79–139. doi: 10.1016/j.ocemod.2018.07.002

Zhai, X., and Greatbatch, R. J. (2007). Wind work in a model of the northwest Atlantic Ocean. *Geophys. Res. Lett.* 34:L04606. doi: 10.1029/2006GL028907

Conflict of Interest: The authors declare that the research was conducted in the absence of any commercial or financial relationships that could be construed as a potential conflict of interest.

frontiers in Marine Science

CORRECTION
published: 06 November 2020
doi: 10.3389/fmars.2020.615078

Corrigendum: Atmospheric-Driven and Intrinsic Interannual-to-Decadal Variability in the Kuroshio Extension Jet and Eddy Activities

Masami Nonaka[1]*, *Hideharu Sasaki*[1], *Bunmei Taguchi*[2] and *Niklas Schneider*[3]

[1] Japan Agency for Marine-Earth Science and Technology, Yokohama, Japan, [2] Faculty of Sustainable Design, University of Toyama, Toyama, Japan, [3] International Pacific Research Center, University of Hawai'i at Mānoa, Honolulu, HI, United States

Keywords: kuroshio extension, eddy activity, interannual-to-decadal variability, predictability, ensemble simulation

OPEN ACCESS

Approved by:
Frontiers Editorial Office, Frontiers Media SA, Switzerland

***Correspondence:**
Masami Nonaka
nona@jamstec.go.jp

Specialty section:
This article was submitted to Physical Oceanography, a section of the journal Frontiers in Marine Science

Received: *08 October 2020*
Accepted: *08 October 2020*
Published: *06 November 2020*

Citation:
Nonaka M, Sasaki H, Taguchi B and Schneider N (2020) Corrigendum: Atmospheric-Driven and Intrinsic Interannual-to-Decadal Variability in the Kuroshio Extension Jet and Eddy Activities. Front. Mar. Sci. 7:615078. doi: 10.3389/fmars.2020.615078

A Corrigendum on

Atmospheric-Driven and Intrinsic Interannual-to-Decadal Variability in the Kuroshio Extension Jet and Eddy Activities

by Nonaka, M., Sasaki, H., Taguchi, B., and Schneider, N. (2020). Front. Mar. Sci. 7:547442. doi: 10.3389/fmars.2020.547442

In the original article, there was a mistake in **Figure 9** as published. The panel was incorrectly included twice. The corrected **Figure 9** appears below.

The authors apologize for this error and state that this does not change the scientific conclusions of the article in any way. The original article has been updated.

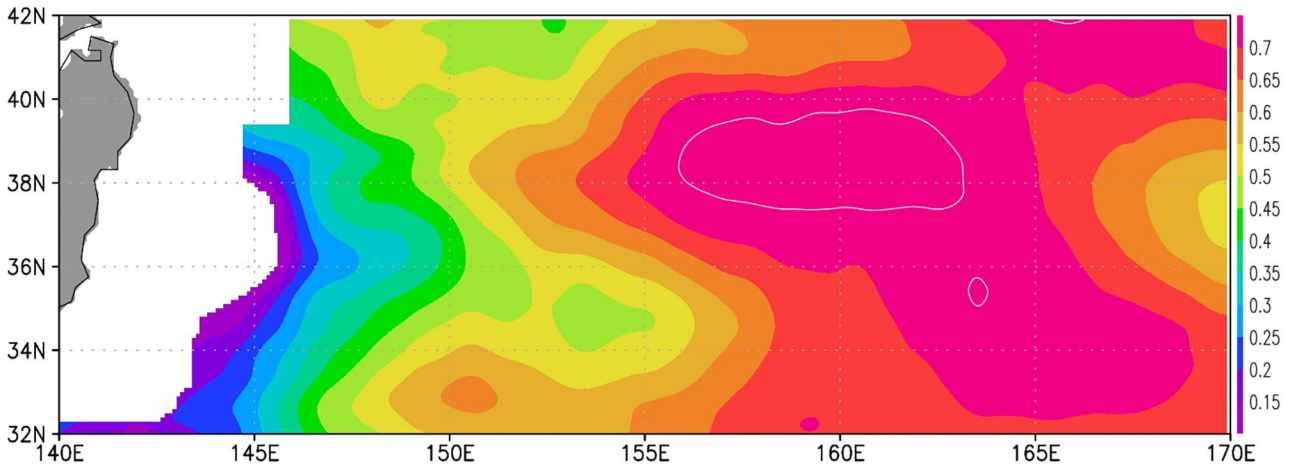

FIGURE 9 | Horizontal map of the square root of the potential predictability (PP) of the simulated 5°–longitude and 5°–latitude averaged EKE. The value is plotted at the grid point of the center of the 5°–longitude and 5°–latitude area. White contours indicate 0.75. A 13-month running-mean is applied to and the linear trend is removed from EKE before estimating PP.

frontiers in Marine Science

ORIGINAL RESEARCH
published: 06 October 2020
doi: 10.3389/fmars.2020.578490

Environmentally Driven Seasonal Forecasts of Pacific Hake Distribution

Michael J. Malick[1], Samantha A. Siedlecki[2], Emily L. Norton[3], Isaac C. Kaplan[4], Melissa A. Haltuch[5], Mary E. Hunsicker[6], Sandra L. Parker-Stetter[5†], Kristin N. Marshall[5], Aaron M. Berger[7], Albert J. Hermann[3], Nicholas A. Bond[3] and Stéphane Gauthier[8]*

[1] NRC Research Associateship Program, Northwest Fisheries Science Center, National Marine Fisheries Service, National Oceanic and Atmospheric Administration, Seattle, WA, United States, [2] Department of Marine Sciences, University of Connecticut, Groton, CT, United States, [3] Joint Institute for the Study of the Atmosphere and Ocean, University of Washington, Seattle, WA, United States, [4] Conservation Biology Division, Northwest Fisheries Science Center, National Oceanic and Atmospheric Administration, Seattle, WA, United States, [5] Fishery Resource Analysis and Monitoring Division, Northwest Fisheries Science Center, National Marine Fisheries Service, National Oceanic and Atmospheric Administration, Seattle, WA, United States, [6] Fish Ecology Division, Northwest Fisheries Science Center, National Marine Fisheries Service, National Oceanic and Atmospheric Administration, Newport, OR, United States, [7] Fishery Resource Analysis and Monitoring Division, Northwest Fisheries Science Center, National Marine Fisheries Service, National Oceanic and Atmospheric Administration, Newport, OR, United States, [8] Institute of Ocean Sciences, Fisheries and Oceans Canada, Sidney, BC, Canada

Changing ecosystem conditions present a challenge for the monitoring and management of living marine resources, where decisions often require lead-times of weeks to months. Consistent improvement in the skill of regional ocean models to predict physical ocean states at seasonal time scales provides opportunities to forecast biological responses to changing ecosystem conditions that impact fishery management practices. In this study, we used 8-month lead-time predictions of temperature at 250 m depth from the J-SCOPE regional ocean model, along with stationary habitat conditions (e.g., distance to shelf break), to forecast Pacific hake (*Merluccius productus*) distribution in the northern California Current Ecosystem (CCE). Using retrospective skill assessments, we found strong agreement between hake distribution forecasts and historical observations. The top performing models [based on out-of-sample skill assessments using the area-under-the-curve (AUC) skill metric] were a generalized additive model (GAM) that included shelf-break distance (i.e., distance to the 200 m isobath) (AUC = 0.813) and a boosted regression tree (BRT) that included temperature at 250 m depth and shelf-break distance (AUC = 0.830). An ensemble forecast of the top performing GAM and BRT models only improved out-of-sample forecast skill slightly (AUC = 0.838) due to strongly correlated forecast errors between models (r = 0.88). Collectively, our results demonstrate that seasonal lead-time ocean predictions have predictive skill for important ecological processes in the northern CCE and can be used to provide early detection of impending distribution shifts of ecologically and economically important marine species.

Keywords: California Current, non-stationary, Pacific hake, climate, temperature, forecast

OPEN ACCESS

Edited by:
Fei Chai,
Ministry of Natural Resources, China

Reviewed by:
Alistair James Hobday,
Commonwealth Scientific and Industrial Research Organization (CSIRO), Australia
Hui Zhang,
Institute of Oceanology (CAS), China

****Correspondence:***
Michael J. Malick
michael.malick@noaa.gov

†Present address:
Sandra L. Parker-Stetter,
Resource Assessment and Conservation Engineering Division,
Alaska Fisheries Science Center, National Marine Fisheries Service, National Oceanic and Atmospheric Administration, Seattle, WA, United States

Specialty section:
This article was submitted to Marine Fisheries, Aquaculture and Living Resources, a section of the journal Frontiers in Marine Science

Received: *30 June 2020*
Accepted: *16 September 2020*
Published: *06 October 2020*

Citation:
Malick MJ, Siedlecki SA, Norton EL, Kaplan IC, Haltuch MA, Hunsicker ME, Parker-Stetter SL, Marshall KN, Berger AM, Hermann AJ, Bond NA and Gauthier S (2020) Environmentally Driven Seasonal Forecasts of Pacific Hake Distribution. Front. Mar. Sci. 7:578490. doi: 10.3389/fmars.2020.578490

INTRODUCTION

Anticipating ecological change is an important component of living marine resource management where decisions often require lead-times of weeks to months. Yet, the lack of advanced warnings about the response of marine taxa to ecosystem shifts limits the ability of management systems to respond to rapidly changing ecosystem conditions (Clark et al., 2001; Dietze et al., 2018). Increasingly, seasonal ecological forecasts provide a means to reduce related uncertainties and play a key role in supporting management of living marine resources into the future (Hobday et al., 2016; Payne et al., 2017; Tommasi et al., 2017). Indeed, over the past decade seasonal ecological forecasts have been developed for a wide range of marine taxa including American lobster in the Gulf of Maine (Mills et al., 2017), sardines in the California Current (Zwolinski et al., 2011; Kaplan et al., 2016), and southern bluefin tuna in eastern Australia (Hobday et al., 2011a, 2016).

Increases in the predictive skill of physical ocean states has partially driven the increased availability of seasonal ecological forecasts and has resulted in the availability of skillful ocean forecasts with seasonal lead-times for many of the world's large marine ecosystems (Stock et al., 2015; Tommasi et al., 2017; Jacox et al., 2020). In the northern California Current Ecosystem (CCE), the J-SCOPE (JISAO's Seasonal Coastal Ocean Prediction of the Ecosystem) model provides forecasts of physical, chemical, and biological ocean states with seasonal lead times (e.g., 6–9 months) (Siedlecki et al., 2016). Skill assessments have shown the J-SCOPE model has considerable predictive skill at seasonal lead times for several ecologically relevant variables including subsurface temperature (Siedlecki et al., 2016). In turn, J-SCOPE seasonal forecasts of ocean conditions can then be used to drive ecological forecasts, such as sardine distribution in the CCE (Kaplan et al., 2016).

Pacific hake (*Merluccius productus*, hereafter just hake) is an important mid-trophic-level species in the CCE that supports one of the largest United States groundfish fisheries outside of Alaska (Ressler et al., 2007; Berger et al., 2019). Hake are distributed from about 25° to 55°N and at depths typically between 100 and 1000 m. The dynamics of the hake stock are characterized by episodic recruitment events with a few large age-classes dominating the stock (Hamel et al., 2015; Berger et al., 2019). Age-structure of the stock, in turn, influences distribution since older and larger hake tend to be distributed further north than smaller and younger conspecifics (Berger et al., 2019). Hake growth is variable across years and is at least partly influenced by ocean conditions (e.g., El Niño events) and availability of prey resources (Ressler et al., 2007; Hamel et al., 2015).

Pacific hake are seasonally migratory, with a northward spring migration from southern spawning grounds off the United States west coast, terminating as far north as southeast Alaska. This migration pattern results in hake being a *trans*-boundary resource fished commercially in the United States and Canada (Bailey et al., 1982). The fraction of the population that migrates into Canadian waters, however, can vary greatly across years, creating challenges for monitoring and management planning (Dorn, 1995). For instance, monitoring of the hake stock is conducted jointly by a United States/Canada summer acoustic-trawl survey that provides an index of hake biomass that is used for stock assessment and management planning (Berger et al., 2019). The ability of the monitoring survey to sample the full spatial extent of the stock partially determines the magnitude of uncertainty associated with the biomass index.

Environmental conditions influence the summer distribution of hake along the west coast of North America (Benson et al., 2002; Ressler et al., 2007; Agostini et al., 2008). Thermal conditions, in particular, have been positively associated with the fraction of the hake stock in Canadian waters, suggesting warmer ocean conditions drive a more northern distribution of hake (Dorn, 1995; Ware and McFarlane, 1995). More recently, evidence has suggested that thermal conditions have a spatially variable effect on hake distribution with strong positive associations with hake biomass north of Vancouver Island, British Columbia (BC) and strong negative associations offshore of Vancouver Island, BC and Washington, United States (Malick et al., 2020). This suggests that ocean temperatures could be a useful predictor of hake distribution in the northern CCE.

Skillful forecasts of hake distribution could help inform management and survey planning decisions in three important aspects. First, early warnings of changes in hake distribution can inform planning of fisheries independent surveys used to monitor the hake stock (Payne et al., 2017). For example, survey planning decisions, such as allocating survey effort between northern and southern areas, are made several months prior to the start of the survey. Thus, forecasts could inform decisions about allocating limited survey effort by predicting areas where hake are unlikely to be present in a given year. If vessel breakdowns or weather forced a reduction in survey effort, transect density could be reduced in regions predicted to have low probability of hake occurrence. Second, skillful forecasts provide information on the projected *trans*-boundary distribution of hake, and thus could help reduce uncertainties in the availability of the hake stock to fishers in Canada and the United States (Hobday et al., 2011b; Mills et al., 2017). Third, skillful forecasts provide early warnings of potential ecosystem shifts that can inform ecosystem-based management (Levin et al., 2009; Malick et al., 2017). For instance, Pacific hake are an important predator of fish and shellfish populations and are prey for larger fish and marine mammals in the CCE, thus advanced warnings of shifts in hake distribution could aid detection of consequential ecological shifts in the CCE (Bailey et al., 1982; Francis, 1983).

In this study, we examined whether seasonal forecasts of physical oceanographic conditions can be used to accurately predict hake distribution in the northern CCE. In particular, we developed and tested 8-month lead-time forecasts of summer hake distribution with the goal of providing forecasts to support management and survey planning decisions. We used 7 years of acoustic-trawl survey data to characterize hake distribution. We then used the J-SCOPE regional ocean model to develop 8-month lead-time forecasts of subsurface temperatures that were used to force environmentally driven species distribution models for hake. We further evaluated whether multi-model ensembles improved forecast skill of hake distribution by comparing ensemble forecasts to single-model forecasts. This process of using oceanographic forecasts to predict hake distributional

shifts in the CCE explicitly addresses fisheries management ecosystem-linkage goals and provides necessary context for short-term oceanographic variability within the scope of longer-term perturbations (e.g., climate change).

MATERIALS AND METHODS

The primary motivation for developing seasonal forecasts of hake distribution was to provide an early warning of changes in hake distribution to support management decisions and Pacific hake acoustic-trawl survey planning. As a result, forecasts were co-developed with survey planners, while stakeholder involvement occurred via meetings associated with the Pacific hake treaty process.

Pacific Hake Data

The hake survey aims to sample the full range of the hake distribution in summer, and survey extent and the number of transects are often adjusted in response to the presence or absence of hake following survey design guidelines. Therefore, we focus on forecasting the probability of hake occurrence, rather than density, because the acoustic-trawl survey is better informed by early warnings in the expansion or contraction of hake distribution than forecasts of hake density in a given location.

We used 7 years of spatially explicit biennial hake occurrence data collected via joint United States/Canada acoustic-trawl surveys from 2009 to 2019, with an additional 2012 survey (**Table 1**). Surveys started in southern California and moved northward along the United States and Canada west coasts until hake were no longer observed (typically around 54.5°N). The spatial extent of data analyzed here, however, was limited to the region 43–50°N – the latitudinal domain of the J-SCOPE model used to generate forecasts of ocean conditions (see below). The number of annual survey transects within the study domain ranged from 34 in 2015 to 49 in 2011 (**Table 1**). Survey timing was fairly consistent across years, with the southern third of the study domain typically sampled during the second half of July and the northern two-thirds typically sampled during August.

Acoustic backscatter measurements attributable to hake were converted to hake biomass using the procedures outlined in Fleischer et al. (2008) and Malick et al. (2020). We aggregated the hake data into 10 km bins to reduce spatial autocorrelation in the data and coded bins with non-zero biomass as hake occurrences. We also tested smaller (e.g., 5 km) and larger (e.g., 20 km) bin sizes and found results were robust across different sized bins.

TABLE 1 | Summary of acoustic-trawl survey data available for analysis.

Year	N transects	N bins	% absent
2009	38	367	73.6
2011	49	427	73.3
2012	38	380	73.7
2013	42	417	76.5
2015	34	340	75.3
2017	39	367	68.7
2019	38	369	63.7

N transects gives the annual number of survey transects. N bins gives the annual number of 10 km bins across the study region. % absent gives the annual percentage of 10 km bins with no Pacific hake.

Ocean Forecasts

We used 8-month lead-time forecasts of temperature at 250 m depth from J-SCOPE to forecast hake distribution (**Supplementary Figure S1**). J-SCOPE is a Regional Ocean Modeling System (ROMS) (Haidvogel et al., 2008) simulation of seasonal ocean conditions spanning 43–50°N on the outer coast of Washington, Oregon, and southern BC (Siedlecki et al., 2016). The J-SCOPE model has a 1.5 km horizontal resolution with 40 vertical levels and includes both rivers and tides. The large scale oceanic and atmospheric forcing comes from NOAA's global Climate Forecast System (CFS). In this study, we focus on retrospective ocean forecasts, i.e., reforecasts, which are true forecasts for a historical period using a free-running model unconstrained by observations after initialization. The aim in using these reforecasts was to test the models skill for jointly predicting future ocean conditions and hake distribution 8-months ahead.

We chose temperature at 250 m depth as our primary ocean variable because (1) previous research has shown strong correlations between temperature at depth and hake distribution (Malick et al., 2020), and (2) 250 m represents depths commonly occupied by hake (Ressler et al., 2007). In areas where bottom depth was less than 250 m, we used bottom temperature instead. July and August temperature forecasts were generated for each survey year using a January initialization period. For 2019, three model runs from CFS were used to quantify the uncertainty related to those forcing variables. The model runs were chosen from the beginning (January 5), middle (January 15), and end (January 25) of the forecast initialization month. The initial conditions for J-SCOPE ROMS consist of the average conditions from CFS-reanalysis for the initialization month of the forecast. As is typical in the oceanographic literature, we focus on anomalies – i.e., differences from the climatology or time-averaged field detailing the seasonal cycle. In this case, the J-SCOPE reforecast climatology was based on 2009–2017, building on Siedlecki et al. (2016).

In addition to the dynamic temperature variable, we also explored a static index of cross-shelf location as a predictor of hake distribution. In particular, we used the distance to the 200 m shelf break, where the distance was defined as the minimum euclidean distance between a hake observation and the 200 m isobath. Positive values of the shelf distance variable indicated the hake observation was offshore of the 200 m isobath and negative values indicated the observation was inshore.

Statistical Forecasting Models

We used both generalized additive models (GAM) and boosted regression trees (BRT) to model species distribution, because previous studies have shown the potential for differences in explanatory power and predictive skill across model types (Abrahms et al., 2019; Brodie et al., 2019).

We used binomial GAMs with a logit link to predict the probability of hake occurrence,

$$y_{t,i} = \alpha + s\left(S_{t,i}\right) + f\left(T_{t,i}\right) + \epsilon_{t,i}$$

where y is the logit transformed probability of occurrence for year t at location i, α is the intercept, s is a univariate smooth function of shelf break distance (S), f is a smooth function that describes the effect of temperature anomaly at 250 m depth (T; i.e., deviations from the long-term mean), and $\epsilon_{t,i}$ are model residuals.

We considered two alternative formulations for the f temperature term (**Table 2**). The first formulation assumed a spatially stationary temperature effect modeled as a univariate smooth function of temperature, $s\left(T_{t,i}\right)$. The second formulation allowed for a spatially variable temperature effect by modeling the temperature effect as the product of $T_{t,i}$ and a bivariate smooth function of longitude (lon) and latitude (lat), i.e., $g\left(lon, lat\right) \cdot T_{t,i}$. Non-parametric thin plate regression splines were used for the univariate (s) and bivariate (g) smooth functions in the GAMs (Wood, 2003).

Two simpler GAMs that included static covariates were considered as alternative null forecast models (**Table 2**). The first simpler model included a univariate smooth of shelf break distance. The second simpler model included a bivariate smooth of longitude and latitude. In total, we evaluated four alternative GAM forecast models (**Table 2**).

The BRT used a Bernoulli distribution. Since BRT models can handle colinearity among predictors, we included four covariates: temperature anomaly at 250 m depth, distance to the shelf break, longitude, and latitude (Elith et al., 2008). BRT models are composed of a large number of decision trees constructed via recursive binary splits of the data with non-linear responses produced by evaluating these splits across many trees (Elith et al., 2008). The BRT was estimated using a maximum of three interactions among covariates, a learning rate of 0.02, and bag fraction of 0.6, which resulted in models with at least 1000 trees (Elith et al., 2008). Standard errors of predicted species distribution were calculated across 100 BRT fits to provide model error estimates (Hazen et al., 2018; Brodie et al., 2019).

Four ensemble model forecasts were generated by averaging each of the GAMs and the BRT, where each model in the ensemble was given equal weight (Clemen, 1989; Araujo and New, 2007). We also tested the sensitivity of our results to the inclusion of temperature in the BRT by re-running the analysis with temperature anomaly at 250 m excluded from the BRT model. All analyses were conducted using R v3.6.0 and the mgcv and dismo packages (Elith et al., 2008; Wood, 2017; R Core Team, 2019).

Forecast Evaluation

Previous work has shown considerable skill for the J-SCOPE temperature forecast model. Siedlecki et al. (2016) evaluated J-SCOPE's predictability for temperature, and found that predictive skill increased with depth. In addition, annual evaluation of J-SCOPE forecasts against observations are available on the NANOOS IOOS portal[1]. Supplementing earlier evaluations of J-SCOPE performance and skill, we further quantified performance of J-SCOPE predictions of bottom temperature by comparing against temperature data from the Northwest Fisheries Science Center's West Coast Groundfish Bottom Trawl Survey (Keller et al., 2017). That survey samples the United States West Coast slope and shelf (55–1280 m) annually from May-October, targeting bottom-dwelling species of commercial importance.

We evaluated the GAM and BRT model performance using a combination of in-sample and out-of-sample metrics including the area-under-the-curve (AUC) and mean squared error (MSE) (Fielding and Bell, 1997). The AUC measures how well a model can discriminate a presence from an absence. The AUC ranges between 0 and 1 where a value of 0.5 indicates a random classifier and values closer to 1 indicate higher forecast skill. The MSE measures the accuracy of the forecast model where lower values indicate a more accurate forecast.

We used leave-one-year-out cross validation to evaluate how the models performed at forecasting hake distribution for unobserved years (Fielding and Bell, 1997). In this procedure, a single year was left-out of the data, each model was re-fit using the remaining years of data, and forecasts were produced for the

[1]http://www.nanoos.org/products/j-scope/home.php

TABLE 2 | Summary of forecast model performance.

Model	Description	MSE_I	AUC_I	MSE_O	AUC_O	MSE_{2019}	AUC_{2019}
GAM1	$y = \alpha + g_1\,(Lon, Lat)$	0.142	0.841	0.156	0.800	0.170	0.834
GAM2	$y = \alpha + s_1\,(Shelf)$	0.147	0.824	0.150	0.813	0.178	0.809
GAM3	$y = \alpha + s_1\,(Shelf) + s_2\,(Temp)$	0.145	0.830	0.164	0.792	0.281	0.712
GAM4	$y = \alpha + s_1\,(Shelf) + g_1\,(Lon, Lat) \cdot Temp$	0.144	0.833	0.154	0.805	0.210	0.725
BRT	$y = Lon + Lat + Shelf + Temp$	**0.091**	**0.938**	0.148	0.828	0.200	0.836
ENS1	Ensemble 1: GAM1 + BRT	0.109	0.914	0.142	0.833	**0.157**	**0.847**
ENS2	Ensemble 2: GAM2 + BRT	0.111	0.909	**0.140**	**0.838**	0.163	0.834
ENS3	Ensemble 3: GAM3 + BRT	0.111	0.909	0.148	0.825	0.221	0.812
ENS4	Ensemble 4: GAM4 + BRT	0.110	0.910	0.142	0.834	0.182	0.800

MSE_I, MSE_O, and MSE_{2019} give the mean squared errors for the in-sample, out-of-sample, and 2019 forecast, respectively. AUC_I, AUC_O, and AUC_{2019} give the area-under-the-curve estimates for the in-sample, out-of-sample, and 2019 forecast, respectively. Bold values indicate the lowest MSE and highest AUC values for a column.

left-out year. This cross-validation was repeated for each year, providing 7 years of out-of-sample forecasts. We then compared the forecasted values for the left-out years to the observed values using the MSE and AUC metrics.

To further test the performance of the forecast models, we generated "true" out-of-sample forecasts for 2019 prior to the hake acoustic-trawl survey. We fit the hake forecast models using data through 2017 and then tested those models using true forecasts of the physical environment from the J-SCOPE January initialized temperature forecasts. True forecasts are produced every January and released on the web in February prior to the conditions being observed, thus referred to as a "true" forecast. In this case, J-SCOPE ocean forecasts were used to generate forecasts of hake distribution for August 2019. To better characterize uncertainty in the ocean forecasts, we generated three forecasts from the J-SCOPE model for 2019 using different initialization dates in January (January 5, January 15, January 25). The spread across the three forecasts was used as a measure of uncertainty in the J-SCOPE temperature forecasts. For each hake forecasting model, we generated separate forecasts for each of the three temperature forecasts and used an average across the three forecasts as our ensemble mean 2019 hake forecast for each model. Performance of the 2019 hake forecasts was evaluated using the AUC and MSE metrics.

RESULTS

J-SCOPE performed well when bottom temperatures observed *in situ* were compared with the simulated bottom temperatures from the same locations (R^2 = 0.88; **Supplementary Figure S2**). The predicted bottom temperatures were biased warm (RMSE = 0.48), which is not uncommon in ROMS applications and is addressed here by focusing on anomalies rather than raw temperature values (Giddings et al., 2014). This strong agreement between observed and predicted temperatures supports the use of numerical ocean model forecasts of sub-surface temperatures to predict suitable hake habitat.

Hake occurred across the latitudinal extent of the study region with the exception of 2011, when no fish were observed off

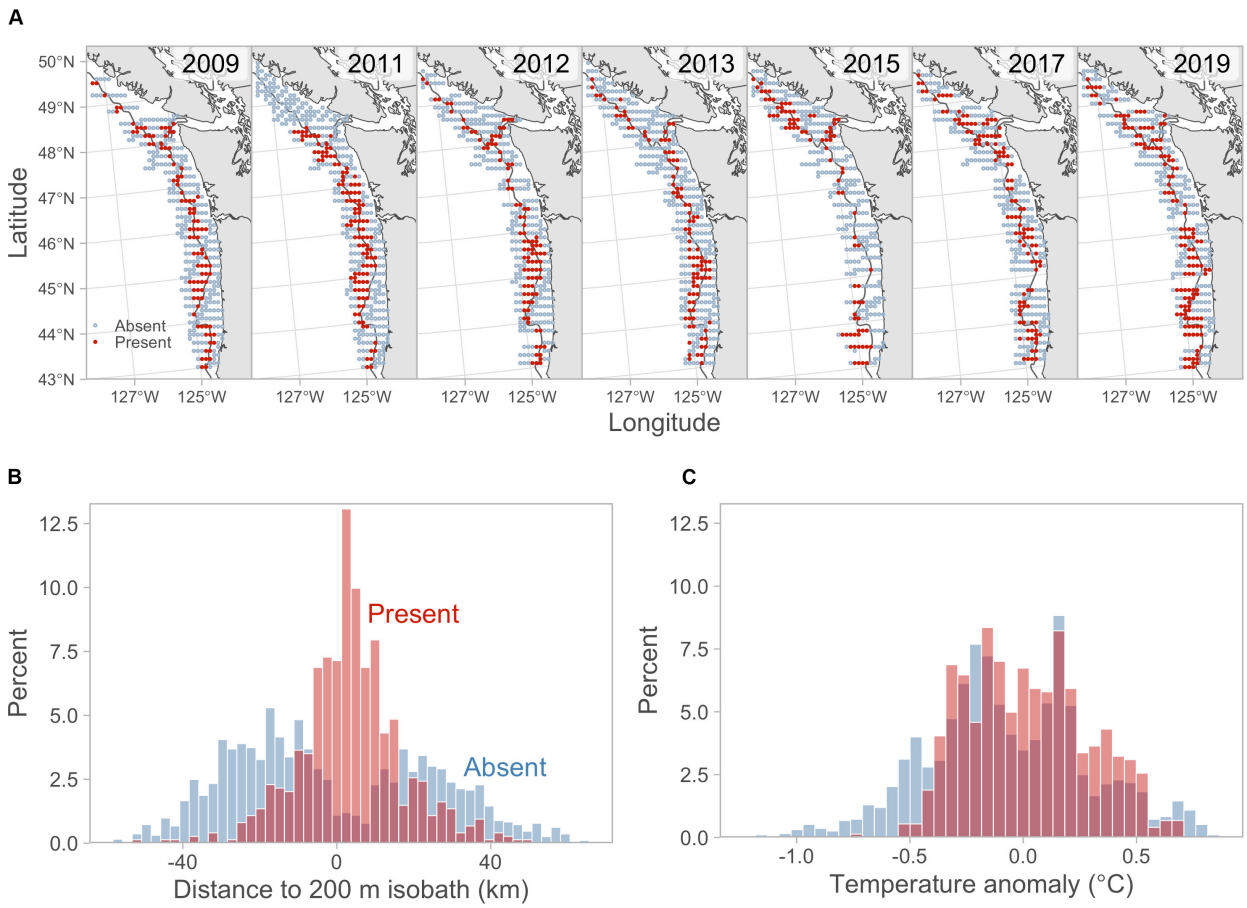

FIGURE 1 | Pacific hake summer distribution as determined by acoustic-trawl surveys. **(A)** Annual occurrences and absences of Pacific hake across the study region. Solid red circles indicate hake occurrences and open blue circles indicate hake absences. Solid gray lines show the 200 m isobath. **(B)** Histograms of distance to the 200 m isobath for Pacific hake occurrences (red) and absences (blue). Darker red bars indicate overlap between the occurrences and absences. **(C)** Histograms of temperature anomaly at 250 m depth for Pacific hake occurrences (red) and absences (blue). Temperature anomalies are reforecasts from the J-SCOPE model.

the west coast of Vancouver Island (**Figure 1**). Across all years, the cross-shelf distribution of hake was concentrated around the 200 m isobath with the majority of hake occurrences (62%) occurring within 10 km of the shelf break (**Figure 1**). The percentage of hake absences across years was consistent ranging from 64% in 2019 to 77% in 2013, although the latitudinal distribution of absences varied across years (**Table 1**). For example, in 2015 hake were absent from most locations off-shore of Washington and Oregon, whereas in 2011 hake occurrences tended to be concentrated in this region (**Figure 1**).

The shelf-break term in the GAM and BRT models confirmed the strong preference of hake to be present slightly offshore of the 200 m shelf-break (**Figures 2A**, **3A–C**). The shelf-break preference was also the dominant pattern in the bivariate smooth of longitude and latitude in model GAM1 (**Figure 2B**). The stationary temperature terms in the GAM3 and BRT models indicated that hake occurrence tended to have a positive association with temperature anomaly (**Figures 2C**, **3D**). In contrast, the non-stationary temperature term in model GAM4 showed negative associations between temperature and hake occurrence off the Washington and Oregon coasts, but positive associations in more northern and southern areas (**Figure 2D**).

All forecasting models had considerable forecast skill (both in-sample and out-of-sample) with AUC values greater than 0.79 and MSE values lower than 0.17 (**Table 2**). The BRT tended to fit the data the best with the highest in-sample AUC (0.93) and lowest in-sample MSE (0.09). For out-of-sample, however, an ensemble model (ENS2) performed best with an overall AUC of 0.84 and MSE of 0.14 (**Table 2**). Among the four GAMs, the longitude-latitude model (GAM1) tended to fit the data the best

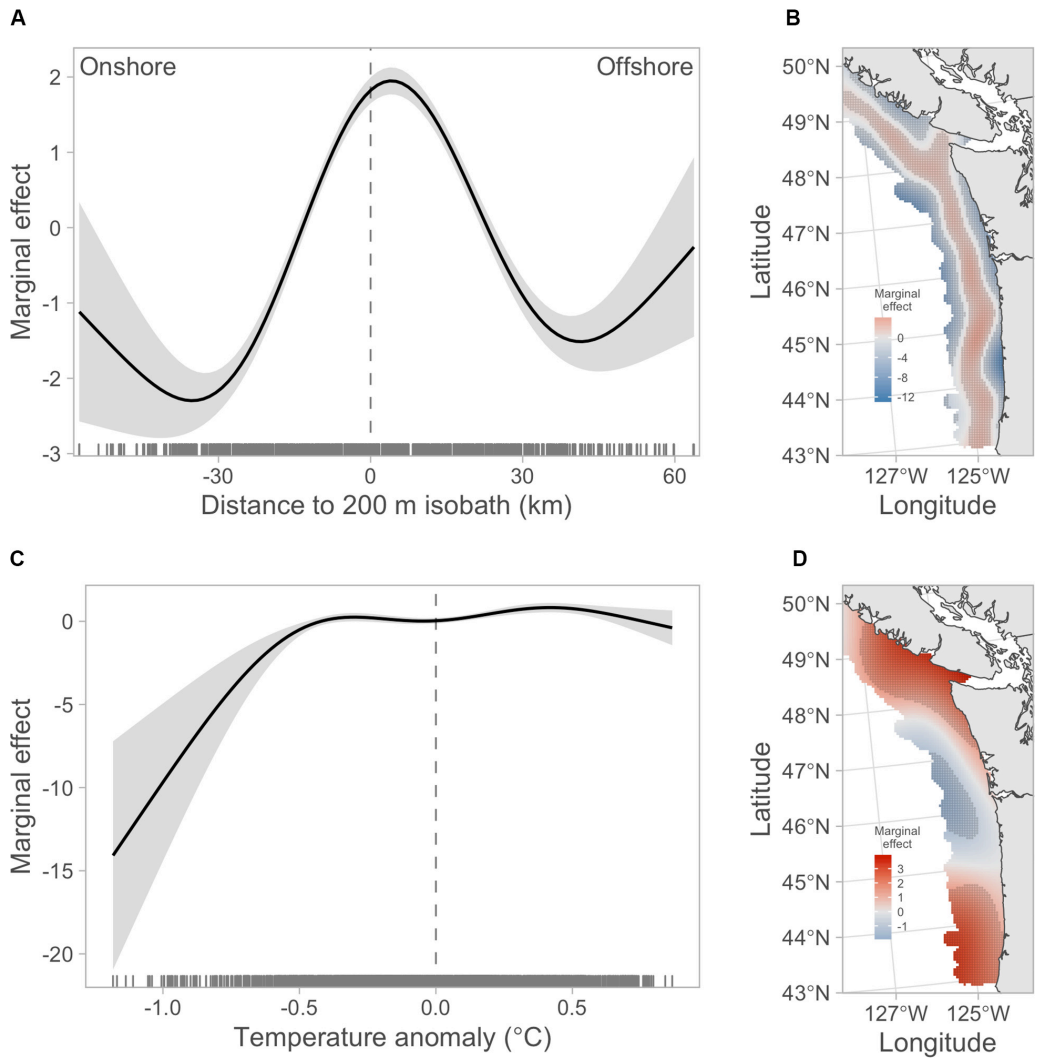

FIGURE 2 | Marginal effects of covariate smooths from the GAMs. **(A)** Marginal effect of shelf break term in model GAM2. **(B)** Marginal effect of bivariate longitude–latitude term in model GAM1. **(C)** Marginal effect of stationary temperature anomaly term in model GAM3. **(D)** Marginal effect of spatially non-stationary temperature anomaly term in model GAM4. In panels **(A,C)**, gray shaded regions show 95% confidence intervals. In panels **(B,D)**, stippling indicates location where the 95% confidence interval for the covariate effect does not include zero.

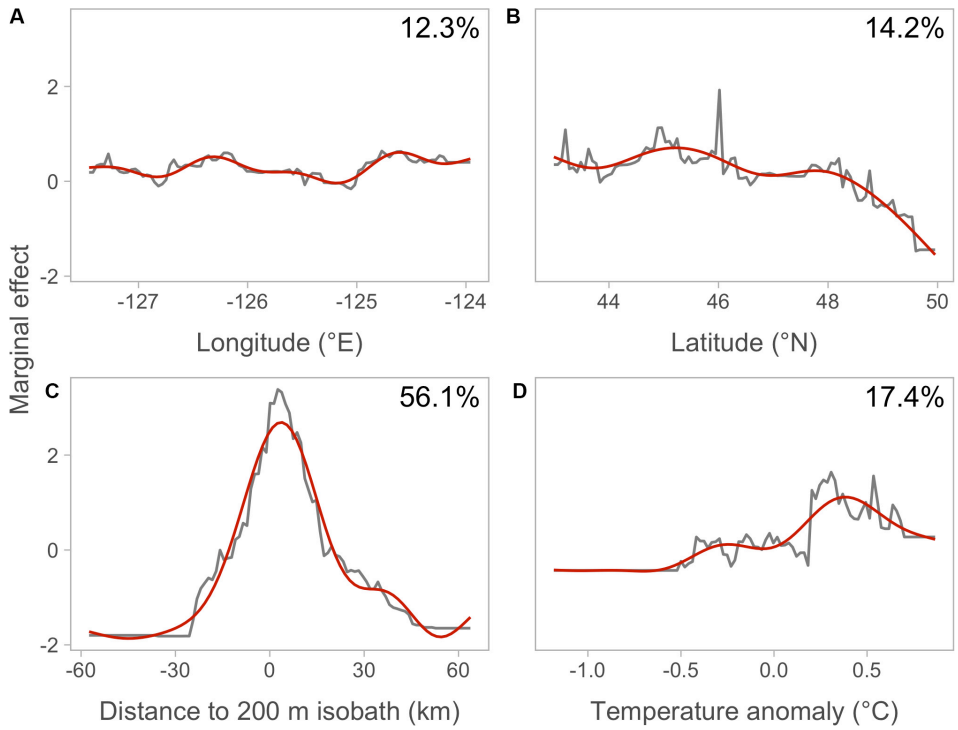

FIGURE 3 | Marginal effects of covariate smooths from the BRT. Each panel shows a single covariate: **(A)** longitude, **(B)** latitude, **(C)** distance to 200 m isobath, and **(D)** temperature anomaly. Gray lines show the marginal effects and red lines show smoothed marginal effects. Percentages give relative influence (i.e., percentage contribution) of each variable in explaining model deviance.

(i.e., had the highest AUC and lowest MSE), whereas the shelf-only model (GAM2) had the best out-of-sample forecast skill (**Table 2**). Between the two GAMs that included a temperature effect (GAM3 and GAM4), there was support for a spatially varying temperature effect with the GAM4 model having better in-sample and out-of-sample performance than GAM2.

The 2019 temperature anomaly forecasts from the J-SCOPE model indicated above average temperatures at depth across the study region (**Figure 4A**) with the warmest forecast (**Figure 4C**) having an average temperature anomaly of 0.78°C and the coolest forecast (**Figure 4B**) having an average anomaly of 0.36°C. The three individual temperature forecasts displayed moderate variability in temperature anomalies with grid cell specific standard deviations across the three temperature forecasts ranging from 0.03 to 1.36 (**Supplementary Figure S3**).

All models had considerable skill in forecasting 2019 hake occurrence with the ENS1 model having the best 2019 forecast skill with an AUC of 0.85 and MSE of 0.16 (**Table 2** and **Figure 5**). The 2019 forecasts showed higher probabilities of hake occurrence near the 200 m isobath, which is consistent with their historical distribution within the study region. The three models that included temperature anomaly (GAM3, GAM4, and BRT) showed more spatial variability in predicted hake occurrence and also tended to have higher standard errors of prediction compared to models that lacked temperature (**Figures 5**, **6**).

When temperature was removed from the BRT, model fit declined compared to the original BRT model that included temperature (i.e., lower in-sample skill; **Table 2** and **Supplementary Table S1**). In addition, the model with the highest out-of-sample skill changed to an ensemble of the BRT without temperature and GAM4, which includes a non-stationary temperature effect, suggesting temperature contributes to out-of-sample forecast skill.

DISCUSSION

Our objective was to develop and test environmentally driven seasonal forecasts of hake distribution to support management and survey planning decisions. The forecast models we tested showed appreciable out-of-sample forecast skill at 8-month time horizons. In addition, we found that: (1) the J-SCOPE model had considerable predictive skill of subsurface temperatures throughout the study domain, (2) distance to the 200 m shelf break was a strong predictor of historical hake occurrence and temperature at depth had a spatially varying effect on the probability of occurrence; and (3) the BRT model had moderately higher forecast skill than the GAMs and a multi-model ensemble forecast had slightly better out-of-sample forecast skill compared to the individual GAM and BRT models. Together, our results suggest that comparatively simple models can forecast hake distribution using seasonal projections of subsurface ocean temperature and distance to the 200 m shelf break.

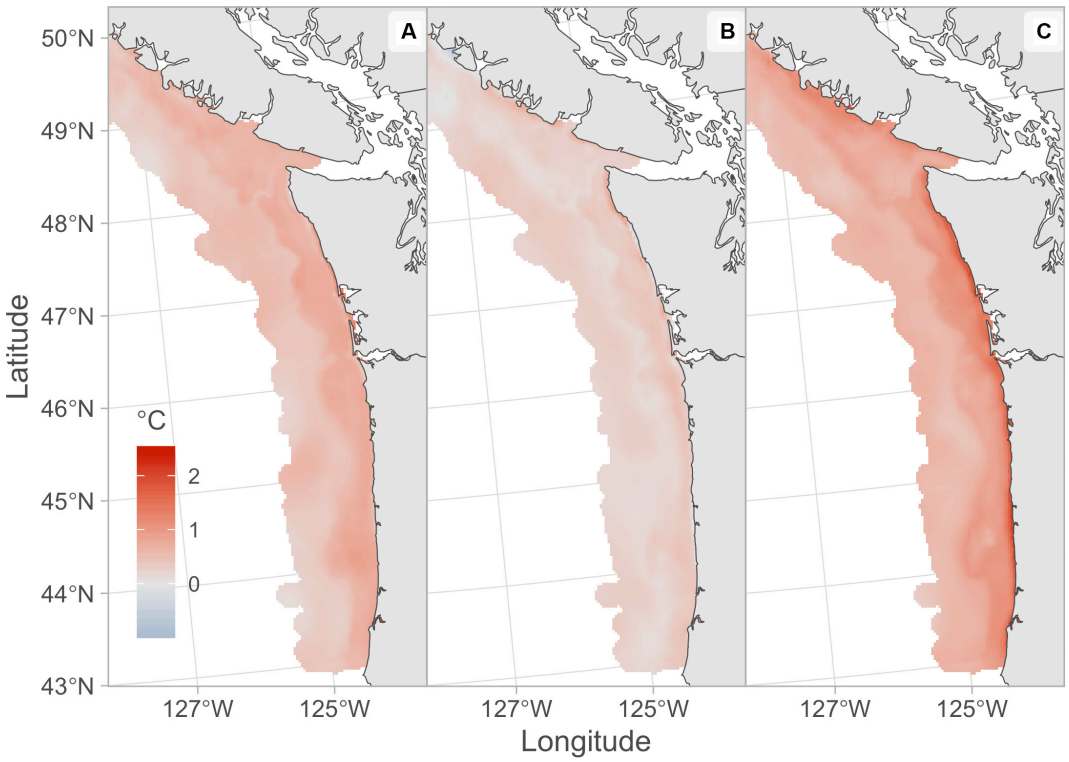

FIGURE 4 | January initialized August 2019 forecasts of temperature anomaly at 250 m depth from the J-SCOPE model. Each panel shows an alternative temperature forecast initialized on different days; **(A)** January 5, **(B)** January 15, **(C)** January 25.

Most of the forecast skill was derived from the 200 m shelf-break covariate. The strong affinity for hake occurrences to be concentrated in areas just-offshore of the 200 m shelf break is consistent with several previous studies that have shown areas near the 200 m isobath and areas with steeply sloping bathymetry provide good hake habitat (Dorn, 1995; Mackas et al., 1997; Swartzman, 1997, 2001). One possible explanation for this is that food availability may be high in these areas. In particular, euphausiids – an important prey item for hake – tend to concentrate in areas of steeply sloping bathymetry and submarine canyons (Buckley and Livingston, 1997; Mackas et al., 1997; Santora et al., 2018). In addition, areas just offshore of the 200 m isobath may also provide good physical ocean conditions. For instance, the California Undercurrent is strongest offshore of the 200 m isobath; the northward flowing undercurrent may act as a migration corridor for hake that could facilitate northward migration of Pacific hake and aggregate prey resources (Bakun, 1996; Agostini et al., 2006).

Our results indicated a moderate subsurface temperature effect on hake occurrence. The best GAMs included a spatially variable temperature effect and the BRT indicated the temperature term accounted for ∼17% of the variability in the response. This result broadly agrees with several previous papers that have shown associations between hake and temperature at depth (Ressler et al., 2007; Hamel et al., 2015; Malick et al., 2020). Temperature most likely acts as a proxy for other processes that have a more direct impact on hake distribution because the temperature ranges analyzed here are comparable to previously observed *in situ* temperature preferences of hake (Bailey et al., 1982; Ressler et al., 2007). Although using variables that have a more direct impact on hake habitat preferences (e.g., food availability) may provide better forecasts, skillful forecast of lower-trophic-level processes relevant for hake (e.g., euphausiid distribution) are currently not available. In contrast, temperature provides an ecologically relevant variable for which there is forecast skill at the lead-times important for decision makers (Kaplan et al., 2016; Siedlecki et al., 2016; Jacox et al., 2017).

The nine forecasting models evaluated here (five individual models + four ensemble models) performed similarly across years when forecasting out-of-sample hake distribution, e.g., most forecasts for 2011 and 2017 had relatively low skill, whereas forecasts for 2009 and 2012 had relatively high skill (**Supplementary Figures S4, S5**). Two factors likely contributed to lower forecast skill in some years. First, gaps in the latitudinal distribution of hake reduced skill, which occurred in 2011 when hake stock size was lower and few were present off the west coast of Vancouver Island. Second, variability in the cross-shelf distribution also appears to reduce skill; in 2017, hake occurrences were concentrated just inshore of the 200 m isobath, but just offshore in all other years (**Figure 1** and **Supplementary Figure S6**). This suggests that the consistency in which hake are present just offshore of the 200 m isobath across the latitudinal range of the study area drives differences in forecast skill among years. A priority

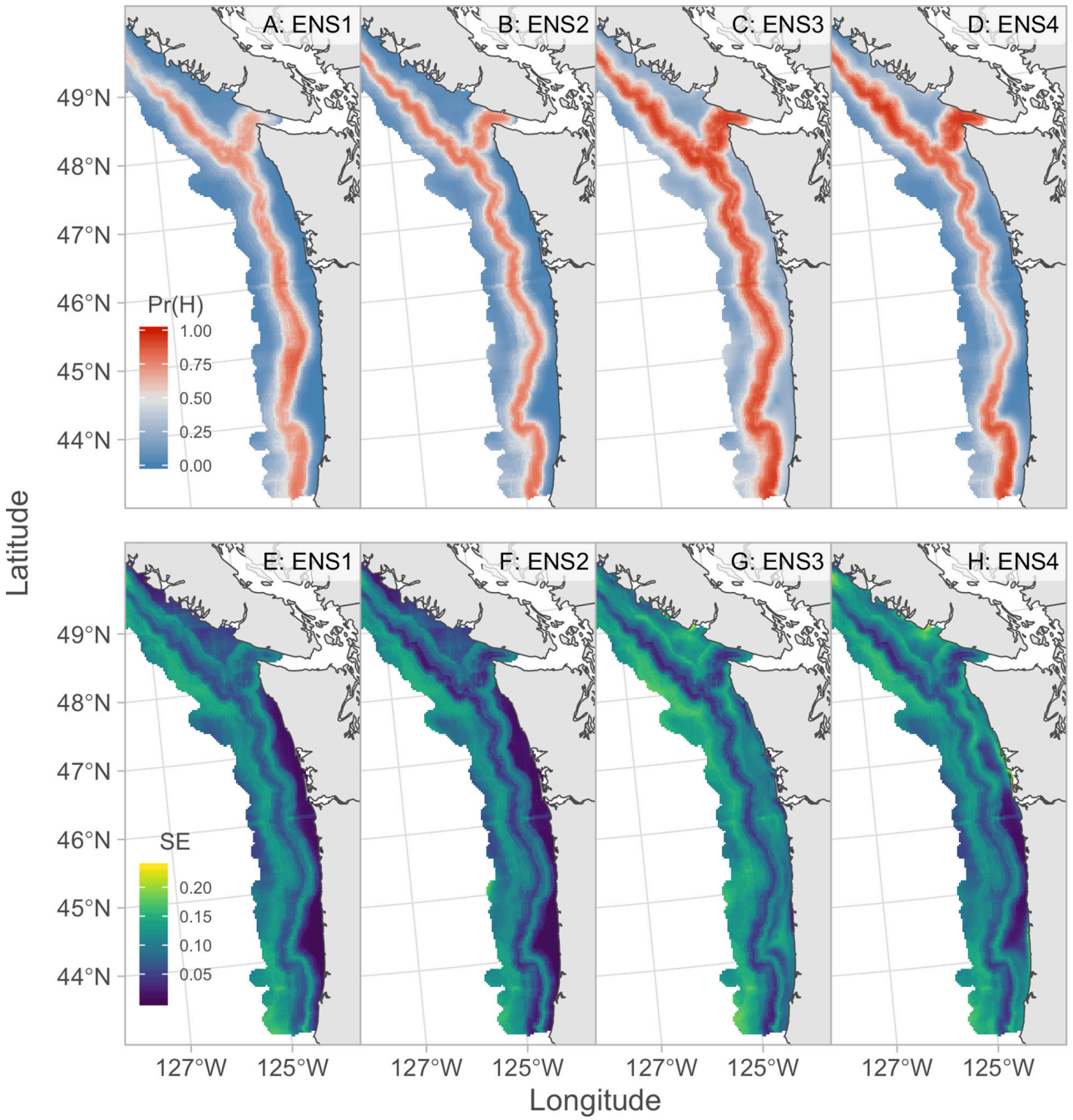

FIGURE 5 | August 2019 forecasts of hake occurrence from ensemble forecast models. Top row **(A–D)** shows the probability of hake occurrence where red indicates probabilities greater than 0.5 and blue indicates probabilities less than 0.5. Bottom row **(E–H)** shows the associated standard errors for each model where brighter colors indicate higher forecast uncertainty.

for future research would be to examine additional covariates to better capture inter-annual deviations in distribution from the shelf-break, e.g., the California Undercurrent or subsurface oxygen concentrations.

Combining multiple forecasts into an ensemble forecast has been widely shown to produce increased forecast precision compared to individual model forecasts, given that the individual forecasts provide some independent information (Bates and Granger, 1969; Clemen, 1989; Abrahms et al., 2019). We found that the ensemble hake forecasts had only slightly better out-of-sample skill compared to the individual model forecasts (**Table 2**). The weak increase in predictive performance for the ensemble models compared to the individual GAM and BRT models is likely due to high correlations among model prediction errors.

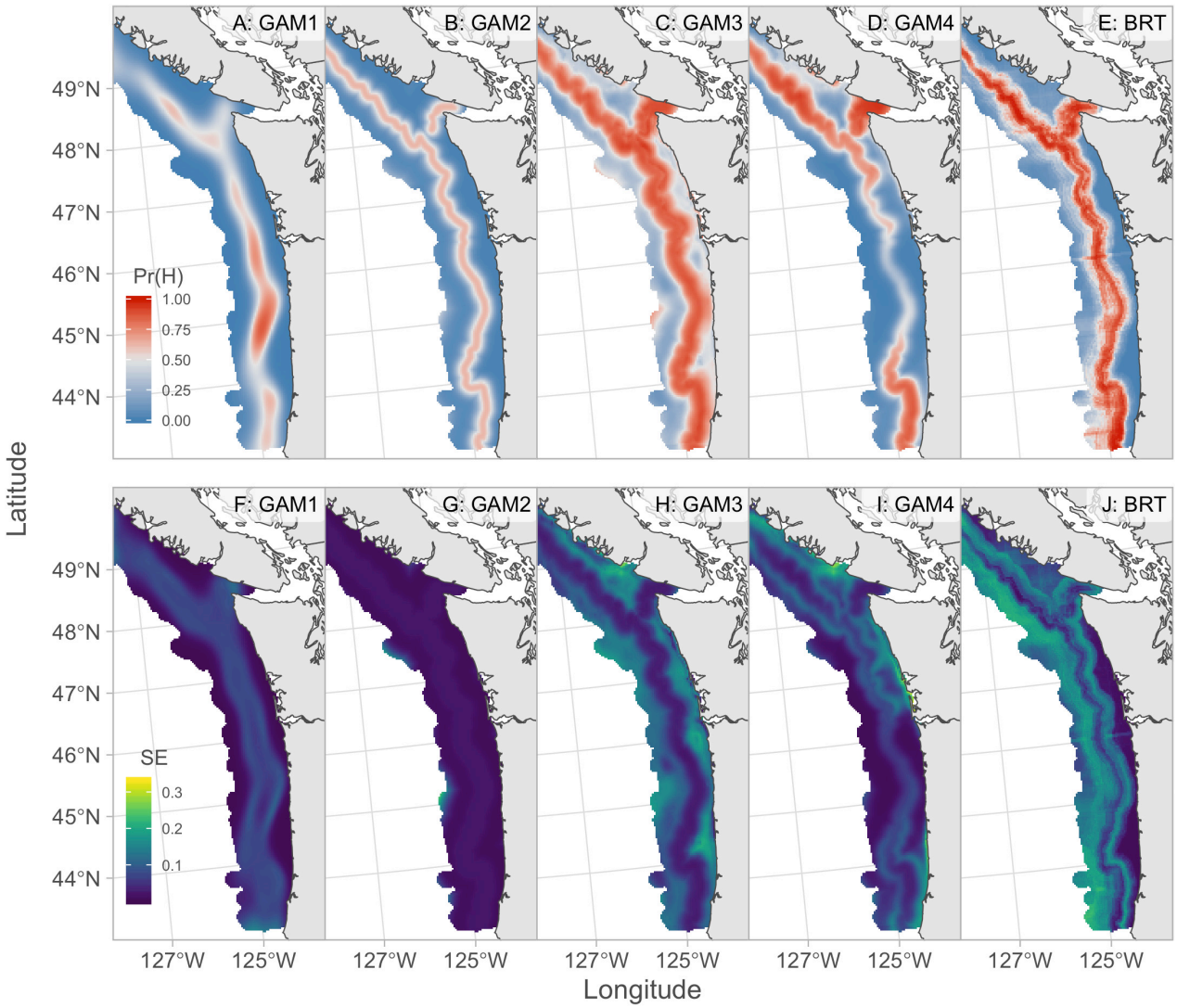

FIGURE 6 | August 2019 forecasts of hake occurrence from individual forecast models. Top row **(A–E)** shows the probability of hake occurrence where red indicates probabilities greater than 0.5 and blue indicates probabilities less than 0.5. Bottom row **(F–J)** shows the associated standard errors for each model where brighter colors indicate higher forecast uncertainty.

Multi-model ensemble models tend to outperform individual model predictions when weakly or negatively correlated model predictions are combined due to cancelation of random errors (Clemen, 1989). In this study, however, the individual model forecast error (i.e., observed hake occurrence - forecasted probability of occurrence), were strongly correlated, e.g., the average pairwise correlation of forecast errors from the GAMs and BRT was 0.91 (**Supplementary Figure S7**). This indicates that the individual forecast models produce similar forecast errors, which reduces the effectiveness of multi-model averaging (Araujo and New, 2007).

The results presented here provide a critical first step in developing an early warning of hake distributional shifts. Yet, we believe future work on three areas could further improve the usefulness of hake forecasts for management and survey planning. First, extending the northern range of this work to include waters through SE Alaska could help inform survey planning by providing additional information on the projected northern extent of Pacific hake, which is a critical uncertainty during survey planning. Second, developing a forecast of hake density could improve how the forecasts inform management decisions by helping to reduce uncertainties regarding the proportion of the population expected to migrate into Canadian waters. Third, if the spatial extent of the study area is extended northward beyond 50°N, the maximum latitudinal domain of this study, accounting for impacts of age-structure on Pacific hake distribution may be important. Exploratory analysis did not identify strong age-based differences in Pacific hake occurrences within the current spatial extent; however, evidence suggests that older and larger hake tend to migrate further north than smaller

hake with few age-2 hake observed north of Vancouver Island (Ressler et al., 2007; Malick et al., 2020).

Collectively, our results provide evidence that hake distribution can be skillfully forecast at lead-times of 8-months in the northern CCE. Our results also illustrate the broader utility of using seasonal lead-time ocean predictions in an ecological context to provide early warnings of distribution shifts of ecologically and economically important marine species. Marine ecosystems are changing rapidly and experiencing extreme events more frequently. Thus, skillful ecological forecasts provide new tools to inform the management process by reducing uncertainties regarding future states of nature that management decisions are often dependent upon (Dietze et al., 2018).

DATA AVAILABILITY STATEMENT

The raw data supporting the conclusions of this article will be made available by the authors, without undue reservation.

AUTHOR CONTRIBUTIONS

MM was the principal author of the manuscript and led the modeling analysis. MM, MH, SP-S, SS, IK, MH, KM, and AB designed the study and contributed to interpreting the results. SP-S and SG performed the data collection and processing. SS, EM, AH, and NB ran the J-SCOPE model forecasts and conducted the skill analysis. All authors contributed to writing and editing of the manuscript.

FUNDING

Funding was provided by NOAA's Fisheries and the Environment (FATE) program (grant #16-08). This study was partially supported by NOAA's Climate Program Office's Modeling, Analysis, Predictions, and Projections Program, Grant #NA17OAR4310112. This publication is partially funded by the Joint Institute for the Study of the Atmosphere and Ocean (JISAO) under NOAA Cooperative Agreement NA15OAR4320063, Contribution No. 2018-0183. The J-SCOPE forecasts were performed on the University of Washington Hyak supercomputer system, supported in part by the University of Washington eScience Institute.

ACKNOWLEDGMENTS

We thank Rebecca Thomas, Dezhang Chu, and John Pohl for assistance with the hake biomass data, as well as for helpful discussions that improved this study. We also thank Lewis Barnett and Nick Tolimieri for useful comments on our manuscript. We are grateful to the captains and crew members of the vessels used to conduct the acoustic-trawl surveys.

SUPPLEMENTARY MATERIAL

The Supplementary Material for this article can be found online at: https://www.frontiersin.org/articles/10.3389/fmars.2020.578490/full#supplementary-material

REFERENCES

Abrahms, B., Welch, H., Brodie, S., Jacox, M. G., Becker, E. A., Bograd, S. J., et al. (2019). Dynamic ensemble models to predict distributions and anthropogenic risk exposure for highly mobile species. *Divers. Distrib.* 25, 1182–1193. doi: 10.1111/ddi.12940

Agostini, V. N., Francis, R. C., Hollowed, A. B., Pierce, S. D., Wilson, C., and Hendrix, A. N. (2006). The relationship between Pacific hake (*Merluccius productus*) distribution and poleward subsurface flow in the California current system. *Can. J. Fish. Aquat. Sci.* 63, 2648–2659. doi: 10.1139/f06-139

Agostini, V. N., Hendrix, A. N., Hollowed, A. B., Wilson, C. D., Pierce, S. D., and Francis, R. C. (2008). Climate–ocean variability and Pacific hake: a geostatistical modeling approach. *J. Mar. Syst.* 71, 237–248. doi: 10.1016/j.jmarsys.2007.01.010

Araujo, M., and New, M. (2007). Ensemble forecasting of species distributions. *Trends Ecol. Evol.* 22, 42–47. doi: 10.1016/j.tree.2006.09.010

Bailey, K. M., Francis, R. C., and Stevens, P. R. (1982). The life history and fishery of Pacific whiting, *Merluccius productus*. *Cal. Coop. Ocean Fish.* 23, 81–98.

Bakun, A. (1996). *Patterns in the Ocean: Ocean Processes and Marine Population Dynamics*. La Paz: California Sea Grant College System.

Bates, J. M., and Granger, C. W. J. (1969). The combination of forecasts. *Oper. Res. Q.* 20, 451–468. doi: 10.2307/3008764

Benson, A. J., McFarlane, G. A., Allen, S. E., and Dower, J. F. (2002). Changes in Pacific hake (*Merluccius productus*) migration patterns and juvenile growth related to the 1989 regime shift. *Can. J. Fish. Aquat. Sci.* 59, 1969–1979. doi: 10.1139/f02-156

Berger, A. M., Edwards, A. M., Grandin, C. J., and Johnson, K. F. (2019). *Status of the Pacific Hake (whiting) Stock in the U.S. and Canadian waters in 2019. Prepared by the Joint Technical Committee for Pacific Hake/Whiting Agreement, National Marine Fisheries Service; Fisheries; Oceans Canada*. Silver Spring, MD: National Marine Fisheries Service, 249.

Brodie, S., Thorson, J. T., Carroll, G., Hazen, E. L., Bograd, S., Haltuch, M. A., et al. (2019). Trade-offs in covariate selection for species distribution models: a methodological comparison. *Ecography* 42, 1–14. doi: 10.1111/ecog.04707

Buckley, T. W., and Livingston, P. A. (1997). Geographic variation in the diet of Pacific hake, with a note on cannibalism. *Cal. Coop. Ocean Fish.* 28, 53–62.

Clark, J. S., Carpenter, S. R., Barber, M., Collins, S., Dobson, A., Foley, J. A., et al. (2001). Ecological forecasts: an emerging imperative. *Science* 293, 657–660. doi: 10.1126/science.293.5530.657

Clemen, R. T. (1989). Combining forecasts: a review and annotated bibliography. *Int. J. Forecast.* 5, 559–583. doi: 10.1016/0169-2070(89)90012-5

Dietze, M. C., Fox, A., Beck-Johnson, L. M., Betancourt, J. L., Hooten, M. B., Jarnevich, C. S., et al. (2018). Iterative near-term ecological forecasting: needs, opportunities, and challenges. *Proc. Natl. Acad. Sci. U.S.A.* 115, 1424–1432. doi: 10.1073/pnas.1710231115

Dorn, M. W. (1995). The effects of age composition and oceanographic conditions on the annual migration of Pacific whiting, *Merluccius productus*. *Cal. Coop. Ocean Fish.* 36, 97–105.

Elith, J., Leathwick, J. R., and Hastie, T. (2008). A working guide to boosted regression trees. *J. Anim. Ecol.* 77, 802–813. doi: 10.1111/j.1365-2656.2008.01390.x

Fielding, A. H., and Bell, J. F. (1997). A review of methods for the assessment of prediction errors in conservation presence/absence models. *Environ. Conserv.* 24, 38–49. doi: 10.1017/s0376892997000088

Fleischer, G. W., Cooke, K. D., Ressler, P. H., Thomas, R. E., de Blois, S. K., and Hufnagle, L. C. (2008). *The 2005 Integrated Acoustic and Trawl Survey of Pacific Hake, Merluccius Productus, in U.S. and Canadian Waters off the Pacific coast*. Seattle, WA: National Oceanic & Atmospheric Administration.

Francis, R. C. (1983). Population and trophic dynamics of Pacific hake *Merluccius productus*. *Can. J. Fish. Aquat. Sci.* 40, 1925–1943. doi: 10.1139/f83-223

Giddings, S. N., MacCready, P., Hickey, B. M., Banas, N. S., Davis, K. A., Siedlecki, S. A., et al. (2014). Hindcasts of potential harmful algal bloom transport pathways on the Pacific Northwest coast. *J. Geophys. Res. Oceans* 119, 2439–2461. doi: 10.1002/2013jc009622

Haidvogel, D. B., Arango, H., Budgell, W. P., Cornuelle, B. D., Curchitser, E., Di Lorenzo, E., et al. (2008). Ocean forecasting in terrain-following coordinates: formulation and skill assessment of the regional ocean modeling system. *J. Comput. Phys.* 227, 3595–3624. doi: 10.1016/j.jcp.2007.06.016

Hamel, O. S., Ressler, P. H., Thomas, R. E., Waldeck, D. A., Hicks, A. C., Holmes, J. A., et al. (2015). "Biology, fisheries, assessment and management of pacific hake (*Merluccius productus*)," in *Hakes: Biology and exploitation Fish and Aquatic Resources Series*, ed. H. Arancibia (Chichester: Wiley-Blackwell). doi: 10.1002/9781118568262.ch9

Hazen, E. L., Scales, K. L., Maxwell, S. M., Briscoe, D. K., Welch, H., Bograd, S. J., et al. (2018). A dynamic ocean management tool to reduce bycatch and support sustainable fisheries. *Sci. Adv.* 4:eaar3001. doi: 10.1126/sciadv.aar3001

Hobday, A. J., Hartog, J. R., Spillman, C. M., and Alves, O. (2011a). Seasonal forecasting of tuna habitat for dynamic spatial management. *Can. J. Fish. Aquat. Sci.* 68, 898–911. doi: 10.1139/f2011-031

Hobday, A. J., Smith, A. D. M., Stobutzki, I. C., Bulman, C., Daley, R., Dambacher, J. M., et al. (2011b). Ecological risk assessment for the effects of fishing. *Fish. Res.* 108, 372–384. doi: 10.1016/j.fishres.2011.01.013

Hobday, A. J., Spillman, C. M., Eveson, J. P., and Hartog, J. R. (2016). Seasonal forecasting for decision support in marine fisheries and aquaculture. *Fish. Oceanogr.* 25, 45–56. doi: 10.1111/fog.12083

Jacox, M. G., Alexander, M. A., Siedlecki, S., Chen, K., Kwon, Y.-O., Brodie, S., et al. (2020). Seasonal-to-interannual prediction of North American coastal marine ecosystems: forecast methods, mechanisms of predictability, and priority developments. *Prog. Oceanogr.* 183:102307. doi: 10.1016/j.pocean.2020.102307

Jacox, M. G., Alexander, M. A., Stock, C. A., and Hervieux, G. (2017). On the skill of seasonal sea surface temperature forecasts in the California Current System and its connection to ENSO variability. *Clim. Dyn.* 53, 7519–7533. doi: 10.1007/s00382-017-3608-y

Kaplan, I. C., Williams, G. D., Bond, N. A., Hermann, A. J., and Siedlecki, S. A. (2016). Cloudy with a chance of sardines: forecasting sardine distributions using regional climate models. *Fish. Oceanogr.* 25, 15–27. doi: 10.1111/fog.12131

Keller, A. A., Wallace, J. R., and Methot, R. D. (2017). *The Northwest Fisheries Science Center's West Coast Groundfish Bottom Trawl Survey: History, Design, and Description*. Seattle, WA: NOAA.

Levin, P. S., Fogarty, M. J., Murawski, S. A., and Fluharty, D. (2009). Integrated ecosystem assessments: developing the scientific basis for ecosystem-based management of the ocean. *PLoS Biol.* 7:e1000014. doi: 10.1371/journal.pbio.1000014

Mackas, D. L., Kieser, R., Saunders, M., Yelland, D. R., Brown, R. M., Moore, D. F., et al. (1997). Aggregation of euphausiids and Pacific hake (*Merluccius productus*) along the outer continental shelf off Vancouver Island. *Can. J. Fish. Aquat. Sci.* 54, 2080–2096. doi: 10.1139/cjfas-54-9-2080

Malick, M. J., Hunsicker, M. E., Haltuch, M. A., Parker-Stetter, S. L., Berger, A. M., and Marshall, K. N. (2020). Relationships between temperature and Pacific hake distribution vary across latitude and life-history stage. *Mar. Ecol. Prog. Ser.* 639, 185–197. doi: 10.3354/meps13286

Malick, M. J., Rutherford, M. B., and Cox, S. P. (2017). Confronting challenges to integrating Pacific salmon into ecosystem-based management policies. *Mar. Policy* 85, 123–132. doi: 10.1016/j.marpol.2017.08.028

Mills, K. E., Pershing, A. J., and Hernández, C. M. (2017). Forecasting the seasonal timing of Maine's lobster fishery. *Front. Mar. Sci.* 4:337. doi: 10.3389/fmars.2017.00337

Payne, M. R., Hobday, A. J., MacKenzie, B. R., Tommasi, D., Dempsey, D. P., Fässler, S. M. M., et al. (2017). Lessons from the first generation of marine ecological forecast products. *Front. Mar. Sci.* 4:289. doi: 10.3389/fmars.2017.00289

R Core Team (2019). *R: A Language and Environment for Statistical Computing*. Vienna: R Foundation for Statistical Computing.

Ressler, P. H., Holmes, J. A., Fleischer, G. W., Thomas, R. E., and Cooke, C. K. (2007). Pacific hake, *Merluccius productus*, autecology: a timely review. *Mar. Fish. Rev.* 69, 1–24. doi: 10.3354/meps006001

Santora, J. A., Zeno, R., Dorman, J. G., and Sydeman, W. J. (2018). Submarine canyons represent an essential habitat network for krill hotspots in a Large Marine ecosystem. *Sci. Rep.* 8:7579. doi: 10.1038/s41598-018-25742-9

Siedlecki, S. A., Kaplan, I. C., Hermann, A. J., Nguyen, T. T., Bond, N. A., Newton, J. A., et al. (2016). Experiments with seasonal forecasts of ocean conditions for the northern region of the California Current upwelling system. *Sci. Rep.* 6:27203. doi: 10.1038/srep27203

Stock, C. A., Pegion, K., Vecchi, G. A., Alexander, M. A., Tommasi, D., Bond, N. A., et al. (2015). Seasonal sea surface temperature anomaly prediction for coastal ecosystems. *Prog. Oceanogr.* 137, 219–236. doi: 10.1016/j.pocean.2015.06.007

Swartzman, G. (1997). Analysis of the summer distribution of fish schools in the Pacific Eastern Boundary Current. *ICES J. Mar. Sci.* 54, 105–116. doi: 10.1006/jmsc.1996.0160

Swartzman, G. (2001). "Spatial patterns of Pacific hake (*Merluccius productus*) shoals and euphausiid patches in the California Current Ecosystem," in *Spatial Processes and Management of Marine Populations*, ed. G. H. Kruse (Fairbanks, AK: Alaska Sea Grant College Program), 495–512.

Tommasi, D., Stock, C. A., Hobday, A. J., Methot, R., Kaplan, I. C., Eveson, J. P., et al. (2017). Managing living marine resources in a dynamic environment: the role of seasonal to decadal climate forecasts. *Prog. Oceanogr.* 152, 15–49. doi: 10.1016/j.pocean.2016.12.011

Ware, D. M., and McFarlane, G. A. (1995). "Climate-induced changes in Pacific hake (*Merluccius productus*) abundance and pelagic community interactions in the Vancouver Island system," in *Climate Change and Northern Fish Populations*, 121 Edn, (Ottawa ON: Canadian Special Publication of Fisheries and Aquatic Sciences), 509–521.

Wood, S. N. (2003). Thin plate regression splines. *J. R. Stat. Soc. B* 65, 95–114. doi: 10.1111/1467-9868.00374

Wood, S. N. (2017). *Generalized Additive Models: An Introduction with R*. Boca Raton, FL: CRC Press.

Zwolinski, J. P., Emmett, R. L., and Demer, D. A. (2011). Predicting habitat to optimize sampling of Pacific sardine (*Sardinops sagax*). *ICES J. Mar. Sci.* 68, 867–879. doi: 10.1093/icesjms/fsr038

Conflict of Interest: The authors declare that the research was conducted in the absence of any commercial or financial relationships that could be construed as a potential conflict of interest.

frontiers in Marine Science

ORIGINAL RESEARCH
published: 20 October 2020
doi: 10.3389/fmars.2020.546587

Skill Assessment of Seasonal-to-Interannual Prediction of Sea Level Anomaly in the North Pacific Based on the SINTEX-F Climate Model

Takeshi Doi, Masami Nonaka and Swadhin Behera*

Application Laboratory (APL), Research Institute for Value-Added-Information Generation (VAiG), Japan Agency for Marine-Earth Science and Technology (JAMSTEC), Yokohama, Japan

OPEN ACCESS

Edited by:
Zhiyu Liu,
Xiamen University, China

Reviewed by:
Debora Bellafiore,
National Research Council (CNR), Italy
Ru Chen,
Tianjin University, China
Soo-Jin Sohn,
APEC Climate Center, South Korea
Kewei Lyu,
Oceans and Atmosphere (CSIRO), Australia

***Correspondence:**
Takeshi Doi
takeshi.doi@jamstec.go.jp
orcid.org/0000-0002-7342-9145

Specialty section:
This article was submitted to Physical Oceanography, a section of the journal Frontiers in Marine Science

Received: *29 March 2020*
Accepted: *22 September 2020*
Published: *20 October 2020*

Citation:
Doi T, Nonaka M and Behera S (2020) Skill Assessment of Seasonal-to-Interannual Prediction of Sea Level Anomaly in the North Pacific Based on the SINTEX-F Climate Model. Front. Mar. Sci. 7:546587. doi: 10.3389/fmars.2020.546587

Extreme sea level rise seriously impacts habitation and is indicative of changes in primary production in the North Pacific. Because of its rising trend associated with global warming, skillful seasonal-to-interannual predictions have become increasingly valuable to guide the introduction of suitable adaptation measures that help us reduce the risks of socioeconomic losses. Here, we have used a dynamical coupled ocean–atmosphere model called "SINTEX-F" to revisit the potential predictability of sea level anomalies at a lead of up to about 2 years. Skillful prediction is found mainly in the tropical Pacific as shown in previous work. Here, we found a new skillful prediction region in the North Pacific (30°–40°N, 180°–150°W) at about 2 years' lead time. We also analyzed the co-variability among ensemble members and found the long-lasting ENSO/ENSO-Modoki in the tropical Pacific seems to contribute to the predictability source. The result may be useful to develop systematic and synergistic attempts to predict marine ecosystem responses to regional and global climate variations.

Keywords: seasonal-interannual prediction, sea level, climate model, dynamical system, skill assessment

INTRODUCTION

The North Pacific marine ecosystems are primary sources of ecosystem services (e.g., fishing, shipping, and recreation) for its surrounding countries including Canada, U.S., China, Russia, Korea, and Japan. Coastlines of the North Pacific are seriously damaged by extreme sea level rise (Nicholls et al., 2007). In particular, the coastal zones are immediately affected by submergence and increased flooding of coastal land, as well as saltwater intrusion of surface waters (Nicholls and Cazenave, 2010).

In addition to the rising sea level trend associated with the global warming, extreme sea level events occur in association with natural climate variability such as the Pacific Decadal Oscillation (PDO), the Interdecadal Pacific Oscillation (IPO), the North Pacific Gyre Oscillation (NPGO), and the El Niño-Southern Oscillation (ENSO) in the North Pacific (Mantua et al., 1997; Zhang et al., 1997; McGowan et al., 1998; Lombard et al., 2005; Di Lorenzo et al., 2008; Hamlington et al., 2019; Han et al., 2019). To address relatively short-term risks, stakeholders desire a forecast of monthly/seasonal rising or falling sea levels caused by those climate variabilities. Hinkel et al. (2019)

analyzed user needs for sea level rise information, and how they are able to be met given the state-of-the-art of sea level forecast science. Jacox et al. (2020) reviewed statistical and dynamical marine ecosystem forecasting methods and highlighted examples of their application along U.S. coastlines for seasonal-to-interannual prediction. Payne et al. (2017) also reviewed the state of the art marine ecological forecasts and suggested forecasts ranging from seasonal to decadal time scales are now a reality. Tommasi et al. (2017a) evaluated the multi-annual SST predictions over Large Marine Ecosystems (LMEs), a coastal scale relevant to managed fisheries stocks. Tommasi et al. (2017b) also highlighted advances in seasonal to decadal prediction of managing living marine resources in a dynamic environment. Those previous studies provide information relevant for supporting coastal adaptation decision making.

Although skillful predictions of SST have already proven useful for a number of marine resource applications (e.g., Hobday et al., 2014; Stock et al., 2015), further studies about sea level anomaly are necessary. Rebert et al. (1985) showed that the oceanic Kelvin and Rossby waves have a direct relation between thermocline depth and sea level, while they have only an indirect relation to SST. These ocean dynamics are responsible for the relatively high skill of sea level prediction relative to SST prediction (Miles et al., 2014). Zainuddin et al. (2017) found that SST was an important variable for detecting hotspots of skipjack tuna distribution, as they are sensitive to the changes in temperature. Sea level anomaly is related to the changes in the depth of the thermocline and mesoscale variability. They combined these variables to improve detection of potential pelagic hotspots for skipjack tuna.

To expand prediction of large-scale sea level anomalies into coastal areas and to further the understanding of its potential predictability, it is necessary to evaluate the lead-time and locations in which a dynamical, physics-based prediction system performs well. It might allow coastal communities to better adapt for the impacts of severe flooding and erosion driven by high sea levels.

Although decadal climate variation is more predictable than previously thought, it is still challenging (Meehl et al., 2014; Smith et al., 2019). Here, our focus is on seasonal-to-interannual prediction. Generally speaking, the most important potential source of seasonal-to-interannual predictability is often from ENSO events, which develop via air-sea coupled feedback. Therefore, application of an ocean-atmosphere coupled general circulation model (GCM) is naturally a proven approach to overcome shortcomings of stand-alone atmospheric/oceanic models. Miles et al. (2014) initially attempted to apply a coupled GCM to predict seasonal sea level anomalies, and assessed the skill globally for up to 7 months in advance. McIntosh et al. (2015) showed the prediction skill by dynamical GCMs is better relative to statistical approaches for coastal sea level. Polkova et al. (2015) used the decadal prediction system and found predictability in the subtropics. Roberts et al. (2016) assessed the predictability of large-scale dynamic sea level anomalies up to 15 months using a climate model and found that prediction of seasonal-to-interannual sea level variability in the extratropics will be governed by the predictability of surface wind stress and modes of atmospheric variability.

This study is a follow-up study of those pioneering studies. Here, we have revisited the predictability of sea level up to about 2 years in advance by analyzing results of a coupled ocean–atmosphere general circulation model "SINTEX-F." Such a long lead time retrospective forecast is beyond most current operational capabilities, and hence a skill assessment of the model results is conducted here as a first attempt. We believe that the obtained result is useful to attempt systematic and synergistic prediction of marine ecosystem responses to regional and global climate variations.

MATERIALS AND METHODS

Dynamical Prediction System

The Scale Interaction Experiment-Frontier ver. 1 (SINTEX-F1) prediction system was used here, which is based on a fully coupled global ocean–atmosphere circulation model (CGCM) developed under the EU-Japan collaborative framework (Luo et al., 2003; Luo et al., 2005; Masson et al., 2005). The atmospheric component has a horizontal resolution of 1.125° (T106) with 19 vertical levels. The oceanic component has a horizontal resolution of about 2° × 2° but with meridional refinement to 0.58° in the tropics. It has 31 vertical levels from the surface to the bottom with a relatively finer resolution of 10 m from the sea surface to 110 m depth. This system adopts a relatively simple initialization scheme based only on the nudging of observed SST. In consideration of uncertainties of both initial conditions and model physics, it has nine ensemble members. More details about the prediction system are available in Luo et al. (2005). This system has demonstrated high performance for prediction of ENSO (Jin et al., 2008). In particular, Luo et al. (2008) showed that several ENSO events can be predicted at lead times of up to 2 years by this system, which can be a strong advantage in this study. The quasi real-time predictions are updated every month and made publicly available from 2005 (see http://www.jamstec.go.jp/aplinfo/sintexf/e/seasonal/outlook.html).

We have analyzed the reforecasting experiments for the 1993–2018 period issued on the first day of March, June, September, and December with about 2-year lead time. The prediction anomalies were determined by removing the model mean climatology at each lead-time over the same period. To evaluate the prediction results, we have used the multi-mission altimeter satellite gridded sea surface heights (SEALEVEL_GLO_PHY_L4_REP_OBSERVATIONS_008_047; available from http://marine.copernicus.eu/services-portfolio/access-to-products/?option=com_csw&view=details&product_id=SEALEVEL_GLO_PHY_L4_REP_OBSERVATIONS_008_047) for sea level, the NOAA OISSTv2 (Reynolds et al., 2002) for SST, and the NCEP/NCAR reanalysis data (Kalnay et al., 1996) for atmospheric variables anomalies. The monthly climatologies of these datasets are also calculated by averaging monthly data over the same period, and then anomalies are derived through deviations from those mean climatologies. All anomalies are linearly detrended, which can

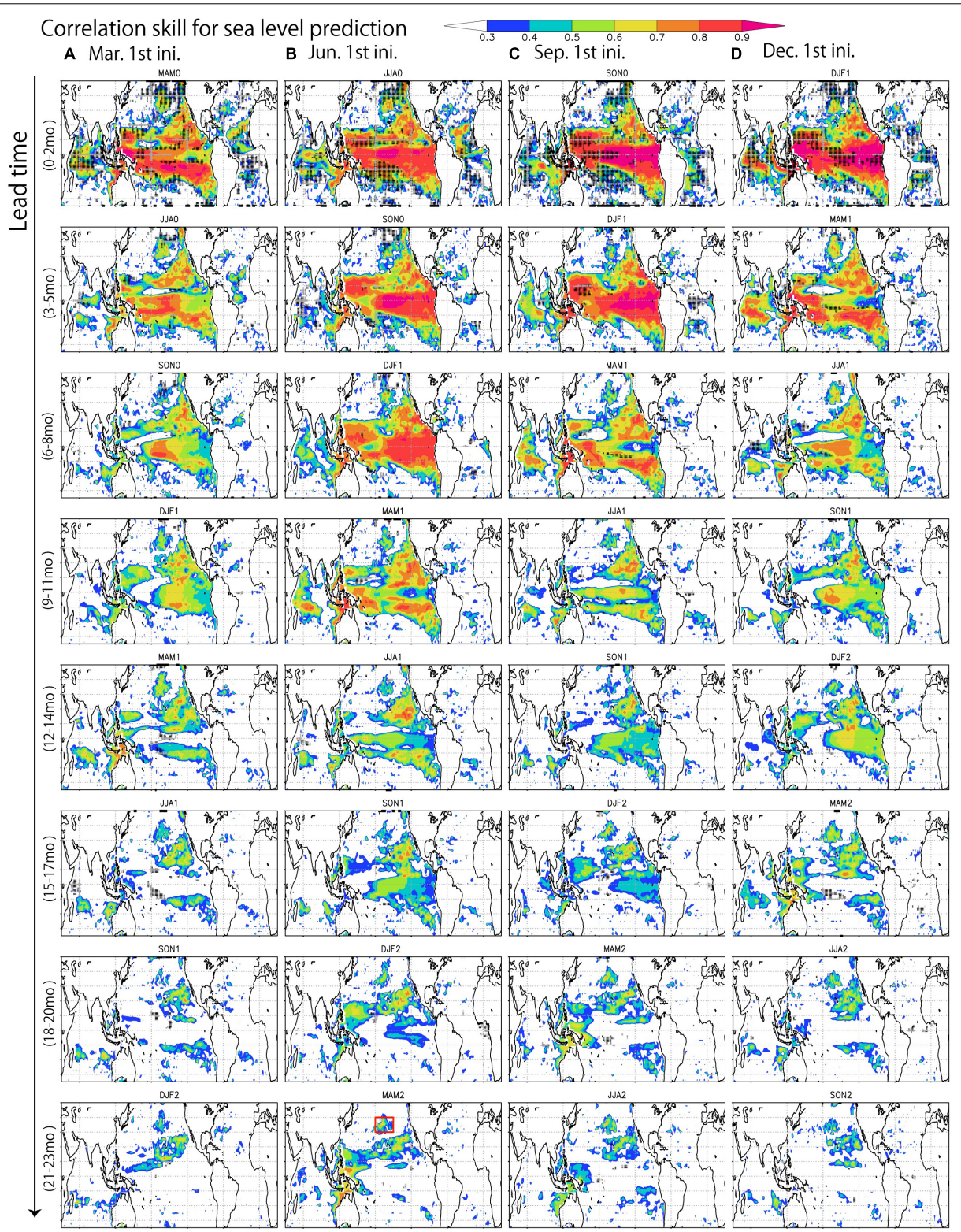

FIGURE 1 | (A) The correlation coefficient for seasonal-to-interannual prediction for sea level anomalies (ensemble mean) from the 0–2 months lead average up to the 21–23 months lead average issued on March 1, 1993–2018. Black dots indicate regions where the correlation is below the persistence (lag autocorrelation of observation). Considering that the degree of freedom based on the sample size, the correlation beyond 0.3 is statistically significant at a 90% level. So, the correlation greater than 0.3 is masked out. **(B–D)** Same as **(A)**, but for the prediction issued on June 1, September 1, and December 1. The target area in the North Pacific (30°–40°N, 180°–150°W) is shown by a red box in MAM2 prediction issued on June 1.

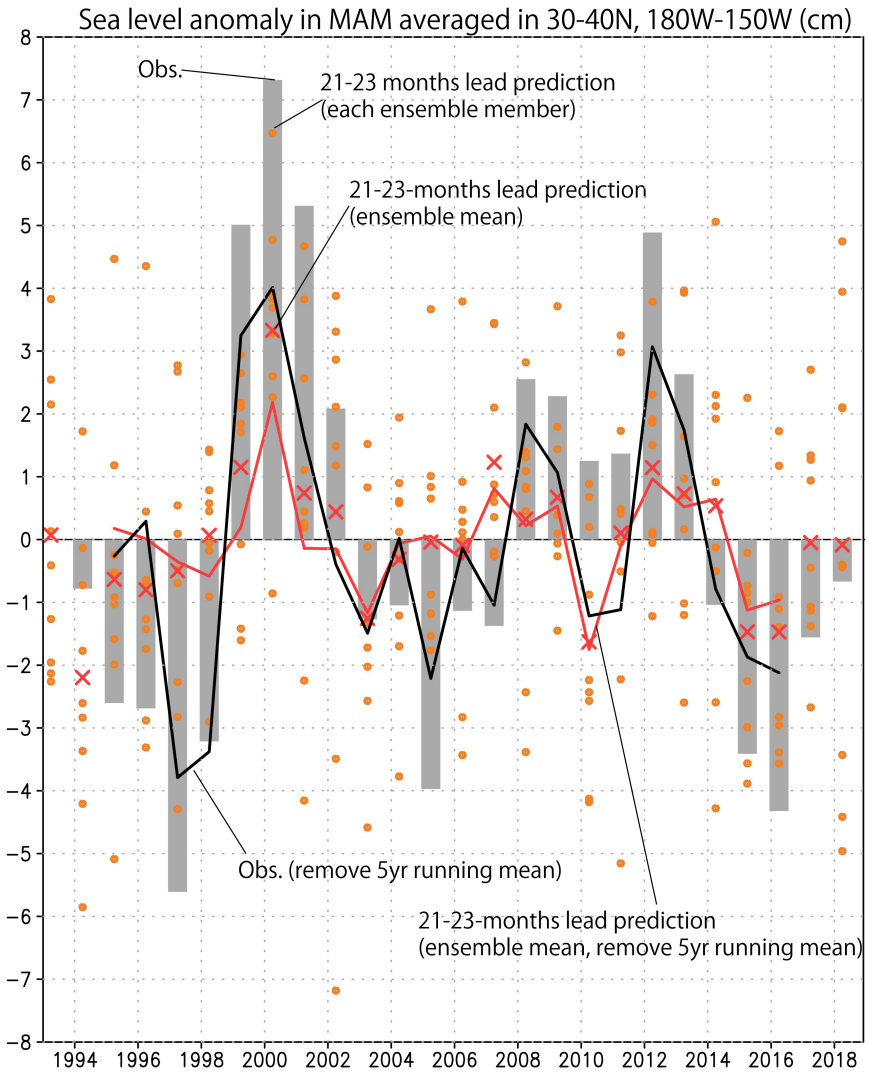

FIGURE 2 | Time series of sea level anomaly averaged over 30°–40°N, 180°–150°W during March-April-May (cm). Gray column: observation, Red cross: ensemble mean prediction issued on June 1, 2-year before (21–23 months lead average), orange dot: each ensemble member prediction, black line: observation after removing 5-years running mean, red line: ensemble mean prediction after removing 5-years running mean.

prevent long time scale changes from artificially increasing correlation analysis.

RESULTS

Skill Assessment up to 2-Year Lead

The correlation coefficient (Pearson's "r") between two time series of observed and predicted anomalies for each grid points is used as a deterministic prediction skill score of the phase variation. The persistence method is the simplest way of producing a forecast; it assumes that the conditions will not change. The persistence method works well when anomalies vary very slowly. Therefore, the correlation of the persistence is generally used to assess the advantage of prediction models. Skillful prediction of sea level is found mainly in the tropical Pacific (**Figure 1**). It drops outside of the oceanic Kelvin, Rossby, and coastally trapped waveguides in the tropical Pacific region. The correlation often exceeds the skill of persistence and 0.6 in many regions within 20° of the equator at the first season (0–2 months lead). The correlation decreases at longer lead times but generally remaining above 0.5 in the waveguides up to 11 months lead times. The advantage of the SINTEX-F prediction relative to the persistence increases at longer lead times. This suggests that the skill is mainly derived from the ability to predict ENSO accurately as expected from the previous works (Miles et al., 2014). It is also found skillful prediction regions off the west coast of Australia and California, which may be related to the successful predictions of the Ningaloo Niño/Niña (Doi et al., 2013, 2015a) and the California Niño/Niña (Doi et al., 2015b); some of those events are strongly linked with coastally trapped ocean waves forced by ENSO events.

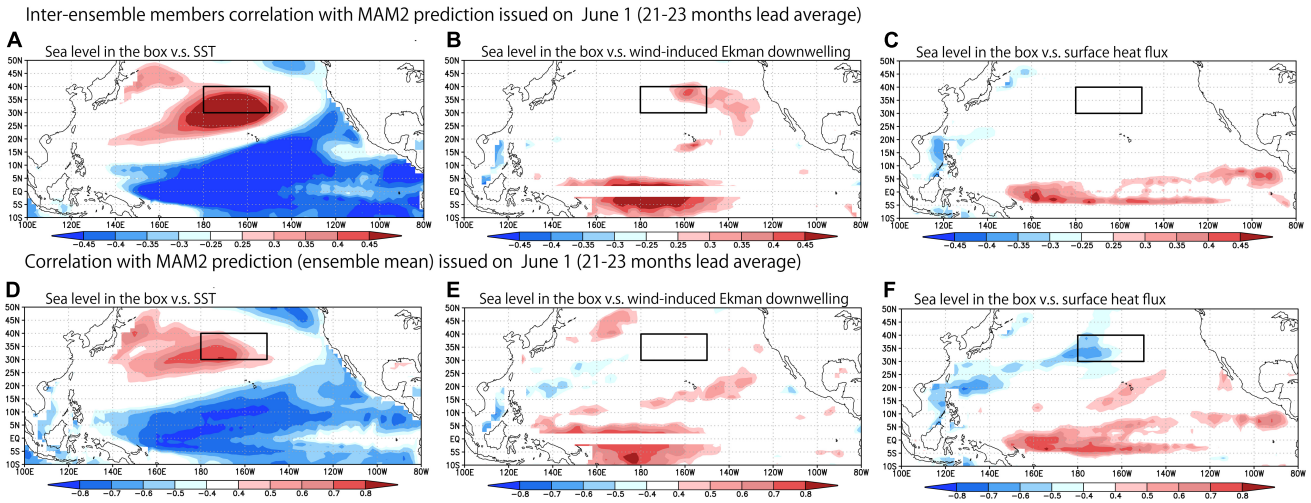

FIGURE 3 | (A) Inter-ensemble member correlation between sea level anomaly averaged in 30°–40°N, 180°–150°W (shown by a box) and a horizontal distribution of SST anomaly in a nine-member ensemble reforecast for the 21–23 months lead average issued on June 1. **(B)** Same as **(A)**, but for regional wind-induced Ekman downwelling. **(C)** Same as **(A)**, but for surface heat flux. **(D–F)** Same as **(A–C)**, but for correlation using the ensemble mean prediction. The color scale is different from that in **(A–C)** because the sample size is different (198 and 22). Considering the degree of freedom based on the sample size, the correlation below 0.25 (0.40) is masked out in the upper (lower) panel.

We can also find the seasonal dependence of the correlation, likely because of the so-called spring predictability barrier in forecasting the development of ENSO (e.g., Latif et al., 1998). Prediction of sea level anomalies in the 3–5 months lead average issued on March 1 shows low correlation in many regions relative to that issued on other seasons. Also, we see a quick decrease in the correlation from prediction of the December-January-February (DJF) average into that of the March-April-May (MAM) average.

At the extratropical latitudes in 20°–30°N, the skill still remains in some regions in the North Pacific up to about 2-year lead. This is likely due to the slowly propagating Rossby wave features and some stationary anomalies. In the extratropics of the North Pacific, which is often defined the latitude bands of 30°–60°N, interestingly, we found the predictability of a region in the North Pacific (30°–40°N, 180°–150°W) to be skillful up to 2 years ahead. This is not yet discussed by the previous work. **Figure 2** shows its time series for the MAM seasonal average. The time series at first glance shows the presence of a decadal variability. The correlation of the 2-year lead prediction is 0.67 for 26 samples (1993–2018 years). After removing the 5-years running mean, it is 0.65 for 22 samples (1995–2016 years). The spread of the ensemble of prediction provides information about the uncertainty inherent. The large uncertainty suggests low potential predictability of sea level anomalies here. Interestingly, however, the sea level anomaly in 2000 exhibits relatively high predictability. We will discuss the details later.

How about the other oceans? We can find some skillful prediction regions in the southern Indian Ocean beyond 1-year lead (**Figure 1**). This may be related to the successful prediction of the Subtropical Indian Ocean Dipole (Beherea and Yamagata, 2001; Yuan et al., 2014). In the Atlantic, prediction beyond 1-year lead is relatively challenging. For example, the pattern associated with the North Atlantic Oscillation, which is the dominant climate mode in the Atlantic Ocean, is not represented well by the model. We need further analysis to understand similarities and differences among the ocean basins.

Inter-Ensemble Members Relationship

Why is the skillful prediction found about 2-year lead in a region in the North Pacific (30°–40°N, 180°–150°W)? Investigating co-variability of inter-member anomalies (defined as deviations from the ensemble mean) may provide useful insights into possible precursors and teleconnection patterns related to a climate event considering the intrinsic variability (Ma et al., 2017; Ogata et al., 2019; Doi et al., 2020a,b). **Figure 3A** shows the correlation coefficients among the inter-ensemble members of the reforecast for the March–May average of 1995–2016 (198 sample: 9 members times 22 years after removing 5-years running mean) at 2-year lead. In this analysis, the conventional time dimension could be enlarged by the ensemble dimension. The co-variability between the sea level anomaly in that region and the tropical Pacific condition shows a pattern resembling a mixture of the Modoki-type and the canonical-type of ENSO (Ashok et al., 2007; Karnauskas, 2013). Also, a similar co-variability is seen between the sea level and local wind-induced Ekman downwelling in that region (**Figure 3B**). Since the similar features are able to be captured by liner regression analysis to ENSO (Vimont, 2005; Zhang and Church, 2012; Han et al., 2019), the successful prediction of ENSO and/or ENSO-Modoki in the tropical Pacific may be related to the success in predicting sea level anomaly in that region at about 2-year lead. Note that a corresponding co-variability with the surface heat flux was not found in that region (**Figure 3C**). This may suggest that the dynamic process is more important in that region than the thermodynamic process.

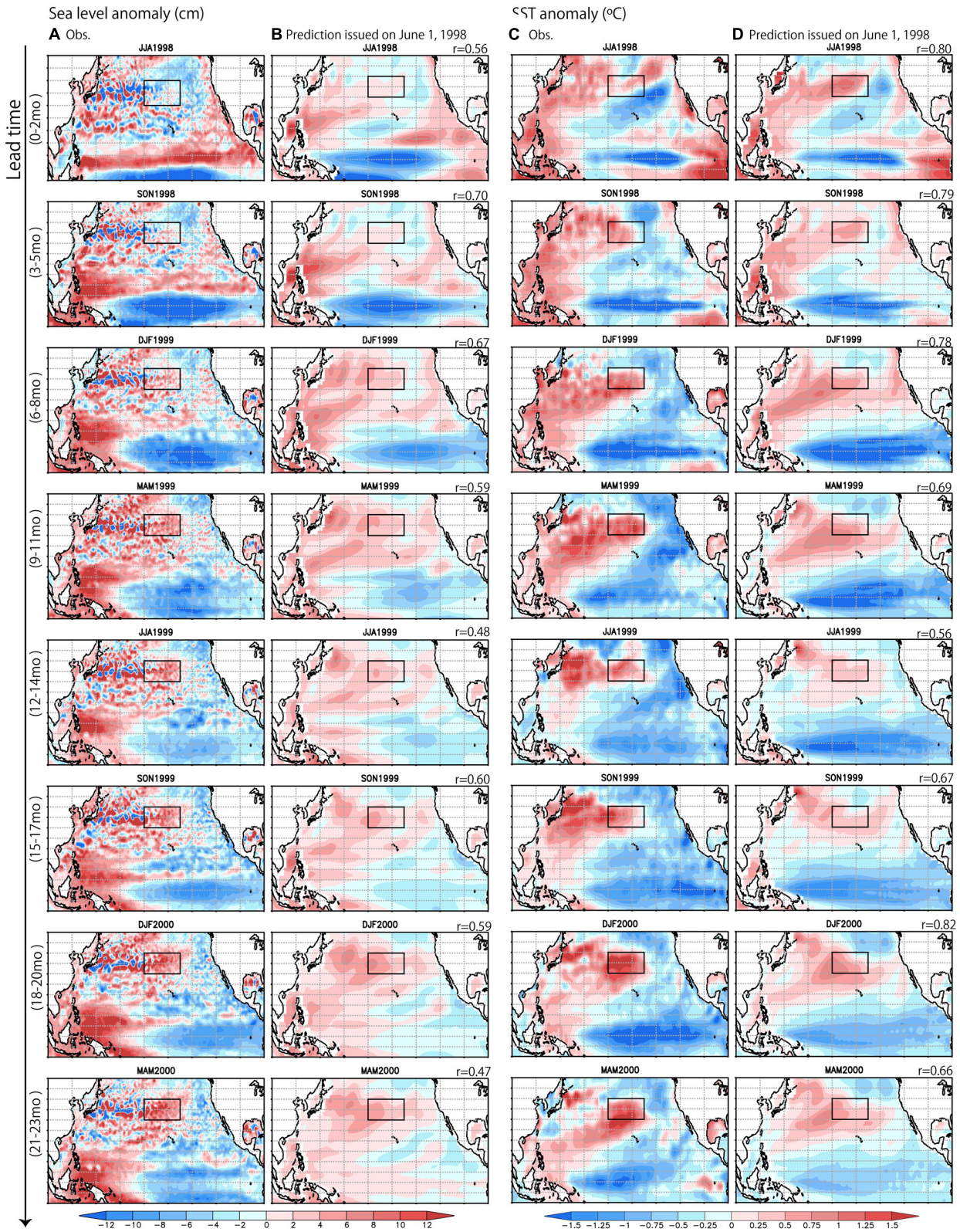

FIGURE 4 | (A) Three-month averaged variations of sea level anomaly (cm) from June–August 1998 (upper) through March–May 2000 (bottom). The box shows the study region of 30°–40°N, 180°–150°W based on observation. **(B)** Same as **(A)**, but for prediction issued on June 1, 1998 (ensemble mean). Pattern correlation is shown in the upper right corner. **(C,D)** Same as **(A,B)**, but for SST (°C).

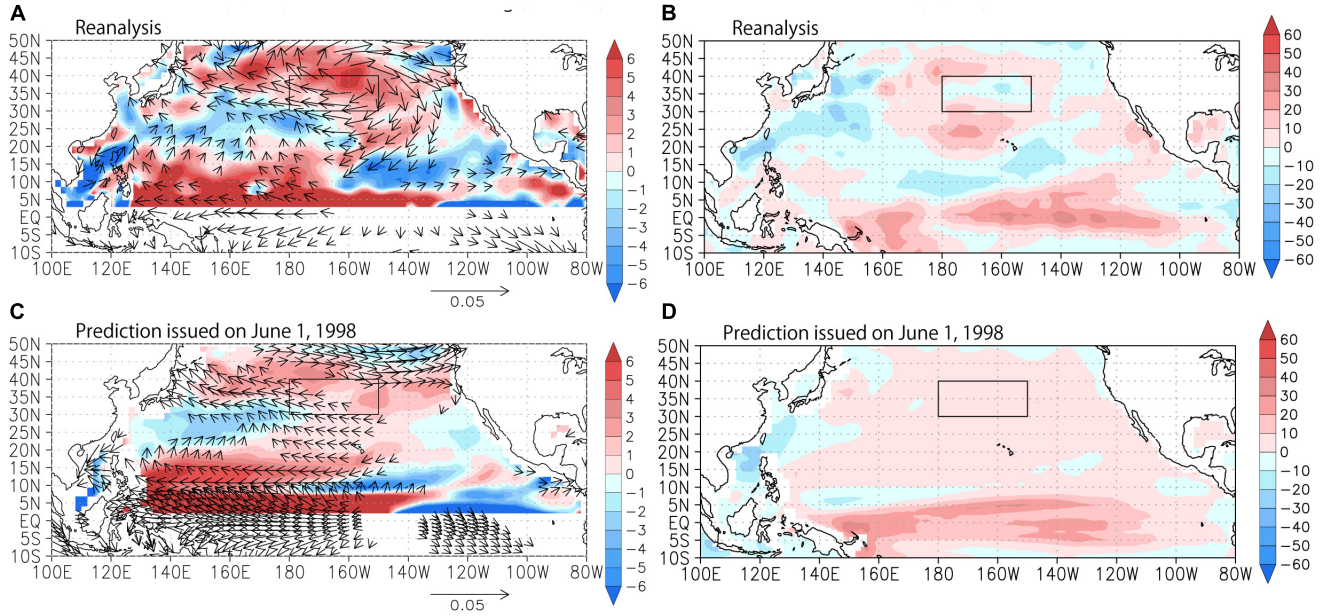

FIGURE 5 | (A) Anomalous surface wind stress (vector: N m^{-2}) and its induced-Ekman vertical velocity (shaded: 10^{-6} m s^{-1}) averaged in June 1998–February 2000 based on the reanalysis data. Positive values show downwelling. The rectangle box demarcates the region of 30°–40°N, 180°–150°W. **(B)** Same as **(A)**, but for surface heat flux (W m^{-2}). Positive values show that it warms ocean. **(C,D)** Same as **(A,B)**, but for prediction issued on June 1, 1998 (ensemble mean).

We see a similar relation with SST anomalies when an ensemble mean of the prediction was considered (**Figure 3D**), which shows the horizontal map of the correlation coefficients between the ensemble mean of the sea level anomalies averaged in the box and the ensemble mean of the SST fields (22 sample: 22 years of the reforecast). However, the correlation with local wind-induced Ekman downwelling does not show a clear relation (**Figure 3E**). Since the signal-to-noise ratio is relatively low in the mid-latitude atmosphere (Scaife and Smith, 2018), the sample size of 22 may not be enough to capture the signal reasonably in the ensemble mean.

Case Study for the 2000 Event

The successful prediction of the high sea level in 2000 (**Figure 2**) demonstrates the model's high skill to predict such events. As in the observations, the sea level anomaly developed from boreal summer of 1998 and reached about 7 cm during March–May 2000. The prediction issued on June 1, 1998, captured the subsequent development in the tropical Pacific and the target region (30°–40°N, 180°W–150°W), albeit a bit weaker than in observations (**Figures 4A,B**). This is supported by the pattern correlations shown in the upper right corner of each panel of **Figure 4B**, which are calculated after interpolating the horizontal distributions of the observational data to those of the prediction output. At 3–5 months lead, the pattern correlation for the sea level prediction is 0.70. At this time, a La Niña Modoki was observed (**Figures 4C,D**) in the tropical Pacific. Then, the pattern correlation reduced at longer lead time, however it is still 0.47 at 21–23 months lead time. Local processes seem to contribute to the variability in 30°–40°N, 180°–150°W relative to remote processes such as a propagation of Rossby waves. Dynamic process associated with the local wind-driven Ekman downwelling may be responsible for that (**Figures 5A,C**), while the heat flux anomaly acted as the damping of the anomaly in the reanalysis (**Figure 5B**) and showed very weak values in the model (**Figure 5D**). Those features are consistent with the results shown by the previous subsection. We note that the signal in the Kuroshio Extension region was not represented well in this prediction system. Nonaka et al. (2016) revealed that stochastic variability in that region limits deterministic potential predictability of its interannual variability through three-member ensemble simulations with an eddy-resolving ocean model. Even if the spatial resolution of the SINTEX-F is enhanced, it might be intrinsically difficult to improve the prediction skill in that region.

DISCUSSION

Sea level anomalies in the region of (30°–40°N, 180°–150°W) may be related to the PDO. The PDO is now interpreted as an empirical mode, which includes teleconnection from ENSO and stochastic atmospheric/oceanic fluctuations (Schneider and Cornuelle, 2005; Newman et al., 2016). Decadal or longer timescale signals appear also to be important for the 2000 event. About 50% of the sea level anomaly averaged over 30°–40°N, 180°–150°W during March-April-May 2000 is due to the decadal signal in the prediction (**Figure 2**). Actually, 2000 is an extreme year for decadal variations in the IPO index and also basin-wide

sea level in the Pacific (see **Figure 3** in Lyu et al., 2017), which is closely related to the ENSO-like low-frequency variability. Although low-frequency sea level variations with periods longer than interannual time scales are interesting, it might be difficult to clearly separate the interannual variations from the decadal and longer timescale variations mainly due to limitation of the sample size and the lead time of the reforecast experiments. Although the focus of this study is on seasonal-to-interannual scale prediction, in the future, we may need to develop skillful seamless prediction abilities from seasonal-to-decadal (S2D) timescale.

Tropical and North Pacific processes are interlinked, which means that the North Pacific processes might also contribute to ENSO predictability (e.g., Ogata et al., 2019). The build-up of subsurface ocean heat content in the tropical western Pacific as well as the northeastern subtropical Pacific is identified as ENSO precursors (Capotondi et al., 2015; Yu and Paek, 2015). Chikamoto et al. (2015) also showed that the low-frequency trans-basin tropical climate variations between the Pacific and the other two adjacent ocean basins can be predicted up to 3 years ahead. Further studies are necessary to estimate the role of the inter-basin coupling on multi-year predictability of the tropical and North Pacific using partial assimilation reforecast experiments.

Since our results are based on a single-model system, we need to check them by a multi-model ensemble system (e.g., Kirtman et al., 2014; Tompkins et al., 2017; Widlansky et al., 2017).

A noble path to systematic and synergistic prediction of marine ecosystem variations may be to develop an earth system model, to incorporate biogeochemical processes into a climate model to represent the interacting physical, chemical, and biological processes. It can provide outlooks for marine-resource–relevant changes beyond physical variables. Along this line, Park et al. (2019) showed that an earth system model can skillfully predict seasonal to multiannual chlorophyll fluctuations in many regions.

Although predictability of open-ocean anomalies was the focus in this study, its connection to coastal sea level is also important. However, it is still challenging to resolve the complicated topography near the coastal regions for the resolution used in current climate models. Therefore, downscaling techniques are helpful to capture the open-ocean and coastal region connections (e.g., Jacox et al., 2020) in a manner similar to successful examples for atmospheric downscaling (e.g., Ratnam et al., 2016, 2017).

Enhancement of the relatively coarse ocean model grid will help to resolve more accurately some islands and narrow upwelling regions. Higher resolution in the atmospheric model may also help to improve winds that are an important component of the ENSO teleconnection. In addition, the accuracy should be improved by better initial conditions by explicit use of altimeter data and *in situ* subsurface ocean temperature and salinity observation from the expendable bathythermographs (XBTs), mooring buoys, sea stations, Argo floats, etc. Increasing the ensemble size may be beneficial for improving prediction of the extratropics, where the signal-to-noise ratio is relatively low. Actually, we have been developing the new version of the SINTEX-F prediction system called as SINTEX-F2 based on a high-resolution model by updating the initialization scheme and increasing the ensemble size (Doi et al., 2016, 2017, 2019, 2020a; Morioka et al., 2019). However, because the computational cost is expensive, the SINTEX-F2 mainly targets for prediction up to 11-month lead time at this stage. We are now extending the lead time up to 23 months because its benefit was shown in this paper.

CONCLUSION

We assessed the prediction skill of sea level anomaly up to 23 months in advance by the SINTEX-F system and found a skillful prediction region in the North Pacific (30–40 N, 180–150 W) at about 2-year lead. The successful prediction of the long-lasting ENSO/ENSO-Modoki in the tropical Pacific seems to contribute to that sea level predictability. The result may be useful to attempt systematic and synergistic prediction of marine ecosystem responses to regional and global climate variations.

DATA AVAILABILITY STATEMENT

The datasets generated for this study can be found in the online repositories. The names of the repository/repositories and accession number(s) can be found below: https://fbox.jamstec.go.jp/public/3vnQgARS2EDAjpEBzL10R3qP8jcy2W-xWLfXy5mE7u8Z/m/3x5AD2lA.

AUTHOR CONTRIBUTIONS

TD performed the seasonal prediction experiments, and analyzed the observation data and model prediction outputs. All authors contributed to designing the research, interpreting results, and writing the manuscript.

FUNDING

This research was supported by the JSPS KAKENHI Grant 20K04074.

ACKNOWLEDGMENTS

The SINTEX-F seasonal climate prediction system was run by the Earth Simulator at JAMSTEC (see http://www.jamstec.go.jp/es/en/index.html, for the system overview). We are grateful to Wataru Sasaki, Jing-Jia Luo, Sebastian Masson, Antonio Navarra, and Toshio Yamagata and our European colleagues of INGV/CMCC, L'OCEAN, and MPI for their valuable contributions in developing the prototypes of the systems. We would also like to thank Shoshiro Minobe for his helpful comments and suggestions. The GrADS software was used to create the figures and maps.

REFERENCES

Ashok, K., Behera, S. K., Rao, S. A., Weng, H., and Yamagata, T. (2007). El Niño Modoki and its possible teleconnection. *J. Geophys. Res. Ocean.* 112, 1–27. doi: 10.1029/2006JC003798

Beherea, S. K., and Yamagata, T. (2001). Subtropical SST dipole events in the southern Indian ocean. *Geophys. Res. Lett.* 28, 327–330. doi: 10.1029/2000GL011451

Capotondi, A., Wittenberg, A. T., Newman, M., Di Lorenzo, E., Yu, J. Y., Braconnot, P., et al. (2015). Understanding ENSO diversity. *Bull. Am. Meteorol. Soc.* 96, 921–938. doi: 10.1175/BAMS-D-13-00117.1

Chikamoto, Y., Timmermann, A., Luo, J.-J., Mochizuki, T., Kimoto, M., Watanabe, M., et al. (2015). Skilful multi-year predictions of tropical trans-basin climate variability. *Nat. Commun.* 6:6869. doi: 10.1038/ncomms7869

Di Lorenzo, E., Schneider, N., Cobb, K. M., Franks, P. J. S., Chhak, K., Miller, A. J., et al. (2008). North Pacific Gyre Oscillation links ocean climate and ecosystem change. *Geophys. Res. Lett.* 35, 2–7. doi: 10.1029/2007GL032838

Doi, T., Behera, S. K., and Yamagata, T. (2013). Predictability of the Ningaloo Niño/Niña. *Sci. Rep.* 3:2892. doi: 10.1038/srep02892

Doi, T., Behera, S. K., and Yamagata, T. (2015a). An interdecadal regime shift in rainfall predictability related to the Ningaloo Niño in the late 1990s. *J. Geophys. Res. Ocean.* 120, 1388–1396. doi: 10.1002/2014JC010562

Doi, T., Yuan, C., Behera, S. K., and Yamagata, T. (2015b). Predictability of the California Niño/Niña. *J. Clim.* 28, 7237–7249. doi: 10.1175/JCLI-D-15-0112.1

Doi, T., Behera, S. K., and Yamagata, T. (2016). Improved seasonal prediction using the SINTEX-F2 coupled model. *J. Adv. Model. Earth Syst.* 8, 1847–1867. doi: 10.1002/2016MS000744

Doi, T., Behera, S. K., and Yamagata, T. (2019). Merits of a 108-member ensemble system in ENSO and IOD predictions. *J. Clim.* 32, 957–972. doi: 10.1175/jcli-d-18-0193.1

Doi, T., Behera, S. K., and Yamagata, T. (2020a). Predictability of the super IOD event in 2019 and its link with El Niño Modoki. *Geophys. Res. Lett.* 47:e2019GL086713. doi: 10.1029/2019gl086713

Doi, T., Behera, S. K., and Yamagata, T. (2020b). Wintertime impacts of the 2019 super IOD on East Asia. *Geophys. Res. Lett.* 47:e2020GL089456. doi: 10.1029/2020GL089456

Doi, T., Storto, A., Behera, S. K., Navarra, A., and Yamagata, T. (2017). Improved prediction of the Indian Ocean Dipole Mode by use of subsurface ocean observations. *J. Clim.* 30, 7953–7970. doi: 10.1175/JCLI-D-16-0915.1

Hamlington, B. D., Cheon, S. H., Piecuch, C. G., Karnauskas, K. B., Thompson, P. R., Kim, K. Y., et al. (2019). The dominant global modes of recent internal sea level variability. *J. Geophys. Res. Ocean.* 124, 2750–2768. doi: 10.1029/2018JC014635

Han, W., Stammer, D., Thompson, P., Ezer, T., Palanisamy, H., Zhang, X., et al. (2019). Impacts of basin-scale climate modes on coastal sea level: a review. *Surv. Geophys.* 40, 1493–1541. doi: 10.1007/s10712-019-09562-9568

Hinkel, J., Church, J. A., Gregory, J. M., Lambert, E., Le Cozannet, G., Lowe, J., et al. (2019). Meeting user needs for sea level rise information: a decision analysis perspective. *Earth's Futur.* 7, 320–337. doi: 10.1029/2018EF001071

Hobday, A. J., Maxwell, S. M., Forgie, J., McDonald, J., Darby, M., et al. (2014). Dynamic ocean management: integrating scientific and technological capacity with law, policy and management. *Stanford Environ. Law J.* 33, 125–165.

Jacox, M. G., Alexander, M. A., Siedlecki, S., Chen, K., Kwon, Y., Brodie, S., et al. (2020). Seasonal-to-interannual prediction of U.S. coastal marine ecosystems: forecast methods, mechanisms of predictability, and priority developments. *Prog. Oceanogr.* 183:102307. doi: 10.1016/j.pocean.2020.102307

Jin, E. K., Kinter, J. L., Wang, B., Park, C. K., Kang, I. S., Kirtman, B. P., et al. (2008). Current status of ENSO prediction skill in coupled ocean-atmosphere models. *Clim. Dyn.* 31, 647–664. doi: 10.1007/s00382-008-0397-393

Kalnay, E., Kanamitsu, M., Kistler, R., Collins, W., Deaven, D., Gandin, L., et al. (1996). The NCEP/NCAR 40-year reanalysis project. *Bull. Am. Meteorol. Soc.* 77, 437–471.

Karnauskas, K. B. (2013). Can we distinguish canonical El Niño from Modoki? *Geophys. Res. Lett.* 40, 5246–5251. doi: 10.1002/grl.51007

Kirtman, B. P., Min, D., Infanti, J. M., Kinter, J. L., Paolino, D. A., Zhang, Q., et al. (2014). The North American multimodel ensemble: phase-1 seasonal-to-interannual prediction; phase-2 toward developing intraseasonal prediction. *Bull. Am. Meteorol. Soc.* 95, 585–601. doi: 10.1175/BAMS-D-12-00050.1

Latif, M., Anderson, D., Barnett, T., Cane, M., Kleeman, R., Leetmaa, A., et al. (1998). A review of the predictability and prediction of ENSO. *J. Geophys. Res.* 103, 14375–14393. doi: 10.1029/97JC03413

Lombard, A., Cazenave, A., Le Traon, P. Y., and Ishii, M. (2005). Contribution of thermal expansion to present-day sea-level change revisited. *Glob. Planet. Change* 47, 1–16. doi: 10.1016/j.gloplacha.2004.11.016

Luo, J. J., Masson, S., Behera, S., Delecluse, P., Gualdi, S., Navarra, A., et al. (2003). South Pacific origin of the decadal ENSO-like variation as simulated by a coupled GCM. *Geophys. Res. Lett.* 30, 4–7. doi: 10.1029/2003GL018649

Luo, J. J., Masson, S., Behera, S., Shingu, S., and Yamagata, T. (2005). Seasonal climate predictability in a coupled OAGCM using a different approach for ensemble forecasts. *J. Clim.* 18, 4474–4497. doi: 10.1175/JCLI3526.1

Luo, J. J., Masson, S., Behera, S. K., and Yamagata, T. (2008). Extended ENSO predictions using a fully coupled ocean-atmosphere model. *J. Clim.* 21, 84–93. doi: 10.1175/2007JCLI1412.1

Lyu, K., Zhang, X., Church, J. A., Hu, J., and Yu, J. Y. (2017). Distinguishing the Quasi-decadal and multidecadal sea level and climate variations in the pacific: implications for the ENSO-like low-frequency variability. *J. Clim.* 30, 5097–5117. doi: 10.1175/JCLI-D-17-0004.1

Ma, J., Xie, S. P., and Xu, H. (2017). Contributions of the North Pacific meridional mode to ensemble spread of ENSO prediction. *J. Clim.* 30, 9167–9181. doi: 10.1175/JCLI-D-17-0182.1

Mantua, N. J., Hare, S. R., Zhang, Y., Wallace, J. M., and Francis, R. C. (1997). A pacific interdecadal climate oscillation with impacts on salmon production. *Bull. Am. Meteorol. Soc.* 78, 1069–1079. doi: 10.1175/1520-0477(1997)078<1069:apicow>2.0.co;2

Masson, S., Luo, J. J., Madec, G., Vialard, J., Durand, F., Gualdi, S., et al. (2005). Impact of barrier layer on winter-spring variability of the southeastern Arabian Sea. *Geophys. Res. Lett.* 32, 1–4. doi: 10.1029/2004GL021980

McGowan, J. A., Cayan, D. R., and Dorman, L. R. M. (1998). Climate-ocean variability and ecosystem response in the Northeast Pacific. *Science* 281, 210–217. doi: 10.1126/science.281.5374.210

McIntosh, P. C., Church, J. A., Miles, E. R., Ridgway, K., and Spillman, C. M. (2015). Seasonal coastal sea level prediction using a dynamical model. *Geophys. Res. Lett.* 42, 6747–6753. doi: 10.1002/2015GL065091

Meehl, G. A., Goddard, L., Boer, G., Burgman, R., Branstator, G., Cassou, C., et al. (2014). Decadal climate prediction an update from the trenches. *Bull. Am. Meteorol. Soc.* 95, 243–267. doi: 10.1175/BAMS-D-12-00241.1

Miles, E. R., Spillman, C. M., Church, J. A., and McIntosh, P. C. (2014). Seasonal prediction of global sea level anomalies using an ocean–atmosphere dynamical model. *Clim. Dyn.* 43, 2131–2145. doi: 10.1007/s00382-013-2039-2037

Morioka, Y., Doi, T., Iovino, D., Masina, S., and Behera, S. K. (2019). Role of sea-ice initialization in climate predictability over the Weddell Sea. *Sci. Rep.* 9, 1–11. doi: 10.1038/s41598-019-39421-w

Newman, M., Alexander, M. A., Ault, T. R., Cobb, K. M., Deser, C., Di Lorenzo, E., et al. (2016). The pacific decadal oscillation, revisited. *J. Clim.* 29, 4399–4427. doi: 10.1175/JCLI-D-15-0508.1

Nicholls, R. J., and Cazenave, A. (2010). Sea-level rise and its impact on coastal zones. *Science* 328, 1517–1520. doi: 10.1126/science.1185782

Nicholls, R. J., Wong, P. P., Burkett, V. R., Codignotto, J. O., Hay, J. E., and McLean, R. F. (2007). "Coastal systems and low-lying areas," in *Climate Change 2007: Impacts, Adaptation and Vulnerability. Contribution of Working Group II to the Fourth Assessment Report of the Intergovernmental Panel on Climate Change*, eds M. L. Parry, O. F. Canziani, J. P. Palutikof, P. J. van der Linden, and C. E. Hanson (Cambridge: Cambridge University Press), 315–356.

Nonaka, M., Sasai, Y., Sasaki, H., Taguchi, B., and Nakamura, H. (2016). How potentially predictable are midlatitude ocean currents? *Sci. Rep.* 6:20153. doi: 10.1038/srep20153

Ogata, T., Doi, T., Morioka, Y., and Behera, S. (2019). Mid-latitude source of the ENSO-spread in SINTEX-F ensemble predictions. *Clim. Dyn.* 52, 2613–2630. doi: 10.1007/s00382-018-4280-4286

Park, J., Stock, C. A., Dunne, J. P., Yang, X., and Rosati, A. (2019). Seasonal to multiannual marine ecosystem prediction with a global Earth system model. *Science* 288, 284–288. doi: 10.1126/science.aav6634

Payne, M. R., Hobday, A. J., MacKenzie, B. R., Tommasi, D., Dempsey, D. P., Fässler, S. M. M., et al. (2017). Lessons from the first generation of marine ecological forecast products. *Front. Mar. Sci.* 4:289. doi: 10.3389/fmars.2017.00289

Polkova, I., Köhl, A., and Stammer, D. (2015). Predictive skill for regional interannual steric sea level and mechanisms for predictability. *J. Clim.* 28, 7407–7419. doi: 10.1175/JCLI-D-14-00811.1

Ratnam, J. V., Behera, S. K., Doi, T., Ratna, S. B., and Landman, W. A. (2016). Improvements to the WRF seasonal hindcasts over South Africa by bias correcting the driving sintex-F2v CGCM fields. *J. Clim.* 29, 2815–2829. doi: 10.1175/JCLI-D-15-0435.1

Ratnam, J. V., Doi, T., and Behera, S. K. (2017). Dynamical downscaling of SINTEX-F2v CGCM seasonal retrospective austral summer forecasts over Australia. *J. Clim.* 30, 3219–3235. doi: 10.1175/JCLI-D-16-0585.1

Rebert, J. P., Donguy, J. R., Eldin, G., and Wyrtki, K. (1985). Relations between sea level, thermocline depth, heat content, and dynamic height in the tropical Pacific Ocean. *J. Geophys. Res.* 90, 11719–11725. doi: 10.1029/jc090ic06p11719

Reynolds, R. W., Rayner, N. A., Smith, T. M., Stokes, D. C., and Wang, W. (2002). An improved in situ and satellite SST analysis for climate. *J. Clim.* 15, 1609–1625. doi: 10.1175/1520-0442(2002)015<1609:aiisas>2.0.co;2

Roberts, C. D., Calvert, D., Dunstone, N., Hermanson, L., Palmer, M. D., and Smith, D. (2016). On the drivers and predictability of seasonal-to-interannual variations in regional sea level. *J. Clim.* 29, 7565–7585. doi: 10.1175/JCLI-D-15-0886.1

Scaife, A. A., and Smith, D. (2018). A signal-to-noise paradox in climate science. *npj Clim. Atmos. Sci.* 1:28. doi: 10.1038/s41612-018-0038-34

Schneider, N., and Cornuelle, B. D. (2005). The forcing of the Pacific Decadal Oscillation. *J. Clim.* 18, 4355–4373. doi: 10.1175/JCLI3527.1

Smith, D. M., Eade, R., Scaife, A. A., Caron, L.-P., Danabasoglu, G., DelSole, T. M., et al. (2019). Robust skill of decadal climate predictions. *npj Clim. Atmos. Sci.* 2, 1–10. doi: 10.1038/s41612-019-0071-y

Stock, C. A., Pegion, K., Vecchi, G. A., Alexander, M. A., Tommasi, D., Bond, N. A., et al. (2015). Seasonal sea surface temperature anomaly prediction for coastal ecosystems. *Prog. Oceanogr.* 137, 219–236. doi: 10.1016/j.pocean.2015.06.007

Tommasi, D., Stock, C. A., Alexander, M. A., Yang, X., Rosati, A., and Vecchi, G. A. (2017a). Multi-annual Climate predictions for fisheries: an assessment of skill of sea surface temperature forecasts for large marine ecosystems. *Front. Mar. Sci.* 4:201. doi: 10.3389/fmars.2017.00201

Tommasi, D., Stock, C. A., Hobday, A. J., Methot, R., Kaplan, I. C., Eveson, J. P., et al. (2017b). Managing living marine resources in a dynamic environment: the role of seasonal to decadal climate forecasts. *Prog. Oceanogr.* 152, 15–49. doi: 10.1016/j.pocean.2016.12.011

Tompkins, A. M., Ortiz, de Zárate, M. I., Saurral, R. I., Vera, C., Saulo, C., et al. (2017). The climate-system historical forecast project: providing open access to seasonal forecast ensembles from centers around the globe. *Bull. Am. Meteorol. Soc.* 98, 2293–2301. doi: 10.1175/BAMS-D-16-0209.1

Vimont, D. J. (2005). The contribution of the interannual ENSO cycle to the spatial pattern of decadal ENSO-like variability. *J. Clim.* 18, 2080–2092. doi: 10.1175/JCLI3365.1

Widlansky, M. J., Marra, J. J., Chowdhury, M. R., Stephens, S. A., Miles, E. R., Fauchereau, N., et al. (2017). Multimodel ensemble sea level forecasts for tropical Pacific Islands. *J. Appl. Meteorol. Climatol.* 56, 849–862. doi: 10.1175/JAMC-D-16-0284.1

Yu, J.-Y., and Paek, H. (2015). Precursors of ENSO beyond the tropical Pacific. *US CLIVAR Var.* 13, 15–20.

Yuan, C., Tozuka, T., Luo, J. J., and Yamagata, T. (2014). Predictability of the subtropical dipole modes in a coupled ocean-atmosphere model. *Clim. Dyn.* 42, 1291–1308. doi: 10.1007/s00382-013-1704-1701

Zainuddin, M., Farhum, A., Safruddin, S., Selamat, M. B., Sudirman, S., Nurdin, N., et al. (2017). Detection of pelagic habitat hotspots for skipjack tuna in the gulf of bone-flores sea, southwestern Coral Triangle tuna. Indonesia. *PLoS One* 12:e0185601. doi: 10.1371/journal.pone.0185601

Zhang, X., and Church, J. A. (2012). Sea level trends, interannual and decadal variability in the Pacific Ocean. *Geophys. Res. Lett.* 39, 1–8. doi: 10.1029/2012GL053240

Zhang, Y., Wallace, J. M., and Battisti, D. S. (1997). ENSO-like interdecadal variability: 1900-93. *J. Clim.* 10, 1004–1020. doi: 10.1175/1520-0442(1997)010<1004:eliv>2.0.co;2

Conflict of Interest: The authors declare that the research was conducted in the absence of any commercial or financial relationships that could be construed as a potential conflict of interest.

frontiers in Marine Science

ORIGINAL RESEARCH
published: 30 October 2020
doi: 10.3389/fmars.2020.557940

Identification of Shared Spatial Dynamics in Temperature, Salinity, and Ichthyoplankton Community Diversity in the California Current System With Empirical Dynamic Modeling

Peter T. Kuriyama[1,2], George Sugihara[1], Andrew R. Thompson[2] and Brice X. Semmens[1]*

[1] Scripps Institution of Oceanography, University of California, San Diego, La Jolla, CA, United States, [2] Fisheries Resources Division, Southwest Fisheries Science Center, National Marine Fisheries Service, National Oceanic and Atmospheric Administration, La Jolla, CA, United States

OPEN ACCESS

Edited by:
Antonietta Capotondi, University of Colorado Boulder, United States

Reviewed by:
Aneesh Subramanian, University of Colorado Boulder, United States
Hui Liu, Texas A&M University, United States

***Correspondence:**
Peter T. Kuriyama
peter.kuriyama@noaa.gov

Specialty section:
This article was submitted to Marine Fisheries, Aquaculture and Living Resources, a section of the journal Frontiers in Marine Science

Received: *30 April 2020*
Accepted: *25 September 2020*
Published: *30 October 2020*

Citation:
Kuriyama PT, Sugihara G, Thompson AR and Semmens BX (2020) Identification of Shared Spatial Dynamics in Temperature, Salinity, and Ichthyoplankton Community Diversity in the California Current System With Empirical Dynamic Modeling. Front. Mar. Sci. 7:557940. doi: 10.3389/fmars.2020.557940

Identifying spatially shared dynamics is a key component of community ecology studies as they provide evidence of common responses to environmental factors. We apply co-prediction, an empirical dynamic modeling method (EDM), where values in one time series are predicted from another to quantify shared dynamics in the California Cooperative Fishery Oceanographic Investigation (CalCOFI) dataset composed of spatially explicit physical and biological measurements. Co-prediction can arise in the absence of correlation between two time series. The survey dates to 1951 and consists of a semi-regular, fixed-station design off the west coast of the USA. While the California Current is a dynamic system with multiple identified regimes, we found evidence of coherence measured in terms of spatially shared dynamics in salinity, temperature, Shannon index of ichthyoplankton abundance, and single-species ichthyoplankton abundance throughout the CalCOFI survey area. Leave-one-out hindcast skill, without including any knowledge of shared dynamics was significant in 27 stations for salinity data, 36 for temperature data, and 33 for Shannon index (out of 81 total stations). We then evaluated hindcast skill when including shared dynamics via composite libraries, in which correlated or co-predicted time series are concatenated to produce denser attractors. The number of correlated stations was generally higher than the number of co-predicted stations, but hindcast skill from composite libraries of correlated stations did not increase hindcast skill. Composite libraries of co-predicted stations had significant leave-one-out hindcast skill in 60 stations for salinity data, 60 for temperature, and 72 for Shannon index. Additionally, we found evidence of nonlinear relationships, as nonlinear hindcasts accounted for nearly all of these significant stations. While there were high levels of correlation among stations, co-prediction proved a more robust method of identifying shared dynamics. Shared dynamics were largely concentrated

south of Point Conception, considered an oceanographic and biological breakpoint, although in some cases shared dynamics spanned this boundary. Taken together, we apply EDM to present the first, to our knowledge, evaluation of station-specific hindcast skill and provide a view of the realized spatial structure occurring in the physical and biological dynamics of the California Current system.

Keywords: California Current, empirical dynamic modeling, ocean observing, synchrony, community diversity

INTRODUCTION

One main objective of ecology is to understand how the environment influences biological organisms from individual to ecosphere scales, and identification of shared dynamics or synchrony across space and time is a valuable tool for achieving this goal (Hsieh et al., 2005). For example, marine fish populations shift distributions in response to ocean warming (Pinsky et al., 2013), and this kind of knowledge is necessary to inform resilient fisheries management (Wilson et al., 2018) or ecosystem-based fisheries management (Pikitch et al., 2004). Application of modern statistical analyses have the capacity to further understanding of synchronous dynamics and holds the potential to improve forecasting (Sugihara et al., 2012). Augmenting forecasting skill is paramount to effective marine management and is particularly important in times of rapid environmental change (Jacox et al., 2020).

The abundance of species can fluctuate in response to combinations of abiotic and biotic factors, and these dynamics can be shared across species-specific populations in space and time. Ecological studies have focused on identifying patterns of synchrony, defined to be shared fluctuations between time series of population abundance. Synchrony exists for species across a spectrum of sizes ranging from protists (Holyoak and Lawler, 1996), insects (Williams and Liebhold, 2000; Tobin and Bjørnstad, 2003), fish (Myers et al., 1995, 1997; Fromentin et al., 2000), and birds (Bellamy et al., 2003). In terrestrial and marine systems, synchrony between two populations decreases as a function of distance (Ranta et al., 1995; Sutcliffe et al., 1996; Bjørnstad et al., 1999), and estimation of this decay is a key component of spatiotemporal models (Cressie and Wikle, 2015; Thorson et al., 2015).

Synchrony can be quantified with parametric statistical methods (Gouhier and Guichard, 2014), and the specific definition of synchrony can depend on methodology (Liebhold et al., 2004). For the most part, parametric methods involve computing some metric (e.g., correlation, variance, or semivariance) between two time series (Bjørnstad et al., 1999; Koenig, 1999). Spatial synchrony is measured by relating the calculated metric to the geographic distances between survey sites. Analysis of residual correlation is one approach of relating synchrony to environmental changes (Buonaccorsi et al., 2001). Analysts will fit a model to the data, e.g., autoregressive models or linear models, then quantify correlations between residuals. Correlated residuals suggest that both time series experienced a common response to an external (e.g., environmental) factor (Buonaccorsi et al., 2001). The challenge with this approach is that correlated residuals may be the result of model misspecification, which is difficult to identify.

Empirical dynamic modeling (EDM) is a non-parametric analytic method that may be an alternative method to quantify shared dynamics without requiring assumptions of independence or statistical distributions. Broadly, the EDM approach focuses on identifying the factors that govern dynamics in natural systems. Takens' theorem of time-delay embedding, a key component of EDM, demonstrates that lags of a single time series can reconstruct the dynamics of the unobservable system (Takens, 1981). This approach primarily distinguishes between observational noise and chaotic dynamics, but has proven applicable to ecological systems. Prediction with EDM outperforms parametric predictions in simulated chaotic ecological systems (Perretti et al., 2013a,b; Munch et al., 2017), and improves forecast skill in salmon runs (Ye et al., 2015) and fish recruitment (Munch et al., 2018). The methods also identify causal relationships between sardine landings and sea surface temperature (Deyle et al., 2013).

Time series can be synchronous even when not fluctuating in unison, and EDM can identify shared dynamics in the absence of traditional correlation (Sugihara et al., 2012). Co-prediction is a method of identifying time series driven by the same forces in ways that are not readily apparent. Technically, co-prediction involves predicting values of one time series from another time series. If predictions are significant (see methods for significance criteria), the time series are assumed to have dynamic similarity. Applications of co-prediction can identify interspecific dynamics (Liu et al., 2012) and relationships between fish populations and environmental covariates (Liu et al., 2014).

In addition to identifying synchrony, correlation and co-prediction can inform forecasting through composite libraries. Composite libraries are a means of using spatial replicates of comparatively short time series to understand system dynamics (Hsieh et al., 2008), but potentially have the same benefits for longer time series. Composite libraries are composed of multiple time series concatenated together. Individual time series that contain as few as five observations can form composite libraries that detect causal relationships in simulated data with both observation and process error (Clark et al., 2015). In an *in vivo* ecological setting, composite libraries can identify the shared dynamics of albacore (*Thunnus alalunga*) across the North Pacific Ocean (Glaser et al., 2014). Composite libraries may be a powerful approach to improve both hindcasting and forecasting in the California Current ecosystem.

The California Cooperative Oceanographic Fisheries Investigation (CalCOFI) program is among the longest-running

oceanographic surveys in the world (Gallo et al., 2019). The survey has a fixed station design that has at times collected physical oceanographic (e.g., temperature, salinity) and plankton (e.g., zooplankton, ichthyoplankton) samples from southern Baja California, Mexico to Vancouver Island, Canada. However, the most comprehensive temporal coverage ranges from the US-Mexico border to the San Francisco Bay area extending from the nearshore to roughly 500 km offshore (Gallo et al., 2019). Although the original intent of CalCOFI was to better elucidate the factors causing the collapse of the Pacific sardine population in the 1940s (Hewitt, 1988), data from the survey now extend beyond fisheries applications and serve as an indicator of overall ecosystem status (Sugihara et al., 2011; Thompson et al., 2018; Harvey et al., 2019). As climate change continues to impact ocean dynamics, CalCOFI is poised to contextualize changes in the California Current Ecosystem (CCE) and help predict changes in fish and zooplankton communities.

The CCE is highly dynamic and characterized by interannual and interdecadal variability (Rykaczewski and Checkley, 2008; Thompson et al., 2018). Distinct water masses mix in the CCE (Bograd et al., 2015), and each body of water is associated with a particular biological community (McClatchie et al., 2018). As a result, fish assemblages fluctuate interannually (McClatchie et al., 2018). The CCE is also subject to larger scale climatic forcing (Thompson et al., 2019). For example, there was a rather abrupt shift from relatively cold to warm conditions in 1976 that induced long-lasting increases in warm water associated fishes in southern California (Peabody et al., 2018). Given the complicated and dynamic nature of physical and biological properties of the CCE, EDM may be a tool to better understand shared dynamics and augment forecasting across the system.

Here, we leverage the rich spatial and temporal resolution of CalCOFI to identify shared dynamics and measure the ability of these similarities to improve hindcast (as a proxy for forecast) prediction skill. We focus on physical (salinity and temperature) and biological time series (species-specific ichthyoplantkon and Shannon index of ichthyoplankton diversity). The goals of this study are both methodological and empirical.

The first methodological goal is to quantify the degree of correlation and co-prediction to identify shared dynamics of physical and biological data among sample stations. The second methodological goal is test whether composite libraries made up of co-predicted time series (significantly predict one time series from another) improve hindcast skill in comparison with composite libraries of correlated sites. Our attempts to improve hindcast skill can serve as a template to conduct forecasts in the future. We hypothesize that there is synchrony in the CalCOFI data and that co-prediction will be a more robust method of identifying shared dynamics than correlation. That is, composite libraries of co-predicted stations will have higher hindcast skill than composite libraries of correlated stations. Notably, we explore synchrony and hindcasting within each variable (e.g., can temperature at station X be predicted by temperature at station Y) but do not search for patterns between variables (e.g., we do not test if temperature can predict fish abundance or diversity).

The ecological goal is to evaluate the extent of shared dynamics within physical and biological time series. We hypothesize that shared dynamics in the physical and biological time series will be mostly localized either north or south of Point Conception, a known biogeographic and oceanographic breakpoint (Hubbs, 1948). Knowledge of both shared dynamics and the spatial scale of dynamics may have important implications for survey design. Depending on the strength of shared dynamics, it may be possible to identify relatively redundant sampling locations to optimize sampling effort.

MATERIALS AND METHODS

Data Preparation

CalCOFI currently collects physical and biological data from each of 104 stations in winter and spring between the United States/Mexico border and San Francisco and 75 stations from the United States/Mexico border to approximately San Luis Obispo in summer and fall (**Figure 1**). Because some stations are sampled more regularly than others, we culled the analysis to include 81 stations (**Figure 1**), with observations spanning from 1951 to 2017. We used observations from winter and spring surveys as the temporal and spatial coverage was highest. CalCOFI shifted from annual to mostly triennial sampling from 1971 to 1983, resulting in no seasonal surveys in some years. Although CalCOFI strives to collect from exactly the same location for a given station, in reality the precise location can vary somewhat from cruise to cruise. Hence, for a particular station, we average observations (see below) within 5 km of a cardinal station location.

CalCOFI samples a myriad of physical factors throughout the water column with a conductivity temperature depth instrument (McClatchie, 2014; Gallo et al., 2019). We focus here on temperature and salinity because these variables are known to impact the distribution and abundance of many marine species (Thompson et al., 2014, 2017). For each station, we calculate mean temperature and salinity between the surface and 100 m and average these means across winter and spring cruises for each station.

The main, long-running CalCOFI biological observations are collected with plankton nets. We focus on ichthyoplankton collected with bongo nets lowered to 210 m (or within 10 m of the bottom at shallow stations) and towed to the surface at a constant speed and at a 45° angle (McClatchie, 2014). Quantifying the abundance of larval fishes is a comprehensive method for assessing the dynamics of most fishes in an ecosystem because although adults occupy different habitats, larval fishes from most species reside in the upper 200 m of the water column and can thus be sampled simultaneously. Several studies demonstrate that ichthyoplankton abundance correlates with the spawning stock biomass of fishes (Moser and Watson, 1990; Moser et al., 2001; Ralston et al., 2003; Ralston and MacFarlane, 2010). CalCOFI plankton samples are preserved at sea in a tris-buffered 5% formalin solution. Ichthyoplankton are identified in a laboratory based on morphology (Moser, 1996). CalCOFI provides time series for hundreds of fishes. Raw larval counts are multiplied by a standard haul factor that accounts for differences in water filtered and divided by the percent of the

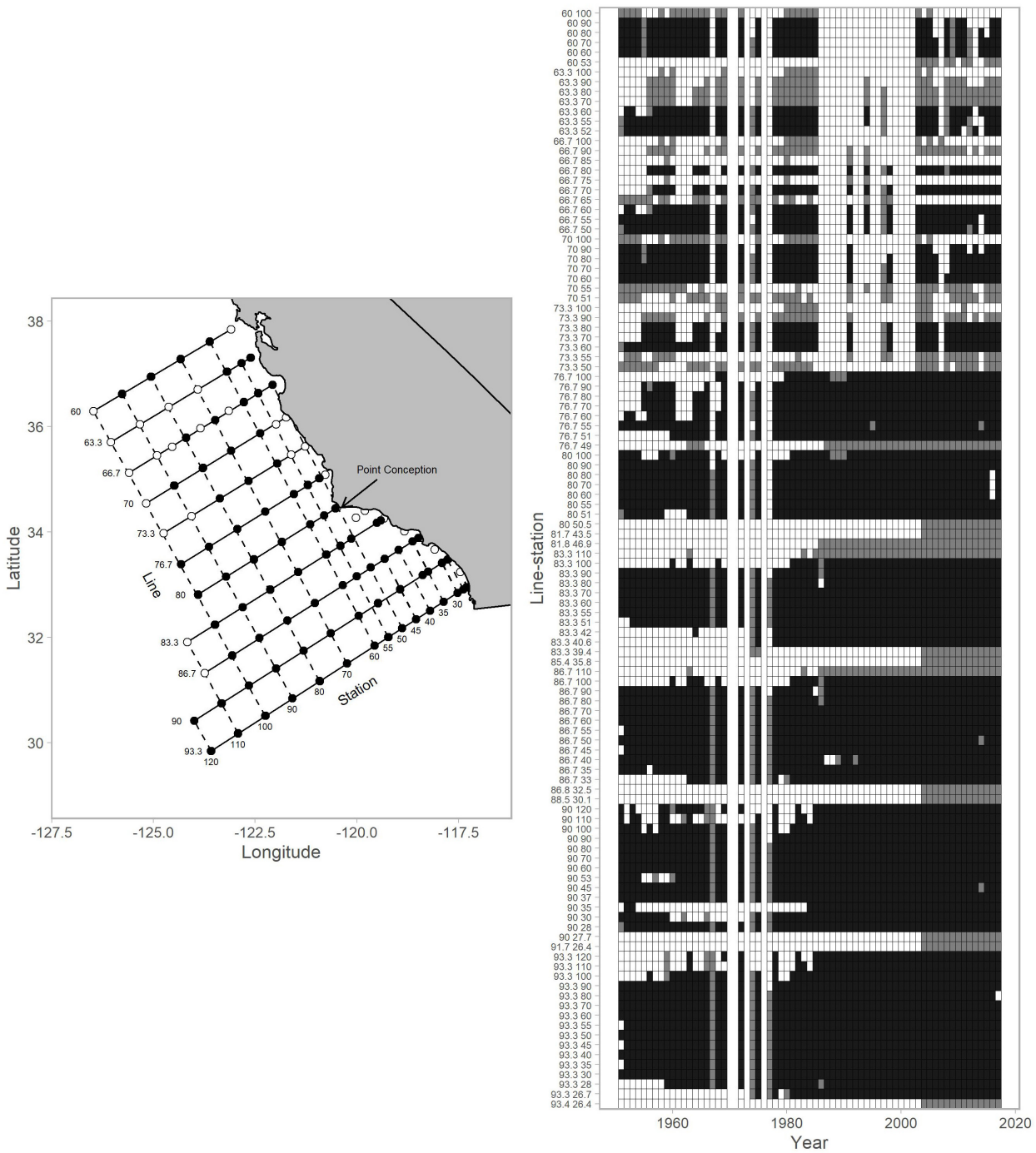

FIGURE 1 | Map of stations within the CalCOFI survey grid and the data availabilities for each individual station (referenced by line-station) for 1951–2017. The map (left column) shows stations used for this analysis (black points) and those that were not (white points). The arrow indicates the location of Point Conception. The data availability plot (right column) shows survey records for years with winter-spring values (black tiles), summer-autumn values (gray tiles; not used in analysis), and no coverage (white tiles). CalCOFI shifted from annual to mostly triennial sampling from 1971–1983 resulting in no surveys in some years. In the early years of CalCOFI, the survey area extended north to British Columbia, Canada and south to Baja California, Mexico (not shown).

samples with high zooplankton volumes are often subsampled (Smith, 1977). Final abundances are expressed as larvae per 10 m^2 surface area. CalCOFI surveys typically sample each of the stations we use in this study 1–4 times per year (**Figure 1**), and we calculate annual averages from winters and springs. Note that CalCOFI shifted from annual to mostly triennial sampling from 1971 to 1983 resulting in no surveys in some years (e.g., 1979).

Many of the fishes in this study share similar adult habitat affinities and are subject to comparable fishing pressure. Both factors are known to comparably and predictably affect fish population dynamics (Hsieh et al., 2005). To evaluate whether fishes in particular groups exhibit similar patterns of synchrony, we assign each taxa to five groups delineated by Hsieh et al. (2005): oceanic-unfished, coastal-fished, coastal-oceanic-fished, coastal-bycatch, and coastal-unfished. For each species, we select time series with at least 25% non-zero values as some species are only rarely observed at particular stations. For example, some mesopelagic fishes are never or very rarely found at shallow, coastal stations.

Finally, we generate time series of single value Shannon diversity index values ($H_{s,t}$) using the equation:

$$H_{s,t} = -\sum_{i=1}^{R} p_{i,s,t} \log\left(p_{i,s,t}\right) \quad (1)$$

at each station (s) in year (t) for species (i). The proportional abundance (p) is multiplied by the natural logarithm of p and summed from species i to the total number of species (R). A single H value was calculated across winter and spring for each year and station. Additionally, the Shannon diversity values were calculated based on all the species reported, which in most cases included additional species to the 36 fish taxa in the single-species analysis. Although we can now identify almost all taxa to species, taxonomic knowledge was less developed at the beginning of CalCOFI. To keep time series used to calculated diversity consistent, we group some species to the 1950s level taxonomic resolution. We use 60 taxa in calculations of Shannon diversity and focus on the 36 most common species for single-species analyses.

Synchrony

We conduct and compare correlational and co-prediction analyses to evaluate synchrony among stations for two physical parameters (temperature and salinity), abundances of 36 fish taxa, and fish diversity. In addition, we evaluate the spatial extent of shared dynamics north and south of Point Conception. Specifically, we quantify the proportion of stations that are significantly synchronous with paired stations within and between northern and southern regions. We follow this analysis by calculating the mean Euclidian distance (km) separating significantly synchronous stations in the north and south. Finally, we assess if synchrony patterns vary among the five fish groups (e.g., ocean-nonfished, coastal-fished). We determine if north-south synchrony patterns differ depending on whether synchrony was assessed with correlation vs. co-prediction analyses.

Correlation

We calculate correlation coefficients (i.e., correlational synchrony) between time series from combinations of station pairs with time lag-0. Our criteria for significance is a statistically significant Spearman's rho coefficient ($p < 0.05$). We do not apply sequential Bonferroni corrections that alleviate type-1 error that can arise with multiple testing because our objective is to compare results from correlation and co-prediction analyses rather than evaluate the significance of any one particular time-series.

Co-prediction

A key step in EDM co-prediction analysis is to identify the dimensionality of the data. In nature, a number of physical and environmental factors drive a population; a time series is a one-dimensional observation of the factors' effects on the population. Fortunately, ecological models do not require analysts to identify all of the factors, rather a comparatively few number of variables can be representative of the dynamics (Schaffer and Kot, 1985). Similarly, Takens' theorem, a tenet of EDM, formalizes this idea that a single time series and some number of lags (dimension; E) are representative of system dynamics (Takens, 1981; Sugihara and May, 1990). Per Takens' theorem, an M-dimensional system converges to a d-dimensional attractor, and a single time series of observations y_t, $t = 1, 2, \ldots, T$ and lagged coordinates of y (at time step τ) $\mathbf{Y_t} = \{y_t, y_{t-\tau}, \ldots, y_{t-E\tau}\}$ can reconstruct the d-dimensional attractor (Takens, 1981). This requires that a time series is sufficiently long to capture attractor dynamics.

Simplex projection (hereafter referred to as simplex) along with sequentially locally weighted global linear maps (s-map) are two key EDM forecasting methods. The distinction is that simplex identifies the dimensionality of the system, and s-map characterizes the data as linear or non-linear (Sugihara, 1994). S-map will generally outperform simplex if system dynamics are non-linear.

We first identify the dimensionality of time series in the CalCOFI dataset with simplex. Simplex projection takes a weighted average of the nearest neighbors' trajectories depending on the specified dimension (E). Given an E, a time series and its E-lagged coordinates, we seek to predict a value $\hat{y}_{t+1}$. In order to predict this value, we use the Euclidean distance $d(y_t, y_s)$ between y_t and y_s and calculate the weights $w_i(t)$ as:

$$w_i(t) = \exp\left(\frac{-d\left(y_t, y_{n(t,i)}\right)}{d\left(y_t, y_{n(t,1)}\right)}\right), \quad (2)$$

where $n(t, i)$ specifies the index of the i-th closest neighbor to $y_{n(t,1)}$. The prediction $\hat{y}_{t+1}$ is:

$$\hat{y}_{t+1} = \frac{\left(\sum_{i=1}^{E+1} w_i(t) y_{n(t,i)+1}\right)}{\sum_{i=1}^{E+1} w_i(t)} \quad (3)$$

We use leave-one-out cross-validation and select the E with the highest correlation between predicted and observed values. We evaluate E values ranging from 1 to 10 and identify the best-fitting E for each time series.

Next, we evaluate co-prediction in which we take the best-fitting E for one time series (library) and predict values in another time series (predictee) with simplex. Co-prediction quantifies the dynamic similarity between time series, and has been used to identify interspecific and species-environment dynamics (Liu et al., 2014) and nonlinearities (Liu et al., 2012) in the

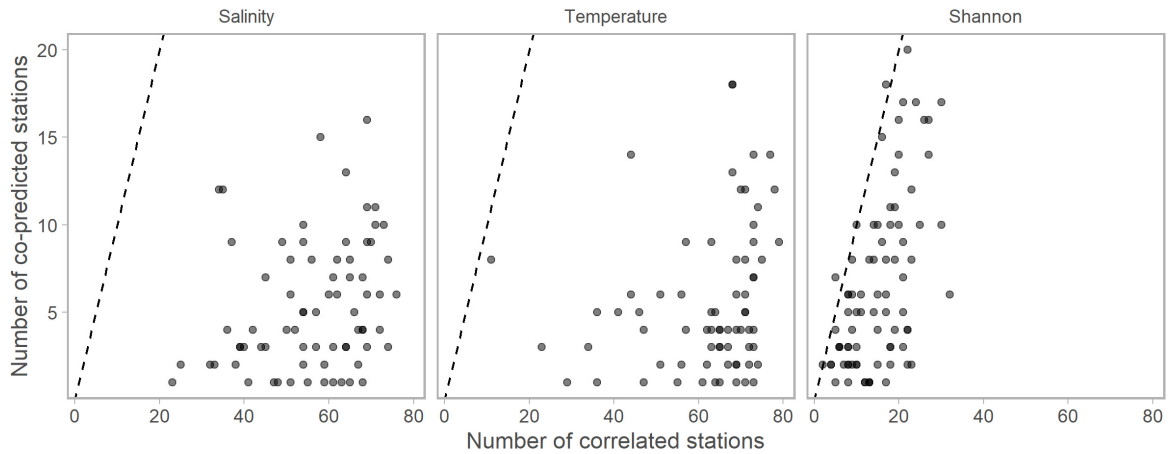

FIGURE 2 | The numbers of significantly correlated vs. numbers of significantly co-predicted stations for salinity, temperature, and Shannon indices of diversity. Each point represents the numbers of each correlated or co-predicted with a particular station (e.g., station A is correlated with 70 stations and co-predicted with 10 stations). Points are slightly transparent to allow overplotting. For nearly all stations, the numbers of correlated stations were higher than the number of co-predicted stations. Dashed lines indicate the one to one line. Composite libraries were composed of correlated or co-predicted stations based on these results.

Northwest Atlantic. We conclude significant co-prediction if there are positive and statistically significant correlations between predicted and observed values ($\rho > 0$; $p < 0.05$) and mean absolute scaled error (MASE) values less than 1. Consider a dataset from timesteps $t = 1, \ldots, n$. We generated a hindcast prediction, F_t, at each timestep. Forecast error was:

$$e_t = Y_t - F_t \tag{4}$$

where Y_t is the observation at time t. Scaled error q_t was:

$$q_t = \frac{e_t}{\frac{1}{n-1}\sum_{i=2}^{n} |Y_i - Y_{i-1}|} \tag{5}$$

and MASE was:

$$MASE = mean\left(\left|q_t\right|\right) \tag{6}$$

A MASE value less than 1 indicates that the prediction had lower error than that from a naïve predictor, which uses the prior year value as a prediction (Hyndman and Koehler, 2006). Again, we evaluate co-predictability between stations for each set time series (i.e., salinity, temperature, Shannon index of abundance, and single-species ichthyoplankton) for each station, but do not attempt to conduct co-prediction across sets of time series (e.g., we do not predict salinity from temperature).

Further details on EDM are available in the documentation for the R package "rEDM"[1] and Chang et al. (2017).

Hindcasting

We construct composite libraries (i.e., concatenated time series) of the significantly correlated and significantly co-predicted stations identified here.

We generate hindcast predictions from three data scenarios for each time series. Consider time series A from a specific station for a particular data set (e.g., salinity). We s-map hindcast (leave-one-out) values of time series A from: (1) time series A; (2) the composite library of time series A and time series correlated with A; and (3) the composite library of time series A and time series co-predicted by A. Once again, we replicate these three scenarios for each of the time series but do not attempt comparisons between data sets (e.g., predicting Shannon index from salinity). Our goal here is to quantify the ability of correlated and co-predicted stations to improve hindcast skill.

We use s-map with leave-one-out cross validation to evaluate hindcast skill. S-map is an extension of simplex that has an additional parameter (θ) that controls the strength of nearest-neighbor weighting. S-map can make both linear ($\theta = 0$) and non-linear ($\theta > 0$) predictions (Sugihara, 1994). We select E

TABLE 1 | Percentages of correlated and co-predicted (number of unique station pairs in parantheses) for salinity, temperature, and Shannon index.

	Point Conception	Correlated	Co-predicted
Salinity	Across	35% ($n = 2262$)	38% ($n = 328$)
	N-N	7% ($n = 2262$)	11% ($n = 328$)
	S-S	58% ($n = 2262$)	51% ($n = 328$)
Temperature	Across	38% ($n = 2507$)	36% ($n = 341$)
	N-N	8% ($n = 2507$)	18% ($n = 341$)
	S-S	54% ($n = 2507$)	46% ($n = 341$)
Shannon	Across	18% ($n = 613$)	26% ($n = 430$)
	N-N	17% ($n = 613$)	6% ($n = 430$)
	S-S	65% ($n = 613$)	68% ($n = 430$)

The Point Conception column indicates whether the library and predicted stations crossed (Across), both north (N-N), or both south (S-S) of Point Conception. Generally the highest percentage of relationships were both south of Point Conception. Often correlated stations were commutative (e.g., station A correlated with station B; Station B correlated station A), and pairs like this were only tallied once.

[1]https://github.com/ha0ye/rEDM

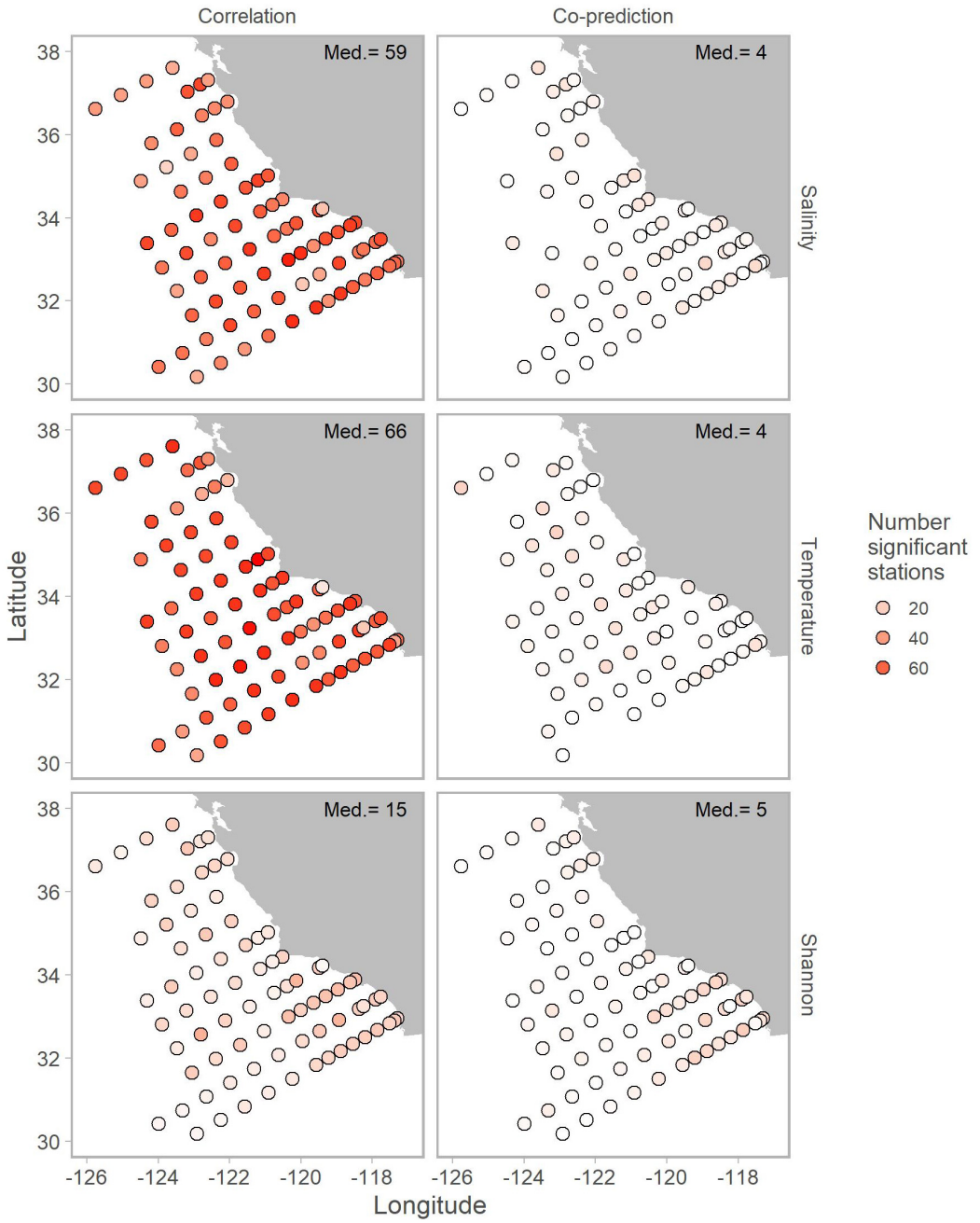

FIGURE 3 | Map of correlated (left column) and co-predicted (right column) stations shown with shades of red. The number of correlated stations was highest for salinity (first row) and temperature (second row). Median number of significant stations are shown in the top right of each panel.

and θ from time series A based on the values that maximize the correlation between the leave-one-out predictions and observations. We then use the E and θ values with s-map to hindcast values for time series A from time series A, correlated composite libraries, and co-predicted composite libraries. The criteria for statistical significance is positive correlations between predicted and observed values ($\rho > 0$, $p < 0.05$) and lower error than that of a naïve prior year predictor (MASE < 1).

RESULTS

Synchrony

We found evidence of synchrony between stations within all time series (salinity, temperature, Shannon index, and 36 single-species ichthyoplankton abundances) with both correlational and co-prediction analyses. Generally, there were many more correlational relationships than

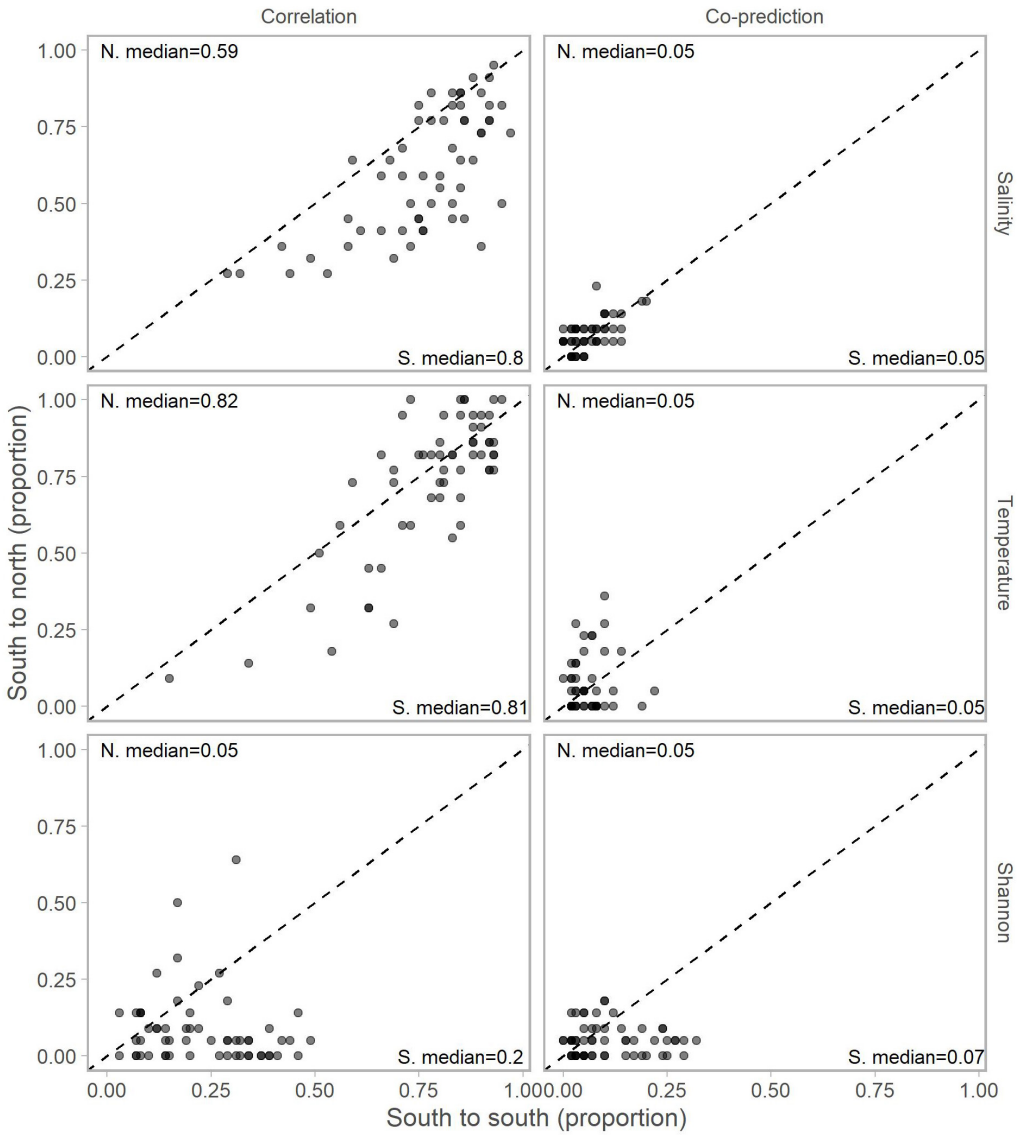

FIGURE 4 | Proportions of south stations correlated (left column) and co-predicted (right column) with stations south (x-axis) and north (y-axis) of Point Conception.There were 59 stations south and 22 stations of Point Conception. Panels show results for the three data types: salinity (top row), temperature (middle row), and Shannon indices (bottom row). The median proportions for predicted stations south (bottom right of each panel) and north (top left of each panel) of Point Conception. The dashed line shows the one-to-one line.

co-predicted relationships (**Figure 2**). Each of the 81 stations was correlated and co-predicted with at least one other station for each of the temperature, salinity, and Shannon index data.

Correlated and co-predicted stations were most concentrated south of Point Conception. A minority of the correlated pairs are north of Point Conception: 7% for salinity, 8% for temperature, and 17% for Shannon index (**Table 1**). We found a similar pattern for co-predicted pairs north of Point Conception: 11% for salinity, 18% for temperature, and 6% for Shannon index (**Table 1**). Note, that 22 of the 81 stations (27%) were located north and 59 of 81 stations (73%) were located south of Point Conception. Generally, stations closer to shore and south had the highest correlation and co-prediction with other stations (**Figure 3**).

Adjusting for the distribution of stations north (22 stations) and south (59) of Point Conception by representing values in terms of proportions (e.g., 10 out of a possible 22 and 12 of a possible 59) for each library station resulted in slightly more balanced relationships across Point Conception. Stations south of Point Conception co-predicted with roughly the same proportions of stations north and south for salinity, temperature, and Shannon index (**Figure 4**). Library stations north of Point Conception were more co-predicted with stations north for salinity and temperature, whereas the proportions for Shannon index were roughly equal (**Figure 5**).

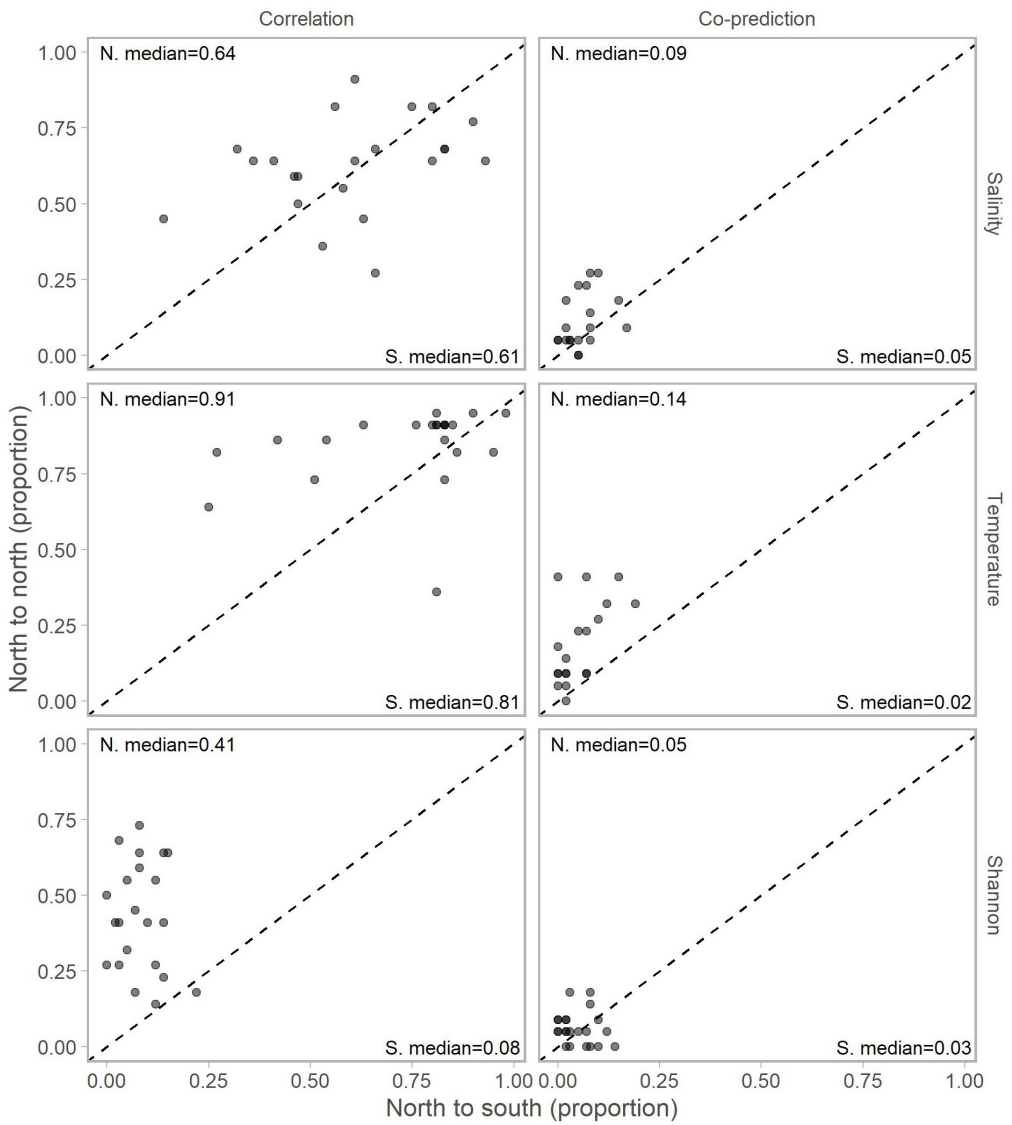

FIGURE 5 | Proportions of north stations correlated (left column) and co-predicted (right column) with stations south (x-axis) and north (y-axis) of Point Conception.There were 59 stations south and 22 stations of Point Conception. Panels show results for the three data types: salinity (top row), temperature (middle row), and Shannon indices (bottom row). The median proportions for predicted stations south (bottom right of each panel) and north (top left of each panel) of Point Conception. The dashed line shows the one-to-one line.

A majority of the predictee stations for single-species ichthyoplankton library stations were concentrated south of Point Conception (**Table 2**). For library stations north of Point Conception, at least half of the predicted stations were south of Point Conception for coastal-oceanic-fished and oceanic species (**Table 2**). For library stations south of Point Conception, at least half of the predicted stations were also south for coastal-fished, coastal-oceanic-fished, and oceanic species categories (**Table 2**).

Composite Libraries

Individual stations showed evidence of hindcast skill. Leave-one-out predictions for a particular time series were significant in 27 stations for salinity, 36 for temperature, and 33 for Shannon index of 81 total stations (**Table 3**).

Composite libraries generally resulted in a greater number of significantly predicted stations. The number of significantly predicted stations from composite libraries of correlated stations was 28 for salinity, 36 for temperature, and 42 for Shannon index (**Table 3**). Predictions from composite libraries of co-predicted stations were significant in 60 stations for salinity, 60 for temperature, and 72 stations for Shannon index (**Table 3**). For salinity and Shannon index, co-prediction was a more robust method of identifying shared dynamics than correlation.

Generally, significant hindcast skill was highest with nonlinear predictions, indicated by θ values greater than 0. Nonlinear

TABLE 2 | Percentages of correlated and co-predicted (number of unique station pairs in parantheses) for individual species grouped by category.

Common name	Scientific name	Pt. Conception	Correlated	Co-predicted
Oceanic				
California flashlightfish	*Protomyctophum* crockeri	Across	36% ($n = 727$)	39% ($n = 364$)
		N-N	9% ($n = 727$)	6% ($n = 364$)
		S-S	55% ($n = 727$)	55% ($n = 364$)
Blue lanternfish	*Tarletonbeania crenularis*	Across	42% ($n = 615$)	54% ($n = 162$)
		N-N	17% ($n = 615$)	20% ($n = 162$)
		S-S	41% ($n = 615$)	26% ($n = 162$)
Northern lampfish	*Stenobrachius leucopsarus*	Across	23% ($n = 455$)	36% ($n = 236$)
		N-N	8% ($n = 455$)	9% ($n = 236$)
		S-S	69% ($n = 455$)	55% ($n = 236$)
Broadfin lampfish	*Nannobrachium spp.*	Across	34% ($n = 443$)	35% ($n = 200$)
		N-N	15% ($n = 443$)	7% ($n = 200$)
		S-S	51% ($n = 443$)	58% ($n = 200$)
Longfin lanternfish	*Diogenichthys atlanticus*	Across		9% ($n = 56$)
		S-S	100% ($n = 153$)	91% ($n = 56$)
Highsnout bigscale	*Melamphaes spp.*	Across	35% ($n = 136$)	41% ($n = 109$)
		N-N	12% ($n = 136$)	9% ($n = 109$)
		S-S	53% ($n = 136$)	50% ($n = 109$)
Mexican lampfish	*Triphoturus mexicanus*	S-S	100% ($n = 104$)	100% ($n = 40$)
California lanternfish	*Symbolophorus californiensis*	Across	7% ($n = 95$)	
		S-S	93% ($n = 95$)	100% ($n = 37$)
Pacific viperfish	*Chauliodus macouni*	Across	52% ($n = 84$)	51% ($n = 43$)
		N-N	18% ($n = 84$)	19% ($n = 43$)
		S-S	30% ($n = 84$)	30% ($n = 43$)
Panama lightfish	*Vinciguerria lucetia*	S-S	100% ($n = 77$)	100% ($n = 13$)
Pacific blacksmelt	*Bathylagus pacificus*	Across	10% ($n = 39$)	12% ($n = 17$)
		N-N	90% ($n = 39$)	82% ($n = 17$)
		S-S		6% ($n = 17$)
Lanternfishes	*Myctophidae spp.*	S-S	100% ($n = 18$)	100% ($n = 9$)
Dogtooth lampfish	*Ceratoscopelus townsendi*	S-S	100% ($n = 16$)	100% ($n = 7$)
Blackbelly dragonfish	*Stomias atriventer*	S-S	100% ($n = 1$)	100% ($n = 6$)
Bluethroat argentine	*Nansenia candida*	Across	100% ($n = 1$)	
Pearly lanternfish	*Myctophum nitidulum*	S-S	100% ($n = 1$)	
Slender lanternfish	*Hygophum reinhardtii*	S-S	100% ($n = 1$)	
Coastal-fished				
Chilipepper	*Sebastes goodei*	Across	42% ($n = 302$)	50% ($n = 147$)
		N-N	23% ($n = 302$)	12% ($n = 147$)
		YS-S	35% ($n = 302$)	38% ($n = 147$)
Cow rockfish (cowcod)	*Sebastes levis*	Across	42% ($n = 302$)	50% ($n = 147$)
		N-N	23% ($n = 302$)	12% ($n = 147$)
		S-S	35% ($n = 302$)	38% ($n = 147$)
Mexican rockfish	*Sebastes macdonaldi*	Across	42% ($n = 302$)	50% ($n = 147$)
		N-N	23% ($n = 302$)	12% ($n = 147$)
		S-S	35% ($n = 302$)	38% ($n = 147$)
Rockfishes	*Sebastes spp.*	Across	42% ($n = 302$)	50% ($n = 147$)
		N-N	23% ($n = 302$)	12% ($n = 147$)
		S-S	35% ($n = 302$)	38% ($n = 147$)
Splitnose rockfish	*Sebastes diploproa*	Across	42% (n=302)	50% ($n = 147$)
		N-N	23% ($n = 302$)	12% ($n = 147$)
		S-S	35% ($n = 302$)	38% ($n = 147$)
Stripetail rockfish	*Sebastes saxicola*	Across	42% ($n = 302$)	50% ($n = 147$)
		N-N	23% ($n = 302$)	12% ($n = 147$)
		S-S	35% ($n = 302$)	38% ($n = 147$)

(Continued)

TABLE 2 | Continued

Common name	Scientific name	Pt. Conception	Correlated	Co-predicted
Bocaccio	*Sebastes paucispinis*	Across	41% ($n = 115$)	45% ($n = 42$)
		N-N	13% ($n = 115$)	14% ($n = 42$)
		S-S	46% ($n = 115$)	41% ($n = 42$)
English sole	*Parophrys vetulus*	Across		33% ($n = 6$)
		N-N		17% ($n = 6$)
		S-S	100% ($n = 2$)	50% ($n = 6$)
Aurora rockfish	*Sebastes aurora*	Across	33% ($n = 3$)	20% ($n = 5$)
		N-N		20% ($n = 5$)
		S-S	67% ($n = 3$)	60% ($n = 5$)
Coastal-oceanic-fished				
Northern anchovy	*Engraulis mordax*	Across	22% ($n = 692$)	23% ($n = 527$)
		N-N	3% ($n = 692$)	2% ($n = 527$)
		S-S	75% ($n = 692$)	75% ($n = 527$)
California smoothtongue	*Leuroglossus stilbius*	Across	31% ($n = 667$)	43% ($n = 166$)
		N-N	9% ($n = 667$)	9% ($n = 166$)
		S-S	60% ($n = 667$)	48% ($n = 166$)
Pacific hake or whiting	*Merluccius productus*	Across	29% ($n = 363$)	36% ($n = 307$)
		N-N	11% ($n = 363$)	6% ($n = 307$)
		S-S	60% ($n = 363$)	58% ($n = 307$)
Jack mackerel	*Trachurus symmetricus*	Across	13% ($n = 239$)	13% ($n = 98$)
		N-N	1% ($n = 239$)	
		S-S	86% ($n = 239$)	87% ($n = 98$)
Pacific sardine (pilchard)	*Sardinops sagax*	S-S	100% ($n = 122$)	100% ($n = 179$)
Medusafish	*Icichthys lockingtoni*	Across	37% ($n = 93$)	44% ($n = 73$)
		N-N	25% ($n = 93$)	28% ($n = 73$)
		S-S	38% ($n = 93$)	28% ($n = 73$)
Coastal-bycatch				
Shortbelly rockfish	*Sebastes jordani*	Across	28% ($n = 101$)	43% ($n = 54$)
		N-N	3% ($n = 101$)	6% ($n = 54$)
		S-S	69% ($n = 101$)	51% ($n = 54$)
Hornyhead turbot	*Pleuronichthys verticalis*	S-S	100% ($n = 1$)	
Coastal-unfished				
Pacific argentine	*Argentina sialis*	Across	33% ($n = 12$)	56% ($n = 9$)
		S-S	67% ($n = 12$)	44% ($n = 9$)

The Point Conception column indicates whether the library and predicted stations crossed (Across), both north (N-N), or both south (S-S) of Point Conception. Generally the highest percentage of relationships were both south of Point Conception.

predictions resulted in significance for roughly 80% of the stations in the single station and composite library scenarios (**Table 3**). For the co-predicted composite library scenario, nonlinear s-map predictions accounted for nearly all the significant results (**Table 3**).

The CalCOFI survey has variable temporal and spatial sampling frequencies due to logistical and financial challenges common to any long-term ecological survey. Stations off northern California in the CalCOFI grid had stretches with no winter and spring surveys. Because we compare s-map predictions to lagged observations, assuming a lagged observation from say 10 years prior may bias MASE calculations. In other words, a poor predictor compared to a lagged observation from many years prior may result in lower MASE values. To control for this, we filtered time series such that the maximum gap was 3 years or less and recalculated MASE. The number of significant stations was relatively unchanged, and the number of significantly co-predicted composite library stations decreased by 1–3 stations (**Supplementary Table 1**).

TABLE 3 | Numbers of significantly predicted stations for salinity, temperature, and Shannon indices of diversity.

	Single station	Correlated composite	Co-predicted composite
Salinity	27 (85% nonlinear)	28 (86%)	60 (97%)
Temperature	36 (83%)	36 (78%)	60 (100%)
Shannon Index	33 (82%)	42 (79%)	72 (99%)

Predictions were made with s-map using either a single station, composite library of correlated stations, or composite library of co-predicted stations. Values in parentheses show the percentage of significant stations with θ values greater than 0 (indicating nonlinearity).

Inclusion of co-predicted stations improved hindcast skill of Shannon index for mostly offshore stations (**Figure 6**).

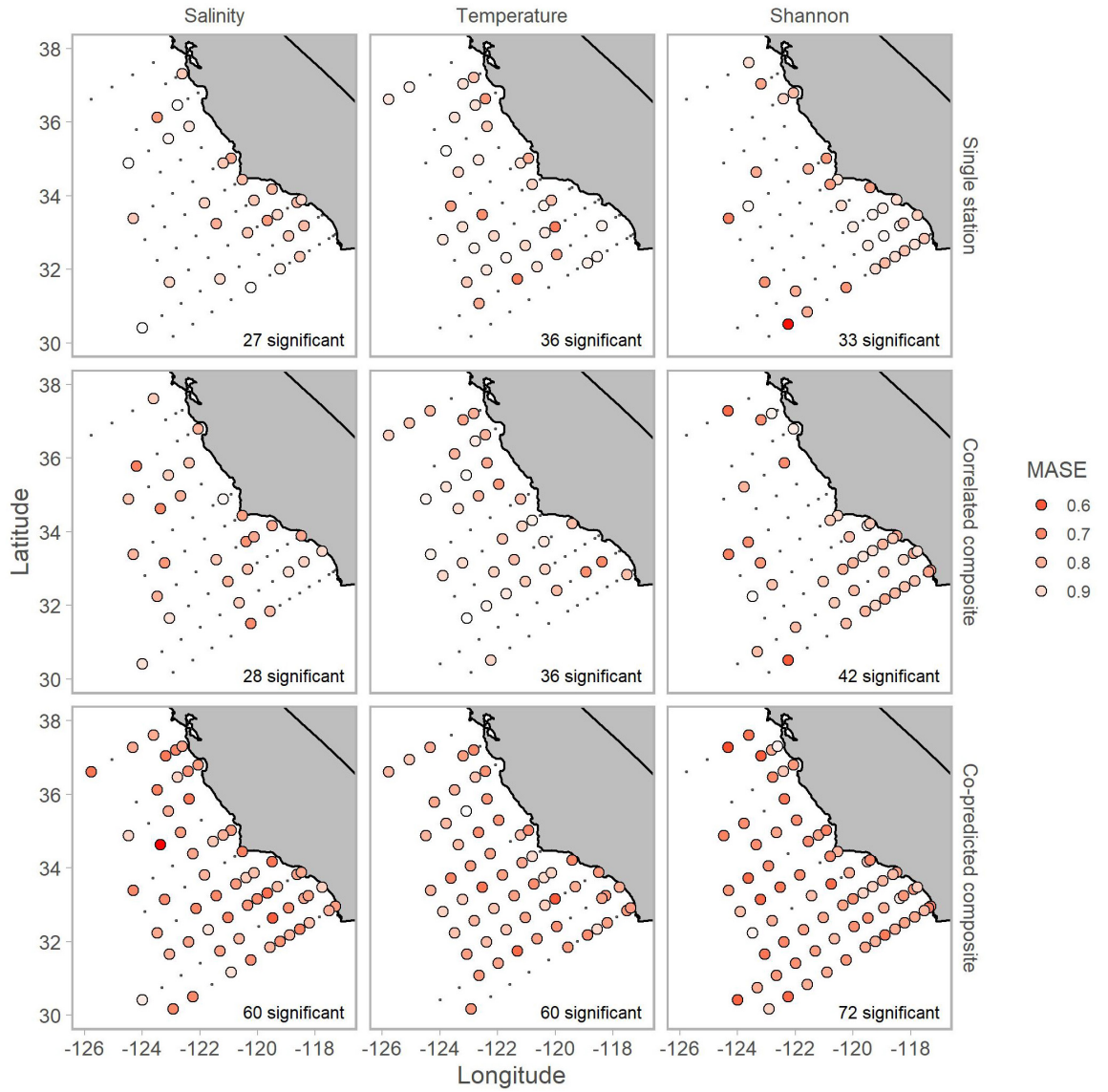

FIGURE 6 | Locations of stations with significant hindcast s-map predictive skill for salinity (left column), temperature (middle column) and Shannon index (right column). Predictions used single station (top row), correlated composite libraries (middle row) and co-predicted composite libraries (bottom row). Shading indicates MASE values. A MASE of 0.6, for example, indicates that the error from s-map predictions is on average 60% of the error from a naïve predictor (i.e., lagged observation). The number of significant stations is shown in the bottom right of each panel.

Additionally, composite libraries resulted in significant predictability for all three of salinity, temperature, and Shannon index in 38 of 81 stations. Although there were some cases, particularly for salinity and Shannon index, where predictions from composite libraries of co-predicted stations had MASE values of 0.6 (indicating that error from predictions was 60% the error from a lagged observation; **Figure 6**).

Prediction for individual species was highest with co-predicted composite libraries. For many species, hindcast skill was highest with composite libraries of co-predicted stations, and this trend was strongest in oceanic and coastal-fished species (**Table 4**).

DISCUSSION

We find evidence of spatially shared dynamics in salinity, temperature, Shannon index, and individual ichthyoplankton species as measured by correlation and co-prediction. Leveraging knowledge of shared dynamics via composite libraries of correlated or co-predicted stations generally improved hindcast skill across all data types. However, although synchrony is more evident from correlation than co-prediction, co-prediction is a more robust method to significantly hindcast salinity, temperature, Shannon index, and nearly all single-species ichthyoplankton. Taken together, we demonstrate the utility of

TABLE 4 | Numbers of significantly predicted stations with s-map prediction for each species, arranged by category.

Category	Common name	Station	Correlation	Co-prediction
Oceanic	California flashlightfish	17	25	42
	Broadfin lampfish	10	11	28
	Pinpoint lampfish	10	11	28
	Blue lanternfish	9	11	20
	Highsnout bigscale	8	3	17
	Little bigscale	8	3	17
	Northern lampfish	4	9	14
	Longfin lanternfish	3	6	10
	Pacific viperfish	5	4	9
	California lanternfish	7	1	6
	Mexican lampfish	4	7	6
	Pacific blacksmelt	2	3	6
	Blackbelly dragonfish	1	0	3
	Panama lightfish	2	4	2
	Dogtooth lampfish	1	1	1
	Pearly lanternfish	1	1	0
	Blackgill rockfish	5	10	11
Coastal-fished	Chilipepper	5	10	11
	Cowcod	5	10	11
	Mexican rockfish	5	10	11
	Splitnose rockfish	5	10	11
	Stripetail rockfish	5	10	11
	Bocaccio	3	4	5
	Northern anchovy	21	28	26
	California smoothtongue	7	13	17
Coastal-oceanic-fished	Pacific hake or whiting	7	7	14
	Pacific sardine	5	10	12
	Medusafish	5	6	9
	Jack mackerel	8	6	7
	Shortbelly rockfish	2	3	1
	Pacific argentine	0	4	2

Columns show predictions from the same predictor station and composite libraries of correlated and co-predicted stations. Composite libraries included correlated or co-predicted stations.

co-prediction in identifying shared dynamics and find evidence of widespread nonlinear spatial structure in physical and biological observations across the CalCOFI survey area. To our knowledge, this study serves as the first evaluation of station-specific hindcast skill of the CalCOFI data set.

Identifying shared dynamics with co-prediction is an important step in constructing composite libraries. Previous studies that implemented composite libraries used all available time series from individual species (Hsieh et al., 2008) or locations (Glaser et al., 2014; Clark et al., 2015). Our results show that identifying shared dynamics with co-prediction is an important step to improve hindcast skill. Longer composite libraries composed of more stations (identified through correlation) did not result in higher hindcast skill than co-predicted stations, with the exception of Shannon index. While we did not explicitly have a scenario of composite libraries with all 81 stations, composite libraries for salinity and temperature mostly included between 70 and 80 correlated stations. Co-prediction quantifies the degree to which two time series are generated from the same underlying process and has the potential to identify relationships in the absence of positive correlation (Engle and Granger, 1987).

We found evidence of nonlinear relationships in the CalCOFI survey data. A majority of the significant results came from nonlinear predictions, with s-map θ values greater than 0, across data types and composite library scenarios. These findings are consistent with previous analyses of CalCOFI data which found nonlinearities in biological time series (Hsieh et al., 2005). These studies utilized out-of-sample forecasting, in contrast to the methods used here, but found that physical time series had high dimensionality and linear dynamics. Thus, it is likely that fish populations have nonlinear responses to environmental forces and have nonlinear relationships across space.

While this study focuses on hindcasting, the methods used here may be extended to out-of-sample forecasting to better identify and predict regime shifts. The transition to out-of-sample forecasting may yield insight to the characteristics of a system undergoing a regime shift. For example, a system undergoing a regime shift may be characterized by a composite library of co-predicted stations undergoing a decrease in forecast skill. Additional indicators may be a shift in the number and orientation of co-predicted stations or a transition between linear and nonlinear dynamics. If analyses extend to include multivariate analyses, there may be time-varying changes in interactions, similar to those identified in Deyle et al. (2016).

The California Current is characterized by physical and biological regimes, and here we show that stations across space demonstrate shared dynamics through multiple regimes over the roughly 70 year span of CalCOFI observations. Studies of principal components in over 100 time series, both physical and biological, found regime shifts in 1976 and 1989 (Ebbesmeyer et al., 1991; Hare and Mantua, 2000). Shifts in the Pacific Decadal Oscillation from a negative to positive phase were hypothesized to precede shifts in biological regimes (McFarlane and Beamish, 2001; Moser et al., 2001). Indeed, a previous study has identified five ichthyoplankton assemblage regimes in analysis of the southern portion of the CalCOFI survey area (Peabody et al., 2018). The combination of co-prediction, composite libraries, and s-map can potentially improve the capability to track system dynamics of a regime change. This work remains to be done but is a logical next step.

We found shared dynamics to be largely concentrated south of Point Conception, although this result may be influenced by skewed station distributions north and south of Point Conception. Point Conception is a well-known biogeographic break within the CCE (Allen et al., 2006) with sharply contrasting water masses north and south of Point Conception (Lynn et al., 2003). Ocean conditions north of Point Conception tend to be dominated by the equatorward-flowing California Current which is cold and relatively fresh as well as cold, salty upwelled water closer to shore that is induced by strong equatorward winds (Checkley and Barth, 2009). As a result, water temperature often increases abruptly south of Point Conception within the Southern California Bight (Checkley and Barth, 2009; Thompson et al.,

2016). Co-prediction identifies shared dynamics between two time series but does not measure causal relationships. Convergent cross mapping (Sugihara et al., 2012) can identify causality between time series, and analyses that apply this method may identify mechanistic relationships between stations. Inclusion of additional oceanographic measurements such as oxygen, phosphate, and silicate may further enhance analyses of the movement and forcing of distinct water masses.

Shannon index have significant hindcast skill in 89% of stations (n = 81). While our focus is on the 60 most-caught taxa (used to calculate Shannon index), our results indicate that there are likely common factors driving shared dynamics across space. Physical conditions cascade to affect zooplankton abundances, which fluctuated in synchrony from 1949 to 1969 (Bernal and McGowan, 1981). Additionally, taxa with similar life histories and adult habitats track each other even when they are uncorrelated with environmental conditions (Hsieh et al., 2005). This is another area of future research, and convergent cross mapping, another EDM method, is one extension to identify causal relationships between populations and environmental conditions or interspecific interactions.

There are multiple possible ecological explanations for the predictability in species like Northern anchovy and bigscales. Recruitment may be an important factor influencing shared ichthyoplankton dynamics in the CalCOFI data. Recruitment generally stabilizes metacommunities (Gouhier et al., 2010, 2011) although the relative levels of recruitment can influence synchrony and stability differently (Townsend and Gouhier, 2019). Additionally, local recruitment synchronizes mussel populations across 1,800 km of coast (Gouhier et al., 2010). The rich time series of available data in the Southern California Bight would allow for analyses relating egg time series (collected on CalCOFI cruises) to ichthyoplankton time series to young-of-year surveys and adult catches to evaluate interactions across all life history stages. EDM works best at predicting recruitment for short-lived, fast-growing species (Munch et al., 2018), and the inclusion of multiple variables may further improve forecast skill. Oceanographic currents in the Southern California Bight have been characterized to identify metapopulation networks (Watson et al., 2011).

While the EDM approach is generally robust to some missing values, additional modeling approaches may not be. The composite library approach has higher predictive skill than using the previous year's value as the forecast. In an analysis of multiple time series forecast methods, this naïve predictor had the highest short-term predictive skill for 2,379 time series of vertebrate population indices (Ward et al., 2014). Shannon index results were likely more predictable as they integrate the year-to-year variability in individual species. Species like bigscales, blue lanternfish, rockfish, Northern anchovy, and Pacific hake all had the most predictable dynamics suggesting that there may be a small number of species driving Shannon index in each year.

Evaluation of out-of-sample predictability was beyond the scope of this study but is a logical next step. Out-of-sample forecasting skill will likely increase if causal relationships exist in the CalCOFI data. Convergent cross mapping (Sugihara et al., 2012) and its spatial applications (Clark et al., 2015) are natural extensions of this analysis and may identify relationships between physical variables like temperature and salinity and biological variables like Shannon index of diversity. The CalCOFI dataset is an ideal dataset for such analysis due to the high spatiotemporal resolution and multiple types of observations. Comparing temperature and salinity directly to ichthyoplankton time series misses key components of the community structure. Likely, there are multiple levels of interactions relating physical conditions to phytoplankton to zooplankton to ichthyoplankton (Thompson et al., 2018). Additionally, analysis may need to adopt a finer temporal scale to identify seasonal drivers. Here, we used averages of physical and biological measurements across winter and spring, which may have smoothed signal in the data. S-map coefficients may elucidate time-varying interactions between biological and physical data sets (Deyle et al., 2016; Ushio et al., 2018). Finally, additional methodologies such as EDM Gaussian processes (Munch et al., 2017; Rogers and Munch, 2020) and regularized s-map (Cenci et al., 2019) may offer improvements in both in-sample and out-of-sample prediction skill.

The analysis we have presented here, and the analytic next steps outlined above, are motivated by both the desire to understand the ecological dynamics of the CCE and the need to identify analytic methods that can support future survey design/reorganization efforts. There are numerous financial and logistical challenges associated with conducting large-scale surveys, and it is difficult to maintain constant sampling efforts year to year. Co-prediction and composite libraries can provide a means of prioritizing survey sites by identifying partial redundancies in the CalCOFI survey grid. In the case that sampling efforts reduce, locations with strongly shared dynamics may be redundant, in that sampling in these areas may not provide additional information. Locations without shared dynamics may be high priorities because they contribute to a more comprehensive survey of an area.

DATA AVAILABILITY STATEMENT

Publicly available datasets were analyzed in this study. This data can be found here: https://calcofi.org/ccdata.html.

AUTHOR CONTRIBUTIONS

PTK, GS, ART, and BXS designed the study. PTK conducted that analysis and wrote the manuscript. GS, ART, and BXS contributed and edited the text. All authors contributed to the article and approved the submitted version.

FUNDING

PTK and BXS received funding from the NOAA Quantitative Ecology and Socioeconomics Training program. GS was supported by DoD-Strategic Environmental Research and Development Program 15 RC-2509, NSF DEB-1655203, NSF ABI-1667584, DOI USDI-NPS P20AC00527, the McQuown

Fund and the McQuown Chair in Natural Sciencies, University of California, San Diego.

ACKNOWLEDGMENTS

We express our deep gratitude to the crews of the CalCOFI research vessels for helping collect the samples, including, but not limited to, David Ambrose, Noelle Bowlin, Sherri Charter, Dave Griffith, Amy Hays, Bryan Overcash, and Sue Manion. Hao Ye, Ethan Deyle, and Chase James provided valuable technical advice regarding EDM analyses. Thanks to the reviewers for providing comments that improved the quality of the manuscript.

SUPPLEMENTARY MATERIAL

The Supplementary Material for this article can be found online at: https://www.frontiersin.org/articles/10.3389/fmars.2020.557940/full#supplementary-material

REFERENCES

Allen, L. G., Pondella, D. J., and Horn, M. H. (2006). *Ecology of Marine Fishes: California and Adjacent Waters*. Berkeley, CA: University of California Press.

Bellamy, P., Rothery, P., and Hinsley, S. (2003). Synchrony of woodland bird populations: the effect of landscape structure. *Ecography* 26, 338–348. doi: 10.1034/j.1600-0587.2003.03457.x

Bernal, P. A., and McGowan, J. A. (1981). *Advection and Upwelling in the California Current. In: Coastal Upwelling*. Washington, DC: American Geophysical Union, 381–399.

Bjørnstad, O. N., Ims, R. A., and Lambin, X. (1999). Spatial population dynamics: analyzing patterns and processes of population synchrony. *Trends Ecol. Evol.* 14, 427–432. doi: 10.1016/s0169-5347(99)01677-8

Bograd, S. J., Buil, M. P., Di Lorenzo, E., Castro, C. G., Schroeder, I. D., Goericke, R., et al. (2015). Changes in source waters to the Southern California bight. *Deep Sea Res. Part II Top. Stud. Oceanogr.* 112, 42–52. doi: 10.1016/j.dsr2.2014.04.009

Buonaccorsi, J. P., Elkinton, J. S., Evans, S. R., and Liebhold, A. M. (2001). Measuring and testing for spatial synchrony. *Ecology* 82, 1668–1679. doi: 10.1890/0012-9658(2001)082%5B1668:matfss%5D2.0.co;2

Cenci, S., Sugihara, G., and Saavedra, S. (2019). Regularized S−map for inference and forecasting with noisy ecological time series. *Methods Ecol. Evol.* 10, 650–660. doi: 10.1111/2041-210x.13150

Chang, C.-W., Ushio, M., and Hsieh C-h. (2017). Empirical dynamic modeling for beginners. *Ecol. Res.* 32, 785–796. doi: 10.1007/s11284-017-1469-9

Checkley, D. M. Jr., and Barth, J. A. (2009). Patterns and processes in the California current system. *Prog. Oceanogr.* 83, 49–64. doi: 10.1016/j.pocean.2009.07.028

Clark, A. T., Ye, H., Isbell, F., Deyle, E. R., Cowles, J., Tilman, G. D., et al. (2015). Spatial convergent cross mapping to detect causal relationships from short time series. *Ecology* 96, 1174–1181. doi: 10.1890/14-1479.1

Cressie, N., and Wikle, C. K. (2015). *Statistics for Spatio-temporal Data*. Hoboken, NJ: John Wiley & Sons.

Deyle, E. R., Fogarty, M., Hsieh C-h, Kaufman, L., MacCall, A. D., Munch, S. B., et al. (2013). Predicting climate effects on Pacific sardine. *Proc. Natl. Acad. Sci. U.S.A.* 110, 6430–6435. doi: 10.1073/pnas.1215506110

Deyle, E. R., May, R. M., Munch, S. B., and Sugihara, G. (2016). Tracking and forecasting ecosystem interactions in real time. *Proc. R. Soc. B Biol. Sci.* 283:20152258. doi: 10.1098/rspb.2015.2258

Ebbesmeyer, C. C., Cayan, D. R., McLain, D. R., Nichols, F. H., Peterson, D. H., and Redmond, K. T. (1991). "1976 step in the Pacific climate: forty environmental changes between 1968-1975 and 1977-1984," in *Proceedings of the Seventh Annual Pacific Climate (PACLIM) Workshop*, Pacific Grove, CA.

Engle, R. F., and Granger, C. W. (1987). Co-integration and error correction: representation, estimation, and testing. *Econometrica* 55, 251–276. doi: 10.2307/1913236

Fromentin, J.-M., Gjøsæter, J., Bjørnstad, O. N., and Stenseth, N. C. (2000). Biological processes and environmental factors regulating the dynamics of the Norwegian Skagerrak cod populations since 1919. *ICES J. Mar. Sci.* 57, 330–338. doi: 10.1006/jmsc.1999.0638

Gallo, N. D., Drenkard, E., Thompson, A. R., Weber, Wilson-Vandenberg, D., McClatchie, S., et al. (2019). Bridging from monitoring to solutions-based thinking: lessons from CalCOFI for understanding and adapting to marine climate change impacts. *Front. Mar. Sci.* 6:695.

Glaser, S. M., Ye, H., and Sugihara, G. (2014). A nonlinear, low data requirement model for producing spatially explicit fishery forecasts. *Fish. Oceanogr.* 23, 45–53. doi: 10.1111/fog.12042

Gouhier, T. C., and Guichard, F. (2014). Synchrony: quantifying variability in space and time. *Methods Ecol. Evol.* 5, 524–533. doi: 10.1111/2041-210x.12188

Gouhier, T. C., Guichard, F., and Menge, B. A. (2010). Ecological processes can synchronize marine population dynamics over continental scales. *Proc. Natl. Acad. Sci. U.S.A.* 107, 8281–8286. doi: 10.1073/pnas.0914588107

Gouhier, T. C., Menge, B. A., and Hacker, S. D. (2011). Recruitment facilitation can promote coexistence and buffer population growth in metacommunities. *Ecol. Lett.* 14, 1201–1210. doi: 10.1111/j.1461-0248.2011.01690.x

Hare, S. R., and Mantua, N. J. (2000). Empirical evidence for North Pacific regime shifts in 1977 and 1989. *Prog. Oceanogr.* 47, 103–145. doi: 10.1016/s0079-6611(00)00033-1

Harvey, C. J., Garfield, N., Williams, G. D., Tolimieri, N., Schroeder, I., Andrews, K. S., et al. (2019). "Ecosystem status report of the california current for 2019: a summary of ecosystem indicators compiled by the california current integrated ecosystem assessment team (CCIEA)," in US Department of Commerce, NOAA Technical Memorandum. NMFS-NWFSC-149.

Hewitt, R. P. (1988). Historical review of the oceanographic approach to fishery research. *Calif. Coop. Oceanic Fish. Invest. Rep.* 29, 27–41.

Holyoak, M., and Lawler, S. P. (1996). Persistence of an extinction−prone predator−prey interaction through metapopulation dynamics. *Ecology* 77, 1867–1879. doi: 10.2307/2265790

Hsieh, C-H., Anderson, C., and Sugihara, G. (2008). Extending nonlinear analysis to short ecological time series. *Am. Naturalist* 171, 71–80. doi: 10.1086/524202

Hsieh, C-H., Reiss, C., Watson, W., Allen, M. J., Hunter, J. R., Lea, R. N., et al. (2005). A comparison of long-term trends and variability in populations of larvae of exploited and unexploited fishes in the Southern California region: a community approach. *Prog. Oceanogr.* 67, 160–185. doi: 10.1016/j.pocean.2005.05.002

Hubbs, C. L. (1948). Changes in the fish fauna of western North America correlated with changes in ocean temperature. *J. Mar. Res.* 7, 459–482.

Hyndman, R. J., and Koehler, A. B. (2006). Another look at measures of forecast accuracy. *Int. J. Forecasting* 22, 679–688. doi: 10.1016/j.ijforecast.2006.03.001

Jacox, M. G., Alexander, M. A., Siedlecki, S., Chen, K., Kwon, Y.-O., Brodie, S., et al. (2020). Seasonal-to-interannual prediction of North American coastal marine ecosystems: forecast methods, mechanisms of predictability, and priority developments. *Prog. Oceanogr.* 183:102307. doi: 10.1016/j.pocean.2020.102307

Koenig, W. D. (1999). Spatial autocorrelation of ecological phenomena. *Trends Ecol. Evol.* 14, 22–26. doi: 10.1016/s0169-5347(98)01533-x

Liebhold, A., Koenig, W. D., and Bjørnstad, O. N. (2004). Spatial synchrony in population dynamics. *Annu. Rev. Ecol. Evol. Syst.* 35, 467–490.

Liu, H., Fogarty, M. J., Glaser, S. M., Altman, I., Hsieh C-h, Kaufman, L., et al. (2012). Nonlinear dynamic features and co-predictability of the Georges Bank fish community. *Mar. Ecol. Prog. Ser.* 464, 195–207. doi: 10.3354/meps09868

Liu, H., Fogarty, M. J., Hare, J. A., Hsieh C-h, Glaser, S. M., Ye, H., et al. (2014). Modeling dynamic interactions and coherence between marine zooplankton and fishes linked to environmental variability. *J. Mar. Syst.* 131, 120–129. doi: 10.1016/j.jmarsys.2013.12.003

Lynn, R. J., Bograd, S. J., Chereskin, T. K., and Huyer, A. (2003). Seasonal renewal of the California current: the spring transition off California. *J. Geophys. Res. Oceans* 108:C8.

McClatchie, S. (2014). "Oceanography of the Southern California current system relevant to fisheries," in *Regional Fisheries Oceanography of the California Current System*, (Dordrecht: Springer), 13–60. doi: 10.1007/978-94-007-7223-6_2

McClatchie, S., Gao, J., Drenkard, E. J., Thompson, A. R., Watson, W., Ciannelli, L., et al. (2018). Interannual and secular variability of larvae of mesopelagic and forage fishes in the Southern California current system. *J. Geophys. Res. Oceans* 123, 6277–6295. doi: 10.1029/2018jc014011

McFarlane, G. A., and Beamish, R. J. (2001). The re-occurrence of sardines off British Columbia characterises the dynamic nature of regimes. *Prog. Oceanogr.* 49, 151–165. doi: 10.1016/s0079-6611(01)00020-9

Moser, H. G. (1996). *The Early Stages of Fishes in the California Current Region: California Cooperative Oceanic Fisheries Investigations: Atlas No 33*. Chicago, IL: University of Chicago.

Moser, H. G., Charter, R. L., Watson, W., Ambrose, D., Hill, K., Smith, P., et al. (2001). The CalCOFI ichthyoplankton time series: potential contributions to the management of rocky-shore fishes. *Calif. Coop. Oceanic Fish. Invest. Report* 42, 112–128.

Moser, H. G., and Watson, W. (1990). Distribution and abundance of early life history stages of the California halibut, Paralichthys californicus, and comparison with the fantail sole, Xystreurys liolepis. *Calif. Dep. Fish. Game Fish. Bull.* 174, 31–84.

Munch, S. B., Giron-Nava, A., and Sugihara, G. (2018). Nonlinear dynamics and noise in fisheries recruitment: a global meta-analysis. *Fish Fish.* 19, 964–973. doi: 10.1111/faf.12304

Munch, S. B., Poynor, V., and Arriaza, J. L. (2017). Circumventing structural uncertainty: a bayesian perspective on nonlinear forecasting for ecology. *Ecol. Complexity* 32, 134–143. doi: 10.1016/j.ecocom.2016.08.006

Myers, R., Mertz, G., and Bridson, J. (1997). Spatial scales of interannual recruitment variations of marine, anadromous, and freshwater fish. *Can. J. Fish. Aqua. Sci.* 54, 1400–1407. doi: 10.1139/f97-045

Myers, R. A., Mertz, G., and Barrowman, N. (1995). Spatial scales of variability in cod recruitment in the North Atlantic. *Can. J. Fish. Aquatic Sci.* 52, 1849–1862. doi: 10.1139/f95-778

Peabody, C. E., Thompson, A. R., Sax, D. F., Morse, R. E., and Perretti, C. T. (2018). Decadal regime shifts in southern California's ichthyoplankton assemblage. *Mar. Ecol. Prog. Series* 607, 71–83. doi: 10.3354/meps12787

Perretti, C. T., Munch, S. B., and Sugihara, G. (2013a). Model-free forecasting outperforms the correct mechanistic model for simulated and experimental data. *Proc. Natl. Acad. Sci. U.S.A.* 110, 5253–5257. doi: 10.1073/pnas.1216076110

Perretti, C. T., Sugihara, G., and Munch, S. B. (2013b). Nonparametric forecasting outperforms parametric methods for a simulated multispecies system. *Ecology* 94, 794–800. doi: 10.1890/12-0904.1

Pikitch, E. K., Santora, C., Babcock, E. A., Bakun, A., Bonfil, R., Conover, D. O., et al. (2004). Ecosystem-based fishery management. *Science* 405, 346–347. doi: 10.1126/science.1098222

Pinsky, M. L., Worm, B., Fogarty, M. J., Sarmiento, J. L., and Levin, S. A. (2013). Marine taxa track local climate velocities. *Science* 341, 1239–1242. doi: 10.1126/science.1239352

Ralston, S., Bence, J. R., Eldridge, M. B., and Lenarz, W. H. (2003). An approach to estimating rockfish biomass based on larval production, with application to Sebastes jordani. *Fish. Bull.* 101, 129–146.

Ralston, S., and MacFarlane, B. R. (2010). Population estimation of bocaccio (Sebastes paucispinis) based on larval production. *Can. J. Fish. Aqua. Sci.* 67, 1005–1020. doi: 10.1139/f10-039

Ranta, E., Kaitala, V., Lindström, J., and Linden, H. (1995). Synchrony in population dynamics. *Proc. R. Soc. Lond. Ser. B Biol. Sci.* 262, 113–118.

Rogers, T. L., and Munch, S. B. (2020). Hidden similarities in the dynamics of a weakly synchronous marine metapopulation. *Proc. Natl. Acad. Sci. U.S.A.* 117, 479–485. doi: 10.1073/pnas.1910964117

Rykaczewski, R. R., and Checkley, D. M. (2008). Influence of ocean winds on the pelagic ecosystem in upwelling regions. *Proc. Natl. Acad. Sci. U.S.A.* 105, 1965–1970. doi: 10.1073/pnas.0711777105

Schaffer, W. M., and Kot, M. (1985). Do strange attractors govern ecological systems? *BioScience* 35, 342–350. doi: 10.2307/1309902

Smith, P. E. (1977). Standard techniques for pelagic fish egg and larva surveys. *FAO Fish. Tech. Pap.* 175, 1–100.

Sugihara, G. (1994). Nonlinear forecasting for the classification of natural time series. *Philos. Trans. R. Soc. Lond. Ser. A Phys. Eng. Sci.* 348, 477–495. doi: 10.1098/rsta.1994.0106

Sugihara, G., Beddington, J., Hsieh, C-H, Deyle, E., Fogarty, M., Glaser, S. M., et al. (2011). Are exploited fish populations stable? *Proc. Natl. Acad. Sci. U.S.A.* 108, E1224–E1225.

Sugihara, G., May, R., Ye, H., Hsieh, C-H, Deyle, E., Fogarty, M., et al. (2012). Detecting causality in complex ecosystems. *Science* 338, 496–500. doi: 10.1126/science.1227079

Sugihara, G., and May, R. M. (1990). Nonlinear forecasting as a way of distinguishing chaos from measurement error in time series. *Nature* 344, 734–741. doi: 10.1038/344734a0

Sutcliffe, O. L., Thomas, C. D., and Moss, D. (1996). Spatial synchrony and asynchrony in butterfly population dynamics. *J. Anim. Ecol.* 65, 85–95. doi: 10.2307/5702

Takens, F. (1981). "Detecting strange attractors in turbulence," in *Dynamical Systems and Turbulence, Warwick 1980*. eds D. Rand and L.S. Young (Berlin: Springer), 366–381. doi: 10.1007/bfb0091924

Thompson, A. R., Auth, T. D., Brodeur, R. D., Bowlin, N. M., and Watson, W. (2014). Dynamics of larval fish assemblages in the California current system: a comparative study between Oregon and southern California. *Mar. Ecol. Prog. Ser.* 506, 193–212. doi: 10.3354/meps10801

Thompson, A. R., Hyde, J. R., Watson, W., Chen, D. C., and Guo, L. W. (2016). Rockfish assemblage structure and spawning locations in southern California identified through larval sampling. *Mar. Ecol. Prog. Ser.* 547, 177–192. doi: 10.3354/meps11633

Thompson, A. R., Chen, D. C., Guo, L. W., Hyde, J. R., and Watson, W. (2017). Larval abundances of rockfishes that were historically targeted by fishing increased over 16 years in association with a large marine protected area. *R. Soc. Open Sci.* 4:170639. doi: 10.1098/rsos.170639

Thompson, A. R., Schroeder, I. D., Bograd, S. J., Hazen, E. L., Jacox, M. G., Leising, A., et al. (2018). State of the California current 2017–18: still not quite normal in the north and getting interesting in the south. *Calif. Coop. Oceanic Fish. Invest. Data Rep.* 59, 2–4.

Thompson, A. R., Schroeder, I. D., Bograd, S., Hazen, E. L., Jacox, M., Leising, A. W., et al. (2019). State of the California current 2018-19: a novel anchovy regime and a new marine heatwave? *Calif. Coop. Oceanic Fish. Invest.* 60, 2–10.

Thorson, J. T., Shelton, A. O., Ward, E. J., and Skaug, H. J. (2015). Geostatistical delta-generalized linear mixed models improve precision for estimated abundance indices for West Coast groundfishes. *ICES J. Mar. Sci.* 72, 1297–1310. doi: 10.1093/icesjms/fsu243

Tobin, P. C., and Bjørnstad, O. N. (2003). Spatial dynamics and cross-correlation in a transient predator-prey system. *J. Anim. Ecol.* 72, 460–467. doi: 10.1046/j.1365-2656.2003.00715.x

Townsend, D. L., and Gouhier, T. C. (2019). Spatial and interspecific differences in recruitment decouple synchrony and stability in trophic metacommunities. *Theor. Ecol.* 12, 319–327. doi: 10.1007/s12080-018-0397-9

Ushio, M., Hsieh C-h, Masuda, R., Deyle, E. R., Ye, H., Chang, C.-W., et al. (2018). Fluctuating interaction network and time-varying stability of a natural fish community. *Nature* 554, 360–363. doi: 10.1038/nature25504

Ward, E. J., Holmes, E. E., Thorson, J. T., and Collen, B. (2014). Complexity is costly: a meta−analysis of parametric and non−parametric methods for short−term population forecasting. *Oikos* 123, 652–661. doi: 10.1111/j.1600-0706.2014.00916.x

Watson, J. R., Siegel, D. A., Kendall, B. E., Mitarai, S., Rassweiller, A., and Gaines, S. D. (2011). Identifying critical regions in small-world marine metapopulations. *Proc. Natl. Acad. Sci. U.S.A.* 108, E907–E913.

Williams, D. W., and Liebhold, A. M. (2000). Spatial synchrony of spruce budworm outbreaks in eastern North America. *Ecology* 81, 2753–2766. doi: 10.1890/0012-9658(2000)081%5B2753:ssosbo%5D2.0.co;2

Wilson, J. R., Lomonico, S., Bradley, D., Sievanen, L., Dempsey, T., Bell, M., et al. (2018). Adaptive comanagement to achieve climate−ready fisheries. *Conserv. Lett.* 11:e12452. doi: 10.1111/conl.12452

Ye, H., Beamish, R. J., Glaser, S. M., Grant, S. C., Hsieh C-h, Richards, L. J., et al. (2015). Equation-free mechanistic ecosystem forecasting using empirical dynamic modeling. *Proc. Natl. Acad. Sci. U.S.A.* 112, E1569–E1576.

Conflict of Interest: The authors declare that the research was conducted in the absence of any commercial or financial relationships that could be construed as a potential conflict of interest.

frontiers in Marine Science

ORIGINAL RESEARCH
published: 05 November 2020
doi: 10.3389/fmars.2020.578165

Marine Ecosystem Variations Over the North Pacific and Their Linkage to Large-Scale Climate Variability and Change

Emi Yati[1,2], Shoshiro Minobe[1,3], Nathan Mantua[4], Shin-ichi Ito[5] and Emanuele Di Lorenzo[6]*

[1] Department of Natural History Sciences, Graduate School of Science, Hokkaido University, Sapporo, Japan, [2] Remote Sensing Application Center, Indonesian National Institute of Aeronautics and Space, Jakarta, Indonesia, [3] Department of Earth and Planetary Sciences, Faculty of Science, Hokkaido University, Sapporo, Japan, [4] Fish Ecology Division, Southwest Fisheries Science Center, National Marine Fisheries Service, National Oceanographic and Atmospheric Administration, Santa Cruz, CA, United States, [5] Atmosphere and Ocean Research Institute, University of Tokyo, Kashiwa, Japan, [6] School of Earth and Atmospheric Sciences, Georgia Institute of Technology, Atlanta, GA, United States

OPEN ACCESS

Edited by:
Athanassios C. Tsikliras, Aristotle University of Thessaloniki, Greece

Reviewed by:
Michael Adam Alexander, National Oceanic and Atmospheric Administration (NOAA), United States
Brett W. Molony, Oceans and Atmosphere (CSIRO), Australia

***Correspondence:**
Shoshiro Minobe
minobe@sci.hokudai.ac.jp

Specialty section:
This article was submitted to Marine Fisheries, Aquaculture and Living Resources, a section of the journal Frontiers in Marine Science

Received: *30 June 2020*
Accepted: *12 October 2020*
Published: *05 November 2020*

Citation:
Yati E, Minobe S, Mantua N, Ito S and Di Lorenzo E (2020) Marine Ecosystem Variations Over the North Pacific and Their Linkage to Large-Scale Climate Variability and Change. Front. Mar. Sci. 7:578165. doi: 10.3389/fmars.2020.578165

In order to understand how North Pacific (NP) marine ecosystems have varied, 120 marine biological time series for both the western (29 time series) and eastern (91 time series) NP were analyzed with a Principal Component Analysis (PCA) for the period 1965–2006. This is the first attempt to conduct a multivariate analysis for a large number of marine biological data in the western and eastern NP combined. We used Monte-Carlo simulation to evaluate confidence levels of correlations and explained variance ratio of PCA modes while accounting for auto-correlation within the analyzed time series. All first mode principal components (PC1s), which are the time coefficients of the first PCA modes, calculated for the data in the whole, western, and eastern NP exhibit a long-term trend. The PC1s were associated with an overall increase of Alaskan and Japanese/Russian salmon, and decreases of groundfish across the basin. This mode was closely related to the warming of sea-surface temperature over the NP and over the global oceans, thereby suggesting that the strongest mode of the NP marine ecosystem was already influenced by global warming. The eastern NP PC2, characterized by multi-decadal variability, was correlated positively with salmon and negatively with groundfish. On the other hand, the western NP PC2 exhibited slightly shorter timescale interdecadal variability than the eastern NP PC2 and was negatively correlated with zooplankton and two small pelagic fish time series around Japan. The eastern NP PC2 was most strongly related to the Pacific (inter-)Decadal Oscillation index, while the western NP PC2 was most closely related to the North Pacific Gyre Oscillation index. Consequently, the present analysis provides a new and unified view of climate change and marine ecosystem variations across the western and eastern NP. In particular, it is suggested that global warming has already substantially influenced the NP marine ecosystem, and that groundfish may suffer more than pelagic fish in response to future global warming.

Keywords: marine ecosystem, decadal climate variability, global warming, North Pacific, regime shift

INTRODUCTION

Marine ecosystems are influenced by physical climate variability and change (e.g., Cushing, 1982; Brander, 2007; Bindoff et al., 2019). The effects of physical climate variability on marine species in the North Pacific (NP) have been studied in the last few decades. Earlier studies focused their attention on target marine species such as salmon (e.g., Ebbesmeyer et al., 1991; Beamish and Bouillon, 1993; Francis and Hare, 1994; Mantua et al., 1997; Beamish et al., 1999; Hare et al., 1999), sardine (Kawasaki and Omori, 1995; Noto and Yasuda, 1999; Yasuda et al., 1999), and groundfish (Hoff, 2006). An important finding of these studies was that large-scale decadal variability of climate characterized by Aleutian Low strength changes and associated sea-surface temperature (SST) anomalies, which are known as the Pacific (inter-)Decadal Oscillation (PDO; Minobe, 1997; Mantua et al., 1997), strongly influenced a wide range of marine species in much of the 20th Century (e.g., Mantua et al., 1997; Yasuda et al., 1999; Hare and Mantua, 2000; Chavez et al., 2003; Litzow and Mueter, 2014).

In particular, as evidence of climate influence on the marine ecosystem, step-like shifts commonly occurring in both the marine ecosystem and physical climate attracted attention (e.g., Ebbesmeyer et al., 1991; Beamish and Bouillon, 1993; Francis and Hare, 1994; Mantua et al., 1997), and such a shift is often referred as a climate and ecosystem regime shift. A regime shift for physical climate is defined as a transition from one climatic state to another within a period substantially shorter than the lengths of the individual epochs of each climate state (Minobe, 1997). A marine ecosystem regime shift can also be defined in the same way as the climatic regime shift, i.e., a rapid transition from one state to another (Möllmann and Diekmann, 2012), but sometimes marine ecosystem regimes mean different states of dominant species (e.g., Lluch-Belda et al., 1989). In this article, we use the marine ecosystem regime shift in the former meaning, i.e., a rapid step-like change that persists for a length of time that far exceeds that of the transition.

In order to understand marine ecosystem variability and change in a more holistic way than analyses of selected species, a useful approach is an analysis of a large number of marine biological time series, typically more than several tens, by using a multivariate analysis method. We call this type of analysis a Large-number Multivariate Analysis (LMA). The pioneering first study of LMA was conducted by Hare and Mantua (2000), who analyzed 69 marine species time series data in the eastern NP, from California waters to the Bering Sea, combined with 31 physical climate indices from 1965 to 1997. They applied a Principal Component Analysis (PCA), which is also known as an Empirical Orthogonal Function analysis. They reported that marine ecosystem regime shifts occurred in 1976/77 and 1988/89 over the eastern NP. A decade later, by using 64 eastern NP biological time series with several climate indices in 1965–2008, Litzow and Mueter (2014) also reported shifts in marine biology in the 1976/77 but they did not find a biological shift in the late 1980s. Rather, they emphasized that the time series of the first biological PCA mode, referred to as PC1, was characterized by a gradual change and not a step-like shift. For the western side of basin, Tian et al. (2006) analyzed 58 Japanese fish catch time series from the Sea of Japan in 1958–2003, and Ma et al. (2019) recently analyzed 147 catch time series in the Yellow and East China Seas for 1965–2008. Tian et al. (2006) reported that the biological PC1 is highly correlated with the PDO index (Mantua et al., 1997) and the Arctic Oscillation (AO) index (Thompson and Wallace, 1998), while Ma et al. (2019) found strong correlations between biological PCs with indices for local physical conditions but not with large scale climate indices. LMA was also used for the northeastern North Atlantic by Brunel and Boucher (2007), who reported that the first mode of 40 fish recruitment time series is characterized by the long-term change probably in association with global warming.

It should be noted that previous LMA studies in the NP were limited either on the eastern NP only or marginal seas in the western NP only. This hinders a unified understanding of the marine ecosystem variability and change over the whole NP. It is already known that climate variability causes synchronized changes in marine ecosystems in both the eastern and western NP for sardine and anchovy (Lluch-Belda et al., 1992; Kawasaki and Omori, 1995; Yasuda et al., 1999; Chavez et al., 2003) and for salmon (e.g., Beamish and Bouillon, 1993). These results underline the importance of whole basin analyses.

The purpose of this study is to identify the dominant modes of marine ecosystem variations in the last half century both in the western and eastern NP basin and their relationships to basin-scale physical climate variability and change. To this end, 120 marine species time series, consisting of 91 eastern NP and 29 western NP time series are analyzed. The data consist of biological time series for zooplankton, invertebrates, small-pelagic fish, groundfish and salmon. This is the first LMA study analyzing data from both the western and eastern NP. We applied PCA on biological data and used correlation analysis to understand the relationships between marine ecosystem and physical climate variations with a rigorous estimation of the corresponding confidence level. In addition to indices for climate modes such as the PDO and North Pacific Gyre Oscillation (NPGO) (Di Lorenzo et al., 2008), we analyze the NP and global mean SST time series, which were not examined by the previous NP LMA studies, in order to evaluate the possible relationships between marine ecosystem changes and global warming.

DATA AND METHODS

Data

We used 120 annually sampled marine biological time series (**Supplementary Table 1**) consisting of 29 western NP time series from Japan and Russia, and 91eastern NP time series over areas including the Bering Sea, Gulf of Alaska, and the west coast of the United States of America and Canada. These consist of 54 groundfish recruitment, 13 small-pelagic fish recruitment, 34 salmon abundance, eight invertebrate recruitment, and eleven zooplankton biomass time series. Some of our eastern NP data are overlapped with those used by previous studies; 48% of groundfish, 80% of small-pelagic, 13% of invertebrate, and 25% of salmon were also used by Litzow and Mueter (2014). On the

other hand, western NP data analyzed in this study, which mainly come from analyses of Japan Fisheries Research and Education Agency (Japan Fisheries Agency, and Fisheries Research Agency, 2015), have not been used for previous LMA studies. We set our analysis period from 1965 to 2006 based on a criteria of available data ratio larger than 50%, following Hare and Mantua (2000). This is 10-years longer than the analysis period of Hare and Mantua (2000), but similar to that of Litzow and Mueter (2014). Some of our results will be shown by map-format figures and the correspondences between the spatial positions of the biological time series on the map and index number are summarized in **Figure 1**, along with abbreviations of time series in **Supplementary Table 1**.

In order to understand relationships between variations in marine biology and climate, we analyzed seven annually averaged physical climate indices: 1. global-mean sea-surface temperature (G-SST), 2. NP-mean SST (NP-SST), 3. PDO index, 4. NPGO index, 5. the multivariate El Niño-Southern Oscillation Index (MEI) (Wolter and Timlin, 2011), 6. The North Pacific Index (NPI) (Trenberth and Hurrell, 1994), and 7. AO index (**Table 1**). The NPI represents the strength of the Aleutian Low, a large-scale low-pressure over the NP in winter, and an Aleutian Low is stronger than usual when the NPI anomaly is negative. The NPI is closely related to the PDO index (Mantua et al., 1997; Minobe, 1997). We use the Centennial *in situ* Observation-Based Estimates of the Variability of SST and Marine Meteorological Variables (COBE) version 2 (Hirahara et al., 2014) to calculate the G-SST and NP-SST indices.

Methods

We employed PCA to the marine biological time series, and calculated PCA modes using the biological time series in the whole, western, and eastern NP, separately. Before calculating the PCA modes, marine biological time series were normalized by their respective standard deviations and removing the means. Thus, reflecting the larger number of time series in the eastern NP than in the western NP, the former more strongly contributes to the whole NP PCA than the latter does. By this reason, we mainly show western and eastern NP PCA modes rather than the whole NP modes. A covariance between two biological time series was calculated for the temporal points at which both time series data are available (von Storch and Zwiers, 2012).

The relation between the PC time series and respective biological or physical time series were evaluated by the Pearson correlation, and its statistical significance is estimated with a Monte-Carlo simulation that takes into account effective degrees of freedom. Since co-variability among biological time series mostly occurs on decadal timescales as will be shown later, we evaluated correlations with a 5-year running mean low-pass filter as main results and without it as **Supplementary results**. Statistical significance of correlations was assessed as follows. First, we generated 1,000 surrogate time series for the respective PCs (without the running mean), by using a red noise model, where lag-1 correlation was estimated by using Burg's method (e.g., Kay, 1988). In the case of the significance estimation for correlations with the low-pass filter, the filter was applied to both observed data and surrogate PCs before calculating correlations. Then surrogate correlation coefficients were calculated between observed data (e.g., marine biological time series) and the surrogate PC. The confidence level was estimated as the percentile of the absolute value of the observed correlation with respect to the absolute surrogate correlations. We employ Monte-Carlo simulation instead of using theoretical estimation of effective degrees of freedom (e.g., Metz, 1991; Pyper and Peterman, 1998)

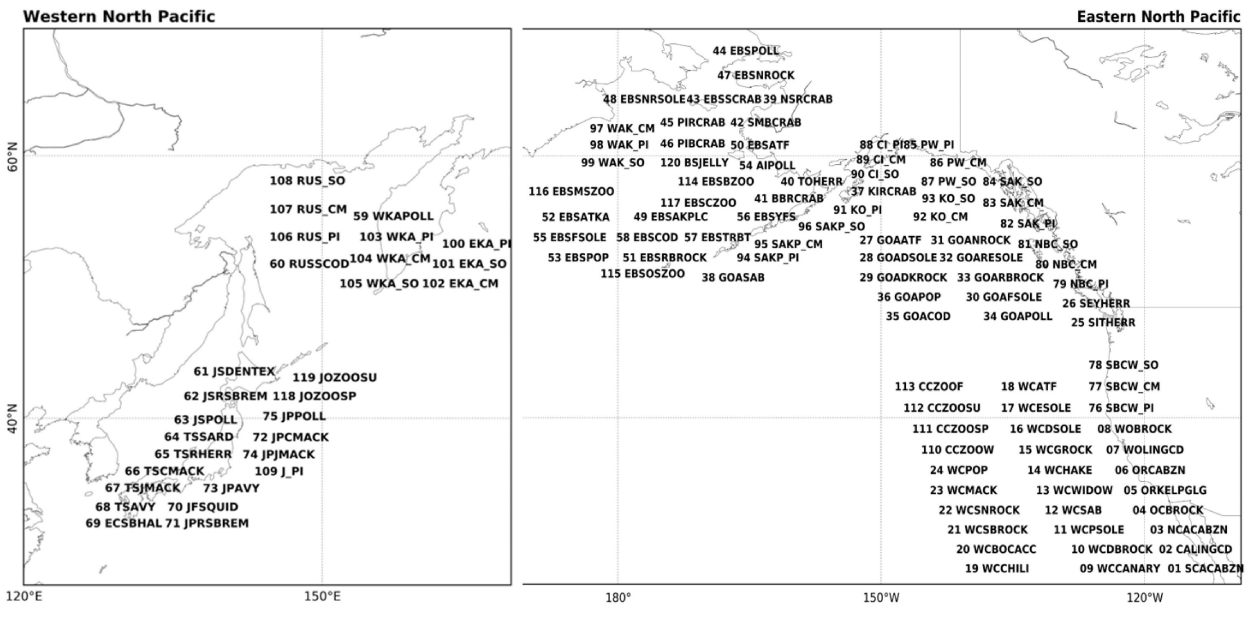

FIGURE 1 | Identification number and alphabetic abbreviations for the 120 marine species data. See **Supplementary Table 1** for a definition of each abbreviation. The locations of the species on the map are approximate.

TABLE 1 | Seven climate indices.

Abbreviation	Name	Description	Data source
G-SST	Global-ocean averaged SST	SST are averaged over the global ocean	Calculated from COBE SST version 2
NP-SST	NP averaged SST	SST are averaged over the NP, north of 20°-68°N	Calculated from COBE SST version 2
PDO	Pacific Decadal Oscillation	First PCA mode of SST anomalies, from which global averaged SST has been removed, over the North Pacific north of 20°N	University of Washington, Joint Institute for the Study of the Atmosphere and Ocean
NPGO	North Pacific Gyre Oscillation	Second PCA mode of sea surface height anomalies in the Northeast Pacific	Emanuele Di Lorenzo, Georgia Institute of Technology
MEI	Multivariate El Nino-Southern Oscillation	An index for El Niño-Southern Oscillation over the tropical Pacific	NOAA Earth System Research Laboratory
NPI	North Pacific Index	The area-weighted sea level pressure over the region 30°N-65°N, 160°E-140°W	NOAA Earth System Research Laboratory
AO	Arctic Oscillation Index	First PCA mode of sea level pressure anomalies north of 20°N	NOAA Climate Prediction Center

All indices are calculated using monthly data and then are averaged to obtain annual average.

because the theoretical estimation is difficult to use for data that have missing values and with time filtering, but these factors are automatically included by the present Monte-Carlo simulation.

We also examined statistical significance of the explained variance ratio (EVR) of PCA modes by using another Monte-Carlo simulation. We use this analysis because the correlations between some biological indices and PCs can become statistically significant just by chance associated with the large number of tests as discussed by Ventura et al. (2004) and Wilks (2016). For the significance test of the EVR for the first mode (EVR1), we generated 1,000 sets of observed biological indices (e.g., 1,000 sets of 120 time series for the whole NP basin) by using a red noise model with a lag-1 auto-correlation for each time series, with missing data in the same years as observed. By considering correlations between biological indices, we reduce the number of surrogate indices by 5% (e.g., from 120 to 114 indices for the whole NP basin) for each set, because the number of statistically significant pairs of biological indices is 9–10% of the number of total pairs in all three PCA domains and removal of 10% of pairs is equivalent to removal of 5% of time series as square root of 0.90 is approximately 0.95. The PCA is calculated for each set of reduced surrogate data, yielding 1,000 surrogate EVR1s. The percentile obtained by the observed EVR1 with respect to the 1,000 surrogate EVR1s gives the confidence level. If EVR1 is larger than any of surrogate EVR1s, the confidence level is higher than 99.9%, and equivalently p-value is smaller than 0.1%. Such a rigorous estimation of statistical significance was not used in previous LMA studies.

RESULTS

First PCA Modes of Marine Biological Time Series

Each of the PC1s for the whole, eastern, and western NP basins show a long-term trend-like feature with the single-phase reversal in the 1980s, and western and eastern NP PC1s are generally similar ($r = 0.90$) especially after 1990 (**Figure 2A**). Interestingly, the 1980s phase reversal is gradual for the eastern NP PC1 as seen in biological PC1s of Hare and Mantua (2000) and Litzow and Mueter (2014), but it is more rapid in the western one. As expected, the whole NP PC1 shares the features of the eastern and western NP PC1s. The EVR1s for the three analysis domains, which ranges between 12.4 and 27.7% (**Figure 2A**), are statistically significant (p-value $< 0.1\%$) according to the Monte-Carlo simulation.

The pattern of PCA first mode is shown (**Figures 2B,C**) as statistically significant correlations at a confidence level of 90% or higher between the PC1s and biological time series with the low-pass filter. The correlations calculated without the filter give essentially the same pattern (**Supplementary Figure 1**). Two fish groups, salmon and groundfish, have significant correlations in both the western and eastern NP. Ten salmon time series (30% of all salmon time series) are positively correlated, including chum salmon (77.S, 83.S, 107.S), pink salmon (82.S, 94.S, 106.S, 109.S), and sockeye salmon (87.S, 93S, 108.S), mainly around Alaska (82.S, 83S, 87.S, 93.S, 94.S), and Russia/Japan (106S, 107.S, 108.S, 109.S). On the other hand, 13 groundfish time series (24% of groundfish time series) have negative correlations with PC1s, including west coast rockfish (09.G, 12.G, 13.G, 20.G, 21.G), walleye pollock (34.G, 54.G, 63G), cod (35.G, 58.G, 60.G), and others (57.G, 61.G). There are exceptions from this general tendency such as negative correlations for salmon (89.S) and positive correlations of groundfish (27.G, 50.S), but these are minor. Therefore, positive correlations of salmon and negative correlations of groundfish are the major feature commonly found in both the western and eastern NP associated with the first PCA mode.

Some species exhibit significant correlations in only either the western or eastern NP (**Figures 2B,C**). In the western NP, PC1 is positively correlated with three small pelagic fish recruitment time series (38% of western NP small pelagic fish) around Japan, i.e., jack mackerel (67.P), anchovy (68.P, 73.P). In the eastern NP, on the other hand, negative correlations are also found for three zooplankton time series (33% of eastern NP zooplankton) (113.Z, 114.Z, 115.Z) and one invertebrate (Bristol Bay red king crab, 41.I), and positive correlation occurs for the large medusae jellyfish in the eastern Bering Sea (120.Z). These basin-specific

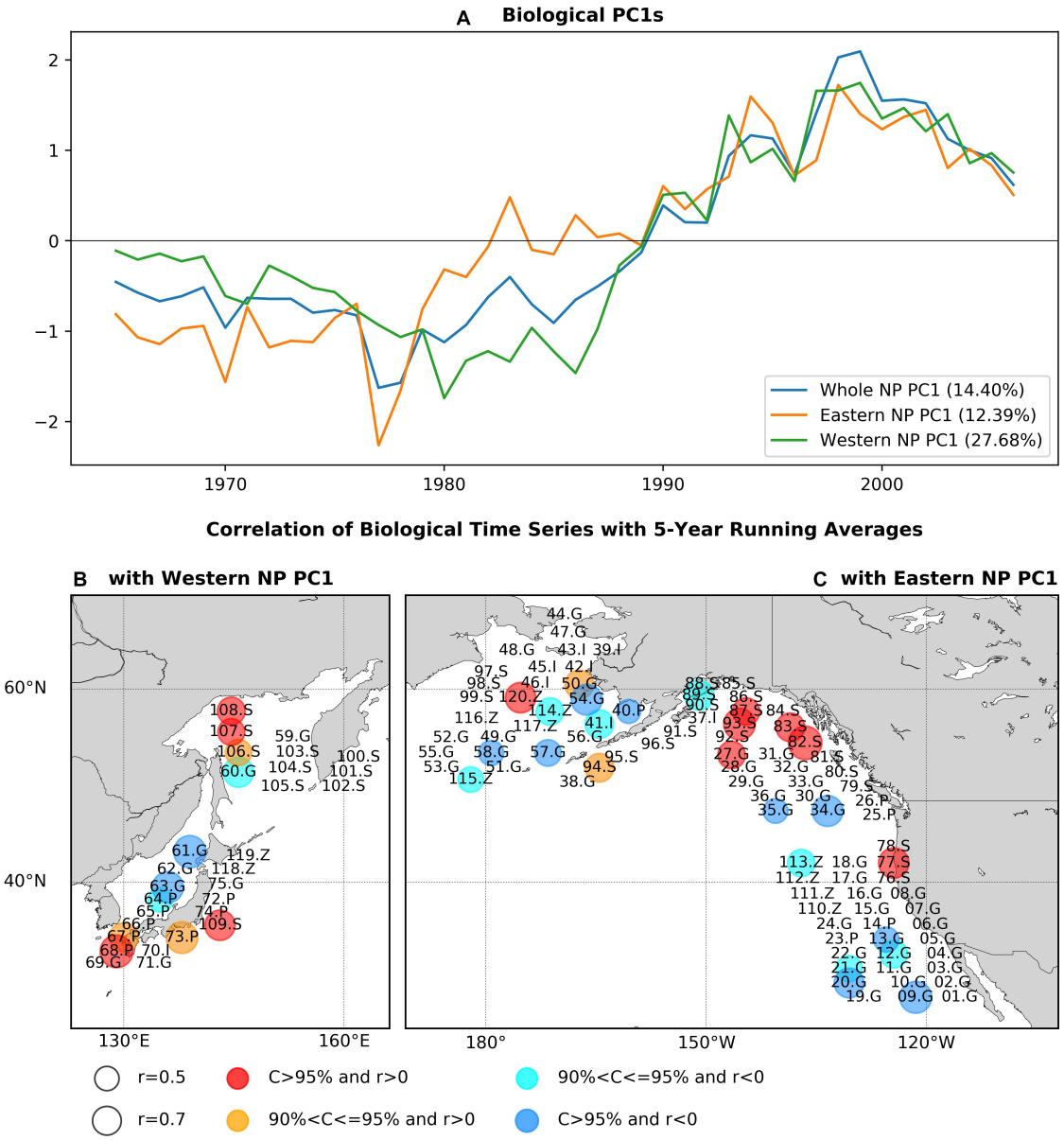

FIGURE 2 | (A) PC1s for the whole NP, eastern NP, and western NP marine biological time series, and statistically significant correlations of marine biological time series **(B)** with the western NP PC1, **(C)** with the eastern NP PC1. Before calculating correlations 5-year running means are applied to PC1s and marine biological time series. In **(B,C)**, numbers indicate species ID in **Supplementary Table 1**, while S, G, P, Z, and I indicate salmon, groundfish, small-pelagic, zooplankton, and invertebrate, respectively. Circle size indicates the absolute values of correlations and colors of the circles (red, orange, cyan, blue) indicate the sign of correlations and the corresponding confidence levels.

associations, especially those for small pelagic fish in the western NP and zooplankton in the eastern NP, are also important aspects of the first PCA mode of the NP ecosystem.

Biological time series that are significantly correlated to the PC1s are compared with those PC1 with the low-pass filter (**Figure 3**). Consistent with the trend-like feature of the PC1s, the biological time series generally exhibit long-term increases for Alaskan and Japanese/Russian salmon and decreases for groundfish irrespective of basins, and increases of small pelagic fish in the western NP and decreases of zooplankton in the eastern NP. It is interesting to note that the time series of the western NP salmon exhibit rapid negative-to-positive phase transition around 1990, which appears consistent with the aforementioned rapid phase reversal of the western NP PC1 (**Figure 3A**). Aside from this rapid transition around 1990, co-variability between biological time series and PC1s occurs on multidecadal and longer timescale. For example, decadal fluctuations are apparent in the eastern NP salmon, but these decadal fluctuations do not occur in the PC1 (**Figure 3D**). Furthermore, the time series comparison without time filtering

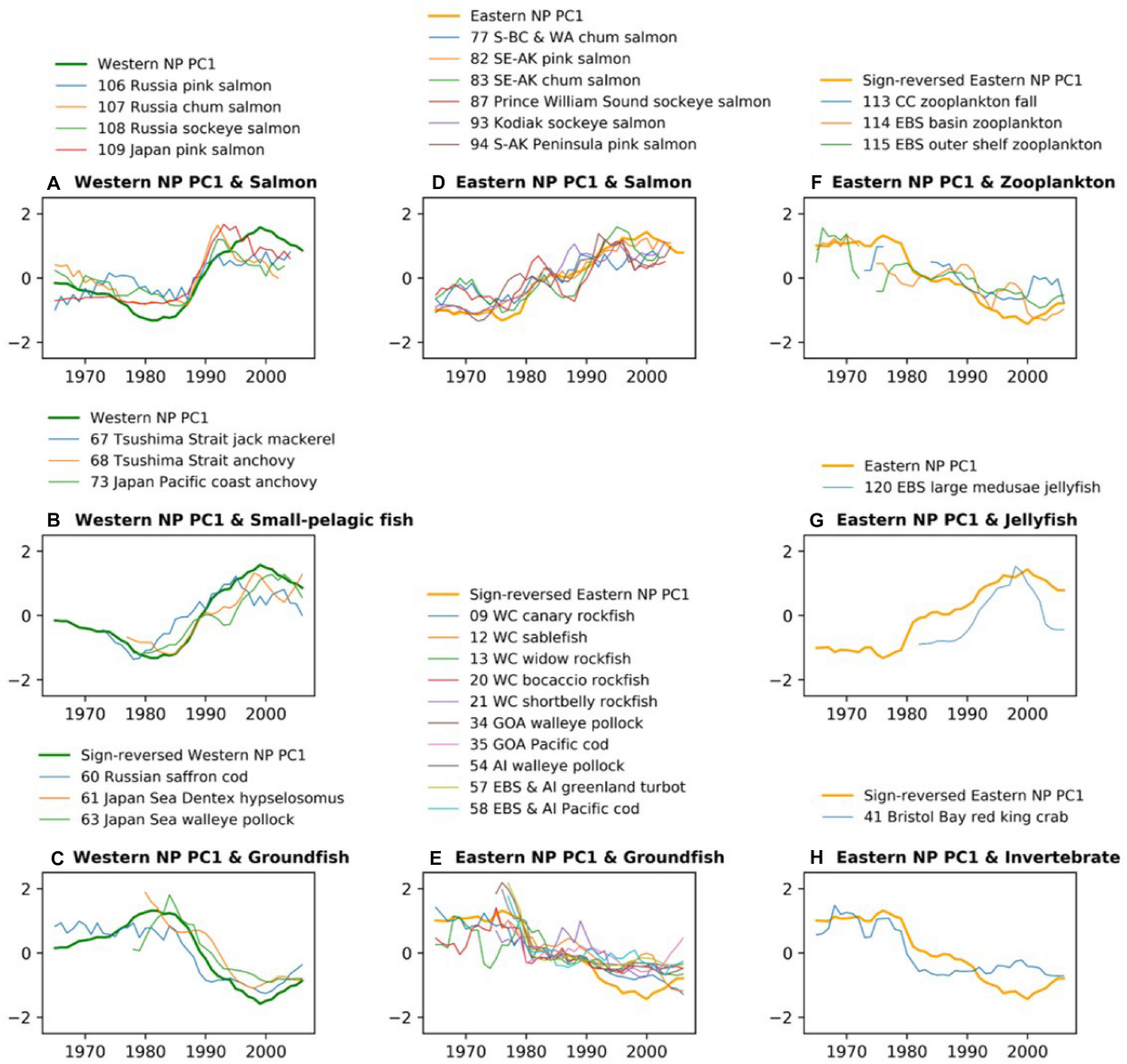

FIGURE 3 | Time-series comparison between marine biological PC1 and biological time series that have significant correlations with that PC1 in each basin shown in **Figures 2B,C**. The time series of western NP **(A)** salmon, **(B)** small pelagic fish, and **(C)** groundfish are shown along with the western NP PC1. The time series of eastern NP **(D)** salmon, **(E)** groundfish, **(F)** zooplankton, **(G)** jellyfish, and **(H)** invertebrate are shown along with eastern NP PC1. All time series are smoothed by 5-year running mean. For an easier comparison, the PC1 time series are sign-reversed (multiplied by –1) for **(C,E,F)**.

(**Supplementary Figure 2**) shows no clear co-variability on interannual timescale. Consequently, in association with the trend-like first PCA mode of the marine ecosystem, the major features are increases in Alaskan and Japanese/Russian salmon, decreases in groundfish in both the western and eastern NP, increases in western NP small pelagic fish, and decreases in eastern NP zooplankton.

Second PCA Modes of Marine Biological Time Series

The PC2s of eastern and western basins exhibit slightly different timescales (**Figure 4A**). The eastern NP PC2 is characterized by multidecadal variability with phase reversals in the 1970s and in the 1990s. The western NP PC2 exhibits three phase reversals and is characterized by shorter timescale interdecadal variability than that of the eastern NP PC2. When PCA modes are calculated using data from which linear trends are removed, the resultant PC1s with detrending are quite similar to the PC2s without detrending ($r = 0.92$ for the eastern NP and $r = 0.82$ for the western NP), thereby indicating the robustness of these modes. Furthermore, the EVR1s for the detrended PC1s are statistically significant (p-value $< 0.1\%$ for the eastern NP and p-value $= 3.3\%$ for the western NP). Here, we apply the statistical significance test for the PCA first mode with detrending, because the present

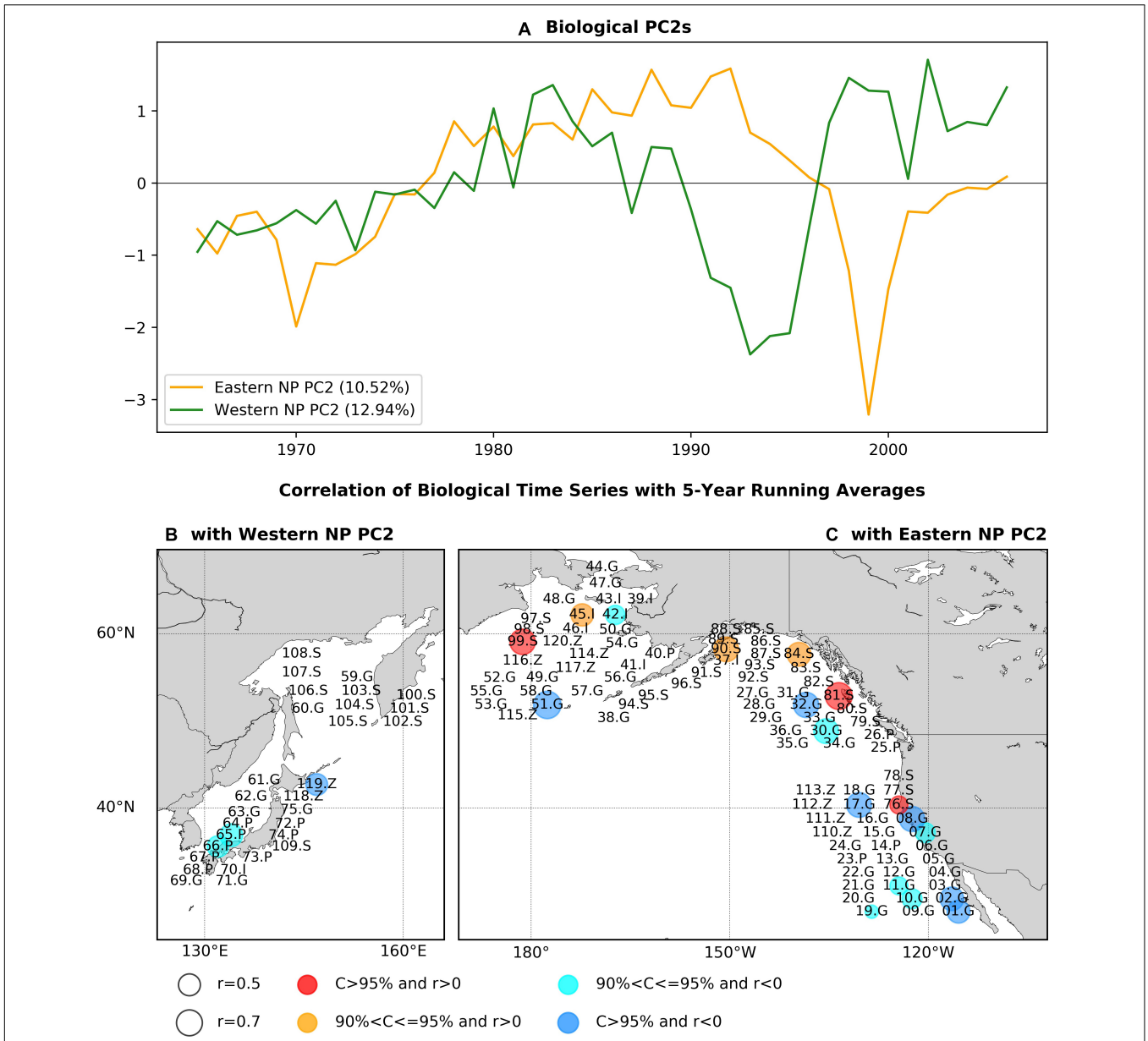

FIGURE 4 | As in **Figure 2**, but for the PCA second modes.

Monte-Carlo simulation, which assume the no-signals, does not work accurately for the second mode when a signal exists in the first mode.

Figures 4B,C shows the statistically significant correlation coefficients of marine ecosystem time series with the respective basin PC2s again using the low-pass filter before calculating correlations. It is interesting to note that, of the time series showing significant correlations with the PC2s, none are significantly correlated with the respective eastern or western NP PC1s. For the western basin (**Figure 4B**), there are three time series with significant correlations consisting of round herring recruitment (65.P), chub mackerel recruitment (66.P), and zooplankton biomass (119Z). When we calculate the correlation map without the low-pass filter, the number of time series with significant correlation is increased by three times to nine in total, with negative correlations for eight biological time series (**Supplementary Figure 3**). This increase of significantly correlated time series can be either due to the increase of effective degrees of freedom in non-filtered analysis or due to the contribution of interannual variability.

On the other hand, significant correlations for the eastern NP PC2 (**Figure 4C**) were positive for mainly salmon abundance (76.S, 81.S, 84.S, 90.S, 99.S) and negative for groundfish recruitment (01.G, 02.G, 07.G, 08.G, 10.G, 11.G, 17.G, 19.G, 30.G, 32.G, 51.G). The opposite sign of correlations between

salmon and groundfish was also found for the first PCA mode (**Figure 2C**). Two invertebrate time series were significantly correlated but with split signs (positive correlation for 45.I and negative for 42.I). The jellyfish in the eastern Bering Sea (120.Z) was negatively correlated, whereas no other zooplankton time series were significantly correlated. The correlation map without time filtering (**Supplementary Figure 3c**) also exhibits positive correlations for salmon and negative correlations for groundfish but with increased number of biological time series that are significantly correlated [from 18 with the filter (**Figure 4C**) to 27 without it (**Supplementary Figure 3c**)].

Figure 5 shows the biological time series that are significantly correlated to the PC2s shown in **Figures 4B,C** with the low-pass filter. The western NP PC2 is characterized by a overall negative trend, small negative anomalies in the 1980s, and large positive anomalies in the 1990s. This feature is shared by zooplankton (119.Z) and chub mackerel (66.P) with a delayed peak in the 1990s (**Figures 5A,B**). In contrast, the

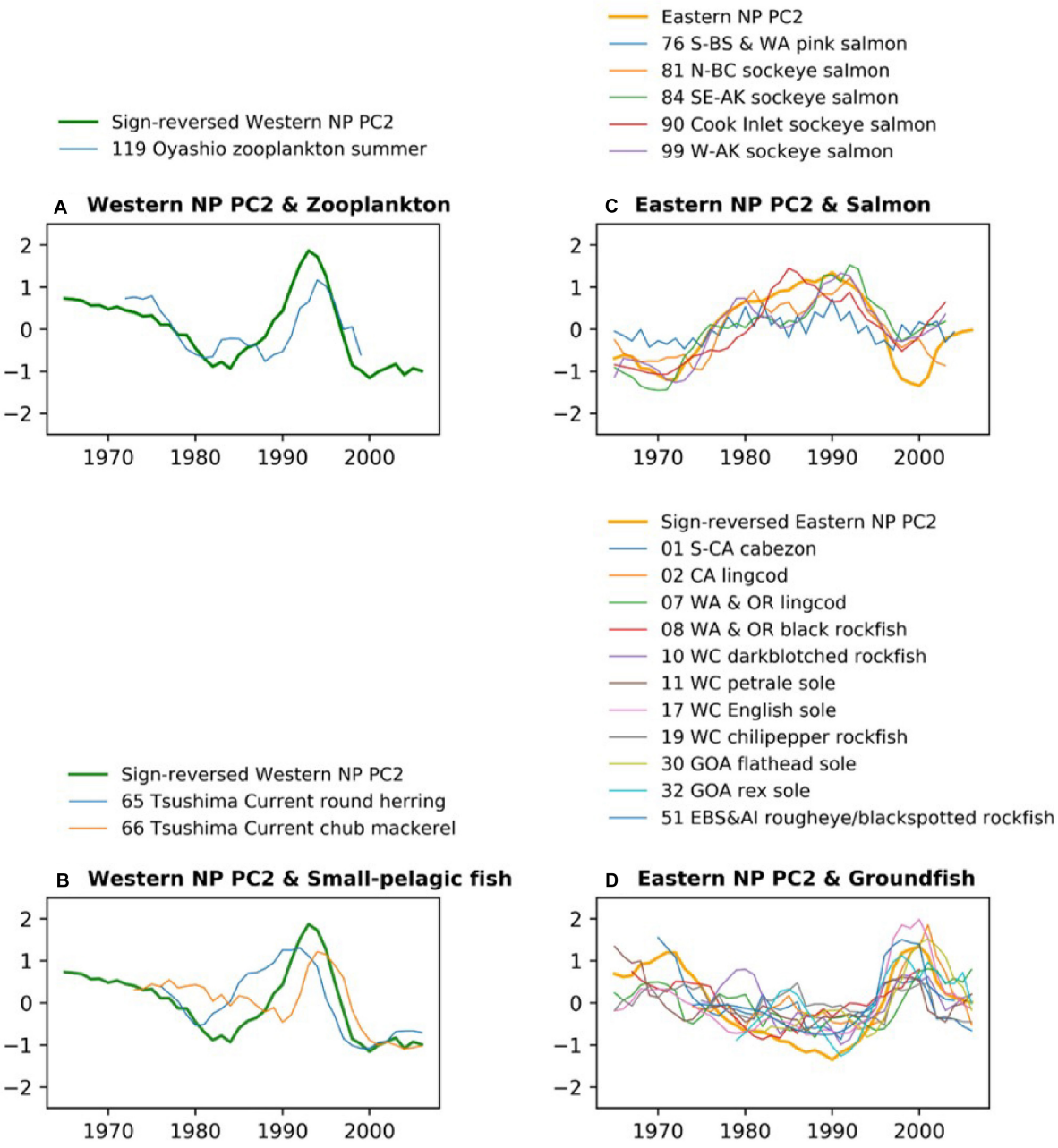

FIGURE 5 | As in **Figure 3**, but for western NP **(A)** zooplankton and **(B)** small pelagic fish along with western NP PC2, and eastern NP **(C)** salmon and **(D)** groundfish along with eastern NP PC2. All time series are smoothed by 5-year running mean. For an easier comparison, the PC2 time series are sign-reversed (multiplied by –1) for **(A,B,D)**.

peak in round herring (65.P) occurs earlier than the peak of the western NP PC2 (**Figure 5B**). The low-pass filtered eastern NP PC2 is characterized by a negative-to-positive change in the 1970s and positive-to-negative change in the 1990s. These two phase transitions generally occur for salmon (**Figure 5C**), but only the later transition is evident in groundfish (**Figure 5D**). Furthermore, non-filtered data show that most of the groundfish time series exhibit a sharp peak at the end of 1990s (**Supplementary Figure 4**) simultaneously in general with the sharp negative peak of the eastern NP PC2 at 1999 shown in **Figure 4C**.

Relation Between Marine Ecosystem PCA and Climate Modes

Table 2 shows correlations between the PCs and climate time series. All PC1s, i.e., the whole NP PC1, the western NP PC1 and the eastern NP PC1, were highly correlated with NP-SST as well as G-SST with correlation coefficients between 0.76 and 0.90. The PC1s are not significantly correlated with other climate time series except for moderate correlations of the eastern NP PC1 with the MEI and NPI. The G-SST and NP-SST time series share multidecadal variability with biological PC1s including the negative-to-positive polarity change in the 1980s (**Figure 6A**). The warming of the G-SST is most likely due to anthropogenic global warming (Bindoff et al., 2019), and the similar trend between the G-SST and NP-SST suggests that global warming caused the warming trend of the NP-SST. Furthermore, the major causality between global warming and the marine ecosystem is that the former influenced the latter and not vise versa (Bindoff et al., 2019). Therefore, the close co-variability between the SST time series and biological PC1s suggests global warming influenced the first mode of the NP marine ecosystem.

The biological eastern NP PC2 is the most strongly correlated with the PDO index (**Table 2**). Consistently, the eastern NP PC2 and PDO index share the phase reversals in the 1970s and 1990s (**Figure 6B**), in association with the previously reported climate and ecosystem regime shifts (Mantua et al., 1997; Minobe, 1997; Chavez et al., 2003). An interesting difference between the two time series occurs around 1990, when the PDO index exhibited negative values for a short time without a similar feature in the eastern NP PC2. Some studies characterized the PDO index phase transition in the late 1980s a climatic regime shift (Yasunaka and Hanawa, 2002), but Minobe (2000) suggested that this was a minor climate regime shift and is different from the major regime shifts in the 1920s, 1940s, and 1970s. The eastern NP PC2 shows no correspondence with this short-lived event. The second strongest correlation with eastern NP PC2 is found for MEI (**Table 2**), probably reflecting the fact that the PDO, the most strongly correlated climate mode to the eastern NP PC2, is accompanied by ENSO-like interdecadal variability in the tropical Pacific (Mantua et al., 1997; Zhang et al., 1997). The relation between the North and tropical Pacific for decadal

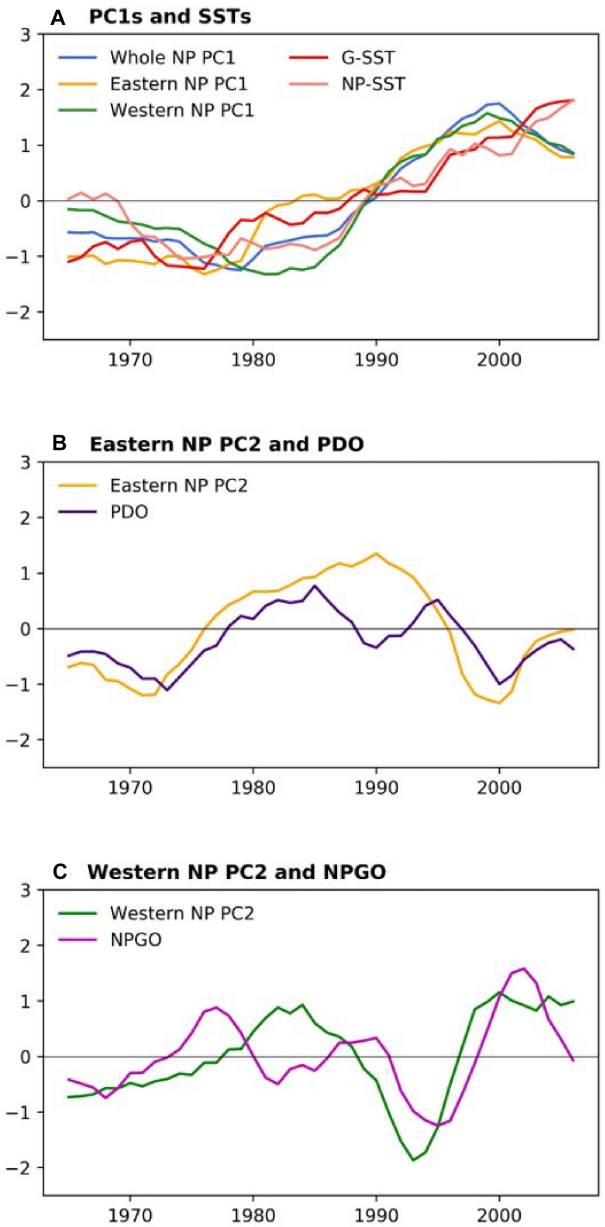

FIGURE 6 | (A) Marine biological PC1s and G-SST and NP-SST **(B)** eastern NP PC2 and PDO index, and **(C)** western NP PC2 and NPGO index. From all climate indices, their respective averages in 1965–2006 have been removed, and G-SST and NP-SST are further divided by their respective standard deviations. All time series are smoothed by 5-year running mean.

TABLE 2 | Correlations between marine ecosystem PCs and climate indices with 5-year running mean.

	G-SSA	NP-SST	PDO	NPGO	MEI	NPI	AO
Whole NP PC1	0.87*	0.88*	−0.12	0.11	0.31	−0.27	0.29
Eastern NP PC1	0.89*	0.76*	0.21	0.07	0.57*	−0.51*	0.37
Western NP PC1	0.77*	0.90*	−0.31	0.1	0.16	−0.05	0.29
Eastern NP PC2	−0.01	−0.26	0.76*	−0.13	0.66*	−0.35	0.43
Western NP PC2	0.46*	0.18	0.03	0.61*	0.01	−0.47	−0.28

Asterisks indicate that the correlations are significant at the 95% confidence level.

variability was at least partly due to the tropical influence on the mid-latitudes (Newman et al., 2003; see also review of Newman et al., 2016), but causality in the opposite direction, i.e., mid-latitude forces the tropics, was also reported (e.g., Vimont et al., 2003, Zhao and Di Lorenzo, 2020; see also review of Amaya, 2019).

In contrast to the relation between eastern NP PC2 and the PDO index, the western NP PC2 is correlated with the NPGO index (**Table 2**). It is noteworthy that the correlations of different combinations, i.e., between eastern NP PC2 and the NPGO index and between western NP PC2 and the PDO index, are very small. The time series comparison shows that the coherent variability between the NPGO index and western NP PC2 is limited to the 1990s and 2000s (**Figure 6C**). This may be related to the recent enhancement of decadal variability of the NPGO (Di Lorenzo et al., 2008; Joh and Di Lorenzo, 2017).

Figure 7 shows that the SST correlation patterns associated with biological PCs. The correlation map associated with the whole NP PC1 (**Figure 7A**) is characterized by overall positive correlations, accompanied by especially strong correlations in the western subtropical gyre and in the East China Sea. The correlations with the whole NP PC1 were weak along the subpolar front near 40°N and the subtropical front near 30°N, 150°W. Similar patterns are produced in correlation maps between gridded SSTA and the western and eastern NP PC1s (**Figures 7B,C**). The correlation map associated with the eastern NP PC2 (**Figure 7D**) is similar to the PDO pattern, which was the first PCA mode of NP SSTs, while the correlation map with the western NP PC2 (**Figure 7E**) is similar to the second mode of SST pattern (Bond et al., 2003), which is known to be closely related to the NPGO. The correlations with the eastern NP PC2 are generally strong in the eastern and central NP rather than in the western NP, consistent with the PDO pattern itself (Mantua et al., 1997). On the other hand, the correlations with the western NP PC2 are generally strong in the subtropical western NP.

DISCUSSION

Comparison of PCA Modes Between the Present and Previous Studies and Possible Future LMAs

The trend-like feature is consistent with the biological PC1s of the previous eastern NP LMAs by Hare and Mantua (2000) and Litzow and Mueter (2014) as well as PC1s of western NP LMAs by Tian et al. (2006) and Ma et al. (2019). The physical-biological combined PC1 of Hare and Mantua (2000) exhibited rapid transition feature, but the changes were much more gradual in biological-only PC1s by Hare and Mantua (2000) and Litzow and Mueter (2014). Although the biological PC1s in this study were similar to those obtained by previous studies as noted above, the relationship between the PC1 and global warming was first identified by the present study. Our results strongly suggest that global warming has already impacted marine ecosystems in the NP.

The eastern NP PC2 was consistent with biological PC2s of Litzow and Mueter (2014). The biological PC2 of Hare and Mantua (2000) also exhibited the 1970s phase reversal, but the second phase change occurred around 1990, earlier than that in this study. The western NP PC2 was different from PCs reported by LMA analyses for western NP marginal seas (Tian et al., 2006; Ma et al., 2019). The different features of western NP PC2 can be due to the different kind of data, i.e., fish catch data in previous studies and recruitment and biomass data along with the abundance in the present study or due to the high spatial heterogeneity in the western NP.

The present and previous LMA studies indicate that the LMA is useful to identify the influence of climate variability and change on marine ecosystems, probably because LMA is effective at extracting the influence of common forcing across the time series even when the magnitude of the response is relatively small. Thus further LMA studies are desirable especially for the regions where LMA analyses have not been conducted yet. For those future LMA studies, it is suggested to use recruitment and/or abundance rather than fish catch data to understand changes in marine ecosystems, because fish catch data are directly influenced by fish catch efforts.

Possible Processes of Global Change Influence

It is interesting to discuss what processes are responsible for the biological variations documented in the present study, especially for the PCA first modes, which are suggested to be related to global warming. It is expected that the temperature increase due to global warming may cause geographical migration of marine species to colder areas, i.e., higher latitudes and deeper depths, and shifts of phenology (e.g., Pinsky et al., 2013; see also review by Poloczanska et al., 2016). The geographical migration increases warm water species and decreases cold water species in each region. This may be consistent with the pattern of small pelagic fishes characterized by increased jack mackerel and anchovy recruitment (P.67, P.68, P.73) in the western NP by the Japanese records. The migration can be more difficult for groundfish than pelagic fish because demersal fish habitat can be constrained by bottom topography (Li et al., 2019). This might partly explain why groundfish generally exhibit declines associated with the PCA first modes across the basin. The increase of salmon mainly occurs for Alaska and Russia, which are generally the northern limit of their habitat in the 20th century. Therefore, there is a possibility that global warming brought better condition for salmon in these areas. Indeed, Kaeriyama et al. (2014) suggested that the increase of salmon in the second half of the 20th century is strongly influenced by global warming, through the enhanced growth of age 1-year salmon in the Okhotsk Sea. Consistently, Pacific salmon catch increases have been noted on the Arctic side of Alaska since the 1990s (Carothers et al., 2019). Therefore, it is suggested that NP warming in the last several decades may have provided a better environment for some Russian and Alaskan salmon, though further temperature increase due to global warming may become harmful even for them. From the latter point of view, it is important to note that the time series

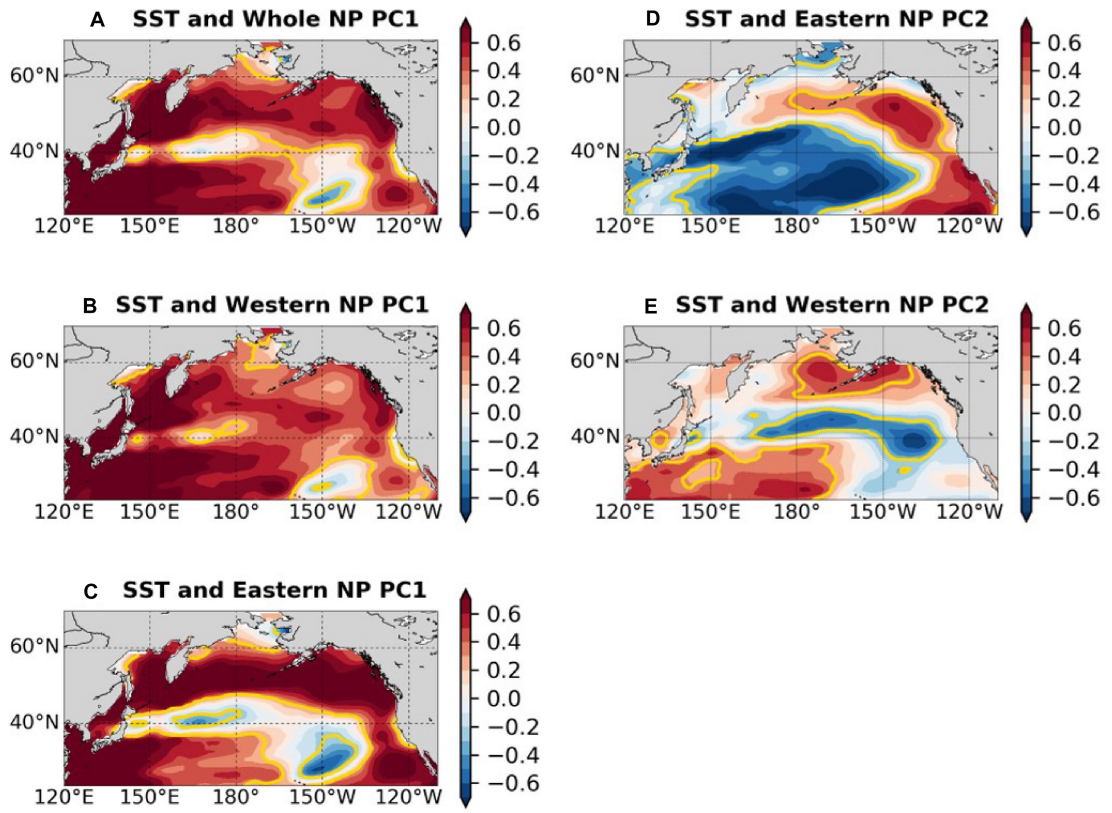

FIGURE 7 | Correlation map between SST and **(A)** whole NP PC1, **(B)** western NP PC1, **(C)** eastern NP PC1, **(D)** eastern NP PC2, **(E)** western NP PC2. The color shade indicates correlation value and the yellow contours indicate that areas have significant correlation at the 95% confidence level. Before calculating correlations 5-year running mean are applied to PCs and SSTs.

of Japanese/Russian salmon decline after 1990 (**Figure 3A**) and that the PC1s exhibit decreasing tendency after 2000 against continuing SSTA warming (**Figure 6A**).

Of course, climate change influences on marine ecosystems are not limited to temperature increases, but also include ocean acidification and ocean deoxygenation. Among these two threats, the species investigated in the present study may be more strongly influenced by the ocean deoxygenation, because the primary species impacted by ocean acidification are likely the species that build calcium carbonate-based shells and other structures (e.g., Doney et al., 2009). On the other hand, the NP is an area where strong ocean deoxygenation has been documented over the last 50–60 years, as reported by recent global analyses (Ito et al., 2017; Schmidtko et al., 2017), and thus the deoxygenation can have negatively impacted marine species, especially groundfish. Indeed, Ono et al. (2001) suggested that the shoaling of the hypoxia upper boundary influenced the deepest habitat of pacific cod over the Pacific continental shelf off northeast of Japan. Oxygen changes also impacted mesopelagic and demersal fish in California Current System (Koslow et al., 2011, 2019). Ocean deoxygenation is generally caused by increased water temperature through the reduced oxygen saturation concentration at the surface and weakened circulation and mixing that supply dissolved oxygen at depth (e.g., Keeling et al., 2010). The strong oxygen decrease over the NP may be due to reduced ventilation caused by weaker cooling in the Okhotsk Sea (Nakanowatari et al., 2007). In addition, vertical displacements of isopycnal surfaces and advection on those surfaces play important roles in varying dissolved oxygen concentration in different regions of the NP (Pozo Buil and Di Lorenzo, 2017; Ito et al., 2019). Further studies are necessary to understand the mechanisms of deoxygenation over the NP basin and its influences on marine ecosystems.

These possible mechanisms suggest that groundfish may have more difficulties than pelagic fish in adjusting to the impacts of global warming. In order to understand this aspect better, we plot the depth ranges of the fish species that have significant correlations with the biological PC1s from our analyses (**Figure 8**). For the first PCA modes, among 17 time series of significant positive correlations 12 time series are for species with depth range shallower than 300 m, while among 20 time series of significant negative correlations 13 time series are for species with depth range deeper than 300 m. This result shows that the sign of the loadings on our ecosystem PCA

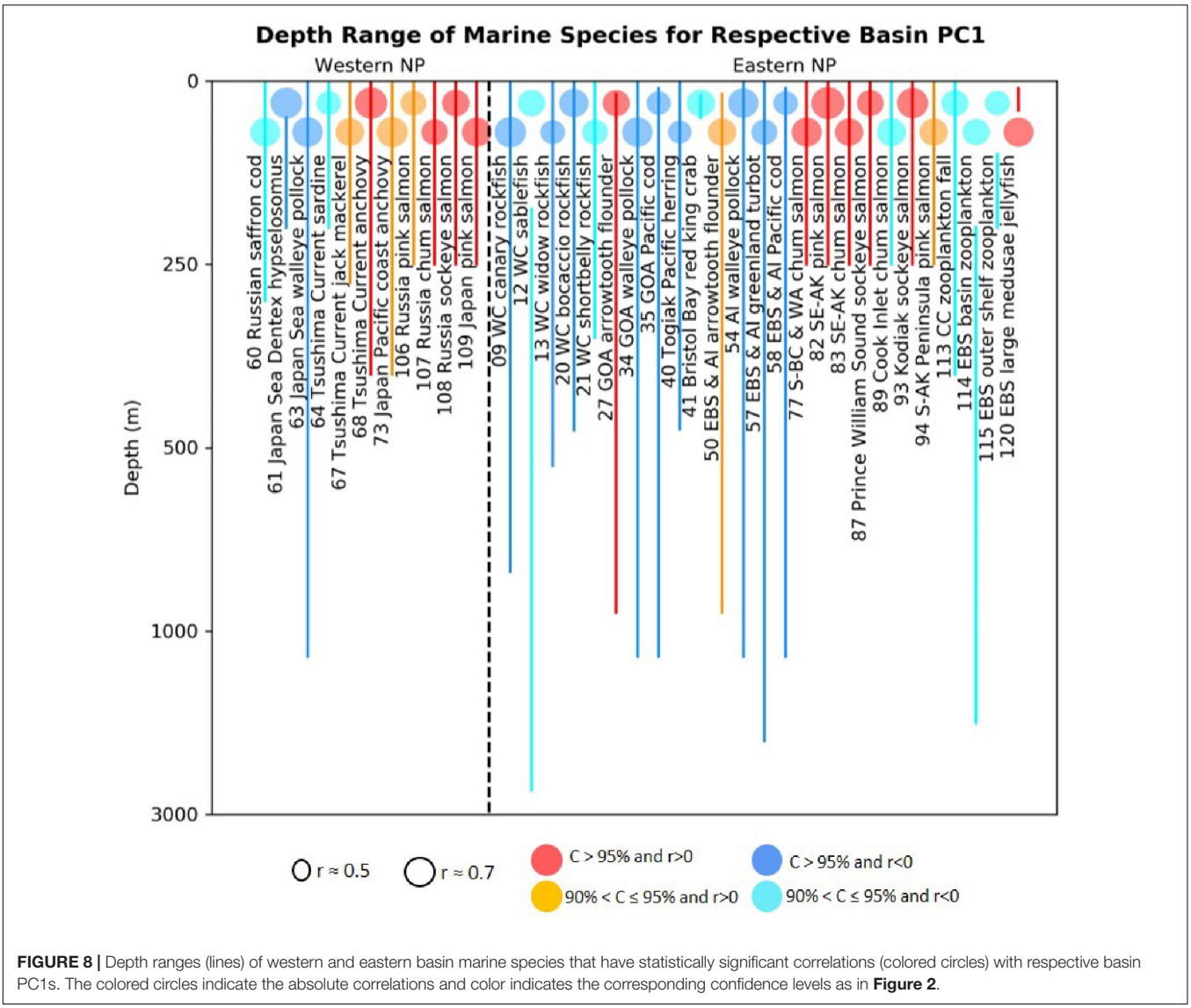

FIGURE 8 | Depth ranges (lines) of western and eastern basin marine species that have statistically significant correlations (colored circles) with respective basin PC1s. The colored circles indicate the absolute correlations and color indicates the corresponding confidence levels as in **Figure 2**.

modes are generally opposite for shallow and deep-water species. Consistently, the LMA in the northeast Atlantic also revealed global-warming related decline of cod and plaice but increase of herring (Brunel and Boucher, 2007). Since the disadvantageous conditions to the ground fish, i.e., bottom topography constraint for habitat and ocean deoxygenation, will not be relaxed in future, we expect that groundfish will suffer more than pelagic fish species in the warming oceans.

Although we consider that the first mode is mainly caused by global warming, but other anthropogenic factors such as fishing may have some influence. Recruitment and abundance, which are the main data used in the present study, are less influenced directly by fishing than fish catch data, which were used in some LMA studies. However, our data are not free from effects of fishing; for example, if a species is substantially removed by fishing, it can impact its predator and prey species. It is difficult to identify these factors from observational data analysis alone. In future, it is desirable that these factors are estimated by using mathematical or numerical models (e.g., Coll et al., 2019; Bueno-Pardo et al., 2020).

Possible Mechanisms of Zooplankton Variations

Among marine species analyzed in the present study zooplankton are important as food for other species. Thus, it is interesting to discuss what mechanisms can work on the observed zooplankton variations.

Three zooplankton biomass time series in the eastern NP, one from California Current waters (113.Z) and two from the eastern Bering Sea (114.Z, 115.Z), were highly correlated with the eastern NP PC1, which is suggested to be influenced by warming ocean temperatures. For California Current waters, Roemmich and McGowan (1995) reported that a substantial decline of zooplankton associated with warming of a surface layer from the 1950s to the 1990s. The warmed surface water enhances

stratification, which in turn reduces the upwelling resulting in weakened productivity due to the reduced upwelled nutrients. Our result shows that the California Current zooplankton stayed low level except for a positive spike 2003 (**Supplementary Figure 2f**). If the hypothesis of Roemmich and McGowan (1995) is true, the decline of California Current zooplankton is an aspect of marine ecosystem response to the global warming discussed in the previous subsection. For the eastern Bering Sea, Sugimoto and Tadokoro (1997) reported an increase in zooplankton biomass in the 1960s and 1970s relative to the preceding decade, and a decline from the 1970s to the 1990s (when the records they examined end). They suggested that on decadal timescales a bottom-up effect may be responsible for zooplankton variations.

In the western NP, summertime zooplankton biomass in Oyashio waters (119.Z) was related to the western NP PC2 (**Figure 4B**). The zooplankton time series is consistent with those in Tadokoro et al. (2005) and Tadokoro et al. (2009). As drivers for the zooplankton variations in Oyashio waters, predation pressure by Japanese sardine (Tadokoro et al., 2005) and surface nutrient variability via primary production (Tadokoro et al., 2009) were suggested. Ito et al. (2007) demonstrated the effect of predation pressure on zooplankton by Japanese sardine on other pelagic fish growth by using a simple box model. The decrease of other small pelagic species in the western NP PC2 was consistent with the estimates generated (**Figure 4B**). Furthermore, the high biomass of zooplankton in Oyashio water in the 1990s in the present study and Tadokoro et al. (2005, 2009) was also seen in zooplankton biomass in the Kuroshio-Oyashio Extension region (Chiba et al., 2013). Chiba et al. (2013) suggested that changes in advection of Kuroshio water in association with the NPGO caused the observed zooplankton biomass changes in this region (see also Di Lorenzo et al., 2008).

SUMMARY

The LMA of marine biological time series for both the western and eastern NP basins was conducted for the first time using PCA of 120 biological time series. Marine biological PC1s both in the eastern and western NP exhibit long-term trends and are associated with overall increased Alaskan and Japanese/Russian salmon abundance and some small pelagic fish recruitment in the western NP, and decreases of groundfish recruitment across the basin and eastern NP zooplankton biomass (**Figures 2**, **3**). This mode is closely related to NP- and G-SSTs (**Figure 6A**). This suggests that the first mode of the NP marine ecosystem is strongly influenced by global warming. These PC1s are consistent with biological PC1s of previous studies for the eastern NP (Hare and Mantua, 2000; Litzow and Mueter, 2014) as well as those for the western NP marginal seas (Tian et al., 2006; Ma et al., 2019), although those studies did not examine relationships with global warming. We expect that future global warming will cause more difficulties for groundfish than pelagic fish. The eastern NP PC2, characterized by multidecadal variability, was correlated positively with salmon abundance and negatively with groundfish recruitment (**Figures 4C**, **5C,D**). On the other hand, the western NP PC2 exhibits slightly shorter timescale interdecadal variability than the eastern NP PC2 and was negatively correlated with zooplankton biomass and two small pelagic fish recruitment records around Japan. The eastern NP PC2 is the most strongly related to the PDO index (**Figures 4A**, **6B**), while the western NP PC2 is the most closely related to the NPGO index (**Figures 4A**, **6C**). Consequently, the present LMA provides a new and unified view for climate change and marine ecosystem variations across the western and eastern NP.

DATA AVAILABILITY STATEMENT

The data analyzed in this study is subject to the following licenses/restrictions: Japanese data of fish recruitment is publically available at http://abchan.fra.go.jp/digests26/index.html (in Japanese) and other data are collected by authors. Requests to access these datasets should be directed to Nathan Mantua for United States/Canada data nate.mantua@noaa.gov.

AUTHOR CONTRIBUTIONS

SM, NM, and ED designed the present study. NM and SI collected the data. EY and SM analyzed the data and wrote the draft manuscript. All authors discussed about the manuscript.

FUNDING

EY thank the Research and Innovation Science and Technology Project, Ministry of Research and Technology/National Research and Innovation Agency of Republic of Indonesia for funded her doctoral course. SM is supported by the Japan Society for the Promotion of Science (JSPS) KAKENHI (JP18H04129). SI is supported by the Japan Society for the Promotion of Science (JSPS) KAKENHI (JP18H03956).

ACKNOWLEDGMENTS

We thank Dr. Kazuaki Tadokoro for providing Japanese zooplankton data and Dr. Yury I. Zuenko for providing Russian Saffron cod data, Dr. Megan M. Stachura for organizing the biological time series data, and Dr. Will Satterthwaite for his helpful comments on a draft of the manuscript. We also thank two reviewers for their constructive comments.

SUPPLEMENTARY MATERIAL

The Supplementary Material for this article can be found online at: https://www.frontiersin.org/articles/10.3389/fmars.2020.578165/full#supplementary-material

REFERENCES

Amaya, D. J. (2019). The Pacific Meridional Mode and ENSO: a review. *Curr. Clim. Change Rep.* 5, 296–307. doi: 10.1007/s40641-019-00142-x

Beamish, R. J., and Bouillon, D. R. (1993). Pacific salmon production trends in relation to climate. *Can. J. Fish. Aquat. Sci.* 50, 1002–1016. doi: 10.1139/f93-116

Beamish, R. J., Noakes, D. J., McFarlane, G. A., Klyashtorin, L., Ivanov, V. V., Kurashov, V., et al. (1999). The regime concept and natural trends in the production of Pacific Salmon. *Can. J. Fish. Aquat. Sci.* 56, 516–526. doi: 10.1139/f98-200

Bindoff, N. L., Cheung, W. W. L., Kairo, J. G., Arístegui, J., Guinder, V. A., Hallberg, R., et al. (2019). "Changing ocean, marine ecosystems, and dependent communities," in *IPCC Special Report on the Ocean and Cryosphere in a Changing Climate*, eds H.-O. Pörtner, D. C. Roberts, V. Masson-Delmotte, P. Zhai, M. Tignor, E. Poloczanska, et al. (Geneva: IPCC).

Bond, N. A., Overland, J. E., Spillane, M., and Stabeno, P. (2003). Recent shifts in the State of the North Pacific. *Geophys. Res. Lett.* 30:2183. doi: 10.1029/2003gl018597

Brander, K. M. (2007). Global fish production and climate change. *Proc. Natl. Acad. Sci. U.S.A.* 104, 709–719.

Brunel, T., and Boucher, J. (2007). Long-term trends in fish recruitment in the north-east Atlantic related to climate change. *Fish. Oceanogr.* 16, 336–349. doi: 10.1111/j.1365-2419.2007.00435.x

Bueno-Pardo, J., Petitgas, P., Kay, S., and Huret, M. (2020). Integration of bioenergetics in an individual-based model to hindcast anchovy dynamics in the Bay of Biscay. *ICES J. Mar. Sci.* 77, 655–667. doi: 10.1093/icesjms/fsz239

Carothers, C., Sformo, T. L., Cotton, S., George, J. C., and Westley, P. A. H. (2019). Pacific salmon in the rapidly changing arctic: exploring local knowledge and emerging fisheries in Utqiaġvik and Nuiqsut, Alaska. *Arctic* 72, 273–288. doi: 10.14430/arctic68876

Chavez, F. P., Ryan, J., Lluch-Cota, S. E., and Niquen, M. (2003). From anchovies to sardines and back: multidecadal change in the Pacific Ocean. *Science* 299, 217–221. doi: 10.1126/science.1075880

Chiba, S., Lorenzo, E. D., Davis, A., Keister, J. E., Taguchi, B., Sasai, Y., et al. (2013). Large-scale climate control of zooplankton transport and biogeography in the kuroshio-oyashio extension region. *Geophys. Res. Lett.* 40, 5182–5187. doi: 10.1002/grl.50999

Coll, M., Albo-Puigserver, M., Navarro, J., Palomera, I., and Dambacher, J. (2019). Who is to blame? Plausible pressures on small pelagic fish population changes in the northwestern Mediterranean Sea. *Mar. Ecol. Prog. Ser.* 617-618, 277–294. doi: 10.3354/meps12591

Cushing, D. H. (1982). *Climate and Fisheries*. London: Academic Press.

Di Lorenzo, E., Combes, J. E., Keister, P. T., Strub, A. C., Thomas, P. J. S., Franks, M. D., et al. (2008). Synthesis of pacific ocean climate and ecosystem dynamics. *Oceanography* 26, 68–81. doi: 10.5670/oceanog.2013.76

Di Lorenzo, E., Schneider, N., Cobb, K. M., Franks, P. J. S., Chhak, K., Miller, A. J., et al. (2008). North Pacific gyre oscillation links ocean climate and ecosystem change. *Geophys. Res. Lett.* 35, 1–6. doi: 10.1029/2007gl032838

Doney, S. C., Fabry, V. J., Feely, R. A., and Kleypas, J. A. (2009). Ocean acidification: the other CO2Problem. *Annu. Rev. Mar. Sci.* 1, 169–192. doi: 10.1146/annurev.marine.010908.163834

Ebbesmeyer, C. C., Cayan, D. R., Mclain, D. R., Nichols, F. H., Peterson, D., Redmond, K., et al. (1991). "1976 step in the pacific climate: forty environmental changes between 1968-1975 and 1977-1984," in *Proceedings of the Seventh Annual Pacific Climate (PACLIM) Workshop, 10-13 April 1990*, (Pacific Grove, CA: Asilomar Conference Center).

Francis, R. C., and Hare, S. R. (1994). Decadal-scale regime shifts in the large marine ecosystems of the north-east pacific: a case for historical science. *Fish. Oceanogr.* 3, 279–291. doi: 10.1111/j.1365-2419.1994.tb00105.x

Hare, S. R., and Mantua, N. J. (2000). Empirical Evidence for North Pacific Regime Shifts in 1977 and 1989. *Prog. Oceanogr.* 47, 103–145. doi: 10.1016/s0079-6611(00)00033-1

Hare, S. R., Mantua, N. J., and Francis, R. C. (1999). Inverse production regimes: Alaska and West Coast Pacific Salmon. *Fisheries* 24, 6–14. doi: 10.1577/1548-8446(1999)024<0006:ipr>2.0.co;2

Hirahara, S., Ishii, M., and Fukudaet, Y. (2014). Centennial-scale sea surface temperature analysis and its uncertainty. *J. Clim.* 27, 57–75. doi: 10.1175/jcli-d-12-00837.1

Hoff, G. R. (2006). Biodiversity as an index of regime shift in the eastern Bering Sea. *Fish. Bull.* 104, 226–237.

Ito, S.-I., Megrey, B. A., Kishi, M. J., Mukai, D., Kurita, Y., Ueno, Y., et al. (2007). On the interannual variability of the growth of Pacific saury (*Cololabis saira*): a simple 3-box model using NEMURO.FISH. *Ecol. Model.* 202, 174–183. doi: 10.1016/j.ecolmodel.2006.07.046

Ito, T., Long, M. C., Deutsch, C., Minobe, S., and Sun, D. (2019). Mechanisms of low-frequency oxygen variability in the North Pacific. *Glob. Biogeochem. Cycles* 33, 110–124. doi: 10.1029/2018gb005987

Ito, T., Minobe, S., Long, M. C., and Deutsch, C. (2017). Upper Ocean O2 trends: 1958–2015. *AGU J.* 44, 4214–4223. doi: 10.1002/2017GL073613

Japan Fisheries Agency, and Fisheries Research Agency (2015). *Marine Fisheries Stock Assessment and Evaluation for Japanese Waters (fiscal year 2014/2015)*. Available online at: http://abchan.fra.go.jp/digests26/index.html (accessed October 25, 2020).

Joh, Y., and Di Lorenzo, E. (2017). Increasing coupling between NPGO and PDO leads to prolonged marine heatwaves in the Northeast Pacific. *Geophys. Res. Lett.* 44, 11,663–11,671. doi: 10.1002/2017gl075930

Kaeriyama, M., Seo, H., and Qin, Y.-X. (2014). Effect of global warming on the life history and population dynamics of Japanese Chum Salmon. *Fish. Sci.* 80, 251–260. doi: 10.1007/s12562-013-0693-7

Kawasaki, T., and Omori, M. (1995). Possible mechanisms underlying fluctuations in the far eastern sardine population inferred from time series of two biological traits. *Fish. Oceanogr.* 4, 238–242. doi: 10.1111/j.1365-2419.1995.tb00147.x

Kay, S. M. (1988). *Modern Spectral Estimation: Theory and Application*. Englewood Cliffs, NJ: Prentice-Hall.

Keeling, R. F., Körtzinger, A., and Gruber, N. (2010). Ocean Deoxygenation in a Warming World. *Annu. Rev. Mar. Sci.* 2, 199–229. doi: 10.1146/annurev.marine.010908.163855

Koslow, J., Goericke, R., Lara-Lopez, A., and Watson, W. (2011). Impact of declining intermediate-water oxygen on deepwater fishes in the California current. *Mar. Ecol. Prog. Ser.* 436, 207–218. doi: 10.3354/meps09270

Koslow, J. A., Davison, P., Ferrer, E., Rosenberg, S. P. A. J., Aceves-Medina, G., and Watson, W. (2019). The evolving response of mesopelagic fishes to declining midwater oxygen concentrations in the southern and central California current. *ICES J. Mar. Sci.* 76, 626–638. doi: 10.1093/icesjms/fsy154

Li, L., Hollowed, A. B., Cokelet, E. D., Barbeaux, S. J., Bond, N. A., Keller, A. A., et al. (2019). Subregional differences in groundfish distributional responses to anomalous ocean bottom temperatures in the Northeast Pacific. *Glob. Change Biol.* 25, 2560–2575. doi: 10.1111/gcb.14676

Litzow, M. A., and Mueter, F. J. (2014). Assessing the ecological importance of climate regime shifts: an approach from the North Pacific Ocean. *Prog. Oceanogr.* 120, 110–119. doi: 10.1016/j.pocean.2013.08.003

Lluch-Belda, D., Crawford, R. J. M., Kawasaki, T., MacCall, A. D., Parrish, R. H., Schwartzlose, R. A., et al. (1989). World-wide fluctuations of sardine and anchovy stocks: the regime problem. *S. Afr. J. Mar. Sci.* 8, 195–205. doi: 10.2989/025776189095045 61

Lluch-Belda, D., Schwartzlose, R. A., Serra, R., Parrish, R., Kawasaki, T., Hedgecock, D., et al. (1992). Sardine and anchovy regime fluctuations of abundance in four regions of the world oceans: a workshop report. *Fish. Oceanogr.* 1, 339–347. doi: 10.1111/j.1365-2419.1992.tb00006.x

Ma, S., Liu, Y., Li, J., Fu, C., Ye, Z., Sun, P., et al. (2019). Climate-induced long-term variations in ecosystem structure and atmosphere-ocean-ecosystem processes in the Yellow Sea and East China Sea. *Prog. Oceanogr.* 175, 183–197. doi: 10.1016/j.pocean.2019.04.008

Mantua, N. J., Hare, S. R., Zhang, Y., Wallace, J. M., and Francis, C. (1997). A pacific interdecadal climate oscillation with impacts on salmon production. *Bull. Am. Meteorol. Soc.* 78, 1069–1079. doi: 10.1175/1520-0477(1997)078<1069:apicow>2.0.co;2

Metz, W. (1991). Optimal relationship of large-scale flow patterns and the barotropic feedback due to high-frequency eddies. *J. Atmos. Sci.* 48, 1141–1159. doi: 10.1175/1520-0469(1991)048<1141:orolsf>2.0.co;2

Minobe, S. (1997). A 50-70 year climatic oscillation over the North Pacific and North America. *Geophys. Res. Lett.* 24, 683–686. doi: 10.1029/97gl00504

Minobe, S. (2000). Spatio-temporal structure of the pentadecadal variability over the North Pacific. *Prog. Oceanogr.* 47, 381–408. doi: 10.1016/s0079-6611(00)00042-2

Möllmann, C., and Diekmann, R. (2012). Marine ecosystem regime shifts induced by climate and overfishing. *Adv. Ecol. Res. Glob. Change Multispecies Syst.* 47, 303–347. doi: 10.1016/b978-0-12-398315-2.00004-1

Nakanowatari, T., Ohshima, K. I., Wakatsuchi, M. (2007). Warming and oxygen decrease of intermediate water in the Northwestern North Pacific, Originating from the Sea of Okhotsk, 1955–2004. *Geophys. Res. Lett.* 34. doi: 10.1029/2006gl028243

Newman, M., Alexander, M. A., Ault, T. R., Cobb, K. M., and Deser, C. E. (2016). The pacific decadal oscillation, revisited. *J. Clim.* 29, 4399–4427. doi: 10.1175/jcli-d-15-0508.1

Newman, M., Compo, G. P., and Alexander, M. A. (2003). ENSO-forced variability of the pacific decadal oscillation. *J. Clim.* 16, 3853–3857. doi: 10.1175/1520-0442(2003)016<3853:evotpd>2.0.co;2

Noto, M., and Yasuda, I. (1999). Population decline of the Japanese sardine, sardinops melanostictus, in relation to sea surface temperature in the kuroshio extension. *Can. J. Fish. Aquat. Sci.* 56, 973–983. doi: 10.1139/f99-028

Ono, T., Midorikawa, T., Watanabe, Y. W., Tadokoro, K., and Saino, T. (2001). Temporal increases of phosphate and apparent oxygen utilization in the subsurface waters of western subarctic pacific from 1968 to 1998. *Geophys. Res. Lett.* 28, 3285–3288. doi: 10.1029/2001gl012948

Pinsky, M. L., Worm, B., Fogarty, M. J., Sarmiento, J. L., and Levin, S. A. (2013). Marine taxa track local climate velocities. *Science* 341, 1239–1242. doi: 10.1126/science.1239352

Poloczanska, E. S., Burrows, M. T., Brown, C. J., Molinos, J. C., Halpern, B. S., Guldberg, O. H., et al. (2016). Responses of marine organisms to climate change across Oceans. *Front. Mar. Sci.* 3:62. doi: 10.3389/fmars.2016.00062

Pozo Buil, M., and Di Lorenzo, E. (2017). Decadal dynamics and predictability of oxygen and subsurface tracers in the california current system. *Geophys. Res. Lett.* 44, 4204–4213. doi: 10.1002/2017gl072931

Pyper, B. J., and Peterman, R. M. (1998). Comparison of methods to account for autocorrelation in correlation analyses of fish data. *Can. J. Fish. Aquat. Sci.* 55, 2127–2140. doi: 10.1139/f98-104

Roemmich, D., and McGowan, J. (1995). Climatic warming and the decline of zooplankton in the california current. *Science* 267, 1324–1326. doi: 10.1126/science.267.5202.1324

Schmidtko, S., Stramma, L., and Visbeck, M. (2017). *Decline in Global Oceanic Oxygen Content during the Past Five Decades*. Berlin: Nature Publishing Group.

Sugimoto, T., and Tadokoro, K. (1997). Interannual-interdecadal variations in zooplankton biomass, chlorophyll concentration and physical environment in the Subarctic Pacific and Bering Sea. *Fish. Oceanogr.* 6, 74–93. doi: 10.1046/j.1365-2419.1997.00031.x

Tadokoro, K., Chiba, S., Ono, T., Midorikawa, T., and Saino, T. (2005). Interannual variation in neocalanus biomass in the oyashio waters of the Western North Pacific. *Fish. Oceanogr.* 14, 210–222. doi: 10.1111/j.1365-2419.2005.00333.x

Tadokoro, K., Ono, T., Yasuda, I., Osafune, S., Shiomoto, A., Sugisaki, H., et al. (2009). Possible mechanisms of decadal-scale variation in PO4 concentration in the Western North Pacific. *Geophys. Res. Lett.* 36. doi: 10.1029/2009gl037327

Thompson, D. W. J., and Wallace, J. M. (1998). The arctic oscillation signature in the wintertime geopotential height and temperature fields. *Geophys. Res. Lett.* 25, 1297–1300. doi: 10.1029/98gl00950

Tian, Y., Kidokoro, H., and Watanbe, T. (2006). Long-term changes in the fish community structure from the tsushima warm current region of the Japan/East Sea with an emphasis on the impacts of fishing and climate regime shift over the last four decades. *Prog. Oceanogr.* 68, 217–237. doi: 10.1016/j.pocean.2006.02.009

Trenberth, K. E., and Hurrell, J. W. (1994). Decadal atmosphere-ocean variations in the Pacific. *Clim. Dyn.* 9, 303–319. doi: 10.1007/bf00204745

Ventura, V., Paciorek, C. J., and Risbey, J. S. (2004). Controlling the proportion of falsely rejected hypotheses when conducting multiple tests with climatological data. *J. Clim.* 17, 4343–4356. doi: 10.1175/3199.1

von Storch, H., and Zwiers, F. (2012). Testing ensembles of climate change scenarios for 'statistical significance.'. *Clim. Change* 117, 1–9. doi: 10.1007/s10584-012-0551-0

Vimont, D. J., Wallace, J. M., and Battisti, D. S. (2003). The seasonal footprinting mechanism in the Pacific: Implications for ENSO. *J. Climate* 16, 2668–2675. doi: 10.1175/1520-0442(2003)016<2668:TSFMIT>2.0.CO;2

Wilks, D. (2016). "The stippling shows statistically significant grid points": how research results are routinely overstated and over-interpreted, and what to do about it. *Bull. Am. Meteorol. Soc.* 97, 2263–2273. doi: 10.1175/bams-d-15-00267.1

Wolter, K., and Timlin, M. S. (2011). El Niño/southern oscillation behaviour since 1871 as diagnosed in an extended multivariate enso index (MEI.ext). *Int. J. Climatol.* 31, 1074–1087. doi: 10.1002/joc.2336

Yasuda, I., Sugisaki, H., Watanabe, Y., Minobe, S. S., and Oozeki, Y. (1999). Interdecadal variations in Japanese sardine and ocean/climate. *Fish. Oceanogr.* 8, 18–24. doi: 10.1046/j.1365-2419.1999.00089.x

Yasunaka, S., and Hanawa, K. (2002). Regime Shifts Found in the Northern Hemisphere SST Field. *J. Meteorol. Soc. Jpn.* 80, 119–135. doi: 10.2151/jmsj.80.119

Zhang, Y., Wallace, J. M., and Battisti, D. S. (1997). ENSO-like interdecadal variability: 1900–93. *J. Climate* 10, 1004–1020. doi: 10.1175/1520-0442(1997)010<1004:ELIV>2.0.CO;2

Zhao, Y., and Di Lorenzo, E. (2020). The impacts of extra-tropical ENSO precursors on tropical Pacific decadal-scale variability. *Sci. Rep.* 10:3031. doi: 10.1038/s41598-020-59253-3

Conflict of Interest: The authors declare that the research was conducted in the absence of any commercial or financial relationships that could be construed as a potential conflict of interest.

frontiers in Marine Science

ORIGINAL RESEARCH
published: 14 January 2021
doi: 10.3389/fmars.2020.576240

Marine Heatwave of Sea Surface Temperature of the Oyashio Region in Summer in 2010–2016

Toru Miyama[1]*, *Shoshiro Minobe*[2,3] *and Hanako Goto*[2]

[1] Application Laboratory, Japan Agency for Marine-Earth Science and Technology, Yokohama, Japan, [2] Department of Earth and Planetary Sciences, Faculty of Science, Hokkaido University, Sapporo, Japan, [3] Department of Natural History Sciences, Graduate School of Science, Hokkaido University, Sapporo, Japan

The sea surface temperature (SST) of the Oyashio region in boreal summer abruptly increased in 2010 and high summertime SST repeated every year until 2016. Observations and an ocean reanalysis show that this marine heatwave occurred not only at the surface but also at deeper depths down to 200 m. Furthermore, salinity in summer also increased in parallel with the temperature. The rises in temperature and salinity indicate the strengthening of the Kuroshio water influence. The sea surface height and velocity show that the southward intrusion of the Oyashio near the coast in summer weakened from 2010 accompanied by an increase in anticyclonic eddies from the Kuroshio Extension. The much more frequent existence of anticyclonic eddies to the east of the first intrusion of the Oyashio in summer is closely associated with the weakening of the first intrusion and the strengthening of the second intrusion. It is suggested that the rise in the water temperature could increase a catch of yellowtail (*Seriola quinqueradiata*) in northern Japan.

Keywords: marine heatwave, Oyashio current, Kuroshio current, anticyclonic eddy, yellowtail

OPEN ACCESS

Edited by:
Lyne Morissette,
M–Expertise Marine, Canada

Reviewed by:
Taku Wagawa,
Japan Fisheries Research and Education Agency (FRA), Japan
Hiroshi Kuroda,
Japan Fisheries Research and Education Agency (FRA), Japan
Ming Feng,
Commonwealth Scientific and Industrial Research Organization (CSIRO), Australia
Fei Yu,
Institute of Oceanology (CAS), China

***Correspondence:**
Toru Miyama
tmiyama@jamstec.go.jp

Specialty section:
This article was submitted to Marine Fisheries, Aquaculture and Living Resources, a section of the journal Frontiers in Marine Science

Received: *25 June 2020*
Accepted: *03 December 2020*
Published: *14 January 2021*

Citation:
Miyama T, Minobe S and Goto H (2021) Marine Heatwave of Sea Surface Temperature of the Oyashio Region in Summer in 2010–2016. Front. Mar. Sci. 7:576240. doi: 10.3389/fmars.2020.576240

INTRODUCTION

Marine heatwave is an event of anomalous warm sea surface temperatures (SST) from several days to years (Hobday et al., 2016). Recently, marine heatwaves have attracted considerable scientific and public interests. Marine heatwaves, combined with the global warming, can have substantial impacts on marine ecosystems. The frequency of marine heatwaves has significantly increased over the past century, with a 54% increase in annual marine heatwave days globally from 1925 to 2016 (Oliver et al., 2018). Marine heatwaves can also be a harbinger of near-future ocean conditions in a warmer world.

A prime example of marine heatwaves is "the blob," which occurred in 2014–2016 in the Northeastern Pacific Ocean (Bond et al., 2015; Lorenzo and Mantua, 2016; Hu et al., 2017), and is characterized by anomalous SST at more than 3°C than normal, exceeding four standard deviations. The blob caused substantial damage to marine ecosystems, including anomalously low near-surface chlorophyll biomass (Whitney, 2015) and massive deaths of sea lions, whales, and seabirds (Welch, 2016). On the other hand, animals favoring warm water temperatures, such as warm-water thresher sharks and ocean sunfish, appeared as far north as the Alaska coast (Welch, 2016).

In the North Pacific Ocean, marine heatwaves in recent years were not limited to the eastern side of the basin, but have also occurred in the western side of the basin with significant impacts

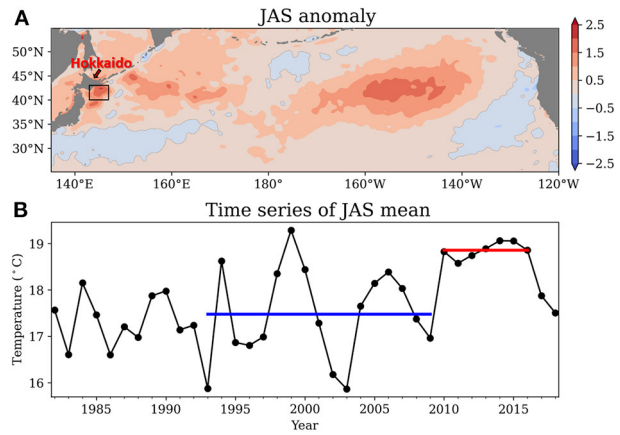

FIGURE 1 | (A) Anomaly of the 2010–2016 mean SST in July–September to the 1993–2009 mean (color; °C). **(B)** Time series from 1982 to 2018 of the July–September mean SST (°C) averaged over the box (143–147°E 40–43°N) enclosed in black lines in **(A)**. The blue line shows the 1993–2009 mean; the red line shows the 2010–2016 mean. OISST version 2 (see section Data) was used for these figures.

on the marine ecosystem there. For example, it has often been reported by mass media and official fisheries statistics in Japan that warm water fishes such as Japanese amberjack or yellowtail (*Seriola quinqueradiata*) are more frequently caught in the coastal region in northern Japan in the 2010s than before (Makino and Sakurai, 2012). Conversely, cold fishes such as saury (*Cololabis saira*) decreased drastically after 2010 (Kuroda and Yokouchi, 2017).

Consistently, in the early and middle 2010s, warm SST anomalies prevailed in the North Pacific off the island of Hokkaido in Japan (**Figure 1A**; in and around the black box). Interestingly, as shown later, this western North Pacific marine heatwave was often limited only in summer. Furthermore, SST anomaly off Hokkaido in summer over the western North Pacific was stable during 2010–2016 in contrast to the relatively high variability before that, indicating a new normal of warm SST (**Figure 1B** explained in section Results).

Recent conditions in the western North Pacific Ocean were studied by a few papers. Kuroda et al. (2015) studied the observational data from 1993 to 2011 and reported the increasing trend of sea-surface height in the region of strong SST anomalies near the coast of Hokkaido, and they suggested that this trend is related to the Oyashio path change from a nearshore path to an offshore path, which was caused by the wind-stress changes over the North Pacific Ocean. By analyzing August and September data, i.e., the season of warm SST anomalies, from 1993 to 2014, Kuroda and Yokouchi (2017) found that positive SST trend off Hokkaido is related to more frequent anticyclonic eddies. Especially for the period 2010–2014, they suggested that the same eddy occupied the region in 3 of 5 years in association with retreated Oyashio intrusion compared with the period 1993–1997. These studies mainly focused on the variability near the surface. The analysis of subsurface water properties by Kuroda et al. (2015) was limited to a single repeat observation line for annual mean.

Qiu et al. (2017) conducted an analysis of SST and head budget analysis of the upper 250 m depth in the western Oyashio Extension region (36–43°N, 141–150°E) and found that eddy advection was important in decadal variability in this region. They did not show the difference with seasons in the decadal variability.

Although these studies give us important information on recent changes and their possible mechanisms in the western North Pacific, previous studies have focused on linear trend or decadal variability. In this study, we paid attention to the apparent change from 2010 in **Figure 1**. We also studied the difference of the summer season from the other seasons, which was not discussed in the previous studies. The purpose of this paper is, therefore, to investigate the anomalous oceanic conditions in summer from 2010 compared with other seasons. In particular, we analyzed the three-dimensional subsurface temperature and salinity field by utilizing an eddy-resolving assimilation dataset of the FRA-JCOPE2 reanalysis (Miyazawa et al., 2009). The reanalysis of FRA-JCOPE2 allows us to understand the three-dimensional structure of the marine heatwave in the 2010s in the western North Pacific Ocean.

This paper is organized as follows. Data used in this study are described in section Data. The results are shown in section Results. The results are summarized and discussed in section Summary and Discussion.

DATA

In this study, we analyzed temperature, salinity, air-sea heat flux, sea surface height (SSH), and velocity data.

For SST, Optimal Interpolation SST (OISST) version 2 (Reynolds et al., 2007) was used. This SST dataset is a satellite observation based on measurements by the Advanced Very High-Resolution Radiometer (AVHRR). The horizontal grid size is 0.25°.

For air-sea heat flux, the ERA5 reanalysis (Copernicus Climate Change Service, 2017) with a 0.25° horizontal grid size was used. The net downward heat flux was calculated as a sum of surface net solar radiation, net thermal radiation, surface latent heat flux, and surface sensible heat flux.

For SSH, Global Ocean Gridded Level 4 Sea Surface Heights of Copernicus Marine Environment Monitoring Service (CMEMS; http://marine.copernicus.eu/) was used. The data is based on the observation of multi-mission satellite altimeters. The horizontal grid size is 0.25°.

The SSH dataset was also used to describe eddies through the eddy-tracking product of AVISO+ (https://www.aviso.altimetry.fr/en/data/products/value-added-products/global-mesoscale-eddy-trajectory-product.html). The daily paths and locations of cyclonic and anticyclonic eddies from 1993 to 2016 were used.

Temperature, salinity, and velocity from the FRA-JCOPE2 reanalysis (Miyazawa et al., 2009) were also used. This reanalysis dataset is the product assimilating satellite data and *in-situ* water temperature and salinity data into an ocean circulation model.

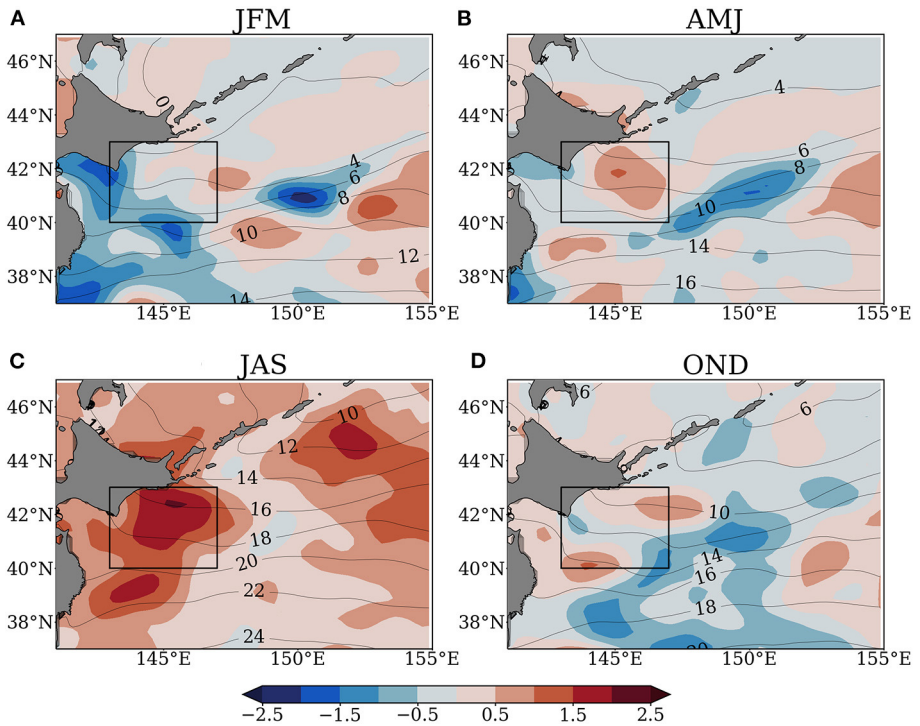

FIGURE 2 | Anomaly of the 2010–2016 mean SST in each season from the 1993–2009 mean (color; °C), and the 2010–2016 mean SST (contour; °C). **(A)** In JFM. **(B)** In AMJ. **(C)** In JAS. **(D)** In OND.

The horizontal grid size is 1/12° × 1/12°. The data from 1993 to 2018 was used.

In this study, we used data from July, August, and September (JAS) for averages for summer. Similarly, we used data from January to March (JFM), April to June (AMJ), and October to November (OND) for averages for winter, spring, and fall, respectively. For the heat flux in summer, the average from June to August was used, assuming that the change in the air-sea heat flux occurs 1 month earlier than the response of the ocean.

Data from 1993 to 2018 were analyzed, unless stated otherwise. The analysis period was decided because the observed SSH product and the FRA-JCOPE2 reanalysis are only available from 1993, though some data (for example, SST) before 1993 are available. We defined anomalies as deviations from the 1993–2009 climatologies.

RESULTS

Observed Sea Surface Temperature

Figure 2 shows the SST anomaly of the 2010–2016 mean from the 1993–2009 mean in each season. The anomaly in **Figure 2C** of JAS is the same as that of **Figure 1A** but magnified to show the detailed structure of the anomaly near Japan. The warming in the 2010s has a distinct seasonality. The temperature increase was particularly large in summer to the southeast off Hokkaido within the black box (143–147°E, 40–43°N). By contrast, SST decreased in most of the same region in winter.

The summertime SST abruptly increased in 2010 and the marine heatwave repeated until 2016. **Figure 1B** shows that the time series of the SST in JAS averaged over the aforementioned box southeast off Hokkaido in **Figure 1** (the same box in **Figure 2**). The SSTs from 2010 to 2016 were continuously higher by more than 1°C than its climatology, 17.5°C, defined for the period between 1993 and 2009 (the blue line) and the SST average between 2010 and 2016 is 18.9°C. The difference between the averages of 1993–2009 and 2010–2016 was statistically significant with Welch's t-test ($p = 3.2 \times 10^{-5} < 0.01$) with an assumption of year each being independent. From 2017 to 2018, the SST anomaly returned to the values close to the 1993–2009 climatology.

Although this study used values from 1993 to 2009 as the climatology according to the availability of the other data, the OISST data are available form 1982 (**Figure 1B**). The average between 1982 and 2009 (17.4°C) was similar to the one between 1993 and 2009. Although there were a few years when the temperature was warmer than the climatology by more than 1°C between 1982 and 2009, consecutive warming like in 2010–2016 did not occur in the past.

Figure 3 shows the anomaly of SST for each year (2010–2016) from the 1993–2009 average. Warming occurred at a similar location southeast off Hokkaido in each year. The SST anomaly in 2012 was located slightly westward of those in the other years and how this feature is associated with other variables will be described later.

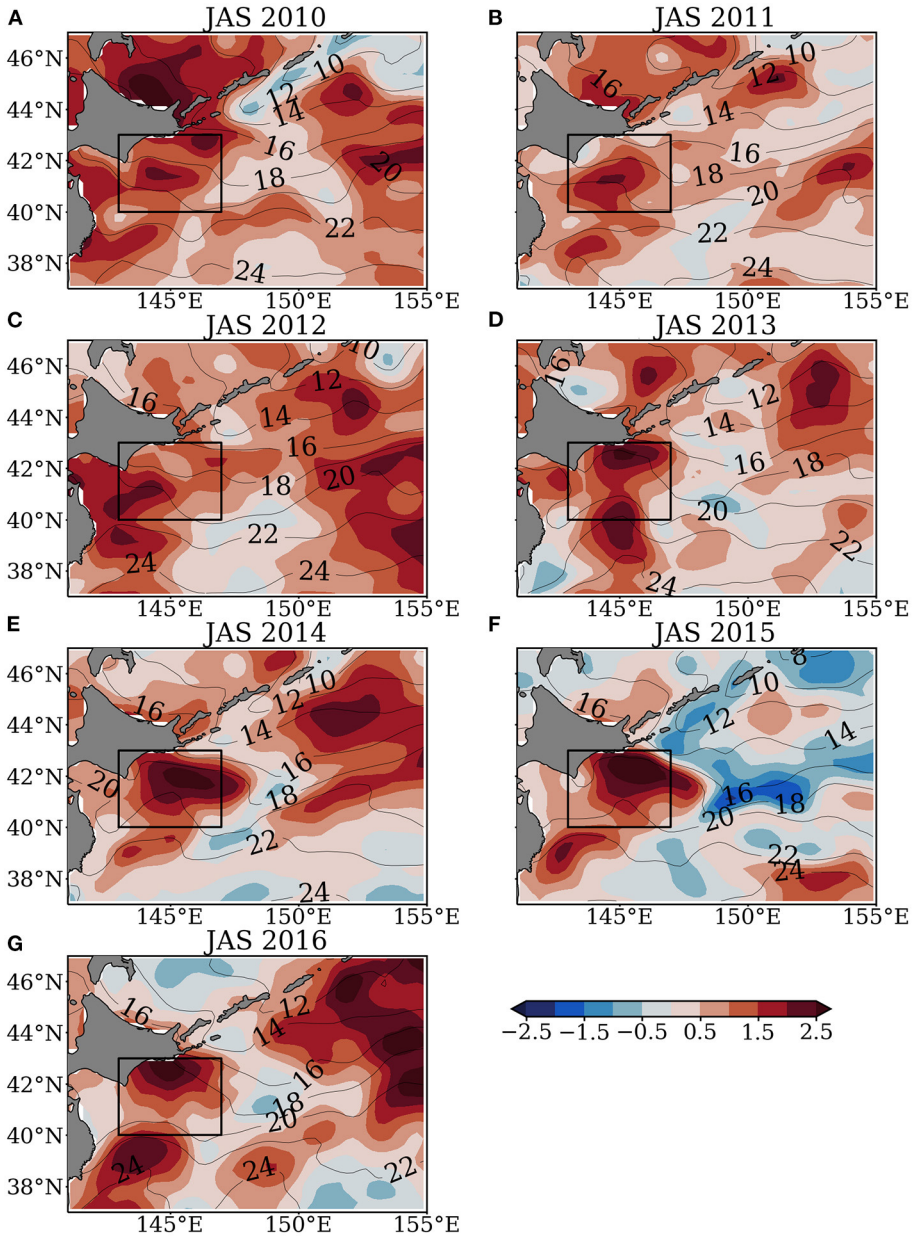

FIGURE 3 | Anomaly of the JAS-mean each year (2010–2016) from the 1993–2009 mean (color; °C) and SST in JAS each year (contour; °C).

Hobday et al. (2016) proposed a definition of marine heatwave as the event where temperature exceed an upper locally determined threshold (90th percentile relative to the local long-term climatology) for at least a five-day period, with no more than two below-threshold days. From daily time series for SST averaged over the box (143–147°E 40–43°N), **Figure 4** shows marine heatwave events in JAS season from 2010 to 2016 using the definition of Hobday et al. (2016). For climatology, 30-year baseline period of 1983–2012 was used as in Hobday et al. (2016). The red filled areas in **Figure 4** indicate the periods of the identified marine heatwaves. In JAS season of all years from 2010 to 2016, marine heatwave events occurred, corresponding to the anomalous SST warming in this region.

Hobday et al. (2018) further proposed a categorization scheme for marine heatwaves. Multiples of the 90th percentile difference (2× twice, 3× three times, etc.) from the mean climatology value define each of the categories I–IV, with corresponding descriptors from moderate to extreme. According to this category, some events in 2010, 2012, 2014 were Category II ("Strong") events, where the maximum temperatures exceeded the 2× difference line (green dashed line).

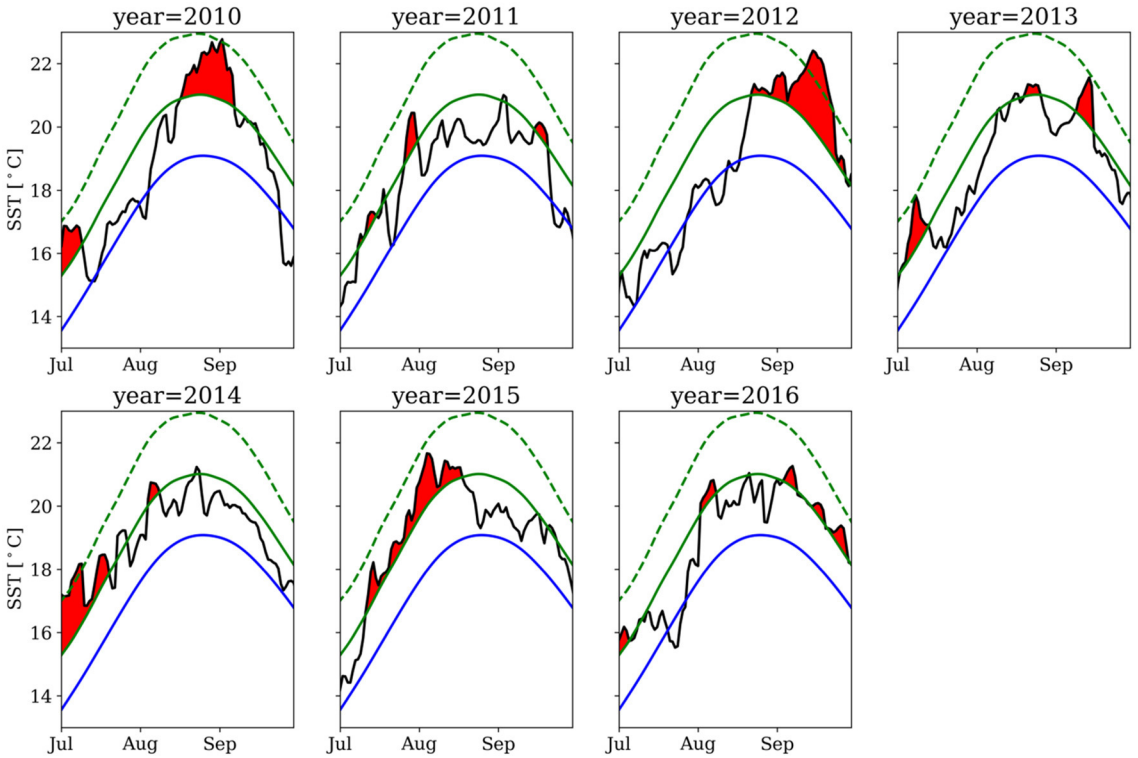

FIGURE 4 | The climatology (blue line), 90th percentile marine heatwave threshold (green solid line), and time series (black line) for SST (°C) averaged over the box (143–147°E 40–43°N). The red filled area indicates the period associated with the identified marine heatwaves. The green line is the twice of the 90th percentile difference from the mean climatology value for the defining Categories II events. Each panel shows time series in JAS of each year from 2010 to 2016.

Heat Flux

One possible cause of the SST increase is an increase in downward net air-sea heat flux. The difference in the net downward air-sea heat flux between the 2010–2016 average and the 1993–2009 average in summer (JJA) is calculated from ERA5 and is shown in **Figure 5**.

Inside the box for southeast off Hokkaido, the anomalous heat flux is upward over the peak of the SST anomaly (**Figure 2C**). Therefore, the air-sea flux could not cause the SST increase. Rather, a comparison between **Figures 2A**, **5** suggests that the increase in SST induced the anomalous upward net-heat flux. A similar spatial pattern of the heat flux change was obtained using the averages in JAS or using the JRA55 reanalysis (Kobayashi et al., 2015) (not shown).

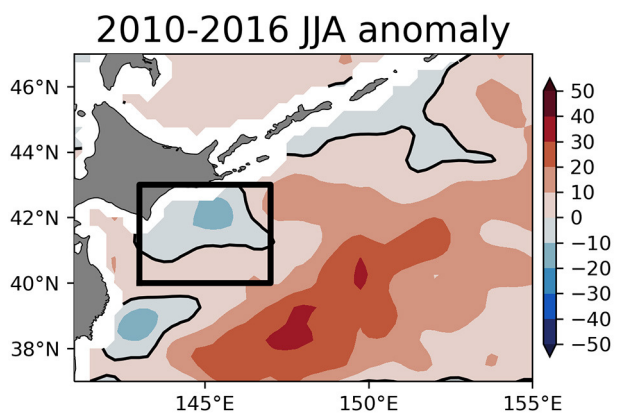

FIGURE 5 | Anomaly of the 2010–2016 average downward net heat flux (color and contour; W m^{-2}) in JJA to the 1993–2009 average in JJA calculated from the ERA5 reanalysis. The box enclosed by the black lines is the same as the previous figures.

Observed Sea Surface Height and Geostrophic Velocity

Because the surface heat flux cannot explain the marine heat wave in 2010–2016, the ocean current is examined as the possible cause of the heat wave in this subsection.

Figure 6 shows (A) the 1993–2009 average, (B) 2010–2016 average, and (C) the difference between the latter and former of SSH and the corresponding geostrophic velocity in JAS.

The 1993–2009 average velocity (**Figure 6A**) shows a typical pattern of the Oyashio, which is schematically shown by the blue arrow in **Figure 6D**. The first and second southward crests of the meandering Oyashio from the west to the east are called the First Oyashio Intrusion (FOI) and the Second Oyashio Intrusion (SOI), respectively (Kawai, 1972). In contrast, the 2010–2016 average (**Figure 6B**) shows that the FOI was significantly weaker

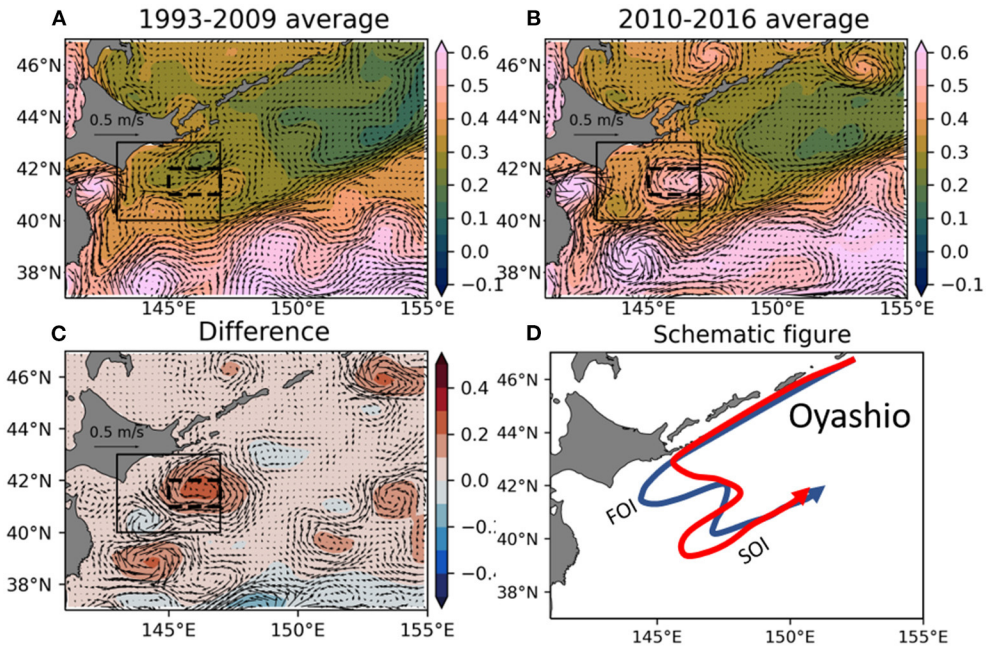

FIGURE 6 | The absolute dynamic heights (color; m) and the corresponding geostrophic velocities (vectors; m s^{-1}) estimated by the altimeters. **(A)** The 1993–2009 average. **(B)** The 2010–2016 average, **(C)** the difference between **(B)** and **(A)**. **(D)** Schematic figure of the Oyashio Current in 1999–2009 (blue line) and in 2010–2016 (red line). The first and second crests of the meandering Oyashio Current from the west to the east are the First Oyashio Intrusion (FOI) and Second Oyashio Intrusion (SOI), respectively.

than that of 1993–2009. Instead, the SOI in 2010–2016 was stronger than that in 1993–2009. The Oyashio's current pattern in this period is shown by the red arrow in **Figure 6D**. Because the area of the SST warming from 2010 discussed in section Observed Sea Surface Temperature corresponds to the FOI area, the weakening of FOI was responsible for the warming from 2010.

The difference between the 1993–2009 and 2010–2016 averages (**Figure 6C**) shows that the anticyclonic eddy-like circulation anomaly between the FOI and the SOI. This anticyclonic eddy-like circulation is clearly visible in 2010–2016 average (**Figure 6B**) but not so in 1993–2009 average (**Figure 6A**). The enhancement of the anticyclone circulation for the period 2010–2016 is closely related to the weakened FOI.

Kuroda et al. (2015) also found that the Oyashio path shifted from the nearshore (FOI) to offshore (SOI). However, they focused their attention on a trend during 1993–2011, not the change from 2010 discussed in this paper.

Meanwhile, there were little differences in the SSH and geostrophic current in the surrounding subpolar gyre and its western boundary current in **Figure 6C** (for example, the region between 44–46°N). This suggests that the local intensification of the anticyclonic eddy rather than the weakening of the whole subpolar gyre caused the weakening of FOI.

Increase in Anticyclonic Eddies

It is interesting to know how the intensification of the anticyclonic eddy-like circulation between the FOI and the SOI shown in **Figure 6** is associated with individual eddies. The region between FOI and SOI is known as the place where eddies from the Kuroshio Extension move northward (Itoh and Yasuda, 2010). Thus, the intensification of the anticyclonic eddy-like

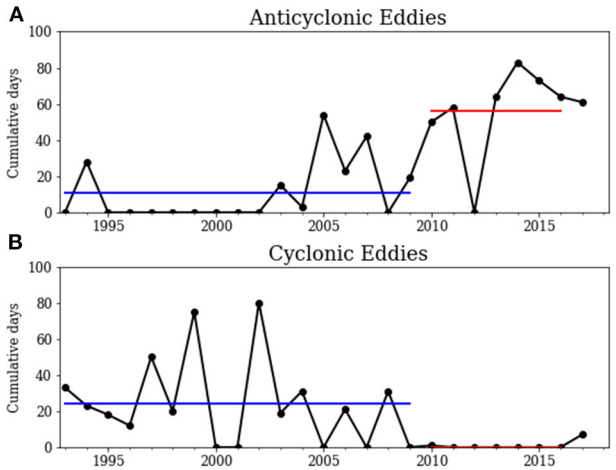

FIGURE 7 | Time series of the total number of days for which eddies remained within the dashed box in **Figures 6A–C** in summer (JAS) each year. For example, if one eddy remained within the box for 30 days and another eddy remained in the box for 20 days during JAS a certain year, the total cumulative days in the year is 50. **(A)** For anticyclonic eddies. **(B)** For cyclonic eddies.

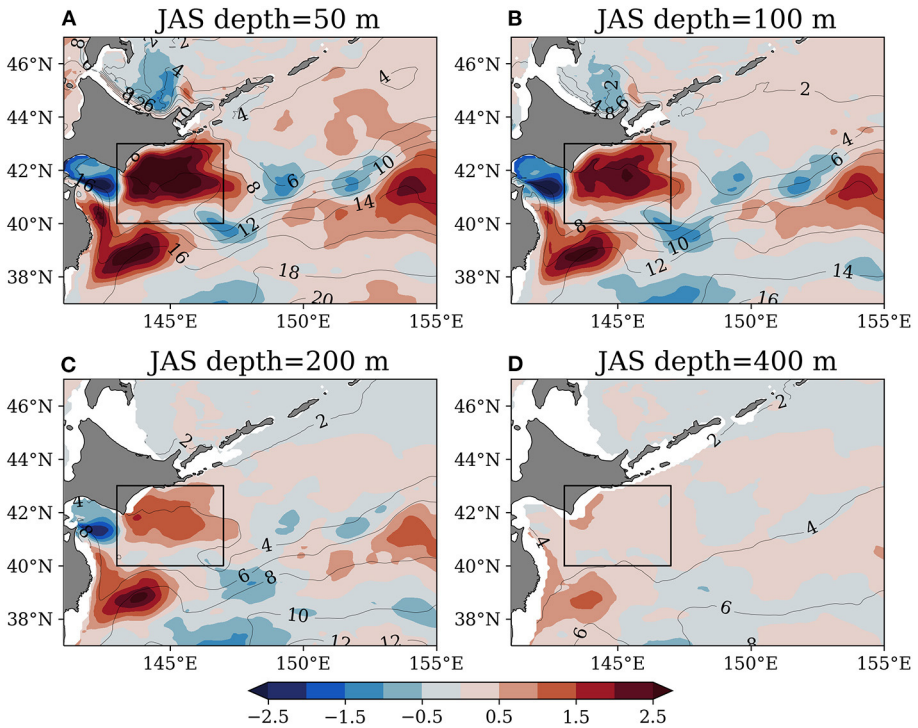

FIGURE 8 | Deviation of the 2010–2016 average temperature at each depth from the 1993–2009 average (color; °C) and the 2010–2016 average temperature at each depth (contour, °C) of the FRA-JCOPE2 reanalysis. **(A)** At 50 m. **(B)** At 100 m. **(C)** At 200 m. **(D)** At 400 m.

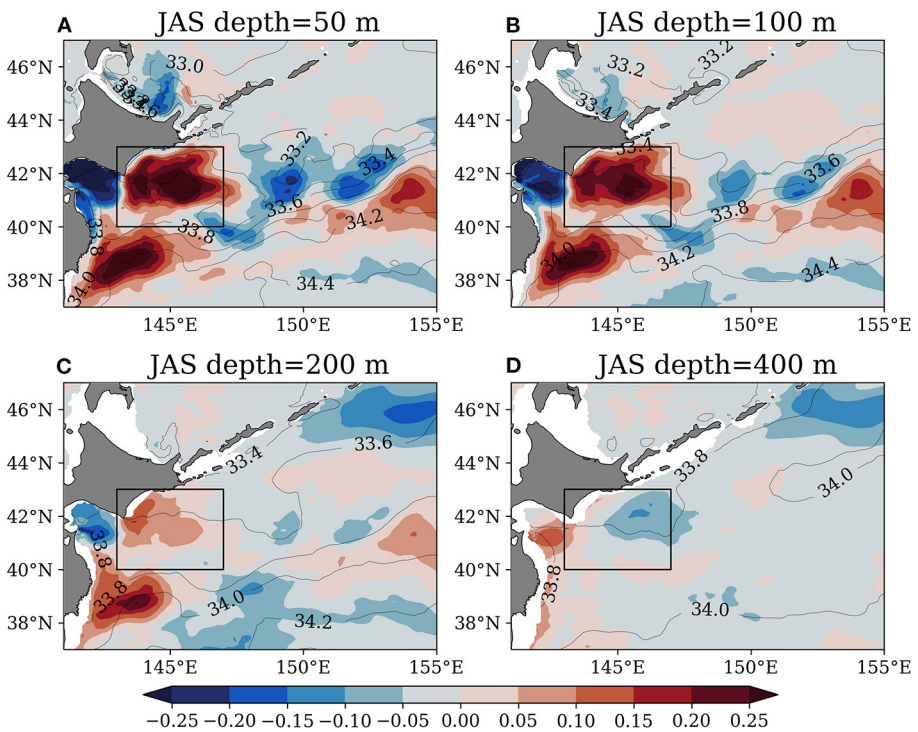

FIGURE 9 | Deviation of the 2010-2016 average salinity at each depth from the 1993-2009 average (color) and the 2010-2016 average salinity at each depth (contour) of the FRA-JCOPE2 reanalysis. **(A)** At 50 m. **(B)** At 100 m. **(C)** At 200 m. **(D)** At 400 m.

circulation may be resulted from the more frequent anticyclonic eddies from the south rather than an intensification of the same eddy at the same place. To examine this idea, the eddy-tracking product of AVISO was analyzed.

Figure 7A shows the time series of the total cumulative days for which anticyclonic eddy centers are contained in the box enclosed by the dashed line between FOI and SOI in **Figure 6B** in summer (JAS) each year. The area shown by the dashed line box is henceforth referred to as east of the FOI. Anticyclonic eddies indeed became more frequent from 2010. While anticyclonic eddies existed for 11 days each year on average during 1993–2009, the number increase five times to 56 days during 2010–2016. The difference was statistically significant ($p = 3.2 \times 10^{-3} < 0.01$ with Welch's t-test).

On the other hand, cyclonic eddies decreased in the east of the FOI (**Figure 7B**). While cyclonic eddies existed for 24 days each year on average during 1993–2009, they are almost absent (0 days) during 2010–2016. The difference was again statistically significant ($p = 9.4 \times 10^{-4} < 0.01$).

During the period 2010–2016, anticyclonic eddies did not exist east of the FOI in 2012. This is because the anticyclonic eddies in summer 2012 remained slightly westward or slightly southwestward. When the cumulative days were counted in the box 144–145°E 40.5–41.5°N, the number was 91 days in 2012, comparable to the number in the other years during 2010–2016. Because of the westward location of the anticyclonic eddies in 2012, the SST anomaly was located westward (**Figure 3C**) compared with the other years in **Figure 3**.

Note that the eddy-tracking suggests that anticyclonic eddies east of the FOI in each year were different ones (not shown), except for the eddy in 2015 and 2016 as discussed in the next section. While Kuroda and Yokouchi (2017) concluded that an identical eddy ("Eddy-A") remained from 2010 to as of September 2016, the product used in this study does not indicate it. The difference of Kuroda and Yokouchi (2017) and the product used in this study might be from the difference of the treatments in the coalescence of eddies. Kuroda and Yokouchi (2017) allowed the coalescence of clockwise eddies. However, they did not determine which clockwise eddy survived or died. Instead, they assumed that the Eddy-A survived at any coalescences. Repeated coalescence processes were essential to revive the Eddy-A, which is much weakened in cold seasons. In Kuroda and Yokouchi (2017), however, source of the eddies absorbed into the Eddy-A were not shown.

Subsurface Water Properties

To further examine the change in the subsurface structure, the ocean reanalysis FRA-JCOPE2 was analyzed.

Figure 8 shows that the anomaly of the temperature at 50, 100, 200, and 400 m depth. **Figures 8A–C** shows that temperature difference occurred not only at the surface but at deeper depths. At 400 m depth, the anomaly was small.

In parallel to the temperature change, the salinity also changed from 2010. **Figure 9** shows the salinity increased at the surface and deeper depths, again at least 200 m (**Figure 9C**). The warming reaching to the subsurface could be important for

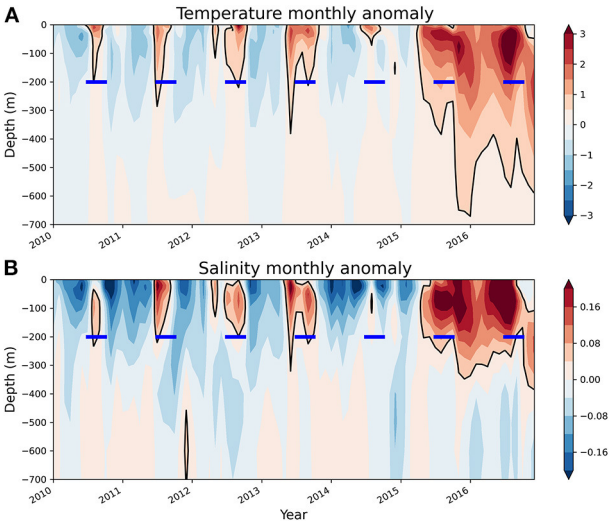

FIGURE 10 | Monthly time-depth diagram from 2010 to 2016 of **(A)** temperature and **(B)** salinity anomaly (°C and salinity unit, respectively; colors and contours) horizontally averaged in the box in **Figures 8**, **9**. The horizontal blue lines at 200 m depth denote JAS period each year.

fisheries because some of the commercially important fisheries in Japan like walleye pollock are demersal (Sakurai, 2007).

Because the water from the Kuroshio Current is warm and saline and the water from the Oyashio Current is cold and fresh, the increases in temperature and salinity in **Figures 8**, **9** are consistent with the idea that the advection from the Oyashio became weak while the eddies from the Kuroshio Extension increased from 2010, as discussed in section Observed Sea Surface Height and Geostrophic Velocity and Increase in Anticyclonic Eddies.

Figure 10 shows the monthly time-depth diagram from 2010 to 2016 of (A) the temperature and (B) salinity anomaly (°C and salinity unit; colors and contours) horizontally averaged in the box in **Figures 8**, **9**. Both the temperature and salinity anomalies extended to a depth of more than a few hundred meters during JAS season each year (the horizontal blue line). This warm and saline anomalies in JAS are separated by opposing cold and fresh anomalies in other seasons until 2014. While the vertical extent in 2014 was relatively small among 2010–2016, the vertical extents in 2015 and 2016 were large.

Another prominent feature of the anomalies in 2015 and 2016 was that the anomaly in 2015 did not end in fall unlike 2010–2014 and continued to summer in 2016. This could be because the warm anticyclonic eddy in 2015 remained until 2016. Sendai district meteorological observatory (2017) reported that the warming in the Oyashio region caused by the anticyclonic eddy continued from June 2015 to October 2016.

Southward Intrusion of the Oyashio

In this subsection, we examine how distribution of the Oyashio water changed in 2010–2016 compared to that in 1993–2009. The temperature colder than 5°C at 100 m depth has been used

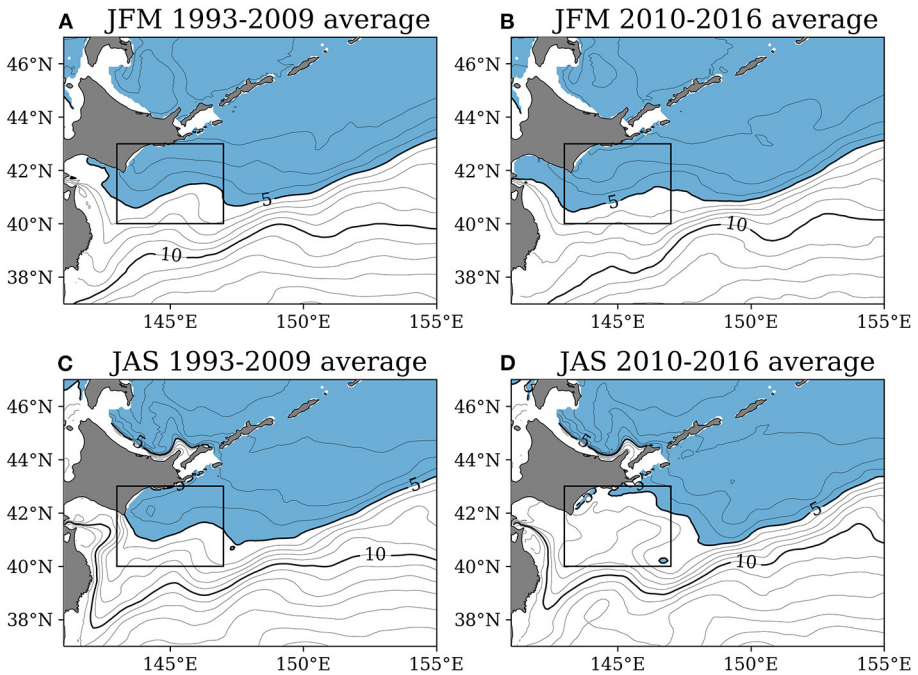

FIGURE 11 | Temperature at 100 m depth of the FRA-JCOPE2 reanalysis (contour). The temperature of <5°C is colored blue. **(A)** The 1993–2009 average in JFM. **(B)** The 2010–2016 average in JFM. **(C)** The 1993–2009 average in JAS. **(D)** The 2010–2016 average in JAS.

for the area of the Oyashio water in previous studies (Ogawa, 1989; Takasugi and Yasuda, 1993). **Figure 11** compares the 1993–2010 and 2010–2016 averages of the temperatures at 100 m depth in winter [JFM, (A) and (B)] and summer [JAS, (C) and (D)]. The Oyashio water indicated by temperature <5°C is colored blue, and southward bulges around 143–144°E and 147–150°E correspond to the FOI and the SOI, respectively. In winter, the distributions of the Oyashio waters are similar between the 1993–2009 (**Figure 11A**) and 2010–2016 (**Figure 11B**) periods. However, in summer, the FOI is clear in 1993–2009 (**Figure 11C**) but not in 2010–2016 (**Figure 11D**). This change of FOI is consistent with the result obtained from the observed SSH and the corresponding weak FOI in section Observed Sea Surface Height and Geostrophic Velocity.

The southernmost latitude of FOI in each month is quantified in **Figure 12** using the FRA-JCOPE2 reanalysis. The southernmost latitude of the FOI was defined as the southernmost latitude of the 5°C isoline east of 145°E at 100 m depth. When there was no 5°C isoline east of 145°E, the latitude was defined as the latitude of the 5°C isotherm closest to the coast of the island of Hokkaido.

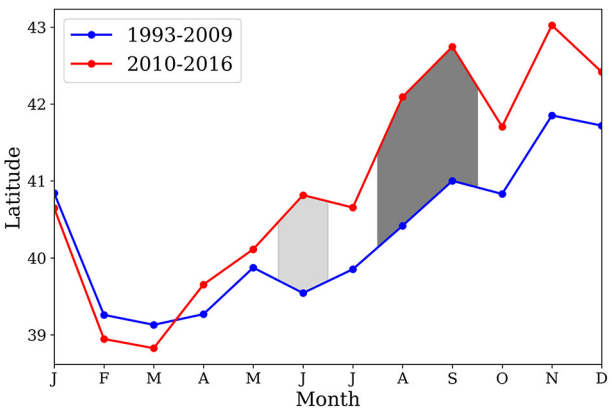

FIGURE 12 | Monthly time series of the southernmost latitude of the FOI. Red and blue curves show the 2010–2016 and 1993–2009 average, respectively. Dark gray and light gray show the differences are significant with $p < 0.05$ and $p < 0.1$, respectively.

Figure 12 shows that the seasonal migrations of the FOI in 1993–2009 and 2010–2016 period. In both periods, the FOI advanced most southward in March, retreated from March to November, and reached its northernmost latitude in November. This seasonal variability is consistent with previous studies (Isoguchi and Kawamura, 2006; Kuroda et al., 2017). The seasonal migration is likely controlled by the seasonally fluctuating Aleutian Low pressure system via barotropic adjustment in the subarctic North Pacific Ocean (Qiu, 2019).

The significant differences in FOI latitude occur in the summertime retreating phase. The FOI in 2010–2016 period retreat faster and thus was located northward to the FOI in 1993–2009, while the southward intrusions in winter were not significantly different. The difference in the latitude of FOI was statistically significant in August and September ($p < 0.05$ with

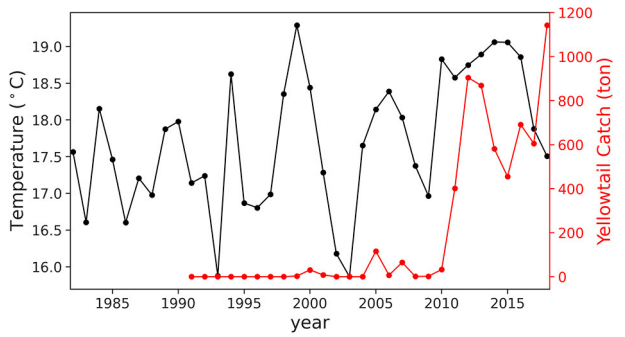

FIGURE 13 | Time series of the SST averaged over the black box of **Figure 2** in JAS (black curve; °C on the left axis; the same as **Figure 1B**) and the time series of the catch of yellowtail (red curve; ton on the right axis) in southeastern Hokkaido (Hidaka, Tokachi, and Kushiro areas). The catch data is taken from Annual Statistics on Fishery and Aquaculture Production in Hokkaido (in Japanese) at: http://www.pref.hokkaido.lg.jp/sr/sum/03kanrig/sui-toukei/suitoukei.htm.

Welch's t-test) and in June ($p < 0.1$). **Figure 12** reaffirms that the warming in FOI from 2010 was concentrated in summer.

SUMMARY AND DISCUSSION

The SST in the Oyashio region off the Island of Hokkaido in boreal summer abruptly increased from 2010 and stayed high until 2016. The temperature rise cannot be explained with the downward heat flux, because there is no agreement between the regions of the large downward net heat flux and the large temperature rise. Therefore, it is inferred that water advection is important. The importance of the advection is also supported by the fact that the change of water temperature and salinity extended to a deeper depth of more than a few hundred meters. The increase in the salinity in addition to temperature suggests that strengthening (weakening) of the influence from the Kuroshio (Oyashio) water.

SSH as well as the temperature change shows the weakening of the Oyashio first intrusion (FOI). The weakening of FOI was closely associated with more frequent warm and saline anticyclonic eddies east of the FOI. The Eddy-tracking analysis shows that more anticyclonic eddies coming from the Kuroshio Extension.

As mentioned in the Introduction, temperature changes in the Oyashio region have affected fisheries. As a striking example, the catch data of yellowtail in southeastern Hokkaido (Hidaka, Tokachi, and Kushiro areas) is shown in **Figure 13**. Yellowtail is one of the most commercially important predatory fishes in Japan. Tian et al. (2012) showed that there was close correspondence between water temperature and catch in the Japan Sea. **Figure 13** shows the catch of yellowtail, which was close to zero before 2010, sharply increased with the SST rise from 2010. Spearman rank correlation between the SST and the catch is 0.65 ($p = 1.7 \times 10^{-4}$).

Fisheries of yellowtail are conducted in the Western Central Pacific Ocean, from Japan and the eastern Korean Peninsular to the Hawaiian Islands (Dhirendra, 2005). The Pacific area off southeast Hokkaido is regarded as the northeasternmost habitat or distribution of yellowtail in Japan (Tian et al., 2012; Stock assessment report, 2020). In addition, around the Hokkaido coast, most of yellowtail (e.g., 99% in 2018) was caught by fixed nets in coastal waters according to the Stock assessment report (2020). Hence, the abrupt increase of the Yellowtail catches during 2010–2016 suggests the expansion of the habitat/distribution. This strongly suggests that the marine heat wave southeast off Hokkaido from 2010, which is closely associated with the weakening of the FOI and more frequent anticyclonic eddies from the Kuroshio Extension, have impacted fishery in Hokkaido. Indeed, Hakodate, a city in the southwestern part of Hokkaido, was famous as a "squid town" because of many catches of squid in the past, but it is now trying to become also a "yellowtail town" to adjust to decreased squid catch and increased yellowtail catch. The sharp increase of the yellowtail catch in the Pacific Ocean was not found in Tian et al. (2012), who used the data before 2010.

The present paper documented the major features of the marine heat wave southeast off Hokkaido and associated the FOI change in 2010–2016, but the driving mechanism of this long-lasting marine heat wave has not been identified. Kuroda et al. (2015) proposed one possible reason for the shift of the Oyashio path from FOI to SOI during 1993–2011 is the change of the wind stress over the North Pacific Ocean (decrease of the wind stress curl and the northward shift of the meridional position). However, this change in the stress is the trend from 1993 to 2011 and does not indicate the abrupt change around 2010 (their Figure 15). **Figure 6C** in this study also suggests that the change from 2010 was local one rather than the large-scale change of the subarctic gyre.

Kuroda et al. (2015) also proposed an increase in anticyclonic eddies as another possible reason for the change in the Oyashio Current. The eddy-tracking analyses by us and Kuroda and Yokouchi (2017) support the role of anticyclonic eddies as the plausible reason for the warming from 2010. Qiu et al. (2017) also concluded that the western Oyashio front variability is controlled by the decadal mesoscale eddy modulations in the upstream Kuroshio Extension. However, **Figure 3A** in Qiu et al. (2017) does not indicate an increase in eddy generation from the Kuroshio Extension around 2010. Further analysis of not only eddy generation but also eddy propagation is needed to elucidate the behavior of eddies. Further studies are needed to identify the driver for the warming in summer and increase of anticyclonic eddies after 2010.

Hosoda et al. (2015) found the temperature increase since 2008 from the surface to several 100 m depth in another western Pacific region (35°–45°N, 160°–180°E) in early summer. The warming at the surface can also be seen in **Figure 1** of our paper. Hosoda et al. (2015) suggested that the oceanic frontal structure change (more northward Kuroshio Extension) was a possible cause, but the reason for the warming has not been confirmed. The current study and Hosoda et al. (2015) share some similarities (abrupt warming from a certain year and the importance of the ocean current) and dissimilarities (from 2010 vs. from 2008, in summer vs. in early summer, and in the Oyashio

region vs. 160°–180°E). The investigation on the link or the independence between these warmings is an interesting subject in future studies.

The anthropogenic climate change will have a large impact on the marine environments in the North Pacific Ocean (Holsman et al., 2018). Abrupt warming caused by marine heatwaves like the event discussed in this paper will amplify the impacts. Further understanding of the cause and impacts of marine heatwaves is required to adapt to the rapidly changing ocean climate.

DATA AVAILABILITY STATEMENT

The datasets presented in this study can be found in online repositories. The names of the repository/repositories and accession number(s) can be found in the article/supplementary material.

AUTHOR CONTRIBUTIONS

HG and SM conceived of the presented idea and did initial analysis. TM continued the analysis and verified the conclusion. All authors discussed the results and contributed to the final manuscript.

FUNDING

This work is a part of the Japan Coastal Ocean Predictability Experiment (JCOPE) promoted by the Japan Agency for Marine-Earth Science and Technology (JAMSTEC). This work was supported by a Grant-in-Aid for Scientific Research on Innovative Areas 6102 (KAKENHI Grant No. JP19H05697 and JP19H05701) from JSPS of Japan.

REFERENCES

Bond, N. A., Cronin, M. F., and Freeland, H. (2015). The blob: an extreme warm anomaly in the Northeast Pacific [in "State of the Climate in 2014"]. *Bull. Amer. Meteorol. Soc.* 96, S62–S63. doi: 10.1175/2015BAMSStateoftheClimate.1

Copernicus Climate Change Service (C3S) (2017). *ERA5: Fifth Generation of ECMWF Atmospheric Reanalyses of the Global Climate*. Available online at: https://cds.climate.copernicus.eu/cdsapp#!/dataset/reanalysis-era5-pressure-levels-monthly-means (accessed May 10, 2020).

Dhirendra, P. T. (2005). *Cultured Aquatic Species Information Programme. Seriola quinqueradiata*. Rome: Cultured Aquatic Species Information Programme, FAO Fisheries Division. Available online at: http://www.fao.org/fishery/culturedspecies/Seriola_quinqueradiata/en (accessed November 12, 2020).

Hobday, A., Oliver, E., Sen Gupta, A., Benthuysen, J., Burrows, M., Donat, M., et al. (2018). Categorizing and naming marine heatwaves. *Oceanography* 31, 162–173. doi: 10.5670/oceanog.2018.205

Hobday, A. J., Alexander, L. V., Perkins, S. E., Smale, D. A., Straub, S. C., Oliver, E. C. J., et al. (2016). A hierarchical approach to defining marine heatwaves. *Prog. Oceanogr.* 141, 227–238. doi: 10.1016/j.pocean.2015.12.014

Holsman, K., Hollowed, A., Ito, S., Bograd, S., Hazen, E., King, J., et al. (2018). "Climate change impacts, vulnerabilities, and adaptations: North Pacific and Pacific Arctic marine fisheries," in *Impacts of Climate Change on Fisheries and Aquaculture*, eds M. Barange, T. Bahri, M. C. Beveridge, K. L. Cochrane, S. Funge-Smith, and F. Poulain (Rome: Food and Agriculture Organization of the United Nations), 113–138.

Hosoda, S., Nonaka, M., Sasai, Y., and Sasaki, H. (2015). Early summertime interannual variability in surface and subsurface temperature in the North Pacific. *J. Oceanogr.* 71, 557–573. doi: 10.1007/s10872-015-0307-3

Hu, Z.-Z., Kumar, A., Jha, B., Zhu, J., and Huang, B. (2017). Persistence and predictions of the remarkable warm anomaly in the Northeastern Pacific Ocean during 2014–16. *J. Clim.* 30, 689–702. doi: 10.1175/JCLI-D-16-0348.1

Isoguchi, O., and Kawamura, H. (2006). Oyashio seasonal intensification and its effect on subsurface temperature variation off the Sanriku coast. *J. Geophys. Res.* 111:C10006. doi: 10.1029/2006JC003628

Itoh, S., and Yasuda, I. (2010). Characteristics of mesoscale eddies in the Kuroshio–Oyashio extension region detected from the distribution of the sea surface height anomaly. *J. Phys. Oceanogr.* 40, 1018–1034. doi: 10.1175/2009JPO4265.1

Kawai, H. (1972). "Hydrography of the Kuroshio extension," in *Kuroshio, It's physical aspects*, eds. H. Stommel and K. Yoshida (Tokyo: University of Tokyo Press), 235–352.

Kobayashi, S., Ota, Y., Harada, Y., Ebita, A., Moriya, M., Onoda, H., et al. (2015). The JRA-55 reanalysis: general specifications and basic characteristics. *J. Meteorol. Soc. Japan Ser. II* 93, 5–48. doi: 10.2151/jmsj.2015-001

Kuroda, H., Wagawa, T., Kakehi, S., Shimizu, Y., Kusaka, A., Okunishi, T., et al. (2017). Long-term mean and seasonal variation of altimetry-derived Oyashio transport across the A-line off the southeastern coast of Hokkaido, Japan. *Deep Sea Res. Part I Oceanogr. Res. Pap.* 121, 95–109. doi: 10.1016/j.dsr.2016.12.006

Kuroda, H., Wagawa, T., Shimizu, Y., Ito, S., Kakehi, S., Okunishi, T., et al. (2015). Interdecadal decrease of the Oyashio transport on the continental slope off the southeastern coast of Hokkaido, Japan. *J. Geophys. Res. Oceans* 120, 2504–2522. doi: 10.1002/2014JC010402

Kuroda, H., and Yokouchi, K. (2017). Interdecadal decrease in potential fishing areas for Pacific saury off the southeastern coast of Hokkaido, Japan. *Fish. Oceanogr.* 26, 439–454. doi: 10.1111/fog.12207

Lorenzo, E. D., and Mantua, N. (2016). Multi-year persistence of the 2014/15 North Pacific marine heatwave. *Nat. Clim. Change* 6, 1042–1047. doi: 10.1038/nclimate3082

Makino, M., and Sakurai, Y. (2012). Adaptation to climate-change effects on fisheries in the Shiretoko World Natural Heritage area, Japan. *ICES J. Mar. Sci.* 69, 1134–1140. doi: 10.1093/icesjms/fss098

Miyazawa, Y., Zhang, R., Guo, X., Tamura, H., Ambe, D., Lee, J.-S., et al. (2009). Water mass variability in the western North Pacific detected in a 15-year eddy resolving ocean reanalysis. *J. Oceanogr.* 65, 737–756. doi: 10.1007/s10872-009-0063-3

Ogawa, Y. (1989). Variation of the southern end latitude of the first Oyashio Intrusion (in Japanese with English abstract and captions). *Bull. Tohoku Reg. Fish. Lab.* 51, 1–9.

Oliver, E. C. J., Donat, M. G., Burrows, M. T., Moore, P. J., Smale, D. A., Alexander, L. V., et al. (2018). Longer and more frequent marine heatwaves over the past century. *Nat. Commun.* 9:1324. doi: 10.1038/s41467-018-03732-9

Qiu, B. (2019). "Kuroshio and Oyashio currents," in *Encyclopedia of Ocean Sciences, 3rd Edn*, eds J. K. Cochran, H. Bokuniewicz, and P. Yager (Cambridge, MA: Academic Press), 384–394.

Qiu, B., Chen, S. M., and Schneider, N. (2017). Dynamical links between the decadal variability of the Oyashio and Kuroshio extensions. *J. Clim.* 30, 9591–9605. doi: 10.1175/JCLI-D-17-0397.1

Reynolds, R. W., Smith, T. M., Liu, C., Chelton, D. B., Casey, K. S., and Schlax, M. G. (2007). Daily high-resolution-blended analyses for sea surface temperature. *J. Clim.* 20, 5473–5496. doi: 10.1175/2007JCLI1824.1

Sakurai, Y. (2007). An overview of the Oyashio ecosystem. *Deep Sea Res. Part II Top. Stud. Oceanogr.* 54, 2526–2542. doi: 10.1016/j.dsr2.2007.02.007

Sendai district meteorological observatory (2017). *Press Release From on March 21, 2017 (in Japanese)*. Available online at: https://www.jma-net.go.jp/sendai/kouhou/houdou/17/20170321_tohoku_sea.pdf (accessed November 28, 2020).

Stock assessment report (2020). *Stock Assessment of Yellowtail in 2019 (in Japanese)*. Available online at: http://abchan.fra.go.jp/digests2019/details/201945.pdf (accessed November 12, 2020).

Takasugi, S., and Yasuda, I. (1993). Index temperature at 100 m depth of the Oyashio front in the Iwate coastal region (in Japanese with English abstract and captions). Japan. *J. Fish. Oceanogr.* 57, 333–344.

Tian, Y., Kidokoro, H., Watanabe, T., Igeta, Y., Sakaji, H., and Ino, S. (2012). Response of yellowtail, Seriola quinqueradiata, a key large predatory fish in the Japan Sea, to sea water temperature over the last century and potential effects of global warming. *J. Mar. Syst.* 91, 1–10. doi: 10.1016/j.jmarsys.2011.09.002

Welch, C. (2016). The blob that cooked the Pacific. *Natl. Geogr.* 230, 54–64.

Whitney, F. A. (2015). Anomalous winter winds decrease 2014 transition zone productivity in the NE Pacific. *Geophys. Res. Lett.* 42, 428–431. doi: 10.1002/2014GL062634

Conflict of Interest: The authors declare that the research was conducted in the absence of any commercial or financial relationships that could be construed as a potential conflict of interest.

frontiers | Frontiers in Marine Science

ORIGINAL RESEARCH
published: 12 July 2022
doi: 10.3389/fmars.2022.814053

Effects of Ocean Chlorophyll on the Mode Water Subduction Rate in the Northwestern and Central Pacific Ocean

Jinfeng Ma[1], *Qian Yang*[2], *Hailong Liu*[1,3,4]*, *Pengfei Lin*[1,3] *and Juan Liu*[5]

[1] State Key Laboratory of Numerical Modeling for Atmospheric Sciences and Geophysical Fluid Dynamics, Institute of Atmospheric Physics, Chinese Academy of Sciences, Beijing, China, [2] State Key Laboratory of Cryospheric Science, Northwest Institute of Eco-Environment and Resources, Chinese Academy of Sciences, Lanzhou, China, [3] College of Earth and Planetary Sciences, University of Chinese Academy of Sciences, Beijing, China, [4] Center for Ocean Mega-Science, Chinese Academy of Sciences, Qingdao, China , [5] Beijing Institute of Applied Meteorology, Beijing, China

The effects of ocean chlorophyll on the mode water subduction rate in the subtropical mode water (STMW) and central mode water (CMW) in Pacific Ocean are investigated by performing two ocean-only experiments, using two different solar radiation penetration schemes, one with and one without chlorophyll effects. The biological impacts on mixed layer depth (MLD), upper ocean temperature and density are analyzed. Results show that the subduction rates of both STMW and CMW are increased with the effects of ocean chlorophyll. The increase in the subduction rate is mainly caused by the increased lateral induction term, which is related to larger MLD gradient in early spring in the chlorophyll experiment.

Keywords: subduction rate, ocean model, biological effects, North Pacific Ocean, mode water

OPEN ACCESS

Edited by:
Shoshiro Minobe,
Hokkaido University, Japan

Reviewed by:
Yizhen Li,
Woods Hole Oceanographic Institution, United States
Shusaku Sugimoto,
Tohoku University, Japan

***Correspondence:**
Hailong Liu
lhl@lasg.iap.ac.cn

Specialty section:
This article was submitted to Physical Oceanography, a section of the journal Frontiers in Marine Science

Received: *12 November 2021*
Accepted: *03 June 2022*
Published: *12 July 2022*

Citation:
Ma J, Yang Q, Liu H, Lin P and Liu J (2022) Effects of Ocean Chlorophyll on the Mode Water Subduction Rate in the Northwestern and Central Pacific Ocean. Front. Mar. Sci. 9:814053. doi: 10.3389/fmars.2022.814053

INTRODUCTION

The winter mixed layer depth (MLD) in the northwestern and central Pacific Ocean shows significant seasonal variation. It reaches a maximum (approximately 200 m) in March (**Figure 1A**) along the Kuroshio Extension region. Separating the deep mixed layer from the shallow one in the rest of the subtropical gyre is a transition zone called the MLD front. At the cross point of the MLD front and outcropping line, water is inducted from the deep mixed layer into the main thermocline by the southeastward Sverdrup flow, forming a local potential vorticity (PV) minimum (Kubokawa, 1999; Xie et al., 2000; Xie et al., 2010). These vertically homogeneous water masses are called mode water. The subtropical mode water (STMW) was identified by Masuzawa (1969) and with vertical uniform layer of 25.2-25.6 σ_θ. It is formed just south of the Kuroshio and Kuroshio Extension between ~132°E and near the dateline. Nakamura (1996) identified the central mode water (CMW) with uniform layer of σ_θ 26.0-26.5. CMW is formed north of the Kuroshio Extension. A composite analysis of Argo data in 2003-2008 demonstrated that lighter (denser) CMW is formed at 33°-39°N (39°-43°N) extending from ~142°E to 160°W (Oka et al., 2011).

The winter MLD in the mode water formation region is mainly caused by local surface cooling (Iwamaru et al., 2010) and ocean dynamic associated with westward propagating Rossby waves from the central North Pacific (Qiu and Chen, 2005), which could cause pycnocline depth anomalies, modify the upper ocean stratification and wintertime mixed layer (Sugimoto and Hanawa, 2010; Lin et al., 2020). Mode water memorizes wintertime ocean-atmosphere interactions and might

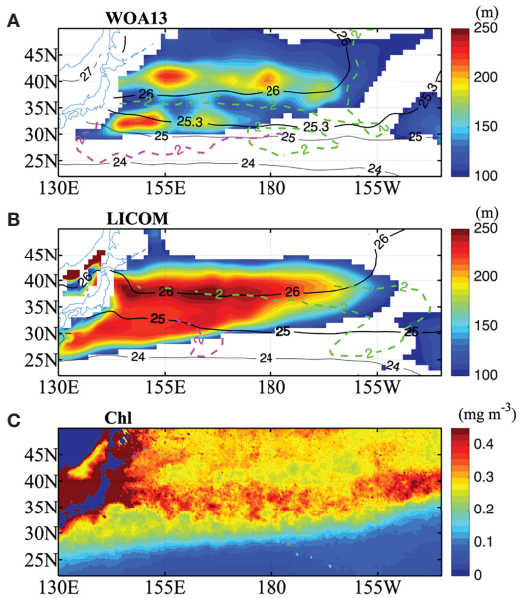

FIGURE 1 | (A) March climatology of the mixed layer depth larger than 100 m (shaded) and the density at the surface (black solid line) for WOA13 along with the PV= 2.0×10^{-10} m^{-1} s^{-1} on 25.3 σ_θ (magenta dashed) and 26 σ_θ (green dashed), bold solid black contour shows surface density at 25.3 σ_θ and 26 σ_θ . **(B)** is the same as **(A)** but for LICOM except dashed contour for PV= 2.0×10^{-10} m^{-1} s^{-1} on 25 σ_θ and 26 σ_θ , and bold solid contour for surface density at 25 σ_θ and 26 σ_θ . The lighter low PV layer (megenta dashed) corresponds to the core layer of the STMW, while the denser layer (green dashed) corresponds to the core layer of the CMW. **(C)** March climatology of chlorophyll concentration in mg m^{-3}. The chlorophyll data is satellite-retrieved from the Sea-viewing Wide Field-of-view Sensor (SeaWiFS) covering the period from September 1997 to December 2007.

reemerge in the surface mixed layer in the subsequent winter (Bingham, 1992; Qiu and Chen, 2006; Oka and Qiu, 2012) and is believed to play an important role in climate variability (Hanawa and Kamada, 2001).

In addition to dynamic and thermodynamic processes, some biological processes, such as phytoplankton in the euphotic layer, can also affect the upper mixed layer through their impacts on the vertical distribution of solar radiation (Lewis et al., 1983; Lin et al., 2007; Ma et al., 2014; Ma et al., 2021). The chlorophyll in the ocean could trap more heat in the upper layer, and less solar radiation could reach the subsurface. As a result, chlorophyll could affect the vertical distribution of penetrative solar radiation and modulate the upper ocean temperature and MLD. Earlier studies have shown that the existence of phytoplankton could result in surface warming, subsurface cooling, and mixed layer shoaling (e.g., Lewis et al., 1983; Lewis et al., 1990; Sathyendranath et al., 1991; Siegel et al., 1995). Other studies found that ocean biological effects could lead to SST cooling in the equatorial Pacific upwelling region (Nakamoto et al., 2001; Anderson et al., 2007; Lin et al., 2007), the eastern tropical Indian Ocean (Liu et al., 2012a; Ma et al., 2015) and the South China Sea (Ma et al., 2012). With the uneven distribution of chlorophyll in the upwelling region, horizontal and vertical density gradients could change, and lead to strengthened upwelling, decreased sea surface temperature (SST) and shallower MLD. In addition, the ocean chlorophyll also has a cooling effect in strong vertical mixing regions like the north Arabian Sea (Ma et al., 2014) and in mid-latitudes of the world's oceans (Ma et al., 2021). In strong mixing regions, biological impacts on MLD are weak as solar penetration cannot affect such a deep depth. So, the biological impacts on MLD are closely related to the local dynamics.

Most previous studies on the effects of ocean chlorophyll have focused on the tropics, and little attention has been given to the mid-latitudes. In fact, ocean biological effects should not be neglected in the mid-latitudes. The chlorophyll concentration (Chl) shows a band of high values (>0.3 mg m^{-3}) in the region of 30°-40°N in the North Pacific during the spring bloom (**Figure 1C**). Ma et al. (2021) found that SST cools (warms) and MLD shoals with biological effects in the mid-latitudes of the North Pacific Ocean during winter (spring). And the biological impacts on MLD are not evenly distributed. According to Xie et al. (2000), the winter MLD distribution is key to mode water formation. Therefore, we further want to know whether and to what extent ocean biological effects could impact the mode water subduction rate in the north and central Pacific region.

In the present study, the effects of ocean chlorophyll on the mode water subduction rate in the northwestern and central Pacific region were investigated by comparing two numerical experiments. The rest of the paper is organized as follows. In Section 2, we describe the model and experiments used in the study. In Section 3, we analyze the biological effects on the mode water subduction rate and investigate the mechanism. In Section 4, we summarize these results.

MODEL AND EXPERIMENTS

Observational Data

The climatological ocean temperatures and salinities used for density and PV are from World Ocean Atlas 2013 (WOA13) (Locarnini et al., 2013; Zweng et al., 2013), with a resolution of 1° × 1°. Satellite-retrieved Chl data from the Sea-viewing Wide Field-of-view Sensor (SeaWiFS) (http://oceandata.sci.gsfc.nasa.gov/SeaWiFS/Mapped/Monthly/9km/chlor/) are used in the present study to analyze the ocean chlorophyll effect. The data are monthly and cover the period from September 1997 to December 2007.

Model Description

The model used in this study is the State Key Laboratory of Numerical Modeling for Atmospheric Sciences and Geophysical Fluid Dynamics (LASG)/Institute of Atmospheric Physics (IAP) Climate System Ocean Model (LICOM), version 2 (Liu et al., 2004a; Liu et al., 2004b; Liu et al., 2012b). The zonal resolution of LICOM in the present study is 1°. The meridional resolution is 0.5° between 10°S and 10°N and then gradually decreases to 1° at 20° (N/S). The model has 30 levels in the vertical direction, with 15 uniform 10 m levels in the upper ocean and 15 nonuniform levels below 150 m. The forcing of the ocean model comes

from both the Corrected Inter-Annual Forcing (CIAF) and the Corrected Normal Year Forcing (CNYF) of the Common Ocean-ice Reference Experiments (CORE) dataset (Large and Yeager, 2004).

A double exponential formula is employed to describe the penetration of solar radiation in LICOM:

$$T_r = I / I_0 = R \times e^{-Z/L_1} + (1-R)e^{-Z/L_2} \quad (1)$$

Where T_r is called transmission function, I is downward solar radiation penetrating to a certain depth z and I_0 is the downward solar radiation at sea surface. The first term on the right side of Eq. (1) represents the rapid attenuation in the upper 5m due to absorption of the red end of the spectrum, and the second term represents the attenuation of blue-green light below 10m (Paulson and Simpson, 1977). Jerlov (1968) classified the seawater according to the seawater transparency, and type I is considered to be clear water and with no biology. In LICOM, the seawater was hypothesized to be type I. Following Jerlov (1968), and R, L_1 and L_2 are set to 0.58, 0.35m and 23m, respectively. The pure water experiment referred to as NOCHL.

In the sensitivity run, the scheme proposed by Ohlmann (2003) is employed to represent the influence of Chl on solar radiation penetration (hereafter referred to as CLIMCHL). In CLIMCHL, all four parameters are functions of Chl (see Equation 5 and 6 of Ohlmann, 2003). In the CLIMCHL run, the 23 m penetration depth approximately corresponds to a Chl of 0.057 mg.m^{-3}. The chlorophyll concentration in present study region is more than 0.057 mg.m^{-3} and the penetration depth is shallower than 23 m (figure not shown). Therefore, more solar radiation will be absorbed by the upper layer in the CLIMCHL run than in the NOCHL run and less solar radiation will penetrate below. The chlorophyll data used in the CLIMCHL run are the climatological SeaWiFS monthly mean. Both experiments were run for 10 years (1998-2007). More details about the model configuration can be found in Lin et al. (2007).

Model Evaluation

PV is defined as $Q = -\frac{f}{\rho_0}\frac{\partial \rho}{\partial z}$. ρ_0 is the reference water density (1024 kg m^{-3}), $\frac{\partial \rho}{\partial z}$ is the verticwal gradient of potential density, and f is the Coriolis parameter. The MLD is defined as the depth at which the water density is 0.125 kg m^{-3} denser than the sea surfaces (Levitus, 1983). In observations, the MLD maxima at approximately 200 m show two zonal bands at 40°N and 30°N (**Figure 1A**), which are key regions for the formation of low PV waters (Kubokawa, 1999). The simulated MLD does not fully capture this feature, with one zonal maxima band in the north of 35°N and with southern edge of MLD front slanting northeastward (**Figure 1B**). The maximum MLD in the model is deeper than that in the observations, with the maximum simulated MLD reaching up to 250 m. The biases of the MLD are mainly caused by the coarse horizontal resolution of this simulation.

Figure 2 shows the total volume of low PV water (less than 1.5×10^{-10} m^{-1} s^{-1}) over the northwestern and central Pacific (135°E-155°W, 25°N-40°N) for the observations from the WOA13 and the LICOM simulation. Low PV water is clustered at 24.9-25.6 σ_θ and 25.7-26.5 σ_θ in WOA13. The lighter one is related to subtropical mode water (STMW) and the denser one is related to central mode water (CMW). In LICOM, the total volume of the low PV water for each density class shows a single peak in the CMW range and is clustered at 25.7-26.5 σ_θ. The mode water properties of CMW in the model are almost matched to the observation in both core layer density and total volume, with a peak at 26 σ_θ (**Figure 2B**). For STMW, low PV water in WOA13 is concentrated in narrow density ranges with higher magnitudes, with a peak at 25.3 σ_θ (**Figure 2A**). In LICOM, volume of low PV water in each density range is weaker and is almost equally distributed in a broad density range (**Figure 2B**).

The weaker PV minimum volume of STMW in model could also be seen in the horizontal distribution of PV minimum in **Figure 1**. The region between the 25.3 σ_θ (25 σ_θ) contour and magenta dashed contour shows the core layers of the STMW formation region for observation (LICOM). According to Kubokawa (1999) and Xie et al. (2000), an isopycnal PV minimum forms where the outcrop line (surface density isoline) intersects a MLD front. In observation, the MLD front is almost zonal, which is almost parallel to the outcrop line especially in the west of dateline (**Figure 1A**), so the PV minimum is in a broad region but concentrated only in a narrow density range. In the coarse resolution LICOM, the MLD front slants northeastward from the southwestern region of the subtropical gyre, the outcrop lines slant slightly southeastward (**Figure 1B**). As mode water with minimum PV forms where the outcrop line intersects the MLD front by lateral induction (Xie et al., 2000), the PV minimum is limited to a narrow region but in a wide density range (**Figure 1B**) and almost equally distributed (**Figure 2B**). So the low PV tongue of the STMW is smaller in the LICOM than in the observations. The meridional MLD gradient maximum west of dateline in LICOM lies eastward compared to WOA13, so the location of core layer PV minimum in STMW also lies eastward in LICOM.

The northern band of the deep MLD extending to approximately 160°W is related to the CMW, with a denser PV minimum layer (**Figure 1**). The region between the 26 σ_θ contour and green dashed contour shows the core layers of the CMW formation region for both observation and LICOM. As the MLD front east of date line in LICOM lies eastward compared to

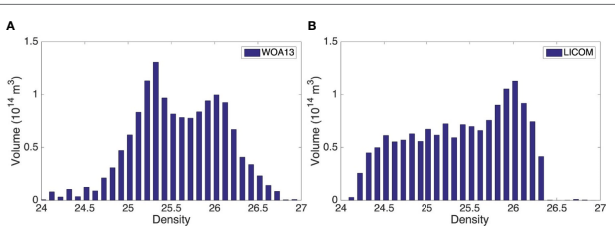

FIGURE 2 | Volume of low PV water (less than 1.5×10^{-10} m^{-1} s^{-1}) in March for each density class in the northwestern and central Pacific (135°E-155°W, 25°N-40°N) for **(A)** WOA13 and **(B)** LICOM. The interval is 0.1 kg m^{-3}. Depth range is 0-300m.

WOA13, the low PV region of CMW in the model extends much farther eastward (**Figure 1B**).

The seasonal variation in the simulated MLD agrees well with the observations, with the deepest MLD (more than 200 m) in March and the shallowest MLD (less than 20 m) in summer, except that the simulated MLD is deeper than the observed MLD, especially in early spring (**Figure 3A**). The observed and simulated SSTs also show similar seasonality, except the SST in the model is warmer than that in the observations on average (**Figure 3B**). The subsurface temperature shows warmer water in the south and cooler water in the north (figure not shown), which leads to lighter water in the south and denser water in the north. As we focus on the difference between experiments, the effects of these biases could be canceled out.

RESULTS AND DISCUSSION

Impacts of Ocean Chlorophyll on SST and MLD

Chl in the 30°N-40°N shows strong seasonal variability. Chl could reach to higher than 0.4 mg m^{-3} during spring bloom (**Figures 4A–C**) and with a maximum in April (**Figure 4B**). The SST differences between CLIMCHL and NOCHL are negative in winter and turn to positive in late spring (**Figures 4D–F**), and reaches a positive peak during June and July (>0.15°C, figure not shown). The statistical significance of SST difference is evaluated using a Student's t-test. The negative/positive SST difference indicates that chlorophyll could trap less/more solar radiation in the mixed layer. The Chl variation leads to a SST difference of approximately two months. This is because chlorophyll directly affects solar radiation, which controls the temperature tendency, not the temperature (according to the equation for the mixed layer heat budget). Therefore, the temperature difference reaches its peak when chlorophyll decreases.

Notably, the MLD differences are negative during the spring (**Figures 4G–I**), with the largest differences in April (>20 m) (**Figure 4H**). The negative MLD difference indicates that the existence of chlorophyll leads to a shallower MLD. This indicates that the spring bloom in this region could obviously impacts the MLD, and the MLD could be lifted more quickly during April with the existence of chlorophyll. The large negative MLD difference values lies around the MLD front in March (**Figure 4G**) and almost the whole study region in April (**Figure 4H**). The more quickly lifted MLD in the CLIMCHL run, which is caused by the larger buoyancy frequency (figure not shown), has a potential impact on the subduction rates in the spring season.

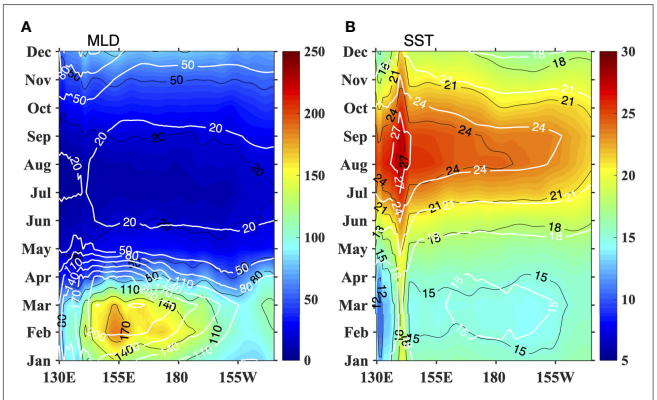

FIGURE 3 | The seasonal variation in **(A)** MLD (m), **(B)** SST (°C) averaged between 30°N and 40°N in the north Pacific. The shaded and black contours are for WOA13, and the while contours are for LICOM.

Impacts of Ocean Chlorophyll on Subsurface Density and PV

In addition to the impacts on SST and MLD, chlorophyll can also alter the subsurface temperature and density (**Figure 5**). At 165°E, the subsurface temperature at approximately 50-300 m for the CLIMCHL run cools by approximately 0.1-0.3°C and further leads to denser water in the subsurface (50 -300 m) in all three months. This could decrease the vertical density gradient at this depth. The temperature differences in the upper 50 m become positive in April, which leads to lighter water. The situation is similar for the section at 170°W but with larger temperature and density differences between experiments. The statistical significance of potential density difference is evaluated using a t-test.

Due to the biological effect on the vertical distribution of solar radiation, the change of vertical density gradient could impact the PV. Mode waters with low PV (less than 2×10^{-10} m^{-1} s^{-1}) (Suga and Hanawa, 1995; Nakamura, 1996; Qu et al., 2002) tend to form where the winter MLD front intersects with the outcrop line. Compared with the NOCHL run, the decrease of vertical density gradient (50-300m) in CLIMCHL run leads to a lower PV in the mode water formation region (gray shade in **Figure 6**). PV decreases about 0.05×10^{-10} m^{-1} s^{-1} in the STMW formation region around 25°-30°N at 165°E (**Figure 6A**) and about 0.05 - 0.1×10^{-10} m^{-1} s^{-1} in the CMW formation region around 33°-38°N at 170°W (**Figure 6B**). The statistical significance of PV difference is evaluated using a t-test. Lower PV and more quickly lifted MLD might make the mode water subduct beneath the mixed layer more easily.

Impacts of Ocean Chlorophyll on Subduction Rate

According to Qiu and Huang (1995) and Qu et al. (2002), the annual subduction rate Sann can be obtained by integrating the instant subduction rate over one year (T) from the end of the first winter t1 to that of the second winter t2 in a Lagrangian framework. The subduction rate is defined as

$$S_{ann} = \frac{1}{T}\int_{t_1}^{t_2} S(t)\,dt \qquad (2)$$

$$= -\frac{1}{T}\int_{t_1}^{t_2} w_{mb}\,dt + \frac{1}{T}\left(h_m(t_1) - h_m(t_2)\right)$$

The first term on the right-hand side represents the contribution from vertical pumping at the base of the mixed layer, where w_{mb}

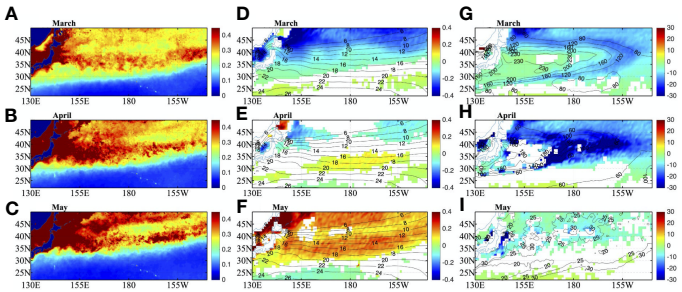

FIGURE 4 | Climatological mean of SeaWiFS chlorophyll concentration (mg m^{-3}) for **(A)** March, **(B)** April and **(C)** May. Shaded in **(D–F)** are for SST differences between CLIMCHL and NOCHL, and contours are for SST of NOCHL (°C). Shaded in **(G–I)** are for MLD differences between CLIMCHL and NOCHL, and contours are for MLD of NOCHL (M). SST and MLD differences are at 95% significant level.

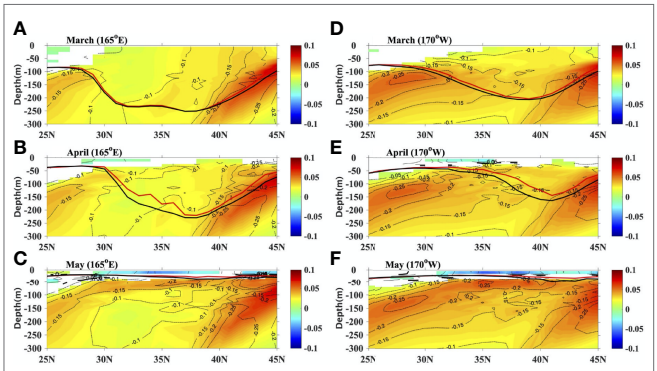

FIGURE 5 | The potential density differences (shaded, CLIMCHL-NOCHL, kg m^{-3}), temperature difference (black contours at 0.05 °C intervals, CLIMCHL-NOCHL) and MLD for NOCHL (blue line, m) and CLIMCHL (red line, m) at 165°E in **(A)** March, **(B)** April and **(C)** May. **(D–F)** are the same as **(A–C)** but for 170°W. Only the potential density differences that are statistically significant are shown (95% significant level).

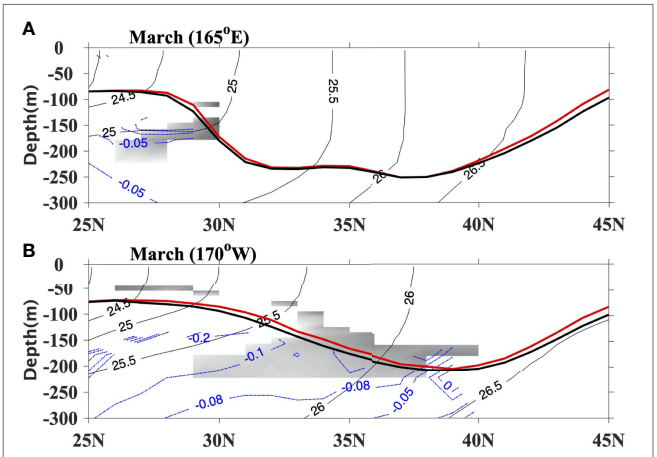

FIGURE 6 | The mean potential density (thin black contours at 0.5 σ_θ intervals, kg m^{-3}) and PV (gray shade< 2×10^{-10} m^{-1} s^{-1}) for NOCHL at **(A)** 165°E and **(B)** 170°W in March. Blue contours are PV differences between two experiments ($\times10^{-10}$ m^{-1} s^{-1}, CLIMCHL-NOCHL), and thick lines show MLD for NOCHL (black line, m) and CLIMCHL (red line, m) in March, respectively. PV< 0.8×10^{-10} m^{-1} s^{-1} are shaded in white. Only the PV differences that are statistically significant are shown (95% significant level).

stands for the vertical velocities at the base of the mixed layer, t_1 and t_2 denote the first and second March, respectively, and T is one year. The second term represents the contribution from lateral induction due to the slope of the mixed layer base or the MLD gradient, where h_m is the MLD. In Lagrangian coordinates, the lateral induction term can be estimated by the difference in the mixed layer depth in the first and second March. In equation 2, the vertical velocities and mixed layer are both from model output. Here, we trace water parcels with a time interval of 5 days and obtain Lagrangian trajectories of the mode water.

The subduction rates due to vertical pumping, lateral induction and the total NOCHL run in the northwestern and central Pacific are shown in **Figures 7A–C**. The annual subduction rate due to vertical pumping is less than 50 m yr^{-1} and shows little spatial variation in the NOCHL run (**Figure 7A**). Lateral induction shows a maximum between 30°N and 40°N, 145°E and 160°W, with values exceeding 100 m yr^{-1} (**Figure 7B**). The maximum center lies in a long narrow band around (29°-35°N, 140°E-180) for STMW and a broad region (35-42°N, 180-160°W) for CMW (**Figure 7B**). The total subduction rate is dominated by the latter and shows a similar pattern to lateral induction, with maximum values exceeding 150 m yr^{-1} (**Figure 7C**). The maximum subduction rate lies where the outcrop line intersects the MLD front (**Figure 1B**).

The differences in annual subduction rates between the two experiments are shown in **Figures 7D–F**. Compared with the NOCHL run, the horizontal distribution of annual subduction rates in CLIMCHL run is similar to the NOCHL run, just with larger value in the center of the subduction region (Figure not shown). The CLIMCHL run shows little difference (less than 5 m yr^{-1}) from the NOCHL run in the vertical pumping term (**Figure 7D**) but shows an evident increase in the lateral induction term (5-15 m yr^{-1}) in the region between 30° and 40°N, 145°E and 160°W (**Figure 7E**), slanting northeastward. The increase is

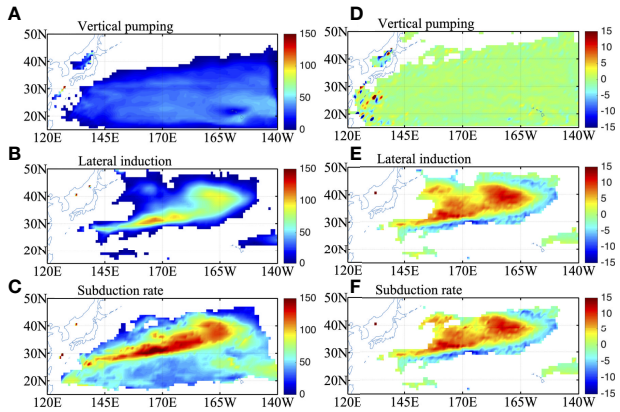

FIGURE 7 | (A) vertical pumping, **(B)** lateral induction and **(C)** the total subduction rate in NOCHL run in the north Pacific (m/year). **(D–F)** are the same as **(A–C)** but for the differences between the two experiments (CLIMCHL-NOCHL).

more than 10m/year in the center of the STMW (30°N-35°N, 150°E-180) and CMW (35°N-42°N, 180-160°W). As a result, the total annual subduction rate increases about 5-10% in the key subduction regions (**Figure 7F**).

To delineate the impacts of ocean chlorophyll on the subduction rate, we computed the distribution with the potential density by integrating it for each 0.1 kg m^{-3} interval of the density field at the base of the March mixed layer in the northwestern and central Pacific (145°E-160°W, 29°-42°N). In the NOCHL, subduction rate is around 1.0 Sv in density range of 24.8-25.6 kg m^{-3} and the maximum subduction rate could reach up to 1.4 Sv (**Figure 8**). The average subduction rate of the CLIMCHL run is larger than that of the NOCHL run in almost all density ranges. The largest differences occur in density range of 26.0-26.4 kg m^{-3} with an increase of about 5-10%.

We have known that the ocean biological effects mainly impact lateral induction, which is associated with MLD front strength. Lateral induction is determined by the MLD difference between the first and second March on the water parcel trajectory (second term on the right-hand side of Eq. (2)). Therefore, either the deeper MLD in the first year or the shallower MLD in the second year could increase lateral induction. Besides, the larger horizontal movement of water parcels could also lead to increase of lateral induction. To investigate how ocean chlorophyll impacts lateral induction, Lagrangian trajectories are compared for the two experiments (**Figure 9**). Most water parcels between 30°N and 40°N move eastward, and the water parcels in the south (approximately 30°N) move southeastward, with little difference between the CLIMCHL and NOCHL runs, except in regions between 25°N and 35°N near the western boundary (**Figure 9**). Little difference between trajectories shows that the lateral induction differences between CLIMCHL and NOCHL runs are mainly caused by strength of the MLD front differences, not by the difference of the trajectories.

To check whether the lateral induction increase is related to the stronger MLD front, the MLD differences between the two experiments in the first and second years and their differences are shown in **Figure 10**. In general, the MLD of CLIMCHL is shallower compared with the NOCHL run due to the biological effect, especially in the shallower MLD region. In the first March, MLD differences between CLIMCHL and NOCHL are negative in the study region, with less than 5 m differences in the center of 30°N-40°N and more than 5 m differences around the MLD front (**Figure 10A**). This indicates that the horizontal MLD gradient of the CLIMCHL run is stronger than that of the NOCHL run. As the water parcels move to the east and south, the MLD is shallower, and the MLD differences between the two experiments increase to more than 10 m in the second March (**Figure 10B**). As a result, the lateral induction differences between experiments show positive values in the region of 30°N-40°N (**Figure 10C**), with magnitude more than 10m/year in the center of the STMW (30°N-35°N, 150°E-180) and CMW (35°N-42°N, 180-160°W). That is, the much shallower MLD in

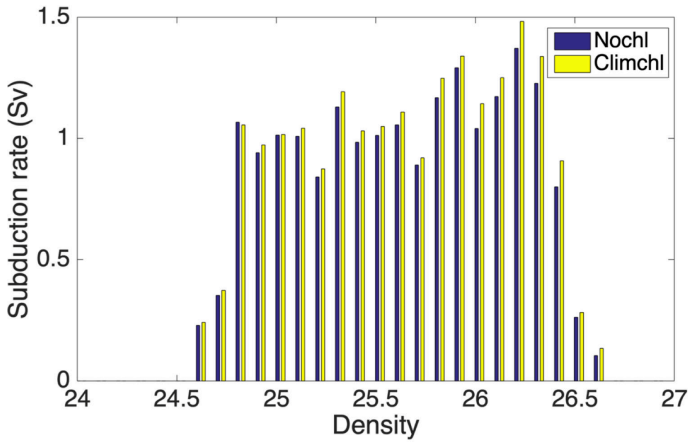

FIGURE 8 | Subduction rate (Sv) for each σ_θ interval of 0.1 kg m^{-3} in the northwestern and central Pacific (145°E-160°W, 29°N-42°N) for the NOCHL run (blue bars) and CLIMCHL run (yellow bars).

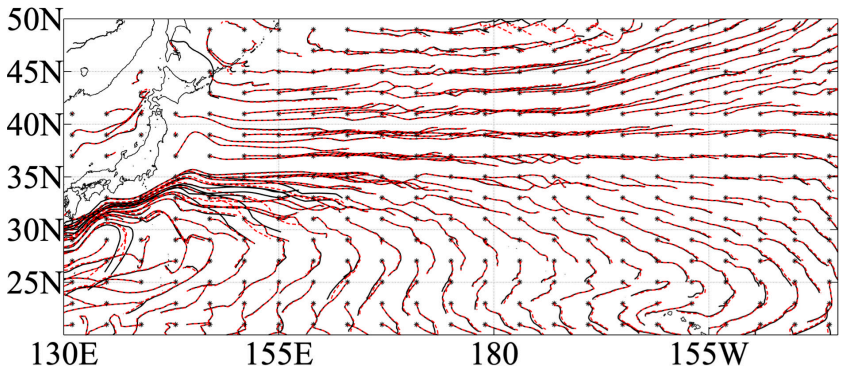

FIGURE 9 | One-year Lagrangian trajectories of water parcels released at the base of the March mixed layer in 2006 for NOCHL (black line) and CLIMCHL (red line). Stars indicate the starting point of the released parcels.

the second year leads to an increase in lateral induction in the CLIMCHL run, which is caused by biological effects.

CONCLUSIONS

In the present study, we investigated the effects of ocean chlorophyll on the temperature and subduction rate of mode water in the northwestern and central Pacific Ocean. Two ocean model experiments with and without chlorophyll indicate that biology-induced feedback could impact the temperature and density in the northwestern and central Pacific Ocean. The Chl reaches a maximum (>0.3 mg m $^{-3}$) during spring and a minimum during summer and autumn. During spring blooms, surface water warms, and subsurface water cools with the existence of chlorophyll. The changes in temperature could also impact the vertical density gradient, which lead to a lower PV at 50 m-250 m.

Biological effects also obviously impact the MLD. With the effect of ocean chlorophyll, the MLD is shallower compared with the NOCHL run, and the MLD lifts more quickly in April in the CLIMCHL run. Analysis shows that biological effects could increase the total annual subduction rate about 5-10% in the northwestern and central Pacific Ocean. The subduction rate increase is mainly caused by the increased lateral induction term (5-15 m yr^{-1}). The results show that the increase of lateral induction is affected by the increased horizontal MLD gradient. Ocean chlorophylls lead to a larger MLD gradient in the CLIMCHL run than in the NOCHL run. In the first March, the MLDs of the CLIMCHL and NOCHL runs have little difference in the deep mixed layer region near Kuroshio Extension region. As the water parcels move to the east and south, the much shallower MLD in the second year leads to an increase in lateral induction in the CLIMCHL run.

The present study focused on the effects of seasonal variations in chlorophyll on the mode water subduction rate. On a decadal scale, the chlorophyll trends in the north Pacific Ocean might also play an important role in mode water formation and ultimately impact climate variability. A study by Gregg and Rousseaux (2019) showed total primary production increases decreases in the North Pacific over the 1998 to 2015 time series. The increased

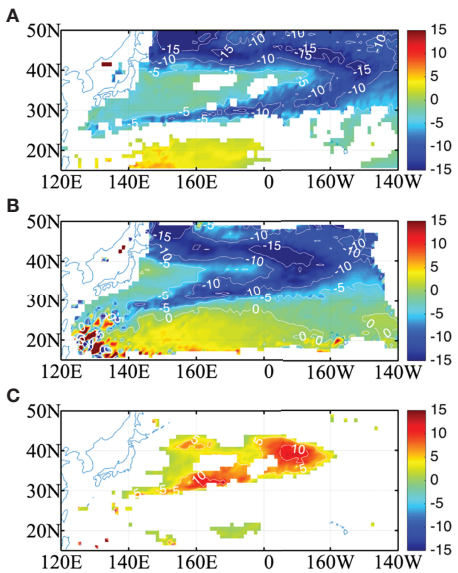

FIGURE 10 | The MLD difference (m) between the two experiments (CLIMCHL-NOCHL) in March of **(A)** the first year and **(B)** the second year. **(C)** is the difference between **(A)** and **(B) (A, B)**. The MLD differences in **(A)** are at 95% significant level.

chlorophyll might lead to a shallower MLD in the MLD front zone and increase the mode water subduction rate. How the variability in primary production and MLD impacts the mode water subduction rate and climate variability needs to be investigated in future studies.

This study is based on a coarse resolution ocean model not including the effect of mesoscale eddy. According to previous studies, mesoscale eddies also enhance the mode water subduction rate, and the magnitude of lateral advection is comparable to the mean flow (Xu et al., 2016; Wang et al., 2020). The biological impacts on subduction rate might be underestimated in present study. Ocean chlorophyll also affects mesoscale activities, such as tropical instability waves (Tian et al., 2019); therefore, the biological

effects in the eddy-resolving model need to be investigated. As the ocean-only model are forced by the same wind forcing, there is no atmospheric feedback, the biological effects might be mitigated in the atmosphere–ocean coupled models. This needs to be investigated in future.

DATA AVAILABILITY STATEMENT

The original contributions presented in the study are included in the article/supplementary material. Further inquiries can be directed to the corresponding author.

AUTHOR CONTRIBUTIONS

JM, do most of the work and write the manuscript; QY, drafting the work and do some analysis; HL, substantial contributions to the conception or design of the work; PL, revising it critically for important intellectual content. JL, provide advice during revision. All authors contributed to the article and approved the submitted version.

FUNDING

This study was supported by the Special Founds for Creative Research (2022C61540), the National Key R&D Program for Developing Basic Sciences (2020YFA0608902 and 2018YFA0605703), and the Key Program of the National Natural Science Foundation of China (grants 41931183 and 41931182). The authors, HLL and PFL, also acknowledge the technical support from the National Key Scientific and Technological Infrastructure project "Earth System Science Numerical Simulator Facility" (EarthLab).

REFERENCES

Anderson, W. G., Gnanadesikan, A., Hallberg, R., Dunne, J. and Samuels, B. L. (2007). Impact of Ocean Color on the Maintenance of the Pacific Cold Tongue. *Geophys. Res. Lett.* 34 (11), L11609. doi: 10.1029/2007gl030100

Bingham, F. M. (1992). The Formation and Spreading of Subtropical Mode Water in the North Pacific. *J. Geophys. Res.* 97, 11177–11189. doi: 10.1029/92JC01001

Gregg, W. W. and Rousseaux, C. S. (2019). Global Ocean Primary Production Trends in the Modern Ocean Color Satellite Record, (1998–2015). *Environ. Res. Lett.* 14 (12), 124011. doi: 10.1088/1748-9326/ab4667

Hanawa, K. and Kamada, J. (2001). Variability of Core Layer Temperature (CLT) of the North Pacific Subtropical Mode Water. *Geophys. Res. Lett.* 28 (11), 2229–2232. doi: 10.1029/2000GL011716

Iwamaru, H., Kobashi, F. and Iwasaka, N. (2010). Temporal Variations of the Winter Mixed Layer South of the Kuroshio Extension. *J. Oceanogr.* 66 (1), 147–153. doi: 10.1007/s10872-010-0012-1

Jerlov, N. G. (1968). Optical Oceanography. Elsevier, pp. 194.

Kubokawa, A. (1999). Ventilated Thermocline Strongly Affected by a Deep Mixed Layer: A Theory for Subtropical Countercurrent. *J. Phys. Oceanogr.* 29, 1314–1333. doi: 10.1175/1520-0485

Large, W. and Yeager, S. (2004). *Diurnal to Decadal Global Forcing for ocean and Sea-Ice Models: The Data Sets and Flux Climatologies* (Boulder, Colorado: National Center for Atmospheric Research), p.105. doi: 10.5065/D6KK98Q6

Levitus, S. (1983). Climatological Atlas of the World Ocean. *Eos Trans. Am. Geophysical Union* 64 (49), 962–963. doi:10.1029/EO064i049p00962-02

Lewis, M. R., Carr, M.E., Feldman, G. C., Esias, W. and McClain, C. (1990). Influence of Penetrating Solar Radiation on the Heat Budget of the Equatorial Pacific. *Nature* 347, 543–546. doi: 10.1038/347543a0

Lewis, M. R., Cullen, J.J. and Platt, T. (1983). Phytoplankton and Thermal Structure in the Upper Ocean: Consequences of Nonuniformity in Chlorophyll Profile. *J. Geophys. Res.* 88 (C4), 2565–2570. doi: 10.1029/JC088iC04p02565

Lin, P., Liu, H. and Zhang, X. (2007). Sensitivity of the Upper Ocean Temperature and Circulation in the Equatorial Pacific to Solar Radiation Penetration Due to Phytoplankton. *Adv. Atm. Sci.* 24(5), 765-780. doi: 10.1007/s00376-007-0765-7

Lin, P., Ma, J., Chai, F., Xiu, P. and Liu, H. (2020). Decadal Variability of Nutrients and Biomass in the Southern Region of Kuroshio Extension. *Prog. Oceanogr.* 188, 102441. 10.1016/j.pocean.2020.102441

Liu, H., Lin, P., Yu, Y. and Zhang, X. (2012b). The Baseline Evaluation of LASG/IAP Climate System Ocean Model (LICOM) Version 2. *Acta Meteor. Sin.* 26, 318–329. doi: 10.1007/s13351-012-0305-y

Liu, H., Ma, J., Lin, P. and Zhan, H. (2012a). Numerical Study of the Effects of Ocean Color on the Sea Surface Temperature in the Southeast Tropical Indian Ocean: The Role of the Barrier Layer. *Environ. Res. Let* 7 (2), 024010. doi: 10.1088/1748-9326/7/2/024010

Liu, H. L., Yu, Y., Li, W. and Zhang, X. (2004b). *Manual of the LASG/IAP Climate System Ocean Model* (Beijing: Science Press), pp.128. doi: 10.1007/BF02916365

Liu, H., Zhang, X., Li, W., Yu, Y. and Yu, R. (2004a). A Eddy-Permitting Oceanic General Circulation Model and its Preliminary Evaluations. *Adv. Atm. Sci.* 21, 675–690.

Locarnini, R. A., Mishonov, A. V., Antonov, J. I., Boyer, T. P., Garcia, H. E., Baranova, O. K., et al. (2013). World Ocean Atlas 2013, Volume 1: Temperature. S. Levitus, Ed., A. Mishonov Technical Ed.;. *NOAA Atlas NESDIS* 73, 40pp. doi: 10.7289/V55X26VD

Ma, J., Liu, H., Lin, P. and Zhan, H. (2014). Seasonality of Biological Feedbacks on Sea Surface Temperature Variations in the Arabian Sea: The Role of Mixing and Upwelling. *J. Geophys. Res. – Oceans* 134, 12–19. doi: 10.1002/2014JC010186

Ma, J., Liu, H., Lin, P. and Zhan, H. (2015). Effects of the Interannual Variability in Chlorophyll Concentrations on Sea Surface Temperatures in the East Tropical Indian Ocean. *J. Geophys. Res.- Oceans* 120 (10), 7015–7027. doi: 10.1002/2015JC010862

Ma, J., Liu, H., Lin, P. and Zhan, H. (2021). Effects of the Seasonal Variation in Chlorophyll Concentration on Sea Surface Temperature in the Global Ocean. *Acta Oceanol. Sin.* 40(11), 50–61. doi: 10.1007/s13131-021-1765-7

Ma, J., Liu, H., Zhan, H., Lin, P. and Du, Y. (2012). Effects of Chlorophyll on Upper Ocean Temperature and Circulation in the Upwelling Regions of the South China Sea. *Aquat. Ecosyst. Health Manag.* 15 (2), 127–134. doi:10.1080/14634988.2012.687663

Masuzawa, J. (1969). Subtropical Mode Water. *Deep Sea Res.* 16 (5), 463–472. doi: 10.1016/0011-7471(69)90034-5

Nakamoto, S., Kumar, S. P., Oberhuber, J. M., Ishizaka, J., Muneyama, K. and Frouin, R. (2001). Response of the Equatorial Pacific to Chlorophyll Pigment in a Mixed Layer Isopycnal Ocean General Circulation Model. *Geophys. Res. Lett.* 28 (10), 2021–2024. doi: 10.1029/2000gl012494

Nakamura, H. (1996). A Pycnostad on the Bottom of the Ventilated Portion in the Central Subtropical North Pacific: Its Distribution and Formation. *J. Oceanogr.* 52 (2), 171–188. doi: 10.1007/BF02235668

Ohlmann, J. C. (2003). Ocean Radiant Heating in Climate Models. *J. Clim.* 16 (9), 1337–1351. doi: 10.1175/1520-0442(2003)16<1337:Orhicm>2.0.Co;2

Oka, E., Kouketsu, S., Toyama, K., Uehara, K., Kobayashi, T., Hosoda, S., et al. (2011). Formation and Subduction of Central Mode Water Based on Profiling Float Data 2003–08. *J. Phys. Oceanogr.* 41 (1), 113–129. doi: 10.1175/2010jpo4419.1

Oka, E. and Qiu, B. (2012). Progress of North Pacific Mode Water Research in the Past Decade. *J. Oceanogr.* 68 (1), 5–20. doi: 10.1007/s10872-011-0032-5

Paulson, C. A. and Simpson, J. J. (1977). Irradiance Measurements in the Upper Ocean. *J. Phys. Oceanogr.* 7(6), 952-956. doi: 10.1175/1520-0485(1977)007<0952:imituo>2.0.co;2

Qiu, B. and Chen, S. (2005). Variability of the Kuroshio Extension Jet, Recirculation Gyre, and Mesoscale Eddies on Decadal Time Scales. *J. Phys. Oceanogr.* 35 (11), 2090–2103. doi: 10.1175/jpo2807.1

Qiu, B. and Chen, S. (2006). Decadal Variability in the Formation of the North Pacific Subtropical Mode Water: Oceanic Versus Atmospheric Control. *J. Phys. Oceanogr.* 36 (7), 1365–1380. doi: 10.1175/jpo2918.1

Qiu, B. and Huang, R. X. (1995). Ventilation of the North Atlantic and North Pacific: Subduction Versus Obduction. *J. Phys. Oceanogr.* 25 (10), 2374–2390. doi: 10.1175/1520-0485

Qu, T., Xie, S.-P., Mitsudera, H. and Ishida, A. (2002). Subduction of the North Pacific Mode Waters in a Global High-Resolution GCM*. *J. Phys. Oceanogr.* 32 (3), 746–763. doi: 10.1175/1520-0485

Sathyendranath, S., Gouveia, A. D., Shetye, S. R., Ravindran, P. and Platt, ,. T. (1991). Biological Control of Surface Temperature in the Arabian Sea. *Nat.* 349 (6304), 54–56. doi: 10.1038/349054a0

Siegel, D. A., Ohlmann, J. C., Washburn, L., Bidigare, R. R., Nosse, C. T., Fields, E., et al. (1995). Solar Radiation, Phytoplankton Pigments and the Radiant Heating of the Equatorial Pacific Warm Pool. *J. Geophys. Res.* 100 (C3), 4885– 4891. doi: 10.1029/94jc03128

Suga, T. and Hanawa, K. (1995). The Subtropical Mode Water Circulation in the North Pacific. *J. Phys. Oceanogr.* 25 (5), 958–970. doi: 10.1175/1520-0485

Sugimoto, S. and Hanawa, K. (2010). Impact of Aleutian Low Activity on the STMW Formation in the Kuroshio Recirculation Gyre Region. *Geophys. Res. Lett.* 37, L03606. doi: 10.1029/2009GL041795

Tian, F., Zhang, R.-H. and Wang, X. (2019). A Positive Feedback Onto ENSO Due to Tropical Instability Wave (TIW)-Induced Chlorophyll Effects in the Pacific. *Geophys. Res. Lett.* 46 (2), 889–897. doi: 10.1029/2018GL081275

Wang, R., Cheng, X., Xu, L. and Chen, J. (2020). Mesoscale Eddy Effects on the Subduction of North Pacific Eastern Subtropical Mode Water. *J. Geophys. Res.: Oceans* 125 (5), e2019JC015641. doi: 10.1029/2019jc015641

Xie, S.-P., Kunitani, T., Kubokawa, A., Nonaka, M. and Hosoda, S. (2000). Interdecadal Thermocline Variability in the North Pacific for 1958–97: A GCM Simulation. *J. Phys. Oceanogr.* 30 (11), 2798–2813. doi: 10.1175/1520-0485(2000)030<2798:Itvitn>2.0.Co;2

Xie, S.-P., Xu, L., Liu, Q. and Kobashi, F. (2010). Dynamical Role of Mode Water Ventilation in Decadal Variability in the Central Subtropical Gyre of the North Pacific. *J. Clim.* 24 (4), 1212–1225. doi: 10.1175/2010jcli3896.1

Xu, L., Li, P., Xie, S.-P., Liu, Q., Liu, C. and Gao, W. (2016). Observing Mesoscale Eddy Effects on Mode-Water Subduction and Transport in the North Pacific. *Nat. Commun.* 7 (1), 10505. doi: 10.1038/ncomms10505

Zweng, M. M., Reagan, J. R., Antonov, J. I., Locarnini, R. A., Mishonov, A. V., Boyer, T. P., et al. (2013). *World Ocean Atlas 2013.* Washington, D.C: U.S. Government Printing Office. *Volume 2: Salinity* . Ed. Levitus, S.Mishonov A.Technical Ed. (NOAA Atlas NESDIS), 74 39 pp

Conflict of Interest: The authors declare that the research was conducted in the absence of any commercial or financial relationships that could be construed as a potential conflict of interest.

Publisher's Note: All claims expressed in this article are solely those of the authors and do not necessarily represent those of their affiliated organizations, or those of the publisher, the editors and the reviewers. Any product that may be evaluated in this article, or claim that may be made by its manufacturer, is not guaranteed or endorsed by the publisher.

frontiers | Frontiers in Marine Science

PERSPECTIVE
published: 01 August 2022
doi: 10.3389/fmars.2022.855965

Toward Regional Marine Ecological Forecasting Using Global Climate Model Predictions From Subseasonal to Decadal Timescales: Bottlenecks and Recommendations

Shoshiro Minobe[1]*, *Antonietta Capotondi*[2,3], *Michael G. Jacox*[3,4,5], *Masami Nonaka*[6] *and Ryan R. Rykaczewski*[7,8]

[1] Faculty of Science, Hokkaido University, Sapporo, Japan, [2] Cooperative Institute for Research in Environmental Sciences, University of Colorado, Boulder, CO, United States, [3] Physical Sciences Laboratory, National Oceanic and Atmospheric Administration (NOAA), Boulder, CO, United States, [4] Southwest Fisheries Science Center, National Oceanic and Atmospheric Administration (NOAA), Monterey, CA, United States, [5] Institute of Marine Sciences, University of California Santa Cruz, Santa Cruz, CA, United States, [6] Application Laboratory, Japan Agency for Marine-Earth Science and Technology, Yokohama, Japan, [7] Pacific Islands Fisheries Science Center, National Oceanic and Atmospheric Administration (NOAA), Honolulu, HI, United States, [8] Department of Oceanography, School of Ocean and Earth Science and Technology, University of Hawaii, Honolulu, HI, United States

OPEN ACCESS

Edited by:
Doran M. Mason,
NOAA-Great Lakes Environmental Research Laboratory, United States

Reviewed by:
Albert J. Hermann,
University of Washington, United States
Claire M. Spillman,
Bureau of Meteorology, Australia

***Correspondence:**
Shoshiro Minobe
minobe@sci.hokudai.ac.jp

Specialty section:
This article was submitted to Marine Fisheries, Aquaculture and Living Resources, a section of the journal Frontiers in Marine Science

Received: 16 January 2022
Accepted: 06 June 2022
Published: 01 August 2022

Citation:
Minobe S, Capotondi A, Jacox MG, Nonaka M and Rykaczewski RR (2022) Toward Regional Marine Ecological Forecasting Using Global Climate Model Predictions From Subseasonal to Decadal Timescales: Bottlenecks and Recommendations. Front. Mar. Sci. 9:855965. doi: 10.3389/fmars.2022.855965

This perspective paper discusses how the research community can promote enhancement of marine ecosystem forecasts using physical ocean conditions predicted by global climate models (GCMs). We review the major climate prediction projects and outline new research opportunities to achieve skillful marine biological forecasts. Physical ocean conditions are operationally predicted for subseasonal to seasonal timescales, and multi-year predictions have been enhanced recently. However, forecasting applications are currently limited by the availability of oceanic data; most subseasonal-to-seasonal prediction projects make only sea-surface temperature (SST) publicly available, though other variables useful for biological forecasts are also calculated in GCMs. To resolve the bottleneck of data availability, we recommend that climate prediction centers increase the range of ocean data available to the public, perhaps starting with an expanded suite of 2-dimensional variables, whose storage requirements are much smaller than 3-dimensional variables. Allowing forecast output to be downloaded for a selected region, rather than the whole globe, would also facilitate uptake. We highlight new research opportunities in both physical forecasting (e.g., new approaches to dynamical and statistical downscaling) and biological forecasting (e.g., conducting biological reforecasting experiments) and offer lessons learned to help guide their development. In order to accelerate this research area, we also suggest establishing case studies (i.e., particular climate and biological events as prediction targets) to improve coordination. Advancing our capacity for marine biological forecasting is crucial for the success of the UN Decade of Ocean Science, for which one of seven desired outcomes is "A Predicted Ocean".

Keywords: dynamical downscaling, statistical downscaling, biological forecast, marine ecosystem prediction, GCM prediction

INTRODUCTION

Marine ecosystem forecasting, often leveraging predictions of physical ocean conditions, is an emerging research area that has rapidly attracted significant attention (Payne et al., 2017; Tommasi et al., 2017; Hobday et al., 2018; Capotondi et al., 2019a; Park et al., 2019; Jacox et al., 2020; Bolin et al., 2021). The development and improvement of marine biological forecasts are motivated by a number of ecological and socioeconomic aims, including management of fisheries and aquaculture, conservation of endangered marine species, and protection of human health. At present, most marine ecosystem predictions are in the experimental stage, but in the future, they could be operationalized with a wide range of applications.

Many different statistical and dynamical methods can be used for ecological prediction on subseasonal to decadal timescales (Tommasi et al., 2017; Jacox et al., 2020). However, perhaps the most promising approach is to start with general circulation or global climate model (GCM) predictions of the physical environment and use them as the basis for ecological prediction. GCM predictions are conducted for a range of forecast lead times (i.e., the length of time between the time of initial condition and the time for which conditions are being predicted[1]). Forecasts with subseasonal to seasonal lead time (i.e., several weeks to a year) are operationally produced by a number of modeling centers, and multiannual predictions (i.e., 1-10 years) are also being examined. These global climate forecasts offer a foundation to be used for an array of marine ecosystem predictions. While alternative methods may also be leveraged to generate biological predictions (for example, forecasting fish population dynamics by monitoring earlier life stages), they are beyond the scope of this paper.

Forecasting marine ecosystems using physical predictions consists of a multi-step process, typically including a GCM prediction, the dynamical or statistical downscaling of the GCM fields, and biological estimation (**Figure 1**) (e.g., Jacox et al., 2020). The data transfer between the tasks is an important consideration for the workflow. The most intensive data transfer is needed for dynamical downscaling, in which the three-dimensional (3D) output of a GCM prediction is needed to force a regional model (**Figure 1A**). A prime example of this workflow is J-SCOPE (JISAO's Seasonal Coastal Ocean Prediction of the Ecosystem), for which dynamical downscaling using the Regional Ocean Modeling System (ROMS) is conducted using surface and lateral boundary conditions taken from version 2 of the National Oceanic and Atmospheric Administration (NOAA) Climate Forecast System (CFSv2) (Kaplan et al., 2016; Siedlecki et al., 2016). This system is supported by publicly available, 6-hourly, 3D forecast outputs of ocean variables for CFSv2. However, such data availability is exceptional; 3D GCM forecast output at higher than monthly resolution is typically not publicly available for other projects. Thus, in most cases, this workflow requires a close collaboration between the climate prediction center and the user institute.

A more practical workflow for many researchers is to use two-dimensional (2D) GCM output for key fields such as SST (**Figure 1B**). This workflow was employed by a series of Australian studies in fisheries forecasting applications (Spillman et al., 2013; Spillman and Hobday, 2014; Eveson et al., 2015; Brodie et al., 2017). In this case, users may employ statistical downscaling rather than dynamical downscaling. A promising future extension of this workflow is to use multiple GCM outputs (**Figure 1C**) because a multi-model ensemble can better capture reality than a single model due to the reduction of model-specific errors, as found for SST (Hervieux et al., 2019; Yati and Minobe, 2021) and for sea-surface height (Widlansky et al., 2017; Long et al., 2021). Furthermore, the reduction of model-specific errors can lead to a better estimation of prediction uncertainty, which can be useful for applications using predictions.

For marine ecosystem forecasts based on physical predictions, some bottlenecks and gaps need to be resolved. In order to address those problems, coordination across institutes is needed, and a large body of research is required. Thus, researchers, managers, and funding agencies need a strategy to work across climate and oceanographic disciplines in pursuit of the larger goal. The purpose of this perspective paper is twofold: (1) to review major ongoing activities related to climate predictions at subseasonal to decadal lead times, and (2) to outline new research opportunities for marine ecosystem forecasting.

PRESENT STATUS OF PREDICTIONS OF OCEANIC PHYSICAL CONDITIONS

In this section, we review how predictions of oceanic physical conditions, which are the basis of marine ecosystem prediction, are conducted from subseasonal (two weeks to two months), seasonal (from two months to one year), and to multiannual (from a year to ten years) lead times, including information on publicly available oceanic variables (**Table 1**). As noted above, our focus here is on physical predictions obtained using GCMs. Other prediction products may be suitable for some applications but are outside the scope of this paper (for example, forecasts produced with statistical methods such as linear inverse models[2] and ocean-only model forecasts such as 10-day ocean weather forecasts around Japan[3]).

The subseasonal to seasonal (S2S) prediction project of the World Climate Research Programme (WCRP) (Vitart et al., 2017) provides S2S prediction datasets for forecast lead-times up to 60 days (**Table 1**). The data are available at the European Centre for Medium-Range Weather Forecasts (ECMWF)[4] and at the Chinese Meteorological Administration (CMA)[5]. Several modeling centers participating in the project provide various oceanic variables as 2D outputs, including SST, sea-surface

[1]This definition of lead time is widely used for research, though for practical use of forecasts, the lead time may be defined based on a time when a forecast is issued instead of the time of the initial condition.

[2] https://psl.noaa.gov/forecasts/sstlim/ (access January 15, 2022).
[3] https://www.eorc.jaxa.jp/ptree/ocean_model/index.html (access January 15, 2022).
[4] https://apps.ecmwf.int/datasets/data/s2s (access January 15, 2022).
[5] http://s2s.cma.cn/index (access January 15, 2022).

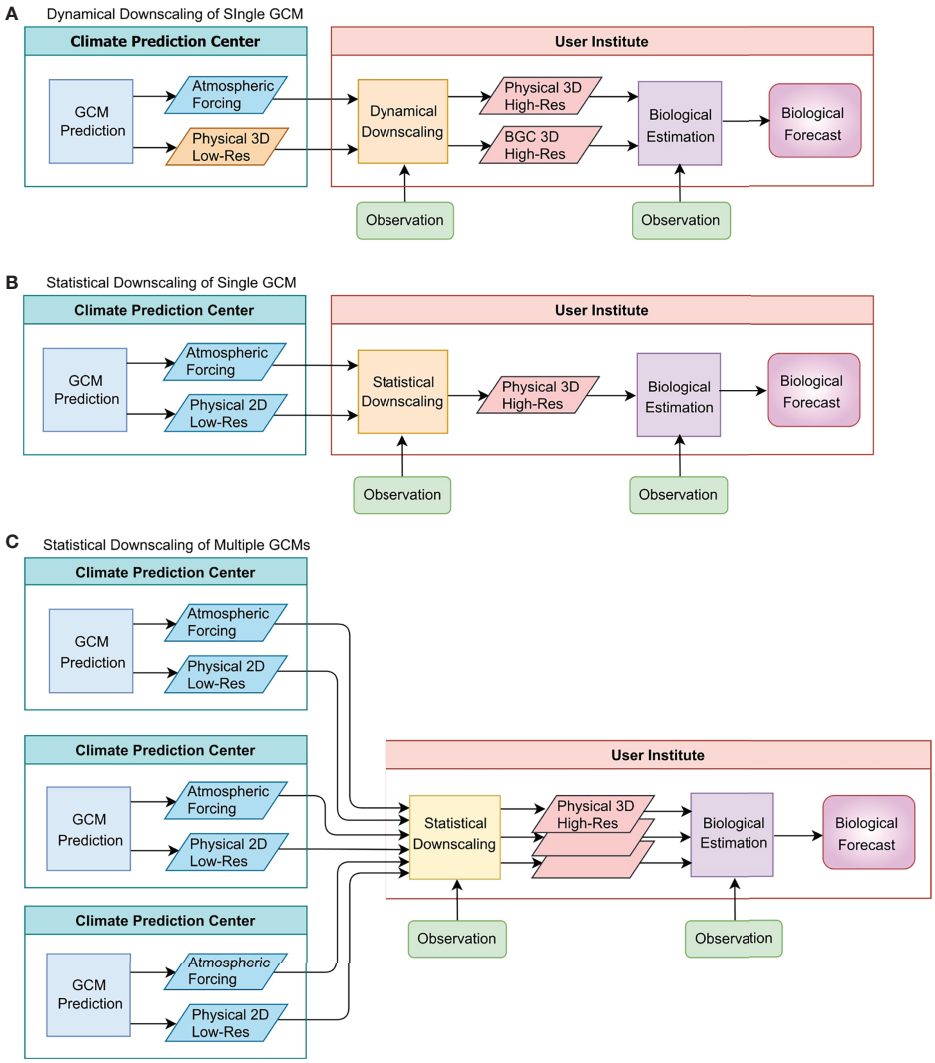

FIGURE 1 | Typical workflows of biological forecasts based on physical GCM predictions. The squares indicate systems that produce predictions, downscaling or biological estimation, whereas the parallelograms indicate the outputs from the systems. Panel **(A)** and panel **(B)** indicate the workflows with dynamical and statistical downscalings, respectively, using outputs of a single GCM prediction, and panel **(C)** indicates the workflow using outputs of multiple GCMs with statistical downscaling. The stacked parallelograms in the middle of panel **(C)** indicate downscaling of different GCM predictions. "BGC" in the figure indicates information about biogeochemistry and lower-trophic level biology. Downscaling can be skipped if GCM predictions are of adequate resolution and acceptable bias. The physical prediction is assumed to be conducted by GCMs, but it can be made by ESMs, which also include BGC.

salinity, surface currents, sea-surface height, mixed-layer depth, and 0-300 m averaged temperature and salinity.

For other subseasonal-to-seasonal prediction projects, currently SST is the only oceanic variable made publicly available. Those projects include the Subseasonal Experiment (SubX) project (Pegion et al., 2019), the North American Multi-Model Ensemble (NMME) (e.g., Becker et al., 2014; Kirtman et al., 2014), and seasonal prediction by the Copernicus Climate Change Service (C3S) (**Table 1**). However, it should be noted that ocean output from CFSv2 seasonal forecasts, which can be obtained from NOAA[6], includes a suite of 2D variables (temperature, salinity, and currents at fixed depths; isotherm depths, sea-level height, 0-300 m heat content) as well as 3D fields (temperature, salinity, and horizontal and vertical velocities) at monthly-mean or 6-hourly resolution.

Multiannual prediction, which is often called "decadal prediction" (Boer et al., 2016), is in its experimental stage. The first systematic collection of multiannual predictions was conducted in the context of the Climate Model Intercomparison Project Phase 5 (CMIP5) (Taylor et al., 2012) and has been enhanced in CMIP6 (Eyring et al., 2016). The data of CMIP5 and CMIP6 are available *via* the Earth System Grid Federation (ESGF)[7]. In CMIP6, multiannual prediction is coordinated under the Decadal Climate Prediction Project (DCPP), and DCPP

[6]https://www.ncei.noaa.gov/products/weather-climate-models/climate-forecast-system (access May 18, 2022).

[7] https://esgf-node.llnl.gov/projects/esgf-llnl/ (access May 1, 2022).

TABLE 1 | Currently available ocean forecast output from major climate prediction projects on subseasonal to decadal timescales.

Project Name	SubX[13]	S2S[14]	C3S seasonal forecasting[15]	NMME[16]	CMIP6/DCPP[17]
Maximal prediction lead-time	45 days	60 days	5 months	11 months	10 years for most models
Number of models that have near real-time forecasts and have the ocean model	7 models	8 models	9 models	6 models	5 models for dcppB-forecast[18]
Number of Ensembles	1-21	4-50	24-60	4-30	10-40
Ocean model resolutions	0.08(1)-1 degree	0.25-1 degree	0.25-1 degree	0.25-1 degree	50-100 km as nominal resolutions
2D ocean data availability for forecast data	SST only	sea-surface height; temperature, salinity, and current speeds at the sea surface; 0-300 m averaged temperature and salinity; 20°C isotherm depth; mixed-layer thickness; sea-ice thickness	SST only	SST only	Surface values; vertically integrated values; depth of specific features
3D ocean data availability	No	No	No	No	Yes
Downloading selected region data	Yes	No	Yes	Yes	No

[13] http://cola.gmu.edu/subx/ (access May 17, 2022).
[14] http://s2sprediction.net/ (access May 17, 2022).
[15] https://climate.copernicus.eu/seasonal-forecasts (access May 17, 2022).
[16] https://www.cpc.ncep.noaa.gov/products/NMME (access May 17, 2022).
[17] https://www.wcrp-climate.org/modelling-wgcm-mip-catalogue/cmip6-endorsed-mips-article/1065-modelling-cmip6-dcpp (access January 15, 2022).
[18] https://esgf-node.llnl.gov/search/cmip6/ (access May 17, 2022).
(1) Only the US Navy Earth System Model has an eddy-resolving high resolution (0.08 degrees).

experiments contain both reforecasts (i.e., forecasts simulated for a retrospective period; called dccpA) and near real-time forecasts (called dccpB) (Boer et al., 2016). Early evaluations of multiannual prediction skill have found that it mainly arises from initial conditions in the first few years, and at longer lead times is associated with the forced response to climate change, especially for temperatures (e.g., Branstator and Teng 2010; Yeager et al., 2018). CMIP6/DCPP provides a suite of 2D ocean variables as well as 3D ocean temperature, salinity and currents, all available as monthly or annual means. Recently, the World Meteorological Organization has established the Lead Centre for Annual to Decadal Climate Prediction, which annually issued a Global Annual to Decadal Climate Update[8]. The latest report documented forecasts for the target years from 2022 to 2026 (see also Hermanson et al., 2022).

Most of these prediction projects use GCMs, but a few modeling centers use Earth System Models (ESMs), i.e., GCMs coupled with a biogeochemical and lower-trophic ecosystem model. The Seasonal-to-Multiyear Large Ensemble (SMYLE) (Yeager et al., 2022) and the Decadal Prediction Large Ensemble (DPLE) (Yeager et al., 2018), both produced by the National Center for Atmospheric Research (NCAR), use the Community Earth System Model (CESM). The outputs of DPLE are publicly available on the NCAR web site[9]. Also, biogeochemical and biological variables for near real-time multiannual prediction under DCPP (dcppB) are available for one model (for the Canadian Earth System Model version 5) and for six models for reforecast (dcppA) at the present[10].

In addition to considering the availability of data, it is also helpful to know whether a subset of the data for a selected region can be easily downloaded. The downloading of a selected region is possible for the C3S seasonal forecast data using the Application Programming Interface and for the SubX, NMME, and CFSv2 data *via* Open-source Project for a Network Data Access Protocol (OPeNDAP); but such an option is not available for the S2S and CMIP6/DCPP data.

This summary of available output from global climate forecast systems highlights both the considerable potential in ongoing efforts and several major bottlenecks for marine ecosystem prediction, specifically the availability of already-computed data and the ability to download them efficiently.

NEW OPPORTUNITIES

A wide range of new studies needs to be conducted to successfully develop marine ecological forecasts built on physical predictions. These studies can be broadly divided into two main categories: physical downscaling and biological prediction (**Figure 1**). The physical downscaling can be viewed as an intermediate goal that can be undertaken by physical researchers. An appropriate intermediate goal will allow researchers of physical oceanography to publish their own papers and obtain funding as principal investigators, and these prospects are important to attract young researchers (Minobe, 2014). To highlight the many specific opportunities for research in physical and biological aspects of marine ecosystem forecasting, we describe them separately below. But of course, even research in specialized areas can benefit from interdisciplinary collaboration.

Physical Research

GCM prediction skill should be examined for various oceanic variables that are useful for biological forecasts, because skillful ocean predictions of quantities that drive biological models are needed to achieve skillful ecological forecasts. To date, oceanic

[8] https://www.wmolc.org/ (access January 10, 2022).
[9] https://www.cesm.ucar.edu/projects/community-projects/DPLE/data-sets.html (access December 26, 2021).
[10] https://esgf-node.llnl.gov/projects/cmip6/ (access May 3, 2022).

prediction skill has been examined mainly for SST (e.g., Becker et al., 2014; Doi et al., 2019; Hervieux et al., 2019) including marine heatwaves (Jacox et al., 2022), sea-surface height (e.g., Widlansky et al., 2017; Long et al., 2021; Shin and Newman, 2021; Amaya et al., 2022), and upper-layer temperatures (e.g., Yeager et al., 2018; Doi et al., 2020), because these variables are important in describing physical climate variability and relatively easy to evaluate with observation-based products. However, for biological predictions, other variables (e.g., mixed-layer depth, upwelling, salinity, bottom temperature, vertical profiles of temperature and density) can also be important, as they impact nutrient availability and the habitat of marine species, and they may be associated with a higher degree of predictability (e.g., Siedlecki et al., 2016; Capotondi et al., 2019a).

Furthermore, physical predictions from large ensembles and multi-model ensembles should be examined for their use in biological prediction. Recent studies identified an interesting bias in climate prediction systems known as the "predictability paradox" or "signal-to-noise paradox" (Eade et al., 2014; Dunstone et al., 2016; Smith et al., 2020). The basic idea of ensemble prediction is that the reality can be viewed as one member of an ensemble, and thus the difference between the ensemble mean and reality (as approximated by observations) should be similar to the differences between the ensemble mean and each ensemble member. However, when the predictability paradox occurs, the ensemble mean is more similar to reality than to other ensemble members. In this case, averaging over large ensembles is helpful to obtain a better prediction than those from smaller ensembles. To increase the size of ensembles, it is generally effective to use output from multiple models, and as discussed in Section 1, the use of multiple models also has the effect of reducing problems specific to individual models. Therefore, we suggest that using outputs of large ensembles from multiple GCMs can also have advantages for marine biological prediction (**Figure 1C**), and this possibility should be explored.

For regional marine ecosystem prediction efforts, the resolution of the global ocean models may not be sufficient, and thus dynamical or statistical downscaling of the predicted data at higher spatial resolutions may be necessary. Dynamical downscaling is used for J-SCOPE, as mentioned above, and various machine learning techniques are used for statistical downscaling (Stengel et al., 2020; Kashinath et al., 2021). Statistical downscaling schemes can be constructed using observations at specific sites together with coarse outputs of numerical models, but they can also be built on the results of dynamically downscaled data from the coarse model outputs (Jacox et al., 2020). The latter approach should be especially useful for variables that are not well observed. Both dynamical and statistical downscaling should be investigated in detail, as they have advantages and limitations. Dynamical downscaling can provide a complete representation of the ocean at the needed resolution, but will inherit the biases of the climate model that was used for the lateral boundary conditions and the surface forcing. The skill of downscaled forecasts should be compared to that of GCMs to quantify the added value of the downscaling procedure. Relative to dynamical downscaling, statistical downscaling can better capture observed relationships, but may be limited by data availability. Furthermore, dynamical downscaling is much more computationally expensive and slower than statistical downscaling, which can be important considerations for operational biological forecasting. Thus, depending on the specific application, different approaches may be more suitable.

Biological Research

It is important to identify which ecological variables are promising targets for prediction. The target for prediction should be relevant to species valued by society and should be sensitive to physical conditions. Candidates of target species can be identified by examining the statistical relationships between physical conditions and marine ecosystem status using the observational data as a first step. A classic example is the relation between the Pacific Decadal Oscillation (PDO) and Pacific salmon catches (Mantua et al., 1997), and that between the PDO and the Japanese sardine population (Yasuda et al., 1999). A more systematic approach using principal component analysis of a large number of marine ecosystem indicators reported that many species are influenced by climate variability and change in the North Pacific and adjacent seas (Hare and Mantua, 2000 ; Tian et al., 2006; Litzow and Mueter, 2014; Ma et al., 2019; Yati et al., 2020) and in the northeast Atlantic (Brunel and Boucher, 2007). Of course, such statistical analysis can only identify correlations, which do not necessarily mean causality, and the relationships may be non-stationary. Furthermore, a causal relationship is not enough for prediction, because if physical conditions that influence marine species are unpredictable, then biological targets are also not predictable (Brodie et al., 2021).

For the potential marine ecosystem targets, prediction skill should be assessed by conducting retrospective forecasts (i.e., reforecasts) evaluated against observations. Reforecasts using global ESMs have demonstrated meaningful prediction skill with lead times of a year or more for certain regions and variables, including surface pH (Brady et al., 2020), ocean carbon uptake (Lovenduski et al., 2019), aragonite saturation state (Yeager et al., 2022), chlorophyll and net primary productivity (Séférian et al., 2014; Rousseaux and Gregg, 2017; Krumhardt et al. 2020), and even annual fish catch in large marine ecosystems (Park et al., 2019). The availability of the biogeochemical model output is very important for better understanding the links between physics and biology in the model context. These links are still poorly constrained by observations due to the sparsity of biogeochemical data (Turi et al., 2018), highlighting the need for expanded and sustained biogeochemical observational networks in support of biological prediction efforts (Capotondi et al., 2019a).

Ecological predictions are also challenged by shifts in the relationships between physical conditions and biological responses through time and with population sizes. Empirical relationships that appear robust for several years can decay over time (Myers, 1998; Deyle et al., 2013). Changes in climate conditions at the basin scale have been linked to shifts in relationships between local physical properties and fisheries recruitment (Litzow et al., 2019). An understanding of the underlying ecological mechanisms that explain empirical relationships between physical and biological properties and how those mechanisms may change over time is necessary to increase confidence in ecological predictions.

In the coming years, regional biological reforecasts should be widely examined. Biological reforecasting is a relatively new study area, but lessons learned from climate reforecasts can be useful to guide similar efforts for biology:

1. Forecast skill should be examined for anomalies, i.e., the differences between forecasted raw values and the forecasted mean seasonal cycle (or climatology). If the forecast skill is examined with raw values, then the skill is likely to be dominated by a seasonal cycle rather than the interannual variability of interest. Furthermore, since model biases tend to grow due to model drift at longer lead times, model climatologies should be lead-time dependent.
2. For the estimation of the statistical significance of a metric, it is important to take into account the serial correlation of the data to be examined. For example, if there are annually sampled predicted and observed data for a period of N -years, and the respective time series have auto-correlation at a one-year lag of. r_a and r_b, then the effective degrees of freedom of the data for the Pearson's correlation can be estimated as $N\,(1-r_a\,r_b)/(1+\,r_a\,r_b)$ (Bretherton et al., 1999). The influence becomes strong when the lag-1 autocorrelation is large. If the lag-1 autocorrelation is 0.6 (0.3) then the effective degrees of freedom are 47% (83%) of the original data samples. The serial correlation is not generally considered in widely used software packages or libraries. Therefore, the p-value obtained by such packages is inappropriate when the serial correlation cannot be ignored. In any case, how degrees of freedom were estimated should be clarified.
3. The separation of training and verification data, known as "cross-validation", is crucial for assessing the performance of statistical estimation (e.g. Arlot and Celisse, 2010). For example, in V-fold cross validation, all data are divided into v "folds," the prediction model is trained using data of v-1 folds, the remaining one fold is used for validation, and the fold to be used for validation is successively changed. Cross-validation is especially important when using a statistical or machine-learning technique that can substantially overfit the training data.
4. Ensembles of prediction should be used appropriately. Since the biological responses to physical conditions may be nonlinear, it is desirable to use the individual ensemble members of physical forecasts to drive biological models, rather than using the ensemble mean of the physical forecasts. A large ensemble size is especially useful to evaluate the probability of extreme events and to evaluate whether the predictability paradox occurs as mentioned above. Furthermore, if biological estimation involves uncertainty in the variables other than the physical prediction, using ensembles for these variables may be useful to understand the uncertainty originating in biological process.

SUMMARY AND RECOMMENDATIONS

Existing subseasonal to decadal climate predictions can potentially be very valuable for the prediction of marine ecosystems. However, availability of forecast output for ocean conditions is generally rather poor; in particular, most seasonal prediction systems do not provide ocean variables other than SST. While there are technical hurdles to providing additional large datasets, one of the reasons for the limited data availability may be that the modeling centers do not see enough demand for those data to be shared. We suggest that the demand actually exists, and we make two recommendations for enabling the uptake of physical forecasts in marine ecosystem prediction: 1) Climate prediction projects should make more ocean prediction data available to the research community. Making an expanded suite of 2D variables available, as done by the S2S project and CFSv2, would be a good starting point. Some currently unavailable 2D variables, such as eddy kinetic energy, could be useful for marine biological forecasts (e.g., Brodie et al., 2018), and thus they would be candidates of variables to be made available in the future. 2) Enable users to download data for selected regions. This capability is useful for a wide range of users who may be interested in specific regions and greatly reduces user requirements for data downloading, storage, and processing.

Combining physical and biological disciplines with the common goal of improved marine ecosystem prediction will be a fruitful area of research with clear applications to society. To facilitate this research area, it would be useful to develop a set of case studies for biological prediction. For example, a massive Northeast Pacific marine heatwave in 2013-2016 involved compound extremes of a heatwave, a low-oxygen extreme, and an ocean acidity extreme (Gruber et al., 2021). While the forecast skill and predictability of SST anomalies during this event have been explored (e.g., Hu et al., 2017; Jacox et al., 2019; Capotondi et al., 2019b; Capotondi et al., 2022), further research could investigate how much these various co-occurring extremes and their impacts on the marine ecosystem could be predicted. Since a regional phenomenon is generally studied by regional researchers, other case studies distributed across the global ocean can be identified to attract the international community's interest.

As the global community increasingly recognizes the sensitivity of marine ecosystems to climate variability and change and the potential consequences to human society, the time is ripe to enhance forecasts of marine ecosystems by pursuing the strategies proposed here. Such efforts are gaining some attraction at the international level. For example, the North Pacific Marine Science Organization (PICES) is in the process of establishing a new working group on "Climate Extremes and Coastal Impacts in the Pacific" with a focus on climate and marine ecosystem predictions[11]. Furthermore, the United Nations Decade of Ocean Science for Sustainable Development (UN Ocean Decade) has been launched for the 2021-2030 decade. The overarching theme of the UN Ocean Decade is "The Science We Need for the Ocean We Want." One of its seven expected outcomes is "A Predicted Ocean."[12]

[11] https://meetings.pices.int/members/working-groups/wg49 (access January 15, 2022).

[12] https://www.oceandecade.org/vision-mission/ (access January 10, 2021).

To know what ocean we can have in the future, the capability of marine biological predictions is essential.

DATA AVAILABILITY STATEMENT

The original contributions presented in the study are included in the article. Further inquiries can be directed to the corresponding author.

AUTHOR CONTRIBUTIONS

SM wrote the first draft, and all authors actively contributed to its improvement. All authors contributed to the article and approved the submitted version.

FUNDING

SM was supported JSPS KAKENHI Grant Numbers JP18H04129, JP19H05704 and MN was by JP19H05701. MGJ was supported by NOAA Southwest Fisheries Science Center, RRR was supported by NOAA Pacific Islands Fisheries Science Center, and AC was supported by the NOAA Climate Program Office Modeling, Analysis, Predictions and Projections (MAPP) program.

ACKNOWLEDGMENTS

This paper is an initiative of the Working Group on "Climate and Ecosystem Predictability", jointly sponsored by the North Pacific Marine Science Organization (PICES) and the Climate and Oceans - Variability, Predictability, and Change (CLIVAR). We thank PICES and CLIVAR for their sponsorship and support. We appreciate two reviewers for their helpful and constructive comments.

REFERENCES

Amaya, D. J., Jacox, M. G., Dias, J., Alexander, M. A., Karnauskas, K. B., Scott, J. D., et al. (2022). Subseasonal-To-Seasonal Forecast Skill in the California Current System and its Connection to Coastal Kelvin Waves. *J. Geophys. Res.: Ocean.* 127, e2021JC017892. doi: 10.1029/2021JC017892

Arlot, S. and Celisse, A. (2010). A Survey of Cross-Validation Procedures for Model Selection. *Stat Surveys.* 4, 40–79. doi: 10.1214/09-SS054

Becker, E., van den Dool, H. and Zhang, Q. (2014). Predictability and Forecast Skill in NMME. *J. Clim.* 27, 5891–5906. doi: 10.1175/JCLI-D-13-00597.1

Boer, G. J., Smith, D. M., Cassou, C., Doblas-Reyes, F., Danabasoglu, G., Kirtman, B., et al. (2016). The Decadal Climate Prediction Project (DCPP) Contribution to CMIP6. *Geosci. Model. Dev.* 9, 3751–3777. doi: 10.5194/gmd-9-3751-2016

Bolin, J. A., Schoeman, D. S., Evans, K. J., Cummins, S. F. and Scales, K. L. (2021). Achieving Sustainable and Climate-Resilient Fisheries Requires Marine Ecosystem Forecasts to Include Fish Condition. *Fish. Fish.* 22, 1067-1084. doi: 10.1111/faf.12569

Brady, R. X., Lovenduski, N. S., Yeager, S. G., Long, M. C. and Lindsay, K. (2020). killful multiyear predictions of ocean acidification in the California Current System. *Nat. Commun.* 11, 2166. doi: 10.1038/s41467-020-15722-x

Branstator, G. and Teng, H. (2010) Potential impact of initialization on decadal predictions as assessed for CMIP5 models. *Geophys. Res. Lett.* 39. doi: 10.1029/2012GL051974

Brodie, S., Abrahms, B., Bograd, S. J., Carroll, G., Hazen, E. L., Muhling, B. A., et al. (2021). Exploring Timescales of Predictability in Species Distributions. *Ecography* 44, 832–844. doi: 10.1111/ecog.05504

Brodie, S., Hobday, A. J., Smith, J. A., Spillman, C. M., Hartog, J. R., Everett, J. D., et al. (2017). Seasonal Forecasting of Dolphinfish Distribution in Eastern Australia to Aid Recreational Fishers and Managers. *Deep. Sea. Res. Part 2. Top. Stud. Oceanogr.* 140, 222–229. doi: 10.1016/j.dsr2.2017.03.004

Brodie, S., Jacox, M. G., Bograd, S. J., Welch, H., Dewar, H., Scales, K. L., et al. (2018). Integrating Dynamic Subsurface Habitat Metrics into Species Distribution Models. *Front. Mar. Sci.* 5:219. doi: 10.3389/fmars.2018.00219

Capotondi, A., Jacox, M., Bowler, C., Kavanaugh, M., Lehodey, P., Barrie, D., et al. (2019a). Observational Needs Supporting Marine Ecosystems Modeling and Forecasting: From the Global Ocean to Regional and Coastal Systems. *Front. Mar. Sci.* 6. doi: 10.3389/fmars.2019.00623

Capotondi, A., Newman, M., Xu, T. and Di Lorenzo, E. (2022). An Optimal Precursor of Northeast Pacific Marine Heatwaves and Central Pacific El Niño Events. *Geophys. Res. Lett.* 49, e2021GL097350. doi: 10.1029/2021GL097350

Capotondi, A., Sardeshmukh, P. D., Di Lorenzo, E., Subramanian, A. and Miller, A. J. (2019b). Predictability of US West Coast Ocean Temperature is Not Solely Due to ENSO. *Sci. Rep.* 9, 10993. doi: 10.1038/s41598-019-47400-4

Deyle, E. R., Fogarty, M., Hsieh, C.-H., Kaufman, L., MacCall, A. D., Munch, S. B., et al. (2013). Predicting Climate Effects on Pacific Sardines. *PNAS* 110, 6430–6435. doi: 10.1073/pnas.1215506110

Doi, T., Behera, S. K. and Yamagata, T. (2019). Merits of a 108-Member Ensemble System in ENSO and IOD Predictions. *J. Clim.* 32, 957–972. doi: 10.1175/JCLI-D-18-0193.1

Doi, T., Nonaka, M. and Behera, S. (2020). Skill Assessment of Seasonal-To-Interannual Prediction of Sea Level Anomaly in the North Pacific Based on the SINTEX-F Climate Model. *Front. Mar. Sci.* 7, 855. doi: 10.3389/fmars.2020.546587

Dunstone, N., Smith, D., Scaife, A., Hermanson, L., Eade, R., Robinson, N., et al. (2016). Skilful Predictions of the Winter North Atlantic Oscillation One Year Ahead. *Nat. Geosci.* 9, 809–814. doi: 10.1038/ngeo2824

Eade, R., Smith, D., Scaife, A., Wallace, E., Dunstone, N., Hermanson, L., et al. (2014). Do Seasonal-to-Decadal Climate Predictions Underestimate the Predictability of the Real World? *Geophys. Res. Lett.* 41, 5620–5628. doi: 10.1002/2014GL061146

Eveson, J. P., Hobday, A. J., Hartog, J. R., Spillman, C. M. and Rough, K. M. (2015). Seasonal Forecasting of Tuna Habitat in the Great Australian Bight. *Fish. Res.* 170, 39–49. doi: 10.1016/j.fishres.2015.05.008

Eyring, V., Bony, S., Meehl, G. A., Senior, C. A., Stevens, B., Stouffer, R. J., et al. (2016). Overview of the Coupled Model Intercomparison Project Phase 6 (CMIP6) Experimental Design and Organization. *Geosci. Model. Dev.* 9, 1937–1958. doi: 10.5194/gmd-9-1937-2016

Gruber, N., Boyd, P. W., Frölicher, T. L. and Vogt, M. (2021). Biogeochemical Extremes and Compound Events in the Ocean. *Nature* 600, 395–407. doi: 10.1038/s41586-021-03981-7

Hare, S. R. and Mantua, N. J. (2000). Empirical Evidence for North Pacific Regime Shifts in 1977 and 1989. *Prog. Oceanogr.* 47, 103–145. doi: 10.1016/S0079-6611(00)00033-1

Hermanson, L., Smith, D., Seabrook, M., Bilbao, R., Doblas-Reyes, F., Tourigny, E., et al. (2022). WMO Global Annual to Decadal Climate Update: A Prediction for 2021–25. *Bull. Am. Meteorological. Soc.* 103 (4), E1117–E1129. doi: 10.1175/BAMS-D-20-0311.1

Hervieux, G., Alexander, M. A., Stock, C. A., Jacox, M. G., Pegion, K., Becker, E., et al. (2019). More Reliable Coastal SST Forecasts From the North American Multimodel Ensemble. *Clim. Dyn.* 53, 7153–7168. doi: 10.1007/s00382-017-3652-7

Hobday, A. J., Spillman, C. M., Eveson, J. P., Hartog, J. R., Zhang, X. and Brodie, S. (2018). A Framework for Combining Seasonal Forecasts and Climate Projections to Aid Risk Management for Fisheries and Aquaculture. *Front. Mar. Sci.* 5. doi: 10.3389/fmars.2018.00137

Hu, Z.-Z., Kumar, A., Jha, B., Zhu, J. and Huang, B. (2017). Persistence and Predictions of the Remarkable Warm Anomaly in the Northeastern Pacific Ocean During 2014–16. *J. Clim.* 30, 689–702. doi: 10.1175/JCLI-D-16-0348.1

Jacox, M. G., Alexander, M. A., Amaya, D., Becker, E., Bograd, S. J., Brodie, S., et al. (2022). Global Seasonal Forecasts of Marine Heatwaves. *Nature* 604, 486–490. doi: 10.1038/s41586-022-04573-9

Jacox, M. G., Alexander, M. A., Siedlecki, S., Chen, K., Kwon, Y.-O., Brodie, S., et al. (2020). Seasonal-To-Interannual Prediction of North American Coastal Marine Ecosystems: Forecast Methods, Mechanisms of Predictability, and Priority Developments. *Prog. Oceanogr.* 183, 102307. doi: 10.1016/j.pocean.2020.102307

Jacox, M. G., Tommasi, D., Alexander, M. A., Hervieux, G. and Stock, C. A. (2019). Predicting the Evolution of the 2014–2016 California Current System Marine Heatwave From an Ensemble of Coupled Global Climate Forecasts. *Front. Mar. Sci.* 6, 497. doi: 10.3389/fmars.2019.00497

Kaplan, I. C., Williams, G. D., Bond, N. A., Hermann, A. J. and Siedlecki, S. A. (2016). Cloudy With a Chance of Sardines: Forecasting Sardine Distributions Using Regional Climate Models. *Fish. Oceanogr.* 25, 15–27. doi: 10.1111/fog.12131

Kashinath, K., Mustafa, M., Albert, A., Wu, J.-L., Jiang, C., Esmaeilzadeh, S., et al. (2021). Physics-Informed Machine Learning: Case Studies for Weather and Climate Modelling. *Philos. Trans. A. Math. Phys. Eng. Sci.* 379, 20200093. doi: 10.1098/rsta.2020.0093

Kirtman, B. P., Min, D., Infanti, J. M., Kinter, J. L., Paolino, D. A., Zhang, Q., et al. (2014). The North American Multimodel Ensemble: Phase-1 Seasonal-to-Interannual Prediction; Phase-2 Toward Developing Intraseasonal Prediction. *Bull. Am. Meteorol. Soc* 95, 585–601. doi: 10.1175/BAMS-D-12-00050.1

Krumhardt, K. M., Lovenduski, N. S., Long, M. C., Luo, J. Y., Lindsay, K., Yeager, S., et al. (2020). Potential Predictability of Net Primary Production in the Ocean. *Global Biogeochem. Cycles.* 34, e2020GB006531. doi: 10.1029/2020GB006531

Litzow, M. A., Ciannelli, L., Puerta, P., Wettstein, J. J., Rykaczewski, R. R. and Opiekun, M. (2019). Nonstationary Environmental and Community Relationships in the North Pacific Ocean. *Ecology* 100 (8), e02760. doi: 10.1002/ecy.2760

Litzow, M. A. and Mueter, F. J. (2014). Assessing the Ecological Importance of Climate Regime Shifts: An Approach From the North Pacific Ocean. *Prog. Oceanogr.* 120, 110–119. doi: 10.1016/j.pocean.2013.08.003

Long, X., Widlansky, M. J., Spillman, C. M., Kumar, A., Balmaseda, M., Thompson, P. R., et al. (2021). Seasonal Forecasting Skill of Sea-Level Anomalies in a Multi-Model Prediction Framework. *J. Geophys. Res. Ocean.* 126, e2020JC017060. doi: 10.1029/2020JC017060

Lovenduski, N. S., Yeager, S. G., Lindsay, K. and Long, M. C. (2019). Predicting Near-Term Variability in Ocean Carbon Uptake. *J. Earth System. Dynamics.* 10, 45–57. doi: 10.5194/esd-10-45-2019

Ma, S., Liu, Y., Li, J., Fu, C., Ye, Z., Sun, P., et al. (2019). Climate-Induced Long-Term Variations in Ecosystem Structure and Atmosphere-Ocean-Ecosystem Processes in the Yellow Sea and East China Sea. *Prog. Oceanogr.* 175, 183–197. doi: 10.1016/j.pocean.2019.04.008

Mantua, N. J., Hare, S. R., Zhang, Y., Wallace, J. M. and Francis, C. (1997). A pacific interdecadal climate oscillation with impacts on salmon production. *Bull. Am. Meteorol. Soc* 78, 1069–1079. doi: 10.1175/1520-0477(1997)078<1069:apicow>2.0.co;2

Minobe, S. (2014). More Attractive Science Ecosystem Design for FUTURE and Beyond: A Personal View From a Researcher in a Peripheral Field. *PICES. Press. 22.* 2, 6–8. Retrieved from https://www.proquest.com/scholarly-journals/more-attractive-science-ecosystem-design-future/docview/1556456820/se-2?accountid=28258.

Myers, R. A. (1998). When do Environment–Recruitment Correlations Work? *Rev. Fish. Biol. Fish.* 8, 285–305. doi: 10.1023/A:1008828730759

Park, J.-Y., Stock, C. A., Dunne, J. P., Yang, X. and Rosati, A. (2019). Seasonal to Multiannual Marine Ecosystem Prediction With a Global Earth System Model. *Science* 365, 284–288. doi: 10.1126/science.aav6634

Payne, M. R., Hobday, A. J., MacKenzie, B. R., Tommasi, D., Dempsey, D. P., Fässler, S. M. M., et al. (2017). Lessons From the First Generation of Marine Ecological Forecast Products. *Front. Mar. Sci.* 4. doi: 10.3389/fmars.2017.00289

Pegion, K., Kirtman, B. P., Becker, E., Collins, D. C., LaJoie, E., Burgman, R., et al. (2019). The Subseasonal Experiment (SubX): A Multimodel Subseasonal Prediction Experiment. *Bull. Am. Meteorol. Soc* 100, 2043–2060. doi: 10.1175/BAMS-D-18-0270.1

Rousseaux, C. S. and Gregg, W. W. (2017). Forecasting Ocean Chlorophyll in the Equatorial Pacific. *Front. Mar. Sci.* 4, 236. doi: 10.3389/fmars.2017.00236

Séférian, R., Bopp, L., Gehlen, M., Swingedouw, D., Mignot, J., Guilyardi, E., et al. (2014). Multiyear Predictability of Tropical Marine Productivity. *Proc. Natl. Acad. Sci. U. S. A.* 111, 11646–11651. doi: 10.1073/pnas.1315855111

Shin, S.-I. and Newman, M. (2021). Seasonal Predictability of Global and North American Coastal Sea Surface Temperature and Height Anomalies. *Geophys. Res. Lett.* 48, e2020GL091886. doi: 10.1029/2020gl091886

Siedlecki, S. A., Kaplan, I. C., Hermann, A. J., Nguyen, T. T., Bond, N. A., Newton, J. A., et al. (2016). Experiments With Seasonal Forecasts of Ocean Conditions for the Northern Region of the California Current Upwelling System. *Sci. Rep.* 6, 27203. doi: 10.1038/srep27203

Smith, D. M., Scaife, A. A., Eade, R., Athanasiadis, P., Bellucci, A., Bethke, I., et al. (2020). North Atlantic Climate Far More Predictable Than Models Imply. *Nature* 583, 796–800. doi: 10.1038/s41586-020-2525-0

Spillman, C. M., Alves, O. and Hudson, D. A. (2013). Predicting Thermal Stress for Coral Bleaching in the Great Barrier Reef Using a Coupled Ocean-Atmosphere Seasonal Forecast Model. *Int. J. Climatol.* 33, 1001–1014. doi: 10.1002/joc.3486

Spillman, C. M. and Hobday, A. J. (2014). Dynamical Seasonal Ocean Forecasts to Aid Salmon Farm Management in a Climate Hotspot. *Clim. Risk Manage.* 1, 25–38. doi: 10.1016/j.crm.2013.12.001

Stengel, K., Glaws, A., Hettinger, D., and King, R. N. (2020). Adversarial super-resolution of climatological wind and solar data. *Proc. Natl. Acad. Sci.* U.S.A. 117, 16805–16815. doi: 10.1073/pnas.1918964117

Taylor, K. E., Stouffer, R. J. and Meehl, G. A. (2012). An Overview of CMIP5 and the Experiment Design. *Bull. Am. Meteorol. Soc* 93, 485–498. doi: 10.1175/BAMS-D-11-00094.1

Tian, Y., Kidokoro, H. and Watanabe, T. (2006). Long-Term Changes in the Fish Community Structure From the Tsushima Warm Current Region of the Japan/East Sea With an Emphasis on the Impacts of Fishing and Climate Regime Shift Over the Last Four Decades. *Prog. Oceanogr.* 68, 217–237. doi: 10.1016/j.pocean.2006.02.009

Tommasi, D., Stock, C. A., Hobday, A. J., Methot, R., Kaplan, I. C., Eveson, J. P., et al. (2017). Managing Living Marine Resources in a Dynamic Environment: The Role of Seasonal to Decadal Climate Forecasts. *Prog. Oceanogr.* 152, 15–49. doi: 10.1016/j.pocean.2016.12.011

Turi, G., Alexander, M. A., Lovenduski, N. S., Capotondi, A., Scott, J., Stock, C., et al. (2018). Response of O2 and pH to ENSO in the California Current System in a High-Resolution Global Climate Model. *Ocean. Sci.* 14, 69–86. doi: 10.5194/os-14-69-2018

Vitart, F., Ardilouze, C., Bonet, A., Brookshaw, A., Chen, M., Codorean, C., et al. (2017). The Subseasonal to Seasonal (S2S) Prediction Project Database. *Bull. Am. Meteorol. Soc* 98, 163–173. doi: 10.1175/BAMS-D-16-0017.1

Widlansky, M. J., Marra, J. J., Chowdhury, M. R., Stephens, S. A., Miles, E. R., Fauchereau, N., et al. (2017). Multimodel ensemble sea level forecasts for tropical Pacific sslands. *J. Appl. Meteor. Climatol.* 56, 849–862. doi: 10.1175/JAMC-D-16-0284.1

Yasuda, I., Sugisaki, H., Watanabe, Y., Minobe, S. S. and Oozeki, Y. (1999) Interdecadal variations in Japanese sardine and ocean/climate. *Fish. Oceanogr.* 8:18–24. doi: 10.1046/j.1365-2419.1999.00089.x

Yati, E. and Minobe, S. (2021). Sea Surface Temperature Predictability in the North Pacific From Multi-Model Seasonal Forecast. *J. Oceanogr.* 77, 897–906. doi: 10.1007/s10872-021-00618-1

Yati, E., Minobe, S., Mantua, N., Ito, S.-I. and Di Lorenzo, E. (2020). Marine Ecosystem Variations Over the North Pacific and Their Linkage to Large-Scale Climate Variability and Change. *Front. Mar. Sci.* 7. doi: 10.3389/fmars.2020.578165

Yeager, S. G., Danabasoglu, G., Rosenbloom, N. A., Strand, W., Bates, S. C., Meehl, G. A., et al. (2018). Predicting Near-Term Changes in the Earth System: A Large Ensemble of Initialized Decadal Prediction Simulations Using the Community Earth System Model. *Bull. Am. Meteorol. Soc* 99, 1867–1886. doi: 10.1175/BAMS-D-17-0098.1

Yeager, S. G., Rosenbloom, N., Glanville, A. A., Wu, X., Simpson, I., Li, H., et al. (2022). The Seasonal-to-Multiyear Large Ensemble (SMYLE) Prediction System Using the Community Earth System Model Version 2, . *Geosci. Model Dev. Discuss.* doi: 10.5194/gmd-2022-60

Conflict of Interest: The authors declare that the research was conducted in the absence of any commercial or financial relationships that could be construed as a

potential conflict of interest. The reviewer AH declared a past co-authorship with one of the authors MJ to the handling Editor.

Publisher's Note: All claims expressed in this article are solely those of the authors and do not necessarily represent those of their affiliated organizations, or those of the publisher, the editors and the reviewers. Any product that may be evaluated in this article, or claim that may be made by its manufacturer, is not guaranteed or endorsed by the publisher.

frontiers | Frontiers in Marine Science

TYPE Original Research
PUBLISHED 09 November 2022
DOI 10.3389/fmars.2022.969319

OPEN ACCESS

EDITED BY
Francois Bastardie,
Technical University of Denmark,
Denmark

REVIEWED BY
Albert J. Hermann,
University of Washington,
United States
Federico Graef,
Center for Scientific Research and
Higher Education in Ensenada
(CICESE), Mexico

*CORRESPONDENCE
Gian Giacomo Navarra
gnavarra3@gatech.edu

SPECIALTY SECTION
This article was submitted to
Marine Fisheries, Aquaculture and
Living Resources,
a section of the journal
Frontiers in Marine Science

RECEIVED 14 June 2022
ACCEPTED 19 October 2022
PUBLISHED 09 November 2022

CITATION
Navarra GG, Di Lorenzo E,
Rykaczewski RR and Capotondi A
(2022) Predictability and empirical
dynamics of fisheries time series in the
North Pacific.
Front. Mar. Sci. 9:969319.
doi: 10.3389/fmars.2022.969319

Predictability and empirical dynamics of fisheries time series in the North Pacific

Gian Giacomo Navarra[1]*, Emanuele Di Lorenzo[2], Ryan R. Rykaczewski[3] and Antonietta Capotondi[4,5]

[1]Program in Ocean Science & Engineering, Georgia Institute of Technology, Atlanta, GA, United States, [2]Department of Earth and Atmospheric Sciences, Brown University, Providence, RI, United States, [3]NOAA Pacific Islands Fisheries Science Center, Ecosystem Sciences Division, Honolulu, HI, United States, [4]NOAA Earth System Research Laboratory, Physical Sciences Division, Boulder, CO, United States, [5]Cooperative Institute for Research in Environmental Sciences, University of Colorado, Boulder, CO, United States

Previous studies have documented a strong relationship between marine ecosystems and large-scale modes of sea surface height (SSH) and sea surface temperature (SST) variability in the North Pacific such as the Pacific Decadal Oscillation and the North Pacific Gyre Oscillation. In the central and western North Pacific along the Kuroshio-Oyashio Extension (KOE), the expression of these modes in SSH and SST is linked to the propagation of long oceanic Rossby waves, which extend the predictability of the climate system to ~3 years. Using a multivariate physical-biological linear inverse model (LIM) we explore the extent to which this physical predictability leads to multi-year prediction of dominant fishery indicators inferred from three datasets (i.e., estimated biomasses, landings, and catches). We find that despite the strong autocorrelation in the fish indicators, the LIM adds dynamical forecast skill beyond persistence up to 5-6 years. By performing a sensitivity analysis of the LIM forecast model, we find that two main factors are essential for extending the dynamical predictability of the fishery indicators beyond persistence. The first is the interaction of the fishery indicators with the SST/SSH of the North and tropical Pacific. The second is the empirical relationship among the fisheries time series. This latter component reflects stock-stock interactions as well as common technological and human socioeconomic factors that may influence multiple fisheries and are captured in the training of the LIM. These results suggest that empirical dynamical models and machine learning algorithms, such as the LIM, provide an alternative and promising approach for forecasting key ecological indicators beyond the skill of persistence.

KEYWORDS

empirical dynamical model, fishery indicators, climate variability, climate change, forecast, biomass anomalies, landings, catches

1. Introduction

The Kuroshio-Oyashio system is composed of the western boundary currents (WBC) of the North Pacific's subtropical and subpolar gyres. In the transition region between the two gyres, quasi-stationary meanders form the Kuroshio-Oyashio Extension jet (KOE). The KOE is flanked to the south by an anticyclonic recirculation gyre which has been observed to increase the eastward transport of the jet [Mizuno et al. 1983; Qiu and Chen, 2005; Qiu et al., 2017]. Atmosphere-ocean interactions are particularly intensified in the WBC. Almost 70% of the latent and sensible heat transferred to the atmosphere from the ocean in the northern hemisphere is transferred in the region between 25°N and 45°N latitude [Kwon et al., 2010]. This heat transfer is crucial in controlling surface baroclinicity and increasing storm activity. As a result, the KOE jet is one of the regions with the greatest eddy kinetic energy in all the North Pacific. [Kelly et al., 2010]

The internal dynamics of the KOE play a critical role in explaining the decadal fluctuations of the Kuroshio-Oyashio system [Mitsudera et al., 2001; Qiu, 2003]. However, it is now well established that the interactions with external modes of variability are important in triggering the quasi-stationary meanders in the KOE jet. Recent study confirms that the surface Chl-a concentration, nutrient concentration, and catches of fish stocks are associated with two dominant modes of variability of the North Pacific [Yati Emi et al., 2020] which are the Pacific Decadal Oscillation (PDO) [Mantua et al., 1997] and the North Pacific Gyre Oscillation (NPGO) [Di Lorenzo et al., 2008; Yatsu et al., 2013; Lin et al., 2014]. One way in which the PDO-related dynamics influences the marine ecosystems is through the control of seasonal mixed layer processes. For the northwestern Pacific, a positive phase of the PDO is associated with a negative anomaly in the SST with an associated increase in the mixed layer depth, leading to a weakening of the KOE [Yatsu, et al., 2013]. The opposite happens in a negative phase. These climate regime shifts are well correlated with fluctuations in biological characteristics [Yati et al., 2020; Möllmann and Diekmann, 2012]. The weakening of the KOE is hypothesized to increase the catches of Japanese sardine in the northwestern Pacific, while during a strengthening of the jet, catches of Japanese anchovies are relatively high [Chavez et al., 2003].

While the patterns of climate variability are well established [Liu and Di Lorenzo, 2018], the mechanism by which the marine ecosystems are influenced by climate fluctuations remains unclear [see review in Bograd et al., 2019]. As climate processes induce fluctuations in marine ecosystems, human societies are often negatively impacted, as food security and coastal economies are dependent on the stability of marine resources [Yunne-Jai et al., 2010; Shin et al., 2010]. This means that improved predictions of future changes in the fisheries of the Kuroshio-Oyashio system can have important socioeconomic impacts.

Forecasting marine ecosystems presents a series of challenges because the interactions of the ecosystem with human society often have been nonlinear and occur over a range of spatial and temporal scales. Also, the lack of long and accurate time series challenges our ability to study climate and fisheries interactions and develop forecasts that are accurate at long lead times. To address these challenges, past studies have focused on identifying the observational needs for ecosystem forecasting [Capotondi et al., 2019] and on exploring the use of dynamical model approaches to account for non-linearities present in marine ecosystems dynamics [Jacox et al., 2019; Tommasi et al., 2017]. Yet, numerical dynamical models still have biases, including erroneous representations of the WBCs and their separation latitude, limiting their usefulness for capturing many complex, fine-scale processes. Given that we still do not have adequate dynamical models that capture the dynamics of climate, fish, and human interactions, previous studies [Koul et al., 2021] have investigated the use of simple statistical models (linear regression and multiple linear regression) for fishery forecasting. These studies have offered successful predictions of cod stocks in the Barents Sea on decadal time scales.

In this article we have considered an alternative approach to predict of time series of fisheries indices by using an empirical dynamical model (EDM) method or linear inverse modeling (LIM). These approaches have proved very useful for understanding the variability of North Pacific physical ecosystems drivers, including extremes [Capotondi et al., 2022], and have exhibited promising results when applied to North and tropical Pacific SST forecasts [Newman, 2007]. Here, we apply the LIM approach to explore the predictability of a set of fisheries time series describing the temporal changes of specific stocks. These time series can be viewed as proxies that simplify complicated biological and socioeconomic conditions over time [Blanchard et al., 2010; Tam et al., 2019]. The three fisheries databases considered in this study are (1) stock biomass anomalies from scientific stock assessments performed for a limited number of stocks in different regions (RAM database, [Ricard et al., 2012]), (2) landings of stocks as reported by the country targeting the species (LME database, [Pauly et al., 2020]), and (3) the catches of species that are estimated from data reported to the United Nations (FAO database [Pauly et al., 1998]).

These data sources are useful in the context of EDMs because they provide a large number of time series that capture physical, ecological and human factors inherent to commercial fisheries statistics. Also, EDMs like the LIM have the added advantage of being able to capture some of the human-forced dynamics that are implicitly reflected in the fish indicators and yet are not explicitly known.

The purpose of the paper is to analyze the ability of the EDM to forecast fisheries time series. While the use of complex dynamical models could be another possible approach [Park

et al., 2019], the inclusion of fisheries information in dynamical models is not straightforward. In addition, dynamical models often suffer from biases in the representation of physical climate features, such as the Western Boundary Currents, and are much more computationally intensive. The EDM approach explored here, if skillful, may provide a useful alternative for forecasting fisheries indices. Here, we consider the forecasting skill related to the fisheries metrics and partition the fisheries predictability between the component associated with climatic variables, i.e., sea surface temperature (SST) and sea surface height (SSH) and that related to stock-stock interactions or socioeconomic factors.

2. Methods

2.1 Reanalysis data

The physical data that we included in the LIM were extracted from the ECMWF Ocean Reanalysis System 4 (ORAS4) on a 1°C by 1°C latitude–longitude spatial resolution between 1958-2016, for a spatial region of 15°S-62°N, 100°E-290°E, which includes the tropical and North Pacific. It is important to include in the LIM all North and tropical pacific basin for the physical state. This allows us to capture the dynamics of the large-scale climate modes such as PDO and NPGO and their tropical forcing linked to the different flavors of the El Niño Southern Oscillation [Di Lorenzo and Ohman, 2013].

As is often done with the LIM [Newman, 2007; Zhao et al., 2021], the SSH and SST data were first coarsened by averaging them into a box of 2 degrees of latitude and 5 degrees of longitude. As a next step, the data were smoothed to remove sub seasonal variations with a 3 months running mean. The SSH and SST anomalies were computed by removing the mean monthly climatology. Further description and access to the data can be found at https://icdc.cen.uni-hamburg.de/daten/reanalysis-ocean/easy-init-ocean/ecmwf-ocean-reanalysis-system-4-oras4.html

2.2 Fisheries databases

The first database considered for the fisheries was the RAM Legacy Stock Assessment Database (RAM), https://www.ramlegacy.org, [Ricard et al., 2012]. Globally, this database contains 331 stock assessments divided into 295 marine fish stocks and 36 invertebrate stocks. The species considered from the RAM database are displayed in Supplementary Table 1 and included 20 species from the northwest Pacific region of interest (Figure 1A). For some species, the associated time series have a time duration of 63 years from (1950-2012). However, most of the fish indicators are only available after 1979. For this reason we selected data after 1979 with less than 5 years of data gaps for developing the LIM.

The second database considered was the commercial catches from a database aggregated by Large Marine Ecosystem (LME), https://www.lmehub.net/, [Cornillon, Peter. (2007)] (Figure 1B). An LME is defined as an area of 200,000 km^2 or greater whose extent is determined by similarities in relevant variables such as bathymetry, productivity, or trophic relationships [Sherman, 2014]. The database contains 10,438 stocks in all regions of the world with 55 years of data, from 1950 to 2004. Three LMEs were considered in this study (the Kuroshio, the Oyashio Current and the Sea of Japan LMEs), and those included catches for 225 stocks that have data gaps for less than 5 years. The catches were defined as the weight of fish caught in the open sea independently of the way they have been taken (i.e., gear type or as target or non-target catch). We have considered catches data from 1959 to the most recent data. Here, catches in FAO region 61 (Figure 1J) were analyzed (a region of the Northwest Pacific from about 20°CN to 65°CN and from the coast of Vietnam east to the Bering Strait). The discarded fish have not been filtered out in the two databases; the stocks of the LME database are referred as "catches" as the database contains more catches in weight than the FAO database.

The last database considered included the landings obtained from the Food and Aquaculture Organization (FAO) of the United Nations (https://www.fao.org/fishery/en/statistics) [Pauly et al., 1998] (Figure 1C). Landings for each region offer insight into variability in commercial fishing operations and the fish populations that support them. WE have used 171 landings data with data gaps less than 5 years. As for the LME database we have started the data from 1959.

The stocks considered for the landings and the catches are displayed in Tables 1, 2 and 3 of Supplemental Materials.

2.3 Detrending and standardization

Before proceeding in developing the LIM, we detrended the fisheries and physical time series so to increase their stationarity (i.e., no linear trends are present in any record).

Specifically, the time series extracted from the fisheries databases were standardized by dividing by the standard deviation for each individual stock ID and detrended by removing the best linear trend fit. Consequently, the time series are represented in STD units, and the total number of fish species is described by the StockID (Figures 1A - C). The fish information relative to the fish stocks are provided in Table 1, 2, and 3 of the Supplemental Materials. To examine the percentage of variance excluded by the detrending, we calculated the

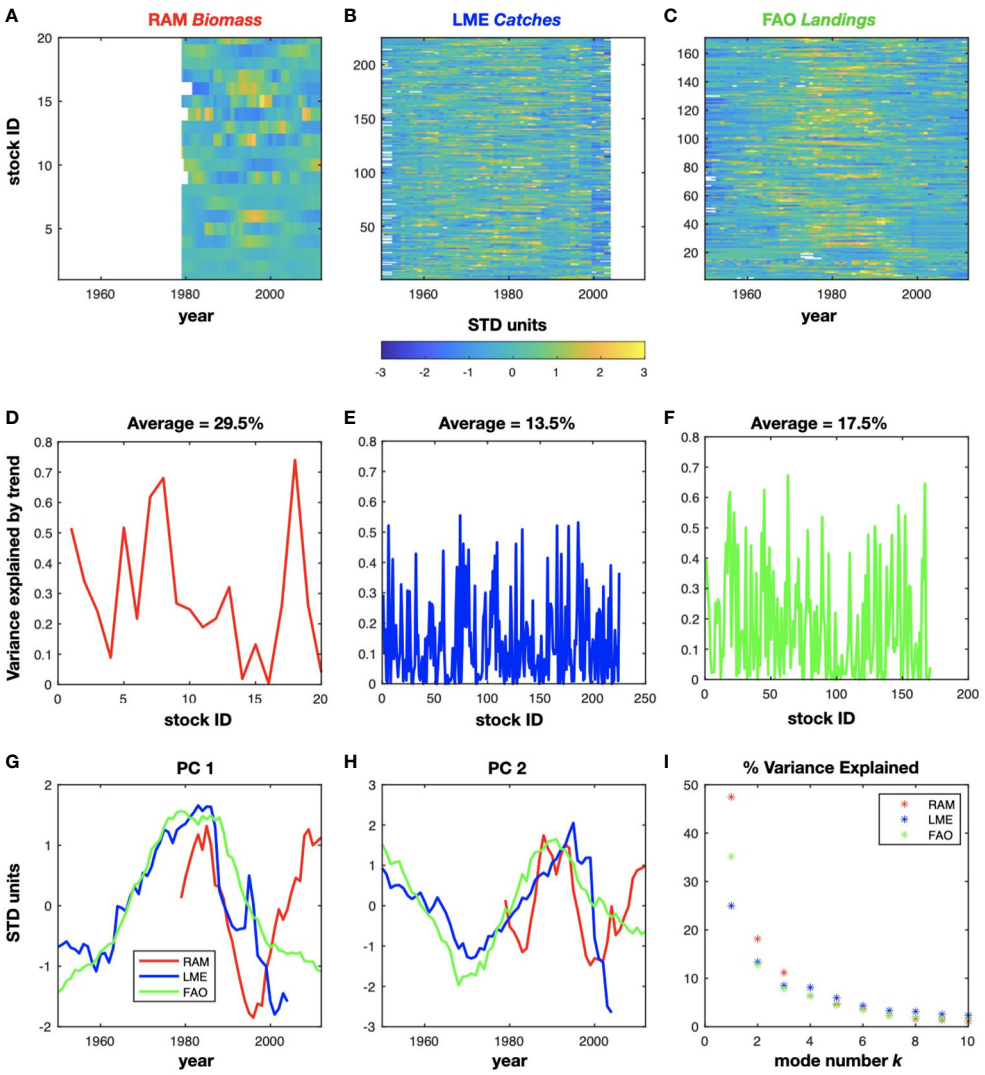

FIGURE 1
Timeseries of detrended and normalized fish stocks for the RAM **(A)**, LME **(B)**, and FAO **(C)** datasets. The variance explained by the removed trend is represented in **(D, E)**, and **(F)**. The mean variance excluded by the detrending has been inserted in the plots. The associated variability is described by the first and second principal component **(G)** and **(H)**, while the corresponding EOFs are displayed in Supplementary Figure S1. The percentage of variance explained by the PCs in each dataset is shown in **(I)**.

difference in variance between the total original data and the detrended time series. The mean variance explained by the trend is 29.5% for the RAM biomass (Figure 1D). In particular, the *Red seabream Inland sea of Japan* (stockID *18*) displays the highest variance associated with the trend. For the LME catches and the FAO landings, the variance excluded by removing the trend is 13.5% and 17.5% respectively, as displayed in Figures 1E, F. The associated sign of the removed trend displays a mixture of positive and negative trends in the stock time series of all the three databases (see supplemental Figure S1).

2.4 Principal components and empirical orthogonal functions

To reduce the dimensionality of the detrended and standardized fish indicators, we have used a classic principal components (PCs) analysis. To extract the PCs we first compute the covariance matrix of each fish dataset $\mathbf{F}_i(s,t)$, where s denotes the stock id, t its time values, and $\mathbf{i}$ the dataset label:

$$C(s,s) = \mathrm{F}_i(s,t)\mathrm{F}_i(t,s)^T$$

By performing an eigenvalue decomposition of C(*s*,*s*),

$$\mathrm{E}_i(s,k)\Lambda(k,k)\mathrm{E}_i(k,s)^T = \mathrm{C}_i(s,s)$$

we derive the eigenvector $\mathbf{E}_i(s,k)$ for the eigenmodes k=1…K where K=7 or RAM, and K=8 for LME and FAO that are associated with the K largest eigenvalues $\lambda(k)$ from the diagonal of the eigenvalue matrix $\Lambda(k,k)$. The choice of K modes retained in each dataset is explained in section 2.5. Physically, these eigenvectors, referred to as the Empirical Orthogonal Functions (EOFs), are the dominant patterns of variance across the stocks and provide an orthogonal basis onto which we can decompose the original fish datasets as:

$$\mathrm{P}_i(k,t) = \mathrm{E}_i(k,s)^T\mathrm{F}_i(s,t)$$

where $\mathbf{P}_i(k,t)$ are the PCs for each dataset **i**. Using this approach we reduce the dimensionality of the fish dataset from *s* (*order* ~100)→*k*(*order* ~10) Prior to the computation of the covariance, years with missing data in any given stock were set to zero to void any contribution to the covariance. Given that for any given year there were only few missing data across all the stocks, the impact of setting to zero the missing values has negligible impact the estimation of the EOFs.

The first two dominant PCs for each of the fish dataset are reported in Figures 1G, H and are discussed further in the results section 3.1. The EOFs structures for the first two modes are reported in supplemental material Figure S1.

By normalizing the eigenvalue om the EOFs decomposition, we measure the fraction of variance explained by each pair of PC/EOF mode k as $\lambda(k)/\sum_{1}^{K}\lambda(k)$. The spectrum of explained variance is reported in Figure 1I.

2.5 Linear inverse model and forecast

Inverse modeling can be defined as the extraction of dynamical properties of a physical-biological system from its observed statistics. The LIM model suggests that on interannual time scales, our system may be viewed as a linear system driven by Gaussian white noise. The idea is that the climate timescales underpinning the dynamics of our system are longer than the noise. An example of noise are the fast air sea interactions. In this framework the N component state vector of anomalies X volves accordingly to the linear equation,

$$\frac{dX(\mathrm{t})}{dt} = LX(\mathrm{t}) + \xi(\mathrm{t}) \tag{1}$$

In this equation **L** represents a matrix that describes the feedback among different components of **X** while ξ is the stochastic forcing term.

For the purpose of this study, the components of the state vector **X** and of the operator **L** in equation (1) are:

$$\frac{dX(t)}{dt} = \begin{bmatrix} X(t)_{fishery} \\ X(t)_{SST} \\ X(t)_{SSH} \end{bmatrix} = \begin{bmatrix} L_{fishery-fishery} & L_{SST-SSH} & L_{SST-fishery} \\ L_{SSH-SST} & L_{SST-SST} & L_{SSH-fishery} \\ L_{fishery-SST} & L_{SST-SST} & L_{SSH-SSH} \end{bmatrix} \begin{bmatrix} X(t)_{fishery} \\ X(t)_{SST} \\ X(t)_{SSH} \end{bmatrix} + \begin{bmatrix} \xi(t)_{fishery} \\ \xi(t)_{SST} \\ \xi(t)_{SSH} \end{bmatrix} \tag{2}$$

In this framework, the state vector **X** is made of three substate vectors representing the fishery, SST, and SSH dataset. Each of these substate vectors is constructed using the PCs to reduce the dimensionality of the problem. For example,

$$X(t)_{SST} = [\,SST\_PC_1(t),\ SST\_PC_2(t),\ \ldots..,\ SST\_PC_K(t)\ ]$$

where K is number of dominant PC retained for each dataset.

In equation (2), the operator **L** as in the main diagonal the interaction terms of each variable with itself (LSST-SST,Lfisheyr-fishery,LSSH-SSH), while the terms outside the main diagonal are the interaction terms of each variable with the other ones (LSST-SSH,LSST-fishery, LSSH-fishery,LSSH-SST,Lfishery-SST, Lfishery-SSH).

As discussed by Penland et al. [1989], the statistics of a system modeled by the LIM must be Gaussian [Penland et al., 1995]. The operator **L** can therefore be determined from the state vector **X** by discretizing the equation (1).

$$L = \frac{1}{\tau}\ln\left(\langle X(t+\tau)X(t)\rangle\langle X(t)X(t)\rangle\right) \tag{3}$$

After obtaining **L** we can forecast of the state vector for a specific lead time τ using:

$$\hat{X}(t+\tau) = \exp(L\cdot\tau)X(t) \tag{4}$$

An important assumption in the use of the LIM, and the forecast equation (4), is that the statistics of the system are stationary over the period considered. For this reason, the operator **L** must be dissipative, which means its eigenvalues must have negative real parts [Newman et al., 2013]. Similarly, we expect that the statistics of stochastic forcing $Q=\langle\xi\xi^T\rangle$ [Penland et al., 1995], which are determined from the fluctuations-dissipation relationship,

$$Q = -LC(0) + C(0)L^T \tag{5}$$

has positive eigenvalues. In supplemental Figure S2 we have displayed the eigenvalue spectrum for the operator **L** and the matrix **Q** We obtain negative eigenvalues for **L** and positive for **Q** indicating that our statistics are stationary.

2.5.1 LIM forecast configuration

Number of PCs used in the state vector. To implement the LIM forecast model, the number of PCs retained in the physical and biological state vectors were chosen differently. For the physical components of the analysis, we retain 20 PCs for the SST and 17 for the SSH which capture 77% and 76% of the variance, respectively. These numbers were selected following the configuration of a previous Pacific LIM that uses the same data sources and domain area [see Zhao et al., 2021]. Equation 2 is used independently for each of the fish datasets. To establish how many PCs to retain for each dataset (e.g. RAM, LME, and FAO), we performed a series of cross-validated forecasts (explained in the next section 2.6) using equation (4) to identity the number of biological PCs to retain in the LIM that would lead to the highest forecast skill for the reconstructed fish indicators. Based on this cross-validation, we retained 8 PCs for the RAM biomass, corresponding to 94% of the variance of that quantity, 7 PCs for the LME catches, which describes 74% of the catches total variance, and 7 PCs for the FAO landings, which still correspond to 70% of the variance. Also, for the fishery state vectors, we interpolate the data to the same monthly scale of SST and SSH to allow inclusion of physical information at seasonal time scales.

Temporal span of forecast. The dataset used in this study have different spatial coverage. The physical data is only available starting 1959. Thus, we begin our training of the LIM and examination of the forecast skill over the following period: 1959-2016 for SSTa, 1979-2012 for RAM, 1959-2004 for LME, and 1959-2014 for FAO.

2.6 Cross-validation

To ensure that the LIM is tested on independent data, the estimates of **L** and of forecasting skills were cross validated by subsampling the data record. We have removed in total 10% of the data, for both the fishery and the physical part, and computed the operator **L** for the remaining data. The independent years removed are then forecasted using the computed **L**. This procedure is repeated for the entire period. The associated forecasting skills are computed by the correlation $r(\tau)$ between the observational data and the forecast for the different lead times τ For example, to evaluate $r(\tau)$ for the each of the fish datasets, the PCs of the forecasted substate vector $\hat{X}(\tau)_{fishery}$ obtained from (eq. 4) [Newman et al., 2003] are projected into the truncated EOF space,

$$\hat{\mathrm{F}}_i(s,\tau) = \mathrm{E}_i(s,k)^T \hat{\mathrm{P}}_i(k,\tau)$$

to obtain the forecasted fishery time series that are then correlated with the original data $F_i(s,\tau)$ We apply this procedure to the LIM that (1) contains only the physical state variables SST and SSH, and (2) contains the physical variables plus the fishery's principal components.

2.7 LIM τ est

To test the validity of linear approximation of the LIM, we perform the so called a τ test, which is designed to test the ability of the LIM to reproduce the lag covariance statistics using a lag which goes far beyond the training τ=3 *months* . Practically, the test consists of comparing the covariance matrix obtained from the original state vector to the covariance matrix calculated using the LIM for different lags τ=3 .. 12 .. 36 *months* . The LIM is re-computed each time using the different training τ Given that the LIM must be independent of the chosen lag, these two covariance matrices should give a compatible result for the LIM to perform well [Newman et al., 2011; Newman and Sardeshmukh, 2017]. A comparison of the diagonal elements of the observed lag covariances with the one obtained from the LIM is show in the supplemental material for the SST (Figure S3), and each of the fishery datasets (Figures S4–S6). Overall, LIM is able to capture the main structures of the lag autocovariance pattern for both the SST (Figure1 of Supplemental Materials) and the fishery indicator (Figure 2-4 of Supplemental Material) for lags up to τ=*72 months* in the fish dataset.Results from this test indicate that the LIM approximation is valid for long-lead forecasts of this set of physical and fishery indicators.

2.8 Persistence and forecast skill

When evaluating the skill of a forecast it is customary to ask the question of whether the forecast model adds skill beyond the so-called persistence forecast. This is equivalent to forecasting that each future conditions is the same as the condition today. From a mathematical point of view the persistence correlation forecast skill at different lead time τ for a timeseries y*(t).* given by the auto-correlation function

$$ACF(\tau) = \frac{y(0)y(\tau)}{y(0)y(0)}$$

where *y(0)y(0)* is the covariance at zero lag and y(0)y(τ) is the covariance at lag τ.

In climate science, for a forecast model to have higher skill that persistence is a fundamental measure to indicate that the model is able to extend the predictability through its dynamics beyond the natural temporal auto-correlation that exists in the data. A recent discussion of the concept of persistence can also be found in Jacox et al. [2020]. In the article, we compare the LIM forecast skill to persistence as a way to estimate the LIM's ability to capture the dynamics of the system and to use those dynamics to extend the predictability of the fish indicators. Specifically, we use the following definitions for the correlation skill,

$$r_{Persistence}(\tau) = ACF(\tau)$$

$$r_{Forecast}(\tau) = \text{correlation}(\ \hat{y}(\tau),\ y(\tau))$$

where $\hat{y}(\tau)$ is the LIM forecasted state at lead τ and $\hat{y}(\tau)$ is the observed state. As reported in section 2.6, all the forecasted states use a LIM that is trained with a dataset that does not include the observed state, which we also refer to this as the cross-validated forecast skill.

To estimate the statistical significance of the correlation skill we have used a Montecarlo approach. Specifically, we first develop an auto-regressive model of order 1 (AR1) as a null-hypothesis simulation model (i.e., red noise) for a given pair of timeseries that are being compared in the correlation. Next, for each of the timeseries we estimate the lag-1 auto-correlation coefficient and use that to generate 2000 pairs of red noise timeseries using the AR1 model. We compute the probability distribution function (PDF) of correlation coefficients between the red noise timeseries pairs. This PDF is then used to estimate the 95% and 99% confident levels of the correlation between the two original timeseries.

3 Results and discussion

3.1 Fisheries biomass data and relation to physical quantities

Given that the data has been decomposed in EOFs and PCs we first perform an inspection of their statistics. The temporal evolution of the first two dominant modes for the fish datasets are captured by the PC1 and PC2 (Figures 1G, H). Both the PCs1 and PCs2 displays very strong low-frequency variability in each dataset with a significant level of coherency across the datasets. As further discussed in the next sections, these low-frequency variations may be associated not only with decadal climate variability, but also with human influences. For example, these stocks have been heavily exploited in the last 60 years [Pons et al., 2017]. In particular, the increase in fishing pressure coupled with the demography of the fish stocks has led to a collapse and recovery of populations with common trends among stocks as discussed by previous authors [Myers and Worm, 2003; Nye et al., 2009; Wang et al., 2020]. The amount of variance explained by the first two PCs for each fisheries databases (see Methods section 2.4) is very large (Figure 1I). For example, PC1 for the RAM biomass represents 47% of the total variance, while the PC1 of the LME catches and the FAO landings describe respectively 25% and 35% of the variance. This indicates that despite the large number of fish stock indicators, the overall degrees of freedom in the datasets are low and represented by a relatively low number of modes (e.g. pairs of PCs/EOFs).

To quantify the extent to which the low-frequency fluctuations of the fish indicators are tracking climate variability, we perform a correlation analysis between the PCs of the fisheries data and large scale SSTa. Correlations between SST anomalies and the PCs1 for the three fish datasets are reported in Figure 2A. While the patterns show some differences it is evident, especially for the LME and FAO, that stronger correlation existing the region of the KOE. This is more evident by computing a map of the mean correlations across the datasets (Figure 2B), which shows a strong negative correlation from the East China Sea and coastal Japan extending in the central North Pacific. A similar correlation analysis for the PCs2 (Figure 2C) reveals the emergence of the more familiar basin-scale pattern of Pacific decadal variability such as the PDO across all the datasets. Again, this PDO-like pattern becomes clearer in the map of the mean correlations for PCs 2 (Figure 2D) exhibiting strong correlations in the canonical center of actions of the PDO over the central and eastern North Pacific. The correlation patterns of the PCs with the SSTa (Figure 2) gives us confidence that the link between the climate variability and the fish can be exploited for forecasting, especially in the KOE region, where previous studies have shown longer-lead multi-year predictability (see next section 3.2).

3.2 LIM forecasts of the low-frequency variability of the KOE

It is well known that the KOE variability is strongly linked to wind induced Rossby waves formed in the Central North Pacific [Deser et al., 1999; Schneider and Miller, 2001; Seager et al., 2001]. The effect of the wave propagation can be separated into two dynamical modes of variability. The first mode is related to a latitudinal shift of the KOE jet, while the second is associated with a strengthening or weakening of the KOE quasi-stationary meanders [Taguchi et al., 2007; Taguchi et al., 2014; Ceballos et al., 2009]. These dynamical changes in the KOE jet can impact the local marine populations with changes in the wintertime mixing and springtime stratification that control seasonal nutrients and light supply for primary producers [Chiba et al., 2013; Nakata et al., 2003]. Given that it takes approximately 2-3 years for the Rossby waves to propagate in the KOE region, these large-scale dynamics carry an inherent multi-year predictability that can be exploited for longer lead low-frequency forecasts on physics and marine ecosystems.

Thus, before exploring the predictability of the fisheries time series, it is informative to quantify the low-frequency predictability of the KOE physical environment, specifically the SST, which is a state variable with strong links to the dynamics of fish populations.

For this purpose, we build a LIM using only SSTa and SSHa data (see Methods section 2.5) and use equation (4) to perform a series of cross-validated forecasts for lead times of 6, 12, and 24

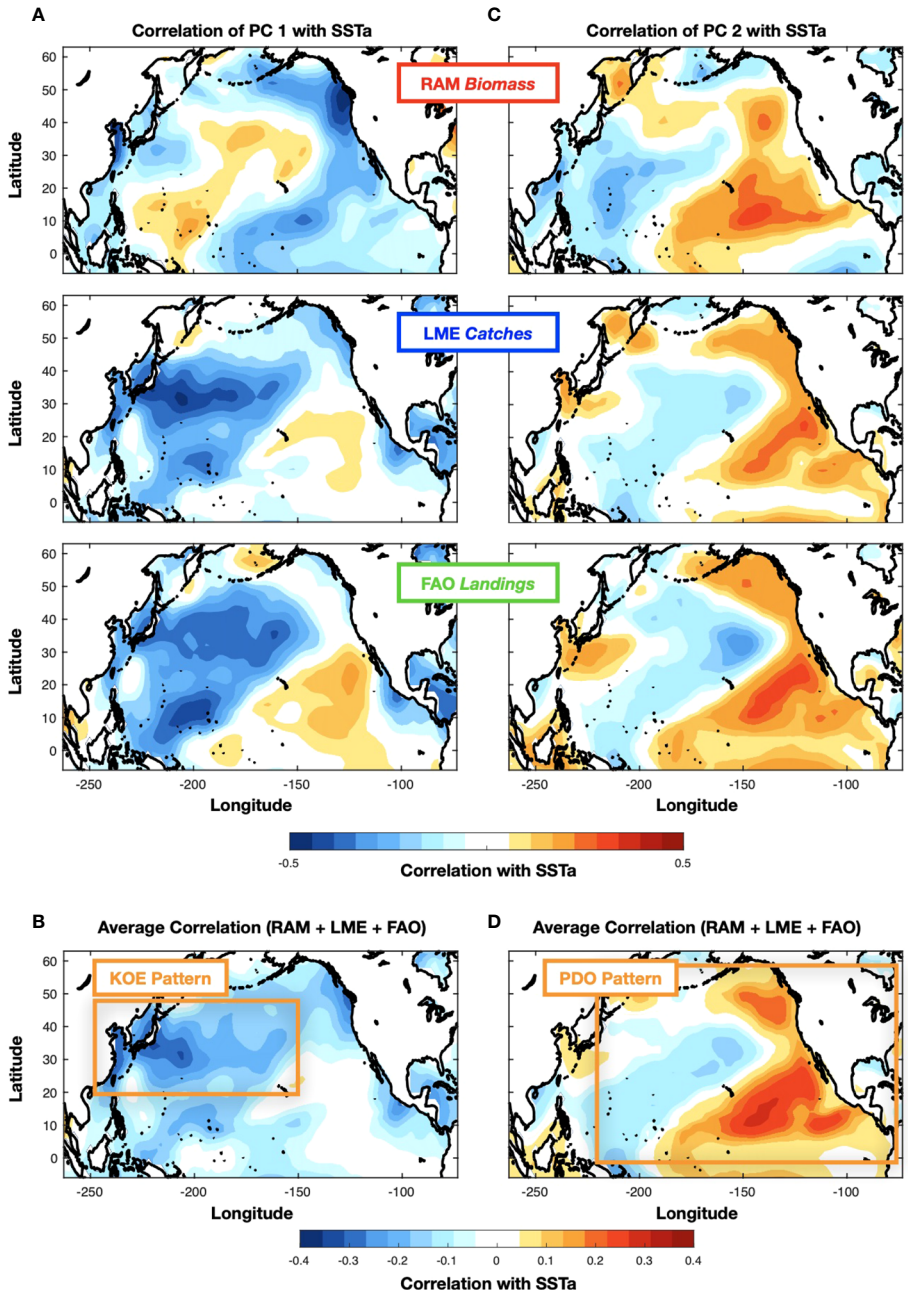

FIGURE 2
Correlation map between SST anomalies and PC1 **(A)** and PC2 **(C)** of the fishery datasets (RAM, LME, FAO). The average correlation maps across the datasets for PC1 and PC2 are shown in **(B)** and **(D)**.

months (Figures 3A, B, C). We find that areas of higher skill are concentrated along the Northeast Pacific coast and the KOE extension and are co-located with centers of actions of the PDO and the KOE low-frequency variability patterns [Matsumura et al., 2016]. We also examine the forecast skill in the KOE region (the average SSTa in the black box of Figure 3A) as a function of the month used to initialize the forecast (Figure 4A). We find that significant forecast skill (correlation >0.6) extends only up to 1.5 year. If we compare this skill level with that obtain from persistence (Figure 4B), we find that the LIM extends this skill beyond persistence up to 10 months (Figure 4C).

Given that the fisheries are predominantly characterized by low-frequency variability, we now quantify the low-frequency predictability of the SSTa in the KOE by applying a 6-year filter

10.3389/fmars.2022.969319

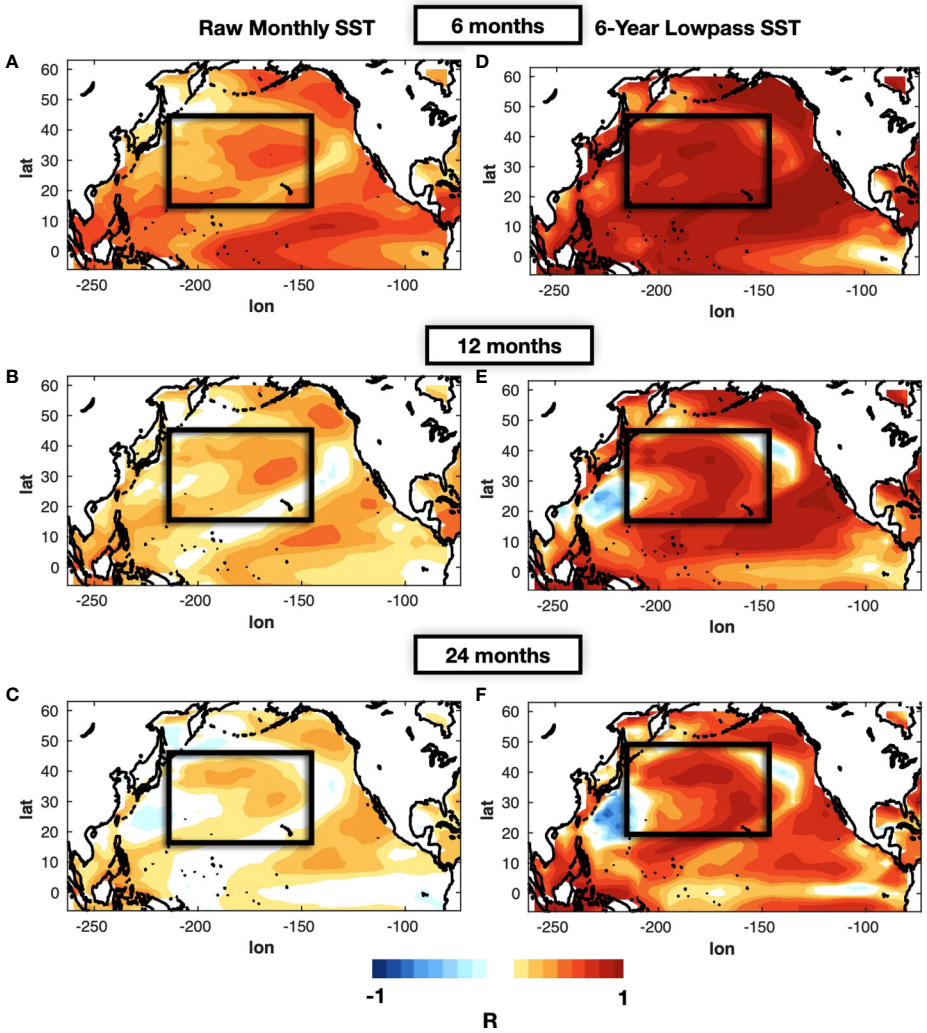

FIGURE 3
Forecast correlation skill of the LIM with physics only (SSTa, SSHa) for lead-times of 6 months **(A)**, 12 months **(B)**, and 24 months **(C)**. In **(D)**, **(E)**, and **(F)** the same correlation skill maps are shown but computed using the 6-year low-pass filter applied on the original and forecasted monthly data.

to the forecasted state vector. As expected when applying a lowpass filter, we find an overall increase in skill spatially at 6, 12, and 24 months (Figures 3D, E, C). If we examine the skill as a function of initialization month (Figure 4D), we find that high skill levels (R>0.6) extends up to lead times of 4-5 years. However, the filtering also leads to longer persistence skill due to the increase in autocorrelation, up to 1.5 years (Figure 4E). Nevertheless, if we look at the difference in skill between the LIM forecast and persistence (Figure 4F), we find that the filtering does extend dynamically the low-frequency predictability by 4-5 years. As emphasized by previous articles [Thompson et al., 2010], the increased skill shows the importance of the low frequency variability of SST anomalies in the KOE jet. These results confirm previous findings that in the KOE, the large-scale climate associated with the propagation of Rossby waves and the modes of decadal variability lead to extended multi-year predictability.

3.3 LIM forecast of fisheries time series

We now analyze if the long-lead, low-frequency predictability of the KOE physical state is important in extending the forecast of fisheries metrics. We construct three independent forecast LIMs for each of the fish datasets (i.e., RAM, LME, FAO) using the definition of the state vector in equation (2) (see Methods section 2.5). The results from the cross-validated forecast are shown in Figures 5A, B, C for leads up to 160 months. Results show high correlation skill values R ~

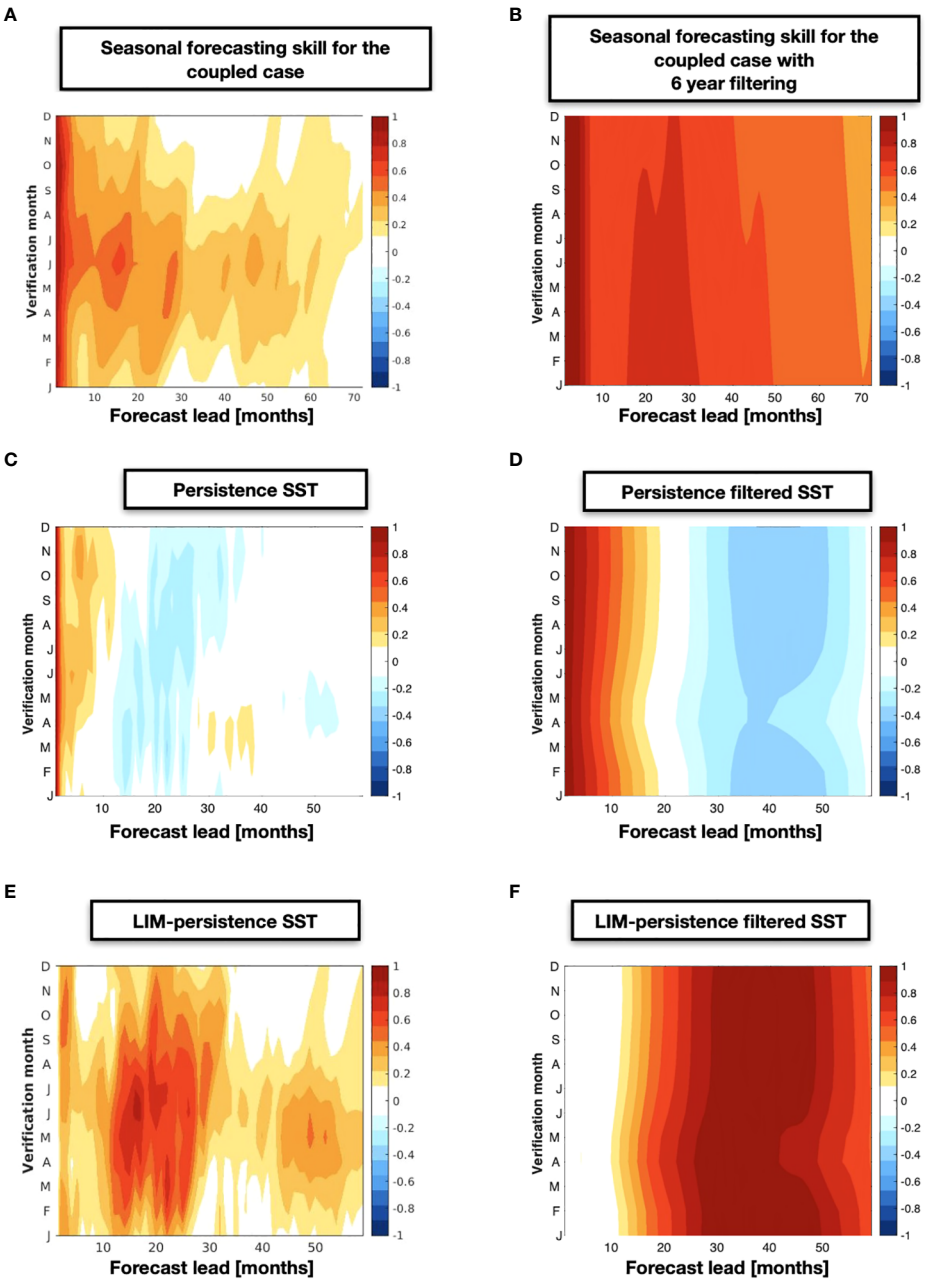

FIGURE 4
KOE SSTa index forecast correlation skill as a function of the initialization month of the year from the physics only LIM **(A)**, the persistence **(B)**, and their difference **(C)**. The same correlation skill maps are shown but computed after applying a 6-year low-pass filter applied on the original and forecasted monthly data **(D, E)**, and **(F)**.

0.7 extending almost to the end of the forecast window. Given that stocks are characterized by timeseries with exceptional low-frequency variability, it is critically important to assess If the correlation skill of the LIM is significant. Using the Montecarlo approach discussed in Method section 2.8, we identify the 95% and 99% significance levels for each of the datasets. These are marked in the colorbar of Figure 5 and show that any correlation above R=0.55 (RAM), R=0.41 ((LME), and R=0.44 (FAO) is significant at the 95%. Correlations above R=0.66 (RAM), R=0.51 (LME), and R=0.54 (FAO) are significant at the 99% with the RAM being higher than the other datasets because of its shorten temporal span, which reduced the degrees of freedom.

We further examine the impact of autocorrelation in the data on the forecast still by computing the persistent forecasts (Figures 5D,

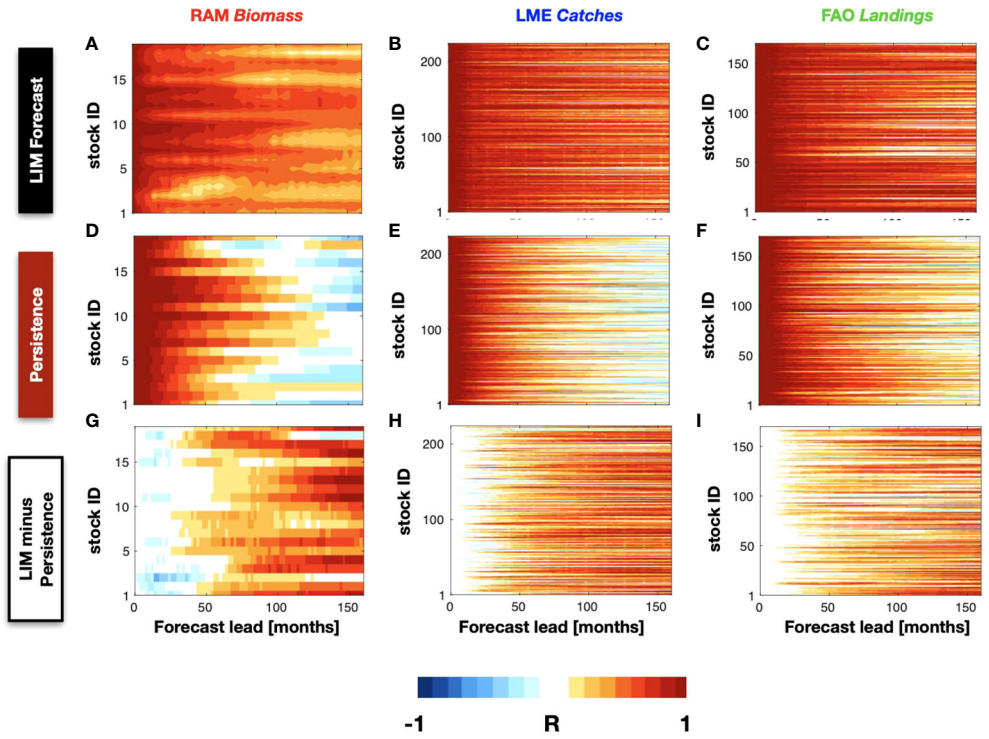

FIGURE 5
The LIM forecasting correlation skill as a function of different lead-times is displayed from the RAM **(A)**, LME **(B)**, and FAO **(C)** stocks. The persistence correlation skill for each of these stock is also shown for comparison in **(D, E)**, and **(F)**. A different between the skill of the LIM minus persistence is shown in **(G**, **H)**, and **(I)**.

E, F). We find significant persistence skill R~0.7 up to 4 years for some of the RAM biomass anomalies (Figure 5D) and up to 3 years for the LME (Figure 5E) catches and FAO landings (Figure 5F). Despite the long-lead forecast skill from persistence, the difference maps between the LIM forecast and persistence skill (Figures 5G, H, I) show that the LIM has higher and extended significant forecast skill beyond the range of persistence by 3-5 year limit.

Despite the statistical measures of skill significance discussed above, it is important to recognize that ultimately the real usefulness of these forecast will depend on how, and what aspects of, this information enables better informed decisions by fishery managers. For this purpose, it is informative to show the timeseries of the LIM forecasts for a few selected species. In each database we picked two species that show extended predictability and displayed their 2- and 5-years composite forecast timeseries (Figure 6, red lines are the cross-validated forecasts, blue line the original data). Focusing on the RAM, Figures 6A, B displays the stock *Striped Marlin North Pacific* and *Yellow sea bream Sea of Japan* from the RAM database. Despite the overall higher frequency variability of the LIM forecast, overall the 2-year LIM well captures the low-frequency evolution of the timeseries including some of the interannual extrema on timescale between 2-5 years. In contrast, for longer lead forecasts such as the 5-year (Figures 6C, D), the LIM is only able to capture the low-frequency variations (6 year and above) and loses information about the interannual fluctuations (e.g. compare Figures 6B vs D). A similar behavior is somewhat evident also in the LME catches stocks *Sardinops sagax* and *Reinhardtius evermanni* (Figures 6E-H) and the FAO landings stocks *Sciaenidae* and *Colorabis saira* (Figures 6I-L). We examine this behavior more systematically across the stocks – that is the LIM loses its ability to forecast interannual fluctuations for longer forecast leads, by applying a 6-year highpass filter on the composite forecasted timeseries for leads times between 0-160 month and re-examine the correlation skill with the original data. We find that the LIM interannual forecast skill is significantly less for longer lead times (Supplemental Figure S7A, B, C) as evident by taking the difference with the non-filtered forecast (Figures S7D, E, F).

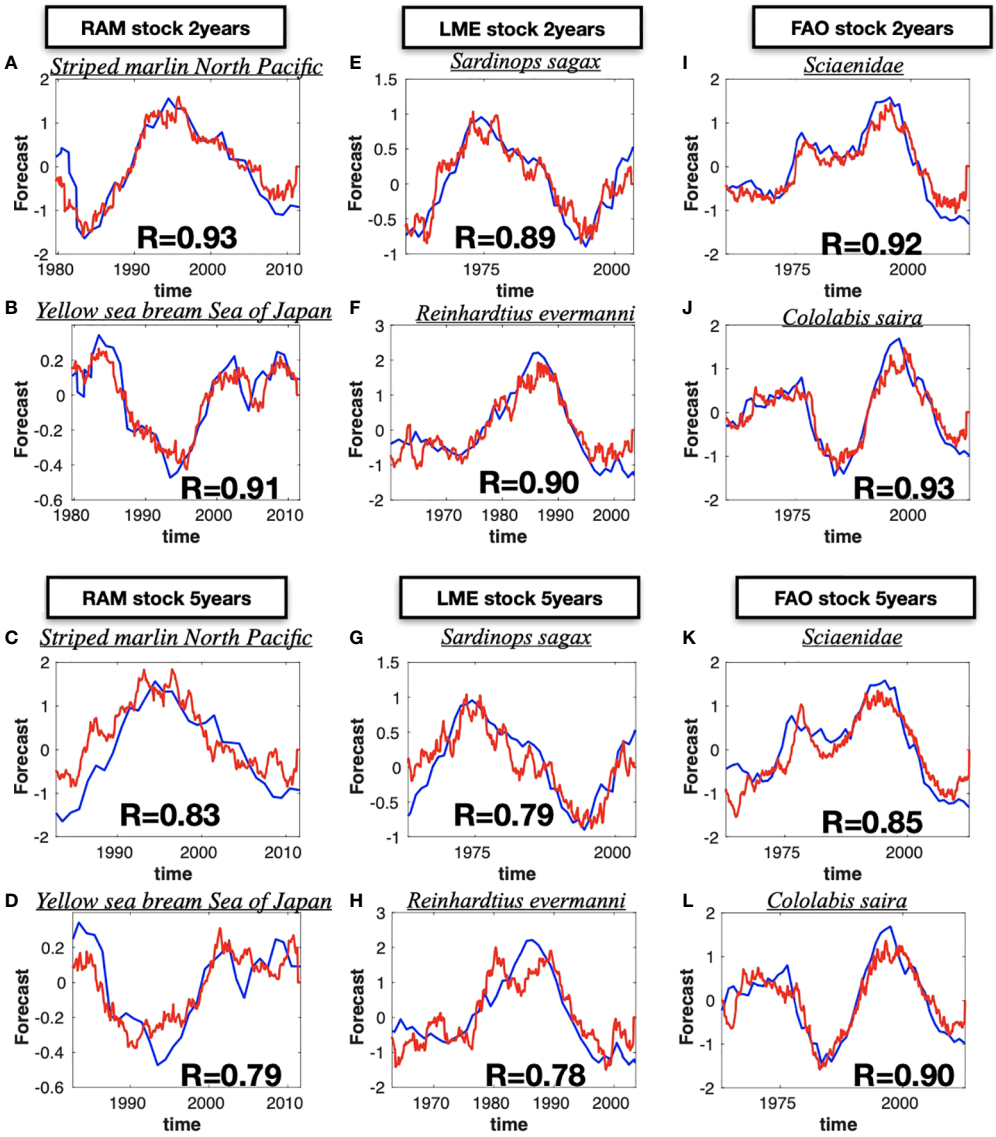

FIGURE 6
Selected single stock time series (blue lines) and the forecasted time series (red lines). The stock have been selected considering those that have the highest difference between forecasting LIM skill and the persistence. The 2-year lead forecast are shown for the RAM **(A**, **B)**, for LME **(E**, **F)** and for the FAO **(I, J)**. The same comparison are shown for the 5-year lead forecast in panels **(C**, **D)** for RAM, **(G**, **H)** for LME, and **(K**, **L)** for FAO. The name of the selected stock is displayed at the top of each panel.

3.4 LIM forecasting skills sensitivity analysis

To better understand how marine ecosystem components and physical components (and their interaction) contribute to the forecast skill, we perform a sensitivity analysis to investigate key physical and biological factors that influence the predictability of the fisheries. More precisely, the purpose of the sensitivity analysis is to quantify how the forecasting skill of individual fisheries time series depends on knowledge of the climate state and to the knowledge of the other fish stocks.

We begin by exploring the role of the physical state variables in the predictability of the fisheries time series by including the constraint that the interaction terms of the fisheries with SSTa and SSHa in the operator **L** are zero. This condition implies that we are excluding the interaction of the SSTa and SSHa PCs with the fishery PCs. The forecast skill of the LIM that does not include the coupling with the physics is shown in Figures 7A - C

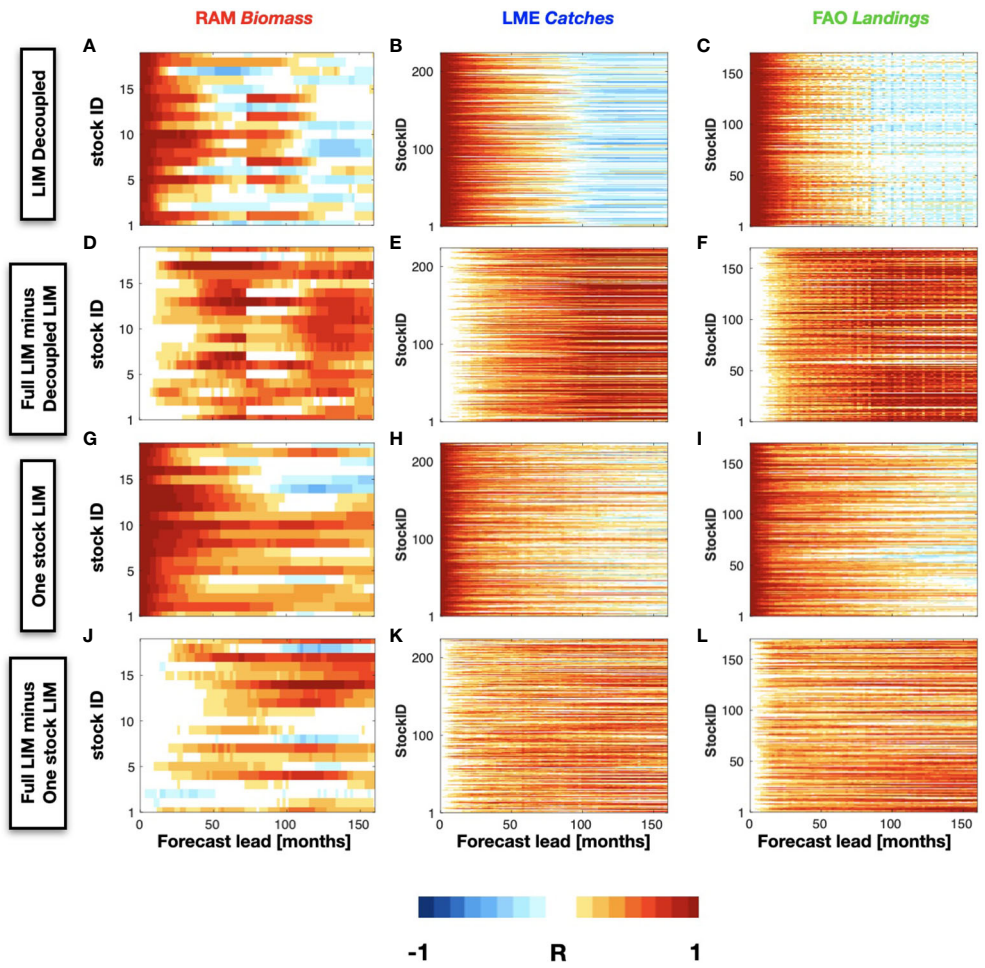

FIGURE 7
Same as Figure 5, except showing the forecast skill of the LIM where the physics and fish sticks are decoupled, **(A)** RAM, **(B)** LME, **(C)** FAO. The differences in skill between the decoupled and the full LIM case are shown in **(D)**, **(E)**, and **(F)**. The forecasting correlation skill as a function of different lead-times is displayed also for a LIM where each stock is forecasted independently are shown for the RAM **(G)**, LME **(H)**, and FAO **(I)** datasets, along with the differences from full LIM case in panels **(J)**, **(K)**, and **(L)**, respectively.

for the different fish datasets. It is immediately apparent that the skill is greatly reduced with compared to the full LIM (Figures 7D–F, show the difference map) suggesting that the information of the phsycial climate variability plays a primary role in extending the LIM forecast skill of the fishery indicators. Specifically, we find that a LIM forecast that depends only on the knowledge of the stock vs. stock interactions (e.g. without the physical information) has limited extended predictability to up to 50 months across the RAM, LME, and FAO timeseries. This reduction in skill can be attributed to several factors, which are not fully investigated in this study. One possible reason regards the role of the Rossby wave propagation in the multiannual prediction of ecological systems [Jacox et al., 2020]. These waves are predominantly initiated in the eastern side of the North Pacific Ocean through modulation of Ekman pumping connected with wind stress curl anomalies induced by the PDO mode [Capotondi and Alexander, 2001; Qiu et al., 2017]. Propagating Rossby waves (RWs) have an important impact on nutrients availability on interannual timescales, which are linked to changes in primary [Sakamoto et al., 2004] and secondary producers as well. In particular, it has been found that RWs modulate the depth of the nutricline by a few tens of meters [Killworth et al., 2004] with corresponding impact on surface nutrient availability. In addition, RW impact surface chlorophyll concentration by a vertical displacement of the chlorophyll maximum, [Dandonneau et al., 2003]. Consequently, it is possible that the exclusion of the physical interactions that are associated with skillful physical predictions from the LIM lead to a much lower forecasting skill for most of the stocks.

Next, we want to examine how the forecast skill depends on the interactions among species. To this end, the full case LIM forecast is repeated by replacing the principal components of the North

Pacific stocks with the data time series for each single stock rather than all stocks together (Figures 7G–I). For each of the three databases, the RAM biomass, the FAO landings, and the LME catches, we find again substantial reduction in forecast skill when data from other stocks are excluded from the LIM (Figures 7K–M, show the difference map). This suggest that interactions between stocks contains information that is useful for predictability.

Through these sensitivity analysis, we conclude that the climate forcing has a considerable impact on the fisheries forecast, but it does not represent the only contribution to the skill. To a lesser extent, skill is contributed from the fisheries data from other stocks in the region.

4 Conclusions

Previous studies [Brander et al., 2007; Yati et al., 2020] have documented how climate variability and change have a significant impact on marine populations and fish species in the North Pacific. However, the mechanisms linking climate fluctuations to the dynamics of marine ecosystems are not fully understood and are currently not well captured by numerical models. Long-term timeseries of data for both climate and fisheries such as population biomass (RAM), catches (LME), and landings (FAO) provide an opportunity to explore the coupled climate-fish predictability using empirical dynamical models and machine learning approaches. These approaches are very promising because the time series of fish indicators also reflect non-climate forcings that are related to the internal stock dynamics, human exploitation by commercial fishing, economic conditions, and technological advancements. These combined interactions are hard to resolve in traditional dynamical models. Each of these non-climate processes and their interactions, can have a substantial influence on metrics of fisheries biomass, landings, and catches. However, the relative importance of these factors on the variability of fish species and their predictability has not been fully explored.

In this paper, we used observationally derived lag covariance statistics to empirically capture the linear and (fast) nonlinear interactions among fish stocks, and of fish stocks with human and climate drivers (e.g. the LIM forecast model). Our results showed that the empirical dynamical forecast of the climate-fish-human multi-variate LIM has long-lead predictability that extends beyond the persistence timescale for up to 5-years with significant skill. This finding is consistent with recent studies showing how both short-lived and long-lived species display a response to climate variability and to the increased fishing pressure [Pinsky and Byler, 2015; Rouyer et al., 2014; Wang et al., 2020]. To further confirm and separate the impacts that climate and non-climate drivers are having on the fisheries, we have implemented a series of sensitivity analyses that selectively included or excluded the interaction terms between climate and fisheries time series in the LIM dynamical operator. Results of the analysis revealed a significant decrease in fish forecast skill when the interaction with the SSH and SST is excluded. While the LIM methodology does not allow us to explicitly diagnose which mechanisms of physical-biological coupling are important for extending the predictability in the KOE region, it does confirm and quantify the critical role of ocean climate dynamics, which previous studies had discussed but not explored with rigorous quantitative measures [see also review from Jacox et al., 2020]. In fact, this study is to our knowledge one of the first attempt to explore empirical model forecasting in the KOE region.

Further analyses also revealed that the forecast skill arising from empirical relationships among the stocks are also important, although less important than the inclusion of physical characteristics. This indicates that the information shared among stocks, which could be reflective of changes in industrial fishing practices, market forces, or species interactions, substantially improves forecasting skill. In particular, we notice a distinction in the RAM data between short-lived species and long-lived species as we compare the results with the first sensitivity analysis. Short living species are highly dependent on the climate factors and much less on the stock-stock interactions. While long-living species have a dependency on climate factors of the North Pacific, but the stock-stock interactions give a high contribution as well to the forecasting skill much more than short living species.

Although more studies are required to understand the joint predictability dynamics between climate and fisheries In the Pacific Ocean, the analyses presented here with a multivariate linear inverse model provide a promising approach for utilizing climate information to predict socio-ecological indicators such as fish catch, biomass, and landings. Our results also suggest that this approach may be successful in accounting for the dynamics of external human forcing (e.g., in this case fishing) that are implicitly incorporated in the stock-stock interaction terms. Lastly, these findings support the idea that predicting the marine ecosystem as a hole (e.g., including multi-variate ecological indicators) is more skillful than focusing on individual stock timeseries.

Data availability statement

The original contributions presented in the study are included in the article/supplementary material. Further inquiries can be directed to the corresponding author.

Author contributions

The authors confirm contribution to the paper as follows: study conception and design: GN, EL. Data collection: GN. Analysis and interpretation of results: GN, EL, RR, AC. Draft manuscript preparation: GN, EL, RR, AC. All authors contributed to the article and approved the submitted version.

Acknowledgments

The work is supported by the Leatherback Trust funds in the Ocean Science and Engineering program at the Georgia Institute of Technology, and was partially supported by the Department of Energy (DOE) RGMA grant DE-SC0019418 and the NSF CCE-LTER. We want thank Dr. Yingying Zhao for helping with the processing of the SST and SSH reanalysis data. No conflicts of interest are present.

Conflict of interest

The authors declare that the research was conducted in the absence of any commercial or financial relationships that could be construed as a potential conflict of interest.

Publisher's note

Supplementary material

The Supplementary Material for this article can be found online at: https://www.frontiersin.org/articles/10.3389/fmars.2022.969319/full#supplementary-material

References

Blanchard, J. L., Coll, M., Trenkel, V. M., Vergnon, Rémi, Yemane, D., Jouffre, D., et al. (2010). Trend analysis of indicators: a comparison of recent changes in the status of marine ecosystems around the world. *ICES J. Mar. Sci.* 67, Issue 4, 732–744. doi: 10.1093/icesjms/fsp282

Bograd, S. J., Kang, S., Di Lorenzo, E., Horii, T., Katugin, O. N., King, J. R., et al. (2019). Developing a social–Ecological–Environmental system framework to address climate change impacts in the north pacific. *Front. Mar. Sci.* 6. doi: 10.3389/fmars.2019.00333

Brander, K. M. (2007). Global fish production and climate change. *Proc Natl Acad Sci USA* 104 (50), 19709–14. doi: 10.1073/pnas.0702059104

Capotondi, A., and Alexander, M. A. (2001). Rossby waves in the tropical north pacific and their role in decadal thermocline variability. *J. Phys. Oceanography* 31 (12), 3496–3515. doi: 10.1175/1520-0485(2002)031<3496:RWITTN>2.0.CO;2

Capotondi, A., Jacox, M, Bowler, C, Kavanaugh, M, Lehodey, P, Barrie, D, et al. (2019). Observational needs supporting marine ecosystem modeling and forecasting: Insights from U.S. *Coast. Appl. Front. Mar. Sci* 6:623. doi: 10.3389/fmars.2019.00623

Capotondi, A., Newman, M., Xu, T., and Di Lorenzo, E. (2022). An optimal precursor of northeast pacific marine heatwaves and central pacific El niño events. *Geophysical Res. Lett.* 49, e2021GL097350. doi: 10.1029/2021GL097350

Ceballos, L. I., Di Lorenzo, E., Hoyos, C. D., Schneider, N., and Taguchi, B. (2009). North pacific gyre oscillation synchronizes climate fluctuations in the Eastern and Western boundary systems. *J. Climate* 22 (19), 5163–5174. doi: 10.1175/2009JCLI2848.1

Cornillon, P (2007). *Fronts in the World Ocean's Large Marine Ecosystems*. 21

Chavez, F. P., Ryan, J., Lluch-Cota, S., and Niquen, M. (2003). From anchovies to sardines and back: Multidecadal change in the pacific ocean. *Science.* 299, 217–221. doi: 10.1126/science.1075880

Chiba, S., Di Lorenzo, E., Davis, A., Keister, J. E., Taguchi, B., Sasai, Y., et al. (2013). Large-Scale climate control of zooplankton transport and biogeography in the kuroshio-oyashio extension region. *Geophys. Res. Lett.* 40, 5182–5187. doi: 10.1002/grl.50999

Dandonneau, Y., Vega, A., Loisel, H., du Penhoat, Y., and Menkes, C. (2003). Oceanic rossby waves acting as a "hay rake" for ecosystem floating by-products. *Science.* 302 (5650), 1548–1551. doi: 10.1126/science.1090729

Deser, C., Alexander, M., and Timlin, M. (1999). Evidence for a wind-driven intensification of the kuroshio current extension from the 1970s to the 1980s. *J. Climate - J. CLIMATE.* 12, 1697–1706. doi: 10.1175/1520-0442(1999)012<1697:EFAWDI>2.0.CO;2

Di Lorenzo, E., Schneider, N., Cobb, K. M., Franks, P. J. S., Chhak, K., Miller, A. J., et al. (2008). North pacific gyre oscillation links ocean climate and ecosystem change. *Geophys. Res. Lett.* 35, L08607. doi: 10.1029/2007GL032838

Di Lorenzo, E., and Ohman, M. (2013). A double-integration hypothesis to explain ocean ecosystem response to climate forcing. *Proc. Natl. Acad. Sci. United States America* 110, 2496–99. doi: 10.1073/pnas.1218022110

Jacox, M., Alexander, M., Siedlecki, S., Chen, Ke, Kwon, Y.-O., Brodie, S., et al. (2020). Seasonal-to-interannual prediction of U.S. coastal marine ecosystems: Forecast methods, mechanisms of predictability, and priority developments. *Prog. Oceanography.* 183, 102307. doi: 10.1016/j.pocean.2020.102307

Kelly, K. A., Small, R. J., Samelson, R. M., Qiu, B., Joyce, T. M., Kwon, Y., et al. (2010). Western Boundary currents and frontal air–Sea interaction: Gulf stream and kuroshio extension. *J. Climate* 23 (21), 5644–5667. doi: 10.1175/2010JCLI3346.1

Killworth, P. D., Cipollini, P., Uz, B. M., and Blundell, J. R. (2004). Physical and biological mechanisms for planetary waves observed in satellite-derived chlorophyll. *J. Geophys. Res.* 109, C07002. doi: 10.1029/2003JC001768

Koul, V., Sguotti, C., Årthun, M., Brune, S, Düsterhus, A, Bogstad, B, et al. (2021). Skilful prediction of cod stocks in the north and barents Sea a decade in advance. *Commun. Earth Environ.* 2, 140. doi: 10.1038/s43247-021-00207-6

Kwon, Y. O., Alexander, M, Bond, NA, Frankignoul, C, Nakamura, H, Qiu, B, et al. (2010). Role of the gulf stream and kuroshio-oyashio systems in Large-scale atmosphere-ocean interaction: A review. *J. Climate* 23 (12), 3249–3281. doi: 10.1175/2010JCLI3343.1

Lin, P., Chai, F., Xue, H., and Xiu, P. (2014). Modulation of decadal oscillation on surface chlorophyll in the kuroshio extension. *J. Geophys. Res. Oceans* 119, 187–199. doi: 10.1002/2013JC009359

Liu, Z., and Di Lorenzo, E. (2018). Mechanisms and predictability of pacific decadal variability. *Curr. Clim Change Rep.* 4, 128–144. doi: 10.1007/s40641-018-0090-5

Mantua, N. J., Hare, S. R., Zhang, Y., Wallace, J. M., and Francis, R. C. (1997). A pacific interdecadal climate oscillation with impacts on salmon production. *Bull. Am. Meteorol. Soc* 78, 1069–1079. doi: 10.1175/1520-0477(1997)078<1069:APICOW>2.0.CO;2

Matsumura, S., and Horinouchi, T. (2016). Pacific ocean decadal forcing of long-term changes in the western pacific subtropical high. *Sci. Rep.* 6, 37765. doi: 10.1038/srep37765

Mitsudera, H., Waseda, T., Yoshikawa, Y., and Taguchi, B. (2001). Anticyclonic eddies and kuroshio meander formation. *Geophys. Res. Lett.* 28, 2025–2028. doi: 10.1029/2000GL012668

Mizuno, K., and White, W. B. (1983). Annual and interannual variability in the kuroshio current system. *J. Phys. Oceanogr.* 10, 1847–1867. doi: 10.1175/1520-0485(1983)013<1847:AAIVIT>2.0.CO;2

Möllmann, C., and Diekmann, R. (2012). Marine ecosystem regime shifts induced by climate and overfishing. *Adv. Ecol. Res. Glob. Change Multispecies Syst.* 47, 303–347. doi: 10.1016/b978-0-12-398315-2.00004-1

Myers, R., and Worm, B. (2003). Rapid worldwide depletion of predatory fish communities. *Nature* 423, 280–283. doi: 10.1038/nature01610

Nakata, K., and Hidaka, K. (2003). Decadal-scale variability in the kuroshio marine ecosystem in winter. *Fisheries Oceanography* 12, 234–244. doi: 10.1046/j.1365-2419.2003.00249.x

Newman, M. (2007). Interannual to decadal predictability of tropical and north pacific Sea surface temperatures. *J. Climate* 20 (11), 2333–2356. doi: 10.1175/JCLI4165.1

Newman, M. (2013). An empirical benchmark for decadal forecasts of global surface temperature anomalies. *J. Climate* 26 (14), 5260–5269. doi: 10.1175/JCLI-D-12-00590.1

Newman, M., Alexander, M., and Scott, J. (2011). An empirical model of tropical ocean dynamics. *Climate Dynamics*. 37, 1823–1841. doi: 10.1007/s00382-011-1034-0

Newman, M., and Sardeshmukh, P. D. (2017). Are we near the predictability limit of tropical indo-pacific sea surface temperatures? *Geophys. Res. Lett.* 44, 8520–8529. doi: 10.1002/2017GL074088

Newman, M., Sardeshmukh, P. D., Winkler, C. R., and Whitaker, J. S. (2003). A study of subseasonal predictability. *Monthly Weather Rev.* 131 (8), 1715–1732. doi: 10.1175//2558.1

Nye, J. A., Link, J. S., Hare, J. A., and Overholtz, W. J. (2009). Changing spatial distribution of fish stocks in relation to climate and population size on the northeast united states continental shelf. *Mar. Ecol. Prog. Ser.* 393, 111–129. doi: 10.3354/meps08220

Park, J. Y., Stock, C. A., Dunne, J. P., Yang, X., and Rosati, A. (2019). Seasonal to multiannual marine ecosystem prediction with a global earth system model. *Science.* 365 (6450), 284–288. doi: 10.1126/science.aav6634

Pauly, D., Christensen, V., Dalsgaard, J., Froese, R., and Torres, F.Jr (1998). Fishing down marine food webs. *Science* 279, 860–863. doi: 10.1126/science.279.5352.860

Penland, C. (1989). Random forcing and forecasting using principal oscillation pattern analysis. *Mon. Weather Rev.* 10, 2165–2185. doi: 10.1175/1520-0493(1989)117<2165:RFAFUP>2.0.CO;2

Penland, C., and Sardeshmukh, P. D. (1995). The optimal growth of tropical Sea surface temperature anomalies. *J. Climate* 8 (8), 1999–2024. doi: 10.1175/1520-0442(1995)008<1999:TOGOTS>2.0.CO;2

Pinsky, M. L., and Byler, D. (2015). Fishing, fast growth and climate variability increase the risk of collapse. *Proc. B.* 282, 20151053. doi: 10.1098/rspb.2015.1053

Pons, M., Branch, T. A., Melnychuk, M. C., Jensen, O. P., Brodziak, J., Fromentin, J. M., et al. (2017). Effects of biological, economic and management factors on tuna and billfish stock status. *Fish Fish* 18, 1–21. doi: 10.1111/faf.12163

Qiu, B. (2003). Kuroshio extension variability and forcing of the pacific decadal oscillations: Responses and potential feedback. *J. Phys. Oceanography* 33 (12), 2465–2482. doi: 10.1175/2459.1

Qiu, B., and Chen, S. (2005). Variability of the kuroshio extension jet, recirculation gyre, and mesoscale eddies on decadal time scales. *J. Phys. Oceanography* 35 (11), 2090–2103. doi: 10.1175/JPO2807.1

Qiu, B., Chen, S., and Schneider, N. (2017). Dynamical links between the decadal variability of the oyashio and kuroshio extensions. *J. Climate* 30 (23), 9591–9605. doi: 10.1175/JCLI-D-17-0397.1

Ricard, D., Minto, C., Jensen, O. P., and Baum, J. K. (2012). Examining the knowledge base and status of commercially exploited marine species with the RAM legacy stock assessment database. *Fish Fish* 13, 380–398. doi: 10.1111/j.1467-2979.2011.00435.x

Rouyer, T., Fromentin, J.-M., Hidalgo, M., and Stenseth, N. C. (2014). Combined effects of exploitation and temperature on fish stocks in the northeast Atlantic. *ICES J. Mar. Sci.* 71, 1554–1562. doi: 10.1093/icesjms/fsu042

Sakamoto, C. M., Karl, D. M., Jannasch, H. W., Bidigare, R. R., Letelier, R. M., Walz, P. M., et al. (2004). Influence of rossby waves on nutrient dynamics and the plankton community structure in the north pacific subtropical gyre. *J. Geophys. Res.* 109, C05032. doi: 10.1029/2003JC001976

Schneider, N., and Miller, A. J. (2001). Predicting Western north pacific ocean climate. *J. Clim.* 20, 3997–4002. doi: 10.1175/1520-0442(2001)014<3997:PWNPOC>2.0.CO;2

Seager, R., Kushnir, Y., Naik, N. H., Cane, M. A., and Miller, J. (2001). Wind-driven shifts in the latitude of the kuroshio–oyashio extension and generation of SST anomalies on decadal timescales. *J. Climate* 14, 4249–4265. doi: 10.1175/1520-0442(2001)014<4249:WDSITL>2.0.CO;2

Sherman, K. (2014). Adaptive management institutions at the regional level: the case of large marine ecosystems. *Ocean Coast. Manage.* 90, 38–49. doi: 10.1016/j.ocecoaman.2013.06.008

Shin, Y.-J., Shannon, L. J., Bundy, A., Coll, M., Aydin, K., Bez, N., et al. (2010). Using indicators for evaluating, comparing, and communicating the ecological status of exploited marine ecosystems. 2. setting the scene. *ICES J. Mar. Sci.* 67, 692–716. doi: 10.1093/icesjms/fsp294

Taguchi, B., and Schneider, N. (2014). Origin of decadal-scale, Eastward-propagating heat content anomalies in the north pacific. *J. Climate* 27 (20), 7568–7586. doi: 10.1175/JCLI-D-13-00102.1

Taguchi, B., Xie, S.-P., Schneider, N., Nonaka, M., Sasaki, H., and Sasai, Y. (2007). Decadal variability of the kuroshio extension: Observations and an eddy-resolving model hindcast. *J. Clim.* 20, 2357–2377. doi: 10.1175/JCLI4142.1

Tam, J., Fay, G., and Link, J. (2019). Better together: The uses of ecological and socio-economic indicators with end-to-End models in marine ecosystem based management. *Front. Mar. Science.* 6. doi: 10.3389/fmars.2019.00560

Thompson, L. A., and Kwon, Y. (2010). An enhancement of low-frequency variability in the kuroshio–oyashio extension in CCSM3 owing to ocean model biases. *J. Climate* 23 (23), 6221–6233. doi: 10.1175/2010JCLI3402.1

Tommasi, D., Stock, C. A., Alexander, M. A., Yang, X., Rosati, A., and Vecchi, G. A. (2017). Multi-annual climate predictions for fisheries: An assessment of skill of Sea surface temperature forecasts for Large marine ecosystems. *Front. Mar. Sci.* 4. doi: 10.3389/fmars.2017.00201

Wang, J. Y., Kuo, T. C., and Hsieh, Ch. (2020). Causal effects of population dynamics and environmental changes on spatial variability of marine fishes. *Nat. Commun.* 11, 2635. doi: 10.1038/s41467-020-16456-6

Yati, E., Minobe, S., Mantua, N., Ito, S., and Di Lorenzo, E. (2020). Marine ecosystem variations over the north pacific and their linkage to Large-scale climate variability and change. *Front. Mar. Sci.* 7. doi: 10.3389/fmars.2020.578165

Yatsu, A., Chiba, S., Yamanaka, Y., Ito, S.-i., Shimizu, Y., Kaeriyama, M., et al. (2013). Climate forcing and the Kuroshio/Oyashio ecosystem. *ICES J. Mar. Sci.* 70 (5), 922–933. doi: 10.1093/icesjms/fst084

Yunne-Jai, S., and Lynne, J.S. (2010). Using indicators for evaluating, comparing, and communicating the ecological status of exploited marine ecosystems. 1. the IndiSeas project. ICES J. Mar. Sci. 67 (4), 686–691. doi: 10.1093/icesjms/fsp273

Zhao, Y. Y., Newman, M., Capotondi, A., Di Lorenzo, E., and Sun, D. X. (2021). Removing the effects of tropical dynamics from north pacific climate variability. *J. Climate* 34 (23), 9249–9265. doi: 10.1175/jcli-d-21-0344.1

Frontiers in Marine Science

Explores ocean-based solutions for emerging global challenges

The third most-cited marine and freshwater biology journal, advancing our understanding of marine systems and addressing global challenges including overfishing, pollution, and climate change.

Discover the latest Research Topics

See more →

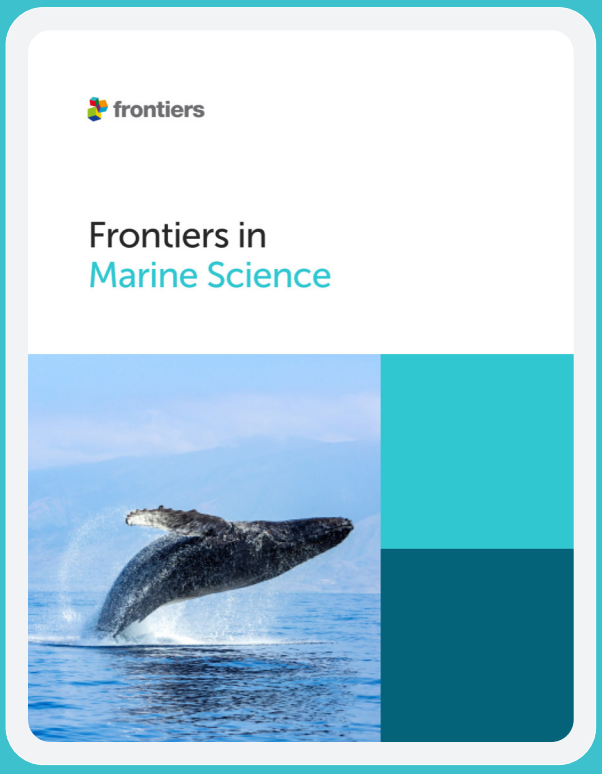

Frontiers

Avenue du Tribunal-Fédéral 34
1005 Lausanne, Switzerland
frontiersin.org

Contact us

+41 (0)21 510 17 00
frontiersin.org/about/contact